



**Universidad de Oviedo**

**Departamento de Química Física y Analítica**

*Programa de Doctorado en Análisis Químico, Bioquímico y Estructural y Modelización  
Computacional*

**NUEVAS HERRAMIENTAS  
(BIO)ANALÍTICAS BASADAS EN  
NANOMATERIALES PARA DIAGNÓSTICO  
CLÍNICO EN EL PUNTO DE ATENCIÓN**

**TESIS DOCTORAL**

Celia Toyos Rodríguez

2023

**Directores:** Dr. Alfredo de la Escosura Muñiz, Dr. Francisco Javier García Alonso

---

---





**Universidad de Oviedo**

**Departamento de Química Física y Analítica**

*Programa de Doctorado en Análisis Químico, Bioquímico y Estructural y Modelización  
Computacional*

**NOVEL (BIO)ANALYTICAL TOOLS  
BASED ON NANOMATERIALS FOR POINT-  
OF-CARE CLINICAL DIAGNOSIS**

**DOCTORAL THESIS**

Celia Toyos Rodríguez

2023

**Directores:** Dr. Alfredo de la Escosura Muñiz, Dr. Francisco Javier García Alonso

---

---



## RESUMEN DEL CONTENIDO DE TESIS DOCTORAL

1.- Título de la Tesis	
Español/Otro Idioma: Nuevas herramientas (bio)analíticas basadas en nanomateriales para diagnóstico clínico en el punto de atención	Inglés: Novel (bio)analytical tools based on nanomaterials for point-of-care clinical diagnosis
2.- Autor	
Nombre: Celia Toyos Rodríguez	DNI/Pasaporte/NIE
Programa de Doctorado: Análisis Químico, Bioquímico y Estructural y Modelización Computacional	
Órgano responsable: Centro Internacional de Postgrado	

### RESUMEN (en español)

El desarrollo de herramientas (bio)analíticas es campo de alto interés dada la sencillez, sensibilidad y bajo coste de estos dispositivos, lo que permite su uso en el punto de atención. Su aplicabilidad es especialmente relevante en el ámbito biomédico, donde obtener un diagnóstico clínico rápido y fiable es imprescindible.

Con el objetivo de mejorar las prestaciones de estas herramientas, los nanomateriales se han venido incorporando a las mismas. Estos materiales, con características superiores a sus equivalentes a gran escala, pueden ser incorporados como marca, en sustitución de las tradicionales marcas enzimáticas, como modificadores de superficies electrónicas o como plataforma sensora.

Por todo ello, la presente Tesis Doctoral se centra en el estudio de nuevas estrategias (bio)analíticas empleando nanomateriales en diversas modalidades. En particular, se investigan nanopartículas con nuevas propiedades electrocatalíticas, y se desarrollan micropartículas magnéticas con alto poder de imanación. Además, se han empleado membranas de alúmina nanoporosas para la detección de biomarcadores y como plataforma para el testeo de nuevos compuestos antimicrobianos. Adicionalmente, se han estudiado nuevas estrategias, como la impresión 3D para el estudio de interacciones microbianas, complementando así los trabajos antes citados.

En el **Capítulo 1** se hace una **Introducción** general sobre los dispositivos en el punto de atención, particularizando en los biosensores y detallando su clasificación en función del elemento de reconocimiento empleado, así como del transductor utilizado. Además, se explican las ventajas y usos que tienen los nanomateriales dentro de estos dispositivos, haciendo hincapié en los empleados en esta Tesis Doctoral. Por último, se hace una revisión bibliográfica de las patologías a las que se han aplicado las herramientas (bio)analíticas desarrolladas en esta Tesis Doctoral: la enfermedad de Alzheimer y la detección y estudio de las infecciones en heridas crónicas.

En el **Capítulo 2** se establecen los **Objetivos** de la presente Tesis Doctoral.

En el **Capítulo 3** se presenta la síntesis y caracterización de **nanopartículas bimetalicas de oro y paladio** (Pd-AuNPs) y se presenta la evaluación de la actividad electrocatalítica de estas frente a la reacción de reducción del oxígeno (ORR) en medio neutro. Además, se emplean dichas partículas en un inmunosensor para la detección de infecciones en heridas crónicas.

En el **Capítulo 4** se presenta la síntesis y caracterización de **nanopartículas magnéticas** y su encapsulación en matrices poliméricas para la formación de micropartículas magnéticas.



El comportamiento de estas micropartículas es comparado con el que presentan las alternativas comercialmente disponibles. Asimismo, estas micropartículas se emplean en un inmunosensor de tipo sándwich para la detección de un biomarcador de la enfermedad de Alzheimer.

En el **Capítulo 5** se introduce el uso de **membranas de alúmina nanoporosa** como plataforma sensora, estudiando diferentes estrategias de detección. En el primer trabajo incluido en este capítulo, se estudia el uso de estrategias de bloqueo de la señal analítica, mediante detección directa antígeno-anticuerpo, de un biomarcador de la enfermedad de Alzheimer. En el segundo trabajo se estudia la estrategia contraria, el desbloqueo de la señal analítica para la detección de un biomarcador enzimático relacionado con las infecciones en heridas crónicas. En estos trabajos se estudia cómo los factores estéricos y electrostáticos afectan al bloqueo conseguido, analizándose factores como el tamaño de los nanoporos (o nanocanales) o el efecto de las cargas en su interior. Estos estudios se completan en un último trabajo, en el que se evalúa como el espesor de las membranas de alúmina nanoporosas afecta a la sensibilidad del método, aplicándolo a la detección de un biomarcador de infecciones en heridas crónicas.

En el **Capítulo 6** se presentan estudios preliminares de **nuevas estrategias para el manejo de infecciones**. En un primer trabajo, realizado durante una estancia internacional, se ha empleado la impresión 3D para estudios preliminares de los mecanismos de toxicidad y las interacciones entre especies bacterianas, siendo de utilidad para el desarrollo de nuevos compuestos antimicrobianos. La evaluación de estos últimos ha sido sujeto de un segundo trabajo enmarcado en este capítulo consistente en el desarrollo de una plataforma (bio)analítica para el testeo de nuevos compuestos antimicrobianos.

Finalmente, en el **Capítulo 7** se discuten las **Conclusiones y Perspectivas de Futuro** extraídas de esta Tesis Doctoral.

## RESUMEN (en Inglés)

The development of (bio)analytical tools is a field of great interest within analytical chemistry, given the simplicity, sensitivity, and low cost of these devices, which allows their use at the point of care. Their applicability is especially relevant in the biomedical field, where obtaining a quick and reliable clinical diagnosis is essential.

Nanomaterials have been incorporated into them to improve the performance of these (bio)analytical tools. These materials, with superior characteristics compared to their large-scale counterparts, can be incorporated either as labels, replacing enzymes, as electrode modifiers or as sensing platforms.

Therefore, this PhD Thesis focuses on the study of novel (bio)analytical strategies, mainly based on electrochemical detection, integrating nanomaterials in. Nanoparticles with enhanced electrocatalytic properties and magnetic microparticles with high magnetisation power are developed. In addition, nanoporous alumina membranes have been used for biomarker detection based on blocking and unblocking strategies, leading to a change in the analytical signal recorded. These membranes have also been used as a platform for the rapid screening of new antimicrobial compounds. Additionally, new strategies, such as 3D printing, have been explored to study microbial interactions.

**Chapter 1** provides a general **Introduction** to point-of-care devices, focusing on biosensors and detailing their classification according to the recognition element used, as well as the transduction system employed. In addition, the advantages, and uses of nanomaterials in these devices are explained, with emphasis on those used in this PhD Thesis. Finally, a bibliographical review is made of the clinical cases studied in this PhD Thesis: Alzheimer's disease and the detection and study of chronic wound infection.



**Chapter 2** sets out the **Objectives** of this PhD Thesis.

**Chapter 3** presents the synthesis and characterisation of **gold-palladium bimetallic nanoparticles (Pd-AuNPs)** and the evaluation of their electrocatalytic activity against the oxygen reduction reaction (ORR) in neutral medium. Furthermore, these particles are used in an immunosensor for the detection of chronic wound infection.

**Chapter 4** presents the synthesis and characterisation of **magnetic nanoparticles** and their encapsulation in polymeric matrices forming magnetic microparticles. The behaviour of these microparticles is compared with that of commercially available alternatives. Furthermore, these microparticles are used in a sandwich immunosensor for the detection of an Alzheimer's disease biomarker.

**Chapter 5** introduces the use of **nanoporous alumina membranes** as sensing platform, employing different detection strategies. In the first work included in this Chapter, the use of nanochannel blocking strategies is studied and used for the detection of a biomarker of Alzheimer's disease. In a second work, the opposite strategy is studied, using a nanochannel unblocking strategy for the detection of an enzyme biomarker related to chronic wound infection. In these works, the effect that both steric and electrostatic effects have over the nanochannel blocking achieved is studied, evaluating factors such as the size of the nanochannels or the effect of the charges inside them. These studies are completed in a final work, which evaluates how the thickness of the nanoporous alumina membranes affects the sensitivity of the method, applying it to the detection of a biomarker of chronic wound infection.

**Chapter 6** presents preliminary studies of new strategies for **infection management**. In a first work, carried out during an international stay, 3D printing has been used for preliminary studies of the mechanisms of toxicity and interactions between bacterial species, being ultimately useful for the evaluation of new antimicrobial compounds. The latter has been also the subject of a second work included in this chapter, consisting of the development of a (bio)analytical platform for testing new antimicrobial compounds.

Finally, **Chapter 7** discusses the **Conclusions and Future Perspectives** drawn from this PhD Thesis.

**SR. PRESIDENTE DE LA COMISIÓN ACADÉMICA DEL PROGRAMA DE DOCTORADO  
EN ANÁLISIS QUÍMICO, BIOQUÍMICO Y ESTRUCTURAL Y MODELIZACIÓN  
COMPUTACIONAL**

# Index

---

Figure and table index .....	1
Chapter 1. Introduction .....	5
<b>1.1. General considerations</b> .....	<b>1</b>
<b>1.2. Point-of-care (bio)analytical tools in clinical diagnostics</b> .....	<b>3</b>
<b>1.3. (Bio)sensors as analytical point-of-care devices</b> .....	<b>6</b>
1.3.1. (Bio)sensors according to their biological recognition element .....	7
1.3.2. (Bio)sensors according to the transduction system used .....	12
<b>1.4. Electroanalytical point-of-care sensing systems</b> .....	<b>13</b>
<b>1.5. Nanomaterials for electrochemical sensing</b> .....	<b>15</b>
1.5.1. Nanomaterials as labels.....	16
1.5.2. Nanomaterials as electrode modifiers.....	19
<b>1.6. Magnetic particles as electrochemical sensing platforms</b> .....	<b>21</b>
<b>1.7. Nanoporous membranes as integrated (bio)analytical platforms</b> .....	<b>25</b>
<b>1.8. Electrochemical sensors in clinical applications</b> .....	<b>28</b>
1.8.1. Alzheimer’s Disease diagnosis .....	28
1.8.2. Chronic wound infection diagnosis.....	36
1.8.3. Beyond biomarker detection: innovative tools for studying bacterial infection .	42
Chapter 2. Objectives/ Objetivos .....	47
Chapter 3. Electrocatalytic nanoparticles as tags.....	51
<b>3.1. Summary</b> .....	<b>53</b>
<b>3.2. Scientific article 4</b> .....	<b>55</b>
3.2.1. Introduction.....	55
3.2.2. Protocols.....	58
3.2.3. Results and discussion .....	61
3.2.4. Conclusions.....	73
Chapter 4. Magnetic nano and microparticles as sensing platforms.....	75
<b>4.1. Summary</b> .....	<b>77</b>
<b>4.2. Scientific article 5</b> .....	<b>79</b>
4.2.1. Introduction.....	79
4.2.2. Protocols.....	82
4.2.3. Results and discussion .....	86
4.2.4. Conclusions.....	98
Chapter 5. Nanoporous membranes as integrated platforms for biomarkers detection	101
<b>5.1. Summary</b> .....	<b>103</b>
<b>5.2. Scientific article 6</b> .....	<b>105</b>
5.2.1. Introduction.....	105
5.2.2. Protocols.....	108

---

5.2.3.	Results and discussion .....	111
5.2.4.	Conclusions.....	123
<b>5.3.</b>	<b>Scientific article 7 .....</b>	<b>125</b>
5.3.1.	Introduction.....	125
5.3.2.	Protocols.....	129
5.3.3.	Results and discussion .....	131
5.3.4.	Conclusions.....	140
<b>5.4.</b>	<b>Scientific article 8 .....</b>	<b>143</b>
5.4.1.	Introduction.....	143
5.4.2.	Protocols.....	145
5.4.3.	Results and discussion .....	147
5.4.4.	Conclusions.....	153
Chapter 6.	Innovative tools for antimicrobial screening.....	155
<b>6.1.</b>	<b>Summary .....</b>	<b>157</b>
<b>6.2.</b>	<b>Scientific article 9 .....</b>	<b>159</b>
6.2.1.	Introduction.....	159
6.2.2.	Protocols.....	164
6.2.3.	Results and discussion .....	167
6.2.4.	Conclusions.....	178
<b>6.3.</b>	<b>Scientific article 10 .....</b>	<b>179</b>
6.3.1.	Introduction.....	179
6.3.2.	Protocols.....	180
6.3.3.	Results and discussion .....	182
6.3.4.	Conclusions.....	188
Chapter 7.	Conclusions and future perspectives / Conclusiones y perspectivas de futuro	189
7.1.	Conclusions.....	191
7.2.	Future Perspectives .....	195
7.3.	Conclusiones.....	197
7.4.	Perspectivas de futuro .....	201
Annexes	203	
<b>Annex A. Theoretical concepts .....</b>	<b>205</b>	
A.1.	Antibody structure.....	205
A.2.	Electrochemical techniques.....	206
A.3.	Immobilization techniques .....	208
<b>Annex B. Scientific production .....</b>	<b>211</b>	
<b>B.1. List of scientific articles included in this PhD Thesis .....</b>	<b>211</b>	
<b>B.2. List of communications in scientific conferences.....</b>	<b>213</b>	
<b>B.3. Additional publications.....</b>	<b>215</b>	

---

# Figure and table index

---

<b>Figure 1.1.</b> Scheme of the types of biological samples analyzed through POC devices together with the molecules more frequently detected (middle). On the side, examples of benchtop and handheld POC analysers.	5
<b>Figure 1.2.</b> Representation of a bioaffinity biosensor device including the different affinity molecules that could be used.	8
<b>Figure 1.3.</b> Scheme of the different possible conformations of an immunosensor: A) Direct or indirect and in this second category B) competitive and sandwich-based immunoassays.	11
<b>Figure 1.4.</b> Scheme of an electrochemical cell.	14
<b>Figure 1.5.</b> Representation of the two possible routes for the synthesis of nanomaterials: top-down and bottom-up.	16
<b>Figure 1.6.</b> Representation of the relation between the diameter of a magnetic material and the magnetization presented.	22
<b>Figure 1.7.</b> Schematic representation of the two-step anodization procedure	27
<b>Figure 1.8.</b> Schematic representation of the main AD biomarkers and the typical nanomaterials used in electrochemical biosensors for AD detection	32
<b>Figure 1.9.</b> Schematic representation of biosensors for the detection of Tau protein.	35
<b>Figure S.3.1.</b> Nanoparticle track analysis (NTA) of the obtained Pd-AuNP-3, revealing the size distribution.	59
<b>Figure 3.1.</b> Schematic representation of PdNPs and Pd-AuNPs synthesis and further conjugation with polyclonal anti-hyaluronidase (HYAL) antibodies	62
<b>Figure 3.2.</b> HRTEM micrographs of bimetallic Pd-AuNPs.	62
<b>Table 3.1.</b> Summary of the different synthesized Pd-AuNPs and characterization in terms of their Pd and Au average composition obtained through STEM-EDX analysis.	63
<b>Figure 3.3.</b> LSV for the obtained electrocatalytic nanoparticles.	64
<b>Figure 3.4.</b> Electrochemical characterization of Pd-AuNPs with different Au content.	66
<b>Figure 3.5.</b> Chronoamperograms of Pd-AuNP-3 at different concentrations.	67
<b>Figure 3.6.</b> Suitability of the optimal Pd-AuNP-3 as labels in an immunosensor.	69
<b>Figure 3.7.</b> Calibration plot signals for hyaluronidase using Pd-AuNP-3 as labels.	70
<b>Table 3.2.</b> Comparison with other reported biosensors for hyaluronidase detection.	71
<b>Table S 4.1.</b> Different ZnFeNPs synthesized with different Zn content and its saturation magnetization (Ms) and coercivity (Hc) obtained.	87
<b>Figure 4.1.</b> Characterization of ZnFeNPs.	88
<b>Figure 4.2.</b> Schematic representation of the encapsulation-based assembly method for the synthesis of MB@NAV.	89
<b>Figure 4.3.</b> Characterization of MBs.	93
<b>Figure 4.4.</b> Direct immunoassay for the evaluation of MB@NAV performance.	95
<b>Figure 4.5.</b> Use of the obtained MBs in an immunosensor for Tau protein detection.	96
<b>Table 4.1.</b> Spike and recovery assay data for Tau protein	97
<b>Figure S5.1.</b> Schematic illustration of the silanization procedure used for the immobilization of anti-Tau antibody in the inner walls of AAO nanoporous membranes.	108



<b>Figure S5.2.</b> Illustration of the protocol performed for nanoporous alumina membrane cleaning between steps.	109
<b>Figure S5.3.</b> Size distribution of the diameter of nanochannels used.	111
<b>Figure 5.1.</b> Representation of nanoporous alumina membranes used for Tau detection.	112
<b>Figure 5.2.</b> Optimization of the concentration of anti-Tau antibody immobilized inside the nanochannels	115
<b>Figure S5.3.</b> Calculation of the pI of Tau-441 human protein (UniProt code P10636-8) using ProtParam tool	117
<b>Figure 5.3.</b> Effect of the pH of the measurement buffer in the analytical system.	119
<b>Figure 5.4.</b> Tau protein detection through antibody recognition inside the nanochannels.	120
<b>Figure S5.4.</b> Long-term stability study of the anti-Tau antibody modified membranes after the addition of Tau at 100 ng/mL.	121
<b>Table 5.1.</b> Spike and recovery assay data in plasma for AD concentrations of 5 and 25 ng/mL, corresponding to the lower and medium values of the calibration curve.	122
<b>Figure 5.5.</b> Scheme of the biosensing system based on nanochannel steric/electrostatic blocking by peptidoglycan and further unblocking after enzymatic cleavage by lysozyme.	131
<b>Figure 5.6.</b> Effect of the peptidoglycan concentration on the nanochannels blockage.	133
<b>Figure 5.7.</b> Measurement buffer pH effect on the nanochannels blockage.	135
<b>Figure 5.8.</b> Effect of the nanopore size on the nanochannels blockage.	136
<b>Figure 5.9.</b> Lysozyme determination through the enzymatic cleavage of peptidoglycan, leading to nanochannels unblockage.	138
<b>Figure S5.5.</b> Calibration curve for the ELISA test developed to validate the lysozyme concentration observed using the electrochemical sensor.	140
<b>Figure 5.10.</b> Characterization of the synthesized nanoporous alumina membranes.	148
<b>Figure 5.11.</b> Electrochemical characterization of bare ITO/PET electrodes and hydrophilized ITO/PET electrodes. Cyclic voltammetry using $[\text{Fe}(\text{CN})_6]^{4-}$ in Tris-HCl 0.1 M pH 7.2.	149
<b>Figure 5.12.</b> Study of the effect of membrane thickness in the sensitivity of an HIgG immunosensors.	150
<b>Table 5.2.</b> Analytical characteristics obtained with nanoporous alumina membranes with variable thicknesses.	151
<b>Figure 5.13.</b> Effect of the pH used for measurement	152
<b>Figure 6.1.</b> Mechanism of internalization of colicins through the outer membrane of susceptible cells.	160
<b>Figure 6.2.</b> Schematic representation of the results obtained through droplet 3D printing confirming that patterning affects bacteria interaction.	161
<b>Figure 6.3.</b> Scheme of how the computational models considers toxin absorption rates.	162
<b>Figure 6.4.</b> Conclusions obtained with the computational model developed, pointing out that patterning has an effect over cell survival.	163
<b>Figure 6.5.</b> Response of <i>E. coli</i> strains under the presence of IPTG as inductor molecule and glucose as repressor.	168
<b>Figure 6.6.</b> Susceptibility tests with different colicins showing no differences between the BtuB receptor expression conditions.	169
<b>Table 6.1.</b> Diameter size (in mm) of the inhibition rings obtained with colicins at a dilution of $10^2$ for <i>E. coli</i> BZB1011 with BtuB expression at different proportions.	169
<b>Figure 6.7.</b> Disk diffusion method performed with bacteria expressing BtuB at different levels.	170
<b>Figure 6.8.</b> SDS-PAGE of the protein extracted from a culture with IPTG induction and without it.	172

---

<b>Figure 6.9.</b> Characterization of the Col-E9 fusion protein during A. FPLC separation and B. after separation	173
<b>Figure 6.10.</b> Characterization of the extracted ColE9-GFP protein through MS.....	173
<b>Figure 6.11.</b> Optimization of the ColE9-GFP concentration for the co-localization assay. ....	174
<b>Figure 6.12.</b> Co-localization assay of strains containing different BtuB expression profiles with ColE9-GFP.	175
<b>Figure 6.13.</b> 3D-printer system used. ....	176
<b>Figure 6.14.</b> Results obtained through 3D-printing with A. one strain and B. two strains.....	176
<b>Figure 6.15.</b> Encapsulation of <i>S. aureus</i> and <i>P. aeruginosa</i> in TSB, molten agar droplets. ....	177
<b>Figure 6.16.</b> Comparison of the average current recorded with two redox pairs alone and in combination with different electrolyte salts.....	183
<b>Figure 6.17.</b> Comparison of the growth (considered as the OD <sub>600</sub> ) for <i>S. aureus</i> under different conditions.	185
<b>Figure 6.18.</b> Comparison of the growth (considered as the OD <sub>600</sub> ) for <i>P. aeruginosa</i> under different conditions.	186
<b>Figure 6.19.</b> Voltamperograms corresponding to the evaluation of enterotoxin blockage for A. pH 5 and B. pH 7.2.	187



# Chapter 1. Introduction

---

<b>1.1.</b>	<b><u>General considerations</u></b> .....	<b>1</b>
<b>1.2.</b>	<b><u>Point-of-care (bio)analytical tools in clinical diagnostics</u></b> .....	<b>3</b>
<b>1.3.</b>	<b><u>(Bio)sensors as analytical point-of-care devices</u></b> .....	<b>6</b>
1.3.1.	<u>(Bio)sensors according to their biological recognition element</u> .....	7
1.3.2.	<u>(Bio)sensors according to the transduction system used</u> .....	12
<b>1.4.</b>	<b><u>Electroanalytical point-of-care sensing systems</u></b> .....	<b>13</b>
<b>1.5.</b>	<b><u>Nanomaterials for electrochemical sensing</u></b> .....	<b>15</b>
1.5.1.	<u>Nanomaterials as labels</u> .....	16
1.5.2.	<u>Nanomaterials as electrode modifiers</u> .....	19
<b>1.6.</b>	<b><u>Magnetic particles as electrochemical sensing platforms</u></b> .....	<b>21</b>
<b>1.7.</b>	<b><u>Nanoporous membranes as integrated (bio)analytical platforms</u></b> .....	<b>25</b>
<b>1.8.</b>	<b><u>Electrochemical sensors in clinical applications</u></b> .....	<b>28</b>
1.8.1.	<u>Alzheimer’s Disease diagnosis</u> .....	28
1.8.2.	<u>Chronic wound infection diagnosis</u> .....	36
1.8.3.	<u>Beyond biomarker detection: innovative tools for studying bacterial infection</u> .	42

---







## 1.1. General considerations

This Doctoral Thesis concerns the evaluation of novel (bio)analytical tools for clinical applications, with the incorporation of innovative nanomaterials. The nanomaterials developed in this Thesis have been integrated in (bio)analytical tools both as sensing platforms and as labels. More precisely, novel metallic electrocatalytic nanoparticles (NPs) and magnetic nano and micromaterials have been studied and embraced, together with screen-printed carbon electrodes (SPCEs), in immunosensors for biomarkers detection. Additionally, nanoporous alumina membranes, composed of multiple nanochannels used as sensing platforms has been also exploited in this Thesis. The sensing principle is based on the blocking and unblocking of the nanochannels, leading to a change in the analytical signal recorded.

The developed (bio)analytical platforms studied in this Thesis have been applied to the identification of biomarkers related with Alzheimer's Disease (AD) and chronic wound infections. In parallel, a work has been initiated for the evaluation of novel antimicrobial compounds using a nanoporous alumina membrane-based electrochemical platform.

In the frame of an international research stay, droplet 3D printing of bacterial structured communities has been studied as a model for the evaluation of toxicity mechanisms between bacterial strains and, ultimately, for predicting the effect of antimicrobial compounds.

This first introduction chapter is intended to give the reader a summary of the importance and principles of point-of-care (POC) (bio)analytical platforms in clinical biomedicine, paying special attention to electrochemical ones. The integration of nanomaterials and their role has been also explained, distinguishing according to their use.

Ultimately, general considerations of AD, chronic wounds and antimicrobial screening have been included to help the reader to understand the clinical relevance of these conditions and the need of POC devices.

Most of the information included in this chapter is in preparation or has been previously published by the author of this Thesis in the following articles:



## Scientific article 1:



Review

# Electrochemical Biosensors Based on Nanomaterials for Early Detection of Alzheimer's Disease

Celia Toyos-Rodríguez <sup>1,2</sup> , Francisco Javier García-Alonso <sup>2,3</sup> and Alfredo de la Escosura-Muñiz <sup>1,2,\*</sup>

<sup>1</sup> NanoBioAnalysis Group-Department of Physical and Analytical Chemistry, University of Oviedo, Julián Clavería 8, 33006 Oviedo, Spain; toyoscelia@uniovi.es

<sup>2</sup> Biotechnology Institute of Asturias, University of Oviedo, Santiago Gascon Building, 33006 Oviedo, Spain; fja@uniovi.es

<sup>3</sup> NanoBioAnalysis Group-Department of Organic and Inorganic Chemistry, University of Oviedo, Julián Clavería 8, 33006 Oviedo, Spain

\* Correspondence: alfredo.escosura@uniovi.es; Tel.: +34-985103521

## Scientific article 2:

Analytical and Bioanalytical Chemistry (2023) 415:1107–1121  
<https://doi.org/10.1007/s00216-022-04449-x>

REVIEW



### Advances in the screening of antimicrobial compounds using electrochemical biosensors: is there room for nanomaterials?

Celia Toyos-Rodríguez<sup>1,2</sup> · David Valero-Calvo<sup>1,2</sup> · Alfredo de la Escosura-Muñiz<sup>1,2</sup>

## Scientific article 3: Under preparation

Nanomaterial-based electrochemical platforms for the monitoring of chronic wounds

Celia Toyos-Rodríguez, David Valero-Calvo, Francisco Javier García-Alonso,  
Alfredo de la Escosura-Muñiz

## 1.2. Point-of-care (bio)analytical tools in clinical diagnostics

The ongoing outbreak of rapid-evolving diseases<sup>1</sup> and the increasingly overcrowding of primary care points<sup>2</sup>, has made clear that the current diagnostic and testing procedures are no longer efficient. The need of fast and accurate detection strategies, both for non-communicable and infectious diseases is rising exponentially<sup>3</sup>. This healthcare challenge, that is highly concerning in developed countries, is even worse in low income countries, where the access to large laboratory facilities is scarce<sup>4</sup>.

The detection of 50% of diseases relies on laboratory diagnostic techniques<sup>5</sup>, that are carried out in purpose-built centralized laboratories. Molecular biology techniques as polymerase chain reaction (PCR) or enzyme-linked immunosorbent assay (ELISA)<sup>6</sup>, cell culture<sup>7,8</sup> or chromatographic techniques, such as mass spectrometry are mainly used<sup>9</sup>. Although they are highly precise and robust techniques that have evolved to more automatized procedures with a rapid turnaround<sup>10</sup>, they still present disadvantages. The need of specialized equipment and highly trained staff and the high cost of these bioanalysis, make them inaccessible in many parts of the world.

Hence, there is a growing tendency in analytical chemistry towards a more decentralized, cost-effective, on-site disease diagnosis with the so-called POC devices.

POC devices are meant to be used directly at a physicians' office, hospital bed, patients' homes or at a remote location<sup>11</sup>. The term POC was first coined in 1980s by Dr. Kost, who developed a device to detect ionized calcium in whole blood using an ion-selective electrode<sup>12</sup>. The POC was directly used at the bedside of patients undergoing

---

<sup>1</sup> R.E. Baker, A.S. Mahmud, I.F. Miller, M. Rajeev, F. Rasambainarivo, B.L. Rice, S. Takahashi, A.J. Tatem, C.E. Wagner, L.-F. Wang, A. Wesolowski, C.J.E. Nat. Rev. Microbiol. 20 (2022).

<sup>2</sup> M. Sartini, A. Carbone, A. Demartini, L. Giribone, M. Oliva, A.M. Spagnolo, P. Cremonesi, F. Canale, M.L. Cristina. Healthcare. 10 (2022) 1625

<sup>3</sup> A. Bernabé-Ortiz, J.H. Zafra-Tanaka, M. Moscoso-Porrás, R. Sampath, B. Vetter, J.J. Miranda, D. Beran. Glob. Health. 17 (2021) 26.

<sup>4</sup> S. Malcolm, J. Cadet, L. Crompton, V. DeGennaro. Glob. Health Epidemiol. Genomics. 4 (2019) e7.

<sup>5</sup> P.B. Lippa, C. Müller, A. Schlichtiger, H. Schlebusch. TrAC Trends Anal. Chem. 30 (2011) 887–898

<sup>6</sup> A.P. Sokolenko, E.N. Imyanitov. Front. Mol. Biosci. 5 (2018) 76

<sup>7</sup> M. Rak, D. Barlič-Maganja, M. Kavčič, R. Trebše, A. Cör. FEMS Microbiol. Lett. 343 (2013) 42–48.

<sup>8</sup> O. Opoa, A. Croxatto, G. Prod'hom, G. Greub. Clin. Microbiol. Infect. 21 (2015) 313–322.

<sup>9</sup> A. Unlu, S. Abusoglu. Turk. J. Biochem. 47 (2022) 548–556.

<sup>10</sup> A.S. Brown, T. Badrick. Clin. Chem. Lab. Med. CCLM. 61 (2023) 37–43

<sup>11</sup> O. Clerc, G. Greub. Clin. Microbiol. Infect. 16 (2010) 1054–1061.

<sup>12</sup> G.J. Kost, M.A. Jammal, R.E. Ward, A.M. Safwat. Am. J. Clin. Pathol. 86 (1986) 61–70.

hepatic transplantation and the results obtained were immediately communicated to the anesthesiology and surgical team, thus facilitating decision-making. Since then, highly efforts have been done to make POC get closer to the patient. Even the European Commission has included the harnessing of POC devices in health care applications as part of their work program for 2023-2024 (European Commission Decision C(2023)2178 of 31 March 2023) and the World Health Organization (WHO) has pointed out POC devices as a tool for health systems to mitigate the spreading of infectious diseases<sup>13</sup>.

It is precisely this organization who has elaborated a guide for a proper selection of POC devices in resource-constrained settings, following the ASSURED rule (Affordable, Sensitive, Specific, User-friendly, Rapid and robust, Equipment-free and Deliverable to end-users)<sup>14</sup>. This term has been proposed to be updated in 2019, adding real-time connectivity and ease of specimen collection as characteristics of POC, being now called REASSURED<sup>15</sup>. However, it is complex for all POC devices to achieve all the components of (RE)ASSURED criteria, and in some applications, not all of them are even required.

POC test are typically classified depending on their size in two types: small benchtop devices and handheld analyzers (Figure 1.1.)<sup>16</sup>.

The first category embraces mainly small laboratory analyzers based on built-in fluidics for process automatization. This type of POC devices have been already implemented in the market, with examples as the Alere Affinon AS 100 Analyzer (Abbot, US), that quantitatively analyzes C-reactive protein (CRP) and glycosylated haemoglobin (HbA1c) in whole blood in less than 20 minutes. The system works by the incorporation of different cartridges into which the user must add a droplet of blood, without any pre-treatment or further manipulation, making diagnosis user-friendly<sup>17</sup>.

---

<sup>13</sup> I. Toskin et al. *Sex. Transm. Infect.* 96 (2020) 342–347.

<sup>14</sup> C.S. Kosack, A.-L. Page, P.R. Klatser. *Bull. World Health Organ.* 95 (2017) 639–645.

<sup>15</sup> K.J. Land, D.I. Boeras, X.-S. Chen, A.R. Ramsay, R.W. Peeling. *Nat. Microbiol.* 4 (2018) 46–54.

<sup>16</sup> S.J. Kassinger, M.L. van Hoek. *Synth. Syst. Biotechnol.* 5 (2020) 1–10.

<sup>17</sup> St John, C.P. Price. *Synth. Syst. Biotechnol.* 5 (2020) 1–10.

Handheld analyzers in contrast are truly portable devices normally used directly by healthcare professionals or patients themselves. The use of these devices is extended, with well-known commercial examples as the strip-based glucometer<sup>18</sup>, the urine dipsticks<sup>19</sup> or the more recently developed lateral flow tests for the early detection of coronavirus diseases 2019 (COVID-19)<sup>20</sup>. Hand-held POC test have evolved including multiplexing (measuring different analytes with a same cartridge)<sup>21</sup>, incorporating smartphone-assisted diagnostics<sup>22</sup> or coupling machine learning algorithms<sup>23,24</sup> to facilitate results acquisition and interpretation.

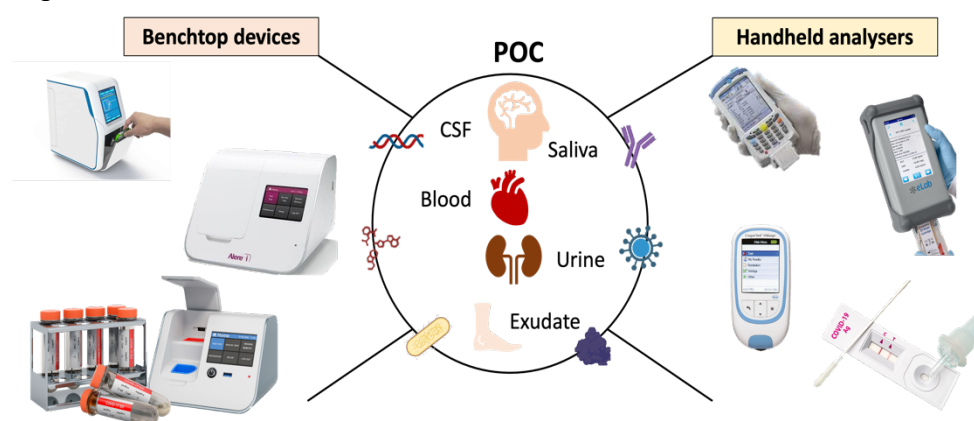


**Figure 1.1.** Scheme of the types of biological samples analyzed through POC devices together with the molecules more frequently detected (middle). On the side, examples of benchtop and handheld POC analysers.

The above mentioned POC devices are fabricated using different materials, being paper and electric strips, the predominant ones owing to their reduced cost and accuracy. Independently of the variety used, almost all have in common that they are coupled to biological recognition elements that assure their specificity, entering in what it is called a biosensor. Most of the (bio)analytical systems developed in this Thesis fall under this category, so that a more detailed description of what it is considered a (bio)sensor will be given below.

<sup>18</sup> O. Didyuk, N. Econom, A. Guardia, K. Livingston, U. Klueh. *J. Diabetes Sci. Technol.* 15 (2021) 676–683.

<sup>19</sup> Z. Zhang, J. Liu, Y. Cheng, J. Chen, H. Zhao, X. Ren. *Front. Anal. Sci.* 1 (2022) 812301.

<sup>20</sup> J. Budd et al. *Nat. Rev. Bioeng.* 1 (2023) 13–31.

<sup>21</sup> C. Dincer, R. Bruch, A. Kling, P.S. Dittrich, G.A. Urban. *Trends Biotechnol.* 35 (2017) 728–742.

<sup>22</sup> M. Zhang, X. Cui, N. Li. *Mater. Today Bio.* 14 (2022) 100254.

<sup>23</sup> A. Stranieri, S. Venkatraman, J. Minicz, A. Zarnegar, S. Firmin, V. Balasubramanian, H.F. Jelinek. *Smart Health.* 24 (2022) 100279.

<sup>24</sup> X. Jin, A. Cai, T. Xu, X. Zhang. *Interdiscip. Mater.* 2 (2023) 290–307.

### 1.3. (Bio)sensors as analytical point-of-care devices

As it has been mentioned previously, the development and commercialization of POC devices for a fast disease detection is a demanded field in continues update.

Sensors are a type of POC devices able to detect and provide information of a defined system. Most of the sensors used in our daily life are physical sensors that measure parameters as temperature, pressure, or air quality<sup>25</sup>.

On the other hand, chemical sensors are defined, according to the IUPAC, as devices able to provide a useful analytical signal from qualitative, quantitative, or semi-quantitative chemical information<sup>26</sup>. A chemical sensor is composed of (i) a receptor, that recognizes the analyte of interest, and (ii) a transduction system, that converts the chemical reaction into a measurable physical signal<sup>27</sup>.

When the receptor is mediated by a specific biochemical reaction<sup>28</sup>, we are talking about a biosensor. The first example of a biosensor was developed by Leland C. Clark in 1962 for the detection of glucose using the enzyme glucose oxidase (GO) as recognition element. This sensor was based on a previous work by Clark for the detection of O<sub>2</sub><sup>29</sup> using a Platinum electrode to measure the oxygen reduction reaction (ORR) of the O<sub>2</sub> present in blood to monitor oxygenation. Later, Clark incorporated the O<sub>2</sub> sensor into a dialysis membrane functionalized with GO to selectively detect glucose<sup>30</sup>. The device developed by Clark was a large equipment compared to the actual portable glucometer used every day by millions of diabetic patients. This major achievement in POC devices represents nowadays the 85% of the biosensors market, being in constant re-invention, adapting to novel technical improvements such as artificial intelligence (AI)<sup>24</sup> or being integrated in wearable devices<sup>31</sup>.

Biosensors could be both classified attending to the biological recognition element used or according to their transduction system, as detailed in the following sections.

---

<sup>25</sup> M. Javaid, A. Haleem, S. Rab, R. Pratap Singh, R. Suman. *Sens. Int.* 2 (2021) 100121.

<sup>26</sup> A. Hulanicki, S. Geab, F. Ingman, *Pure & App. Chern.*, (1991) 63, 9, 1247-1250.

<sup>27</sup> Abdul, S., Judit, T., Ilona, F. Nikoletta, M. In *Fundamentals of Nanoparticles*, 485–519

<sup>28</sup> B. Nagel, H. Dellweg, L.M. Gierasch. *Pure Appl. Chem.* 64 (1992) 143–168

<sup>29</sup> L.C. Clark, R. Wolf, D. Granger, Z. Taylor. *J. Appl. Physiol.* 6 (1953) 189–193.

<sup>30</sup> L.C. Clark, C. Lyons. *Ann. N. Y. Acad. Sci.* 102 (2006) 29–45.

<sup>31</sup> L. Johnston, G. Wang, K. Hu, C. Qian, G. Liu. *Front. Bioeng. Biotechnol.* 9 (2021) 733810

### **1.3.1. (Bio)sensors according to their biological recognition element**

In Clark's first biosensor, molecular recognition consisted of the selective interaction between an enzyme, GO, immobilized in the transducer surface and the target molecule glucose. However, enzymes are not the only molecular recognition molecules used in biosensing. According to the recognition used, biosensors may be classified in two groups, those that use a biocatalytic recognition element or those based on bioaffinity (or biocomplexity) reactions<sup>32</sup>. In the first ones, the biological recognition element generates a catalytic reaction with the analyte of interest, while in the second, recognition is based in the formation of a complex between the immobilized molecule and the analyte.

#### **Biocatalytic recognition elements**

Biocatalytic molecules are characterized by performing a catalytic activity over a target molecule that they could specifically recognize. After the catalytic process, the biocatalytic molecule can be re-generated, being suitable for an ulterior use. In this group of recognition elements are enclosed the enzymes and cells or tissues. Enzymes are defined as biomolecules able to catalyze a chemical reaction that is mediated by the formation of a complex between the substrate (the reactive complex) and the enzyme (enzyme-substrate complex)<sup>33</sup>. Transduction of the analytical signal, in this case, is mediated by the detection of a product or co-reactant of the biocatalytic reaction.

Enzymes have been integrated in biocatalytic biosensors, being directly immobilized in the transducer surface, or as labels in bioaffinity biosensors. Enzymes as GO, horseradish peroxidase (HRP) or alkaline phosphatase (AP) are predominantly used, as they are commercially available at a reduced cost and have a high catalytic activity.

The main advantages of enzymatic biosensors are their high selectivity, fast response, easiness, and regeneration of the recognition molecule. However, they are not highly stable under pH, ionic strength, or temperature variations. To increase stability and

---

<sup>32</sup> R. Monošík, M. Stred'anský, E. Šturdík. *Acta Chim. Slov.* 5 (2012) 109–120.

<sup>33</sup> C.I.L. Justino, A.C. Freitas, R. Pereira, A.C. Duarte, T.A.P. Rocha Santos. *TrAC Trends Anal. Chem.* 68 (2015) 2–17.

selectivity, wild-type enzymes can be genetically modified<sup>34</sup> by site-directed mutagenesis<sup>35</sup> or direct evolution<sup>36</sup>.

Nevertheless, their cost-effectiveness is reduced, what has prompted their incorporation together with nanomaterials or their substitution by alternative recognition biomolecules to increase stability. One of them is the use of whole cells or tissues, as they still contain enzymes but present a reduced cost due to the absence of purification procedures<sup>37</sup>. However, their selectivity is worse compared to pure enzymes and their kinetics are slower.

### Bioaffinity recognition elements

The other major group of biological recognition elements integrated in biosensors are those based on bioaffinity reactions (Figure 1.2.). Bioaffinity recognition is based on the reversible formation of a non-covalent bonding between two complementary (in size, shape, and chemical reactivity) chemical species forming a complex.

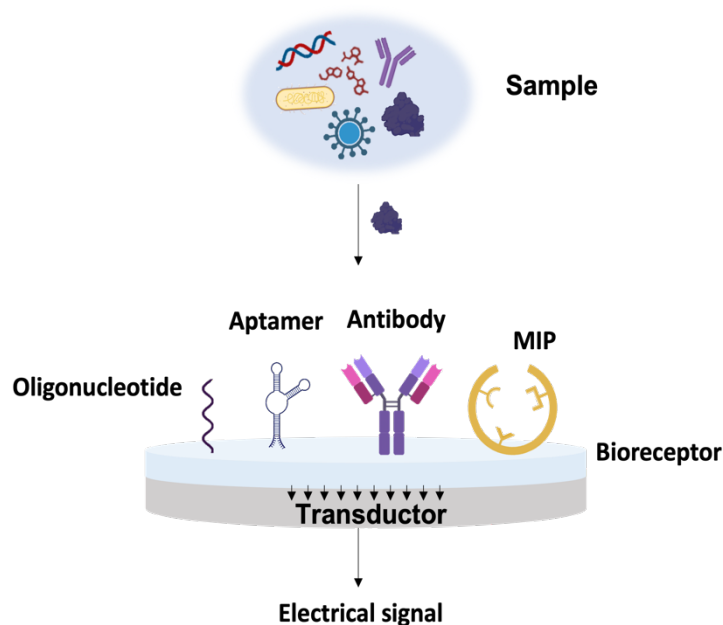


**Figure 1.2.** Representation of a bioaffinity biosensor device including the different affinity molecules that could be used.

<sup>34</sup> B. Bucur, C. Purcarea, S. Andreescu, A. Vasilescu. *Sensors*. 21 (2021) 3038.

<sup>35</sup> K. Hiraka, W. Tsugawa, R. Asano, M.A. Yokus, K. Ikebukuro, M.A. Daniele, K. Sode. *Biosens. Bioelectron.* 176 (2021) 112933.

<sup>36</sup> M.A. Crum, B.T. Sewell, M.J. Benedik. *Front. Microbiol.* 7 (2016).

<sup>37</sup> J. Liu, J.-Z. Xu, Z.-M. Rao, W.-G. Zhang. *Biosens. Bioelectron.* 216 (2022) 114681.

In this category are included genosensors<sup>38</sup> (employing nucleic acids as recognition element), aptamer-based biosensors or aptasensors (sequence of synthetic oligonucleotides as biological recognition element) molecularly imprinted polymers (MIPs)<sup>39</sup> and immunosensors (using antigen-antibody interactions)<sup>40</sup>.

❖ Genosensors

Genosensors, that employ nucleic acids as deoxyribonucleic acid (DNA) and ribonucleic acid (RNA), are characterized by having a sequence of oligonucleotides (probe) as biological recognition element<sup>41</sup>. The principle of these sensors is based on the specific hybridization between the oligonucleotides immobilized in the transducer and the complementary analyte in such a way that they could be applied for the detection of polymorphisms in the DNA and RNA associated with genetic-related diseases. Compared to traditional techniques for the detection of DNA and RNA sequences that include polymerase chain reaction (PCR)<sup>42</sup> or fluorescence in situ hybridization (FISH)<sup>43</sup>, genosensors are simpler, less time-consuming and more sensible.

❖ Aptasensors

Aptasensors have recently gained special interest as they present an enhanced efficiency compared to antibodies, being more stable, easier to bioconjugate and less toxic<sup>44,45</sup>. Aptamers are synthetic materials formed by single-stranded nucleic acids of around 20-100 base pairs long with specificity against certain proteins or molecules<sup>46</sup>. Although they are a promising alternative to immunosensors, a wider characterization in terms of affinity and selectivity is still required to outcompete antibodies. The integration of both aptamers and antibodies in dual hybrid systems has been raised to overcome the limitations of both types of recognition elements<sup>47</sup>.

❖ Molecularly imprinted polymers (MIPs)-based biosensors

---

<sup>38</sup> Y.E. Goumi. *Int. J. Biosens. Bioelectron.* 3 (2017).

<sup>39</sup> S. Ding, et al. *Biosens. Bioelectron.* 149 (2020) 111830.

<sup>40</sup> D.R. Thévenot, K. Toth, R.D. Durst, G.S. Wilson. *Int. Union Pure Appl. Chem.* (1999) 2333–2348.

<sup>41</sup> M. Pividori. *Biosens. Bioelectron.* 15 (2000) 291–303.

<sup>42</sup> S. Campuzano, P. Yáñez-Sedeño, J. Pingarrón. *Sensors.* 17 (2017) 866.

<sup>43</sup> J.G.J. Bauman, J. Weigant, P. Borst, P. van Duijn. *Exp. Cell Res.* 128 (1980) 485–490.

<sup>44</sup> A.D. Ellington, J.W. Szostak. *Nature.* 346 (1990) 818–822.

<sup>45</sup> F. Odeh, et al. *Molecules.* 25 (2019) 3.

<sup>46</sup> G. Ștefan, O. Hosu, K. De Wael, M.J. Lobo-Castañón, C. Cristea. *Electrochimica Acta.* 376 (2021) 137994

<sup>47</sup> M. Jarczewska, E. Malinowska. *Anal. Methods.* 12 (2020) 3183–3199.

---



MIPs, also known as plastic antibodies<sup>48</sup>, are polymeric materials with holes in their structure that mimic the 3D structure of a determine molecule against which they have a high selectivity. MIPs are synthesized by polymerization of functional monomers in the presence of a template molecule. After this process, the imprinted molecule is removed leaving a polymeric matrix containing cavities with identical size and shape to the template molecule used<sup>49</sup>.

#### ❖ Immunosensors

Immunosensors have been widely studied in clinical diagnostics through (bio)analytical tools due to the high affinity reached by antigen-antibody interactions. Immunosensors have numerous applications in biomedicine<sup>50</sup>, food control and environmental monitoring<sup>51</sup> and are the main type of recognition element used in this Thesis. As will be detailed in the following chapters, antibodies have been used in i) wound infection diagnosis by detecting hyaluronidase (HYAL) and catalase biomarkers, ii) for the screening of novel antimicrobial compounds by detecting enterotoxin B (*Staphylococcus aureus* virulence factor) and pyocyanin (*Pseudomonas aeruginosa* virulence factor), and iii) in AD diagnosis by detecting Tau protein biomarker.

In all these works, both polyclonal and monoclonal antibodies have been used, that differ between them in their specificity. Monoclonal antibodies are produced by identical immune cells, hence are identical antibodies with specificity against one single epitope of the antigen. In contrast, polyclonal antibodies are produced by different immune cells and can recognize variable epitopes of the antigen, being less specific and more prompt to provide cross-reactivity but more versatile for immunosensing<sup>525354</sup>. The epitope selectivity of an antibody is an important parameter in immunosensing, especially if paired antibodies are used, what occurs in certain types of biosensing formats. A deeper explanation on the structure of an antibody and how antigen recognition is reached has been included in the Annex section.

---

<sup>48</sup> K. Haupt. Nat. Mater. 9 (2010) 612–614.

<sup>49</sup> Y. Saylan, Ö. Erdem, F. Inci, A. Denizli. Biomimetics. 5 (2020) 20.

<sup>50</sup> B. Gil Rosa, O.E. Akingbade, X. Guo, L. Gonzalez-Macia, M.A. Crone, L.P. Cameron, P. Freemont, K.-L. Choy, F. Güder, E. Yeatman, D.J. Sharp, B. Li. Biosens. Bioelectron. 203 (2022) 114050.

<sup>51</sup> S. Campuzano, P. Yáñez-Sedeño, J.M. Pingarrón. Sensors. 20 (2020) 5125.

<sup>52</sup> S. Patris, M. Vandeput, J.-M. Kauffmann. TrAC Trends Anal. Chem. 79 (2016) 239–246.

<sup>53</sup> F. Ricci, G. Adornetto, G. Palleschi. Electrochimica Acta. 84 (2012) 74–83.

<sup>54</sup> S.C.B. Gopinath, T.-H. Tang, M. Citartan, Y. Chen, T. LakshmiPriya. Biosens. Bioelectron. 57 (2014) 292–302.

In immunosensors, both biomolecules (antigen or antibody) could be used as recognition element depending on the application. According to the detection strategy used, immunosensors could be based in direct or indirect detection (Figure 1.3.A.)<sup>55</sup>. Direct immunoassays are label-free strategies in which the analytical signal detected is generated through the direct antigen-antibody interaction<sup>56</sup>. Although this strategy is simpler as it does not require the use of labels, it is normally less sensible. Direct immunoassays have been used in this Thesis for the detection of Tau protein (Chapter 5.1), catalase (Chapter 5.3) and enterotoxin B and pyocyanin (Chapter 6), all using nanoporous alumina membranes as sensing platform. Indirect immunoassays, in contrast, use labels to monitor the antigen-antibody complex formation. These labels are normally enzymes and more recently nanomaterials<sup>57</sup>.

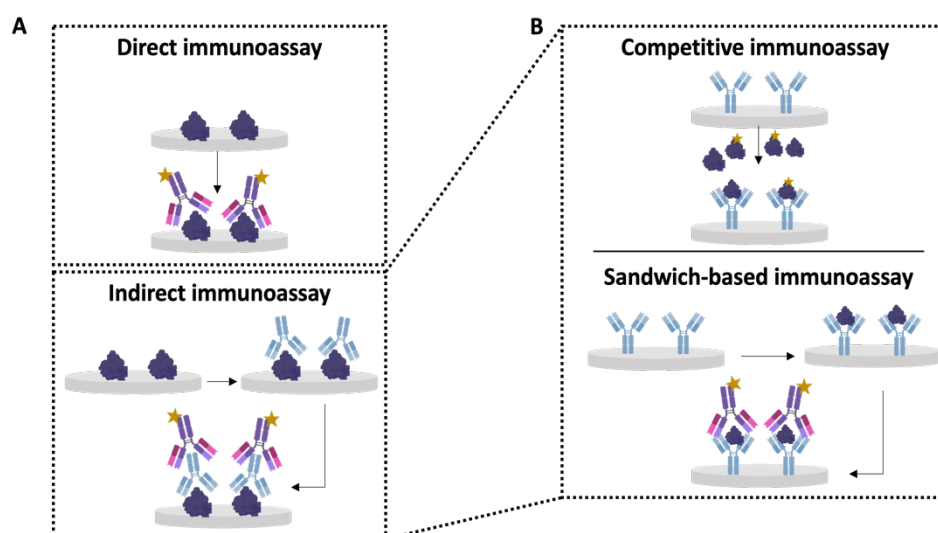


**Figure 1.3.** Scheme of the different possible conformations of an immunosensor: A) Direct or indirect and in this second category B) competitive and sandwich-based immunoassays.

Indirect immunosensors could be sub-classified in competitive and non-competitive assays (Figure 1.3.B.). Competitive assays consist of measuring the target analyte in the presence of a known labeled quantity of analyte. In this way, both analytes compete for the binding to the immobilized antibodies. The analytical signal recorded is inversely proportional to the concentration of target analyte<sup>58</sup>. These assays are mainly used with small molecules, more difficult to detect with non-competitive assays. This

<sup>55</sup> Mollarasouli, Kurbanoglu, Ozkan, *Biosensors*. 9 (2019) 86.

<sup>56</sup> E. Rapp, F.J. Gruhl, K. Länge. *Anal. Bioanal. Chem.* 398 (2010) 2403–2412.

<sup>57</sup> A. Iglesias-Mayor, O. Amor-Gutiérrez, A. Costa-García, A. de la Escosura-Muñiz. *Sensors*. 19 (2019) 5137.

<sup>58</sup> J. Mandli, A. Attar, M.M. Ennaji, A. Amine. *J. Electroanal. Chem.* 799 (2017) 213–221.

type of immunosensor has been used in a collaborative work not included in this Thesis for the detection of p53<sup>59</sup>.

Non-competitive assays, usually sandwich-based assays, are used for antigens with more than one epitope. The assay consists of the capturing of the target antigen in between two antibodies (“sandwiched”). A primary or capture antibody is immobilized in the sensing surface and first captures the target antigen, separating it from a complex sample. Then, a secondary labeled antibody is added and binds to the antigen-antibody complex. In these assays, used for the detection of larger molecules (>1000 Da), signal is directly proportional to the target analyte concentration. They have a higher sensitivity and specificity than direct immunosensors because of the use of paired antibodies. Non-specific binding is an issue in these assays, as both protein and antibodies could be adsorbed to the sensing surface. To avoid this, the addition of physical and chemical blocking agents such as bovine serum albumin (BSA), poly(ethylene glycol) (PEG) or surfactants such as Tween-20 are used<sup>60</sup>. Sandwich-based immunoassays have been used in this Thesis, together with nanomaterials, for the detection of HYAL (Chapter 3) and Tau protein (Chapter 4).

### ***1.3.2. (Bio)sensors according to the transduction system used***

As stated in previous sections, (bio)sensors could be classified according to the recognition element used and according to the transduction system in which they rely on. Transduction systems convert a physical or chemical output into a measurable electrical signal, in a process of energy conversion known as signalization.

The main types of chemical transduction use are the optical (based on light absorption or scattering, fluorescence, or surface plasmon resonance), piezoelectric, calorimetric, bioluminescent, or electrochemical. Electrochemical methods are by far the most used and are the subject of study of this Thesis, so from this point on, only these transduction systems are going to be addressed.

---

<sup>59</sup> S. García, O. Amor-Gutiérrez, M. Palomares-Albarrán, C. Toyos-Rodríguez, F. Cuetos, C. Martínez, A. Costa-García, M.T. Fernández-Sánchez, A. de la Escosura-Muñiz, A. Novelli, *Curr. Alzheimer Res.* 18 (2021) 695–700.

<sup>60</sup> J.Y. Lichtenberg, Y. Ling, S. Kim. *Sensors.* 19 (2019) 2488.

## 1.4. Electroanalytical point-of-care sensing systems

Electrochemistry is defined as the branch of chemistry implicated in the interrelation between electrical and chemical effects<sup>61</sup>, which includes the study of the production of electricity by chemical reactions and the chemical changes generated by the passage of an electrical current. Both these phenomena are used in the development of electroanalytical POC devices. These systems use as a transducer an electronic conducting, semi-conducting or ionic conducting material, that allows measuring analytical samples with a high sensitivity and ease of miniaturization. Electrochemical transduction systems are selected over other options as optical transduction, as they are fast and simple devices that could be used even in turbid samples (unlike optical systems).

In most electrochemical processes, the measured reaction occurs in the interface between the electrode and the solution. At least two electrodes are required to record changes in an electrochemical process: a working electrode (WE), that responds to the concentration of the target analyte, and a reference electrode (RE), that has a constant potential independently of the solution measured. A third electrode, the counter electrode (CE), used to facilitate current passage to the WE, is normally added. All together forms what it is known as the electrochemical cell<sup>61</sup>. Although electrochemical cells started being large-scale containers with a capacity of 20 mL, they have been little by little substituted by solid, integrated electrodes, as screen-printed electrodes (SPEs). These SPEs integrate the three electrodes required in an electrochemical cell into just one ceramic/plastic card (Figure 1.4.). The main advantage of SPEs over conventional electrochemical cells is the low sample volume required (typically around 30  $\mu$ L). This is of special relevance for the analysis of samples like blood and CSF which require invasive extraction. SPEs are constructed by thick film deposition of carbon and metallic inks on the surface of plastic or polymeric substrates. SPEs have a peculiarity over conventional electrodes, that is that the RE is actually a pseudo reference electrode, as it

---

<sup>61</sup> A.J. Bard, L.R. Faulkner, *Electrochemical methods: fundamentals and applications*, 2nd ed, Wiley, New York, 2001.

is composed just of Ag (as opposed to Ag/AgCl conventional RE) so that the stability of the potential is lower, varying depending on the electrolyte used<sup>62</sup>.

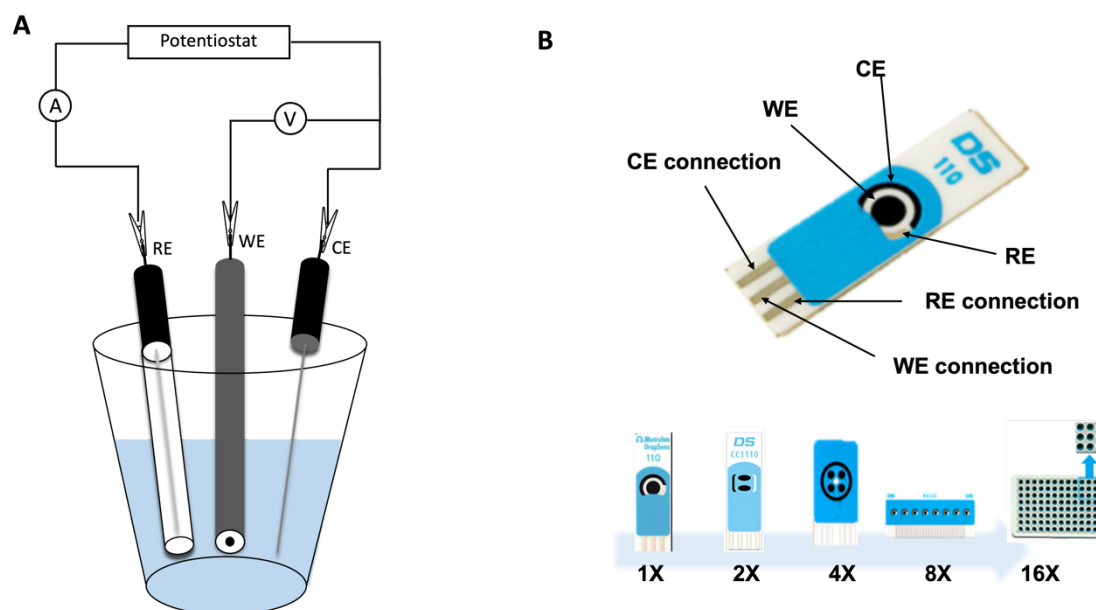


**Figure 1.4.** Scheme of an electrochemical cell. A) conventional electrochemical cell with a working (WE), reference (RE) and counter (CE) electrode and B) screen-printed electrodes containing three electrodes integrated into a strip. At the right bottom of the image, examples of screen-printed electrodes containing more than one working electrode, allowing the simultaneous detection of more than one analyte.

Another type of semi-conducting material used as WE is indium tin oxide (ITO). ITO is a transparent conductive oxide highly used in biosensing due to the high electrical transference and biocompatibility that presents. If combined with polyethylene terephthalate (PET), constitutes a flexible matrix that has increasing potential in the development of biocompatible biosensors<sup>63</sup> and even wearable devices<sup>64</sup>.

Electrochemical (bio)sensing may be classified according to the transduction signal used in amperometric/voltammetric (current intensity), potentiometric (potential), conductometric (conducting properties) or impedimetric (resistance), among others<sup>65</sup>. Using this transduction systems, there are different possible electrochemical techniques available. In this Thesis, amperometric and voltammetric techniques have been used. To

<sup>62</sup> G. Paimard, E. Ghasali, M. Baeza. *Chemosensors*. 11 (2023) 113.

<sup>63</sup> A. de la de la Escosura-Muñiz, K. Ivanova, T. Tzanov. *ACS Appl. Mater. Interfaces*. 11 (2019) 13140–13146.

<sup>64</sup> K. Sakamoto, H. Kuwae, N. Kobayashi, A. Nobori, S. Shoji, J. Mizuno. *Sci. Rep.* 8 (2018) 2825.

<sup>65</sup> F. Bettazzi, G. Marrazza, M. Minunni, I. Palchetti, S. Scarano. *Biosens. Bioanal. Tools Anal. Chem. Tribute Profr. Marco Mascini, I. Pachetti, P. Hansen, D. Barceló, Elsevier, 2017: pp. 1–440.*

better understand the principles behind these techniques, a deeper explanation has been included in the Annex section.

## 1.5. Nanomaterials for electrochemical sensing

Although electrochemical biosensors have gained importance as POC devices over the past few years, their performance still needs to be improved in terms of resolution, miniaturization, and precision<sup>66</sup>. This is especially relevant in clinical diagnosis, where biomarkers could be present in low levels, particularly in early stages of the disease, what makes their detection a challenge.

In this sense, the noise reduction and the integration of signal amplification strategies, such as nanotechnology or biotechnology-based approaches, are required<sup>67,68,69</sup>. Nanotechnology is defined as the branch of science that studies those materials that have at least one dimension in the nanoscale. According to the last definition provided in 2022 by the European Commission (EU 2022/C 229/01), a nanomaterial is considered as a “natural, incidental or manufactured material consisting of solid particles that are present, either on their own or as identifiable constituent particles in aggregates or agglomerates, and where 50% of them have at least one dimension between 1-100 nm”.

Nanomaterials present intrinsic properties not seen in their corresponding bulk materials<sup>70</sup>, as their high electron transfer, biocompatibility and electrocatalytic activity. This is due to the order of their atoms and the electronic behavior of their electronic structure. In the last decades, significant progress has been made in the synthesis of nanomaterials with tailored characteristics (size, shape or surface charge) and on their functionalization and combination between them and with polymers or biomolecules<sup>71</sup>.

The synthesis of nanomaterials can be done following two strategies: bottom-up and top-down approaches (Figure 1.5.)<sup>72</sup>. In top-down methodologies, the starting material is

---

<sup>66</sup> B.D. Malhotra, Md.A. Ali, *Nanomaterials in Biosensors*, in: *Nanomater. Biosens.*, Elsevier, 2018: pp. 1–74.

<sup>67</sup> H. Ju, X. Zhang and J. Wang, *NanoBiosensing*, Springer New York, New York, NY, 2011

<sup>68</sup> J. Wu, H. Liu, W. Chen, B. Ma, H. Ju. *Nat. Rev. Bioeng.* (2023).

<sup>69</sup> J. Lei, H. Ju. *Chem. Soc. Rev.* 41 (2012) 2122.

<sup>70</sup> P. Carneiro, S. Morais, M.C. Pereira. *Nanomaterials.* 9 (2019) 1663.

<sup>71</sup> A. Hayat, G. Catanante, J. Marty. *Sensors.* 14 (2014) 23439–23461.

<sup>72</sup> N. Abid, A.M. Khan, S. Shujait, K. Chaudhary, M. Ikram, M. Imran, J. Haider, M. Khan, Q. Khan, M. Maqbool. *Adv. Colloid Interface Sci.* 300 (2022) 102597.

in the macroscale, and it is reduced to the nanoscale using techniques as laser ablation or ball milling. This approach is easy to perform but it is difficult to obtain reproducible nanoparticles with small size and homogeneous shape. In contrast, bottom-up approaches construct nanomaterials starting from atoms and molecules that are self-assembled forming materials in the nanoscale following, among others, vapor deposition or hydrothermal methods. Bottom-up approaches allow a finer control over NPs size but requires a higher supervision over the synthetic process.

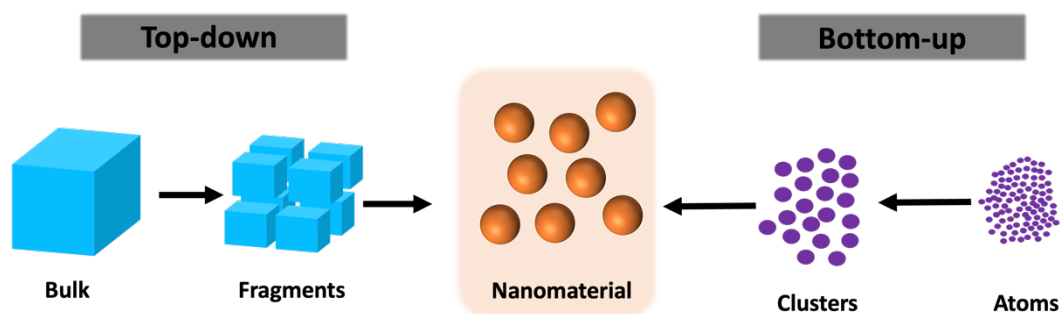


**Figure 1.5.** Representation of the two possible routes for the synthesis of nanomaterials: top-down and bottom-up.

Nanoparticles, nanotubes, or even more sophisticated three-dimensional structures as nanoflowers are just some of the multiple examples of nanomaterials seen in biosensing. Their incorporation onto electrochemical POC devices has been as electrotransductor modifiers or as labels. Below, a wider description of the state-of-the-art of the nanomaterials used in these concrete applications will be revised. Additionally, and due to the importance of the immobilization of biological recognition elements in the surface of the nanomaterials used in a (bio)analytical platform, a wider description of different chemical routes used along this Thesis has been included in Annex section.

### ***1.5.1. Nanomaterials as labels***

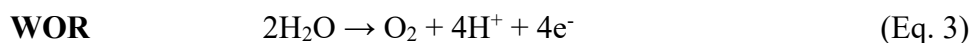
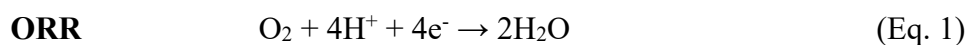
Electrochemical (bio)sensors require, in most cases, the use of a label as a reporter. Even though enzymes are the most common label used in biosensing and more particularly in immunosensing, their low thermal stability and non-conductivity have favored its substitution by nanomaterials. In comparison, nanomaterials have higher stability, signal amplification capacity and sensitive electrochemical response than

traditional enzymes or metal ion probes<sup>57,73</sup>. Metal nanoparticles, carbon-based nanomaterials or electroactive nanovesicles, are some of the prevalent examples used, due to their electroactive and electrocatalytic properties<sup>74</sup>. Their characteristics compared to those of the bulk materials have raised them as fundamental parts of electrochemical biosensors as they are ideal tools for improving sensitivity, time stability and lower limits of detection (LOD).

### Electrocatalytic nanoparticles

Catalysts are those materials that alter the rate of a chemical reaction increasing it without being consumed<sup>75</sup>. Catalyst have become increasingly valuable in the industrial sector, where they have been incorporated into fuel cells or food production among others. If the reaction in which they participate is an electrochemical reaction, they are called electrocatalysts. Electrocatalyst facilitate the electron transfer between electroactive species presence in the electrolyte interface and an electrode (heterogeneous reaction), reducing the potential that is needed to apply for the electrochemical reaction to take place.

There is a wide number of simple electrochemical reactions in which electrocatalytic materials have been incorporated<sup>76</sup>. Oxygen reduction reaction (ORR) (Eq. 1), hydrogen evolution reaction (HER) (Eq. 2) or water oxidation reaction (WOR) (Eq. 3) are just some of them. Such reactions are central to the patterns of conversion of natural and artificial energy.



<sup>73</sup> Y. Zhang, Q. Wei. *J. Electroanal. Chem.* 781 (2016) 401–409.

<sup>74</sup> G. Liu, Y. Lin. *Talanta*. 74 (2007) 308–317.

<sup>75</sup> V. Gold, ed., *The IUPAC Compendium of Chemical Terminology: The Gold Book*, 4th ed., International Union of Pure and Applied Chemistry (IUPAC), Research Triangle Park, NC, 2019.

<sup>76</sup> T. Chao, Y. Hu, X. Hong, Y. Li. *ChemElectroChem*. 6 (2019) 289–303.



In electrochemical biosensors, electrocatalytic reactions have been incorporated as an effective strategy for signal amplification<sup>77</sup>.

Nanoparticles, thanks to their high surface-to-volume ratio, are excellent electrocatalytic materials, that have been recently introduced as labels in immunosensing<sup>78,79</sup>. This approach has prevailed over the use of electroactive nanoparticles with redox properties. Electrocatalytic NPs are predominantly prepared by using transition metals as gold, palladium, or platinum. The high cost of these materials has prompted their use, both in the form of nanomaterials and in combination with other metals, in comparison to traditional bulk electrocatalysts<sup>80</sup>. Additionally, nanomaterials mimicking the activity of enzymes as peroxidase, catalase or oxidase have been also developed and implemented in (bio)analytical systems.

AuNPs have been the most extensively electrocatalytic nanomaterial studied and integrated in (bio)analytical systems, as they are easy to synthesize and bioconjugate with antibodies<sup>81</sup>. AuNPs are normally synthesized through the “Turkevich” method<sup>82</sup>, a simple synthetic procedure using chloroauric acid as precursor and sodium citrate or ascorbic acid as reducing agents. This content will be extended in Chapter 4, where AuNPs have been used as electrocatalytic labels. Owing to their high surface-to-volume ratio, in particles between 1-100 nm and high surface energy, they favour the immobilization of biological recognition elements<sup>83</sup>.

Bimetallic NPs have been also used in biosensing, taking advantage of the biofunctionalization properties of gold and the enhanced electrocatalytic ability that the use of combined metals has over certain reactions<sup>84, 85</sup>.

---

<sup>77</sup> J. Zhou, P. Qing, W. Liu, Y. Liu. *Int. J. Electrochem. Sci.* 17 (2022) 221152.

<sup>78</sup> M. Maltez-da Costa, A. de la Escosura-Muñiz, C. Nogués, L. Barrios, E. Ibáñez, A. Merkoçi. *Small*. 8 (2012) 3605–3612.

<sup>79</sup> A. Merkoçi. *Electroanalysis*. 25 (2013) 15–27.

<sup>80</sup> H. Kim, T.Y. Yoo, M.S. Bootharaju, J.H. Kim, D.Y. Chung, T. Hyeon. *Adv. Sci.* 9 (2022) 2104054.

<sup>81</sup> P. Jiang, Y. Wang, L. Zhao, C. Ji, D. Chen, L. Nie. *Nanomaterials*. 8 (2018) 977.

<sup>82</sup> J. Turkevich, P.C. Stevenson, J. Hillier. *Discuss. Faraday Soc.* 11 (1951) 55–75.

<sup>83</sup> Y. Li, H.J. Schluesener, S. Xu. *Gold Bull.* 43 (2010) 29–41.

<sup>84</sup> A. Iglesias-Mayor, O. Amor-Gutiérrez, A. Novelli, M.-T. Fernández-Sánchez, A. Costa-García, A. de la Escosura-Muñiz. *Anal. Chem.* 92 (2020) 7209–7217.

<sup>85</sup> H. Zhang. *Nat. Mater.* 11 (2012) 4.

### 1.5.2. Nanomaterials as electrode modifiers

Electrode surface is an essential element of electrochemical (bio)sensors, as electrochemical reactions occur heterogeneously in the interface between the electrode and the electrolyte interface. The rate of these reactions is governed by mass transfer to the electrode (diffusion limited) or on the rate through which electrons are transferred to the electrode surface (kinetically limited).

Increasing these rates while reducing background noise is a major requirement of electrochemical sensors to grant the obtaining of low LODs. On the last few years, nanomaterials have been highly incorporated as electrode modifiers to enable these requirements<sup>86</sup>. Integration of nanomaterials on the surface of an electrode is achieved using several methodologies: directly adding them in the electrode fabrication materials (as is the case of the bulk modification of carbon-pasted electrodes with several metallic nanomaterials), through direct absorption of the material by drop-casting, by covalent bonding or through electrodeposition<sup>87</sup>. From the nanomaterials used as electrotransducer modifiers, AuNPs, alone or in combination with other nanomaterials are the preferred choice<sup>88</sup>. In a collaboration work not included in this Thesis, AuNPs were formed by electrodeposition on the surface of SPCEs for the detection of unfolded p53 as biomarker of AD<sup>59</sup>.

Nanomaterials are also incorporated to the electrode surface to facilitate the immobilization of biomolecules. Coating the transducer surface with nanomaterials functionalized with biomolecules allows an appropriate orientation of the biological recognition elements, which is of key relevance for ensuring that the binding sites are accessible and that the redox-active sites in the biomolecule are in contact with the transducer<sup>66899091</sup>. These has a huge impact on the reproducibility, robustness of the assay and time stability, owing to its strong absorption capacity and its biocompatibility compared to bulk materials.

---

<sup>86</sup> J. Xie, L. Zhang, Z. Liu, G. Ling, P. Zhang. *Colloids Surf. B Biointerfaces*. 214 (2022) 112442.

<sup>87</sup> R. Ahmad, O.S. Wolfbeis, Y.-B. Hahn, H.N. Alshareef, L. Torsi, K.N. Salama. *Mater. Today Commun.* 17 (2018) 289–321.

<sup>88</sup> N. Dimcheva. *Curr. Opin. Electrochem.* 19 (2020) 35–41

<sup>89</sup> Holzinger, M., Le Goff, A., & Cosnier, S. *Frontiers in chemistry*, 2, (2014), 63.

<sup>90</sup> A. Walcarius, S.D. Minteer, J. Wang, Y. Lin, A. Merkoçi, *J. Mater. Chem. B*. 1 (2013) 4878.

<sup>91</sup> B.D. Mansuriya, Z. Altintas. *Sensors*. 20 (2020) 1072



## 1.6. Magnetic particles as electrochemical sensing platforms

There is a third strategy in which nanomaterials have been used in (bio)analytical devices. As sensing platforms, nanomaterials have been mainly incorporated to facilitate the anchoring of biological recognition elements.

In this Thesis, magnetic nano and microparticles have been synthesized and integrated into sensing devices. Hence, a deeper explanation on how these materials are obtained and their role in electrochemical (bio)analytical devices will be given below.

Magnetic nanoparticles are traditionally classified into pure metals, metal oxides, and metal nanocomposites. The most common nanoparticles in biosensing and biomedical applications are metal oxides of Co, Fe, Ni, Ti. Of these, iron oxides (both magnetite and maghemite) are the most widely used, due to its high biocompatibility, low-cost and ease of fabrication<sup>92</sup>. Magnetite ( $\text{Fe}_3\text{O}_4$ ) has a cubic symmetry with a spinel structure, in which oxygen atoms are arranged in a face-centered cubic packing (fcc).  $\text{Fe}^{2+}$  atoms occupy 1/4 of the octahedral holes, and  $\text{Fe}^{3+}$  atoms are divided between the remaining octahedral holes and 1/8 of the tetrahedral holes.

The behavior of magnetite in an external magnetic field is determined by the way in which the magnetic dipoles inside them interact. These dipoles are generated by the existence of unpaired electrons. Depending on how these dipoles behave, materials can be classified as: diamagnetic, paramagnetic, ferromagnetic, antiferromagnetic and ferrimagnetic<sup>93</sup>. Ferromagnetic materials are characterized by presenting magnetic domains in which the dipoles are arranged in the same direction. In each domain, the orientation of the dipoles varies with respect to the adjacent domain. However, if the size of a material decreases to a critical value, they become single-domain materials, that flip direction under the influence of temperature. This is what it is considered as a superparamagnetic material, characterized by presenting magnetization only in the presence of an external magnetic field. This property is measured by coercivity, (i.e., the magnetic intensity that needs to be applied to a material to demagnetize it). In

---

<sup>92</sup> X. Li, J. Wei, K.E. Aifantis, Y. Fan, Q. Feng, F.-Z. Cui, F. Watari. *J. Biomed. Mater. Res. A.* 104 (2016) 1285–1296.

<sup>93</sup> R.V. Ramanujan, *Biomed. Mater.*, Springer US, Boston, MA, 2009: pp. 477–491.

superparamagnetic materials, this coercivity tends to zero and it is reached when nanoparticles present a diameter size lower than 20 nm<sup>94</sup> (Figure 1.6.). This property is what makes ferromagnetic materials, and more precisely superparamagnetic materials, highly interesting in biomedical applications, being especially relevant as theragnostic<sup>95</sup>.

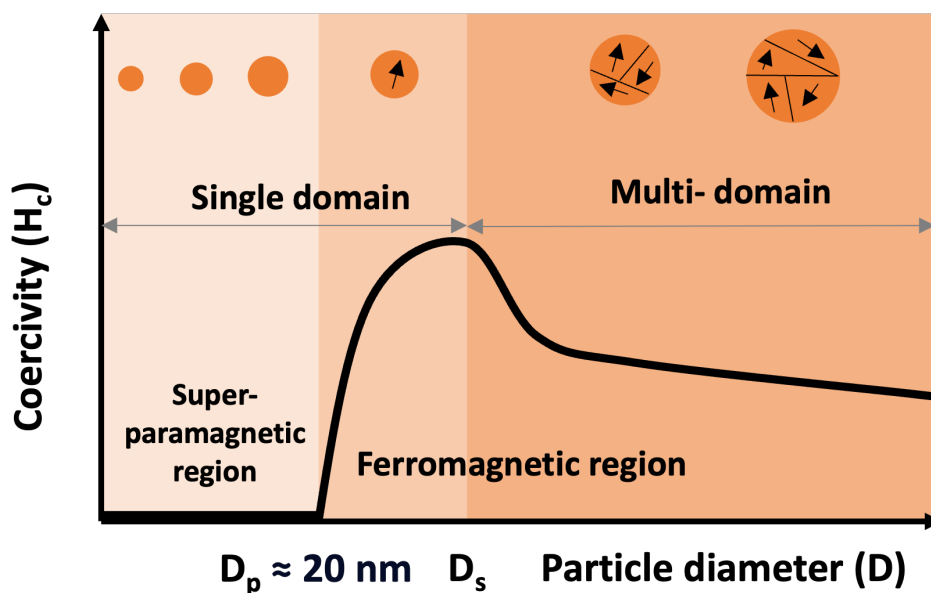


**Figure 1.6.** Representation of the relation between the diameter of a magnetic material and the magnetization presented.

Many synthetic routes have been developed to produce superparamagnetic magnetic NPs (SPIONs) of different sizes and shapes<sup>96</sup>. Depending on the synthetic methodology used, SPIONs of a determined size, shape and magnetic behavior could be obtained<sup>97</sup>. Chemical synthesis is the main choice as allows the obtaining of homogeneous and stable colloidal suspensions, easier to functionalize. Englobed in the chemical synthetic routes are the chemical co-precipitation, thermal decomposition, microemulsion and hydrothermal synthesis.

<sup>94</sup> W. Wu, C.Z. Jiang, V.A. L. Roy. *Nanoscale*. 8 (2016) 19421–1974.

<sup>95</sup> Farjadian F et al. *Front Chem*. 2022 Sep 14;10:952675

<sup>96</sup> S. Laurent, D. Forge, M. Port, A. Roch, C. Robic, L. Vander Elst, R.N. Muller. *Chem. Rev.* 108 (2008) 2064–2110.

<sup>97</sup> A.V. Samrot, C.S. Sahithya, J. Selvarani A, S.K. Purayil, P. Ponnaiah. *Curr. Res. Green Sustain. Chem.* 4 (2021) 100042.

In this Thesis, Zn doped ferrites have been synthesized following a thermal decomposition method. In a previous work not included in this Thesis, magnetite NPs were synthesized and deeply characterized following the same synthetic procedure<sup>98</sup>.

Thermal decomposition consists of the heating of a precursor compound, organometallic compounds as iron oxide or other metal oxides, to break chemical bonds. This process is done in the presence of a reducing agent, required to decrease oxidation states of the organometallic precursors<sup>99</sup>, and a surfactant compound, that acts as capping agent. A capping agents often used is oleic acid<sup>100</sup>, able to bond to the surface of nanoparticles, forming a monolayer that protect from agglomeration<sup>101</sup>. The incorporation of organic compounds that act both as reducing and capping agent, as oleylamine, has been increasingly used, reducing the complexity of the procedure<sup>102</sup>. The proportion in which organometallic precursors and reducing and capping agents are incorporated, together with time of reaction and temperature achieved are of major relevance to control homogeneity and size and shape distribution of the nanoparticles obtained.

The reduced size of magnetic NPs, although beneficial for *in vivo* applications, entails a decrease in the magnetism, which affects their usefulness, especially in biosensing applications. To counter this point, magnetic microparticles, also called magnetic beads (MBs) have been proposed as an alternative, allowing the obtention of an increased magnetism due to the greater amount of magnetic material per particle<sup>103</sup>. Colloidally assembled MBs have been proposed for maintaining superparamagnetic behavior and getting an increased magnetism. These MBs are characterized by consisting of the encapsulation of magnetic NPs of high magnetism into polymeric matrices<sup>104</sup>. These MBs can be obtained by different ways, ranging from polymer encapsulation<sup>105</sup> to emulsion-based bottom-up assembly<sup>104</sup>. A polymer encapsulation protocol has been

---

<sup>98</sup> C. Toyos-Rodríguez, J. Calleja-García, L. Torres-Sánchez, A. López, A.M. Abu-Dief, A. Costa, L. Elbaile, R.D. Crespo, J.S. Garitaonandia, E. Lastra, J.A. García, F.J. García-Alonso. *J. Nanomater.* 2019 (2019) 1–10.

<sup>99</sup> A.T. Odularu. *Bioinorg. Chem. Appl.* 2018 (2018) 1–6.

<sup>100</sup> A. Haryono, S.B. Harmami, D. Sondari. *Mater. Sci. Forum.* 737 (2013) 153–158.

<sup>101</sup> J. Park, K. An, Y. Hwang, J.-G. Park, H.-J. Noh, J.-Y. Kim, J.-H. Park, N.-M. Hwang, T. Hyeon. *Nat. Mater.* 3 (2004) 891–895.

<sup>102</sup> Z. Xu, C. Shen, Y. Hou, H. Gao, S. Sun. *Chem. Mater.* 21 (2009) 1778–1780

<sup>103</sup> Y. Zhang, J. Xu, Q. Li, D. Cao, S. Li. *AIP Adv.* 9 (2019) 015215.

<sup>104</sup> F. Bai, D. Wang, Z. Huo, W. Chen, L. Liu, X. Liang, C. Chen, X. Wang, Q. Peng, Y. Li. *Angew. Chem. Int. Ed.* 46 (2007) 6650–6653.

<sup>105</sup> N.C. Bigall, C. Wilhelm, M.-L. Beoutis, M. García-Hernandez, A.A. Khan, C. Giannini, A. Sánchez-Ferrer, R. Mezzenga, M.E. Materia, M.A. Garcia, F. Gazeau, A.M. Bittner, L. Manna, T. Pellegrino. *Chem. Mater.* 25 (2013) 1055–1062.

followed for the encapsulation of Zn doped magnetic NPs in Chapter 4. Hence, a more detailed description of polymer encapsulation will be given there.

## 1.7. Nanoporous membranes as integrated (bio)analytical platforms

Magnetic particles are not the only surface susceptible to be used as sensing platform. Nanoporous membranes have emerged in the last decade as integrated (bio)analytical platforms with powerful analytical capabilities for (bio)sensing applications<sup>106</sup>. Nanoporous membranes are structures composed of array of nanopores or nanochannels, that are defined as nanoscale holes with a diameter between 1 to 100 nm<sup>107</sup>

The advantage of these nanoporous membranes compared to other sensing platforms is that, not only serve as capturing platforms but also allow the development of a detection methodology itself (the blocking and unblocking of the nanochannel leads to the analytical signal).

Currently existing nanoporous-based sensing devices are influenced by Coulter counter principle, consisting of recording changes in the electrical current or voltage pulse produced by the passage of particles, of different sizes and shapes, through a microchannel system<sup>108</sup>. These microparticle system evolved to the nanometer scale exploiting existing natural protein ion channels, as the  $\alpha$ -haemolysin. This bacteria protein pore was inserted in artificial lipid bilayers, leading the use of these nanochannel systems in sensing applications, using the so-called stochastic sensing<sup>109</sup>. This sensing principle is similar to the Coulter counter, consisting of collocating the nanopore in between two electrolyte solutions and applying a transmembrane potential to record the changes in the ion current going through the nanopore. This system has been employed for the detection of DNA, proteins, or other molecules, achieving selectivity by the engineering of the inner walls of the nanopore or docking biological recognition elements to the cis side of the nanopore.

But it is DNA sequencing the application in which nanochannels have definitively stand out. By detecting the ion current fingerprint produced by each of the nucleotides

---

<sup>106</sup> A. de la Escosura-Muñiz, A. Merkoçi. *TrAC Trends Anal. Chem.* 79 (2016) 134–150.

<sup>107</sup> S. Faucher, et al. *J. Phys. Chem.* 2019, 123, 21309.

<sup>108</sup> W.H. Coulter. *Proc Natl Electron Conf.* 12 (1956) 1034–1040.

<sup>109</sup> H. Bayley, P.S. Cremer. *Nature.* 413 (2001) 226–230.



that composed DNA, this commercially available system (developed by the company Oxford Nanopore) is able to sequence a whole genome in just a few minutes, which has proved highly useful for SARS-CoV-2 detection<sup>110</sup> among other applications.

However, the technical complexity of these systems has prompted the development of alternative nanoporous materials as sensing platforms, as it is the case of solid-state nanoporous membranes. Solid-state nanoporous membranes are obtained through different techniques as: i) electron-beam lithography, ii) ion-bead sculpting: focused ion beam, iii) track-etching, iv) thin film formation of high ordered mesoporous membranes, and v) micromolding.

From the possible solid-state nanoporous membranes that could be obtained with the above-mentioned methodologies, nanoporous alumina membranes stand out. These membranes are composed of multiple arrays of perfectly ordered and sized-controlled nanochannels (pore density of  $1 \times 10^9 / \text{cm}^2$ ) easy to functionalize, what makes them the preferred choice for (bio)analytical applications<sup>111</sup>. Additionally, their low absorption of proteins makes them ideal substrates for filtering applications and their use in complex real samples.

Nanoporous alumina membranes are typically synthesized by a two-step electrochemical anodization of highly pure aluminum at acidic conditions (Figure 1.7.). In this first anodization step, a high voltage is applied, and aluminum oxide is irregularly generated. These defects in the structure favor the oxidation of the aluminum at the bottom of the pore while leaving the inner walls untouched (since they are protected by the electric field from inside). This forms a nanoporous structure with an aluminum protective layer at the top, that it is subsequently removed by chemical etching, leaving a hexagonally ordered of closed-packed cylindrical nanopores. Then, a second electrochemical anodization is applied, that differs from the first one in the acidic conditions used. Then, the membrane is detached from the aluminum surface and the pores are opened<sup>112</sup>.

---

<sup>110</sup> L.W. Meredith et al. *Lancet Infect. Dis.* 20 (2020) 1263–1271.

<sup>111</sup> A.K. Kasi, J.K. Kasi, N. Afzulpurkar, M.M. Hasan, B. Mahaisavariya. *Mater. Process. Meas. Phenom.* 30 (2012) 031805.

<sup>112</sup> Santos, A., Formentín, P., Ferré-Borrull, J., Pallarès, J., & Marsal, L. F. (2012). *Materials Letters*, 67(1), 296-299.

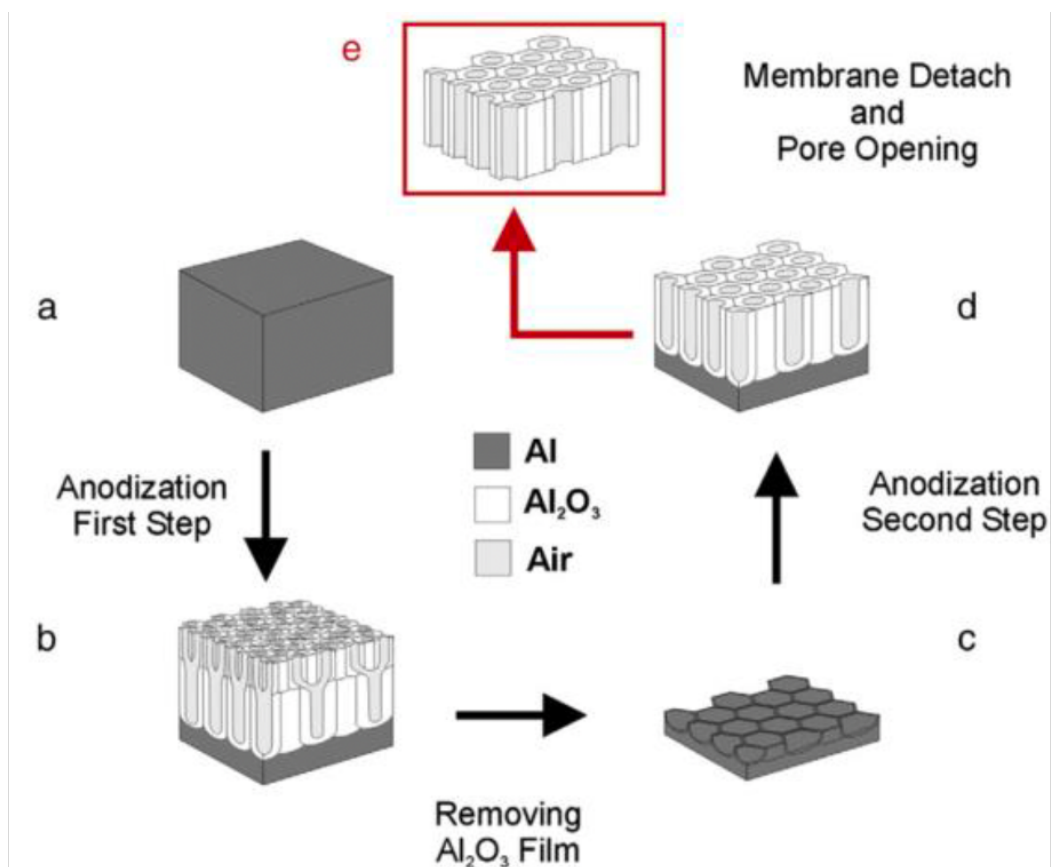


**Figure 1.7.** Schematic representation of the two-step anodization procedure. First (a) the aluminum substrate is treated by annealing and polishing to later (b) apply a first anodization step under hard conditions that leaves a nanoporous alumina structure at the bottom with a top protective layer. c) The oxide film is removed leaving a patterned Al substrate that it is further anodized (d) forming the nanoporous alumina membrane with closed pores that are opened in a last step (e). Adapted with permission from [112].

The surface of these nanoporous membranes is abundant on hydroxyl groups that facilitate the immobilization of biomolecules needed for biosensing applications. The functionalization of these membranes has been deeply explained in Chapter 5, where nanoporous membranes have been used for biosensing applications.

## 1.8. Electrochemical sensors in clinical applications

### 1.8.1. *Alzheimer's Disease diagnosis*

Alzheimer's disease (AD) is a debilitating neurodegenerative disorder and the current main cause of dementia<sup>113</sup>. This untreatable disease affected more than 50 million people in 2019 and this number is estimated to increase to 152 million by 2050 according to Alzheimer's disease international (ADI) and the World health organization (WHO)<sup>114</sup>. Even though AD affects mainly older people, it is considered a multifactorial disease that appears before 65 years in 4% of cases. Commonly, AD starts with an initial phase, known as mild cognitive impairment (MCI), characterized by unclear episodes of memory and non-memory related impairments, that evolve to symptoms of dementia, implying deterioration of cognitive functions, memory loss, inability to perform daily tasks or time and space disorientation<sup>115,116</sup>. Cognitive decline associated with AD has a significant impact not only in patients, but also in families and careers, affecting them both emotionally and economically. In 2022, the estimated economic impact of AD just in the US was of 305 billion US dollars and it is expected to grow to one trillion by 2050<sup>117</sup>.

Due to its socio-economic effect, the Group of eight (G8) inter-governmental political forum stated in 2013 that discovering a therapy before 2025 was a global priority<sup>113</sup>. Unfortunately, there is still no treatment for effectively eradicate AD, although recent research has been focused on disease-modifying drugs for early stages of the disease owing to its increased efficiency<sup>118,119</sup>, what highlights the importance of an early detection. The diagnose of AD can be performed by conducting cognitive tests and by imaging techniques, mainly magnetic resonance imaging (MRI), positron emission tomography (PET) and near infrared (NIR), used to detect abnormalities in patient brains<sup>120</sup>. The analysis of CSF and blood plasma biomarkers by immunohistochemistry

---

<sup>113</sup> P. Scheltens, K. Blennow, M.M.B. Breteler, B. de Strooper, G.B. Frisoni, S. Salloway, W.M. Van der Flier. *The Lancet*. 388 (2016) 505–517.

<sup>114</sup> Alzheimer's Disease International, *World Alzheimer Report 2019: Attitudes to dementia*, 2019.

<sup>115</sup> Alzheimer Association, *2018 Alzheimer's Disease facts and figures*, 2019.

<sup>116</sup> E. Joe, J.M. Ringman. *BMJ*. (2019) 16217.

<sup>117</sup> A. P. Skaria, *Am J Manag Care*. (2022) ;28(10):S188-S196.

<sup>118</sup> O. Hansson, et al. *Alzheimers Dement*. 14 (2018) 1470–1481.

<sup>119</sup> Ana, R. M., José, B. D., Fernando, R., & Renata, S. *Biochemical Pharmacology*, (2023). 115522.

<sup>120</sup> A. Kaushik, R.D. Jayant, S. Tiwari, A. Vashist, M. Nair. *Biosens. Bioelectron*. 80 (2016) 273–287.

and ELISA have also been used<sup>121</sup>. These techniques are time-consuming, expensive, and invasive and do not constitute a generalized method for an early detection of AD. Due to that, there is still a need to develop easy-to-use, low-cost, sensitive methods to facilitate the detection of biomarkers related with AD, as it is the case of electrochemical (bio)analytical systems.

### **Biomarkers of AD**

A biomarker is defined as a substance that is quantifiable and is representative of a pathological process or that represent the evolution of a certain condition under the effect of a pharmacological treatment. Hence, they can be classified in predictive (help to predict the outcome), diagnostic (to identify a condition) or indicative (used to monitor progression)<sup>122</sup>.

Even though molecular bases of AD are not well established, amyloid beta (A $\beta$ ) peptides plaques and Tau protein (both total and hyperphosphorylated) are the most accepted pathological hallmarks of the disease.

A $\beta$  plaques are composed by aggregated A $\beta$  peptides, generated by the proteolysis of amyloid precursor protein (APP), a transmembrane type I glycoprotein that is present in almost all tissues and whose physiological function is still unknown<sup>123</sup>. Any imbalance in the generation or clearance of amyloidogenic A $\beta$  peptides leads to A $\beta$  accumulation and constitutes a risk factor for AD development. After A $\beta$  peptide generation, A $\beta$  monomers tend to form aggregates first in the form of oligomers (A $\beta$ o), protofibrils and then fibrils (A $\beta$ f) that accumulate extracellularly in neuron cell surfaces forming senile plaques.

Another important hallmark is Tau protein and its hyperphosphorylated form<sup>124</sup>. Tau protein is the main microtubule-associated protein of neurons involved in the assembly of tubulin. Normal phosphorylation of tau protein regulates axonal growth, transport, and neuronal polarity. In several neurodegenerative diseases, Tau is hyperphosphorylated in

---

<sup>121</sup> B. Shui, D. Tao, A. Florea, J. Cheng, Q. Zhao, Y. Gu, W. Li, N. Jaffrezic-Renault, Y. Mei, Z. Guo. *Biochimie*. 147 (2018) 13–24.

<sup>122</sup> L.E. Lindley, O. Stojadinovic, I. Pastar, M. Tomic-Canic. *Plast. Reconstr. Surg.* 138 (2016) 18S-28S.

<sup>123</sup> R.J. O'Brien, P.C. Wong. *Annu. Rev. Neurosci.* 34 (2011) 185–204.

<sup>124</sup> K. Iqbal, F. Liu, C.-X. Gong, I. Grundke-Iqbal. *Curr. Alzheimer Res.* 7 (2010) 656–664.

the proline-rich region and tends to aggregate forming pair helical filaments (PHFs)<sup>125</sup>, that form intracellular neurofibrillary tangles (NFTs)<sup>126</sup>, neuropil threads<sup>127</sup> and dystrophic neurons extracellularly accumulated near A $\beta$  plaques<sup>128</sup>.

Tau protein is coded by the gene MAPT, located in the 17q21.3 chromosome containing 16 exons, even though only 11 are expressed in the central nervous system<sup>129</sup>. The alternative splicing of this gene generates six different isoforms<sup>130</sup>. Depending on the number of inserts in the N-terminal end of Tau protein, isoforms are classified in 0N, 1N, 2N. In addition, the C-terminal domain also could be modified, as the presence or absence of exon 10 conducts to the presence of three (3R) or four (4R) of these domains<sup>131</sup>. The combination of these different splicing options leads to the formation of six isoforms, being the longest one the 2N4R isoform.

According to the amyloid cascade hypothesis, Tau aggregates, in a mixture of 3R and 4R, are accumulated in the neocortex after the formation of A $\beta$  plaques<sup>132</sup>. Both total-Tau and phosphorylated Tau have been proposed as early onset biomarkers of neurodegeneration, being the second more specific of AD<sup>133</sup>. Hence, both total and phosphorylated Tau have been detected as biomarkers through electrochemical (bio)sensors, as explained in detail below.

Other type of biomarkers such as ApoE4, unfolded p53, miRNAs, oxidative stress markers or neurotransmitters have been appointed as triggers of AD. However, further research is required to establish these biomolecules as relevance biomarkers for AD detection. Regarding the samples measured, most of the biomarkers studied so far are present in CSF and blood samples but there is an increasing tendency to use salivary samples<sup>48</sup>. However, it is still needed further investigation before their application in biosensing.

---

<sup>125</sup> K. Iqbal, T. Zaidi, G.Y. Wen, I. Grundke-Iqbal, P.A. Merz, S.S. Shaikh, H.M. Wisniewski, I. Alafuzoff, B. Winblad. *The Lancet*. 2 (1986) 421–426.

<sup>126</sup> K. Iqbal, A. del C. Alonso, C.-X. Gong, S. Khatoon, J.-J. Pei, J.Z. Wang, I. Grundke-Iqbal. *Ageing Dement.*, Springer Vienna, Vienna, (1998), 169–180.

<sup>127</sup> H. Braak, E. Braak, I. Grundke-Iqbal, K. Iqbal. *Neurosci. Lett.* 65 (1986) 351–355.

<sup>128</sup> Y. Zhou, J. Shi, D. Chu, W. Hu, Z. Guan, C.-X. Gong, K. Iqbal, F. Liu. *Front. Aging Neurosci.* 10 (2018) 27.

<sup>129</sup> M.S. Wolfe. *Scientifica*. 2012 (2012) 1–20.

<sup>130</sup> M. Coedert, M.C. Spillantini, D. Rutherford, R.A. Crowther. *Neuron*, 3(4) (1989) 519–526.

<sup>131</sup> D. Panda, J.C. Samuel, M. Massie, S.C. Feinstein, L. Wilson. *Proc. Natl. Acad. Sci.* 100 (2003) 9548–9553.

<sup>132</sup> O. Hansson. *Nat. Med.* 27 (2021) 954–963.

<sup>133</sup> C. Wattmo, K. Blennow, O. Hansson. *BMC Neurol.* 20 (2020) 10.

Although the identification of AD biomarkers is a complex and extensive field, diagnosis criteria vary as further as investigations are performed. Moreover, there are at least five different subgroups of AD patients differentiated by the concentration of A $\beta$  and Tau levels in CSF, what affects the establishment of an effective diagnosis criteria and the efficacy of medical treatments<sup>134</sup>. What is clear is that as important as knowing the appropriate biomarkers is being able to identify them, for what electrochemical biosensors emerge as outstanding tools.

### **State-of-the-art in electrochemical sensors for Tau protein detection**

The presence of AD biomarkers in blood and CSF has promoted the development of electrochemical biosensors for their detection, as they allow the obtention of quantitative results in five minutes to two hours. Reaching the low cut-off values of the main AD biomarkers in human samples and improving selectivity and time-stability are the heading challenges in the field. For that purpose, nanomaterials have been introduced in biosensors either as labels or electrode modifiers.

From all biosensors for AD diagnosis (revised in a review paper related with this Thesis that could be found complete in the Annex section) peptides are, by far, the most widely detected biomarkers followed by proteins, as A $\beta$  peptide is, till now, the mainly accepted biomarker. Regarding biological recognition elements, antibodies are predominant even though the use of aptamers is remarkable as well as the combination of these two elements in sandwich type biosensors. From nanomaterials, AuNPs are, without no doubt, the most frequently used materials, both as electrode modifiers and as labels, followed by carbon-based nanomaterials (Figure 1.8.). It is worth remarking that the use of combinations of different nanomaterials, known as nanocomposites, is increasing as in most cases they present a synergistic effect.

---

<sup>134</sup> K. Iqbal, I. Grundke-Iqbal. *Alzheimers Dement.* 6 (2010) 420–424.

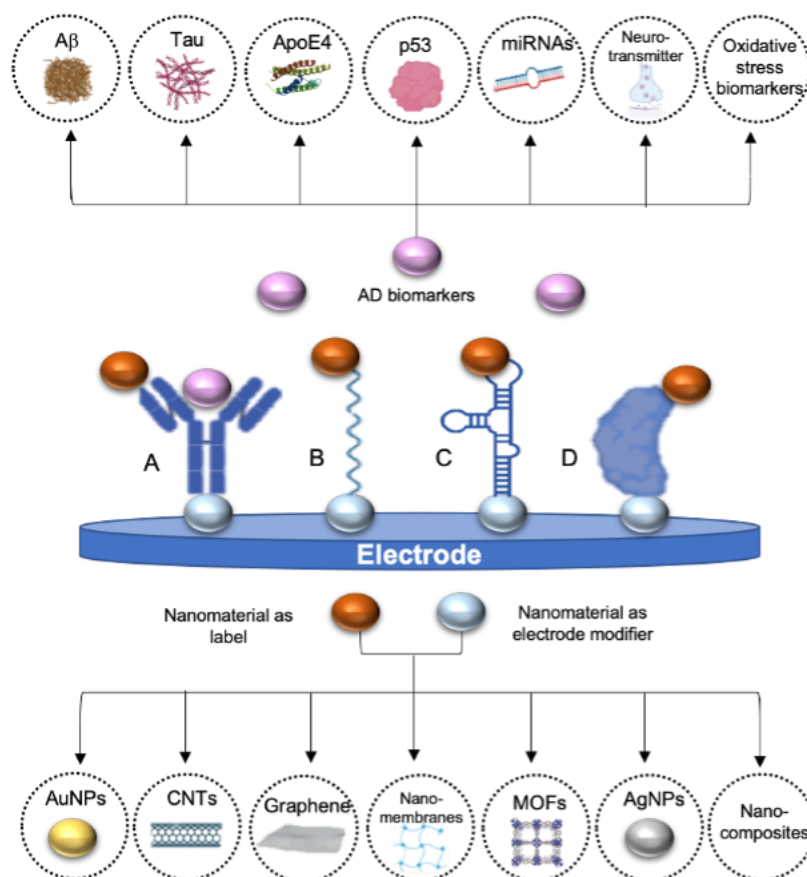


**Figure 1.8.** Schematic representation of the main AD biomarkers and the typical nanomaterials used in electrochemical biosensors for AD detection (gold nanoparticles (AuNPs), carbon nanotubes (CNTs), graphene, nanomembranes, metal-organic frameworks, silver nanoparticles (AgNPs) and nanocomposites). **A.** using antibodies as recognition element, **B.** using oligonucleotides as recognition element, **C.** using aptamers as recognition element and **D.** using affinity proteins as recognition elements. In all cases nanomaterials may be used both to modify the electrode and as label, not being necessary the use of both nanomaterials at the same time in all the detection strategies.

Regarding the detection of Tau protein through electrochemical (bio)sensors, although scarce compared to A $\beta$  determination, there is also examples in the bibliography of its use as AD biomarker in electrochemical biosensors using nanomaterials, mainly using AuNPs both as electrode modifiers and labels.

Tau protein has been using AuNPs – poly(amidoamine) (PAMAM) dendrimer nanocomposite as electrode modifier<sup>135</sup>. In this work, first SPCEs were modified with AuNPs-PAMAM and electrografted *p*-aminobenzoic acid for the ulterior anchoring of

<sup>135</sup> C.A. Razzino, V. Serafín, M. Gamella, M. Pedrero, A. Montero-Calle, R. Barderas, M. Calero, A.O. Lobo, P. Yáñez-Sedeño, S. Campuzano, J.M. Pingarrón. Biosens. Bioelectron. 163 (2020) 112238.

antibodies through glutaraldehyde crosslinking. HRP functionalized with specific antibodies was used for the electrochemical signal generation, upon de addition of hydroquinone and H<sub>2</sub>O<sub>2</sub>, recorded by amperometric detection with a LOD of 0.031 pM (Figure 1.9.A.). Biosensors performance was evaluated in human plasma samples and in brain tissue of healthy and AD diagnosed patients.

Tau-441 protein was detected by Li et al.<sup>136</sup> using multi-walled carbon nanotubes (MWCNTs) and reduced graphene oxide (rGO) as electrode modifiers and AuNPs for signal amplification (Figure 1.9.B.). The synergistic effect of MWCNTs and rGO provided a better electron transfer than with both nanomaterials alone and the binding of chitosan to MWCNTs by electrostatic forces allowed the anchoring through glutaraldehyde of the capturing antibodies. Tau-441 was conjugated to AuNPs through cysteamine for its capturing by the antibodies immobilized onto the electrode. When affinity recognition occurred, electron transfer of [Fe(CN)<sub>6</sub>]<sup>3-/4-</sup> was blocked, reducing the electron transfer process measured by DPV, providing a LOD of 0.46 fM.

Tau-381 protein was also detected in human serum, using an antibody-aptamer based biosensor<sup>137</sup>. In this case, cysteamine-stabilized AuNPs were used as probe for the amplification of the electrochemical signal recorded by DPV. Cysteamine is a stable aminothiol used in nanoparticles synthesis since, due to its -NH<sup>3+</sup> terminus, provides nanoparticles with an external positive charge, preventing aggregation and facilitating the interaction with negatively charged oligonucleotides<sup>138</sup>. The use of AuNPs as signal amplifiers allowed a LOD of 0.42 pM. Human serum of AD patients was tested verifying the feasibility of the biosensor and its potential use as clinical test.

In a more recent work, phosphorylated Tau-181 protein was detected through an immunosensor using SPCEs modified with platinum nanoparticles decorated with MWCNTs as electrode<sup>139</sup>. Modification with these nanomaterials increased significantly the current recorded while favouring antibody immobilization. The sensor was able to

---

<sup>136</sup> X. Li, M. Jiang, J. Cheng, M. Ye, W. Zhang, N. Jaffrezic-Renault, Z. Guo. *Microchim. Acta.* 187 (2020) 302.

<sup>137</sup> D. Tao, B. Shui, Y. Gu, J. Cheng, W. Zhang, N. Jaffrezic-Renault, S. Song, Z. Guo. *Biosensors.* 9 (2019) 84.

<sup>138</sup> J.L. Wai, S.Y. New. *RSC Adv.* 10 (2020) 1088–1094.

<sup>139</sup> M. Eduarda Schneider, L. Guillade, M.A. Correa-Duarte, F.T.C. Moreira. *Bioelectrochemistry.* 145 (2022) 108057.



detect Tau-181 through CV and square-wave voltammetry (SWV) with a LOD of 0.24 pg/mL.

Tau protein has been also detected as part of a pool of AD biomarkers in multianalyte biosensors. Tau protein was detected in combination with TAR DNA binding protein 43 (TDP-43)<sup>140</sup>, a protein involved in the evolution of several neurodegenerative diseases that has been found to form deposits in AD<sup>141</sup>. In this biosensor, AuNPs combined with PAMAM were used as scaffolds for the immobilization of antibodies to dual SPCEs, while HRP functionalized with antibodies was used for the amperometric detection of AD biomarkers using H<sub>2</sub>O<sub>2</sub> / hydroquinone system as reporter, providing a LOD of 50 fM for Tau-441 and 0.287 pM for TDP-43.

In another approximation, four different AD biomarkers (Tau, ApoE4, A $\beta$  and miRNA-101) were detected using a mini-pillar sensor modified with gold nanodendrites<sup>142</sup> (Figure 1.9.C.). This sensor was constructed by using polydimethylsiloxane as prepolymer and a template of polytetrafluoroethylene with holes of ~5 mm of diameter and ~1.65 mm of height. On each hole of the array, they were embedded an Au working electrode, a Pt counter electrode, and a reference electrode of Ag. After the construction of the mini-pillar polydimethylsiloxane electrode, gold nanodendrites were electrodeposited onto the working electrode for favouring the immobilization of both specific antibodies and DNA probes. This open-channel biosensor allowed the simultaneous sensing of trace amounts of different biomarkers, reaching LODs of 91.4 pM for miRNA-101, 1.29 fM for tau, 2.09 fM for ApoE4 and 1.9 fM for A $\beta$ .

---

<sup>140</sup> V. Serafin, C.A. Razzino, M. Gamella, M. Pedrero, E. Povedano, A. Montero-Calle, R. Barderas, M. Calero, A.O. Lobo, P. Yáñez-Sedeño, S. Campuzano, J.M. Pingarrón. *Anal. Bioanal. Chem.* (2020).

<sup>141</sup> X.-L. Chang, M.-S. Tan, L. Tan, J.-T. Yu. *Mol. Neurobiol.* 53 (2016) 3349–3359.

<sup>142</sup> Y. Song, T. Xu, Q. Zhu, X. Zhang. *Biosens. Bioelectron.* 162 (2020) 112253.

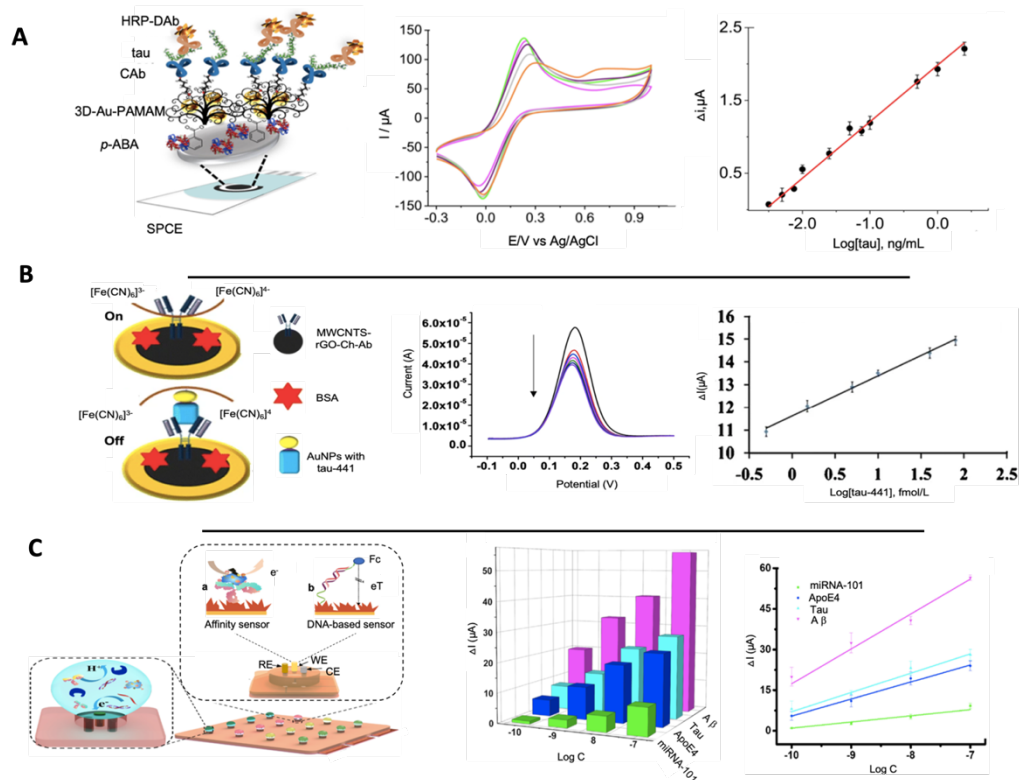


**Figure 1.9.** Schematic representation of biosensors for the detection of Tau protein. **A.** Biosensor for the detection of Tau protein using SPCEs modified with p-aminobenzoic acid (p-ABA), 3D-Au-PAMAM nanocomposites, capture antibody (CAb) and a detection antibody functionalized with HRP enzyme as signal generator (left). At the right side CV curves at different stages of the functionalization process: 3D-Au-PAMAM-p-ABA-SPCE (magenta), GA-3D-Au-PAMAM-p-ABA-SPCE (green), CAb-3D-Au-PAMAM-p-ABA-SPCE (purple), blocked CAb-3D-Au-PAMAM-p-ABA-SPCE (grey) and HRP-DAb-tau-CAb-3D-Au-PAMAM-p-ABA-SPCE (orange) and calibration curve at different tau protein concentrations. Adapted with permission from 135140. **B.** Biosensor for the detection of tau-441 using MWCNTs-rGo with chitosan as electrode modifiers for the immobilization of antibodies and AuNPs conjugated with tau-441 for signal amplification. The biosensor works with an on/off system based on the blocking of electron transference of  $[\text{Fe}(\text{CN})_6]^{3-/4-}$  in the presence of tau-441. At the right side the DPV curves of growing concentrations of tau-441 and the corresponding calibration curve. Adapted from 136. **C.** Mini-pillar sensor of polydimethylsiloxane and gold nanodendrites for the detection of multiple AD biomarkers at the same time. Each hole of the biosensor constitutes a reservoir in which biomarkers interact with the recognition element producing an increase in the surface resistance in the case of affinity biomarkers (Tau, ApoE4 and A $\beta$ ) and reducing the electrochemical signal reported by ferrocene (Fc) in the case of DNA probes for miRNA-101 detection. At the bottom, the electrochemical response of different concentration of the AD biomarkers measured and the corresponding calibration curve (green: miRNA-101, blue: ApoE4, cyan: Tau, magenta: A $\beta$ ). Adapted with permission from 142.

### ***1.8.2. Chronic wound infection diagnosis***

Throughout our lives, wounds can develop in our skin that in most cases we hardly notice. These wounds could be produced by an incision (surgical or combat-related wounds), a burn (burn wounds) or could be chronic wounds, in which they are included diabetic foot ulcers, pressure ulcers and leg ulcers<sup>143</sup>.

After a wound appears in a healthy individual, a process of cutaneous epidermal repair starts to reassemble the damaged tissue and restore integrity. When this process stalls to progress in an orderly and timely manner, it results in chronic non-healing wounds<sup>144</sup>.

Healing of chronic wounds can last from a few months to almost a year, a period in which patients suffer triggering pain and a reduction in the quality of life<sup>145</sup>.

Wound healing is a process composed of four main phases: (a) haemostasis, (b) inflammation, (c) cell proliferation and (d) epithelialization<sup>146</sup>. Haemostasis is the first stage of wound healing in charge of stopping bleeding after vascular damage. Platelet and fibrinogen are the main cells involved in this process, constricting blood vessels and forming a fibrin clot that serves as a platform for upcoming inflammatory cells<sup>147,148</sup>. Inflammatory phase starts with the recruitment of neutrophils as a first line defence against bacteria due to the release by injured cells of  $\text{Ca}^{2+}$  ions<sup>149</sup>, damage associated molecular patterns (DAMP)<sup>150</sup>, hydrogen peroxide ( $\text{H}_2\text{O}_2$ )<sup>151</sup> or chemokines among other molecules. After 48-96 h of the injury, monocytes are also recruited, followed by other immune cells such as T-cells<sup>152</sup>. After completion of the inflammatory phase, wound enters the proliferative stage where occurs the formation of new granulation tissue through activated fibroblasts that serves as a scaffold for the formation of new connective tissue<sup>153</sup>. Wound healing process ends with the re-epithelialization of the skin by the

---

<sup>143</sup> L.J. Bessa, P. Fazii, M. Di Giulio, L. Cellini. *Int. Wound J.* 12 (2015) 47–52.

<sup>144</sup> C.K. Sen, G.M. Gordillo, S. Roy, R. Kirsner, L. Lambert, T.K. Hunt, F. Gottrup, G.C. Gurtner, M.T. Longaker. *Repair Regen.* 17 (2009) 763–771.

<sup>145</sup> C. Dowsett, A. Bielby, R. Searle. *J. Wound Care.* 23 (2014) 552–562.

<sup>146</sup> M. Rodrigues, N. Kosaric, C.A. Bonham, G.C. Gurtner. *Physiol. Rev.* 99 (2019) 665–706.

<sup>147</sup> B. Furie, B.C. Furie. *N. Engl. J. Med.* 359 (2008) 938–949.

<sup>148</sup> R.A.F. Clark. *Ann. N. Y. Acad. Sci.* 936 (2006) 355–367.

<sup>149</sup> A.B.G. Lansdown. *Wound Repair Regen.* 10 (2002) 271–285

<sup>150</sup> M. Rani, S.E. Nicholson, Q. Zhang, M.G. Schwacha. *Burns.* 43 (2017) 297–303.

<sup>151</sup> A. van der Vliet, Y.M.W. Janssen-Heininger. *J. Cell. Biochem.* 115 (2014) 427–435.

<sup>152</sup> J.E. Park, A. Barbul. *Am. J. Surg.* 187 (2004) S11–S16.

<sup>153</sup> G.C. Gurtner, S. Werner, Y. Barrandon, M.T. Longaker. *Nature.* 453 (2008) 314–321.

proliferation of unipotent epidermal stem cells and the de-differentiation of epidermal cells<sup>154</sup>.

During all these four stages, there are many factors that could lead to wound healing impairment, including age of the patient, lifestyle factors as smoking or poor nutrition, or diseases such as autoimmune disorders or diabetes<sup>155</sup>.

But a severe complication that leads to non-healing wound and directly affects the prognosis is infection. When an open wound is exposed to an environment in which microorganisms are present, it could undergo three consecutive stages: i) contamination, when bacteria from the environment get inside the wound, ii) colonization, when bacteria start to replicate inside the wound to a level that interferes with the healing process, and iii) infection, when the spread of bacteria inside the wound overwhelms the host immune system response<sup>156</sup>.

Infection affects patients with chronic wounds, increasing hospitalization, what has an important socioeconomical burden<sup>157</sup>. Preventing infection is still a challenge for healthcare professionals that are not equipped with fast and sensitive diagnostic tools and have to trust in doubtful visual signs such as flushing, swelling or heat<sup>158,159</sup>.

Although normal skin is already colonized by commensal bacteria such as *Staphylococcus epidermis* or *Corinebacterium sp.* that protects from pathogenic colonization through the release of natural antimicrobial peptides<sup>160</sup>, a myriad of microbes take advantage of the compromised situation of a wound and escape skin immunity<sup>161</sup>. Chronic wounds have been largely studied to identify the main pathogenic bacteria present in the wound. In a study developed by Kirketerp-Møller *et al*<sup>162</sup>, 93.5% of the patients analyzed had *Staphylococcus aureus*, 71.7% *Enterococcus faecalis*, 52.2%

---

<sup>154</sup> G. Donati, E. Rognoni, T. Hiratsuka, K. Liakath-Ali, E. Hoste, G. Kar, M. Kayikci, R. Russell, K. Kretzschmar, K.W. Mulder, S.A. Teichmann, F.M. Watt. *Nat. Cell Biol.* 19 (2017) 603–613.

<sup>155</sup> M. Barchitta, A. Maugeri, G. Favara, R. Magnano San Lio, G. Evola, A. Agodi, G. Basile. *Int. J. Mol. Sci.* 20 (2019) 1119.

<sup>156</sup> D.T. Williams, J.R. Hilton, K.G. Harding. *Clin. Infect. Dis.* 39 (2004) S83–S86.

<sup>157</sup> K. Järbrink, G. Ni, H. Sönnegren, A. Schmidtchen, C. Pang, R. Bajpai, J. Car. *Syst. Rev.* 6 (2017) 15.

<sup>158</sup> G. Tegl, D. Schiffer, E. Sigl, A. Heinzle, G.M. Guebitz. *Appl. Microbiol. Biotechnol.* 99 (2015) 4595–4614.

<sup>159</sup> F.A.R. Mota, S.A.P. Pereira, A.R.T.S. Araújo, M.L.C. Passos, M.L.M.F.S. Saraiva. *TrAC Trends Anal. Chem.* 143 (2021) 116405.

<sup>160</sup> M. Coates, S. Blanchard, A.S. MacLeod. *PLOS Pathog.* 14 (2018) e1007353.

<sup>161</sup> M. Tomic-Canic, J.L. Burgess, K.E. O’Neill, N. Strbo, I. Pastar. *Am. J. Clin. Dermatol.* 21 (2020) 36–43.

<sup>162</sup> K. Kirketerp-Møller, P.Ø. Jensen, M. Fazli, K.G. Madsen, J. Pedersen, C. Moser, T. Tolker-Nielsen, N. Hoiby, M. Givskov, T. Bjarnsholt. *J. Clin. Microbiol.* 46 (2008) 2717–2722.

*Pseudomonas aeruginosa*, 45.7% coagulase-negative staphylococci, 41.3% *Proteus* species and 39.1% anaerobic bacteria.

*S. aureus*, a Gram-positive coccus harboring more than 50 virulence factors and immune evasion strategies, is a leading cause of bacterial infection worldwide. *S. aureus* is normally found in the respiratory tract and on the skin as a common commensal and is considered as an opportunistic pathogen. Although mortality rates due to *S. aureus* decreased after the discovery of *penicillin* the appearance of methicillin-resistant *S. aureus* (MRSA) has reconstituted it as a medical challenge<sup>163,164</sup>, listed by the Centre for Disease Control and Prevention (CDC) as a serious threat to human health in 2019<sup>165</sup>. *P. aeruginosa*, in contrast, is a Gram-negative opportunistic pathogen, normally found in the environment in soil and water samples scarce of pristine, or in the surface of medical devices as catheters or ventilators, being more associated with human activities<sup>166</sup>. *P. aeruginosa* presents a large genome that allows to produce numerous secreted molecules and virulence factors, what confers it with a great adaptability<sup>167</sup>.

Their presence, separated or together, is normally treated by the administration of pharmacological drugs, what has been hampered by the increasing acquire antibiotic resistance of these bacteria, making characterization of microorganisms present in the wound an important factor to stop the spreading of this healthcare challenge.

Conventional identification of bacteria is made by culture-based or characterization of biopsies of the wound, using Gram staining, analytical profile index systems, polymerase chain reaction (PCR) and gas chromatography coupled with mass spectrometry (GC-MS) for the identification of volatile compounds as amines<sup>168</sup>. Those techniques are time-consuming, requiring a turn-around time of at least 24h, and needing specialized personnel to perform them, which makes wound infection diagnosis an ideal target for POC devices.

---

<sup>163</sup> M. Matuszewska, G.G.R. Murray, E.M. Harrison, M.A. Holmes, L.A. Weinert. *Trends Microbiol.* 28 (2020) 465–477.

<sup>164</sup> J.P. O’Gara. *Environ. Microbiol.* 19 (2017) 3823–3833.

<sup>165</sup> S.S. Kadri. *Crit. Care Med.* 48 (2020) 939–945.

<sup>166</sup> S. Crone, M. Vives-Flórez, L. Kvich, A.M. Saunders, M. Malone, M.H. Nicolaisen, E. Martínez-García, C. Rojas-Acosta, M. Catalina Gomez-Puerto, H. Calum, M. Whiteley, R. Kolter, T. Bjarnsholt. *APMIS.* 128 (2020) 220–231.

<sup>167</sup> K. Zhao, W. Li, J. Li, T. Ma, K. Wang, Y. Yuan, J.S. Li, R. Xie, T. Huang, Y. Zhang, Y. Zhou, N. Huang, W. Wu, Z. Wang, J. Zhang, B. Yue, Z. Zhou, J. Li, Y.-Q. Wei, X. Zhang, X. Zhou. *Nat. Microbiol.* 4 (2019) 459–469.

<sup>168</sup> N.A. binte Mohamed Salleh, Y. Tanaka, L. Sutarlie, X. Su. *The Analyst.* 147 (2022) 1756–1776.

Both wound exudate (through microbial swabbing) and wound tissue are used as sample. However, it has disadvantages as wounds need to be larger than 1 cm<sup>2</sup> to perform microbial swabbing and they just allow to collect bacteria from the upper layers of the wound. Wound exudates have been used as sample for evaluating the suitability of the sensors developed in Chapters 3 and 5.2.

### **Biomarkers of chronic wound infection**

To substitute gold-standard culture methods, the identification of biomarkers of chronic wounds is a simple strategy that helps to reduce time of analyses.

Biomarkers of wound infection can be classified according to the role they play through the diagnosis. In initial stages of the infection, biomarkers can help to determine the stage and help to select a proper treatment. Later, biomarkers could be used to monitor the disease and to assure that therapies are effective. In this way, the role of biomarkers in chronic wound infections is transversal, covering all stages of the disease and being fundamental to achieve a more personalised treatment.

Depending on the biological nature of the biomarker, they can be also classified in enzymes or proteins and metabolites<sup>169</sup>. The direct detection of bacteria is also widely extended approach that requires in most cases the use of more complex approaches that detect microbial DNA (e.g. PCR or NG Sequencing). Enzymes are, by far, the most studied, as they are predictive biomarkers that appear in early stages of infection. Some of these enzymes are oxidative enzymes as myeloperoxidase (MPO) or xanthine oxidase, proteolytic enzymes, as matrix metalloproteinases (MMPs), cathepsin G or neutrophil elastase, or others as lysozyme (Lys) or hyaluronidase (HYAL).

Protein or metabolic biomarkers of wound infection are those directly produced by bacteria (bacteria metabolites), as is the case of virulence factors, or those produced by the immune system in response to a non-healing stage, as proinflammatory cytokines.

Virulence factors are molecules released directly by a bacteria as a mechanism to infect a host cell<sup>170</sup>. The predominant bacteria present in chronic wounds mainly produce as virulence factors enterotoxins, in the case of *S. aureus* and pyocyanin by *P. aeruginosa*<sup>171,172</sup>.

---

<sup>169</sup> J. Broadbent, T. Walsh, Z. Upton, *Proteom. Clin. Appl.* 4 (2010) 204–214.

<sup>170</sup> A.K. Sharma, N. Dhasmana, N. Dubey, N. Kumar, A. Gangwal, M. Gupta, Y. Singh., *Indian J. Microbiol.* 57 (2017) 1–10.

<sup>171</sup> K. Shettigar, T.S. Murali. *Eur. J. Clin. Microbiol. Infect. Dis.* 39 (2020) 2235–2246.

<sup>172</sup> L. Vilaplana, M.-P. Marco. *Anal. Bioanal. Chem.* 412 (2020) 5897–5912.

Other biomarkers such as microRNAs or physico-chemical parameters, as pH or temperature changes have been also related with infection<sup>173</sup>. Additionally, human metabolic biomarkers as interleukins 1 (IL1) and 6 (IL6), tumor necrosis factor-alpha (TNF $\alpha$ ) or C-reactive protein (CRP), that promote the recovery of damaged tissues are also analysed as biomarkers of healing monitoring.

In this Thesis, biomarkers as lysozyme, hyaluronidase, catalase, pyocyanin or enterotoxin B have been detected. A deeper explanation of all of them will be given in the corresponding Chapters.

### **State-of-the-art in electrochemical sensors for chronic wound infection diagnosis**

The need to reduce the time of analyses of traditional culture-based wound infection diagnostic procedures, makes the development of (bio)sensors for this purpose a necessity. From the biomarkers explained below, *P. aeruginosa* virulence factors are the preferred target analyte for electrochemical sensors, with a few recent review papers summarizing the works in this field<sup>174,175</sup>.

This is mainly due to the electrochemical behavior that pyocyanin, *P. aeruginosa* predominant virulence factor, presents, what enables the direct detection of this metabolite. Pyocyanin is a compound of the phenazines family, a class of antibiotics involved in biofilm formation that are produced by diverse bacteria. In the case of *P. aeruginosa*, the most typical phenazine is pyocyanin, a blue-green pigment that it is specifically produced by this pathogen. Pyocyanin is considered as the most virulent factor of *P. aeruginosa* as it interferes in electron transport, cellular respiration, and innate immune response among other cellular events. Due to its specificity, pyocyanin and other phenazines have been deeply used as biomarkers of *P. aeruginosa* in (bio)sensing.

Pyocyanin was directly detected through CV and SWV using an ITO electrode modified with polyaniline and AuNPs transparent carbon ultramicroelectrode arrays (T-CUAs) modified with gold nanoparticles The sensor was evaluated in corneal ulcer

---

<sup>173</sup> R. Mirzaei, R. Mohammadzadeh, H. Mirzaei, M. Sholeh, S. Karampoor, M. Abdi, M.Y. Alikhani, S. Kazemi, Y. Ahmadyousefi, S. Jalalifar, R. Yousefimashouf. *Life*. 72 (2020) 1856–1869.

<sup>174</sup> F.A. Alatrakchi, W.E. Svendsen, S. Molin. *Sensors*. 20 (2020) 5218.

<sup>175</sup> O. Simoska, K.J. Stevenson. *Sens. Actuators Rep.* 4 (2022) 100072.

samples showing promising results and being able to detect Pyocyanin with a LOD of 0.5  $\mu\text{M}$ <sup>176</sup>.

In relation to *S. aureus*, less biosensors have been developed for the identification of this strain due its polysaccharide layer. Nonetheless, aptamer-based biosensor able to directly detect *S. aureus* have been developed so far<sup>177</sup>. Using single walled carbon nanotubes to modify the transducer, a detection limit of  $8 \times 10^{-2}$  CFU/mL was obtained.

Another strategy for the detection of *S. aureus* is the measurement of its virulence factors. This is the case of enterotoxin B, one of the most potent superantigen produced by *S. aureus*. This molecule has been extensively used to identify food poisoning outbreaks through electrochemical sensors<sup>178</sup>. However, the detection of enterotoxin B in wound fluid samples has not been reported so far.

HYAL is another enzymatic biomarker used for the identification of Gram-positive bacteria. HYAL degrades hyaluronic acid, cleaving the polysaccharide of skin cells and thus promoting pathogen infection. A hyaluronic acid modified porous silicon film was used for the electrochemical detection of HYAL. By monitoring the degradation through DPV and using ferrocyanide/ferricyanide as redox probe, they detected this enzyme in artificial wound fluids<sup>179</sup>.

Moreover, it is worth mentioning a (bio)sensing tendency that it has been highly implemented in wound monitoring as it is smart wound dressing. Wound dressing is the actual standard of care in patients with chronic wounds and it consist of the replacement of the dressing and monitoring of the state of the wound by a specialised healthcare personal. A proper wound dressing is essential for preventing infections and regulating moisture. Due to its importance, wound dressing has evolved and research on bioactive wound dressings containing drug delivery systems<sup>180</sup>. Bioactive wound dressing not only helps to treat wound healing, but it also provides a tool for monitoring wound infections. Davis *et al.* recently constructed a paper-based wound dressing sensor for monitoring *S. aureus* is diabetic foot ulcer. Wound dressing was composed of a screen-printed surface conjugated with a composite of Zeolitic Imidazolate Framework (ZIF-67), carbon nitride

---

<sup>176</sup> M.M. Khalifa, A.A. Elkhawaga, M.A. Hassan, A.M. Zahran, A.M. Fathalla, Waleed A. El-Said, O. El-Badawy. *Sci. Rep.* 9 (2019).

<sup>177</sup> G.A. Zelada-Guillén, J.L. Sebastián-Avila, P. Blondeau, J. Riu, F.X. Rius. *Biosens. Bioelectron.* 31 (2012) 226–232.

<sup>178</sup> X. Xiong, X. Shi, Y. Liu, L. Lu, J. You. *Anal. Methods.* 10 (2018) 365–370.

<sup>179</sup> K.-S. Tücking, R.B. Vasani, A.A. Cavallaro, N.H. Voelcker, H. Schönherr, B. Prieto-Simon. *Macromol. Rapid Commun.* 39 (2018) 1870044.

<sup>180</sup> Q. Pang, F. Yang, Z. Jiang, K. Wu, R. Hou, Y. Zhu. *Mater. Des.* 229 (2023) 111917.



(C<sub>3</sub>N<sub>4</sub>) and *S. aureus* probe DNA<sup>181</sup>. By electrochemical impedance spectroscopy, this biosensor was able to detect *S. aureus* DNA with a LOD of 0.46 fM.

### ***1.8.3. Beyond biomarker detection: innovative tools for studying bacterial infection***

The importance of infection in chronic wounds has been already explained in previous sections. Although reducing detection time is a key aspect in managing chronic wounds, there are other factors that play a pivotal role in this comorbidity.

As already stated above, infection in chronic wounds is not normally governed by a single pathogen but rather as polymicrobial infection. This leads to a higher complexity of both pathogen identification and treatment administration. Therefore, to address the healthcare challenge of chronic wounds, being able to identify the presence of an infection is not enough. For that reason, in this Thesis two important aspects in chronic wounds have been explored: bacteria biogeography and antimicrobial screening.

#### *1.8.3.1. The importance of bacteria biogeography: 3D printing as a tool to study bacteria interaction*

Microorganisms tend to live in communities rather than isolated, forming polymicrobial infections normally in the form of a biofilm<sup>182</sup>. Although it has been extensively associated a disease with a single pathogen, the presence of polymicrobial infections has long been stated as causative of human health disorders<sup>183</sup>. Moreover, it is not important just the presence of polymicrobial infections, the patten in which bacteria are collocated is also relevant as it affects how they interact between them and hence, how they respond to external outputs. Understanding the patterning of microbes withing infection and how it is correlated with their interactions and fitness is an emerging area of research called microbiogeography<sup>184</sup>.

---

<sup>181</sup> S. Roy, K. Bisaria, S. Nagabooshanam, A. Selvam, S. Chakrabarti, S. Wadhwa, R. Singh, A. Mathur, J. Davis. IEEE Sens. J. 21 (2021) 1215–1221.

<sup>182</sup> A. Stacy, L. McNally, S.E. Darch, S.P. Brown, M. Whiteley. Nat. Rev. Microbiol. 14 (2016) 93–105.

<sup>183</sup> Smith, H. Philos. Trans. R. Soc. Lond. B Biol. Sci. 297(1088), 551-561.

<sup>184</sup> S. Azimi, G.R. Lewin, M. Whiteley. Nat. Rev. Microbiol. (2022). 20(10), 579-592

In chronic wounds the predominant co-infection is dominated by *P. aeruginosa* and *S. aureus*, a polymicrobial interaction that it is also present in cystic fibrosis and oral cavity infections. The polymicrobial colonization of wounds is a concurrently process, in which first *S. aureus* and *P. aeruginosa* have a competitive relationship, turning into a synergy in later stages of infection, providing a mutual benefit enhancing their antimicrobial resistance<sup>185</sup>. Their relationship in chronic wounds has probably evolved in this way owing to the interaction with other microorganisms<sup>186</sup>. Over recent years, it has been increasingly clear that this synergy enhances host colonization, virulence, and antimicrobial resistance. However, a thorough understanding on the mechanistic behind polymicrobial interaction in relation to disease are still required.

Culture and PNA-FISH of biopsies from the wound bed have been the primarily used techniques for studying these interactions. However, the lack of reproducibility of the wound microenvironment in the first case and the autofluorescence and sample opacity in the second hinder analysis. What it is known so far with these techniques is that *S. aureus* is present in the top layers of the wound (within 30 µm) while *P. aeruginosa* settles at the bottom of the wound bed (>40 µm from the top layer, depending on the depth of the wound bed) thanks to its ability to produce virulence factors, more concretely rhamnolipid, that destroy polymorphonuclear leukocytes (PMNs), maintaining the wound in an inflammatory stage<sup>187,188</sup>. It has been also stated that the microenvironment and the availability of electron acceptors for metabolic and respiratory rates affects bacteria distribution<sup>189,190</sup>. This situation is not observed in acute wounds, where bacteria aggregate at the edges of the wound leaving free the wound bed<sup>191</sup>. What modulates this differentiated distribution in chronic wounds is still unclear.

---

<sup>185</sup> S. DeLeon, A. Clinton, H. Fowler, J. Everett, A.R. Horswill, K.P. Rumbaugh. *Infect. Immun.* 82 (2014) 4718–4728.

<sup>186</sup> D.A. Hogan, R. Kolter. *Science.* 296 (2002) 2229–2232.

<sup>187</sup> D.B.Y. Yung, K.J. Sircombe, D. Pletzer. *Mol. Microbiol.* 116 (2021) 1–15.

<sup>188</sup> M. Fazli, T. Bjarnsholt, K. Kirketerp-Møller, B. Jørgensen, A.S. Andersen, K.A. Krogfelt, M. Givskov, T. Tolker-Nielsen. *J. Clin. Microbiol.* 47 (2009) 4084–4089.

<sup>189</sup> G.A. James, A. Ge Zhao, M. Usui, R.A. Underwood, H. Nguyen, H. Beyenal, E. deLancey Pulcini, A. Agostinho Hunt, H.C. Bernstein, P. Fleckman, J. Olerud, K.S. Williamson, M.J. Franklin, P.S. Stewart. *Wound Repair Regen.* 24 (2016) 373–383.

<sup>190</sup> M. Lichtenberg, T.H. Jakobsen, M. Kühl, M. Kolpen, P.Ø. Jensen, T. Bjarnsholt. *FEMS Microbiol. Rev.* (2022) 46(5) fuac018.

<sup>191</sup> L. Bay, K.N. Kragh, S.R. Eickhardt, S.S. Poulsen, L.M.R. Gjerdrum, K. Ghathian, H. Calum, M.S. Ågren, T. Bjarnsholt. *Adv. Wound Care.* 7 (2018) 105–113.

And if it is difficult to study their interaction in real wounds, it is even more difficult to reproduce it in *in vitro* models. While it seems that *S. aureus* colonizes the upper regions of wound infection, in static culture conditions it settles at the bottom. In contrast, *P. aeruginosa* produces a biofilm in the air-liquid surface<sup>192,193</sup>. To overcome these issues, the introduction of shaking and flow conditions to enhance the mimicking of physiological conditions of wound exudates have been exploited to obtain more accurate models<sup>194</sup>. However, shaking conditions if too rough would not allow *P. aeruginosa* to adhere to surfaces while during flow conditions the formation of mushroom-like aggregates different to the ones observed in wounds is produced<sup>195</sup>.

Obtaining valuable models to study polymicrobial infections in wounds is then a necessity both to understand the resistant mechanisms that govern this polymicrobial interaction and to harness bacterial models for the screening of new antimicrobial compounds.

For this purpose, 3D printing seems like a promising technology for generating customized complex materials, with great potential to study complex bacteria interactions<sup>196</sup>. This technology was initially developed for large industrial manufacturing materials, but it has evolved been of potential application in biomedicine and more precisely in tissue and organ production<sup>197</sup>. The 3D printing of living cells is known as bioprinting, and it comprises the printing through different techniques (as droplet or extrusion printing) of living cells encapsulated withing hydrogel materials<sup>198</sup>. These techniques have been more recently implemented in microbiology, focused on developing novel functional materials more than studying microbes' behaviors.

In this way, 3D printed bacteria have been even used in the development of a wearable sensor device<sup>199</sup>. This method used a bioink composed of engineered *E. coli* embedded in a hydrogel matrix (composed of Irgacure 2959 as photoinitiator and Pluronic

---

<sup>192</sup> C. Reichhardt, H.M. Jacobs, M. Matwichuk, C. Wong, D.J. Wozniak, M.R. Parsek. *J. Bacteriol.* 202 (2020). 202(19)

<sup>193</sup> L. Friedman, R. Kolter. *Mol. Microbiol.* 51 (2003) 675–690.

<sup>194</sup> P.F. Duckworth, R.S. Rowlands, M.E. Barbour, S.E. Maddocks. *Microbiol. Res.* 215 (2018) 141–147.

<sup>195</sup> T. Bjarnsholt. *APMIS.* 121 (2013) 1–58.

<sup>196</sup> R. Krishna Kumar, K.R. Foster. *Microb. Biotechnol.* 16 (2023) 489–493.

<sup>197</sup> Z. Jin, Y. Li, K. Yu, L. Liu, J. Fu, X. Yao, A. Zhang, Y. He. *Adv. Sci.* 8 (2021) 2101394.

<sup>198</sup> L. Zhou, A.C. Wolfes, Y. Li, D.C.W. Chan, H. Ko, F.G. Szele, H. Bayley. *Adv. Mater.* 32 (2020) 2002183.

<sup>199</sup> X. Liu, H. Yuk, S. Lin, G.A. Parada, T. Tang, E. Tham, C. de la Fuente-Nunez, T.K. Lu, X. Zhao. *Adv. Mater.* 30 (2018) 1704821.

F127 diacrylate micelles in water for physical crosslinking). *E. coli* strains were modified to respond under the presence of the inducers N-acyl homoserine lactone, rhamnose and isopropyl  $\beta$ -D-1-thiogalactopyranoside and rhamnose (IPTG) as chemical-sensing molecules in an initial probe-of-concept of the developed system as a living tattoo. Under the presence of each of these compounds, *E. coli* emitted green fluorescence.

But, although scarce, there is also research on the use of 3D printing for studying microbial patterned communities based on droplet-printing at the microscale<sup>200</sup>. This work demonstrated the importance of spatial arrangement for biogeography and bacteria interaction and lays the groundwork for its expansion to other pathologies as chronic wound infection.

#### 1.8.3.2. *Antimicrobial screening: potential of electrochemical sensors*

As it has been previously presented, the problem of managing chronic wounds goes beyond detection. It has been explained above how important is to understand bacteria interaction in a wound to overcome infection. These information helps to obtain valid models for the development of novel antimicrobial compounds.

The abusive use of antibiotic treatments has enhanced the problem of antimicrobial resistance (AMR)<sup>201,202</sup>. This rising pandemic is making currently available antimicrobial treatments no longer be useful, making the development of novel antimicrobial compounds then a need. Antibiotic screening tests (AST) are used to identify bacteria resistances and novel candidate compounds. Main AST techniques are based on bacterial growth in solid or liquid media and rely on the diffusion or dilution of antibiotics across the media<sup>203</sup>. The longtime of analysis requires by these techniques has prompted the development of alternative screening methodologies that allow, not only to identify resistant bacteria, but also serve as platform for new drug screening.

(Bio)sensors, and more in concrete electrochemical (bio)sensors, have stood out due to their specificity, rapid response, easy to use, portability and low-cost<sup>204</sup>. The use

---

<sup>200</sup> R. Krishna Kumar, T.A. Meiller-Legrand, A. Alcinesio, D. Gonzalez, D.A.I. Mavridou, O.J. Meacock, W.P.J. Smith, L. Zhou, W. Kim, G.S. Pulcu, H. Bayley, K.R. Foster. *Nat. Commun.* 12 (2021) 857.

<sup>201</sup> M. Miethke et al. *Nat. Rev. Chem.* 5 (2021) 726–749.

<sup>202</sup> C.L. Ventola. *Pharm. Ther.* 40 (2015) 277–283.

<sup>203</sup> M. Balouiri, M. Sadiki, S.K. Ibsouda. *J. Pharm. Anal.* 6 (2016) 71–79.

<sup>204</sup> Ü. Anik, *Electrochemical medical biosensors for POC applications*, in: *Med. Biosens. Point Care POC Appl.*, Roger J. Narayan, Woodhead Publishing, 2017, 275–292.

of electrochemical sensors for AST, ranges from the use of different types of electrodes to a variety of electrochemical techniques, using both direct and indirect detection approaches.

Combining the use of a disposable screen-printed electrode coupled to a microfluidic chamber<sup>205</sup>, the antibiotic susceptibility of *P. aeruginosa*, via electrochemical detection of pyocyanin was addressed, against different concentrations of colistin sulphate as antibiotic. The main disadvantage of this methodology is that the time required for completing measurements is of 45 h, comparable with the standard techniques currently used.

Antibiotic compounds are not the only therapeutic target in antimicrobial research. Anti-biofilms have been subject of study for many pathological microorganisms as the formation of biofilms enhances multidrug tolerance. Besides, the incorporation of electrochemical scaffolds together with anti-biofilm compounds has also been confirmed to have a co-adjuvant effect in antimicrobial treatment<sup>206</sup>.

Evaluation of new anti-biofilm forming compounds has also been done using an electrochemical sensor using ferricyanide as redox indicator. In this case, alginate, one of the main components of mucoid *P. aeruginosa* strain biofilms<sup>207</sup>, was immobilized on top of a pyrolytic graphite electrode modified layer-by-layer with poly(diallyldimethylammonium) chloride and polystyrene sulfonate. Both polymers have opposite charge, which allows the retaining of alginate in the upper electrode layer<sup>208</sup>. By the addition of antimicrobial peptides, the alginate was broken and ferricyanide was able to go through the layers and reach the electrode, providing an increase in the oxidation current recorded. In a later work, the same group used the same type of electrodes but in this case with the immobilization of *P. aeruginosa* on the upper layer. Direct electrochemical reduction of phenazine compounds produced by *P. aeruginosa* was recorded through SWV in a label-free sensor. With this sensor, the establishment of the half maximal inhibition concentration (IC<sub>50</sub>) and half maximal effective concentration (EC<sub>50</sub>) of an anti-biofilm compound was possible in just a few minutes<sup>209</sup>.

---

<sup>205</sup> T.A. Webster, H.J. Sismaet, I.J. Chan, E.D. Goluch. *The Analyst*. 140 (2015) 7195–7201.

<sup>206</sup> S.T. Sultana, D.R. Call, H. Beyenal. *Npj Biofilms Microbiomes*. 2 (2016) 2.

<sup>207</sup> D.M. Ramsey, D.J. Wozniak. *Mol. Microbiol.* 56 (2005) 309–322.

<sup>208</sup> S.M. Vinogradov, J.E. Satterwhite-Warden, R.P. Hicks, E. Anderson, E.G. Hvastkovs. *Electrochimica Acta*. 186 (2015) 245–252.

<sup>209</sup> A.J. Robb, S. Vinogradov, A.S. Danell, E. Anderson, M.S. Blackledge, C. Melander, E.G. Hvastkovs. *Electrochimica Acta*. (2018) 276–282.

## **Chapter 2. Objectives/ Objetivos**

---



## Objectives

Considering the information explained in the introduction chapter, the main objective of this Doctoral Thesis is the development of novel (bio)analytical tools based on nanomaterials, in particular nanoparticles and nanoporous alumina membranes, for biomedical applications. This general objective could be divided in the following specific objectives:

1. Synthesis and characterization of novel electrocatalytic nanoparticles and thorough study of their catalytic properties.
2. Application of these novel nanoparticles as electrochemical labels in immunosensors.
3. Synthesis and characterization of polymeric magnetic nanomaterials.
4. Application of these magnetic nanomaterials as sensing platforms in an immunosensor.
5. Development of (bio)analytical platforms based on nanoporous alumina membranes and study of the electrostatic effects that govern them.
6. Use of the nanomaterials developed for the detection of biomarkers related with AD and chronic wound infection.
7. Integration of nanoporous alumina membranes as (bio)analytical platform for the screening of novel antimicrobial compounds.
8. Exploring innovative tools to understand bacteria interactions.



## Objetivos

Considerando la información expuesta en el Capítulo introductorio, el objetivo principal de esta Tesis Doctoral es el desarrollo de nuevas herramientas (bio)analíticas basadas en nanomateriales, en particular nanopartículas y membranas nanoporosas de alúmina, para aplicaciones biomédicas. Este objetivo general podría dividirse en los siguientes objetivos específicos:

1. Síntesis y caracterización de nuevas nanopartículas electrocatalíticas y estudio en profundidad de sus propiedades catalíticas.

2. Aplicación de estas novedosas nanopartículas como etiquetas electroquímicas en inmunosensores.

3. Síntesis y caracterización de nanomateriales magnéticos poliméricos.

4. Aplicación de estos nanomateriales magnéticos como plataformas sensoras en un inmunosensor.

5. Desarrollo de plataformas (bio)analíticas basadas en membranas nanoporosas de alúmina y estudio de los efectos electrostáticos que las gobiernan.

6. Utilización de los nanomateriales desarrollados para la detección de biomarcadores relacionados con la EA y la infección de heridas crónicas.

7. Integración de membranas de alúmina nanoporosa como plataforma (bio)analítica para el cribado de nuevos compuestos antimicrobianos.

8. Exploración de herramientas innovadoras para comprender las interacciones bacterianas.

## Chapter 3. Electrocatalytic nanoparticles as tags

---

<b>3.1. Summary</b> .....	<b>53</b>
<b>3.2. Scientific article 4</b> .....	<b>55</b>
3.2.1. Introduction .....	55
3.2.2. Protocols .....	58
3.2.3. Results and discussion .....	61
3.2.4. Conclusions .....	73

---



### 3.1. Summary

As it has been mentioned previously, one of the main purposes of this Thesis is the evaluation of novel nanomaterials and their integration into (bio)analytical platforms used in biomedical applications.

In this sense, in this Chapter, the synthesis and characterization of novel PdAu nNPs have been studied. In particular, the role that the introduction of increasing concentrations of Au into Pd nanoclusters has in the electrocatalytic activity against the ORR at neutral pH was conducted. Our results indicate that, the synergy between both metals is strongly enhanced when the amount of gold is controlled and occupies the more reactive positions of the cluster, reaching a maximum activity for the NPs containing a 30% of gold, while an excess of this metal leads to a decrease in such activity, as a shelter of the PdNPs is achieved.

As a proof-of-concept, such optimal Pd-AuNPs were used as tags, taking advantage of the bio-functionalities of gold present in the cluster, in an electrochemical immunosensor for the detection of hyaluronidase wound infection biomarker, using magnetic beads as platforms. Hyaluronidase was detected, at levels as low as 74 ng/mL (0.03 U/mL; 437 U/mg) with good reproducibility (RSD below 8 %) and selectivity (evaluated against bovine serum albumin, immunoglobulin G and lysozyme), meeting the clinical requirements. The low matrix effects inherent to the use of magnetic bead platforms allowed us to discriminate between wound exudates with both sterile and infected ulcers without sample pre-treatment. This novel electrocatalytic immunoassay has the advantage of the signal generation in the same neutral medium where the immunoassay takes place, avoiding the use of additional and hazardous reagents, bringing it closer to their use as point-of-care devices.

---

## 3.2. Scientific article 4

Biosensors and Bioelectronics 200 (2022) 113926



Contents lists available at [ScienceDirect](https://www.sciencedirect.com)

Biosensors and Bioelectronics

journal homepage: [www.elsevier.com/locate/bios](http://www.elsevier.com/locate/bios)



### Enhancing the electrocatalytic activity of palladium nanocluster tags by selective introduction of gold atoms: Application for a wound infection biomarker detection

Celia Toyos-Rodríguez<sup>a,b</sup>, Alaa Adawy<sup>c</sup>, Francisco Javier García-Alonso<sup>b,d</sup>, Alfredo de la Escosura-Muñiz<sup>a,b,\*</sup>

<sup>a</sup> NanoBioAnalysis Group-Department of Physical and Analytical Chemistry, University of Oviedo, Julián Clavería 8, 33006, Oviedo, Spain

<sup>b</sup> Biotechnology Institute of Asturias, University of Oviedo, Santiago Gascon Building, 33006, Oviedo, Spain

<sup>c</sup> Unit of Electron Microscopy and Nanotechnology, Institute for Scientific and Technological Resources (SCTs), Edificio Severo Ochoa S/n, Campus de El Cristo, 33006, Oviedo, Spain

<sup>d</sup> NanoBioAnalysis Group-Department of Organic and Inorganic Chemistry, University of Oviedo, Julián Clavería 8, 33006, Oviedo, Spain

#### 3.2.1. Introduction

The use of nanomaterials has been a breakthrough since they were first synthesized and implemented into different research topics with continuous progress<sup>210,211</sup>. Biosensing is among the main areas of application of these materials, in which the usage of nanomaterials, both as electrode modifiers and as labels has implied a significant improvement. Their unique properties, including electron transfer, biocompatibility and electroactive and electrocatalytic activity, among others, has enabled decreasing detection limits and increasing sensitivity, selectivity, and reproducibility of the assays<sup>137</sup>. Their use as labels in immunosensing has been deeply studied, constituting an outstanding alternative to traditionally used enzymes<sup>212</sup>.

In this context, metal nanoparticles have emerged due to their catalytic potential, making them reporters with an outsized sensitivity that is associated with their high surface-to-volume ratios, high mechanical strength and ease of functionalization<sup>213,214</sup>.

<sup>210</sup> S. Bayda, M. Adeel, T. Tuccinardi, M. Cordani, F. Rizzolio. *Molecules*. 25 (2020) 112.

<sup>211</sup> C.M. Welch, R.G. Compton. *Anal. Bioanal. Chem.* 384 (2006) 601–619.

<sup>212</sup> A. de la Escosura-Muñiz, C. Parolo, A. Merkoçi. *Mater. Today*. 13 (2010) 24–34.

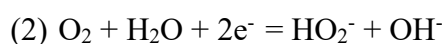
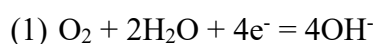
<sup>213</sup> G. Doria, J. Conde, B. Veigas, L. Giestas, C. Almeida, M. Assunção, J. Rosa, P.V. Baptista. *Sensors*. 12 (2012) 1657–1687.

<sup>214</sup> N.J. Wittenberg, C.L. Haynes. *WIREs Nanomedicine Nanobiotechnology*. 1 (2009) 237–254.

---

From all metal nanoparticles, gold nanoparticles are chiefly used. However, in most cases their detection requires the use of highly acidic media, as it is the case of their use as catalysts of HER<sup>215,216</sup>. This extra requisite results in the incorporation of additional steps that increase the time of analysis.

The use of alternative nanoparticles capable of acting as catalysts at neutral pH has been recently explored<sup>217,218</sup>, specially based in the catalysis of reactions as WOR or ORR. ORR is one of the most studied electrocatalytic reactions as it plays a pivotal role in the electrochemical energy conversion<sup>219,220</sup>. This cathodic electrode reaction is a complicated and slow process in which various reaction intermediates are embedded. Thus, the reduction of O<sub>2</sub> has been proposed to take place following two different pathways: a straightforward four electron reaction (1) or an indirect process called the two-electron process (2)<sup>221,222,223</sup>.



The role of metals such as palladium, platinum or silver has been related to the formation first of a superoxide ion ( $\text{O}_2 + \text{e}^- = \text{O}_2^{\cdot-}$ )<sup>224,225,226</sup>.

Platinum (Pt) catalysts have been the benchmark in the ORR catalysis owing to their durability in acidic media and their high activity<sup>227</sup>. However, their high cost is their main drawback. The use of other metals has been postulated as an alternatively cheaper catalyst that also boosts ORR activation<sup>228</sup>.

---

<sup>215</sup> L. Baptista-Pires, A. de la Escosura-Muñiz, M. Balsells, J.C. Zuaznabar-Gardona, A. Merkoçi. *Electrochem. Commun.* 98 (2019) 6–9.

<sup>216</sup> A.-R.H.A.-A. Hassan, A. de la Escosura-Muñiz, A. Merkoçi. *Biosens. Bioelectron.* 67 (2015) 511–515.

<sup>217</sup> L. Cao, J. Cai, W. Deng, Y. Tan, Q. Xie. *Anal. Chem.* 92 (2020) 16267–16273.

<sup>218</sup> L. Rivas, A. de la Escosura-Muñiz, J. Pons, A. Merkoçi. *Electroanalysis.* 26 (2014) 1287–1294.

<sup>219</sup> G. Maduraiveeran. *Mater. Lett.* 283 (2021) 128763.

<sup>220</sup> S.T. Rahman, K.Y. Rhee, S.-J. Park. *Nanotechnol. Rev.* 10 (2021) 137–157.

<sup>221</sup> J.-J. Han, N. Li, T.-Y. Zhang. *J. Power Sources.* 193 (2009) 885–889.

<sup>222</sup> D.-H. Lim, J. Wilcox. *J. Phys. Chem. C.* 116 (2012) 3653–3660.

<sup>223</sup> H.-Y. Wang, C.-C. Weng, Z.-Y. Yuan. *J. Energy Chem.* 56 (2021) 470–485.

<sup>224</sup> K. Kusunoki, D. Kudo, K. Hayashi, Y. Chida, N. Todoroki, T. Wadayama. *ACS Catal.* 11 (2021) 1554–1562.

<sup>225</sup> R. Singh, P. Kesharwani, N.K. Mehra, S. Singh, S. Banerjee, N.K. Jain. *Drug Dev. Ind. Pharm.* (2015) 1–14.

<sup>226</sup> J.S. Spindelov, A. Wieckowski. *Phys. Chem. Chem. Phys.* 9 (2007) 2654.

<sup>227</sup> J.K. Nørskov, J. Rossmeisl, A. Logadottir, L. Lindqvist, J.R. Kitchin, T. Bligaard, H. Jónsson. *J. Phys. Chem. B.* 108 (2004) 17886–17892.

<sup>228</sup> X. Tian, X.F. Lu, B.Y. Xia, X.W. (David) Lou. *Joule.* 4 (2020) 45–68.

In this context, palladium (Pd) as a metal has been proven to be as promising as Pt alloy<sup>229,230,231</sup> or in combination with other metals. Zhang et al.,<sup>85</sup> described the combination of Pd and Au in a crown-jewel structure with a hexagonal Pd core decorated with upper Au atoms mimicking the disposition of a crown. The selective introduction of upper Au atoms in the vertex and corners of the Pd core, provided a synergistic effect increasing the intrinsic catalytic activity of Pd, as shown toward the glucose oxidation and H<sub>2</sub>O<sub>2</sub> decomposition reactions.

In this context, the objective of this work is to explore for the first time the role that the introduction of increasing concentrations of Au into Pd nanoclusters have in their electrocatalytic activity toward the ORR. A careful control of the amount of Au atoms introduced in the cluster and the evaluation of the optimum Pd:Au ratio for getting the maximum catalytic activity is a key study, missing in the bibliography. This may be of great interest not only for biosensing, but also for applications such as energy converting on fuel cells.

As a proof-of-concept of application in biosensing, the synthesized Pd-AuNPs prepared with an optimum Pd/Au rate have been used as tags in a magnetic bead-based immunoassay for the detection of hyaluronidase, a chronic wound infection biomarker. Hyaluronidase is produced by the main pathogenic Gram-positive bacteria that colonize mucosal surfaces and skin, although its role is still being investigated<sup>232</sup>. Even though there are human hyaluronidases, bacterial ones (EC 4.2.2.1 or EC 4.2.99.1) are characterized by producing unsaturated disaccharides through endo-N-acetylhexosaminidase activity<sup>233</sup>. This bacterial specificity makes hyaluronidase a potential biomarker of infection in chronic wounds, also allowing to discern between bacterial genders.

---

<sup>229</sup> X. Wang, M. Vara, M. Luo, H. Huang, A. Ruditskiy, J. Park, S. Bao, J. Liu, J. Howe, M. Chi, Z. Xie, Y. Xia. *J. Am. Chem. Soc.* 137 (2015) 15036–15042.

<sup>230</sup> X. Wang, S.-I. Choi, L.T. Roling, M. Luo, C. Ma, L. Zhang, M. Chi, J. Liu, Z. Xie, J.A. Herron, M. Mavrikakis, Y. Xia. *Nat. Commun.* 6 (2015) 7594.

<sup>231</sup> Z.-P. Wu, D.T. Caracciolo, Y. Maswadeh, J. Wen, Z. Kong, S. Shan, J.A. Vargas, S. Yan, E. Hopkins, K. Park, A. Sharma, Y. Ren, V. Petkov, L. Wang, C.-J. Zhong. *Nat. Commun.* 12 (2021) 859.

<sup>232</sup> W.L. Hynes, S.L. Walton. *FEMS Microbiol. Lett.* 183 (2000) 201–207.

<sup>233</sup> R. Stern, M.J. Jedrzejka. *Rev.* 106 (2006) 818–839.



---

### **3.2.2. Protocols**

#### *3.2.2.1. Synthesis, bioconjugation and characterization of Pd-AuNPs*

The synthesis of Pd nanoclusters was performed following a previously reported procedure with some modifications<sup>85</sup>. Briefly, 50 mL of a suspension of 0.66 mM palladium (II) chloride prepared in ethanol: water (1:3) were vigorously stirred in a round bottom flask at room temperature for 15 min. Then, 50 mL of a PVP 66 mM solution in ethanol: water (1:3) were added, and the suspension was again stirred at room temperature for additional 15 min. Afterwards, the suspension was heated at 100°C for 2h under reflux and inert atmosphere (Ar, Ar  $\geq$  99,999, ALPHAGAZ™ 1, from AirLiquid, Spain). The final product was purified with centrifugation at 4000 g, 20°C for 30 min using Amicons® with a cut-off value of 10.000 molecular weight. Three washing steps with water and one with ethanol, using the same Amicons® were also done. Then, the remaining ethanol was evaporated, and the final product was resuspended in a 1:3 ethanol: water solution to a final concentration of 0.66 mM Pd.

For the selective introduction of gold, 20 mL of a gold (III) chloride trihydrate solution (0.135 mM, 0.735 mM, 0.835 mM, 0.935 mM or 1.135 mM) were poured into a round bottom flask containing the obtained Pd nanoclusters. The solution was heated for 30 min at 100°C under reflux and inert atmosphere. To reduce aggregation, 2 mL of tri-sodium citrate in a concentration of 0.17 M were introduced in the flask and the solution was purified by centrifugation at 8000 g, 4°C for 45 minutes using LoBind tubes. Then, the remaining pellet was washed three times with water by centrifuging at 8000 g, 20°C during 30 min.

The final product was resuspended to a final concentration of  $1.45 \times 10^{12}$  NPs/mL according to Nanoparticle tracking analysis (NTA) measurements (Figure S3.1).

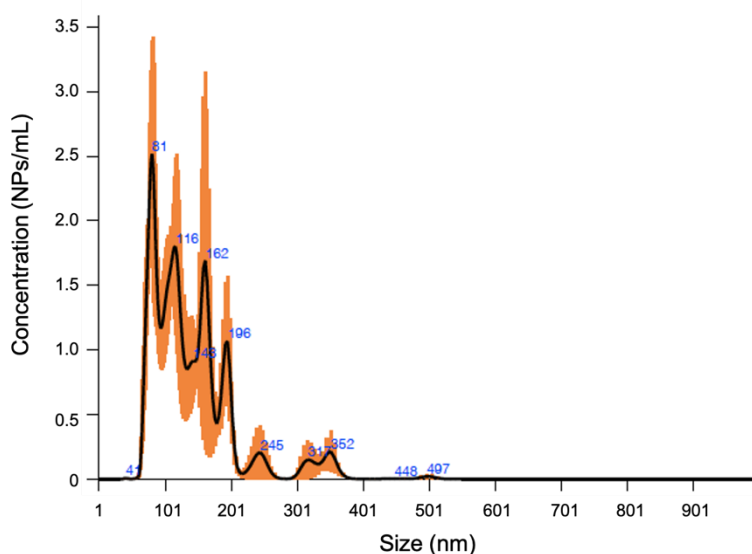


**Figure S.3.1.** Nanoparticle track analysis (NTA) of the obtained Pd-AuNP-3, revealing the size distribution. By the same analysis, the final NPs concentration was established ( $1.45 \times 10^{12}$  NPs/mL).

Meanwhile, 690  $\mu\text{L}$  of the Pd-AuNPs suspension were transferred into a 1.5 mL LoBind Eppendorf® tube and centrifuged at 7500 g, 20°C for 20 min with the addition of 10  $\mu\text{L}$  of 1.75% Tween-20. After centrifugation, the pellet was resuspended in 700  $\mu\text{L}$  of 2 mM trisodium citrate pH 7.4 solution. Then, 57.5  $\mu\text{L}$  of 50  $\mu\text{g/mL}$  solution of a polyclonal antibody anti-hyaluronidase were added and incubated for 1 h. For purification, the solution was centrifuged at 7500 g, 4°C for 15 min, the supernatant was removed, and the pellet resuspended in 0.1M PBS pH 7.2 with 1% BSA.

### 3.2.2.2. *Electrochemical measurements*

The electrocatalytic activity of the obtained Pd and Pd-AuNPs toward the ORR was electrochemically evaluated by dropping 10  $\mu\text{L}$  of the NP suspension onto the working electrode of an SPCE. Then, the solution was kept until complete absorption, when 40  $\mu\text{L}$  of 10 mM PBS pH 7.4 were added. For obtaining the background signals, 50  $\mu\text{L}$  of a 10 mM PBS pH 7.4 solution were used. LSV scans were recorded in the range from 0 V to -0.8 V at a scan rate of 0.1 V/s.

Chronoamperometric scans were obtained maintaining a fixed potential of -0.45V for 50s. Signal at 5s was selected as analytical signal for the evaluation of the electrocatalytic activity of the different Pd-AuNPs toward the ORR and for the quantitative studies.

---

In all the experiments, measurements were performed by triplicate at room temperature, using a different SPCE.

### *3.2.2.3. Immunoassay for the detection of hyaluronidase wound infection biomarker*

Hyaluronidase was detected using magnetic bead (MB) platforms and Pd-AuNPs tags, adapting a previously reported immunoassay format<sup>84</sup>. Briefly, 15  $\mu\text{L}$  (10 mg/mL) of commercially available streptavidin modified MBs were conveyed to a 0.5 mL LoBind Eppendorf tube and washed three times with B&W buffer. Then, MBs were resuspended in 135  $\mu\text{L}$  of B&W buffer and 15  $\mu\text{L}$  of 15  $\mu\text{g}/\text{mL}$  biotin-linked monoclonal anti-hyaluronidase antibody were added, and the solution was incubated for 30 min at 25°C, 650 rpm in a thermo shaker incubator. Past this time, the excess of biotin-linked anti-hyaluronidase antibody was removed with the help of a MagRack®, and the solution was washed three-times with B&W buffer. Then, 150  $\mu\text{L}$  of blocking buffer (PBS 0.1 M pH 7.2 with 5% BSA) were added to each tube and incubated for 1 h at the same heating and stirring conditions to minimized unspecific absorptions.

Once the MBs-anti hyaluronidase conjugate was obtained, 100  $\mu\text{L}$  of hyaluronidase solutions ranging from 0-4600 ng/mL were added and incubated for 30 min at 25°C, 650 rpm. The final product was washed three times with B&W buffer.

Then, 150  $\mu\text{L}$  of the Pd-AuNP conjugate were added to with the MBs final conjugate and incubated for 1h at 25°C and 650 rpm. The resulting immunocomplex was washed twice with B&W buffer and twice with 10 mM PBS pH 7.4 and reconstituted in 150  $\mu\text{L}$  of this buffer. The final conjugate was chronoamperometrically measured by placing 40  $\mu\text{L}$  of the final solution on the working area of a SPCEs (with a magnetic support on the reverse side) and applying a voltage of -0.45 V for 50 s, being the value of the current recorded at 5 s selected as analytical signal.

Selectivity was evaluated following the above detailed procedure but with the addition of solutions at 750 ng/mL of albumin from bovine serum (BSA), immunoglobulin G (IgG) or lysozyme (Lys) instead of 750 ng/mL hyaluronidase. Exudates from patients with both sterile and infected ulcers were also measured following the same immunoassay procedure than the detailed for the hyaluronidase standard solutions. Both control and infected swabs were provided by the Chronic Ulcers Unit of the Hospital Universitario

Central de Asturias (HUCA), where they were analyzed by traditional culture techniques to corroborate the presence of bacterial infection in the infected swab.

### **3.2.3. Results and discussion**

#### *3.2.3.1. Characterization of the PdNPs and Pd-AuNPs with variable Pd/Au content*

Pd-AuNPs were prepared adapting a previously described procedure consisting in the selective introduction of Au atoms on vertex or corner positions of Pd nanocluster, following a galvanic replacement reaction (Figure 3.1). The obtained PdNPs follow a “crown-jewel” model that was first described by Zhang et al.<sup>85</sup>, being this name related to the decoration that Au atoms do in the PdNPs, acting as jewels decorating a crown. This method is based on the synthesis of PdNPs, prepared by alcohol reduction in the presence of polyvinylpyrrolidone, and the subsequent introduction of Au atoms on top positions rather than sheltering the PdNPs. The introduction of Au atoms in these positions has been previously attributed to the difference in free energies associated to top, edges, and face atoms of a cluster, that affect the preference of Au atoms to occupy first top positions<sup>234,235</sup>.

The presence of both metals has a synergistic effect that increases their electrocatalytic activity. Moreover, the presence of external Au atoms facilitates the further conjugation of the obtained Pd-AuNPs with antibodies, owing to the Au affinity to the cysteine groups that are present in the immunoglobulin structure<sup>236,237</sup>.

---

<sup>234</sup> C.T. Campbell. *Science*. 306 (2004) 234–235

<sup>235</sup> N. Toshima, M. Kanemaru, Y. Shiraishi, Y. Koga. *J. Phys. Chem. B*. 109 (2005) 16326–16331.

<sup>236</sup> A. Ambrosi, M.T. Castañeda, A.J. Killard, M.R. Smyth, S. Alegret, A. Merkoçi. *Anal. Chem.* 79 (2007) 5232–5240.

<sup>237</sup> M. Brust, M. Walker, D. Bethell, D.J. Schiffrin, R. Whyman. *J Chem Soc Chem Commun.* 0 (1994) 801–802.

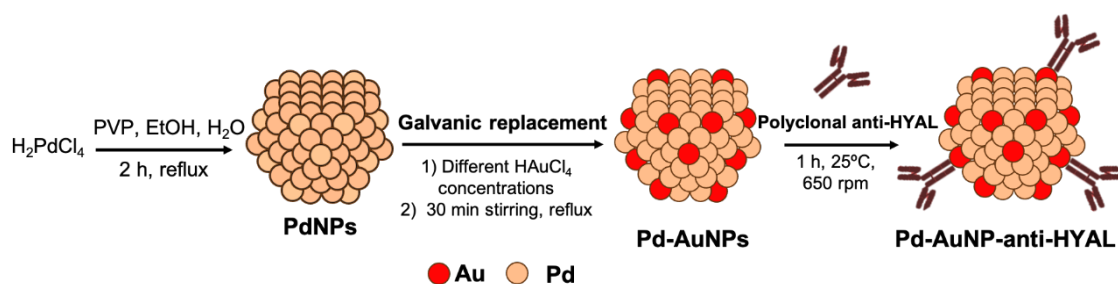


**Figure 3.1.** Schematic representation of PdNPs and Pd-AuNPs synthesis and further conjugation with polyclonal anti-hyaluronidase (HYAL) antibodies

Pd-AuNPs prepared with 0.835 mM  $H_2AuCl_4$  were selected as representative for their comparison with the starting PdNPs. High resolution-transmission electron microscopy (HRTEM) (Figure 3.2A-B) characterization showed spherical nanoparticles with a diameter of  $4 \pm 1$  nm for the PdNPs, while a slight increase in the size to  $5 \pm 1$  nm was noticed for Pd-AuNPs. It is worthy to mention that a slight aggregation is observed compared to initial PdNPs, probably due to the introduction of Au. Nevertheless, we observed that the introduction of tri-sodium citrate after the synthesis seems to regulate this effect. Moreover, STEM-TEM mode EDX analysis demonstrated the presence of both Pd and Au in the Pd-AuNPs structure, as expected (Figure 3.2C-E).

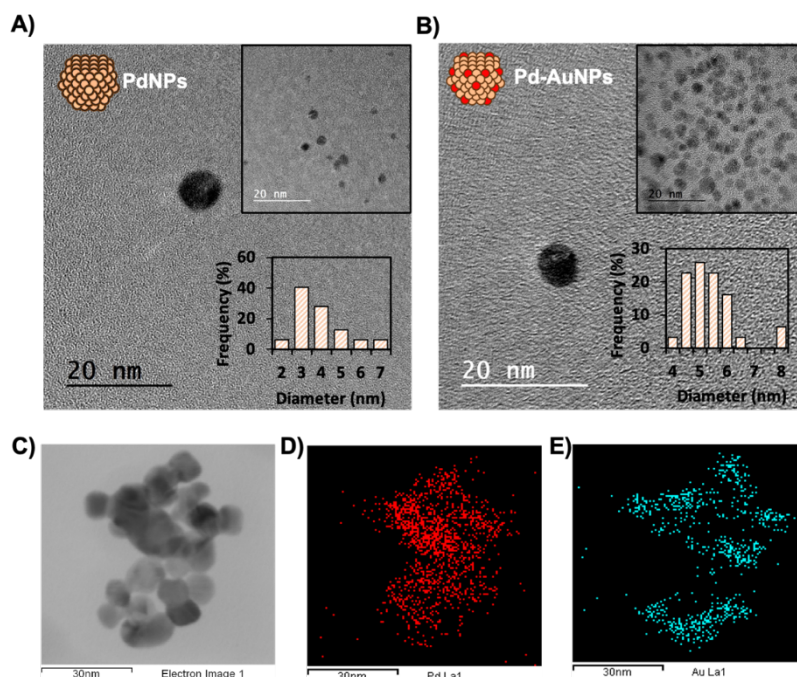


**Figure 3.2.** HRTEM micrographs of bimetallic Pd-AuNPs. PdNPs (A) and Pd-AuNP (B) (prepared with 0.835 mM  $H_2AuCl_4$ ) and their particle size distribution analysis (insets); The difference in the particle density observed in both pictures is due to the different samples dilution used for the analysis. C. Bright-field STEM micrograph showing Pd-AuNPs with the performed EDX area maps showing the presence of Pd elements (D) and Au elements (E).

The selective introduction of increasing amounts of Au slightly leads to the galvanic replacement of Pd surface atoms by Au atoms, leading to a higher covering and affecting the electrocatalytic activity of the final NPs. So bimetallic Pd-AuNPs were prepared by adding HAuCl<sub>4</sub> solutions at different concentrations ranging from 0.135 mM to 1.135 mM to the Pd nanocluster. The average elemental analysis done relying on EDX spectroscopy of the obtained Pd-AuNPs confirmed the presence of increasing proportions of Au on the NPs with increasing the incorporated Au concentration in the reaction (Table 1). This continued to be the case until reaching equal proportions of Pd and Au.

**Table 3.1.** Summary of the different synthesized Pd-AuNPs and characterization in terms of their Pd and Au average composition obtained through STEM-EDX analysis. Data are given as average  $\pm$  SD (n = 5).

Sample	[HAuCl <sub>4</sub> ] (mM)	STEM-EDX analysis	
		% Pd atom	% Au atom
Pd-AuNP-1	0.135	97 $\pm$ 1	3 $\pm$ 1
Pd-AuNP-2	0.735	83 $\pm$ 6	17 $\pm$ 3
Pd-AuNP-3	0.835	70 $\pm$ 3	30 $\pm$ 3
Pd-AuNP-4	0.935	56 $\pm$ 16	44 $\pm$ 16
Pd-AuNP-5	1.135	48 $\pm$ 3	52 $\pm$ 3

### 3.2.3.2. Evaluation of the electrocatalytic activity of Pd-AuNPs toward the oxygen reduction reaction (ORR): effect of the selective introduction of Au atoms in the Pd nanocluster

The electrocatalytic activity of the synthesized Pd-AuNPs toward the oxygen reduction reaction (ORR) was first evaluated by lineal sweep voltammetry (LSV) on SPCEs. LSV scans were recorded from 0 to -0.8V in PBS 10 mM pH 7.4 at a scan rate of 0.1 V/s. Pd-AuNP-3 (as described in Table 1) were chosen for this study, being the results compared with those obtained for the unmodified PdNPs. Commercial AuNPs of 5 nm in

diameter were also evaluated for comparison purposes (Figure 3.3). NPs concentration was  $1.45 \times 10^{12}$  NPs/mL in all cases.

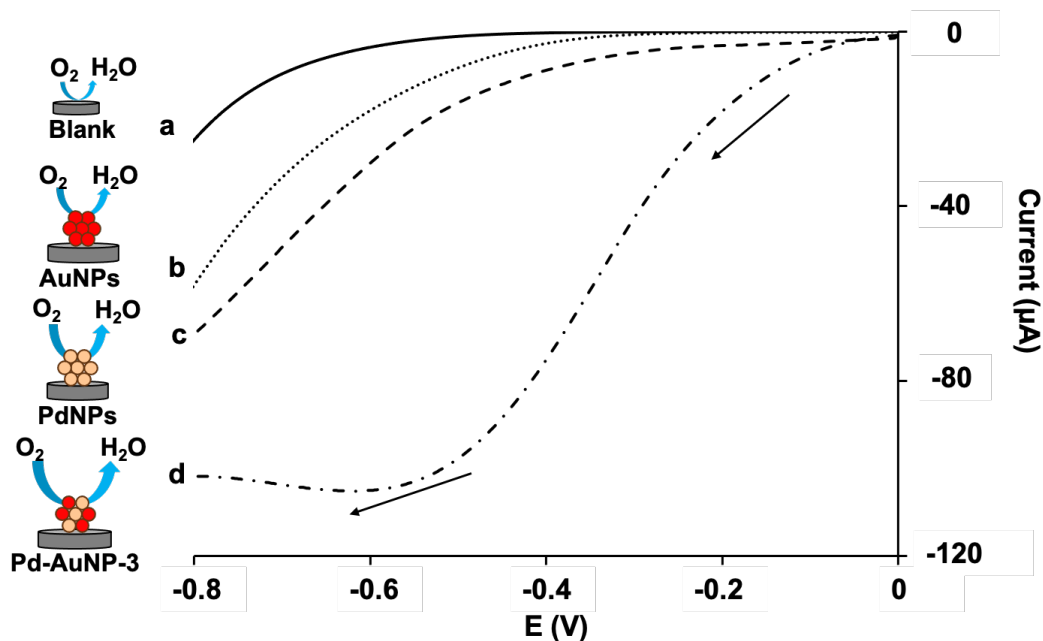


**Figure 3.3.** LSV for the obtained electrocatalytic nanoparticles. Recorded from 0 to -0.8 V at a scan rate of 0.1 V/s in 10 mM PBS pH 7.4, for a bare electrode (background; a) and for electrodes modified with AuNPs (b), PdNPs (c) and Pd-AuNP-3 (d). NPs concentration:  $1.45 \times 10^{12}$  NPs/mL.

The background (curve a) reveals that the oxygen reduction starts at approximately -0.70 V, and this value slightly shifts to -0.55 V in the presence of AuNPs (curve b). A notable shift of the half-wave potential to around -0.47 V is noticed for PdNPs, also noticing an increase in the associated current. Interestingly, this effect is dramatically enhanced for the Pd-AuNP-3, where the potential shifts to around -0.18 V, accompanied with a high increase in the associated current. This behaviour is in agreement with what was expected, due to the synergy in the catalytic activity of bimetallic NPs<sup>238,239,240,241</sup>, which assist on the cleavage of the O=O bond, lowering the energy barrier<sup>242</sup> of such intermediate.

Once corroborated the higher electrocatalytic activity of the bimetallic Pd-AuNPs compared with the individual PdNPs and AuNPs, the effect of the selective introduction

<sup>238</sup> J. Sha, S. Paul, F. Dumeignil, R. Wojcieszak. RSC Adv. 9 (2019) 29888–29901.

<sup>239</sup> J. Tang, D. Tang. Microchim. Acta. 182 (2015) 2077–2089.

<sup>240</sup> A. Wang, X.Y. Liu, C.-Y. Mou, T. Zhang. J. Catal. 308 (2013) 258–271.

<sup>241</sup> D. Zhao, B.-Q. Xu. Angew. Chem. Int. Ed. 45 (2006) 4955–4959.

<sup>242</sup> R. Ma, G. Lin, Y. Zhou, Q. Liu, T. Zhang, G. Shan, M. Yang, J. Wang. Npj Comput. Mater. 5 (2019) 78.

of Au atoms in the Pd nanocluster was studied, taking advantage of the chronoamperometric mode due to its high sensitivity, simplicity and speed. In agreement, with what was observed in the LSV study, a fix potential of -0.45 V was selected for the chronoamperometric measurements, being it applied for 50 s (Figure 3.4A). The absolute value of the current generated at 5 s (response time of the sensor; current profiles were not stable for shorter times) was chosen as the analytical signal used for the comparison between the different Pd-AuNPs prepared (Figure 3.4B). As observed, the NPs with only a 12% of Au (Pd-AuNP-1), give an absolute electrocatalytic current like that of the PdNPs cluster (around 11  $\mu\text{A}$ ). This suggests that although Au atoms are first introduced in the more reactive top positions (vertex and corner) of the cluster, due to the lower free energies of such atoms, this small amount is not enough to significantly enhance the catalytic activity of the Pd nanocluster. However, a dramatic increase in the absolute signal (to approx. 34  $\mu\text{A}$ ) is observed for the NPs with a 21% of Au (Pd-AuNP-2). A slight increase in the signal (to approx. 38  $\mu\text{A}$ ) is then observed when increasing the Au content to 30% (Pd-AuNP-3). Interestingly, increasing amounts of Au in the nanocluster (44% for Pd-AuNP-4 and 54% for Pd-AuNP-5) exert the opposite effect. These results indicate that the maximum synergy between both metals is reached for a Pd:Au ratio of approximately 2.3:1. The majority presence of the Au atoms in the vertex and corner positions of the cluster, with a high degree of coordinative unsaturation, makes them available for participating in the ORR reaction, also being responsible of such effect. in such positions of the cluster. However, for increasing amounts of Au synergy begins to lose, dominating the presence of Au, which is a worse catalyst than Pd, as corroborated by the small current (1.54  $\mu\text{A}$ ) recorded for AuNPs.



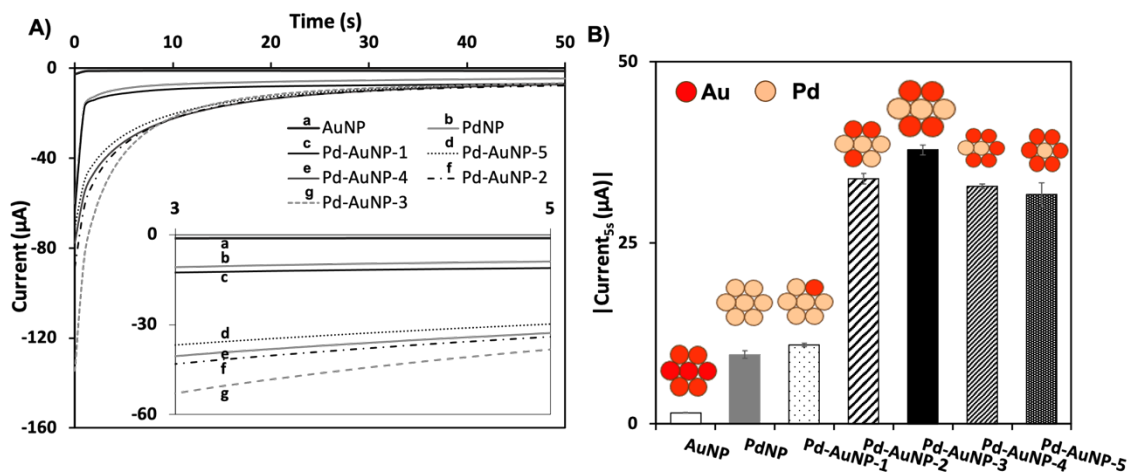


**Figure 3.4.** Electrochemical characterization of Pd-AuNPs with different Au content. A. Chronoamperograms recorded at -0.45 V for 50 s in PBS 10 mM pH 7.4 for AuNPs (a), PdNPs (b), Pd-AuNP-1 (c), Pd-AuNP-2 (f), Pd-AuNP-3 (g), Pd-AuNP-4 (e) and Pd-AuNP-5 (d). Inset corresponds to the region from 3 s to 5 s and from 0  $\mu\text{A}$  to -60  $\mu\text{A}$ . B. Comparison of the analytical signal (absolute value of current recorded at 5 s) for each NPs. Data are given as average  $\pm$  SD ( $n = 3$ ). NPs concentration:  $1.45 \times 10^{12}$  NPs/mL. NPs composition as detailed in Table 1.

According to these results, Pd-AuNP-3 were selected for their further use as electrocatalytic labels in biosensing. Before that, the ability of our electroanalytical method to quantify small amounts of such NPs was evaluated. Chronoamperometry, under the same conditions than the described above, was also selected for such quantitative studies. As observed in Figure 3.5A, a proportional increase of catalytic cathodic current was observed with corresponding increases in the concentration of Pd-AuNP-3. As shown in Figure 3.5B, a linear relationship between the analytical signal (current recorded at 5 s) and the Pd-AuNP-3 concentration was found in the range between  $1 \times 10^{10}$  and  $1.2 \times 10^{11}$  NPs/mL, adjusted to the following equation:

$$|\text{Current}_{5s}| (\mu\text{A}) = 1.63 \times 10^{-10} [\text{Pd-AuNP-3}] (\text{NPs/mL}) - 0.05$$

The calibration curve presented a good correlation coefficient ( $r$ ) of 0.9985 and reproducibility, with a standard deviation below 8.0% ( $n=3$ ). The limit of detection

(LOD), calculated as three times the standard deviation of the intercepted divided by the slope, was of  $5.97 \times 10^9$  NPs/mL.

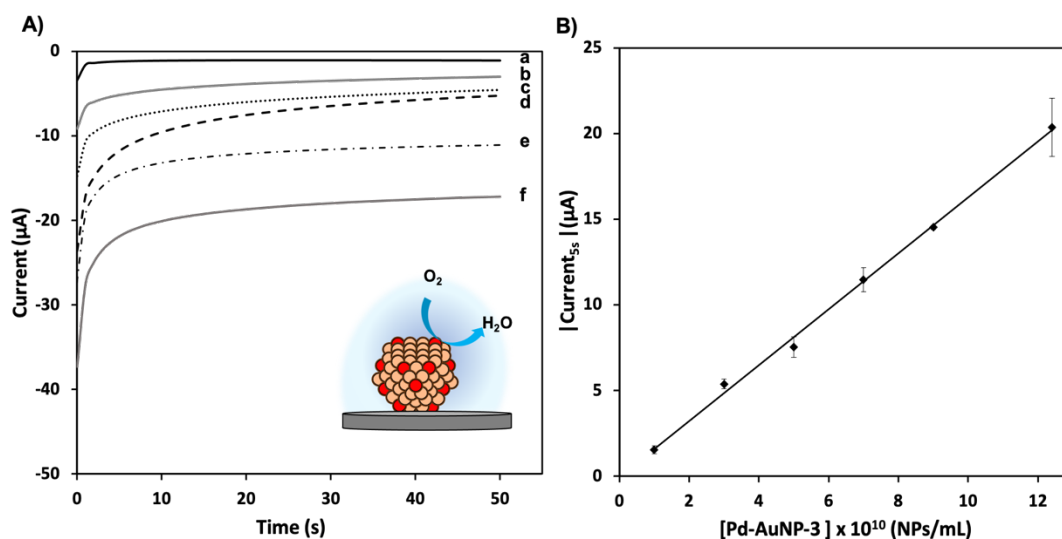


**Figure 3.5.** Chronoamperograms of Pd-AuNP-3 at different concentrations. A. Recorded at -0.45 V during 50 s in 10 mM PBS pH 7.4 for increasing concentrations of Pd-AuNP-3:  $1.00 \times 10^{10}$  NPs/mL (a),  $3.00 \times 10^{10}$  NPs/mL (b),  $5.00 \times 10^{10}$  NPs/mL (c),  $7.00 \times 10^{10}$  NPs/mL (d),  $9.00 \times 10^{10}$  NPs/mL (e) and  $1.20 \times 10^{11}$  NPs/mL (f). B. Relationship between the analytical signal (current at 5 s) and Pd-AuNP-3 concentration. Data are given as average  $\pm$  SD (n=3).

### 3.2.3.3. Electrocatalytic detection of hyaluronidase wound infection biomarker using Pd-AuNP tags

Hyaluronidase is an enzyme secreted as virulence factor by Gram-positive bacteria during a chronic wound infection. Hyaluronidase detection is useful for the identification of bacterial infection to provide the patients with the correct antibiotic treatment and thus reducing any bacterial antibiotic resistances. As a proof-of-concept of the suitability of the high electrocatalytically active Pd-AuNP-3 as labels, an immunosensor for the detection of hyaluronidase was developed. In this context, the evaluation of the Pd-AuNP-3 activity after conjugation with antibodies is of key relevance for the further biosensing application. As observed in Figure 3.6A, such Pd-AuNP-3/antibody conjugate retained most of the catalytic activity, allowing for its use as an electrochemical tag. The little decrease in activity compared with bare Pd-AuNP-3 could be attributed to a partial blocking of the Au surface by the antibodies, which might somehow affect the synergy

---

between both metals. This behavior was previously observed for other metallic and bimetallic NPs catalyzing different reactions<sup>243</sup>.

The developed immunosensor takes advantage of the use of MB as platforms to facilitate separation and minimizing matrix effects<sup>244,245</sup> (Figure 3.6B). The advantages of the MB-based immunoassays are well-known. First, the fact that the reactions take place in liquid phase, with stirring, allows to improve their kinetics, reducing the incubation times to approximately 20 minutes (typically 90 minutes for assays performed in solid phase). The magnetic separation performed after each incubation step also allows to pre-concentrate the sample, which leads to improved sensitivities. Moreover, such separation after capturing the analyte allows to remove the rest of compounds present in the sample which may interfere in the electrochemical measurement. This leads to a reduction of matrix effects and to an increase in selectivity.

Briefly, biotinylated monoclonal anti-hyaluronidase antibody (biotin anti-HYAL) was immobilized onto streptavidin-modified commercial magnetic beads and the conjugate was incubated with increasing concentrations of hyaluronidase. The resulting complex was put in contact with the MBs-hyaluronidase conjugate, forming the final immunosandwich. The use of antibodies as recognition elements confers the immunosensor with selectivity against hyaluronidase.

The resulting complex was placed on a SPCE, to which working electrode was attracted by the action of a small external magnet placed on its reverse side. The analytical method consists in applying a potential of -0.45 V in chronoamperometric mode and measuring the current recorded at 5 s (analytical signal), as optimized for the Pd-AuNP-3 determination.

---

<sup>243</sup> A. de la Escosura-Muñiz, C. Sánchez-Espinel, B. Díaz-Freitas, Á. González-Fernández, M. Maltez-da Costa, A. Merkoçi. *Anal. Chem.* 81 (2009) 10268–10274.

<sup>244</sup> M. Ahmadi, A. Ghoorchian, K. Dashtian, M. Kamalabadi, T. Madrakian, A. Afkhami. *Talanta*. 225 (2021).

<sup>245</sup> A. de la Escosura-Muñiz, L. Baptista-Pires, L. Serrano, L. Altet, O. Francino, A. Sánchez, A. Merkoçi. *Small*. 12 (2016) 205–213.

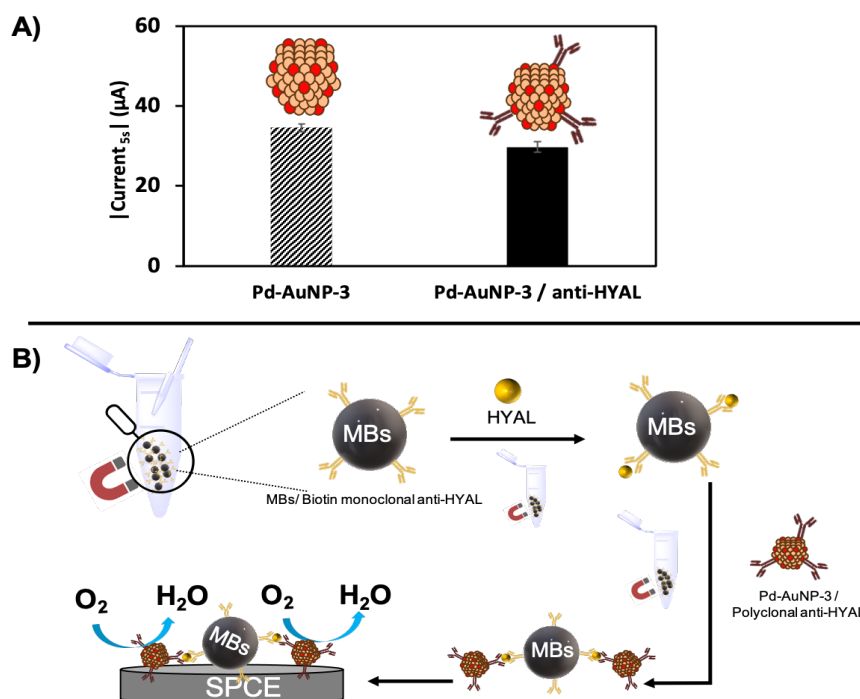


**Figure 3.6.** Suitability of the optimal Pd-AuNP-3 as labels in an immunosensor. A. Comparison of the analytical signals (coming from chronoamperograms obtained applying a potential of -0.45 V and measuring the current recorded at 5 s) for Pd-AuNP-3 and Pd-AuNP-3/ anti-HYAL conjugate. Data are given as average  $\pm$  SD (n=3). B. Schematic representation of the immunosensor developed for the detection of hyaluronidase (HYAL) using Pd-AuNP-3 tags and magnetic beads (MBs) platforms.

The absolute value of this current increases with the Pd-AuNP-3 concentration, due to their catalytic activity toward the ORR. So, when higher is the concentration of hyaluronidase in the immunoassay, higher is the amount of the Pd-AuNPs-3 tags, being the signals correlated with the analyte concentration, as shown in Figure 3.7A.

Dose-response experiments were performed in the range of 125 to 4600 ng/mL of hyaluronidase with a good linear relationship ( $r= 0.9982$ ) according to the following equation:

$$|Current_{5s}| (\mu A) = 0.003 [Hyaluronidase] (ng/mL) + 0.4432$$

The obtained LOD, calculated as three-times the SD of the intercepted divided by the slope was 50 ng/mL, equivalent to 0.02 U/mL (437 U/mg)<sup>63</sup>. The reproducibility of the method was also good with an RSD below 8% (n=3).

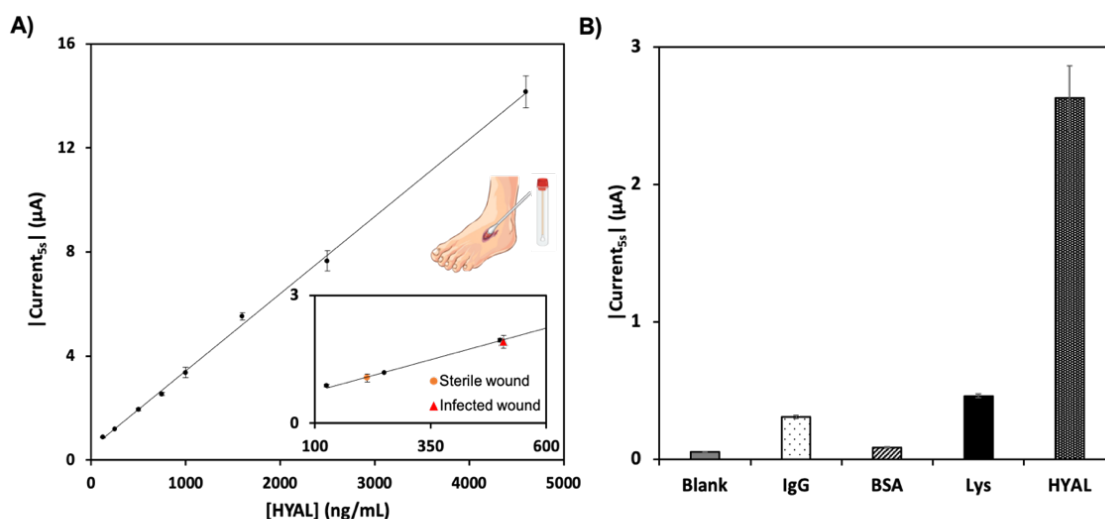


**Figure 3.7.** Calibration plot signals for hyaluronidase using Pd-AuNP-3 as labels. A. Coming from chronoamperograms obtained applying a potential of  $-0.45$  V and measuring the current recorded at 5 s, obtained for standard solutions of hyaluronidase (from 125 to 4600 ng/mL) as well as the analytical signals obtained for swab exudates from patients with sterile (circle) and infected (triangle) ulcers (inset). Data are given as average  $\pm$  SD ( $n=3$ ). B. Sensor response to different potential interferences, all of them at a concentration of 750 ng/mL. Data are given as average  $\pm$  SD ( $n=3$ ).

The obtained LOD is one of the lowest found in the biosensors-related bibliography (Table 3.2), demonstrating the excellent performance of our method based on the use of Pd-AuNP-3 tags.

#### 3.2.3.4. Selectivity studies and hyaluronidase determination in chronic wound exudates

Bacterial identification in chronic wound exudates in a short time and with a high selectivity is desirable for achieving a better screening methodology in wound infection handling. For that reason, attaining an analytical method with a high selectivity and good performance in real samples is advantageous. In this context, the use of MBs in the here developed immunosensor supposes a major advantage as they allow to separate biomolecules from complex samples, reducing matrix effects<sup>244245</sup>.

**Table 3.2.** Comparison with other reported biosensors for hyaluronidase detection.

Sensing principle	Transduction technique	Limit of detection (U/mL)	Sample	Ref
Bimetallic gold/silver nanoclusters-gold nanoparticles as fluorescence quencher	Fluorescence	0.3	Spike and recovery	246
Conjugated polymer nanoparticles and Au nanorods	Fluorescence	0.003	Spike and recovery	247
Water soluble fluorescence molybdenum disulfide quantum dots quenched by hyaluronic acid gold nanoparticles	Fluorescence	0.7	Spike and recovery	248
Carbon Dot/ Naphthalimide and hyaluronic acid Förster resonance energy transfer (FRET) mechanism	Fluorescence	0.09	Not tested	249
Electrostatic interaction between hyaluronic acid and Ru(bpy) <sub>3</sub> <sup>2+</sup>	Electrochemiluminescence	0.33	Spike and recovery	250
Methylene blue-hyaluronic acid complexes and enzymolysis through hyaluronidase	Differential pulse voltammetry (DPV)	0.28	Urine samples	251
Nanopores blocking by hyaluronidase	Differential pulse voltammetry (DPV)	64	Bacteria culture	63
Pd-AuNP-3 / MB immunosensor based on electrocatalytic activity toward the ORR	Chronoamperometry	0.02	Exudates from human wounds	This work

<sup>246</sup> Q. Liu, X. Yan, Q. Lai, X. Su. *Sens. Actuators B Chem.* 282 (2019) 45–51.

<sup>247</sup> Q. Wang, W. Fu, R. Ma, Q. Lu, Z. Liu, J. Yao, Q. Liu, X. Zhang, H. Zhao. *Dyes Pigments.* 197 (2022) 109844.

<sup>248</sup> W. Gu, Y. Yan, C. Zhang, C. Ding, Y. Xian. *ACS Appl. Mater. Interfaces.* 8 (2016) 11272–11279.

<sup>249</sup> P. Raj, S. Lee, T.Y. Lee. *Materials.* 14 (2021) 1313

<sup>250</sup> Z. Li, H. Chen, Z. Zhuo, D. Huang, F. Luo, L. Chen, J. Wang, L. Guo, B. Qiu, Z. Lin. *Sens. Actuators B Chem.* 275 (2018) 409–414.

<sup>251</sup> Z.-X. Li, J.-L. Zhang, J. Wang, F. Luo, B. Qiu, L.-H. Guo, Z.-Y. Lin. *J. Anal. Test.* 5 (2021) 69–75.

---

Selectivity of the Pd-AuNP-3 based immunosensor was evaluated against common analytes present in human samples, as it is BSA, IgG and lysozyme, another well-known infection biomarker<sup>252,253</sup>. Analytical signals recorded for each condition were insignificant comparing with hyaluronidase (Figure 3.7B), even in the presence of common wound exudate biomolecules as lysozyme. Thus, the Pd-AuNP-3/MBs based immunosensor had enhanced selectivity to hyaluronidase sensing without significant interferences.

Moreover, the immunosensor was evaluated in real samples obtained from exudates of patients with open wounds, being one from a patient with a sterile wound and the other one from an infected wound (Figure 3.7A, inset). The hyaluronidase concentration was directly extrapolated from the calibration curve, considering the low matrix effects observed in the presence of MBs. It can be clearly observed a difference between the hyaluronidase concentration detected in a clean ( $213 \pm 18$  ng/mL,  $0.09 \pm 0.008$  U/mL) and an infected wound ( $507 \pm 40$  ng/mL,  $0.22 \pm 0.017$  U/mL), attesting the suitability of the immunosensor to discriminate between them.

These levels are much lower than the provided by the gold standard turbidimetric assay, which has a linear range from 2-5 U/mL<sup>254</sup>. This makes it difficult to apply this method for validation. In addition, turbidimetric method requires a complex methodology that implies the use of hyaluronic acid for the enzymatic reaction, in contrast with the simplicity of our immunosensor.

Moreover, there is not a clear consensus in bibliography about the expected levels of hyaluronidase in infected and non-infected samples. Considering this, and the limitations of the turbidimetric assay, our immunosensor provides a useful tool for further carefully evaluation in a high number of patient samples. A threshold value for discriminating infected and non-infected samples should be further defined for a practical application of this method in a real scenario.

---

<sup>252</sup> A. Hasmann, E. Wehrschuetz-Sigl, G. Kanzler, U. Gewessler, E. Hulla, K.P. Schneider, B. Binder, M. Schintler, G.M. Guebitz. *Diagn. Microbiol. Infect. Dis.* 71 (2011) 12–23.

<sup>253</sup> N.H.C.S. Silva, P. Garrido-Pascual, C. Moreirinha, A. Almeida, T. Palomares, A. Alonso-Varona, C. Vilela, C.S.R. Freire. *Int. J. Biol. Macromol.* 165 (2020) 1198–1210.

<sup>254</sup> D. Chen, X. Zhu, W. Tao, Y. Kong, Y. Huag, Y. Zhang, R. Liu, L. Jiang, Y. Tang, H. Yu, Q. Hao, X. Yang, H. Zou, J. Chen, Y. Lu, H. Zhang, W. Li. *J. Controlled Release.* 324 (2020) 545–559.

### ***3.2.4. Conclusions***

In this work, we study for the first time the role that slight changes into the Pd/Au proportion have in the electrocatalytic activity of bimetallic Pd-AuNPs toward the ORR, together with their application as novel tags for the determination of an infection biomarker in chronic wound exudates.

The selective introduction of gold atoms on the palladium nanocluster, following a galvanic substitution procedure, is quantitatively evaluated by STEM-EDX analysis. Our findings indicate that, the synergy between both metals is strongly enhanced when the amount of gold is controlled and occupies the more reactive positions of the cluster, affecting the obtained electrocatalytic activity. This is of key relevance since it is observed that an excess of gold leads to a decrease in such activity. These findings may be of great interest not only for the biosensing application given in this work, but also for applications such as energy converting on fuel cells.

The optimal Pd-AuNPs (70% Pd, 30% Au) are used as tags, taking advantage of the bio-functionalities of gold present in the cluster, in an electrochemical immunosensor for the detection of hyaluronidase wound infection biomarker, using magnetic beads (MBs) platforms. The low matrix effects inherent to the use of MBs platforms allow us to discriminate between wound exudates with both sterile and infected ulcers without sample pre-treatment, meeting the clinical requirements. This novel electrocatalytic immunoassay has the advantage, over common methods for NP tags electrochemical detection, of the signal generation in the same neutral medium where the immunoassay takes place (10 mM PBS pH 7.4), avoiding the use of additional and hazardous reagents, bringing it closer to their use as point-of-care devices. This is particularly relevant in highly integrated systems such as lateral-flow assays, where our Pd-AuNPs have also potential interest since their optical properties (violet color with maximum of absorbance at 530 nm) allows to postulate them as tags for dual electrochemical/optical detection.



---

## Chapter 4. Magnetic nano and microparticles as sensing platforms

---

<b>4.1.</b>	<b><u>Summary</u></b> .....	<b>77</b>
<b>4.2.</b>	<b><u>Scientific article 5</u></b> .....	<b>79</b>
4.2.1.	<u>Introduction</u> .....	79
4.2.2.	<u>Protocols</u> .....	82
4.2.3.	<u>Results and discussion</u> .....	86
4.2.4.	<u>Conclusions</u> .....	98

---

---

## 4.1. Summary

Magnetic beads (MBs) have been notably used as platforms in biosensing thanks to their magnetic behavior as they allow to simplify purification and separation by preconcentrating the sample and also to minimize matrix effects, what facilitates the analysis of real samples. Even though it exists a variety of commercially available ones, there is still great interest to develop alternative MBs with improved performance. In this work, we propose the synthesis of novel, reliable and low-cost MBs by colloidal assembly of zinc doped magnetite for their use as electrochemical immunosensing platforms. First, zinc doped magnetite  $Zn_xFe_{3-x}O_4$  nanoparticles (ZnFeNPs) of a diameter of  $13 \pm 3$  nm and a saturation magnetization of 80 emu/g were synthesized and encapsulated in a polymeric matrix of poly(lactic-co-glycolic) acid (PLGA), generating polymeric MBs that were covered with polyethyleneimine (PEI) (MB@PEI), obtaining particles of  $96 \pm 16$  nm. The PEI external layer provides MBs with a higher degree of encapsulation and stability and with functional groups that convert MB@PEI particles in versatile tools for their use as immunosensing platforms. In order to compare the suitability of the obtained MBs with commercially available ones, the affinity protein neutravidin (NAV) was linked to the MB@PEI surface through glutaraldehyde crosslinking. The obtained MB@NAV exhibited a significantly higher saturation magnetization than commercially available NAV-modified MBs, and also a better reproducibility (RSD of 4% for MB@NAV and 12% for commercial MBs) and enhanced surface functionalization ability when used as immunosensing platforms in a model assay using gold nanoparticle tags. As proof-of-concept of application in real samples, MB@NAV were finally applied for the detection of Tau protein, a well-known Alzheimer's Disease (AD) biomarker, with a detection limit (LOD) of 63 ng/mL and an excellent performance in human serum samples.

---

## 4.2. Scientific article 5

Microchemical Journal 175 (2022) 107211



Contents lists available at [ScienceDirect](#)

Microchemical Journal

journal homepage: [www.elsevier.com/locate/microc](http://www.elsevier.com/locate/microc)



### Novel magnetic beads with improved performance for Alzheimer's disease biomarker detection

C. Toyos-Rodríguez<sup>a,b</sup>, A. Llamedo-González<sup>c,d</sup>, D. Pando<sup>c</sup>, S. García<sup>e</sup>, J.A. García<sup>f</sup>, F. J. García-Alonso<sup>b,d</sup>, A. de la Escosura-Muñiz<sup>a,b,\*</sup>

<sup>a</sup> NanoBioAnalysis Group-Department of Physical and Analytical Chemistry, University of Oviedo, Julián Clavería 8, 33006 Oviedo, Spain

<sup>b</sup> Biotechnology Institute of Asturias, University of Oviedo, Santiago Gascon Building, 33006 Oviedo, Spain

<sup>c</sup> Nanovex Biotechnologies S.L., Parque Tecnológico de Asturias Edificio CEEI, 33428 Llanera, Spain

<sup>d</sup> NanoBioAnalysis Group-Department of Organic and Inorganic Chemistry, University of Oviedo, Julián Clavería 8, 33006 Oviedo, Spain

<sup>e</sup> Department of Psychology, University of Oviedo, Oviedo, Spain

<sup>f</sup> NanoBioAnalysis Group-Department of Physics, University of Oviedo, Calvo Sotelo s/n, 33007 Oviedo, Spain

#### 4.2.1. Introduction

Magnetic particles (MPs), those containing metals like iron or nickel as elements, oxides, or mixed oxides, have emerged as relevant materials in many different areas including bioimaging<sup>255</sup>, drug delivery<sup>256</sup>, wastewater treatment<sup>257</sup>, biosensing<sup>258,244</sup> or in the isolation of complex matrices<sup>259</sup> among other applications.

MPs are typically used in the nanoscale range, from which superparamagnetic nanoparticles (SPIONs) are very appreciated by their stability and low toxicity<sup>260</sup>. In the nanoscale, the magnetic properties of these particles are size-dependent<sup>261</sup>. At lower diameters, lower than 20 nm, their saturation magnetization (Ms) increases with increasing particle size, regardless of particle shape. Up to 20 nm, the upper

<sup>255</sup> S. Mirza, M.S. Ahmad, M.I.A. Shah, M. Ateeq, *Met. Nanoparticles Drug Deliv. Diagn. Appl.*, Elsevier, 2020: pp. 189–213.

<sup>256</sup> L.H. Reddy, J.L. Arias, J. Nicolas, P. Couvreur. *Chem. Rev.* 112 (2012) 5818–5878

<sup>257</sup> S.C.N. Tang, I.M.C. Lo. *Water Res.* 47 (2013) 2613–2632.

<sup>258</sup> Y. Xu, E. Wang. *Electrochimica Acta.* 84 (2012) 62–73.

<sup>259</sup> A.-H. Lu, E.L. Salabas, F. Schüth. *Angew. Chem. Int. Ed.* 46 (2007) 1222–1244.

<sup>260</sup> R.B. Nasir Baig, M.N. Nadagouda, R.S. Varma. *Coord. Chem. Rev.* 287 (2015) 137–156.

<sup>261</sup> Y.-T. Chen, A.G. Kolhatkar, O. Zenasni, S. Xu, T.R. Lee. *Sensors.* 17 (2017) 2300.

---

superparamagnetic limit<sup>262</sup> their remanent magnetization ( $M_r$ ) starts to increase<sup>263,264</sup>. These SPIONs form stable liquid dispersions at room temperature<sup>262</sup> and exhibit high mobilities in the presence of external magnetic fields<sup>265</sup>. The most widely used route for the synthesis of SPIONs is the thermal decomposition of iron complexes as it generates high crystalline products with low polydispersity<sup>266</sup>.

The reduced size of SPIONs entails, however, a low magnetic moment ( $m$ ), what difficulties their functionalization without losing their magnetic behavior. An effective way to circumvent this difficulty is doping magnetite nanoparticles with  $Zn^{2+}$  ions, what enhances their magnetic properties, particularly its  $M_s$ , that increases significantly with the incorporation of a modest percentage of zinc(II) ions<sup>267,268,269</sup>.

Another common way to increase magnetism is the encapsulation of magnetic nanoparticles into the so-called magnetic beads (MBs) that is, polymer spheres containing nanomagnetic particles randomly dispersed<sup>270,271,272</sup>, thus the resulting material remains superparamagnetic but exhibits a fast response to external magnetic fields<sup>105</sup>. Accordingly, the employment of ZnFeNPs improves the magnetic moment of the MBs they are part of<sup>273</sup>, taking advantage of both strategies.

There are a huge number of polymers that can be used to synthesize MBs, including poly(lactic-co-glycolic) acid (PLGA)<sup>274,275,276,277</sup>. PLGA is a biocompatible, biodegradable polymer widely used for encapsulation of different compounds for

---

<sup>262</sup> L. Li, Y. Yang, J. Ding, J. Xue. *Chem Mater.* 22 (2010) 3183–3191.

<sup>263</sup> Q. Li, C.W. Kartikowati, S. Horie, T. Ogi, T. Iwaki, K. Okuyama. *Sci. Rep.* 7 (2017) 9894

<sup>264</sup> D. Ling, T. Hyeon. *Small.* 9 (2013) 1450–1466.

<sup>265</sup> C.G.C.M. Netto, H.E. Toma, L.H. Andrade. *J. Mol. Catal. B Enzym.* 85–86 (2013) 71–92

<sup>266</sup> K. Aguilar-Arteaga, J.A. Rodriguez, E. Barrado. *Anal. Chim. Acta.* 674 (2010) 157–165.

<sup>267</sup> J. Jang, H. Nah, J.-H. Lee, S.H. Moon, M.G. Kim, J. Cheon. *Angew. Chem. Int. Ed.* 48 (2009) 1234–1238.

<sup>268</sup> J.M. Byrne, V.S. Coker, E. Cespedes, P.L. Wincott, D.J. Vaughan, R.A.D. Patrick, G. van der Laan, E. Arenholz, F. Tuna, M. Bencsik, J.R. Lloyd, N.D. Adv. *Funct. Mater.* 24 (2014) 2518–2529.

<sup>269</sup> I. Castellanos-Rubio et al., *Chem. Mater.* 33 (2021) 3139–3154.

<sup>270</sup> O. Philippova, A. Barabanova, V. Molchanov, A. Khokhlov. *Eur. Polym. J.* 47 (2011) 542–559.

<sup>271</sup> Z. Lu, Y. Yin. *Chem. Soc. Rev.* 41 (2012) 6874.

<sup>272</sup> J. Guo, W. Yang, C. Wang. *Mater.* 25 (2013) 5196–5214.

<sup>273</sup> J. Park, M.D. Porter, M.C. Granger. *ACS Appl. Mater. Interfaces.* 9 (2017) 19569–19577.

<sup>274</sup> S.H. Chun, S.W. Shin, L. Amornkitbamrung, S.Y. Ahn, J.S. Yuk, S.J. Sim, D. Luo, S.H. Um. *Langmuir.* 34 (2018) 12827–12833.

<sup>275</sup> S.-J. Lee, H.-J. Kim, Y.-M. Huh, I.W. Kim, J.H. Jeong, J.-C. Kim, J.-D. Kim. *J. Nanosci. Nanotechnol.* 18 (2018) 1542–1547.

<sup>276</sup> N. Schleich, et al. *Int. J. Pharm.* 447 (2013) 94–101.

<sup>277</sup> S.-J. Lee, J.-R. Jeong, S.-C. Shin, J.-C. Kim, Y.-H. Chang, K.-H. Lee, J.-D. Kim. *Eng. Asp.* 255 (2005) 19–25.

diagnosis in biomedicine as it is approved by the Food and Drug administration (FDA) and the European Medicines Agency (EMA)<sup>278,279</sup>.

The use of MBs in immunosensing is extensive as they are interesting tools for the immobilization of biological recognition elements due to their high surface-to-volume ratio. As they can be moved by an external magnetic field, they allow the pre-concentration and separation of analytes of interest from complex samples, thus minimizing matrix effects<sup>280,281,282,283</sup>. Although the extensive use of commercially available MBs, there is still a great interest in obtaining alternative MBs for an improved performance<sup>284,285</sup>.

Among the wide variety of analytes detected using MBs as immunosensing platforms, it is worthy to mention their application for the detection of AD biomarkers (as collected in section 1.9.1. of the introduction). A $\beta$  peptides plaques and hyperphosphorylated microtubule-associated protein Tau stand out from the biomarkers used for AD diagnostics. Tau protein is the main microtubule associated protein of the brain, that regulates axonal growth, transport, or neuronal polarity through its phosphorylation. But, an hyperphosphorylation of this protein has been associated to the development of several neurodegenerative diseases, including AD<sup>124,125</sup>. In patients with AD, levels of Tau protein reach values of 195 pg/mL in CSF samples<sup>70</sup>, although further research is needed to stablish reliable methodologies for sample acquisition and measurement that reduce the variability observed in the clinic between protein levels and the development of the disease<sup>135,286</sup>.

In this work, ZnFeNPs with a high magnetization were synthesized following a thermal-decomposition procedure and used for the formation of MBs by encapsulation using PLGA as coating polymer. The obtained MB@PLGA were subsequently coated with polyethyleneimine (PEI) for increasing encapsulation and stability and providing the

---

<sup>278</sup> A. Jonderian, R. Maalouf. *Front. Pharmacol.* 7 (2016).

<sup>279</sup> L. Gomes dos Reis, W.-H. Lee, M. Svolos, L.M. Moir, R. Jaber, N. Windhab, P.M. Young, D. Traini. *Pharmaceutics.* 11 (2019) 12.

<sup>280</sup> T.A.P. Rocha-Santos. *Trends Anal. Chem.* 62 (2014) 28–36.

<sup>281</sup> J. Pansieri, M. Gerstenmayer, F. Lux, S. Mériaux, O. Tillement, V. Forge, B. Larrat, C. Marquette. *Nanomaterials.* 8 (2018) 740.

<sup>282</sup> M. Pedrero, S. Campuzano, J.M. Pingarrón. *Electroanalysis.* 24 (2012) 470–482.

<sup>283</sup> L. Fabiani, et al. *Biosens. Bioelectron.* 171 (2021) 112686.

<sup>284</sup> K. Luo, K.-B. Jeong, S.-M. You, D.-H. Lee, Y.-R. Kim. *J. Agric. Food Chem.* 66 (2018) 6806–6813.

<sup>285</sup> K. Luo, D.-H. Lee, H.J. Adra, Y.-R. Kim. *Carbohydr. Polym.* 218 (2019) 261–268.

<sup>286</sup> L.C. Brazaca, I. Sampaio, V. Zucolotto, B.C. Janegitz. *Talanta.* 210 (2020) 120644.



---

MBs with external functional groups for facilitating the ulterior bioconjugation of the affinity protein neutravidin (NAV) through glutaraldehyde crosslinking. The obtained MB@NAV were used as immunosensing platforms in a model immunoassay using gold nanoparticles (AuNPs) as labels, proving their suitability in immunosensing. Their performance was compared with that of commercially available MBs, showing comparable results with an increased reproducibility (RSD of 4% vs 12%) and an enhanced surface functionalization ability for the immobilization of specific antibodies. As proof-of-concept of application in real samples, MB@NAV were also implemented for the detection of Tau protein with a LOD of 63 ng/mL and a good performance in human serum sample.

## **4.2.2. Protocols**

### *4.2.2.1. Synthesis and characterization of ZnFeNPs*

ZnFeNPs were synthesized following a previously published procedure<sup>98</sup> with slight modifications. For the synthesis, 4 mmol Fe(acac)<sub>3</sub> and 0.68 mmol Zn(acac)<sub>2</sub> were dispersed in a mixture of 20 mL dibenzyl ether, 2.8 mL oleylamine and 2.7 mL oleic acid previously deoxygenated by purging Ar for 30 minutes. The mixture was placed in a three-necked round-bottom flask and heated with vigorous mechanical stirring, refrigeration, and inert atmosphere until reflux. When reflux was achieved, the reaction was maintained for 15 minutes under the same conditions. Afterwards, heating was removed, and the reaction was maintained at vigorous stirring for 15 minutes more, completing the first heating step. Then, a second heating step was performed by reconnecting the heating source and maintaining the reaction under reflux for 2 hours. After this time, heating was removed again, and the reaction was maintained under stirring for 30 minutes, when it was separated and let it cool down. The obtained particles were purified by washing with a mixture 1:1 in volume of 2-propanol and light petroleum ether using an external magnetic disk and dried under vacuum. Dried particles were reconstituted in 2-propanol at a concentration of ~100 mg/mL.

The obtained NPs were characterized through transmission electron microscopy (TEM), XRDP, IR, ICP and magnetic measurement of the room temperature hysteresis loops.

#### 4.2.2.2. *Synthesis and characterization of magnetic beads (MBs)*

MBs were synthesized following a water in oil emulsion procedure. First, 1.0 mL of ZnFeNPs suspension in 2-propanol was added to 2.0 mL of a 25 mg/mL PLGA solution in dimethylformamide (DMF) in a 15 mL centrifuge tube and vortexed for 15 seconds. The mixture was then transferred to a 50 mL centrifuge tube containing 15 mL of PVA 2% solution and then vortexed for 30 seconds and homogenized using a Branson® digital sonifier S450D during 1 minute in pulses of 1 second (30 pulses/min) at a 65% amplitude. The PLGA encapsulated MBs were transferred to a one-necked round bottom flask that contained 10 mL of PVA 1% solution and the suspension was stirred at 100 rpm, 20°C and 950 mbar for 45 minutes using a rotary evaporator to toughen the synthesized MBs. Next, the obtained MBs were washed three times with water using an external magnetic disk, and then resuspended in water for a final concentration of 10 mg/mL.

TEM, DLS (both size and  $\zeta$ -potential), IR and magnetic measurement of the room temperature hysteresis loops were used for the characterization of the MBs obtained here and after further functionalization.

#### 4.2.2.3. *MBs conjugation with neutravidin*

MB@PLGA were also functionalized with a layer of PEI for further conjugation with neutravidin (NAV) through glutaraldehyde linking. First, 1.0 mL of MBs with a concentration of 10 mg/mL in water were transferred to a 1.5 mL LoBind Eppendorf® and separated from the supernatant using a MagRack® 6 from Sigma-Aldrich. Then 1.0 mL of 4.0 mg/mL aqueous solution of PEI was added to the MBs and stirred using a Vortex for 1 hour. The MB@PEI were washed three times with water by using the magnetic rack MagRack® and, then 1.0 mL of 2.5% glutaraldehyde solution. The mixture was maintained under stirring in the Vortex during 30 min. After that, the reaction was washed three times with water using the MagRack® and, again with the supernatant removed, 1.0 mL of a 0.8 mg/mL solution of NAV in PBS 0.1M pH 7.2 was added. This suspension was stirred during 6 h using a Vortex and the excess of NAV was removed by washing three-times with PBS 0.1M pH 7.2 using the MagRack®. Finally, the

---

MB@NAV were suspended in 1 mL of PBS 0.1M pH 7.2 and maintained under refrigeration until its use.

#### *4.2.2.4.Synthesis of AuNPs and conjugation with antibodies*

AuNPs were synthesized following the method developed by Turkevich et al.<sup>82</sup>. Briefly, 100 mL of a solution  $2.94 \times 10^{-4}$  M of gold (III) chloride trihydrate were reduced by 2.5 mL of an aqueous solution  $3.88 \times 10^{-2}$  M of tri-sodium citrate dihydrate at boiling point and under vigorous stirring for 15 minutes. Then, the reaction was moved to a cold magnetic stirrer and maintained under vigorous stirring for 30 minutes. Past this time, 690  $\mu$ L of the as-synthesized AuNPs ( $9.00 \times 10^{14}$  NPs/mL) were transferred to a 1.5 mL LoBind Eppendorf® tube and centrifuged at 7500 g, 20°C for 30 min in the presence of 0.025% Tween-20. The supernatant was removed and 700  $\mu$ L of 2 mM trisodium citrate solution pH 7.3 were added. For the initial direct immunoassay (Section 2.7.), on this solution, 57.5  $\mu$ L of 100  $\mu$ g/ mL antibody (human IgG for positive samples and mouse-IgG for negative control) were added and the solution was incubated for 60 min at 25°C at gentle stirring. Finally, the solution was centrifuged at 7500 g, 4°C for 20 min and the pellet was resuspended in 0.1M PBS pH 7.2 with the addition of 1% BSA.

For the sandwich immunoassay for Tau protein detection (Section 2.8.), AuNPs were conjugated with Anti-Tau antibody, following the same procedure with the addition of Anti-Tau antibody in a concentration of 40  $\mu$ g/mL.

#### *4.2.2.5.Direct immunoassay for the evaluation of MB@NAV performance as immunosensing platforms*

For the evaluation of the ability of MB@NAV to be used as platforms in an immunoassay, they were conjugated with a biotinylated-anti-human IgG (anti-HIgG). Briefly, 15  $\mu$ L of a solution 10 mg/mL of MB@NAV were transferred to a 0.5 mL LoBind Eppendorf® tube and washed three-times with B&W buffer using a MagRack®. Then, MB@NAV were re-suspended in 108  $\mu$ L of B&W buffer, and 42  $\mu$ L of anti-HIgG (200  $\mu$ g/mL) were added. The solution was incubated during 30 min at 25°C and 650 rpm in a Thermo Shaker incubator. After this step, MB@NAV/anti-HIgG were washed three times with B&W buffer and resuspended in 150  $\mu$ L of BB solution followed by an incubation period of 1 h at 25°C and 650 rpm to prevent from unspecific absorption by blocking any

remaining active sites. MB@NAV/anti-HIgG were then washed three times with B&W buffer and the supernatant removed. Then, 150  $\mu\text{L}$  of AuNPs conjugated with human IgG (HIgG-AuNPs) were added and the solution was incubated for 30 min at 25°C and 650 rpm. After this step, MB@NAV/anti-HIgG/HIgG were separated and washed two times with B&W buffer and two times with 0.1M PBS pH 7.2 using a MagRack®. The final product was resuspended in 150  $\mu\text{L}$  of 0.1M PBS pH 7.2. Negative control assays were performed following the same experimental procedure but using mouse IgG (mIgG-AuNPs) instead of HIgG-AuNPs.

The electrochemical measurements were done taking advantage of the potential of AuNPs as catalysts of hydrogen evolution reaction (HER), following a previously optimized procedure<sup>213,243</sup>. For these measurements, 20  $\mu\text{L}$  of sample were placed on the working area of a SPCEs above a magnetic support and 20  $\mu\text{L}$  of a 0.2M HCl solution were added. Electrochemical measurements were done by applying an initial potential of +1.35V for 60 s and then measuring by chronoamperometry at a fixed potential of -1.00 V for 300s. The absolute value of the current at 300s was chosen as the analytical signal.

The same procedure was performed with commercially available streptavidin-modified magnetic beads, for comparison purposes.

#### *4.2.2.6. Sandwich immunoassay for Tau protein detection*

A similar procedure to the previously described for the direct immunosensor was done here for the detection of Tau protein. Briefly, 10  $\mu\text{L}$  of the obtained MB@NAV were re-suspended to a final volume of 150  $\mu\text{L}$  with B&W buffer and washed three-times with the same buffer. Then, MB@NAV were re-suspended in 108  $\mu\text{L}$  of B&W buffer and 42  $\mu\text{L}$  of biotinylated anti-Tau antibody (15  $\mu\text{g}/\text{mL}$ ) were added. The solution was incubated during 30 min at 25°C and 650 rpm in a Thermo Shaker incubator. After incubation MB@NAV/anti-Tau were washed three-times with B&W buffer, and 150  $\mu\text{L}$  of BB solution were added and incubated for 60 min in the same conditions. Then, another washing step was performed, and 100  $\mu\text{L}$  of Tau protein was added in concentrations ranging from 50 to 750 ng/mL and incubated for 30 min. After the incubation, MB@NAV/anti-Tau/Tau conjugate was washed three-times with B&W buffer and 150  $\mu\text{L}$  of the conjugate of AuNPs with anti-Tau antibody were added for the incubation during 60 min at the same conditions.

---

The final product was washed twice with B&W buffer and twice with 0.1M PBS pH 7.2 and measured in SPCEs above a magnetic support with the addition of 20  $\mu$ L of the final product and 20  $\mu$ L of 0.2M HCl, using the same electrochemical procedure as in the direct immunoassay.

#### *4.2.2.7. Spike and recovery protocol*

Spike and recovery experiment was performed to evaluate if the Tau protein detection was affected by the human serum matrix. A pool of serum samples of healthy patients obtained from the University Program for Seniors of Oviedo University, from the Memory Workshop from the Popular University, from Roces Senior Center, from Gijón-Sur Integrated Cultural Center, from Ateneo Integrated Cultural Center, and from San Agustín Senior Social Center (Spain) were used for such purpose. They met the following criteria: (1) no history of past or current psychiatric or neurological disorders and (2) a score higher than 26 in the Mini-Mental State Examination (MMSE). Also, subjects with acute comorbidities were excluded.

The serum was spiked with different concentrations of Tau (50 and 750 ng/mL) and then evaluated in the immunoassay (n=3 for each sample), following the same experimental procedure than the described in section 3.2.2.6.. The analytical signals were compared with those obtained for the standard samples in PBS buffer, calculating the % recovery of the analytical signal in the real matrix sample.

### **4.2.3. Results and discussion**

#### *4.2.3.1. Synthesis and characterization of ZnFeNPs*

ZnFeNPs have been proposed as an alternative to conventional SPIONs since it is known that the introduction of  $Zn^{2+}$  ions at the tetrahedral sites of SPIONs may increase the magnetic properties of these particles<sup>287</sup>. For that reason, their use in the formation of superparamagnetic MBs by encapsulation in polymeric matrixes has been postulated as an alternative to traditional SPIONs based MBs to improve magnetism without the need to increase the particles size. In this work, ZnFeNPs have been synthesized following a

---

<sup>287</sup> W. Szczerba et al. Chem. Chem. Phys. 18 (2016) 25221–25229.

previously published thermal-decomposition method developed by our group but using an appropriate mixture of Zn(acac)<sub>2</sub> and Fe(acac)<sub>3</sub> instead of using only Fe(acac)<sub>3</sub>. This method has advantages over electrochemical-based synthetic routes<sup>288,289</sup> in terms of simplicity, reproducibility and size-controllability<sup>264,290</sup>.

Figure 4.1.A. represents an electron micrograph of ZnFeNPs and the corresponding size distribution. The average size distribution of ZnFeNPs is  $13 \pm 3$  nm with a spherical shape an appropriate polydispersity. ZnFeNPs were also characterized by X-ray powder diffraction (XRDP) (Figure 4.1.B.). Compared to the standard Fe<sub>3</sub>O<sub>4</sub>, ZnFeNPs have a similar profile. To estimate the crystallinity domain size of the nanoparticles, a LeBail fitting method was performed using magnetite as standard sample, showing an average apparent size of  $15 \pm 9$  nm, a value that is within the range of that observed by TEM, also indicating that the ZnFeNPs are monocrystalline.

Composition of ZnFeNPs was also studied by ICP-MS, that provided a Zn/Fe ratio of 12:88 ( $\pm 1$ ), what indicates that the obtained NPs are doped with Zn. Additionally, it was proven that little modifications in the Zn/Fe ratio do not significantly affect their magnetic behavior (Table S.4.1.).

**Table S 4.1.** Different ZnFeNPs synthesized with different Zn content and its saturation magnetization (Ms) and coercivity (Hc) obtained.

Sample	Zn content	Fe content	Ms (emu/g)	Hc (Oe)
ZnFeNPs 1	1.2	1.8	$73.3 \pm 9.5$	$2.8 \pm 3.1$
ZnFeNPs 2	1	2	$79.8 \pm 1.2$	$5.5 \pm 4.0$
ZnFeNPs 3	0.8	2.2	$77.5 \pm 2.8$	$2.0 \pm 2.8$
ZnFeNPs 4	0.74	2.25	$81.7 \pm 4.1$	$9.1 \pm 11.0$
ZnFeNPs 5	0.43	2.57	$80.6 \pm 0.5$	$2.7 \pm 1.4$

<sup>288</sup> M. Rivero, A. del Campo, Á. Mayoral, E. Mazario, J. Sánchez-Marcos, A. Muñoz-Bonilla, RSC Adv. 6 (2016) 40067–40076.

<sup>289</sup> M. Jouyandeh et al. Prog. Org. Coat. 136 (2019) 105246.

<sup>290</sup> A. Ali, H. Zafar, M. Zia, I. ul Haq, A.R. Phull, J.S. Ali, A. Hussain. Nanotechnol. Sci. Appl. Volume 9 (2016) 49–67.

ZnFeNPs were also characterized by IR (Figure 4.1.C.), showing a broad band at  $570\text{ cm}^{-1}$ , due to solid-state vibrations of ferrites. The obtained ZnFeNPs were covered by oleic acid, what is confirmed by the presence of absorption bands of the oleate at  $\sim 2910\text{ cm}^{-1}$ , w, and  $\sim 2840\text{ cm}^{-1}$ , w (CH stretching), and  $\sim 1520\text{ cm}^{-1}$ , w, br and  $\sim 1420\text{ cm}^{-1}$ , w, br (symmetric and antisymmetric stretching of  $-\text{COO}$ ). This IR spectra is equal to the previously described for magnetite NPs<sup>98</sup> what suggests that the incorporation of Zn ions is by doping of the magnetite nanoparticles, as expected.

The magnetic hysteresis curve of ZnFeNPs (Figure 4.1.D.) showed a superparamagnetic behavior at room temperature, with a coercivity of 3 Oe and a saturation magnetization ( $M_s$ ) of  $81 \pm 1\text{ emu/g}$ , which is much higher than the previously described for magnetite NPs obtained by the same synthetic method (12 Oe and  $70\text{ emu/g}$ )<sup>98</sup>. Similar increases in the value of  $M_s$  have been described for other zinc doped magnetite<sup>287</sup>.

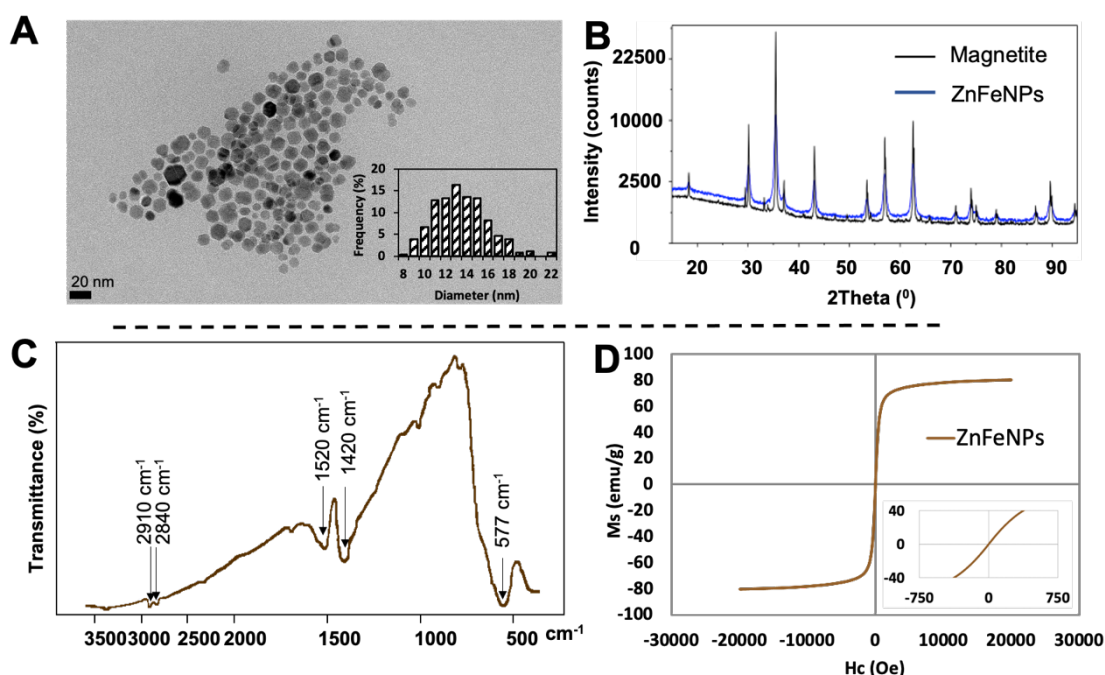


**Figure 4.1.** Characterization of ZnFeNPs. **A.** Electron micrographs of ZnFeNPs and size distribution histogram showing an average size diameter of 13 nm; **B.** XRD analysis of ZnFeNPs compared to magnetite as reference material. ZnFeNPs pattern presents a broadened profile; **C.** IR spectrum of ZnFeNPs; and **D.** Hysteresis curve of ZnFeNPs that shows a superparamagnetic behavior and a  $M_s$  of  $81\text{ emu/g}$  (inset shows amplified the low-field region of the hysteresis curve).

#### 4.2.3.2. Synthesis and characterization of magnetic beads (MBs)

The obtained ZnFeNPs were used for the formation of MBs following the procedure described in Figure 4.2, based on previously published methods with some modifications<sup>291,292</sup>. A dispersion of ZnFeNPs in 2-propanol was mixed with PLGA in DMF solution and incorporated into an aqueous phase of PVA, following a water in oil emulsion method. The contact of these two phases facilitates the assembling of ZnFeNPs and PLGA, leading to the formation of the MBs. PLGA is a biocompatible polymer widely used in drug delivery due to its effective encapsulation capacity and control release<sup>293</sup>, what provides a great versatility to the MBs obtained in this work<sup>294,295</sup>. MB@PLGA were also coated with a layer of PEI (MB@PEI) to achieve an improved encapsulation and stability. Also, PEI was selected as it facilitates the conjugation due to i) the primary amine groups of PEI and to ii) the well-known proton sponge effect of this polymer, associated to its high positive charge that facilitates the electrostatic interaction with negatively charged biomolecules<sup>296,297</sup>.

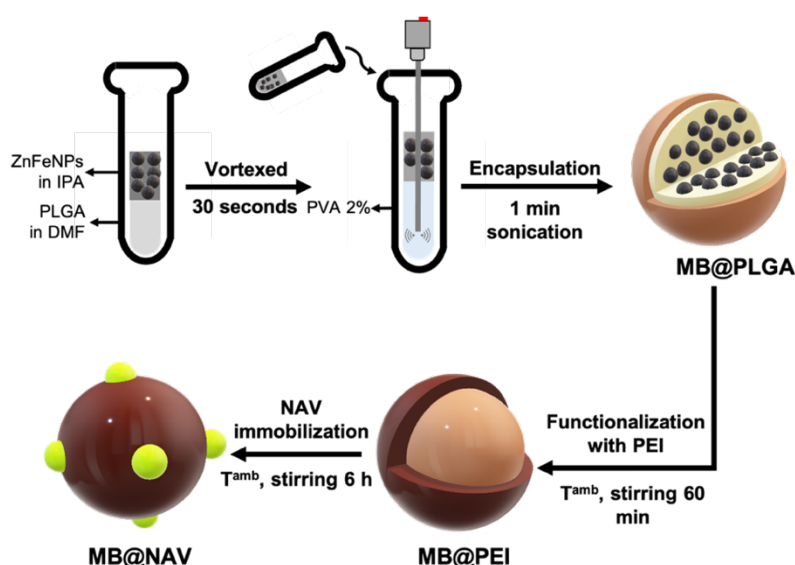


**Figure 4.2.** Schematic representation of the encapsulation-based assembly method for the synthesis of MB@NAV.

<sup>291</sup> J. Mosafer, K. Abnous, M. Tafaghodi, H. Jafarzadeh, M. Ramezani. *Eng. Asp.* 514 (2017) 146–154.

<sup>292</sup> X. Liu, M.D. Kaminski, H. Chen, M. Torno, L. Taylor, A.J. Rosengart. *J. Controlled Release.* 119 (2007) 52–58.

<sup>293</sup> F. Mohamed, C.F. van der Walle. *J. Pharm. Sci.* 97 (2008) 71–87.

<sup>294</sup> Y. Zhang, M. García-Gabilondo, A. Rosell, A. Roig. *Pharmaceutics.* 17 (2020) 16.

<sup>295</sup> J. Ghitman, E.I. Biru, R. Stan, H. Iovu. *Mater. Des.* 193 (2020) 108805.

<sup>296</sup> S. Nimesh, 10 - Polyethylenimine nanoparticles, in: *Gene Ther.*, Woodhead Publishing, 2013: pp. 197–223.

<sup>297</sup> C. Olbrich, U. Bakowsky, C.-M. Lehr, R.H. Müller, C. Kneuer. *J. Controlled Release.* 77 (2001) 345–355.



---

To obtain MBs suitable for their use as immunosensing platforms, the synthesized MB@PEI need to be functionalized with affinity proteins. To facilitate the comparison of the MBs synthesized in this work with commercially available ones, neutravidin (NAV) affinity protein was selected for the conjugation. NAV is, together with streptavidin, a biotin-recognition protein normally used as molecular recognition element in biosensing<sup>298</sup>. In this work, NAV was incorporated through glutaraldehyde as a crosslinker, thanks to its high reactivity<sup>299</sup>. This methodology may also be applied to different affinity proteins, thus increasing the versatility of the obtained MBs.

The obtained MBs were characterized in terms of size, DLS,  $\zeta$ -potential, IR and magnetic behavior by measuring the hysteresis loops at room temperature.

First, MBs were morphologically characterized, showing a spherical shape and an enhanced dispersity with an average diameter of  $89 \pm 18$  nm for MB@PLGA,  $96 \pm 16$  nm for MB@PEI and  $117 \pm 19$  nm for MB@NAV (Figure 4.3.A.) obtained from the TEM images. It is worthy mention that the encapsulation observed in the MB@PLGA is slightly worse as noticed in the left side inset in Figure 3.A., while this state is corrected after the incorporation of PEI. The presence of external NAV is correlated with the increased size of the final NP, as detected by DLS.

As it can be clearly seen, each MB is constituted by many individual ZnFeNPs. Considering the average volume of a MB and the average volume of a single ZnFeNP, it has been estimated that each MB is constituted by approximately 260 individuals ZnFeNPs (assuming that there are no holes inside the particle).

Measurement of the hydrodynamic size of the as-synthesized MBs indicates a change in the diameter of the particles after functionalization, going from 182 nm of MB@PLGA (Polydispersity index (PdI) of 0.098), 216 nm for MB@PEI (PdI of 0.147) to 414 nm (PdI 0.318) after the incorporation of NAV (Figure 4.3.B.), what tallies with the presence of this high molecular weight protein (~60 kDa). It is also worthy to mention that an increase in the PdI of the particles is also noticed, what suggests that the conjugation with NAV slightly favor aggregation compared to previous steps.

Functionalization has also been confirmed by measuring the  $\zeta$ -potential of MBs, which represents the external electrical potential in the surface of the suspended

---

<sup>298</sup> C.M. Pradier, M. Salmain, L.C. Méthievier. *Surf Interface Anal.* (2002) 5.

<sup>299</sup> I. Migneault, C. Dartiguenave, M.J. Bertrand, K.C. Waldron. *BioTechniques.* 37 (2004) 12.

particles<sup>300</sup>. The  $\zeta$ -potential (Figure 4.3.C.) of MB@PLGA suspended in milli-Q water was of  $-10 \pm 5$  mV due to the presence of external carboxylic groups own of acid terminations of the PLGA used. After the coating with PEI, the  $\zeta$ -potential changed to a positive value of  $27 \pm 6$  mV, corresponding to the presence of amine groups, confirming the successful incorporation of PEI.  $\zeta$ -potential of MB@NAV measured in PBS 0.1 M pH 7.2 shifts from  $27 \pm 6$  mV to  $-10 \pm 5$  mV, what correlates with the charge of NAV near its isoelectric point (pH 6.3)<sup>301</sup>.

To furtherly confirm the functionalization, MBs were characterized by IR (Figure 4.3.D.). The presence of the poly(lactic-co-glycolic) matrix in MB@PLGA nanoparticles is denoted mainly by the band at  $1752\text{ cm}^{-1}$ , due to the ester carbonyl group ( $\nu_{\text{C=O}}$ ) of the copolymer. It should be noticed the relative intensities of the peaks at  $1422$  and  $1384\text{ cm}^{-1}$  in the same IR spectrum, assignable to the C-H bending vibrations of the  $\text{CH}_3$  and  $\text{CH}_2$  groups. The stronger intensity of the band at  $1384\text{ cm}^{-1}$  indicates the presence of abundant methyl groups, as it is expected for the lactic repeating unit in PLGA<sup>302</sup>. Other absorptions of interest are those at  $1167$  and  $1090\text{ cm}^{-1}$ , due to the C-O-C groups of the polyester.

On the other hand, the most characteristic band of the PEI assigned to N-H bending should appear at  $1576\text{ cm}^{-1}$ <sup>303</sup>. However, in the infrared spectrum of the MB@PEI this peak is almost completely hidden by a  $\delta_{\text{OH}}$  band at  $1636\text{ cm}^{-1}$ , probably due to the presence of water. It should be mentioned that the intensities of the peaks at  $1422$  and  $1384\text{ cm}^{-1}$  are very similar, as expected, considering the predominant presence of  $\text{CH}_2$  groups in PEI. Additionally, bands corresponding to PLGA still remain, confirming that the incorporation of PEI does not remove the previously present PLGA.

Moreover, the presence of NAV could not be clearly identified through IR due to the multiple functional groups that compose this protein and to the previous structure of the MBs, although it could be seen an increase in the signal corresponding to  $\sim 1545\text{ cm}^{-1}$ . This peak corresponds to amide II band of the secondary amides present in the NAV protein.

---

<sup>300</sup> G.W. Lu, P. Gao, Emulsions and Microemulsions for Topical and Transdermal Drug Delivery, in: Handb. Non-Invasive Drug Deliv. Syst., Elsevier, 2010: pp. 59–94.

<sup>301</sup> I. Barinaga-Rementería Ramírez, L. Ekblad, B. Jergil. J. Chromatogr. B. Biomed. Sci. App. 743 (2000) 389–396.

<sup>302</sup> J. Coates, Interpretation of Infrared Spectra, A Practical Approach, in: R.A. Meyers (Ed.), Encycl. Anal. Chem., John Wiley & Sons, Ltd, Chichester, UK, 2006: p. a5606.

<sup>303</sup> F. Wang, P. Liu, T. Nie, H. Wei, Z. Cui. Int. J. Mol. Sci. 14 (2012) 17–29.

---

Magnetic behavior of all the obtained MBs was measured at room temperature (Figure 4.3.E.). The saturation magnetization ( $M_s$ ) of MB@PLGA was of  $54 \pm 2$  emu/g, while after the coating with PEI this value increased to  $63 \pm 5$  emu/g. Although it should be expected a decrease in  $M_s$  with the increase of non-magnetic components<sup>304</sup>, the higher degree of encapsulation observed through TEM measurements for MB@PEI and the purification stages performed after functionalization has allowed us to separate and purify those MBs with an increased magnetic saturation, what could explain the improvement observed.

Regarding superparamagnetic behavior, MB@PLGA present a reduced remanence with a coercivity of 10 Oe, what indicates that the clustering of individual ZnFeNPs into MBs allows to maintain the superparamagnetic behavior of the individual nanoparticles. This value increases to 14 Oe after the incorporation of PEI. Regarding the magnetic behavior of MB@NAV, it is observed a slight decrease in the  $M_s$  (from  $63 \pm 5$  emu/g to  $54 \pm 1$  emu/g) and an increase in the coercivity (from 14 to 16 Oe) of the particles. Commercially available MB were also measured for comparison purposes, showing a  $M_s$

---

<sup>304</sup> W. Wu, Q. He, C. Jiang. *Nanoscale Res. Lett.* 3 (2008) 397–415

of 11 emu/g with a coercivity of 2 Oe. The low value of total  $m$  noticed for such MBs is probably due to the high proportion of non-magnetic material, as previously reported<sup>273</sup>.

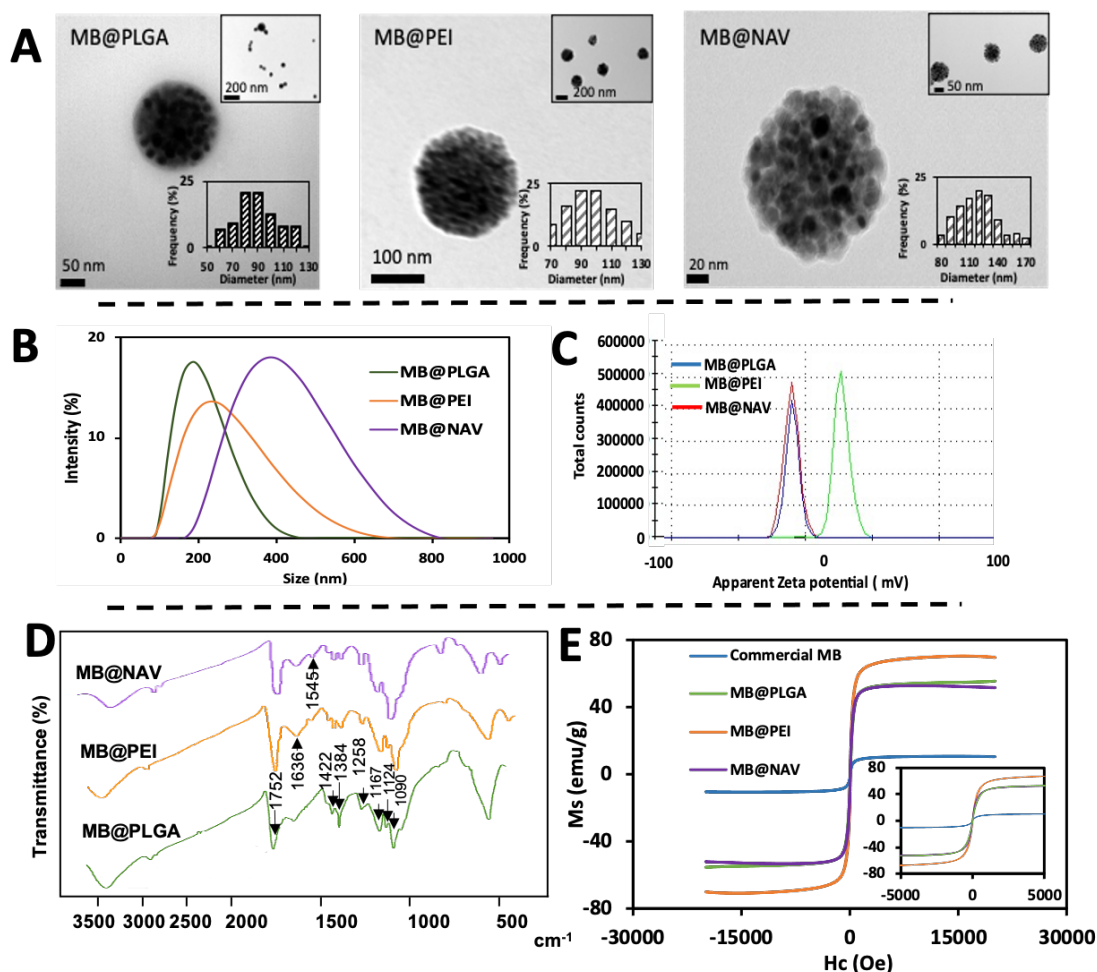


**Figure 4.3.** Characterization of MBs. **A.** TEM micrographs of MB@PLGA, MB@PEI and MB@NAV and the corresponding size distribution histogram. An inset of higher magnification is included in the right side of the micrographs; **B.** Hydrodynamic diameter of all MBs in which it is observed a change after functionalization; **C.**  $\zeta$ -potential showing a shift from a negative value for MB@PLGA (external carboxylic groups) to a positive value for MB@PEI (external amine groups) and again, to a negative value after the incorporation of NAV (external imine groups); **D.** IR spectrum of MB@PLGA, MB@PEI and MB@NAV; and **E.** Hysteresis curves of MB@PLGA (54 emu/g), MB@PEI (63 emu/g), MB@NAV (54 emu/g) and the commercially available MBs (11 emu/g). Inset represents an amplification of the low-field region of the hysteresis curves.

#### 4.2.3.3. Direct immunoassay for the evaluation of MB@NAV performance

A direct immunoassay was performed for i) the evaluation of the ability of the MB@NAV to be used as immunosensing platforms and ii) as a comparison of the performance of the MB@NAV with that of the commercial MBs. Both MB@NAV and

---

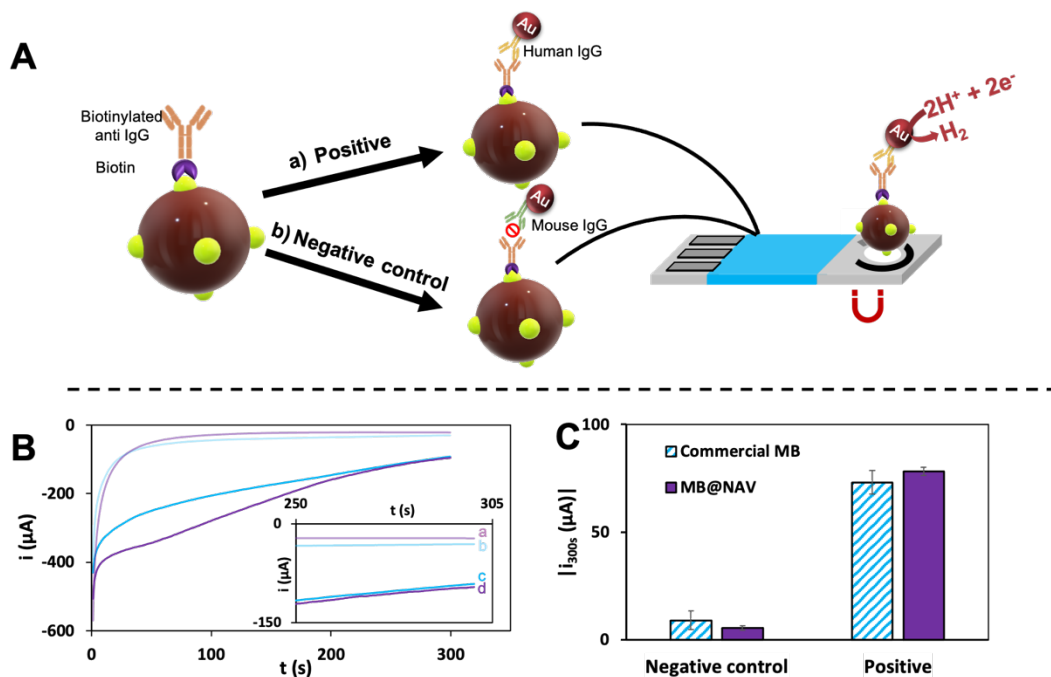
commercial MBs were bioconjugated with biotinylated anti-human IgG (anti-HIgG) and let to react with human IgG (HIgG), previously conjugated with AuNP tags. Mouse IgG (MIgG) conjugated with AuNPs was used as negative control (Figure 4.4.A.). Electrochemical detection was based on the electrocatalytic activity of AuNPs toward the hydrogen evolution reaction (HER)<sup>305</sup>, by applying a potential of -1.0 V during 300 s, selecting the value of the current recorded at 300 s as the analytical signal<sup>213,306</sup>.

Figure 4.4.B. shows the chronoamperograms recorded during the stage of hydrogen ion electroreduction for the different assays evaluated. An increase in the catalytic current is clearly observed for the positive assays compared with the control ones. The comparison of the average analytical signals and their standard deviation (n=3) shown in Figure 4.4.C. suggest that MB@NAV have a better performance than the commercial ones. First, positive samples provide higher signals, which suggests an enhanced ability of the MB@NAV to capture antibodies. Moreover, the signals recorded for negative control samples were smaller for the MB@NAV, what may indicate a lower unspecific absorption of protein/AuNP conjugates. In addition, the reproducibility obtained with MB@NAV was better than that of the commercial MBs, giving a relative standard deviation (RSD) of 4% (RSD of 12% for commercial MBs).

---

<sup>305</sup> T.D. Tran, M.T.T. Nguyen, H.V. Le, D.N. Nguyen, A. Truong, P.D. Tran. *Chem. Commun.* 54 (2018) 3363–3366.

<sup>306</sup> M. Espinoza-Castañeda et al. *Biosens. Bioelectron.* 40 (2013) 271–276.



**Figure 4.4.** Direct immunoassay for the evaluation of MB@NAV performance. **A.** Schematic representation of the direct immunoassay performed for the evaluation of the MB@NAV performance; **B.** Chronoamperograms recorded by applying a potential of  $-1.00$  V for 300 seconds in 1M HCl for: a. Negative control with MB@NAV, b. negative control with commercial MBs, c. positive control with commercial MBs and d. positive control with MB@NAV (inset shows an amplification of the region near 300 s); **C.** Current obtained at 300s (analytical signal) for the negative control and positive control with both MB@NAV synthesized in this work (purple) and commercial MBs (blue lines). Background current of  $16.5$   $\mu\text{A}$  corresponding to the hydrogen evolution in the bare carbon electrode was subtracted from all measurements.

#### 4.2.3.4. Sandwich immunoassay for the detection of Tau protein using MB@NAV

Once evaluated the ability of the MB@NAV to efficiently act as immunosensing platform, they were applied for the detection of Tau protein, an AD biomarker, in a sandwich immunoassay format. The structure of the immunoassay is schematized in Figure 4.5.A. Briefly, a biotinylated anti-Tau antibody was immobilized on the MB@NAV and the conjugate was then incubated with samples containing concentrations of Tau protein ranging from 50-750 ng/mL, in a dose-response assay. The sandwich was then completed with anti-Tau antibody conjugated with AuNPs, that were detected based on the HER reaction, as described above.

The results obtained are represented in Figure 4.5.B. and depict that there is a direct correlation between the catalytic current recorded and the concentration of Tau protein.

Figure 4.5.C. shows that there is a good linear relationship between the two parameters in the range 50-750 ng/mL, with a correlation coefficient of 0.9963, according to the equation:

$$Current_{300s} = 0.1264 [Tau] (ng/mL) + 63.043$$

The limit of detection (LOD) was calculated as three times the standard deviation of the intercepted divided by the slope, resulting in a value of 63 ng/mL. The method showed an excellent reproducibility, with an average relative standard deviation (RSD) of 4 % (n=3).

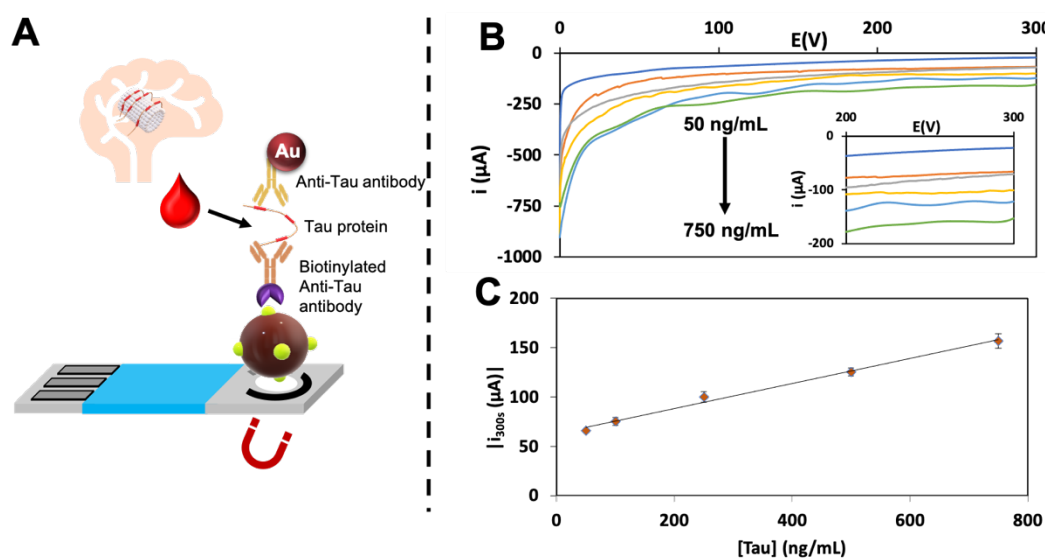


**Figure 4.5.** Use of the obtained MBs in an immunosensor for Tau protein detection. **A.** Schematic representation of the biosensor used for the detection of Tau protein by the immobilization of biotinylated anti-Tau antibodies onto MB@NAV; **B.** Chronoamperograms recorded by applying a potential of -1.00 V for 300 seconds in 0.1M HCl for each Tau concentration ranging between 50-750 ng/mL. Inside, an inset of the signal recorded at the region near 300 s; **C.** Calibration curve of the current recorded at 300s for each Tau concentration.

Tau protein has been selected as model analyte in our proof-of-concept, instead of i.e. hyperphosphorylated one due to the following reasons. Although there is still controversy on the clinical implications of total Tau protein as predictor of neurodegeneration<sup>307,308</sup> and its role in AD, there is no consensus on hyperphosphorylated Tau (p-tau) too, as it is not clear which p-tau isoform is more relevant in AD. Even though p-tau181 has been mainly stated as AD biomarker in blood<sup>309</sup>, the role of p-tau217 has

<sup>307</sup> M.P. Pase, et al. JAMA Neurol. 76 (2019) 598.

<sup>308</sup> M.A. Sugarman, et al. Neurobiol. Aging. 94 (2020) 60–70.

<sup>309</sup> T.K. Karikari, et al. Lancet Neurol. 19 (2020) 422–433.

also stood out<sup>310,311</sup>. The difference between both isoforms relies on the amino acid residue that is phosphorylated. These clinical results point out that the mechanism of action of Tau protein in AD still requires further investigation. For these reasons, the identification of Tau protein as proof-of-concept is an extended practice in immunosensing for AD diagnostics (i.e. Razzino et al., *Biosensors and Bioelectronics* (2020) 163 112238)<sup>135</sup>.

This is way we have selected Tau protein as analyte in our proof-of-concept work. It is worthy to highlight that our biosensing system may be easily adapted to the determination of p-tau, just using suitable antibodies that are commercially available.

#### 4.2.3.5. Tau protein analysis in human serum samples: Spike and recovery

The final objective of the development of an analytic biosensor is the detection of biomolecules in real samples. In this context, it has been evaluated the performance of the biosensor in a serum sample of cognitively healthy patients, demonstrating the selectivity of the analytical method in the real scenario. For that purpose, a spike and recovery method was performed obtaining a high recovery rate at levels around 85-89% (Table 4.1). These results indicate that the presence of other components in real samples do not significantly interfere in the accurate detection of Tau protein, opening the way to the use of the here described methodology to the evaluation of samples from AD patients.

**Table 4.1.** Spike and recovery assay data for Tau protein

Sample	Spiked Tau (ng/mL)	Current in PBS (μA)	Current in real sample (μA)	Recovery (%)
Serum from cognitively healthy subjects	50	-66,12	-56,15	85%
	750	-156,8	-139,0	89%

<sup>310</sup> S. Janelidze, et al. *Nat. Commun.* 11 (2020) 1683.

<sup>311</sup> E.H. Thijssen, et al. *Lancet Neurol.* 20 (2021) 739–752.



---

#### 4.2.4. Conclusions

In this work, we report a novel method for obtaining magnetic beads (MBs) with improved performance as immunosensing platforms, which is applied for the detection of Tau protein, an Alzheimer's disease biomarker in human serum.

First, ZnFeNPs were obtained by a thermal-decomposition method, demonstrating that the doping with Zn atoms of the magnetite nanoparticles, clearly enhances their magnetic behavior. The obtained ZnFeNPs are used for the formation of MBs by encapsulation in a PLGA polymeric matrix. To facilitate their use as immunosensing platform, MB@PLGA were first functionalized with PEI and then NAV was furtherly immobilized on their surface. In all cases, MBs maintained their superparamagnetic behavior with high saturation magnetization values, assuring that encapsulation of single nanoparticles works as a way of maintaining magnetism while allowing further functionalization. Moreover, the saturation magnetization obtained for the as-synthesized MB@NAV was significantly higher than that of commercial MBs, constituting an important practical advantage.

The performance of MB@NAV in a direct immunoassay for detecting HIgG using AuNPs as labels showed lower RSD for MB@NAV compared to commercial MBs, thus improving the reproducibility of the assay. Moreover, the lower and higher net currents recorded with MB@NAV for control and positive samples respectively suggested that the here described MBs provide lower non-specific adsorptions as they have a greater surface functionalization ability.

These results prove the effectivity of the obtained MB@NAV as immunosensing platforms, and their versatility opens the way to their use for a wide variety of applications. The developed immunosensor for Tau protein detection constitutes just a proof-of-concept of the potential ability of such MBs to be used immunosensing platforms for an interesting application in real samples. The low matrix effects (high recoveries) observed in human serum samples demonstrate the excellent performance of our MBs in a real scenario. Although the detection limit obtained in our proof-of-concept study (63 ng/mL) is higher than the required for AD diagnostics (pg/mL levels in human serum), the versatility of both the MBs and the nanoparticle tags allow to make feasible further optimizations for meeting such clinical needs. On the one hand, it is well-known that the magnetic separation performed after each incubation step allows to pre-

concentrate the sample. This means that higher sample volumes than the evaluated in our work (150  $\mu\text{L}$ ) may be assayed, capturing a higher amount of the AD biomarker. After removing the supernatant, MBs may be re-suspended in a smaller volume, leading to the sample pre-concentration. Regarding the tag, current research in our group (and others) is focused on alternative bimetallic nanoparticles with electrocatalytic properties that can be detected at lower levels than the AuNPs.

Such studies, together with a careful evaluation of patient samples will be object of future research.



## Chapter 5. Nanoporous membranes as integrated platforms for biomarkers detection

---

<b>5.1. Summary</b> .....	<b>103</b>
<b>5.2. Scientific article 6</b> .....	<b>105</b>
5.2.1. Introduction.....	105
5.2.2. Protocols .....	108
5.2.3. Results and discussion .....	111
5.2.4. Conclusions.....	123
<b>5.3. Scientific article 7</b> .....	<b>125</b>
5.3.1. Introduction.....	125
5.3.2. Protocols .....	129
5.3.3. Results and discussion .....	131
5.3.4. Conclusions.....	140
<b>5.4. Scientific article 8</b> .....	<b>143</b>
5.4.1. Introduction.....	143
5.4.2. Protocols .....	145
5.4.3. Results and discussion .....	147
5.4.4. Conclusions.....	153

---



## 5.1. Summary

Nanoporous membranes have been increasingly introduced in biosensing applications over the last decade due to their easy functionalization, large surface area, stability, and filtering properties. In these biosensing applications, detection is based on the blocking and unblocking of the nanochannels, leading to a change in the analytical signal recorded. To achieve so, controlling the electrostatic and steric effects that govern blocking is paramount.

In this Chapter, nanoporous membranes have been first used for the detection of Tau protein (Section 5.2.), in a novel work aiming to understand the effect of both the recognition element (in this case an antibody) and the immunocomplex (antibody/antigen) on the overall charges inside the nanochannel. The captured Tau protein blocks the nanochannel and difficulties the passage of red-ox indicator ions, which are voltammetrically monitored using an indium tin oxide/poly(ethylene terephthalate) (ITO/PET) electrode as transducer. The developed biosensing system allows the determination of Tau protein with a detection limit of 4.3 ng/mL, which is within the range of clinical interest, showing also excellent recovery percentages in human plasma samples.

In a later work (Section 5.3.), an unblocking strategy was used for the detection of lysozyme by the immobilization in the inner walls of the nanochannels, peptidoglycan, the native substrate of lysozyme. In this case, both electrostatic and steric effects were evaluated, checking how nanochannel diameter affects the blockage obtained.

The diameter of the nanochannel is not the only factor that affects electrostatic blockage, pore thickness also has an influenced. Therefore, this parameter was also studied in a complementary work (Section 5.4.) observing that a reduced pore thickness helps to achieve a lower limit of detection compared to nanoporous membranes with higher pore thickness but reduced pore diameter sizes.



## 5.2. Scientific article 6

Sensors & Actuators: B. Chemical 380 (2023) 133394



Contents lists available at ScienceDirect

Sensors and Actuators: B. Chemical

journal homepage: [www.elsevier.com/locate/snb](http://www.elsevier.com/locate/snb)



Towards the maximization of nanochannels blockage through antibody-antigen charge control: Application for the detection of an Alzheimer's disease biomarker

Celia Toyos-Rodríguez<sup>a,b</sup>, Francisco Javier García-Alonso<sup>b,c</sup>, Alfredo de la Escosura-Muñiz<sup>a,b,\*</sup>

<sup>a</sup> NanoBioAnalysis Group-Department of Physical and Analytical Chemistry, University of Oviedo, Julián Clavería 8, 33006 Oviedo, Spain

<sup>b</sup> Biotechnology Institute of Asturias, University of Oviedo, Santiago Gascon Building, 33006 Oviedo, Spain

<sup>c</sup> NanoBioAnalysis Group-Department of Organic and Inorganic Chemistry, University of Oviedo, Julián Clavería 8, 33006 Oviedo, Spain

### 5.2.1. Introduction

Neurodegenerative diseases are multifactorial pathologies that act on the central and peripheral nervous system<sup>312</sup>. The incidence of these pathologies increases among age, so that the rise in life expectancy is expected to worsen their burden<sup>313</sup>. From all of them, AD is the most common, affecting 30% of people older than 85 years, a value that is increasing in a 6-8% yearly<sup>314,315</sup>. For that reason, a rapid detection is a major concern and, in this process, AD biomarkers, between which Tau protein is included, have been identified as a research priority<sup>316</sup>.

Tau protein plays a pivotal role in the development of several neurodegenerative diseases, known as tauopathies<sup>317</sup>. AD, frontotemporal lobar dementia (FTD)<sup>318</sup> or corticobasal degeneration (CBD) are some of them. In the case of AD, Tau is related with the formation of neurofibrillary tangles (NFTs)<sup>319</sup>. All of it, constitutes Tau as a common

<sup>312</sup> A.D. Gitler, P. Dhillon, J. Shorter. *Model. Mech.* 10 (2017) 499–502.

<sup>313</sup> G. Deuschl, et al. *Lancet Public Health.* 5 (2020) e551–e567.

<sup>314</sup> H. Checkoway, J.I. Lundin, S.N. Kelada. *IARC Sci. Publ.* 163 (2011) 407–419.

<sup>315</sup> C.P. Ferri, et al. *Lancet*, 366 (2005) 6.

<sup>316</sup> H. Shah, E. et al. *Lancet Neurol.* 15 (2016) 1285–1294.

<sup>317</sup> Y.-L. Gao et al. *Ann. Transl. Med.* 6 (2018) 175–175.

<sup>318</sup> M. Hutton, et al. *FTDP-17*, 393 (1998) 4.

<sup>319</sup> R. Medeiros, D. Baglietto-Vargas, F.M. LaFerla. *CNS Neurosci. Ther.* 17 (2011) 514–524.



pathological hallmark in neurodegeneration, so that its detection is desirable for the sensitive diagnosis of AD and other neurodegenerative disorders. Tau proteins acts as a neuronal microtubule-associated protein that regulates axonal growth and neuronal polarity, as it is mainly found associated to axons<sup>124</sup>. In the normal human brain, Tau regulates the assembly of tubulin into microtubules<sup>320</sup>. This regulation is mediated by the phosphorylation of Tau protein, however, an hyperphosphorylation of this protein increases its tendency to aggregate and to assemble into pair helical filaments (PHFs) and later in the formation of intracellular NFTs, highly related with AD. The formation of NFTs has also been related with  $\beta$ -amyloid (A $\beta$ ), a relevant AD biomarker<sup>123</sup>, as according to the amyloid cascade hypothesis<sup>321</sup>, Tau hyperphosphorylation occurs following (A $\beta$ ) deposition<sup>322,323</sup>.

Current Tau protein detection is based on enzyme-linked immunosorbent assay (ELISA), mass spectrometry or surface plasmon resonance among other techniques<sup>324,325,326</sup>. But these procedures are time-consuming and expensive, so that they are not suitable for their use as generalized screening methods. For that reason, the development of optical and electrochemical biosensors for the detection of AD biomarkers has increased among the last years, obtaining promising results<sup>327</sup>. However, most of these approaches are based on sandwich-based or competitive assays, depending on the analyte size, requiring the use of labels. The complexity of these procedures is meant to be reduced by the implementation of label-free strategies, for what the use of nanochannels as biosensing platforms stands out<sup>328</sup>.

In the 50's Wallace Coulter developed the first microchannel-based biosensing device<sup>108</sup>. The mechanism of action of this system is based on the detection of changes in the electrical conductance between two chambers connected by a microchannel when an analyte passes through it. From this first device, several improvements have been done

---

<sup>320</sup> M.D. Weingarten, A.H. Lockwood, S.Y. Hwo, M.W. Kirschner. Proc. Natl. Acad. Sci. 72 (1975) 1858–1862.

<sup>321</sup> J.A. Hardy, G.A. Giggins. Science. 256 (1992) 184–185.

<sup>322</sup> R. Ismail, et al. J. Neuroinflammation. 17 (2020) 151

<sup>323</sup> M.J. Pontecorvo, et al. Brain. (2017) aww334.

<sup>324</sup> D.L. Sparks et al. Am J Neurodegener Dis. 1 (2012) 99–106.

<sup>325</sup> Y. Liu, H. Qing, Y. Deng. Int. J. Mol. Sci. 15 (2014) 7865–7882.

<sup>326</sup> A. Hye et al. Alzheimers Dement. 10 (2014) 799-807.e2.

<sup>327</sup> M. Ameri et al. Int. J. Biol. Macromol. 162 (2020) 1100–1108.

<sup>328</sup> A. de la Escosura-Muñiz, A. Merkoçi. ACS Nano. 6 (2012) 7556–7583.

until reaching nanometer channel systems<sup>329</sup>, able to detect biomolecules as ssDNA following the so-called stochastic sensing<sup>109,328</sup>.

In the development of nanochannel-based systems, the use of naturally pore forming biomolecules such as pore forming toxins has also been exploited<sup>330</sup>. However, these biological systems in occasions lack from precise pore-size control and stability, so that alternative systems such as solid-state nanochannels have been postulated<sup>331</sup>. As an example of them, nanoporous alumina membranes show up. They are characterized by having reduced pore sizes while maintaining an enhanced pore density, what increases the available surface area<sup>332</sup>. These membranes have already been used for the electrochemical detection of proteins<sup>333</sup>, DNA<sup>334</sup>, enzymes<sup>335</sup> or *in situ* monitoring of cell secreted proteins<sup>336</sup> and anti-virulence agents<sup>337</sup>, using screen printed carbon electrodes (SPCEs) or indium tin oxide/poly (ethylene terephthalate) (ITO/PET) electrodes. The excellent filtering properties and low unspecific adsorption of proteins shown by this material has made it ideal for the analysis of samples with complex matrixes. However, the detection of AD biomarkers is seldom studied within nanochannels<sup>338</sup>.

In this context, we propose here a novel approach for the detection of Tau protein using nanoporous alumina membranes as sensing platforms and ITO/PET electrodes as transducers. The analytical detection technique used is based on the blockage of the signal, both steric and electrostatic, due to the presence of increasing concentrations of Tau protein, captured by specific antibodies. Moreover, the effect of the pH in the blockage capacity and the performance in real plasma samples has also been investigated. The developed biosensor is the first approach, to our knowledge, in which nanochannels are used for Tau protein detection.

---

<sup>329</sup> S.M. Bezrukov, I. Vodyanoy, V.A. Parsegian. *Nature*. 370 (1994) 279–281.

<sup>330</sup> H. Bayley. *Nature*. 459 (2009) 651–652.

<sup>331</sup> Z.S. Siwy, S. Howorka. *Chem Soc Rev*. 39 (2010) 1115–1132.

<sup>332</sup> A. Santos, T. Kumeria, D. Losic. *TrAC - Trends Anal. Chem.* 44 (2013) 25–38.

<sup>333</sup> A. de la Escosura-Muñiz, A. Merkoçi. *Electrochem. Commun.* 12 (2010) 859–863.

<sup>334</sup> A. de la Escosura-Muñiz, A. Merkoçi. *Chem. Commun.* 46 (2010) 9007–9009.

<sup>335</sup> A. Iglesias-Mayor et al. *Biosens. Bioelectron.* 209 (2022) 114243.

<sup>336</sup> A. de la Escosura-Muñiz et al. *Biosens. Bioelectron.* 107 (2018) 62–68.

<sup>337</sup> A. de la Escosura-Muniz, K. Ivanova, T. Tzanov. *ACS Appl. Mater. Interfaces*. 11 (2019) 13140–13146.

<sup>338</sup> L. Zhou, H. Ding, F. Yan, W. Guo, B. Su. *The Analyst*. 143 (2018) 4756–4763.

## 5.2.2. Protocols

### 5.2.2.1. Nanoporous alumina membranes functionalization and anti-Tau antibody immobilization

Anti-Tau antibodies were immobilized in the inner walls of the nanochannels of the nanoporous alumina membranes following a previously optimized procedure, consisting in the functionalization of the alumina with amino groups through a silanization protocol, followed by the immobilization of the antibody through the peptide bond, using the EDC/NHS chemistry (see Figure S5.1)<sup>339</sup>.

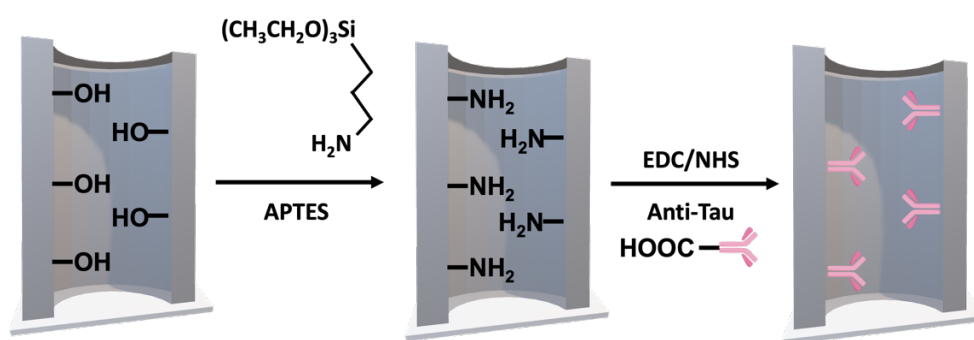


**Figure S5.1.** Schematic illustration of the silanization procedure used for the immobilization of anti-Tau antibody in the inner walls of AAO nanoporous membranes.

Briefly, nanoporous membranes were immersed in ultrapure water and boiled for 1 h. This boiling step is done both for cleaning them and activate the hydroxyl groups present in the surface, what favors the latter silanization process<sup>340</sup>. Then, the membranes were dried under a nitrogen flow and then plunged into a 5% APTES solution in acetone for 1 h. The solution was withdrawn, and the membranes were washed three times with pure acetone. After that, they were dried at 120°C for 30 min. After this process, the silanized membranes could be stored for weeks without losing their activity.

For the optimization of the immobilization of anti-Tau antibodies in the inner wall of the nanochannels, 30  $\mu$ L of a solution of 5 mM EDC/sulfo-NHS in MES pH 5, containing different concentrations of the anti-Tau antibody (0.5, 1, 10 and 50  $\mu$ g/mL) were placed on the top side of the membrane and left at room temperature for incubation

<sup>339</sup> A. de la Escosura-Muñiz, A. Merkoçi. *Small*. 7 (2011) 675–682.

<sup>340</sup> W. Ye, Y. Xu, L. Zheng, Y. Zhang, M. Yang, P. Sun. *Sensors*. 16 (2016) 1767.

for 2h. Control assays were performed in Tris-HCl 10 mM pH 7.00 without antibody being added. After this incubation, membranes were placed on top of a rack and gently washed with Tris-HCl 10 mM pH 7.00 buffer (Figure S5.2).

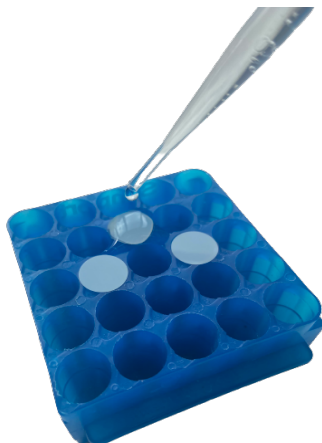


**Figure S5.2.** Illustration of the protocol performed for nanoporous alumina membrane cleaning between steps.

#### 5.2.2.2. *Immunoassay for Tau capturing in the nanochannels*

For that purpose, 30  $\mu\text{L}$  of solutions containing increasing concentrations of Tau protein (5-100 ng/mL) were placed on the membranes and left for incubation at room temperature during 3 h. Then, membranes were put on top of a rack and thoroughly cleaned with Tris-HCl 10 mM. To achieve an enhanced variation between control samples and Tau-containing ones, pH of the final buffer solution used for cleaning and measuring was adjusted, thus trying at pH 7.00, 8.24 and 9.00. Control assays were performed using the same procedure but without the addition of Tau protein. To evaluate the selectivity of the developed sensor, the above-described methodology was followed for 100 ng/mL solutions of  $\beta$ -amyloid, avidin and BSA solutions instead of that of Tau protein.

Long-term stability of the membranes was also evaluated by storing a set of anti-Tau antibody modified membranes at 4°C for one month and adding a 100 ng/mL Tau concentration at different time points.

### 5.2.2.3. *Cell set-up and electrochemical measurements*

The electrochemical measurements were performed fixing the nanoporous membrane on top of an ITO/PET electrode, using a methacrylate cell. First, the membrane was placed with the filtering side up on top of the conductive side of the ITO/PET electrode. The electrode was introduced between two pieces of methacrylate, one of them with a hole that delimitates the ITO/PET working electrode area and the electrochemical cell. Then, the whole system was adjusted with screws to avoid liquid leakage. Ag/AgCl and a Pt wire were used as reference and counter electrodes respectively.

For the electrochemical measurement, the electrochemical cell was filled with 400  $\mu\text{L}$  of a 10 mM solution of  $\text{K}_4[\text{Fe}(\text{CN})_6]$  red-ox indicator. Then, a pre-treatment at -0.55V was applied for 30 s and immediately after, a differential pulse voltammetric (DPV) scan between +0.1V and +1.3V was done applying a step potential of 10 mV, a modulation amplitude of 50 mV and at a scan rate of 33.5 mV/s. As a result, the oxidation of  $[\text{Fe}(\text{CN})_6]^{4-}$  to  $[\text{Fe}(\text{CN})_6]^{3-}$  was observed and the correspondent peak current at approximately +0.6V was selected as analytical signal.

Measurements were performed in triplicate, using different nanoporous alumina membranes and ITO/PET electrodes.

The whole time required for performing the analysis (from the step of adding the sample containing the antigen), including also mounting the cell, is of around 4h (for 20 membranes: analysis of 20 samples) or 6h (for 60 membranes: analysis of 60 samples). Using more cells simultaneously, the number of analysis could be further increased, estimating 1h more per each 20 membranes (i.e. 8 h for analysing 100 samples).

### 5.2.2.4. *Spike and recovery assay*

Spike and recovery is fundamental for the evaluation of the performance of a biosensor in complex samples. A plasma sample from healthy patients was used for such purpose. This experiment was performed by spiking the plasma sample with different concentrations (5 and 25 ng/mL) of Tau protein (n=3 for each sample). Then, the spiked samples were evaluated in the nanochannels-based sensing system, being finally

calculated the % of recovery of the analytical sample in plasma, compared with the obtained in non-spiked plasma.

### 5.2.3. Results and discussion

#### 5.2.3.1. Sensing principle for Tau protein detection: optimization of the main parameters involved

In this work, commercial nanoporous alumina membranes with a pore diameter size of 100 nm (real average diameter of  $108 \pm 16$  nm, Figure S5.3) were selected as sensing platforms due to their easy functionalization, filtering capacities and low unspecific adsorption of proteins. Membranes were first characterized by SEM showing a regular and well dispersed morphology (Figure 5.1.A.).

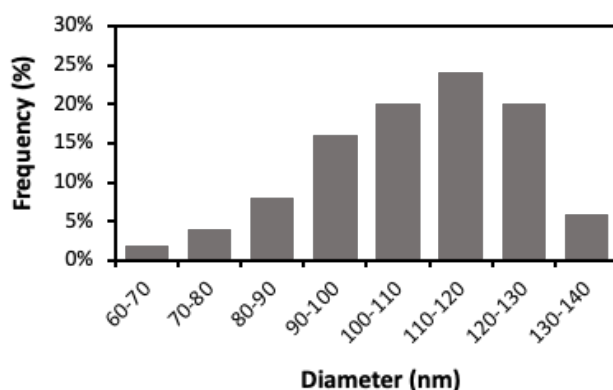


**Figure S5.3.** Size distribution of the diameter of nanochannels used. Measured using Image J from SEM micrographs of commercial AAO membranes with a nominal diameter size of 100 nm and a real average diameter size of  $108 \pm 16$  nm ( $n=50$ ).

The principle of the developed biosensor is based on the nanochannels blocking by the Tau protein captured by the specific antibody. In the presence of this protein, the flow of the  $[\text{Fe}(\text{CN})_6]^{4-}$  red-ox indicator through the nanochannels is reduced, due to both steric and electrostatic impediments (Figure 5.1.B.). This is monitored through the decrease in the voltammetric oxidation of  $[\text{Fe}(\text{CN})_6]^{4-}$  to  $[\text{Fe}(\text{CN})_6]^{3-}$  which is evaluated using the electrochemical set-up detailed at *methods* section, with ITO/PET working electrodes (Figure 5.1.C.). Compared to screen-printed carbon electrodes (SPCEs), previously used together with nanoporous alumina membranes in nanochannels-based electrochemical

biosensing systems<sup>341</sup>, ITO/PET electrodes show important advantages for such particular application. The use of SPCEs as transducers in these systems suffered from important limitations related to: (i) the membrane covers the three electrodes (reference, counter and working), inducing not wanted blocking of the reference electrode, which leads to unstable signals; (ii) the roughness of the working carbon electrode makes difficult the assembling with the membrane, leading to irreproducibility in the signals. In contrast, our experimental set-up allows to improve the system performance, overcoming such limitations. The flatter surface of the ITO/PET electrode allows to improve the membrane/electrode assembling and consequently the system reproducibility. The use of external counter and reference electrodes avoids the electrodes blocking with the membrane, giving much more stable signals. Moreover, the flexibility and biocompatibility of the ITO/PET make them ideal for future applications in wearable electrochemical sensing<sup>342</sup>.

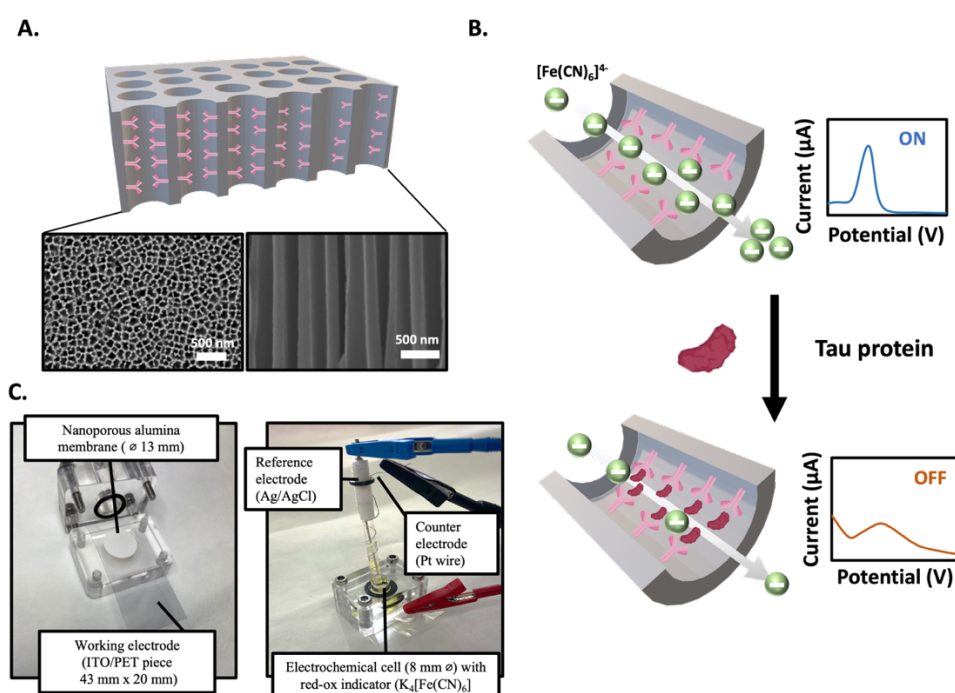


**Figure 5.1.** Representation of nanoporous alumina membranes used for Tau detection. **A.** Schematic representation of the pore distribution inside a nanoporous alumina membrane accompanied by SEM micrographs of both top view (left) and cross- section view (right) of the membranes. **B.** Schematic representation of the principle of the biosensor developed, based on the nanochannels blocking by the Tau

<sup>341</sup> A. de la Escosura-Muñiz, W. Chunglok, W. Surareungchai, A. Merkoçi. *Biosens. Bioelectron.* 40 (2013) 24–31.

<sup>342</sup> Y. Wang, B. Sun, H. Wei, Y. Li, F. Hu, X. Du, J. Chen. *Anal. Chim. Acta.* 1224 (2022) 340217.

protein captured by specific antibodies, which hinders the diffusion of  $[\text{Fe}(\text{CN})_6]^{4-}$  to the electrode, leading to a decrease in its voltammetric oxidation to  $[\text{Fe}(\text{CN})_6]^{3-}$ . C. Electrochemical set-up used in this sensing device.

### 5.2.3.2. Optimization of anti-Tau antibody concentration

As detailed in *methods* section, anti-Tau antibodies are immobilized in the inner walls of the nanochannels through the peptide bond, taking advantage of the carbodiimide chemistry. The minimum concentration for a total covering of the nanochannels surface was evaluated by monitoring the certain blocking effect that the antibodies by themselves exert toward the diffusion of the red-ox indicator ion through to the electrode. This blockage could be associated to both steric and electrostatic effects, as the size of an antibody is considered to be around 10 to 15 nm<sup>343,344</sup>, while the size of the ions of  $[\text{Fe}(\text{CN})_6]^{4-}$  is lower than 1 nm.

Therefore, the first step performed was the immobilization of different anti-Tau antibody concentrations to study the blockage produced. The degree of blockage in the signal has been calculated as described in Equation 1:

$$\text{Index of Antibody Current Blockage } (\Delta I_{\text{ab}}) (\%) = \left( \frac{I_0 \text{ bare membrane} - I \text{ antibody modified membrane}}{I_0 \text{ bare membrane}} \right) \times 100$$

(Eq 1.)

where  $I$  is the value of the peak current corresponding to the voltammetric oxidation of  $[\text{Fe}(\text{CN})_6]^{4-}$  to  $[\text{Fe}(\text{CN})_6]^{3-}$ . The use of this parameter as analytical signal in this experiment has helped to normalize the results and obtain a better conclusion.

Anti-Tau antibody in concentrations ranging from 0.5 to 50  $\mu\text{g/mL}$  were evaluated. The isoelectric point (pI) of the antibody is a key parameter for the selection of the adequate buffer in which the  $[\text{Fe}(\text{CN})_6]^{4-}$  red-ox indicator solution is prepared. Previous experiments have confirmed that the pI for Tau antibodies is between 5 to 8<sup>345</sup> but these values could vary depending on the species in which the antibody has been generated. In this regard, the monoclonal anti-Tau antibody used in this work has been produced in mouse, being the antibody an IgG1 kappa light chain that is associated with a pI of 6.4<sup>346</sup>.

---

<sup>343</sup> Y.H. Tan, M. Liu, B. Nolting, J.G. Go, J. Gervay-Hague, G. L. ACS Nano. 2 (2008) 2374–2384.

<sup>344</sup> Y. Dong, C. Shannon. Anal. Chem. 72 (2000) 2371–2376.

<sup>345</sup> E.E. Congdon et al. EBioMedicine. 42 (2019) 157–173.

<sup>346</sup> Å. Danielsson, A. Ljunglöf, H. Lindblom. J. Immunol. Methods. 115 (1988) 79–88



In view of this information, a Tris-HCl buffer at pH of 7.00 was selected as  $[\text{Fe}(\text{CN})_6]^{4-}$  solution media, so as to have the antibodies negatively charged which should exert a certain repulsion to the diffusion of the  $[\text{Fe}(\text{CN})_6]^{4-}$  ions, what it is translated into an increased blockage of the analytical signal. By selecting this pH, a further confirmation of the pI of the antibody could be done in an easy-to-manage form.

As shown and illustrated in Figure 5.2.A., the increasing amount of anti-Tau antibody produces a gradual decrease in the voltammetric signal, reaching a saturation for 1 ng/mL. This behavior is consistent with our hypothesis, suggesting that the presence of the negatively charged antibodies is hindering the diffusion of the negatively charged red-ox indicator ions. In terms of blockage in the signal (Figure 5.2.B.) at a concentration of 0.5  $\mu\text{g}/\text{mL}$  the index of blockage produced is of 9% while this value is notably enlarged to 41% with a slight increase in the concentration to 1  $\mu\text{g}/\text{mL}$ . This value is maintained at higher concentrations, reaching 42% for 10  $\mu\text{g}/\text{mL}$ , what indicates that the saturation of the nanochannels has been achieved and the increase in anti-Tau antibody concentrations is not translated into a greater immobilization of them inside the nanochannel. The slight decrease to 34% observed for 50  $\mu\text{g}/\text{mL}$  is probably due to the saturation of the signal. These results suggest that the minimum amount of anti-Tau

antibody giving the total covering of the nanochannels corresponds to a concentration of 1  $\mu\text{g/mL}$ , which was selected as optimum for the development of the immunoassay.

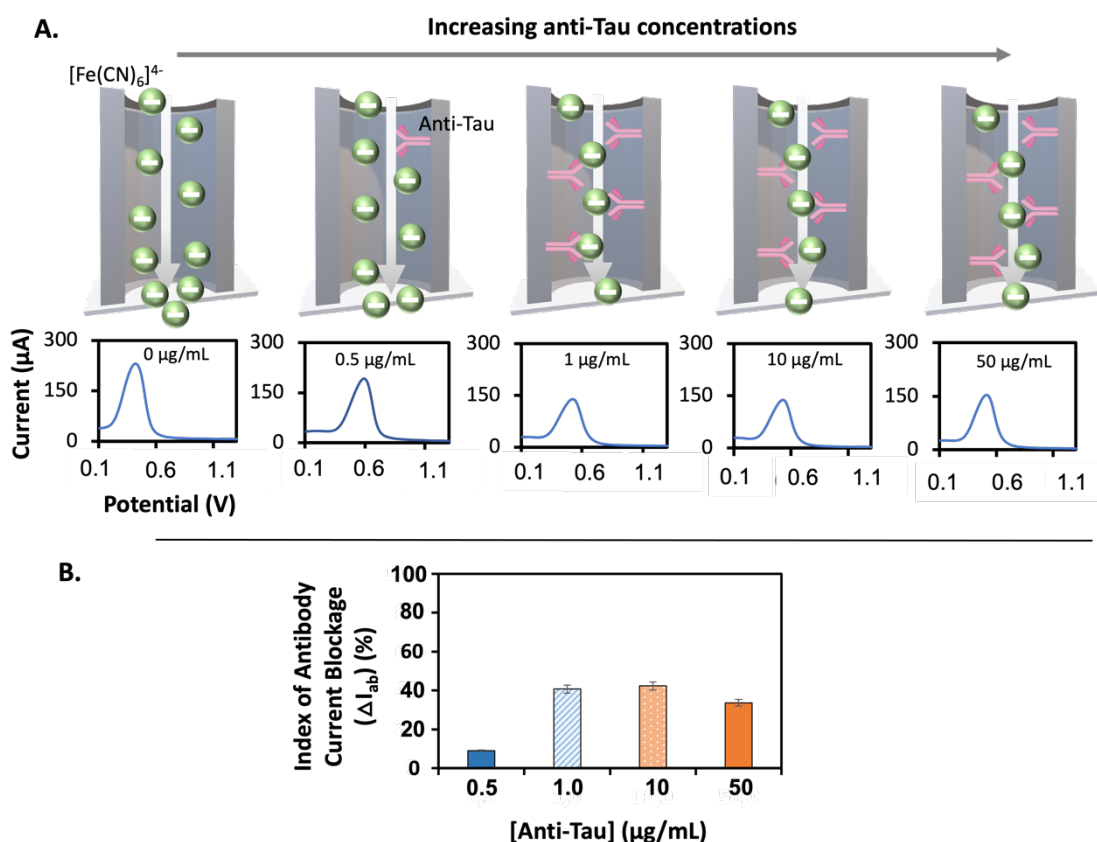


**Figure 5.2.** Optimization of the concentration of anti-Tau antibody immobilized inside the nanochannels. **A.** (Up) Schematic illustration of the different situations with different amounts of antibody immobilized and the blockage on the diffusion of the  $[\text{Fe}(\text{CN})_6]^{4-}$  red-ox indicator ions; (Down) Differential pulse voltammograms (DPV) recorded for each concentration of anti-tau antibody concentration evaluated, using a 10 mM  $\text{K}_4[\text{Fe}(\text{CN})_6]$  solution in 10 mM Tris-HCl buffer at pH 7.00, applying a pre-concentration potential of -0.55V for 30 s and scanning from +0.1V to +1.3V at a step potential of 10 mV, a modulation amplitude of 50 mV and a scan rate of 33.5 mV/s; **B.** Comparative representation of the index of antibody current blockage (as defined in Equation 1) for different anti-Tau antibody concentrations. Data are given as average  $\pm$  SD (n=3).

### 5.2.3.3. *Immunoassay for Tau protein capturing inside the channels and optimization of the pH of the measuring buffer*

After the optimization of the anti-Tau antibody concentration, immunoassays were performed for Tau protein capturing inside the nanochannels. The Tau protein molecule has a size of 69-75 nm in a non-phosphorylated form while this value slightly increases

in a hyperphosphorylated form<sup>347</sup>. These value, together with the presence of anti-Tau antibodies (of around 15 nm) forming a monolayer in the inner walls of the nanochannel, highly increase the steric blockage of the signal, but still provides margin for  $[\text{Fe}(\text{CN})_6]^{4-}$  red-ox indicator ions (1 nm diameter) fluxed through the nanochannels of around 100 nm diameter (real diameter of  $108 \pm 16$  nm).

Moreover, proteins may have a positive or negative external net charge depending on the pH of the measurement solution. This charge will contribute to the signal blockage by electrostatic interactions of the nanochannel due to charge repulsion between the negative ions of the red-ox indicator and the biomolecule. For that reason, to have the maximum blockage by low concentrations of Tau protein, the optimum pH for the buffer used during measurements was evaluated.

In this experiment, a fixed concentration of Tau protein of 100 ng/mL was used. Tau protein behaves as a dipole containing two domains, a N-terminal region which has a pI of 3.8, and a C-terminal region with a pI of 10.8. Tau protein also contains a proline-rich domain with a pI of 11.4. However, posttranslational modifications of this protein could clearly modulate these dipoles<sup>348</sup>. For that reason, the use of a measuring pH that allows to detect a wider range of Tau protein forms is desirable for the real implementation of the biosensor developed in this work for further clinical samples analysis.

In this work, the model Tau-441, recombinant protein, the longest human brain Tau isoform (441 amino acids) was used<sup>349</sup>. The pI value for Tau-441 used was also theoretically calculated using ProtParam tool following previously published procedures (Figure S5.3)<sup>348,350</sup>, providing a pI value of 8.24 which correlates with previously reported values<sup>351</sup>.

---

<sup>347</sup> G.C. Ruben et al. *J. Biol. Chem.* 266 (1991) 22019–22027.

<sup>348</sup> M. Kolarova, F. García-Sierra, A. Bartos, J. Ricny, D. Ripova. *Int. J. Alzheimers Dis.* 2012 (2012) 1–13.

<sup>349</sup> P. Weydt, L. Dupuis, Å. Petersen, Thermoregulatory disorders in Huntington disease, in: *Handb. Clin. Neurol.*, Elsevier, 2018: pp. 761–775.

<sup>350</sup> L. Ferrari, S.G.D. Rüdiger. *Protein Eng. Des. Sel.* 31 (2018) 447–455.

<sup>351</sup> R. Brandt, N.I. Trushina, L. Bakota. *Front. Neurol.* 11 (2020) 590059.

>sp|P10636-8|TAU\_HUMAN Isoform Tau-F of Microtubule-associated protein tau OS=Homo sapiens OX=9606 GN=MAPT

```

ProtParam
User-provided sequence:
      10      20      30      40      50      60
MAEPRQEFEV MEDHAGTYGL GDRKDQGGYT MHQDQEGDTD AGLKESPLQT PTEDGSEEPG
      70      80      90     100     110     120
SETSDAKSTP TAEDVTAPLV DEGAPGKQAA AQPHTEIPFG TTAEAEAGIGD TPSLEDEAAG
      130     140     150     160     170     180
HVTQARHVSK SKDGTGSDDK KAKGADGKTK IATPRGAAPP GQKQGAMATR IPAKTPPAPK
      190     200     210     220     230     240
TPPSSGEPPK SGRDSGYSSP GSPGTPGSRG RTPSLTPPTP REPKKVAVVR TPPKSPSSAK
      250     260     270     280     290     300
SRLQTAPVPM PDLKNVSKI GSTENLKHQP GGGKVQIINK KLDLSNVQSK CGSKDNIKHV
      310     320     330     340     350     360
PGGGSVQIVY KPVDSLKVTG KCGSLGNIHH KPGGGQVEVK SEKLDKDFRV QSKIGSLDNI
      370     380     390     400     410     420
THVPGGGNKK IETHKLTFRG NAKAKTDHGA EIVYKSPVVS GDTSPRHLN VSTGSDIMV
      430     440
DSPQLATLAD EVSASLAKQG L

Number of amino acids: 441
Molecular weight: 45849.91
Theoretical pI: 8.24

```

**Figure S5.3.** Calculation of the pI of Tau-441 human protein (UniProt code P10636-8) using ProtParam tool (<https://web.expasy.org/protparam/>).

Taking into consideration this information, pH values of 7.00, 8.24 and 9.00 were used for preparing the 10 mM  $K_4[Fe(CN)_6]$  red-ox indicator solutions for studying the effect of the pH in the nanochannels blockage, as defined in Equation 2:

$$\text{Index of Tau Current Blockage } (\Delta I_{\text{Tau}}) (\%) = \left( \frac{I_0 \text{ antibody modified membrane} - I \text{ immunoassay}}{I_0 \text{ antibody modified membrane}} \right) \times 100 \quad (\text{Eq. 2})$$

It is worthy to mention that according to the pI of the anti-tau antibodies, they should remain negatively charged for all the pH values evaluated, being their inherent blockage effect considered as a constant background which does not affect the biosensing system.

According to the scheme represented in Figure 5.3.A. at a pH of 8.24, equivalent to the pI of Tau-441, the protein molecules are uncharged, so not electrostatic effects should be induced by the presence of the protein inside the nanochannels. However, a noticeable blockage in the current up to a 32% index (as defined in Equation 2) is measured,

suggesting that steric impediments (size above 69-75 nm in a nanochannel of 100 nm in diameter) have an important contribution in hindering the diffusion of the red-ox indicator ions.

At a pH of 7.00, which is below the pI value of Tau-441, the net charge of the protein is positive, so this should induce an electrostatic attraction effect to the  $[\text{Fe}(\text{CN})_6]^{4-}$  ions and consequently an increase in the voltammetric signal. This is corroborated by the decrease in the blockage index (18%) obtained, as depicted in Figure 5.3.B., induced by the steric blockage of the protein (size above 69-75 nm in a nanochannel of 100 nm in diameter).

Interestingly, increasing the pH to 9.00, a value which is higher than the pI of the Tau-441, the protein is negatively charged, impeding the diffusion of the  $[\text{Fe}(\text{CN})_6]^{4-}$  ions. This leads to a dramatic increase in the current blockage index to 73% (Figure 5.3.B.). According to these results, pH 9.00 is selected as the optimum value for obtaining the maximum response regarding the analytical signal. Moreover, this pH value allows to cover a wide spectrum of pIs, so that all variants of Tau protein, independently of their phosphorylation state and isoform, could be detected with a high precision. The quite basic pH does not significantly affect the chemical stability of the ferro/ferricyanide pair as it has been previously stated that this redox molecule retains its activity even at pH 14<sup>352</sup>. Although a small decrease in the analytical signal is recorded at pH 9.00 compared to measurements at pH 7.00, the use of normalized blocking indexes eliminates the impact of these small variations in the result, facilitating comparison between conditions.

---

<sup>352</sup> J. Luo, A. Sam, B. Hu, C. DeBruler, X. Wei, W. Wang, T.L. Liu. *Nano Energy*. 42 (2017) 215–221.

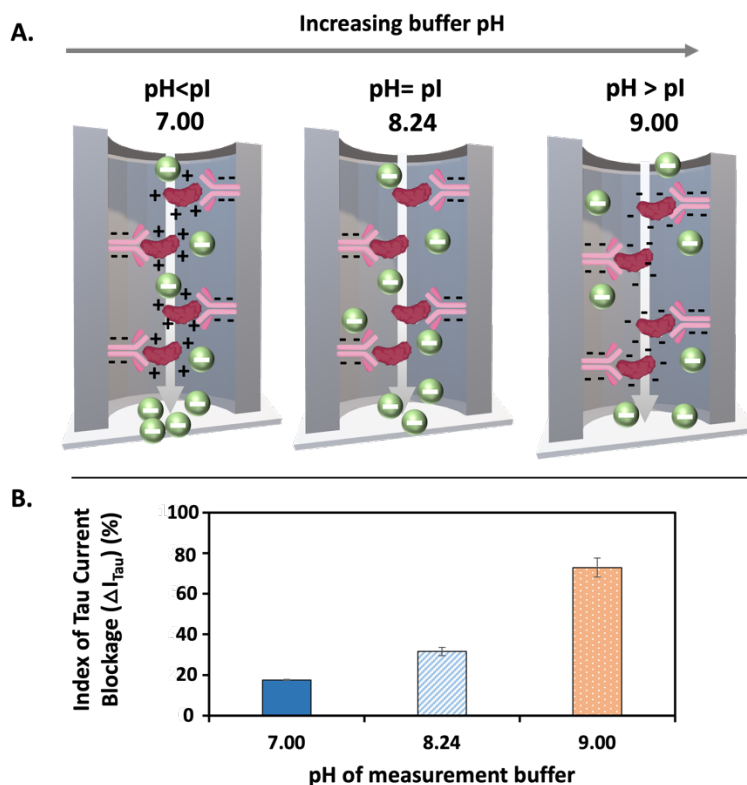


**Figure 5.3.** Effect of the pH of the measurement buffer in the analytical system. **A.** Representation of the different charges of both anti-Tau antibody and Tau protein depending on the pH of the measurement solution and how it affects the diffusion of the  $[\text{Fe}(\text{CN})_6]^{4-}$  red-ox indicator ions through the channel; **B.** Effect of the pH on the index of Tau current blockage (as defined in Equation 2) represented by the average  $\pm$  SD ( $n=3$ ).

#### 5.2.3.4. *Electrochemical detection of Tau protein*

After the optimization of the main parameters involved in the detection of Tau protein, the biosensor developed was used for the determination of different concentrations of this biomarker. First, anti-Tau antibodies were immobilized in the inner walls of the AAO membranes followed by the antigen-antibody interaction at a pH 7. In this initial incubation step, a pH of 7 was selected as the immunoreaction has been proved to be more efficient and stable at a neutral pH<sup>353</sup>. After this incubation step, AAO membranes are measured using a  $[\text{Fe}(\text{CN})_6]^{4-}$  redox solution at pH 9. At this pH value, both anti-Tau antibody and Tau are negatively charged, what optimizes the blockage

<sup>353</sup> S.C. Devanaboyina et al. MAbs. 5 (2013) 851–859.

obtained as proved in previous sections. Due to the short duration of the measurement, the chemical stability of the antigen-antibody interaction should not be compromised.

As expected, the presence of increasing concentrations of Tau protein leads to a decrease in the voltammetric peak current corresponding to the oxidation of the red-ox indicator  $[\text{Fe}(\text{CN})_6]^{4-}$  to  $[\text{Fe}(\text{CN})_6]^{3-}$  at approximately +0.6 V (Figure 5.4.A.), which is the analytical signal selected for the quantitative analysis. It was found a linear relationship between such analytical signal and the Tau protein concentration within the range 5-100 ng/mL (Figure 5.4.B.) with a correlation coefficient ( $r$ ) of 0.9981, adjusted to this equation:

$$\text{Peak current } (\mu\text{A}) = -0.112 [\text{Tau}] (\text{ng/mL}) + 20.4 \quad (\text{Eq. 3})$$

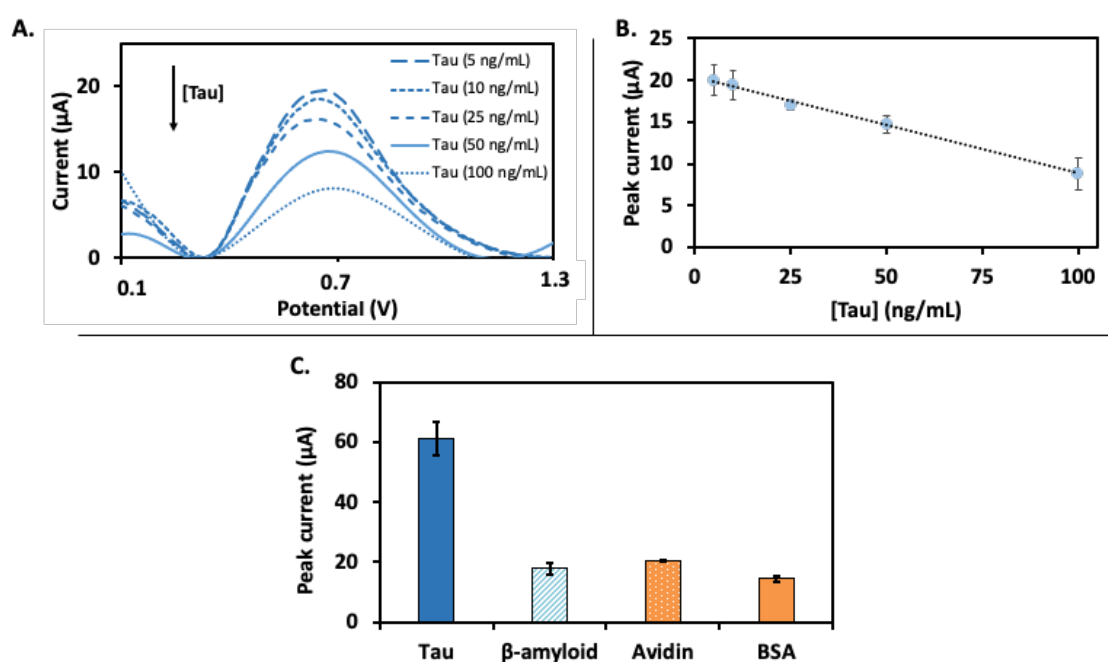


**Figure 5.4.** Tau protein detection through antibody recognition inside the nanochannels. **A.** Differential pulse voltammograms (DPV) recorded for different Tau concentrations, using as red-ox indicator 10 mM  $\text{K}_4[\text{Fe}(\text{CN})_6]$  in buffer at pH 9.00. Anti-Tau antibody concentration: 1  $\mu\text{g/mL}$ . Pre-concentration potential: -0.55V for 30 s; scan range: +0.1V to +1.3V; step potential: 10 mV; modulation amplitude: 50 mV; scan rate: 33.5 mV/s. **B.** Calibration curve obtained by representing the analytical signal (value of the peak current at +0.6 V)  $\pm$  SD ( $n=3$ ), obtained for the different concentrations of Tau protein assayed. **C.** Selectivity assay using a concentration of 100 ng/mL of Tau protein,  $\beta$ -amyloid, avidin or BSA.

The biosensing system developed has a limit of detection (LOD, calculated as three times the standard deviation of the intercepted divided by the slope) of 4.32 ng/mL and

an appropriate reproducibility with a relative standard deviation (RSD) of 9%. This value meets the average levels of total Tau detected in AD patients' blood ( $61.91 \pm 42.19$  ng/mL)<sup>354</sup> in a faster and cheaper approach than ELISA kits and without the need of any label, providing a result in less than 3.2h from the the sample addition step, from what 3h are from the incubation step common to other techniques. This is possible due to the long-term stability of the membranes (Figure S5.4) till 21 days. Moreover, the developed biosensor could be long-term coupled to a portable potentiostat<sup>355</sup>, what it would mean a significant advantage compared to the previously mentioned detection techniques as it would allow a fast and point-of-care detection of Alzheimer's Disease.

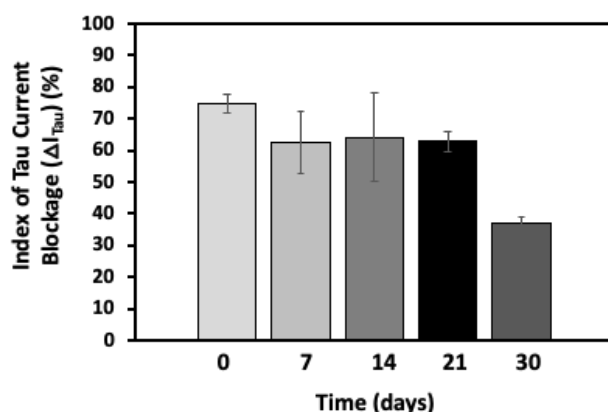


**Figure S5.4.** Long-term stability study of the anti-Tau antibody modified membranes after the addition of Tau at 100 ng/mL.

#### 5.2.3.5. System selectivity and performance in real samples

Selectivity of the biosensor was evaluated against common analytes present in human samples, as  $\beta$ -amyloid, another common AD biomarker, avidin and BSA (Figure 5.4.C.). It has been observed that the blockage produced in the presence of the abovementioned analytes is lower than 20%, what supposes an irrelevant value compared to the one obtained by Tau protein (61%), proving the selectivity of the method. Additionally, long-term stability of the developed sensor has been preliminary addressed (Figure S5.4), showing no reduction of the blocking capacity after 21 days. Although this aspect requires further optimization, it opens the possibility of reducing the time required by the developed sensor to provide a result, being just the last incubation step needed to be done by the final user.

<sup>354</sup> T.T. Vu Nu et al. RSC Adv. 8 (2018) 7855–7862.

<sup>355</sup> O. Parlak. Sens. Actuators Rep. 3 (2021) 100036.



Tau protein is well-known to be a suitable biomarker for the detection of AD and other neurodegenerative disorders, as high levels of this protein are present in cerebrospinal fluid (CSF) and plasma samples of patients with different pathologies<sup>356</sup>.

The main obstacle to overcome for measuring Tau protein is the complexity of real samples as possible interferences could occur<sup>357,358</sup>. For addressing this drawback, nanoporous alumina membranes are suitable platforms, as it is well known that this material has a low protein adsorption rate, acting as efficient filter in complex matrixes<sup>339,341</sup>.

For evaluating this issue, a spike and recovery procedure was performed in plasma samples adding different Tau concentrations spiked in commercial plasma from healthy patients. The plasma samples are then incorporation, in substitution of Tau protein dissolved in buffer solution, in the incubation step. After that a 10 mM  $K_4[Fe(CN)_6]$  in buffer at pH 9.00 red-ox solution was used for measuring the decrease in current produced by Tau protein, hence assuring that both antibody and antigen are negatively charged and maximizing electrostatic blockage. The spiked assay showed an excellent recovery rate at levels around 95% (Table 5.1). These results clarify that the performance of the biosensor is not altered by the presence of interfering compounds, thus opening the way to its use for the detection of AD.

**Table 5.1.** Spike and recovery assay data in plasma for AD concentrations of 5 and 25 ng/mL, corresponding to the lower and medium values of the calibration curve.

Sample	Spiked Tau (ng/mL)	Current in PBS ( $\mu$ A)	Current in real sample ( $\mu$ A)	Recovery (%)
Plasma from healthy subjects	5.00	18.9	18.2	96.3
	25.0	17.0	16.3	95.6

<sup>356</sup> S. Schraen-Maschke et al. *Biomark. Med.* 2 (2008) 363–384.

<sup>357</sup> M.L. Chiu, W. Lawi, S.T. Snyder, P.K. Wong, J.C. Liao, V. Gau. *J. Assoc. Lab. Autom.* 15 (2010) 233–242.

<sup>358</sup> J.-F. Masson. *ACS Sens.* 5 (2020) 3290–3292.

#### **5.2.4. Conclusions**

Tau protein, a well-known AD biomarker, has been detected in this work using a novel nanochannel-based platform. The mechanism of this biosensor is based on the voltammetric determination of the blockage that Tau protein produces to the diffusion of the red-ox indicator  $[\text{Fe}(\text{CN})_6]^{4-}$ . It was already known that both steric and electrostatic interactions affect the nanochannel blockage obtained, but the contribution of both components of the antigen-antibody pair used in nanochannels-based immunosensors was less research. Our findings confirm that the control of the charge of both components by changing the buffer measurement pH is required to maximize the blockage upon the immunocomplex formation. Considering antibody pI is particularly crucial not only for the overall blockage obtained but also to properly select the antibody concentration required in the immunoassay, reducing the concentration needed and thus the immunosensor cost.

In main, our method let detecting Tau protein with a good performance in human real samples and with a LOD of 4.3 ng/mL, which is in correlation with clinical values and with those detected by gold-standard techniques. It is worthy to mention that our methodology does not require neither labels nor competitive assays. As far as we know, this is the first time that Tau protein is detected through a nanochannel-based electrochemical sensor. This label-free sensor allows to detect Tau protein in a cheaper and faster approach, getting closer to clinical practice requirements, opening the way to a point-of-care diagnosis of AD.

Overall, our findings related to the effect of both the anti-Tau antibody and the anti-Tau/ Tau immunocomplex charges on the nanochannels-based biosensing system may be extended to any other antibody/antigen pair, just paying attention to the isoelectric point of such proteins, targeting applications in medicine, food analysis and environmental control among others.



## 5.3. Scientific article 7

Biosensors and Bioelectronics 209 (2022) 114243



Contents lists available at [ScienceDirect](#)

Biosensors and Bioelectronics

journal homepage: [www.elsevier.com/locate/bios](http://www.elsevier.com/locate/bios)



### Electrical monitoring of infection biomarkers in chronic wounds using nanochannels

Alba Iglesias-Mayor<sup>a</sup>, Olaya Amor-Gutiérrez<sup>a</sup>, Celia Toyos-Rodríguez<sup>a</sup>, Arnau Bassegoda<sup>b</sup>, Tzanko Tzanov<sup>b</sup>, Alfredo de la Escosura-Muñiz<sup>a,c,\*</sup>

<sup>a</sup> NanoBioAnalysis Group - Department of Physical and Analytical Chemistry, University of Oviedo, Julián Clavería 8, 33006, Oviedo, Spain

<sup>b</sup> Grup de Biotecnologia Molecular i Industrial, Department of Chemical Engineering, Universitat Politècnica de Catalunya, Terrassa, Spain

<sup>c</sup> Biotechnology Institute of Asturias, University of Oviedo, Santiago Gascon Building, 33006, Oviedo, Spain

#### 5.3.1. Introduction

Healing of chronic wounds, affecting 1 to 2 percent of the population in developed countries, represents a major healthcare challenge with important financial burden<sup>359,360</sup>. Chronic wounds are usually heavily colonized with bacteria, while providing bacteria-free environment is a prerequisite for wound healing. An early detection and treatment of infection is one of the most important factors in wound management. Although classical signs of infection - like redness, heat, swelling, exudate production and pain<sup>361</sup> - are still the main criteria in the clinical examination of the wound status, they are ambiguous and depend on the experience of the healthcare practitioner<sup>362</sup>. More precise, but still questioned are the (semi)quantitative microbiological investigations, including the gold-standard biopsy method, a time-consuming technique which is not often carried out in ambulatory clinical practice to avoid patient's morbidity, mostly local bleeding and infection spread<sup>363</sup>. The correct microbiological identification of the microorganisms

<sup>359</sup> A. Clinton, T. Carter. *Lab Med.* 46 (2015) 277–284.

<sup>360</sup> K. Järbrink, G. Ni, H. Sönnergren, A. Schmidtchen, C. Pang, R. Bajpai, J. Car. *Syst. Rev.* 5 (2016) 152.

<sup>361</sup> S.E. Gardner, R.A. Frantz, B.N. Doebbeling. *Wound Repair Regen.* 9 (2001) 178–186.

<sup>362</sup> A.R. Siddiqui, J.M. Bernstein. *Clin. Dermatol.* 28 (2010) 519–526.

<sup>363</sup> S.E. Gardner, R.A. Frantz, C.L. Saltzman, S.L. Hillis, H. Park, M. Scherubel. *Wound Repair Regen.* 14 (2006) 548–557.

infecting a wound to prescribe the suitable antibiotic treatment may take up to 3 days to come from the Microbiology lab in many hospitals. Until then, the patient is subjected to a broad-spectrum unspecific antimicrobial therapy with important side effects on human microbiome. For this reason, alternative tools for the rapid detection of infections in chronic wounds are strongly required.

Although physical parameters such as temperature<sup>364</sup>, pH<sup>365</sup> or odour<sup>366</sup> have been studied as qualitative indicators of wound infection<sup>367,368</sup>, main efforts have been dedicated in the last decades in the identification of biomolecules which presence in wound exudates evidences a bacterial infection<sup>369</sup>. Enzymes with increased activity in infected wound fluids are considered as reliable infection biomarkers<sup>370</sup>. Lysozyme<sup>371</sup> is of special relevance since it is produced by the human immune system as the main component of the host innate defence mechanism<sup>372</sup>. Lysozyme is a glycosidase enzyme<sup>373</sup> capable of hydrolysing the  $\beta$ -(1,4)-glycosidic bonds between N-acetylmuramic acid and N-acetylglucosamine residues of its native substrate, the peptidoglycan<sup>374</sup>, a polymer which constitutes the core component of almost all bacterial cell walls<sup>375</sup>. This polymer is composed of linear glycan strands (alternating N-acetylglucosamine and N-acetylmuramic acid residues linked by  $\beta$ -(1,4) bonds) cross-linked by short peptides. Gram positive bacteria have a thick peptidoglycan layer and no outer lipid membrane whilst Gram negative bacteria have a thin peptidoglycan layer and an outer lipid membrane<sup>376</sup>. The presence of high lysozyme activity in serum and urine samples has been associated with chronic granulomatous inflammatory disorders as tuberculosis or sarcoidosis<sup>377</sup> and myelomonocytic leukaemia<sup>378</sup>, respectively. Moreover, the increase in lysozyme levels in serum is an indicator of active chronic inflammation<sup>371</sup>.

---

<sup>364</sup> G. Matzeu, M. Losacco, E. Parducci, A. Pucci, V. Dini, M. Romanelli, F. Di Francesco. IECON Proc. Ind. Electron. Conf. (2011) 3533–3535.

<sup>365</sup> S. Trupp et al. Sens. Actuators B Chem. 150 (2010) 206–210.

<sup>366</sup> K.C. Persaud. Int. J. Low. Extrem. Wounds. 4 (2005) 50–56.

<sup>367</sup> K.F. Cutting, R.J. White. Ostomy Wound Manag. 51 (2005) 28–34.

<sup>368</sup> A.M. Caliendo et al. Clin. Infect. Dis. 57 (2013) S139–S170.

<sup>369</sup> D.R. Yager, R.A. Kulina, L.A. Gilman. Int. J. Low. Extrem. Wounds. 6 (2007) 262–272.

<sup>370</sup> D. Schiffer et al. Expert Rev. Mol. Diagn. 15 (2015) 1125–1131.

<sup>371</sup> A. Hasmann et al. Diagn. Microbiol. Infect. Dis. 71 (2011) 12–23.

<sup>372</sup> E.F. Osserman, M. Klockars, J. Halper, R.E. Fischel. Nature. 243 (1973) 331–335.

<sup>373</sup> L. Callewaert, C.W. Michiels. J. Biosci. 35 (2010) 127–160.

<sup>374</sup> M.R.J. Salton. Bacteriol. Rev. 21 (1957) 82–100.

<sup>375</sup> H.J. Rogers, H.R. Perkins, J.B. Ward, Microbial cell walls and membranes, Springer, 2013.

<sup>376</sup> W. Vollmer, D. Blanot, M.A. de Pedro. FEMS Microbiol. Rev. 32 (2008) 149–167

<sup>377</sup> R. Jain, D. Yadav, N. Puranik, R. Guleria, J.-O. Jin. J. Clin. Med. 9 (2020) 1081

<sup>378</sup> E.F. Osserman, D.P. Lawlor. J. Exp. Med. 125 (1966) 921–952.

The analysis of lysozyme activity has been traditionally based on its lytic action against the cell wall of *Micrococcus luteus* (*M. lysodeikticus*), by measuring the decrease in turbidity<sup>379</sup>. However, this methodology is affected by the pH, ionic strength and matrix effects, what implies that these parameters must be thoroughly controlled to obtain a proper result<sup>380</sup>. Colorimetric methods based on i) the release of coloured fragments of Remazol brilliant blue-labelled *Micrococcus luteus* upon hydrolysis<sup>381,382</sup> and ii) peptidoglycan stabilized-gold nanoparticles aggregation after enzymatic cleavage<sup>383</sup> have also been proposed for such purpose. However, these methods are laborious and require additional separation steps, having as main drawback the low contrast observed in some procedures between signal and background. Chromatographic<sup>384</sup> and both antibody<sup>385</sup> and aptamer-based<sup>386</sup> methods have also been reported for lysozyme detection, suffering from important limitations related to their high cost and the need of bioreceptors.

Biosensing systems based on nanochannels emerge as outstanding tools to overcome these limitations and meet such clinical demand. The use of nanopores/nanochannels has become one of the most promising fields of research in the biosensing area in the last years<sup>387</sup>. Proteins, DNA sequences and viruses have been detected through the so-called stochastic sensing on single natural/artificial nanopores. Special mention deserves the commercial implementation of DNA sequencing systems based on the same principles<sup>388</sup>. Nanoporous membranes have also been proposed as platforms for both electrochemical and optical biosensing through the monitoring of the nanochannels steric blockage upon biocomplex formation<sup>389</sup>. The easy functionalization and capacity for mass production of nanoporous alumina have made this material as the most extensively used for such applications<sup>390</sup>. Size and charge effects in nanochannels have been approached for biosensing purposes for more than ten years. However, the use

---

<sup>379</sup> D. Shugar. *Biochim. Biophys. Acta.* 8 (1952) 302–309.

<sup>380</sup> P. Mörsky. *Anal. Biochem.* 128 (1983) 77–85

<sup>381</sup> Y. Ito, H. Yamada, T. Imoto. *Chem. Pharm. Bull. (Tokyo).* 40 (1992) 1523–1526.

<sup>382</sup> M. Hardt, Y. Guo, G. Henderson, R.A. Laine. *Anal. Biochem.* 312 (2003) 73–76.

<sup>383</sup> F. Fu, L. Li, Q. Luo, Q. Li, T. Guo, M. Yu, Y. Song, E. Song. *Analyst.* 143 (2018) 1133–1140.

<sup>384</sup> X. Fang, Z. Wang, N. Sun, C. Deng. *Talanta.* 226 (2021) 122143.

<sup>385</sup> M.-L. Vidal, J. Gautron, Y. Nys. *J. Agric. Food Chem.* 53 (2005) 2379–2385.

<sup>386</sup> Ostatná, V. Kasalová-Vargová, L. Kékedy-Nagy, H. Černocká, E.E. Ferapontova. *Bioelectrochemistry.* 114 (2017) 42–47.

<sup>387</sup> A. de la Escosura-Muñiz, A. Merkoçi. *ACS Nano.* 6 (2012) 7556–7583.

<sup>388</sup> J. Clarke, H.C. Wu, L. Jayasinghe, A. Patel, S. Reid, H. Bayley. *Nat. Nanotechnol.* 4 (2009) 265–270

<sup>389</sup> A. de la Escosura-Muñiz, A. Merkoçi. *TrAC - Trends Anal. Chem.* 79 (2016) 134–150.

<sup>390</sup> D. Losic, A. Santos, *Nanoporous Alumina: Fabrication, Structure, Properties and Applications*, 2015.

of nanoporous membranes for monitoring enzymatic cleavage processes, leading to analytical methods for enzyme determination has not been deeply explored so far.

In this context, we propose a novel methodology for the determination of lysozyme using nanoporous alumina membranes as sensing platforms and indium tin oxide/poly(ethylene terephthalate) (ITO/PET) electrodes as transducers. This analytical method is based on the electrical monitoring of steric/electrostatic nanochannels blocking upon peptidoglycan immobilization and further lysozyme digestion of the peptidoglycan leading to unblockage of the nanopores. Steric and electrostatic contributions to the nanopore blocking/unblocking mechanism are thoroughly studied, before analysing samples of wound exudates from both patients with clean and infected ulcers.

Our novel methodology presents important advantages compared with the lysozyme detection methodologies reported so far, related to: i) no need of bioreceptors (antibodies or aptamers); ii) no need of competitive assays; iii) low matrix effects thanks to the filtering-like properties and low protein adsorption rate of the nanoporous alumina membranes; iv) quantitative analysis; v) rapid analysis at the point-of-care, using cheap and portable instruments.

### 5.3.2. Protocols

#### 5.3.2.1. Nanoporous alumina membranes functionalization, peptidoglycan immobilization and enzymatic cleavage by lysozyme

Peptidoglycan immobilization on the inner walls of the nanochannels was performed adapting an experimental procedure previously optimized for antibodies<sup>391</sup>. It consists first in the generation of amino groups in the nanochannels *via* silanization, followed by carbodiimide-mediated peptidoglycan binding through its carboxyl groups. Briefly, nanoporous alumina membranes were first boiled in ultrapure water for 1 h, so as to clean the membranes and the hydroxyl groups of the alumina, which favour the later silanization process<sup>392</sup>. After drying in nitrogen, they were immersed in a 5 % acetone solution of APTES for 1 h. Then, membranes were washed in acetone and baked at 120 °C for 30 min. After that, 30 µL of peptidoglycan solution in 10 mM MES pH 5 buffer, containing 5 mM EDC/sulfo-NHS, was placed on the filtering side of the membrane and left there for 2 h.

After thoroughly washing with 10 mM Tris-HCl (10 mM ionic strength coming from NaCl) pH 8 buffer, the enzymatic reaction was performed by incubating 30 µL of lysozyme solution (concentration range from 1 to 50 µg/mL) in 10 mM Tris-HCl pH 8 on the membrane filtering side at 37 °C for 30 min. Finally, the membranes were washed again and stored in the measurement buffer before the electrochemical experiments. Control assays were performed following the same protocol but using 10 mM phosphate buffered saline (PBS) pH 7.4 solution instead of peptidoglycan solution (bare silanized nanoporous membranes). Exudates from wound ulcers were analysed following the same experimental procedure but using a 1 to 10 dilution (in 10 mM Tris-HCl pH 8) of the wound exudate instead of lysozyme solution.

Selectivity assays were performed following the same experimental procedure but using a 25 µg/mL concentration of avidin, HYAL and BSA. The long-term stability of the peptidoglycan-modified membranes was evaluated by storing a set of them (peptidoglycan concentration: 5 mg/mL) at 4°C for one month. The nanochannel blocking was evaluated in different days during this period.

---

<sup>391</sup> A. de la Escosura-Muñiz, A. Merkoçi. *Small*. 7 (2011) 675–682.

<sup>392</sup> W. Ye, Y. Xu, L. Zheng, Y. Zhang, M. Yang, P. Sun. *Sensors*. 16 (2016) 1767.



### 5.3.2.2. *Nanoporous cell set-up and electrochemical detection*

Nanoporous alumina membranes were measured following the experimental set-up used in the previous section. Nanoporous membranes were physically attached onto the ITO/PET electrode, placing it onto a methacrylate block and putting the membrane with the filtering side up over the electrode surface. Then, a second block containing a hole of 8 mm in diameter was placed onto the membrane, with an insulating O-ring between them to avoid liquid leakage. Finally, the system was fixed with screws, defining an electrochemical cell that was filled with the 10 mM  $K_4[Fe(CN)_6]$  red-ox indicator solution. All measurements were carried out with a working volume of 400  $\mu$ L, which was enough to cover the three-electrode system (silver/silver chloride reference electrode, platinum wire counter electrode and ITO/PET working electrode).

A pre-treatment at -0.1 V was applied for 30 s and, immediately after, a differential pulse voltammetric (DPV) scan was performed from -0.1 V to +1.1 V (step potential: 10 mV, modulation amplitude: 50 mV, and scan rate: 33.5 mV/s), resulting in a voltammetric signal due to oxidation of  $[Fe(CN)_6]^{4-}$  to  $[Fe(CN)_6]^{3-}$ , which peak current at approximately +0.40 V was chosen as the analytical signal. The measurements were carried out in triplicate at room temperature under non-stirring conditions. Each measurement was performed with a single nanoporous membrane and an ITO/PET electrode, discarded after the measurement.

### 5.3.3. Results and discussion

#### 5.3.3.1. Nanochannels blockage by peptidoglycan: steric and electrostatic contributions

As illustrated in Figure 5.5, it is envisaged that the immobilization of peptidoglycan in the nanochannels produces a blockage in the diffusion of the electroactive species through the nanoporous membranes to the electrochemical transducer surface. Furthermore, it is also expected that the degradation of peptidoglycan by lysozyme will lead to the unblockage of the nanopores.

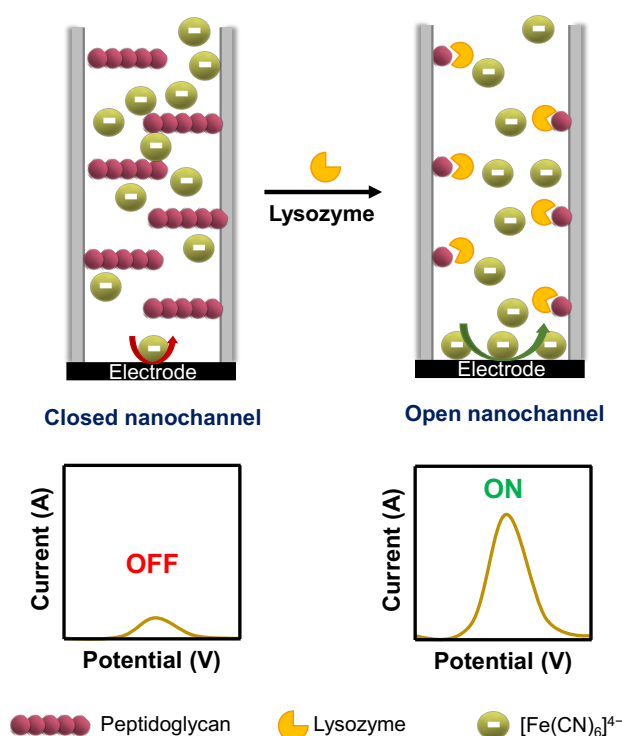


**Figure 5.5.** Scheme of the biosensing system based on nanochannel steric/electrostatic blocking by peptidoglycan and further unblocking after enzymatic cleavage by lysozyme.

Such nanochannels blocking after peptidoglycan immobilization can be attributed to a dual effect based on both steric and charge repulsion effects. Considering the size of both peptidoglycan (around 10 nm)<sup>393</sup> and  $[\text{Fe}(\text{CN})_6]^{4-}$  red-ox indicator ions (< 1 nm), it is expected that in absence of peptidoglycan the red-ox ions can freely flow through the nanochannel to the electrode, whereas the presence of peptidoglycan will hinder their passage due to steric impairments.

<sup>393</sup> I. Tulum, Y.O. Tahara, M. Miyata. *Microscopy*. 68 (2019) 441–449.

On the other hand, it is worthy to note that the peptidoglycan can be negatively charged, positively charged or without a net charge depending on the pH of the measurement buffer solution. Peptidoglycan electronic charge may influence the nanopores blockage due to charge repulsion effects. If the peptidoglycan is negatively charged (working at a pH higher than peptidoglycan's isoelectric point) a repulsion effect between the negative charges of the peptidoglycan and the negative ones from the red-ox indicator ions is expected. This charge repulsion will hinder the ions diffusion to the electrode.

Therefore, before carrying out lysozyme determination, a series of optimizations were made with the aim of achieving the maximum steric/electrostatic blocking of the nanochannels by immobilizing peptidoglycan on their inner walls.

With the aim to simplify and normalize the results, in the studies shown along the following sections, the degree of blockage will be expressed in terms of % of decrease in the analytical signal, compared with the one obtained for the bare silanized membrane, calculated as follows:

$$\text{Blockage (\%)} = \left| \left( \frac{(i_p \text{ peptidoglycan modified membrane} - i_p \text{ bare membrane})}{i_p \text{ bare membrane}} \right) \times 100 \right|$$

#### 5.3.3.2. *Effect of the peptidoglycan concentration*

The effect of peptidoglycan concentration on the nanochannels blockage and thus on the analytical signal was first studied with membranes containing nanopores of 20 nm. Peptidoglycan from solutions at different concentrations (1 and 5 mg/mL) was immobilized in the nanochannels through carbodiimide chemistry, as detailed in the methods section. The nanochannels blocking was evaluated by the voltammetric monitoring of the diffusion of the  $[\text{Fe}(\text{CN})_6]^{4-}$  ions in buffer at pH 7.2.

As shown in Figure 5.6.A, when increasing the amount of peptidoglycan in the nanochannels, the  $[\text{Fe}(\text{CN})_6]^{4-}$  ions diffusion is hindered, probably due to both steric and electrostatic effects, leading to a decrease in the voltammetric signal from the oxidation of  $[\text{Fe}(\text{CN})_6]^{4-}$  to  $[\text{Fe}(\text{CN})_6]^{3-}$ . As summarized in Figure 5.6.B, the 18 % blocking in the signal recorded at 1 mg/mL peptidoglycan increased up to 47 % when using 5 mg/mL peptidoglycan. Higher concentrations were not assayed for cost saving considerations. In

view of these results, a peptidoglycan concentration of 5 mg/mL was selected as the optimum for the biosensor development.

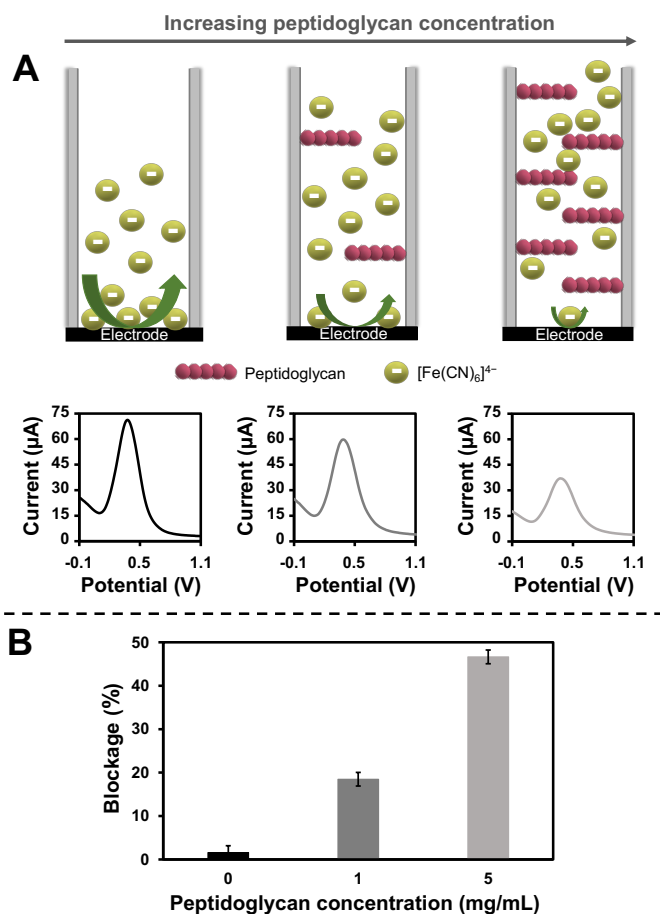


**Figure 5.6.** Effect of the peptidoglycan concentration on the nanochannels blockage. (A) Schematic illustration of the different amount of immobilized peptidoglycan, and its effect on the  $[\text{Fe}(\text{CN})_6]^{4-}$  ions diffusion to the electrode. Differential pulse voltammograms registered in 10 mM  $\text{K}_4[\text{Fe}(\text{CN})_6]/0.1$  M (in buffer at pH 7.2) for nanoporous membranes (20 nm pore size), bare silanized (left) and modified with 1 mg/mL (middle) and 5 mg/mL (right) of peptidoglycan. DPV parameters: pre-concentration potential: -0.1 V; pre-concentration time: 30 s; step potential: 10 mV, modulation amplitude: 50 mV, and scan rate: 33.5 mV/s. (B) Comparative bar chart of the signal blockage (expressed in percentage) for different peptidoglycan concentrations. Data are given as average  $\pm$  SD ( $n = 3$ ).

### 5.3.3.3. Effect of the pH: electrostatic forces involved in nanochannel blocking

pH is a key parameter affecting the ionic transport in nanochannels. In our particular case, the pH of the measurement buffer solution drives the peptidoglycan electronic charge, affecting the electrostatic forces involved in the nanochannels blocking.

Considering the isoelectric point of the peptidoglycan (pI: 6.5)<sup>394</sup> solutions of the 10 mM K<sub>4</sub>[Fe(CN)<sub>6</sub>] red-ox indicator were prepared in different buffers at pH below, equal and above this value. Typical buffers for each range of pH were selected: 0.1 M NaAc (for pH 4.5), 0.1 M MES (for pH 6.5) and 0.1 M Tris-HCl (for pH 7.2). The evaluation of any of these buffers at a pH different from their typical value was not considered appropriate. Membranes containing nanopores of 20 nm, where the peptidoglycan is immobilized from a 5 mg/mL, solution were used for this study.

As shown in Figure 5.7, when the pH of the measurement buffer solution is higher than the pI of the peptidoglycan (pH 7.2), a high blocking (47 % decrease in the signal) is observed. These experimental results are in line with the hypothesis about the effect of the nanochannel charges on the diffusion of [Fe(CN)<sub>6</sub>]<sup>4-</sup> anions, which has also been proposed by other authors<sup>395</sup>. At this pH the peptidoglycan is negatively charged, and such charges attract cations and repel anions, forming a negatively charged electric field, also called electrostatic repulsion region. Such hindrance region decreases the pathway of anion passing through the nanochannels, resulting in a decreased flux of [Fe(CN)<sub>6</sub>]<sup>4-</sup> and consequently a lower voltammetric signal, what we call a high blockage. However, when working below the pI of the peptidoglycan (pH 4.5), it is positively charged and the situation is the opposite: a positively charged electric field is generated, allowing the [Fe(CN)<sub>6</sub>]<sup>4-</sup> anions to permeate preferentially for maintaining the electroneutral condition in the nanochannel, leading to a higher voltammetric signal, what we call a low blockage (5 % decrease in the signal). At pH of the red-ox indicator medium equal to the pI of the peptidoglycan (pH 6.5), the peptidoglycan molecules are uncharged and the [Fe(CN)<sub>6</sub>]<sup>4-</sup> ions diffusion through the nanochannel is neither electrostatically favored nor hindered, obtaining a 15 % of signal blockage, probably only due to steric issues.

---

<sup>394</sup> H. Yoshida, K. Kinoshita, M. Ashida. *J. Biol. Chem.* 271 (1996) 13854–13860

<sup>395</sup> S. Li, J. Li, K. Wang, C. Wang, J. Xu, H. Chen, X. Xia, Q. Huo. *ACS Nano.* 4 (2010) 6417–6424

Considering these findings, in further experiments the electrochemical measurements were performed at the maximum electrostatic blockage conditions, that is using a buffer of pH 7.2 as red-ox indicator medium solution.

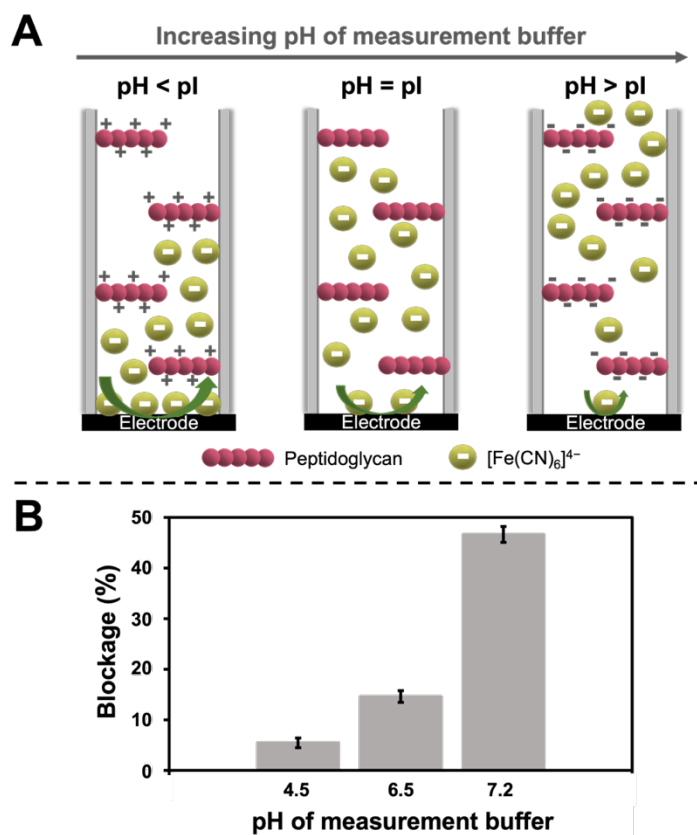


**Figure 5.7.** Measurement buffer pH effect on the nanochannels blockage. (A) Schematic illustration of the different net charge of the peptidoglycan (pI: 6.5) depending on the pH of the measurement buffer, and its effect on the  $[\text{Fe}(\text{CN})_6]^{4-}$  ions diffusion to the electrode. (B) Comparative bar chart of the signal blockage (expressed in percentage) for measurement buffer solutions at different pH. Data are given as average  $\pm$  SD ( $n = 3$ ). Peptidoglycan concentration: 5 mg/mL.  $\text{K}_4[\text{Fe}(\text{CN})_6]$  concentration: 10 mM (at different pH measurement buffer solutions).

#### 5.3.3.4. Effect of the nanopore size

The steric blockage of the nanochannels will depend not only on the peptidoglycan concentration but also on the nanopore size, expecting a lower degree of blockage when increasing the nanopore size. Nanoporous membranes containing nanopores of 20 nm, 100 nm and 200 nm were evaluated for such purpose. A peptidoglycan concentration of 5 mg/mL and a red-ox indicator medium solution at pH 7.2 were fixed for this study.

As schematized in Figure 5.8.A, for the smaller nanopore size (20 nm) the peptidoglycan molecules in the opposite walls of the nanochannels are very close, and this proximity leads to a steric blockage that prevents the flow of  $[\text{Fe}(\text{CN})_6]^{4-}$  ions. However, when increasing the nanopore size, the distance between the nanochannel walls increases, which facilitates the ions' flow, leading to a decrease in the steric blockage.

From the obtained results (Figure 5.8.B) it can be concluded that the higher is the nanopore size, the lower the steric blockage. The blocking percentage found for the 20 nm membranes (47 %) decreases to 17 % when using the intermediate nanopore size (100 nm) membranes, and further to 6 % for the higher nanopore size (200 nm) membranes. In line with these results, nanoporous membranes containing pores of 20 nm, for which the maximum signal blocking by the peptidoglycan was achieved, were chosen for lysozyme sensing.

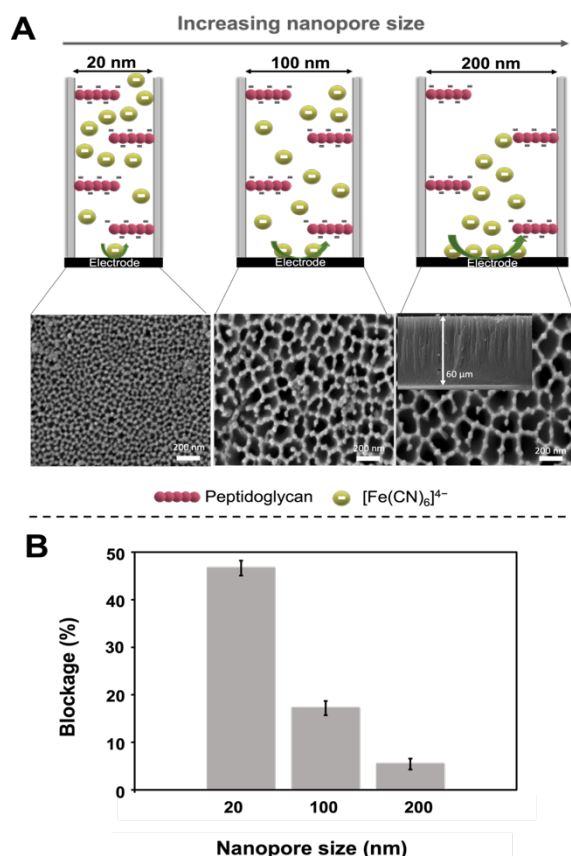


**Figure 5.8.** Effect of the nanopore size on the nanochannels blockage. (A) Schematic representation of the effect of different nanopore sizes on the  $[\text{Fe}(\text{CN})_6]^{4-}$  ions diffusion to the electrode, together with SEM top-view micrographs of the nanoporous membranes. The inset in the image of the 200 nm-pores membrane corresponds to a cross-section view. (B) Comparative bar chart of the signal blockage (expressed in percentage) for nanoporous membranes with different nanopore sizes. Data are given as average  $\pm$  SD ( $n = 3$ ). Peptidoglycan concentration: 5 mg/mL.  $\text{K}_4[\text{Fe}(\text{CN})_6]$  concentration: 10 mM (in buffer at pH 7.2).

### 5.3.3.5. *Electrochemical detection of lysozyme*

As previously detailed, the proposed sensing system is based on the specific cleavage of the  $\beta$ -(1,4)-glycosidic bonds of the peptidoglycan by lysozyme, which leads to the unblockage of the nanochannels. For this purpose, the peptidoglycan-modified membranes were incubated with lysozyme (concentration range from 1 to 50  $\mu\text{g/mL}$ ) at the optimum conditions for the enzymatic reaction (37  $^{\circ}\text{C}$ , 30 min)<sup>396</sup>.

As expected, (Figure 5.9.A.), the voltammetric signal obtained for the peptidoglycan-modified membranes (blue continuous line) gradually increases with the amount of lysozyme (dotted lines), evidencing the unblockage of the nanochannels by specific degradation of the peptidoglycan. As a result, the analytical signal ( $[\text{Fe}(\text{CN})_6]^{4-}$  oxidation peak current at +0.40V) increases with the lysozyme concentration in the range 0-50  $\mu\text{g/mL}$ . Both parameters are adjusted to a linear relationship (Figure 5.9.B), with a correlation coefficient of 0.9994, according to the following equation:

$$\text{Peak current } (\mu\text{A}) = 2.2 [\text{Lysozyme}] (\mu\text{g/mL}) + 31$$

The method shows a good reproducibility, with a relative standard deviation (RSD) of 5 % (n=3). A limit of detection (LOD, calculated as three times the standard deviation of the intercept divided by the slope) of 280 ng/mL of lysozyme was found. This value is in agreement with the obtained by standard ELISA assays (260 ng/mL)<sup>397</sup>, being our method considerably simpler, faster and cheaper, without the need of labels or competitive immunoassay formats.

---

<sup>396</sup> J. Sambrook, E.F. Fritsch, T. Maniatis, *Molecular Cloning: A Laboratory Manual*, Cold Spring Harbor, New York: Cold Spring Harbor Laboratory, 1989, 1989.

<sup>397</sup> M.-L. Vidal, J. Gautron, Y. Nys. *J. Agric. Food Chem.* 53 (2005) 2379–2385



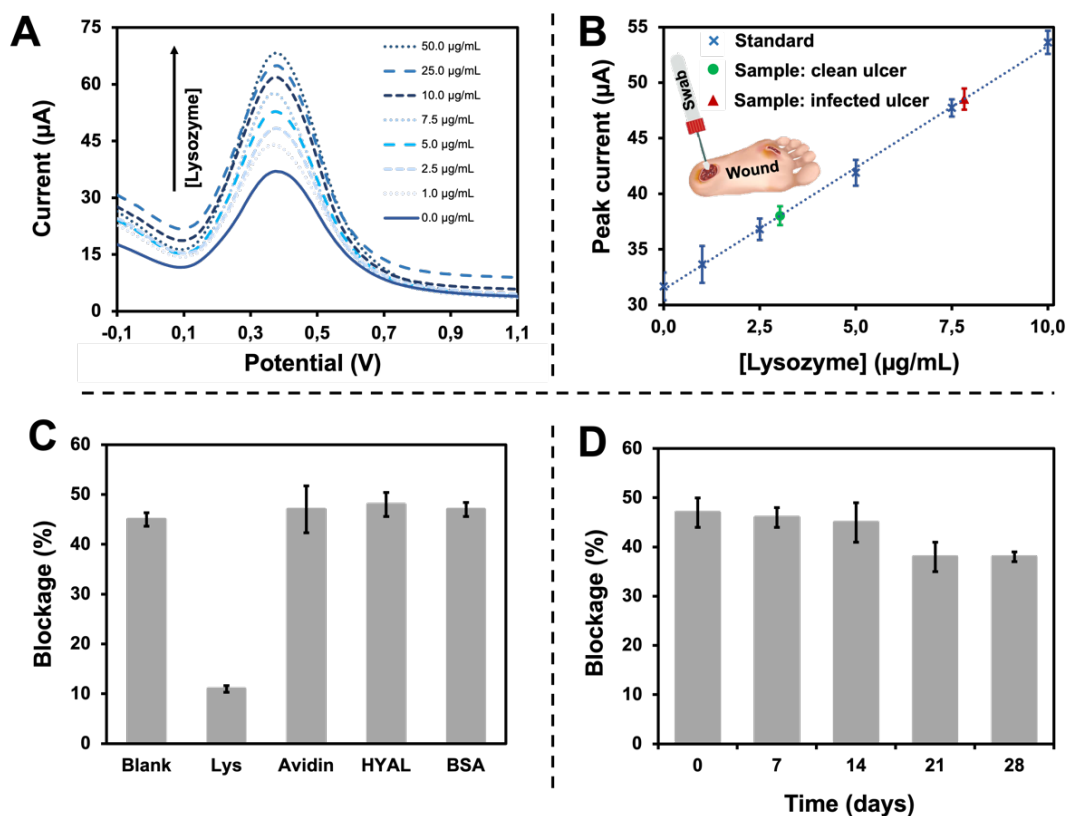


**Figure 5.9.** Lysozyme determination through the enzymatic cleavage of peptidoglycan, leading to nanochannels unblockage. (A) Differential pulse voltammograms registered in 10 mM  $K_4[Fe(CN)_6]$ /0.1 M (in buffer at pH 7.2) for 5 mg/mL peptidoglycan-modified membranes (20 nm nanopores) after incubation with increasing concentrations of lysozyme (0-50  $\mu\text{g/mL}$ , from down to up). DPV parameters: pre-concentration potential: -0.1 V; pre-concentration time: 30 s; step potential: 10 mV, modulation amplitude: 50 mV, scan rate: 33.5 mV/s. (B) Calibration plot obtained for standard solutions of lysozyme as well as the analytical signals obtained for swab exudates (diluted 1:10) from patients with potentially clean and clearly infected ulcers. Data are given as average  $\pm$  SD ( $n = 3$ ). (C) Selectivity study of Lysozyme detection, evaluated against avidin, HYAL and BSA (proteins concentration 5  $\mu\text{g/mL}$ ). (D) Long-term stability study of the peptidoglycan-modified membranes (Peptidoglycan concentration: 5  $\mu\text{g/mL}$ ).

### 5.3.3.6. System selectivity and stability

The selectivity of our system against other proteins that are commonly present in wound exudates, such as avidin, hyaluronidase (HYAL) and bovine serum albumin (BSA) (at a concentration of 5  $\mu\text{g/mL}$ ), was evaluated. As shown in Figure 5.9.C, no significant changes in the nanopore blockage were noticed for any of such proteins, as it is observed for lysozyme, demonstrating the excellent selectivity of the system.

The long-term stability of the peptidoglycan-modified membranes was evaluated by storing a set of them at 4°C for one month. The nanochannel blocking was evaluated in different days during this period. As shown in Figure 5.9.D, the response of the system was stable and reproducible for at least 14 days, noticing a decrease in the effectivity of the immobilized peptidoglycan after 21 days of storage. The response was then stable at least after 28 days. A longer-term stability study was not considered.

#### 5.3.3.7. *Lysozyme determination in chronic wound exudates*

The detection of excessive lysozyme levels in wound exudates is a sign of infection. This would allow to monitor the evolution of the healing status of the wound and to assess the effectiveness of the applied therapies.

Nanoporous alumina membranes are ideal platforms for such real application, thanks to their ability to also act as filter of biomolecules<sup>398,399,400</sup>, which also allows *in situ* studies on live cells and bacteria cultures<sup>401,337</sup>. It is well-known that alumina has a low protein adsorption rate, what is indeed the reason for its use as a filter material. This filter-like property minimizes matrix effects in the analytical signal, allowing for the direct detection of lysozyme, without any pre-treatment of the sample. As detailed in the experimental section, swab exudates from patients with potentially bacteria-free skin ulcers and infected ones were analysed following the experimental procedure previously detailed for lysozyme standard solutions. Dilution of the swab exudates to a 1:10 ratio was necessary to obtain analytical signals within the range of the calibration curve. As observed in Figure 5.9.B, substantially different analytical signals were obtained for both samples evidencing the ability of our method to discriminate them. The concentration of lysozyme in each sample was directly extrapolated from the calibration curve, taking advantage of the above detailed low matrix effects noticed when working with alumina membranes. In this way,  $30 \pm 5$  µg/mL of lysozyme were estimated in the clean ulcer sample while this value increases to  $78 \pm 6$  µg/mL for the infected one. These values

---

<sup>398</sup> A. de La Escosura-Muñiz, A. Merkoçi. *Small*. 7 (2011) 675–682.

<sup>399</sup> A. de la Escosura-Muñiz, W. Chunglok, W. Surareungchai, A. Merkoçi. *Biosens. Bioelectron.* 40 (2013) 24–31.

<sup>400</sup> M. Espinoza-Castañeda, A. de la Escosura-Muñiz, A. Chamorro, C. de Torres, A. Merkoçi. *Biosens. Bioelectron.* 67 (2015) 107–114.

<sup>401</sup> A. de la Escosura-Muñiz, M. Espinoza-Castañeda, A. Chamorro-García, Carlos.J. Rodríguez-Hernández, C. de Torres, A. Merkoçi. *Biosens. Bioelectron.* 107 (2018) 62–68.

correlate with the previously reported<sup>371</sup> thus validating the feasibility of our system for the wound infection diagnosis in a real scenario. Wound exudates have been analysed by ELISA technique (Figure S5.5), providing a value of  $28 \pm 0.3 \mu\text{g/mL}$  for the clean ulcer sample and  $76 \pm 0.8 \mu\text{g/mL}$  for the infected one, what correlates with the values obtained by our method.

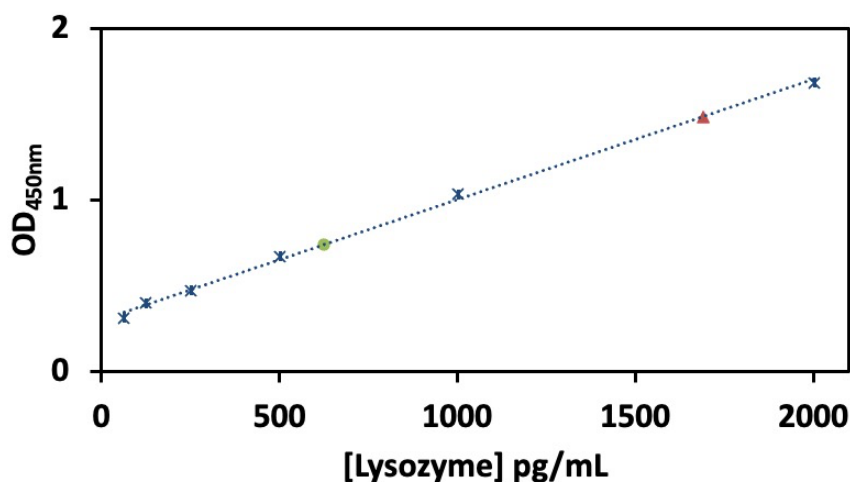


**Figure S5.5.** Calibration curve for the ELISA test developed to validate the lysozyme concentration observed using the electrochemical sensor. Data provided by duplicate  $\pm$  SD. As an inset, measurement for non-infected wound exudate (green circle) and infected exudate (red triangle). Samples were diluted 1:45000.

### 5.3.4. Conclusions

We have demonstrated that the infection biomarker lysozyme can be detected in chronic wound exudates using nanoporous alumina membranes, owing to the enzymatic cleavage of the peptidoglycan substrate used for blocking the alumina nanochannels. Both steric and electrostatic contributions are of key relevance for maximizing the nanochannels blocking by the substrate, which allows detecting low levels of lysozyme. Our findings suggest that while steric blocking is highly dependent on the pore size and the peptidoglycan concentration, the electrostatic blocking mainly depends on the pH of the red-ox indicator solution used for the voltammetric measurements. As far as we know, this is the first time that nanoporous membranes are used for electrochemical monitoring of enzymatic cleavage processes through the unblocking of previously blocked nanochannels, leading to an analytical method for the enzyme determination.

Our electrical method reached a lysozyme detection limit of 280 ng/mL, with a good selectivity and long-term stability. This result is in line with previous reports based on ELISA assays, being our method faster and cheaper, without the need of labels or competitive immunoassay formats.

The proposed method is of particular interest for the discrimination of exudates from infected and non-infected wounds without sample pre-treatment, taking advantage of the low protein absorption rate and thus outstanding filtering properties of the nanoporous alumina membranes. The increased levels of lysozyme in infected ulcer samples (around 78  $\mu\text{g/mL}$ ) compared with non-infected ones (around 30  $\mu\text{g/mL}$ ) correlate with previously reported data for wound fluids, demonstrating the feasibility of our system for the early wound infection diagnosis in the clinical scenario. Early diagnosis would allow to select a correct treatment, avoiding patients' disability and saving resources for hospitalization. Furthermore, the miniaturization and low cost of the proposed analytical methodology would allow its implementation in out-of-hospital settings as well.



## 5.4. Scientific article 8

### **Modifying thickness of nanoporous membranes reduces limit of detection: Application in an electrochemical sensor for chronic wound infection**

C. Toyos-Rodríguez, D. Valero-Calvo, A. Iglesias-Mayor, V. Vega-Martínez, A. de la Escosura-Muñiz

Invited contribution to *Frontiers in Bioengineering and Biotechnology*

#### **5.4.1. Introduction**

Solid-state nanoporous membranes as platforms have emerged as promising tools in biotechnological challenges such as healthcare applications<sup>402</sup>, energy storage<sup>403,404</sup> or as nanoreactors for single-molecule chemistry studies<sup>405,406</sup>.

These type of nanoporous membranes were first synthesized in 2001, and since then many manufacturing methodologies have emerged, reporting membranes diameter sizes between 100 at the beginning to 1 nm more recently<sup>407</sup>.

From the variable solid-state nanoporous membranes available, nanoporous alumina membranes stand out, due to their easy functionalization, large surface area, stability, and filtering properties. This type of membranes is one of the largest platforms used in biosensing, as they present a homogenous and self-ordered nanoporous structure<sup>408</sup>. Nanoporous alumina membranes are formed by the voltage mediated anodization of Al at an acidic pH, which forms a honeycomb like structure characterized by two main parameters involved in biosensing performance: pore diameter and pore thickness.

---

<sup>402</sup> S. Cai J. Y. Y. Sze, A. P. Ivanov, J.B. Edel. *Nature Communications* 2019 10 1797

<sup>403</sup> G. Che, B. B. Lakshmi, E. R. Fisher, C. R. Martin. *Nature*, 1998, 393, 346-349

<sup>404</sup> P. Si et al. *Materials*. 2023, 16(10), 3864

<sup>405</sup> Lee, J. & Bayley, H. *Proc. Natl Acad. Sci. USA* 2015 112, 13768–13773

<sup>406</sup> Qing, Y., Tamagaki-Asahina, H., Ionescu, S. A., Liu, M. D. & Bayley, H. *Nat. Nanotechnol.* 2019 14, 1135–1142

<sup>407</sup> H. Liu et al. *Small*. 2023. 19. 2205680

<sup>408</sup> A. de la Escosura Muñiz, A. Merkoçi. *ACS Nano* 2012, 6, 9, 7556–7583

Although this first one has been deeply researched<sup>409</sup>, studying the effect of pore thickness in the analytical performance of a biosensor using this material as sensing platform is still in the fledgling period. Nanopore thickness has been previously considered in biological nanopores<sup>410</sup>, where reducing it has been correlated with the detected signal. However, in nanoporous alumina membranes, studies in this sense are scarce.

In this work, nanoporous alumina membranes with a fixed pore diameter (~60 nm) and variable pore thicknesses (45, 60, 90  $\mu\text{m}$ ) have been constructed through a two-step anodization process. Commercially available membranes with a diameter of 20 nm and a thickness of 60  $\mu\text{m}$  have been also evaluated. The analytical characteristics of these membranes have been compared developing an immunosensor for the detection of human IgG (HIgG) as analyte. The principle of the developed sensors is based on the immobilization inside nanoporous alumina membranes of an antibody against HIgG. In the presence of this molecule, an immunocomplex is formed inside the channel. The diffusion of a redox indicator solution through the nanochannel is then hindered, changing the electrical signal recorded.

Using this principle, we have observed that a reduced pore thickness (45  $\mu\text{m}$ , 60 nm pore diameter) improves the sensitivity of the biosensor developed while lowers the limit of detection achieved up to 6 times compared to nanoporous membranes with higher pore thickness (60  $\mu\text{m}$ ) but reduced pore diameter sizes (20 nm).

Optimal nanoporous membranes have been applied to the detection of a chronic wound infection biomarker as a proof-of-concept. Chronic wounds are a prevalent healthcare challenge in aging populations, with a prevalence of 1-2% in developed countries<sup>411</sup>. A major complication in the normal healing process of a wound is infection, that delays wound bed recovery and if unattended increasing the risk of sepsis. A fast and accurate identification of an infection is then mandatory to stop the bacteria colonization by providing a suitable antibiotic treatment. However, current identification techniques are based on visual signs of infection<sup>412</sup>. (i.e. redness, swelling, increased temperature of the wound bed...) or gold-standard culture techniques, that are time consuming. The long time required for a result to be obtained leads to the unchecked administration of

---

<sup>409</sup> van den Hout, M. et al. *Nat. Nanotechnology* 21, 115304 (2010).

<sup>410</sup> L. Xue et al. *Nature Review Materials* 2020, 5, 931-951

<sup>411</sup> A. Clinton, T. Carter. *Lab Med.* 46 (2015) 277–284.

<sup>412</sup> A.R. Siddiqui, J.M. Bernstein. *Clin. Dermatol.* 28 (2010) 519–526.

antibiotic treatment, what aggravates the appearance of multi-drug resistant microorganisms<sup>413,414</sup>.

The use of point-of-care (POC) analytical tools, as the one developed in this work, to tackle infection in a cost-effective, fast and accurate manner would be desirable both to alleviate both chronic wound management and antimicrobial resistance ascension. Thus, catalase, a hydrogen peroxidase enzyme established as biomarker of several pathologies as oxidative stress or chronic wound infection<sup>415</sup>. Catalase is produced by certain bacteria, including *Pseudomonas aeruginosa*, a prevalent microorganism present in chronic wounds, as well as *Enterobacteriaceae* or *Staphylococcus* among others<sup>416,417</sup>

The results obtained in this work will illuminate nanoporous membrane biosensing research, considering thickness as a relevant parameter in nanoporous membrane construction. Moreover, the developed sensor will facilitate the identification of chronic wound infection in a timely manner.

## 5.4.2. Protocols

### 5.4.2.1. Nanoporous alumina membranes synthesis and functionalization

Nanoporous alumina membranes were obtained following a previously published procedure<sup>418</sup>. Briefly, a highly pure aluminum disk (composed of Al 99.999% with a size of 0.5 mm in thickness and 25 in diameter) was cleaned with isopropanol and ethanol for further electropolish with a 1:3 v/v of perchloric acid: ethanol. The aluminum was then anodized following a two-step anodization process, using a 0.3 M oxalic acid solution as electrolyte, and applying an anodization voltage of 40 V. The first anodization step was applied for 24h at 0-1°C. The anodization time was modified to adjust the thickness of the resulting membranes. After that, the resulting Al template was washed to remove the aluminum oxide layer with an acidic solution of CrO<sub>3</sub> and H<sub>3</sub>PO<sub>4</sub> at 35°C for 24h. A second anodization step was then performed also applying a 40 V potential and the time

---

<sup>413</sup> Hirsch, E. B.; Tam, V. H. *Expert Rev. Pharmacoeconomics Outcomes Res.* 2010, 10, 441–451.

<sup>414</sup> J.S. Inda-Díaz et al. *Microbiome* 2023 11, 44

<sup>415</sup> A. Clemente et al. *ACS Sensors*, 2020, 5, 3956-3963

<sup>416</sup> B. Chester, L.B. Moskowitz. *J. Clin. Microbiol.* 1987, 25(2), 439-441

<sup>417</sup> D-H. Shin, Y-S. Choi, Y-H. Cho. *J. Bacteriol.* 2008, 190(8), 2663-2670

<sup>418</sup> A.L. Cuevas et al. 2023. *Micromachines* 2023, 14, 839.



was adjusted to obtain a nanoporous membrane thickness of ~60  $\mu\text{m}$ . A last cleaning step was then performed using an aqueous mixture of HCl and  $\text{CuCl}_2$  to remove a  $1\text{ cm}^2$  area of remaining Al at the bottom layer and then, a wet chemical etching using an aqueous solution of  $\text{H}_3\text{PO}_4$  5% at RT for 90 min to open the formed pores. Nanopores were widened in a final step using  $\text{H}_3\text{PO}_4$  5% at  $30^\circ\text{C}$  to adjust diameter size to ~50 nm.

The obtained nanoporous membranes were later functionalized using atomic layer deposition (ALD) using exposure mode and APTES as precursor and Ar as purge and carrier gas.  $\text{O}_3$  was used as oxidation agent used at  $25^\circ\text{C}$  applying a 0.1 s precursor pulse time, 60s exposure time and 120 s purge laps. In between pulses, an Ar flow of 50 sccm was applied for 90 s to remove any excess reactant.

#### 5.4.2.2. *Electrochemical measurements*

The obtained nanoporous membranes were physically attached onto an ITO/PET electrode hydrolysed immersing the electrodes onto a 17:3:1 solution of  $\text{H}_2\text{O}:\text{NH}_3:\text{H}_2\text{O}_2$  for 20 min. Electrodes were washed with acetone, isopropanol and water and let dry. Later, they were electrochemically characterized to confirm that the applied hydrophilization treatment did not affect conductivity. Nanoporous membranes were later placed on top of the ITO/PET electrode and placing it into a methacrylate block. The membranes were maintained inside the cell during the duration of the experiments, performing washing steps with the appropriate buffer inside them.

Measurements were performed using a 10 mM  $\text{K}_4[\text{Fe}(\text{CN})_6]$  red-ox indicator solution and a three-electrode system (silver/silver chloride reference electrode, platinum wire counter electrode and ITO/PET working electrode). A DPV was used to measure the oxidation of  $[\text{Fe}(\text{CN})_6]^{4-}$  to  $[\text{Fe}(\text{CN})_6]^{3-}$ , applying a pre-treatment at -0.1 V for 30 s and, scanning between -0.1 V to +1.1 V (step potential: 10 mV, modulation amplitude: 50 mV, and scan rate: 33.5 mV/s). Measurements were carried out in triplicate using a single nanoporous membrane and an ITO/PET electrode, discarded after the measurement.

#### 5.4.2.3. *IgG immobilization and evaluation of thickness effect*

After functionalizing the inner walls of the nanoporous alumina membranes with amine groups, 30  $\mu\text{L}$  of a solution of 5 mM EDC/sulfo-NHS in MES pH 5, containing a

concentration of 1000  $\mu\text{g/mL}$  of anti-HIgG antibody was placed on top of the nanoporous membrane and left at room temperature for incubation for 2h. After this time, membranes were gently washed with Tris-HCl 10 mM pH 7.00 buffer. Blockage obtained after antibody immobilization was measured at this point on each modified membrane. After measurement, membranes were gently washed with Tris-HCl 10 mM pH 7.00 buffer again and measured again without the addition of further redox indicator, confirming that there was no remaining solution inside the membrane.

Then, 30  $\mu\text{L}$  of solutions containing increasing concentrations of HIgG (100,500 and 1000  $\text{ng/mL}$ ) were placed on the membranes and left for incubation at room temperature during 1h, following a previously optimized protocol for this analyte<sup>419</sup>. After incubation, membranes were washed again and measured using a 10 mM Tris-HCl pH 8 solution.

#### 5.4.2.4. *Catalase detection*

For catalase enzyme detection, anti-catalase antibodies at a concentration of 50  $\mu\text{g/mL}$  were immobilized in the inner walls of nanoporous alumina membranes following the same procedure as described in Section 5.4.2.3. First, the optimum pH used for measurement was evaluated, using the solutions Tris-HCl 0.1M pH 7.0 and Tris-HCl 0.1 M pH 8.0. Catalase was detected in concentrations ranging from 10 to 10000  $\text{ng/mL}$ . Control assays were performed in Tris-HCl 0.1 M pH 7.0 without catalase being added. After this incubation, membranes were placed on top of a rack and gently washed with Tris-HCl 0.1 M pH 8.0 buffer solution.

### 5.4.3. *Results and discussion*

#### 5.4.3.1. *Nanoporous structural characterization and ITO/PET electrochemical characterization*

The effect of the diameter size of a nanochannel has already been correlated with the performance of the sensor, in terms of sensitivity and limit of detection. However, the diameter size is not the only parameter that affects the steric blockage inside nanochannels. We hypothesized that thickness of the nanochannels could also play a

---

<sup>419</sup> De la Escosura-Muñiz A., Merkoçi A. *Electrochemistry Communications* 12 (2010) 859–863

pivotal role in the blockage achieved, being traduced in lowering limits of detection and, additionally, in the amount of reactant needed, lowering the costs of the assay.

Commercial nanoporous alumina membranes have a fixed thickness of 60  $\mu\text{m}$ , making it impossible to evaluate this parameter. For that purpose, we have synthesized nanoporous alumina membranes with thickness of 45, 60 and 90  $\mu\text{m}$ . Nanoporous alumina membranes were obtained following a two-step anodization process. This variability in the membrane thickness is achieved by modifying the time of the second anodization step.

The obtained nanoporous alumina membranes were characterized by SEM, presenting a homogeneous honey-comb structure, with nanochannels of an average diameter size of  $59 \pm 4$  nm (Figure 5.10.B.). A cross-section of the membranes was also characterized, confirming that the nanochannels maintained their structure along the thickness of the membranes (Figure 5.10.C.).

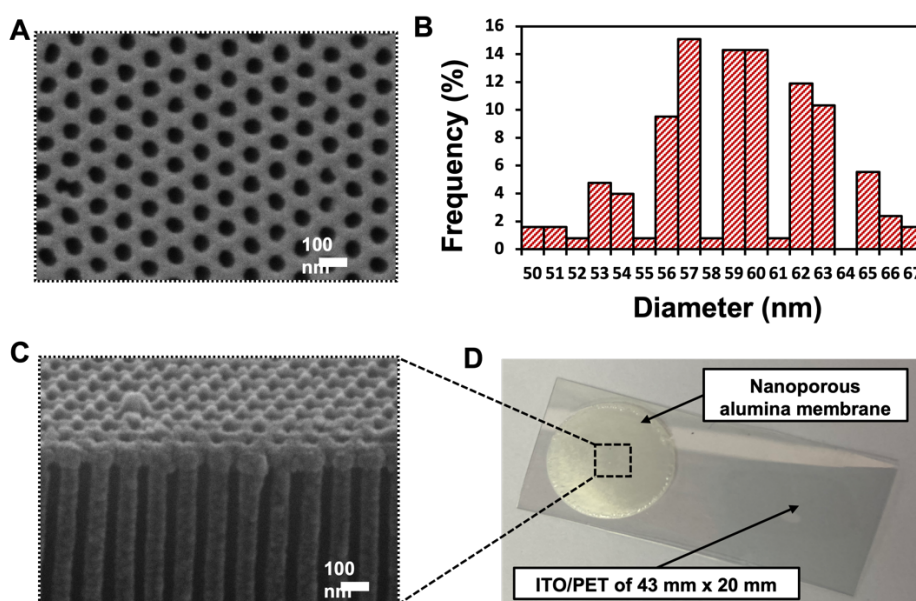


**Figure 5.10.** Characterization of the synthesized nanoporous alumina membranes. A. Top-view of the nanoporous membranes. B. Diameter size distribution of the nanochannels, showing an average diameter size of  $59 \pm 4$  nm. C. Cross-section of the obtained nanoporous alumina membranes with a thickness of 45  $\mu\text{m}$ . D. Non-magnified view of the nanoporous membranes on top of an ITO/PET electrode.

Nanoporous membranes were modified through atomic layer deposition (ALD), forming amine groups in the inner surface of the nanochannels. These amine groups were later used for the immobilization of antibodies used as recognition element. Functionalized membranes were integrated on top of a hydrophilized ITO/PET electrode.

This treatment increased the surface adherence of the membranes without modifying the electrochemical behavior observed (Figure 5.11.).

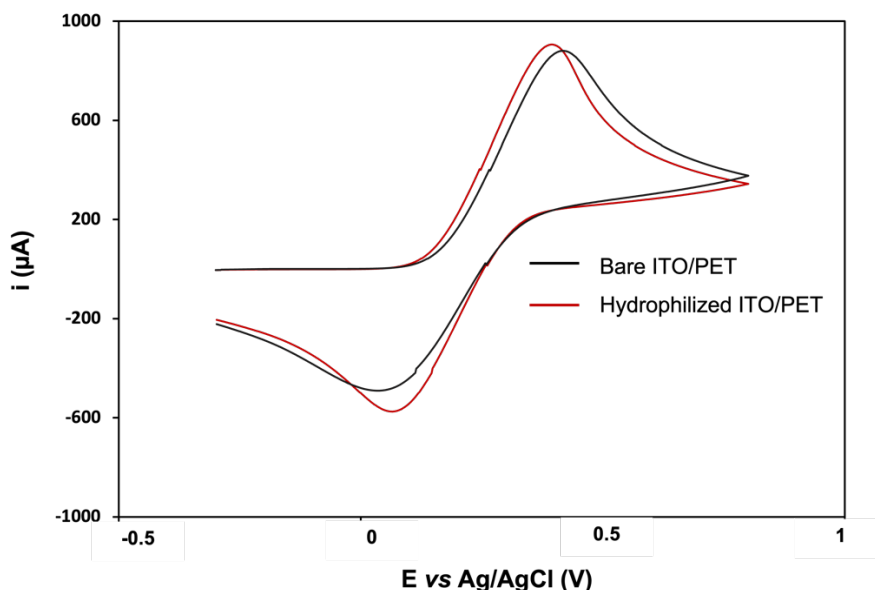


**Figure 5.11.** Electrochemical characterization of bare ITO/PET electrodes and hydrophilized ITO/PET electrodes. Cyclic voltammetry using  $[\text{Fe}(\text{CN})_6]^{4-}$  in Tris-HCl 0.1 M pH 7.2.

#### 5.4.3.2. Evaluation of thickness effect in nanochannel blockage

To evaluate how thickness of a nanochannel affected the sensitivity of a (bio)analytical platform using this material as sensing platform, an immunosensor for the detection of human IgG was constructed through the immobilization of anti-HIgG antibodies in the inner walls of the nanochannels. The principle of the developed platform is based on the specific capturing of HIgG inside the nanochannels, what blocks the passage of the red-ox indicator  $[\text{Fe}(\text{CN})_6]^{4-}$  to the electrode. This blockage reduces the voltammetric signal, associated to the oxidation of  $[\text{Fe}(\text{CN})_6]^{4-}$  to  $[\text{Fe}(\text{CN})_6]^{3-}$ , that it is recorded. All the process is performed using the *setup* depicted in Figure S5.X, where the integrated electrode/membrane platforms is collocated to perform every incubation step inside the cell. This approach increases the reproducibility of the method while facilitates manipulation, what it would be highly desirable for an end-point application.

HIgG has already been detected using commercially available nanoporous alumina membranes<sup>419</sup>. In this work, the authors observed that the diameter of nanoporous membranes affected the blockage, but contrary to what it was expected, the use of nanoporous membranes with a diameter of 200 nm provided a better result than using

membranes with a diameter of 200 nm, due to unspecific interactions. However, the effect of thickness has been hardly studied in these solid-state membranes before.

Three different nanochannel thicknesses, 45, 60 and 90  $\mu\text{m}$  of membranes with an average diameter size of 60 nm and commercial membranes with 60  $\mu\text{m}$  and 20 nm diameter size were tested against HIgG at concentrations 100, 500 and 1000  $\mu\text{g}/\text{mL}$  (Figure 5.12.).

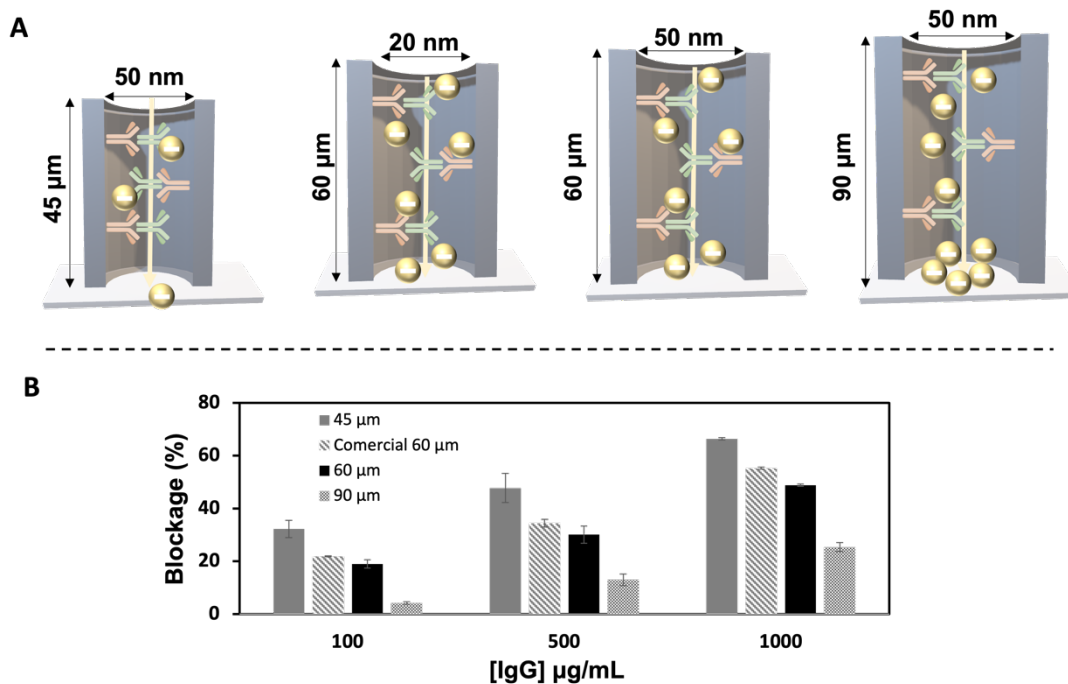


**Figure 5.12.** Study of the effect of membrane thickness in the sensitivity of an HIgG immunosensors. A. Schematic representation of the different membranes used with increasing thickness. B. Results obtained represented as blockage % obtained per each concentration studied.

Results showed that membranes with a thickness of 45  $\mu\text{m}$  provided a higher sensitivity (slope of 0.0379 (blockage %)) and lower limit of detection (24.2  $\mu\text{g}/\text{mL}$ ) compared to the analytical results provided with thicker membranes (Table 5.2). This change in the LOD obtained was particularly notable for commercial membranes with a diameter of 20 nm with a LOD more than 6 times higher (152.8  $\mu\text{g}/\text{mL}$ ). These results confirm that controlling the thickness is also of paramount importance to improve the sensitivity of immunosensors using nanoporous membranes as sensing platform.

**Table 5.2.** Analytical characteristics obtained with nanoporous alumina membranes with variable thicknesses.

Thickness ( $\mu\text{m}$ )	Diameter size (nm)	Slope	LOD ( $\mu\text{g/mL}$ )
45	~60	0.0379	24.2
60	~20	0.0373	152.8
60	~60	0.0332	158.8
90	~60	0.0236	62.5

#### 5.4.3.3. *Catalase detection*

To prove the feasibility of the optimal 45  $\mu\text{m}$  nanoporous membranes, an immunosensor for the detection of catalase was developed. Anti-catalase antibodies were immobilized in the inner walls of the developed membranes through carbodiimide chemistry. The anti-catalase antibody used was a mouse monoclonal antibody. Although the exact isoelectric point (pI) of this antibody was not determined, the approximately pI that mouse IgG present is in the range between 6.3 to 8.0<sup>420</sup>. To maximize the blockage obtained, a measurement pH higher than 8.0 would be required. Regarding human catalase from erythrocytes (UniProt Code P04040), the analyte of interest, it presents a theoretical pI of 6.9, thus a pH higher than this value would be desirable to maximize the blockage obtained. Moreover, catalase, as every enzyme, has an optimum pH range in between it maintains native conformation of the active site. For catalase, it is hypothesized that this value ranges between pH 6 and 8.

The effect of the use of measurement solutions with pH values ranging from 6 to 8 on the blockage obtained was tested. First, the catalytic activity of catalase was easily tested under the different pH values used exposing a catalase concentration of 500 ng/mL against 20  $\mu\text{L}$  of  $\text{H}_2\text{O}_2$  + 20  $\mu\text{L}$  of redox indicator or buffer solution for control assays. Results confirmed that catalytic activity was not affected by neither the pH nor the redox indicator solution.

<sup>420</sup> Robert A. Murgita, Stephen I. Vas; Isoelectric Separation of Mouse Immunoglobulins<sup>1</sup>. *J Immunol* 1 February 1970; 104 (2): 514–517

Once this aspect was confirmed, catalase was detected using nanoporous alumina membranes under redox indicator solutions with pH values of 7.0 and 8.0. According to the scheme depicted in Figure 5.13., at a pH of 7.0, catalase enzyme is negatively charged, as this pH value is under the pI of this molecule. The presence of a negative charge inside the nanochannel should have an electrostatic attraction effect over the  $[\text{Fe}(\text{CN})_6]^{4-}$  redox indicator, what would lead in a decrease in the voltammetric signal recorded. This hypothesis was corroborated, observing an increase in the blockage obtained of 13% (for a catalase concentration of 500 ng/mL), defining the blockage as stated in Equation X.

$$\text{Index of Catalase Current Blockage } (\Delta I_{\text{Cat}}) (\%) = \left( \frac{I_0 \text{ antibody modified membrane} - I_{\text{immunoassay}}}{I_0 \text{ antibody modified membrane}} \right) \times 100$$

(Eq. 4)

At a pH 8, catalase enzyme is still negatively charged while anti-catalase antibody should also have a net positive charge, what should increase the blockage obtained. Although the blockage was on average ~3 times higher (35%), the deviation obtained at this pH concentration also increased, with an RSD of 20% compared to the 1% obtained at pH 7.0. Further optimization of this parameter is then required prior to the quantification of catalase.

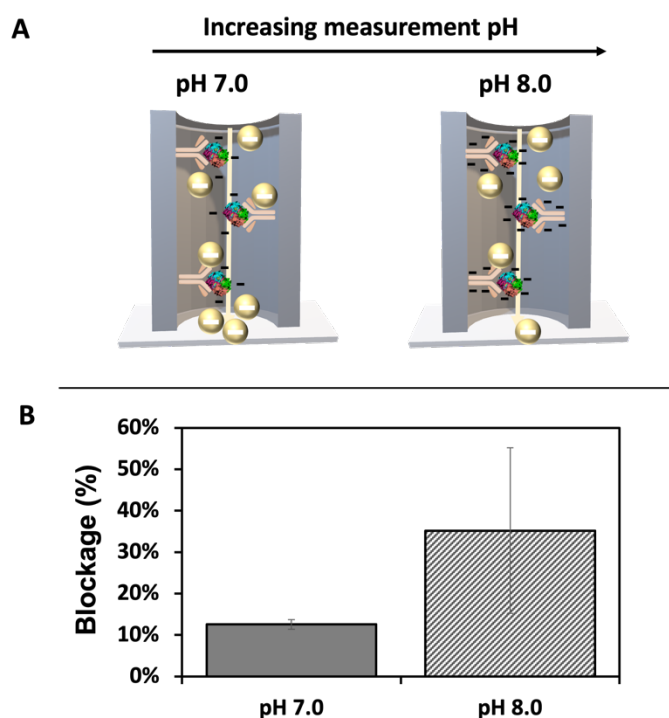


**Figure 5.13.** Effect of the pH used for measurement **A.** Representation of the electrostatic profile of the catalase immunocomplex at varying pH and how it affects the diffusion of the  $[\text{Fe}(\text{CN})_6]^{4-}$  red-ox

indicator ions through the channel; **B.** Effect of the pH on the index of Catalase current blockage (as defined in Equation X) represented by the average  $\pm$  SD (n=3).

#### **5.4.4. Conclusions**

The effect of the thickness of nanoporous alumina membranes in the sensitivity of a sensor developed using this material as sensing platform has been stated in this work. To probe this, an immunosensor based on the determination of the blockage that HIgG produces to the diffusion of the red-ox indicator  $[\text{Fe}(\text{CN})_6]^{4-}$  was developed. In previous works, the diameter of the nanochannels used was optimized and studied, observing that the reduction of this parameter not always favours the performance of the sensor. However, the contributions of the thickness of the nanochannel were less researched. This work confirms that reducing this parameter increases the sensitivity while reduces the LOD achieved. The reduction of the thickness to a value of 45  $\mu\text{m}$  provides 6 times lower LOD than thicker commercially available nanoporous membranes (60  $\mu\text{m}$ ) with narrower diameter (20 nm instead of 60 nm).

The optimized nanoporous membranes were applied for the detection of catalase, an enzyme related with oxidative procedures in the human body and secreted by certain bacteria.

Overall, our findings related to the effect of membrane thickness and the applicability to catalase detection both may be extended to any type of catalase just by changing the immunocomplex formed, being suitable to detect this enzyme in several biomedical applications.





## Chapter 6. Innovative tools for antimicrobial screening

---

<b>6.1.</b>	<b><u>Summary</u></b> .....	<b>157</b>
<b>6.2.</b>	<b><u>Scientific article 9</u></b> .....	<b>159</b>
6.2.1.	<u>Introduction</u> .....	159
6.2.2.	<u>Protocols</u> .....	164
6.2.3.	<u>Results and discussion</u> .....	167
6.2.4.	<u>Conclusions</u> .....	178
<b>6.3.</b>	<b><u>Scientific article 10</u></b> .....	<b>179</b>
6.3.1.	<u>Introduction</u> .....	179
6.3.2.	<u>Protocols</u> .....	180
6.3.3.	<u>Results and discussion</u> .....	182
6.3.4.	<u>Conclusions</u> .....	188

---



## 6.1. Summary

In this Chapter, (bio)analytical tools are used for a purpose far beyond biomarkers detection. As important as detecting a disease is to understand what causes it and how to treat it. This becomes even more important in chronic wound infections.

For that reason, and to complement the achievements made in previous Chapter in the detection of chronic wound infection, in this case, two projects have been developed, complementing (bio)analytical tools with microbiology.

The first one (Section 6.2.) is a work performed as part of a six-month research stay at the University of Oxford to study bacteria interactions through micron-scale droplet 3D-printing. In this way, the ultimate idea was to study the interactions between the predominant bacteria present in chronic wounds, *S. aureus* and *P. aeruginosa*. Due to the complexity of this work and the risk assessments needed to perform it, a model microorganism as it is *E. coli*, was first used to evaluate how computational models could help us understand toxin diffusion mechanisms and how patterning affects them. This kind of work would not only allow a better understanding of the biological mechanisms behind an infection, but also build platforms for the determination of new antimicrobial compounds.

It is precisely this last aspect the main objective of the second work included in this chapter (Section 6.3.). The over-use of antimicrobial treatments has led to the emergence of resistant superbugs, making the development of novel antimicrobial compounds a need. The high cost of development and the long-time required through traditional techniques, has made industries leave the antibiotic innovation race, being mandatory to provide alternative screening technologies. In this work, we have developed an electrochemical sensing platform based on the use of nanoporous alumina membranes for the evaluation of novel antimicrobial compounds. First, nanoporous alumina membranes have been modified for the specific detection of enterotoxin B, a *S. aureus* virulence factor, and pyocyanin a *P. aeruginosa* virulence factor. The change in the amount of both analytes, detected in separate membranes, can be correlated with the effect that antimicrobial compounds have over them. Thanks to the low unspecific absorption and biocompatibility of nanoporous membranes, they are suitable platform for the *in vivo* culture of bacteria.



## 6.2. Scientific article 9

### Studying toxin diffusion mechanisms through droplet 3D-printing

Unpublished results

#### 6.2.1. Introduction

Although the focus of microbiology has been traditionally to address what type of microorganisms are present in a certain sample and what they do there, a question that has gain meaningful insights more recently is who is next to who<sup>421</sup>. This newly field of research is known as biogeography and covers the study of how species are distributed through space and time. The biogeography of bacteria in polymicrobial infections determines how they interact between them and the environment that surrounds them<sup>422</sup>, being the answer relevant to fight against them. This is especially important in managing infection diseases, as chronic wounds, or in understanding microbiome dysbiosis, as those that occur in the gut microbiome, that are related with the appearance of certain diseases<sup>423</sup>.

Having appropriate tools to understand *in vitro* how these bacteria interactions are governed and how patterning affects them is fundamental, not just to comprehend their role in our organism but also to have proper models for texting treatments against pathogenic bacteria. One of these tools is 3D printing of patterned communities, that has been previously used for studying toxin susceptibility in *E. coli* colicin producer strains<sup>424</sup>. *E. coli* is a Gram-negative bacteria highly selected as model organism as its genome is well studied and it is easy to culture. *E. coli*, as other bacteria, can produce a group of toxins known as colicins, released to the environment to outcompete other bacteria strains, including some *E. coli* strains.

---

<sup>421</sup> A. Stacy, L. McNally, S.E. Darch, S.P. Brown, M. Whiteley. Nat. Rev. Microbiol. 14 (2016) 93–105.

<sup>422</sup> S. Azimi, G.R. Lewin, M. Whiteley. Nat. Rev. Microbiol. (2022).

<sup>423</sup> J. Nguyen, D.M. Pepin, C. Tropini. Microbes Infect. 23 (2021) 104815.

<sup>424</sup> R. Krishna Kumar et al. Nat. Commun. 12 (2021) 857.

Colicins are the most studied bacteriocins and are classified, among other parameters, according to the cell surface receptor to which they bind<sup>425</sup>. One of these groups is E colicins that are internalized through the outer membrane receptor BtuB, that it is also responsible of the internalization of vitamin B<sub>12</sub><sup>426</sup>. The nine E colicins are translocated to the cytosol by binding the BtuB receptor and then crossing the outer membrane through the OmpF receptor (Figure 6.1.). Colicins are then pulled through the outer membrane porin OmpF by the Tol system. Some strains of bacteria acquire resistance to colicin by the deletion of the BtuB receptor.

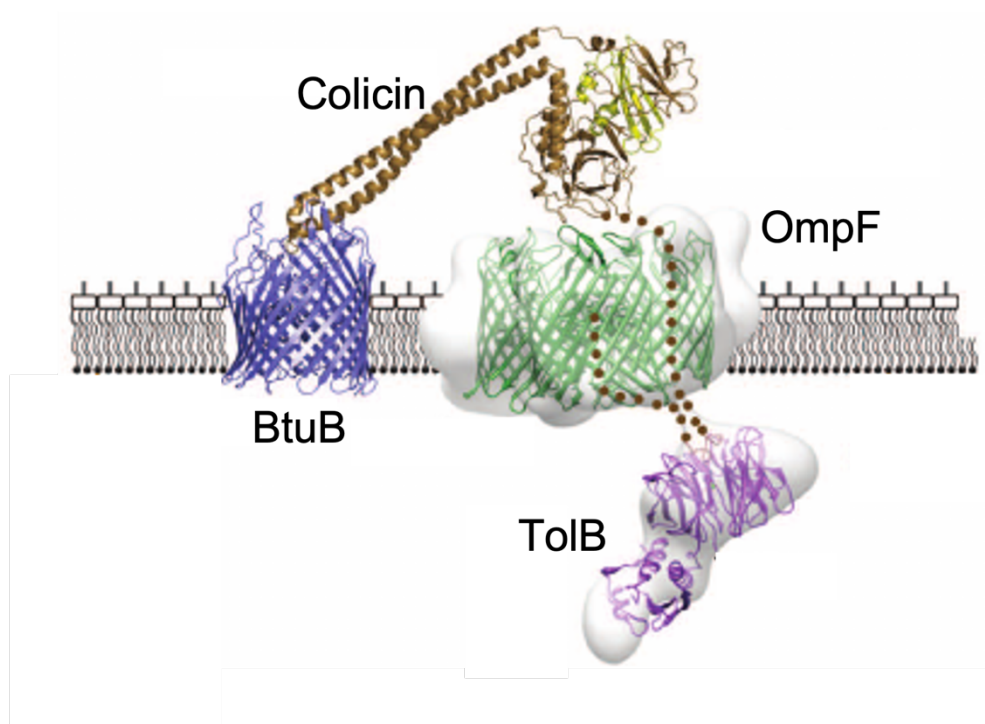


**Figure 6.1.** Mechanism of internalization of colicins through the outer membrane of susceptible cells. Represented with permission from 427.

In a previous work, the effect of patterning in colicin toxicity was addressed<sup>200</sup>. In this work, they confirmed that the elimination of BtuB receptor made bacteria strains resistant to colicin (Figure 6.2.A.). However, they hypothesized that colicin binding through BtuB could be important not just to confirm resistance but also to mop up toxins protecting susceptible strains nearby, creating a refuge effect. To confirm this, they

<sup>425</sup> E. Cascales et al., *MMBR*. (2007) 71 (1) 158-229

<sup>426</sup> T. Pienko et al. *Biophys. J.* (2021) 120, 725–737

<sup>427</sup> N. G. Housden, et al. *Science***340**,1570-1574(2013).

created a resistant strain that expressed the BtuB receptor but had an immunity protein able to bind colicin in the cytosol, inhibiting toxicity (Figure 6.2.B.). These findings indicate that the protective effect brought about by the spatial segregation of producers and susceptible cells is connected to the binding and uptake of diffusing colicins through BtuB receptor.

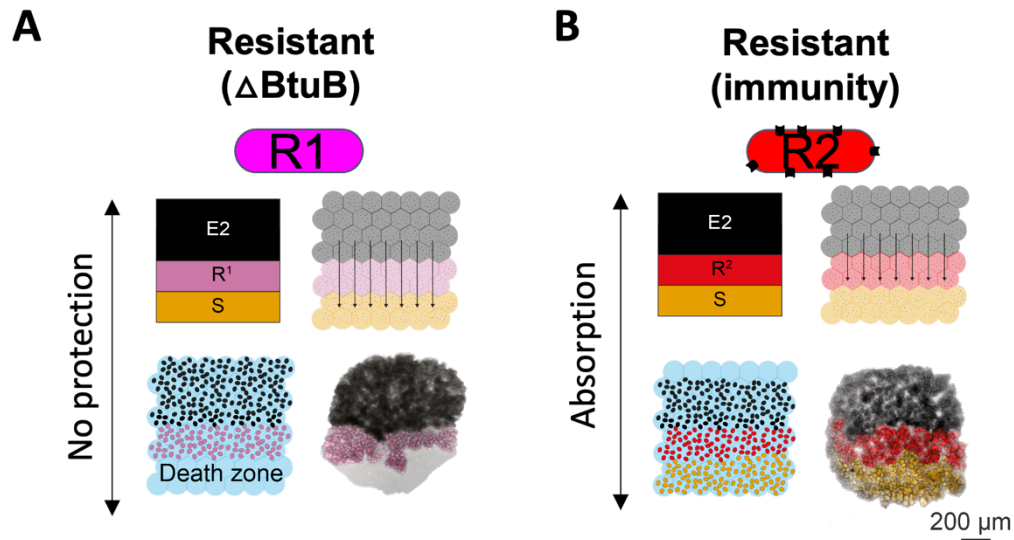


**Figure 6.2.** Schematic representation of the results obtained through droplet 3D printing confirming that patterning affects bacteria interaction. **A.** Printing of resistant strains unable to internalize colicin E2 does not have a protective effect over susceptible strains nearby. However, **B.** if the bacteria is able to internalize the toxin even though it is resistant through immunity (R2), it protects susceptible strains that are just behind.

This factor could have an influence over bacteria competition through diffusible toxins. Therefore, it is desirable to study how toxin removal through BtuB receptor is related with toxin susceptibility. However, studying *in vivo* the possible combinations of toxin removal/toxin susceptibility would be time consuming and impracticable, limiting the information obtained. Due to that, it was decided the introduction of computational modelling to optimize knowledge acquisition.

Mathematical and computational models have been long used to explain, predict, and optimize physical systems. Models can support results from experiments and give aid in elucidating the fundamental ideas that underlie them. Additionally, they allow to predict outcomes that are not yet explored experimentally. Therefore, models can be divided into two groups: forward modelling, which starts from known or hypothesized causalities from which predictions are made, and reverse modelling, which starts from



experimental data and seeks to derive and mathematically express causalities from correlations in the data<sup>428</sup>.

In this project, Dr. William Smith (University of Oxford), together with Daniel Figueiredo de Oliveira (Técnico Lisboa) developed a computational model to explain how spatial segregation affects bacteria warfare using colicin diffusion and toxicity. For that purpose, they developed an individual-based model (IbMs), highly used in microbial science, as addresses local interactions, individual heterogeneity and adaptive behaviour individually.

The model monitors, between other parameters as size, biomass or nutrient diffusion, the toxin production, and the toxin removal. Toxin removal in colicin susceptible strains is achieved by the binding of this molecule to the external receptor BtuB. In this way, toxin removal was associated to the occupancy of receptors in the outer membrane of susceptible cells as depicted in Figure 6.3. Cell death is considered when bacteria reach a certain threshold of occupied receptors.

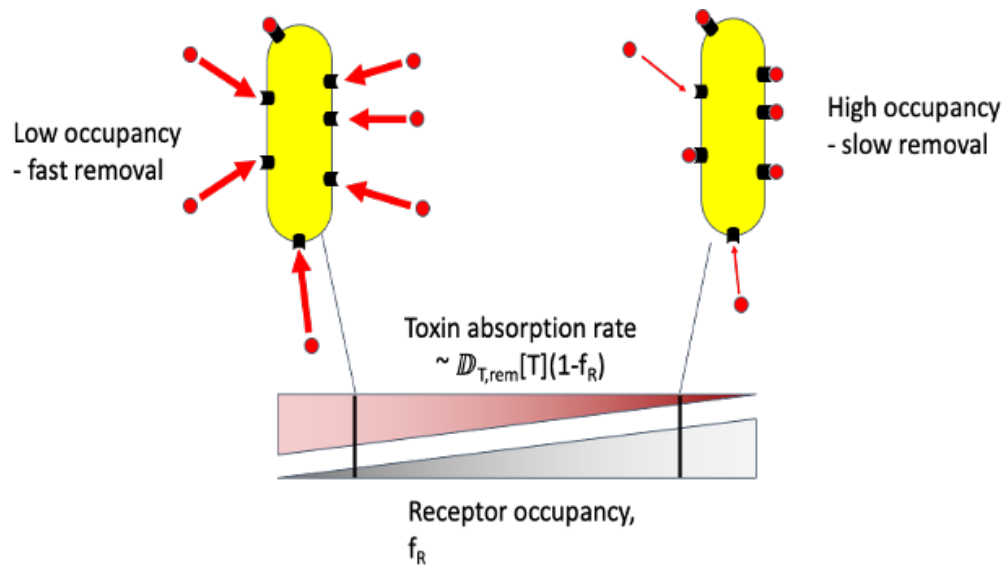


**Figure 6.3.** Scheme of how the computational models considers toxin absorption rates.

The conclusions extracted with this model confirmed that patterning has an effect over toxin susceptibility for determine conditions of toxin removal and toxin production, being irrelevant when the toxin production is too high or too low (Figure 6.4).

<sup>428</sup> Guanawardena J. BMCBiology (2014) 12(1):29

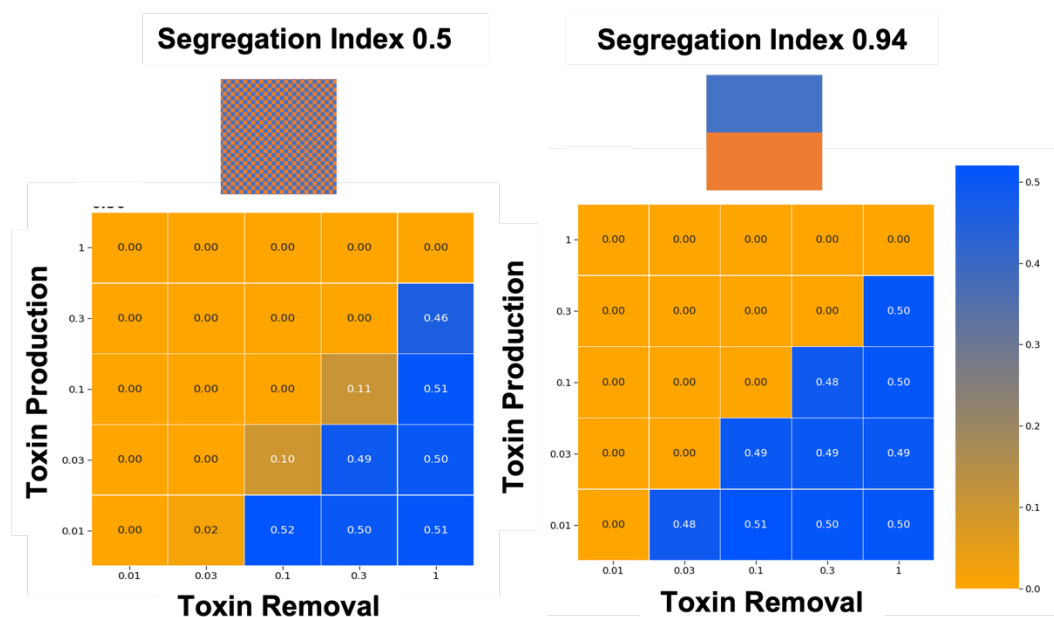


**Figure 6.4.** Conclusions obtained with the computational model developed, pointing out that patterning has an effect over cell survival.

Although this model contemplates a finite toxin removal, which is consistent with colicin diffusion, the authors also demonstrate that the model could be adapted to a continuous toxin removal which is representative of other molecules as antibiotics. This makes this research easily transferrable to other areas, such as the testing of antibacterial agents to treat chronic wound infection.

To validate the feasibility of this computational model in a real scenario, it is necessary to confirm experimentally the conclusions reached. That task has been the purpose of this work, to see through 3D printing if patterning affects bacteria warfare under different toxin production and removal conditions. As the computational model considers toxin removal according to the fraction of unoccupied receptors, it is mandatory to obtain in first instance, bacteria strains that can express BtuB receptor in different proportions to mimic variable unoccupancy states.

In this work, *E. coli* strains expressing BtuB receptor at different proportions have been engineered and their susceptibility against E colicins have been evaluated. Colicins E2, E7 and E8, with variable toxicity have been selected to reproduce the distinct toxin production states considered in the computational model.

This work has been done with a model organism as *E. coli* to evaluate the use of 3D printing and computational models in toxin diffusion studies. As the ultimate goal for

this Thesis would be to incorporate this knowledge in studying bacteria interaction in wound infection and their susceptibility against antibiotic compounds, the encapsulation of *S. aureus* and *P. aeruginosa* in lipid droplets has been evaluated as a previous step to 3D printing.

## **6.2.2. Protocols**

### *6.2.2.1. Bacterial strains*

Bacterial strains used in this work are *E. coli* BZB1011 pBtuB (0-100%), provided by the Foster Lab<sup>424</sup>. *E. coli* BZB1011 pBtuB strains were obtained by constitutive expression of BtuB receptor in *E. coli* BZB1011  $\Delta$ BtuB strains. Briefly, a plasmid (pJ231(X) BtuB) controlled by the Anderson promoter modified to change expression strengths. *P. aeruginosa* PA01 and *S. aureus* were obtained from Foster and Bayley Lab respectively.

### *6.2.2.2. Minimum inhibitory concentration assay*

The susceptibility of the different BtuB expressing strains was tested against extracts of E2 and E7 produced by *E. coli* following a protocol adapted from a microdilution (MIC) assay. Briefly, *E. coli* strains (susceptible and producers) were cultured in LB liquid media supplemented with Antibiotic overnight at 37°C with shaking conditions. Then, culture from E2 and E7 producer strains was centrifuge at 8000g for 10 min. The supernatant was collected and filtered using a 0.2  $\mu$ m filter. Serial dilutions of the colicins in LB were done in a 96-well U-bottom microtiter plate to a total volume of 300  $\mu$ L. Then, *E. coli* strains were added to a final concentration of  $1 \times 10^5$  CFU/mL on each well. Plates were then cultured at 37°C without shaking and OD<sub>600</sub> was measured at different time points. Per each individual condition, three biologically independent replicates were done (n=3).

#### 6.2.2.3. *Growth inhibition assay*

Alternatively to the MIC assay, a growth inhibition was performed following a previously published procedure<sup>429</sup>. Each susceptible strain and BZB1011 pColE2 and BZB1011 pColE7 were inoculated in LB medium and incubated at 37°C and 225 rpm O/N. After this incubation, susceptible strains were diluted to an OD<sub>600</sub> of 0.05 in fresh LB media and cultured again in the same conditions until reaching an OD<sub>600</sub> between 0.6-0.7. In between, BZB1011 pColE2 and BZB1011 pColE7 cultures were centrifuged and the supernatant was serially diluted. Then, 2 µL of each serial dilution was spotted on top of an LB-Agar (1.5 % w/v) plate and left dry. When susceptible strains were in the appropriate OD<sub>600</sub>, 200 µL of the culture were added to molten 0.75% w/v LB-Agar and quickly poured over the agar plate. Plates were left dried and then incubated overnight at 37°C without shaking. The day after, inhibition ales were checked and imaged.

#### 6.2.2.4. *Protein purification*

The plasmid pPGI5, provided by the Kleanthous group<sup>430</sup>, contained the ColE9-GFP gene modified with a His6-tagged. The plasmid was transformed into BL21(DE3) *E. coli* competent cells, using a T7 RNA polymerase-IPTG induction system, by inoculating them overnight at 37°C and 225 rpm in 10 mL of LB-media with ampicillin (100 µg/mL). The day after, 4 mL of the overnight culture were inoculated in a flask containing 400 mL of LB-media with ampicillin (100 µg/mL) and incubated at 30°C with shaking until the culture reached an OD<sub>600</sub> of 0.5-0.6, when expression was induced by IPTG (0.5 mM). Cells were harvested after overnight culture by centrifuging at 5000 rpm for 20 min at 4°C. Pellets were frozen for 3h and then resuspended in lysis buffer (50 mM Tris HCl pH 8, 150 mM NaCl, 10 mM imidazole, 0.1% Triton, 5% glycerol and 2 mM (tris(2-carboxyethyl) phosphine) (TCEP)) supplemented with lysozyme (1 mg/mL, 0.05 U/µL benzonase and 50 µM MgCl<sub>2</sub>) and incubated on ice for 60 min. The lysate was sonicated and then centrifuged at 29.000 g, 45 min, 4°C, and the supernatant was added to a column packed with HisPur Ni-NTA Agarose Resin, equilibrated with lysis buffer. The column was mixed on an orbital shaker for 1h at 4°C. The column was washed with 6 column volumes of washing buffer (50 mM Tris HCl pH 8, 500 mM NaCl, 20 mM imidazole, 0.1% Triton, 5% glycerol and 2 mM (tris(2-carboxyethyl) phosphine) (TCEP)). Then, the

---

<sup>429</sup> B. LaSarre, M.J. Federle. *Mol. Biol. Rev.* 77 (2013) 73–111.

<sup>430</sup> P. Rassam et al. *Nature.* 523 (2015) 333–336.

protein was eluted by adding 6 column volumes of elution buffer (50 mM Tris HCl pH 8, 500 mM NaCl, 250 mM imidazole, 0.1% Triton, 5% glycerol and 2 mM (tris(2-carboxyethyl) phosphine) (TCEP)). The eluted fraction was characterized and separated through fast protein liquid chromatography (FPLC), and later by polyacrylamide gel electrophoresis (SDS-PAGE) and mass spectrometry.

#### 6.2.2.5. *Co-localization assay of Cole9-GFP and BtuB receptor*

The co-localization assay was performed following a previously published procedure with slight modifications<sup>430</sup>. Briefly, *E. coli* BZB1011 p were grown overnight in LB-Media supplemented with antibiotics at 37°C and 225 rpm. The day after, cells were inoculated in fresh LB-Media to an OD<sub>600</sub> and left incubating at the same conditions until reaching an OD<sub>600</sub> of 0.6. Then, 200 µL were taken and centrifuged at 4700 g, 4°C for 3 min. The pellet was washed three times with M9 media and then centrifuged one more time and re-suspended in 200 µL of a solution containing Cole9-GFP at different concentrations (30, 300 and 3000 nM). The solution was incubated with mild shaking at room temperature for 15 min, and then centrifuged and washed three times with M9-media. The final pellet was re-suspended in 100 µL of M9-media. Samples were imaged using a Leica® SP5 confocal microscope using a HC PL Fluotar x 10/0.30 objective at an excitation wavelength of 405 nm and emission cut-off values of 420-520 nm for GFP and RFP.

#### 6.2.2.6. *Preparation of bioinks*

First, bacteria used were incubated in 4 mL LB-Medium for 16 h at 37°C and 225 rpm. After this time, bacteria were inoculated in fresh LB-Media and incubated at the same conditions for 3h. Cultures were then centrifuged at 8000 g, 4°C, 5 min and resuspended in the appropriate volume to reach a cell concentration of 10<sup>9</sup> cells/mL. Then, 150 µL of molten 2.0% w/v ULGT agarose in LB-Miller medium, 30 µL of LB-Miller medium and 20 µL of bacteria were gently mixed in PCR tubes.

#### 6.2.2.7. *Printing bacterial droplet networks containing bacteria*

The printing of bacteria networks was done using a custom-built piezoelectric printer previously developed in the research group<sup>431</sup>. The principle of this printer is based on the transmission of control pulses ( $\pm 130$  V) through a piezoelectric transducer to a chamber with Milli-Q® water connected to a glass nozzle ( $\text{Ø} \approx 100 \mu\text{m}$ ). The glass nozzle was first charged with  $\approx 5 \mu\text{L}$  of undecane oil to separate water from the bioink, that it is also incorporated inside. Then, droplets of the bioink were ejected to a quartz cuvette filled with 1mL of lipid-in-oil solution. All the set-up was warmed up to  $37^\circ\text{C}$  using two IR heating lamps to avoid liquid convection. The quartz cuvette was situated on top a micromanipulator controlled by a custom-made software created in LabVIEW. The printing process was followed using a stereomicroscope and a camera coupled to the printing set-up. For printing two separated bacteria strains at the same time, two nozzles were used. Both nozzles were aligned to allow printing layer-by-layer.

### 6.2.3. *Results and discussion*

#### 6.2.3.1. *Obtaining *E. coli* strains with variable susceptibility*

As it has been explained in the introduction, the computational model that it has been evaluated in this work, is based on the simulation of competition behaviors between colicin producer and susceptible cells. Toxin removal was regulated by the fraction of unoccupied BtuB receptors in the outer membrane of *E. coli* susceptible strains according to the following (simplified) equation (Eq. 6.1):

$$\text{Toxin absorption rate} \approx D_{T,\text{rem}}[T](1-f_R) \quad (\text{Eq 6.1})$$

where,  $D_T$  is the toxin diffusivity and  $f_R$  the receptor occupancy.

---

<sup>431</sup> G. Villar, A.D. Graham, H. Bayley. Science. 340 (2013) 48–52.

To mimic this *in vivo* bacteria strains with different BtuB expression levels were engineered. Firstly, the IPTG inductive expression of BtuB in a knock-out strain was contemplated. The addition of different concentrations of IPTG was used to induce the expression of BtuB at different levels. To confirm this process, a MIC assay against colicin at different concentrations was performed, checking the OD<sub>600</sub> at different time points. However, the IPTG alone generated an excessive growing burden over *E. coli* strains that did not allow to record any differences between the conditions tested (Figure 6.5.).

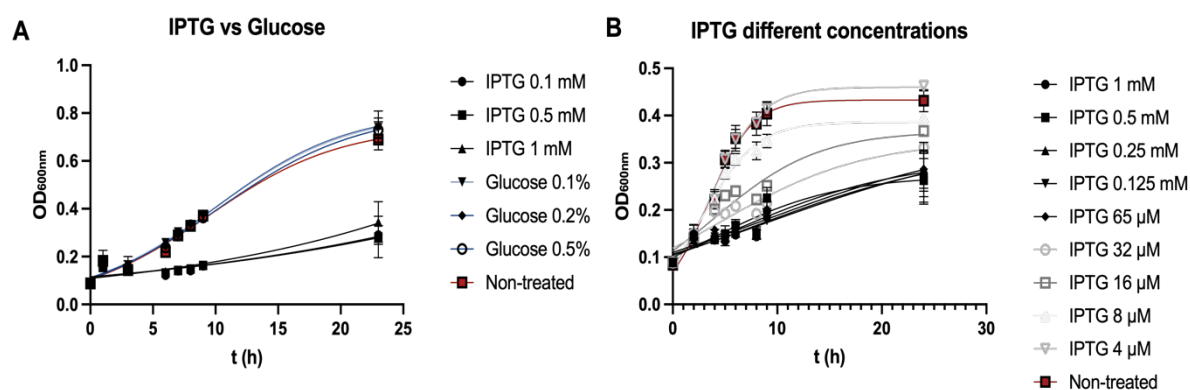


**Figure 6.5.** Response of *E. coli* strains under the presence of IPTG as inducer molecule and glucose as repressor. **A.** The addition of IPTG significantly affects the growth observed, even without the addition of toxin. **B.** This effect could be minimized by decreasing the IPTG concentration added.

A second strategy was then followed, using *E. coli mrfp1::Tn7 ΔBtuB* pJ231(X) BtuB strains constitutively expressing BtuB at different proportions. The use of a constitutive promoter as the Anderson promoter allows to modify the strength to which the protein, in this case the BtuB receptor, is expressed. Strength's equivalent to a 1, 30, 70 and 100% expression of BtuB were engineered and tested against E2, E7 and E8 colicin extracts at different dilutions through a MIC assay. OD<sub>600</sub> was measured at different time points to establish the growing curves of each bacteria. For a proper comparison, OD<sub>600</sub> after 16h of incubation has been represented in Figure 6.6. It is worthy to mention that, over the performance of the experiment, condensation on the lid of the 96-well plate used and irregular measurements in the borders of the plate were occasionally observed.

The susceptibility presented by each strain was comparable between BtuB concentrations, not allowing to determine the variable BtuB expression on each strain. This behavior was observed for the three toxins tested. In all the conditions evaluated, when the toxin was concentrated (1:10 dilution) the maximum OD<sub>600</sub> values reached were lower than those observed when the concentration decreased.

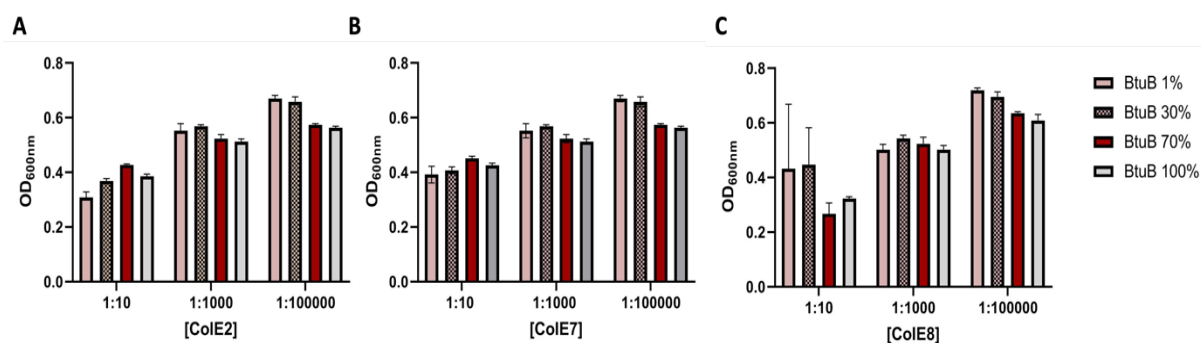


**Figure 6.6.** Susceptibility tests with different colicins showing no differences between the BtuB receptor expression conditions.

As the MIC assay did not allow to clearly differentiate between conditions, a disk diffusion assay was used as an alternative. Following a similar procedure, toxicity of increasing colicin (E2, E7 and E8) concentrations was evaluated. Although there was a clear difference between the toxicity for E8 colicin compared to E2 and E7, presenting inhibition even at a 10<sup>3</sup> dilution, between these two there was no significance (Figure 6.7.).

Regarding the diameter of the inhibition ring obtained in each concentration, there was no significant difference between BtuB expression levels as stated in Table 6.1.

**Table 6.1.** Diameter size (in mm) of the inhibition rings obtained with colicins at a dilution of 10<sup>2</sup> for *E. coli* BZB1011 with BtuB expression at different proportions.

	Inhibition ring diameter (mm)					
	BtuB	ΔBtuB	BtuB 1%	BtuB 30%	BtuB 70%	BtuB 100%
E2 (10 <sup>2</sup> )	5.202	--	4.494	5.072	5.230	4.689
E7 (10 <sup>2</sup> )	4.500	--	5.520	4.275	2.897	4.631
E8 (10 <sup>2</sup> )	6.258	--	6.004	6.016	7.017	4.783



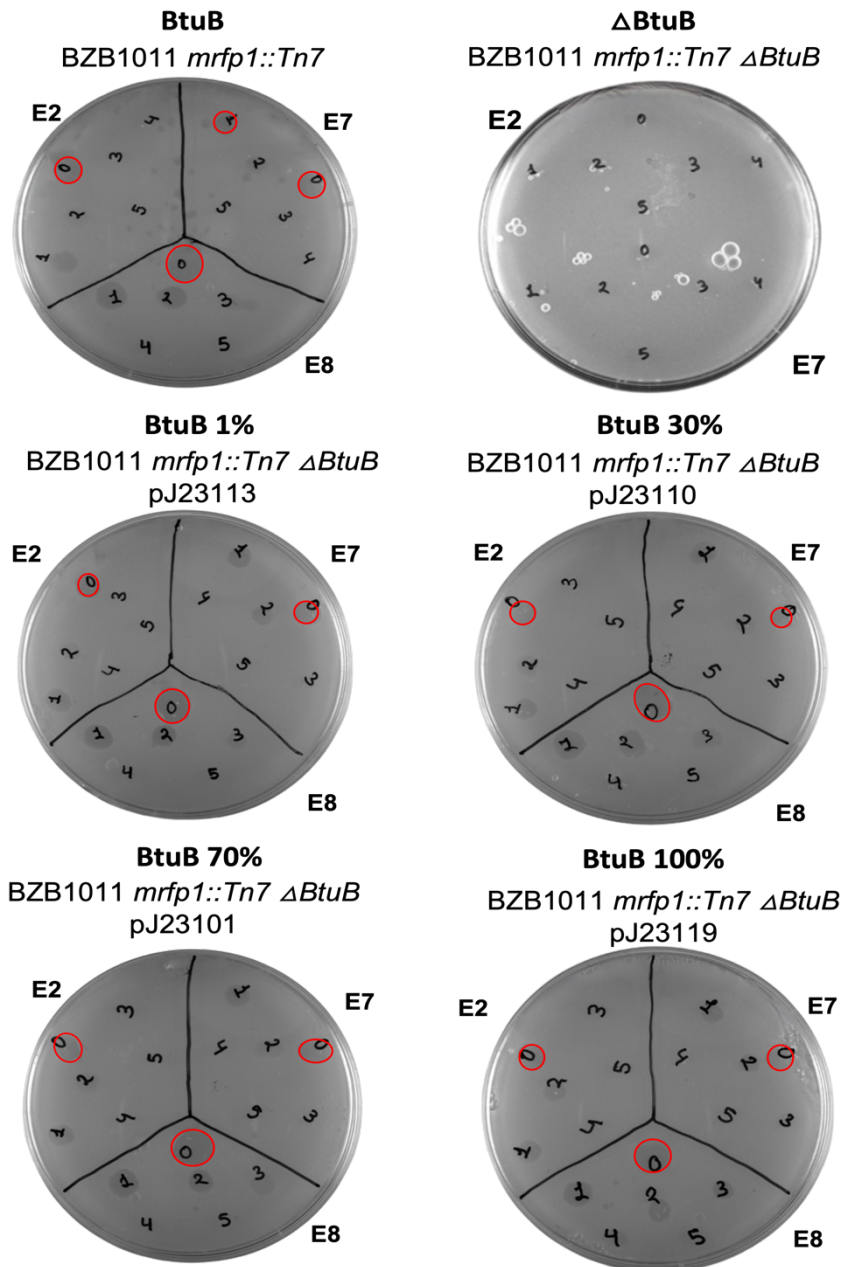


**Figure 6.7.** Disk diffusion method performed with bacteria expressing BtuB at different levels. Control bacteria (*E. coli* BZB1011 naturally expressing BtuB),  $\Delta$ BtuB bacteria that do not show any inhibition zone and *E. coli* BZB1011 constitutively expressing BtuB at different %. The assay did not provide a notable difference between BtuB concentration. No statistical analysis was performed in this case as just one replicate was done per each condition tested.

The results obtained with these methodologies did not allow to determine if strains with variable BtuB receptor expressions are susceptible to colicins in different stents.

Probably, a major limitation of the methodology followed is that the concentration of colicin was not normalized. Colicins were obtained from the supernatant of an overnight culture of the different Colicin producer strains. Although the OD<sub>600</sub> of the cultures was checked prior to be used, not seen notable differences, the exact quantity of colicin was not quantify as there was not stablished methodology for that. Hence, there could be variability between the colicin concentrations between assays, what difficulties comparison between experiments. To overcome this drawback, as a future work, we propose to develop an electrochemical sensor for the quantification of colicin concentration prior to addition.

#### 6.2.3.2. *Co-localization of ColE9-GFP*

In view of the results obtained with the above-described methodologies, an alternative approach raised was the co-localization of a colicin, in this case ColE9, fused with fluorescence protein GFP following a previous work from Kleanthous<sup>432</sup>. They developed a methodology to follow the localization of the Omp receptors, the outer membrane pore through which colicins are internalized inside a susceptible cell. This family of receptors includes nanopore forming proteins that have interestingly been also used in nanopore sensing applications<sup>433,434</sup>.

Prior to internalization to OMP receptors, colicins bind to the BtuB receptor, also localized in the outer membrane as depicted in Figure 6.1.

In the method developed by Kleanthous, the use of a fusion protein modified with the fluorescence reporter molecule GFP allowed the binding of colicin to BtuB receptor but not the internalization through the Omp receptor.

The selection in this work of colicin E9 instead of one of the colicins previously evaluated was due to the availability of the ColE9-GFP fusion protein, already synthesized by the Kleanthous group. Colicin E9 is, together with E2, E7 and E8 part of the group of E toxins with endonuclease activity, all able to bind to the BtuB receptor.

---

<sup>432</sup> Rassam, P., Copeland, N., Birkholz, O. *et al. Nature* **523**, 333–336 (2015).

<sup>433</sup> J. Wang, J. Dahyabhai Prajapati, F. Gao, Y-L Ying, U. Kleinekathöfer, M. Winterhalter, and Y-T Long. *J. Am. Chem. Soc.* 2022, 144, 33, 15072–15078

<sup>434</sup> T. Tosaka and K. Kamiya. *ACS Appl. Nano Mater.* 2022, 5, 6149–6158

The fusion protein was first expressed in competent *E. coli* strains containing the plasmid pPGI5. The expression was induced with the addition of IPTG. After this induction and a first purification step, the obtained protein extract was characterized through SDS-PAGE (Figure 6.8.) presenting a band at approximately 75 kDa, corresponding to the Cole9-GFP fusion protein. The large quantity of protein obtained is observed by the width of the band and how it is slightly displaced. The band corresponding to Cole9-GFP was even observed in the extract of bacteria not induced with IPTG, confirming that there was a residual leaky expression of Cole9-GFP even without the addition of IPTG.

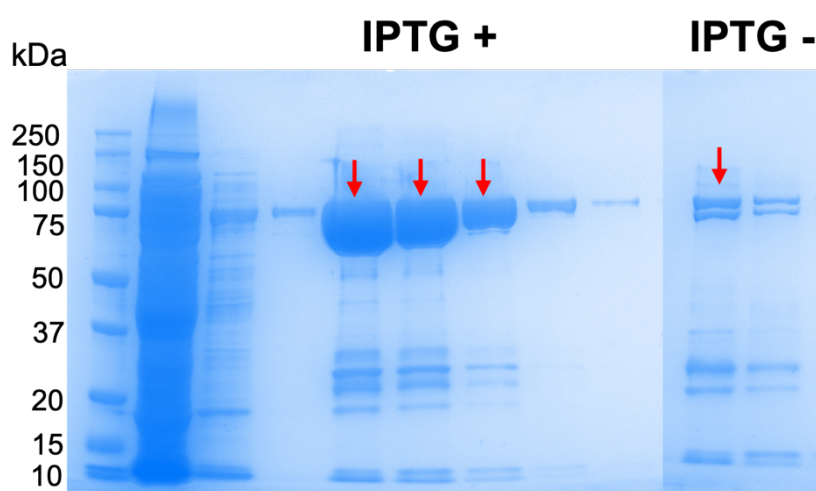


**Figure 6.8.** SDS-PAGE of the protein extracted from a culture with IPTG induction and without it.

The obtained protein extract was further separated through FPLC (Figure 6.9.A.). The different eluted fractions presenting an increase in conductivity were further characterized through SDS-PAGE again (Figure 6.9.B.), resulting in a size of approximately 60 kDa. The theoretical size of the fusion protein Cole9-GFP is of 75.37 kDa (calculated using SnapGene). The difference in size between the theoretical value and the observed in the gel electrophoresis could be associated to an incorrect denaturalization that could lead to the formation of secondary or tertiary structures that might affect gel migration.

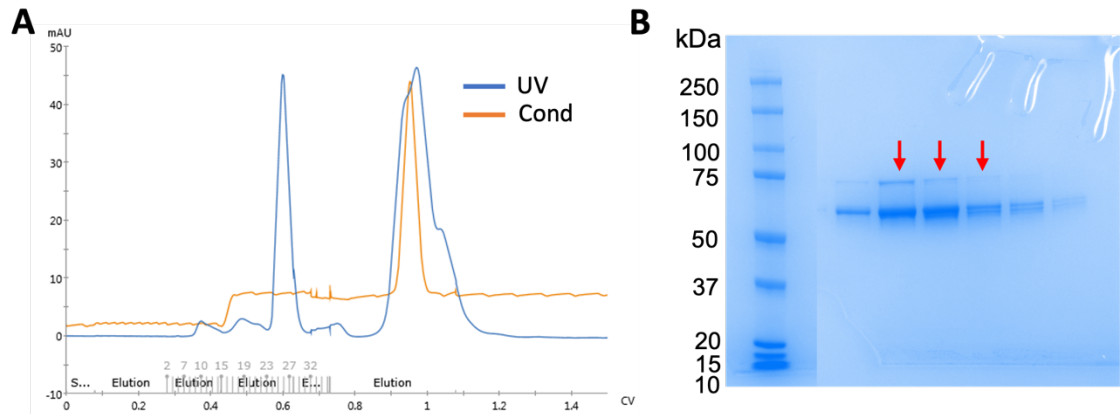


**Figure 6.9.** Characterization of the Col-E9 fusion protein during A. FPLC separation and B. after separation.

To confirm that this was the reason behind the size difference and not that the extracted protein was not the suitable one, we further characterized the obtain protein through MS, obtaining an average protein size of 75.22 kDa (Figure 6.10). This, together with the bright green color of the solutions extracted, confirms that the ColE9-GFP fusion protein was purified.

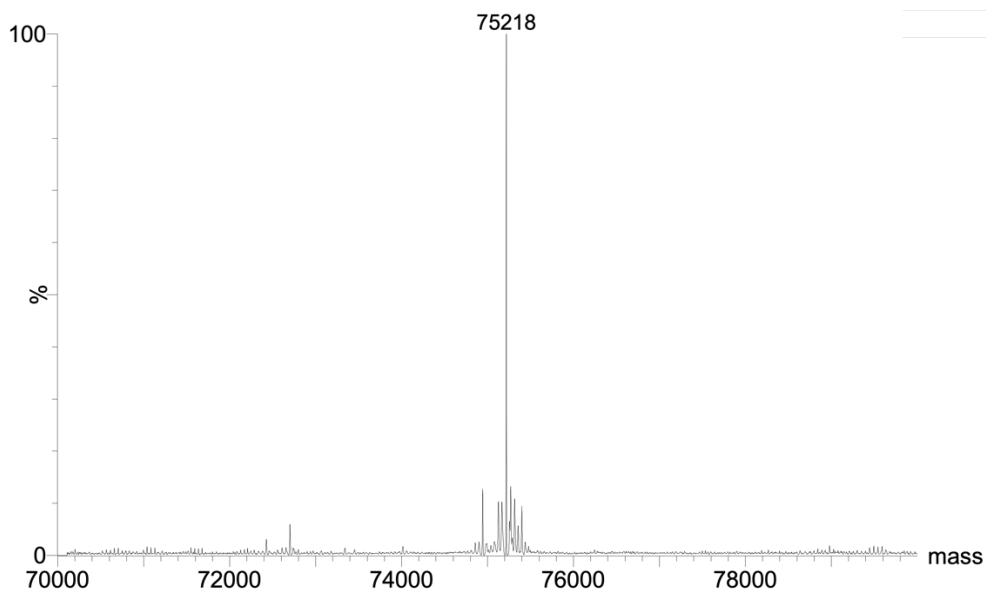


**Figure 6.10.** Characterization of the extracted ColE9-GFP protein through MS.

Once the fusion protein was obtained, a co-localization experiment with *E. coli* strains with different BtuB receptor presence were tested. In a first optimization, BtuB and  $\Delta$ BtuB RFP labeled strains were incubated together with increasing concentrations of ColE9-GFP (30 nM, 300 nM, 3  $\mu$ M), observing that first, there was a significant

difference in terms of the fluorescence obtained between BtuB and  $\Delta$ BtuB strains for the three concentrations tested (Figure 6.11.).

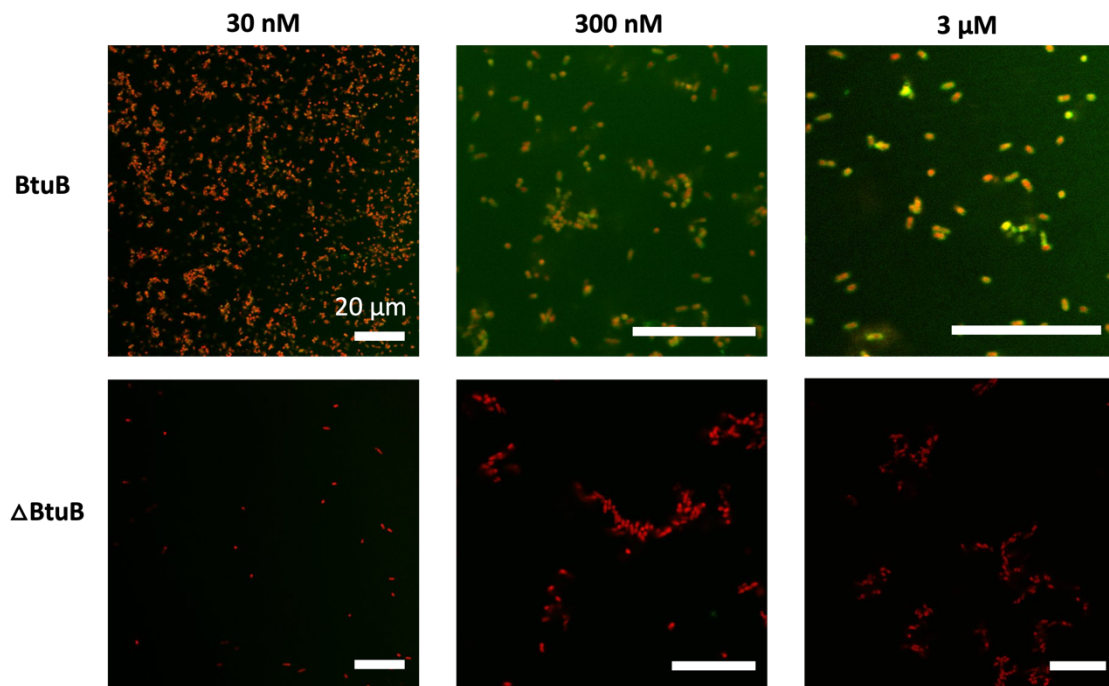


**Figure 6.11.** Optimization of the ColE9-GFP concentration for the co-localization assay.

Regarding fusion protein concentration, 300 nM was selected as the optimum one and used in the following experiments. Then, a co-localization experiment with the BtuB (1-100%) expressing strains was done, observing that fluorescence was notably higher in BtuB strains expressing a 70 or 100% BtuB receptor than those expressing it at 1 or 30% (Figure 6.12.).

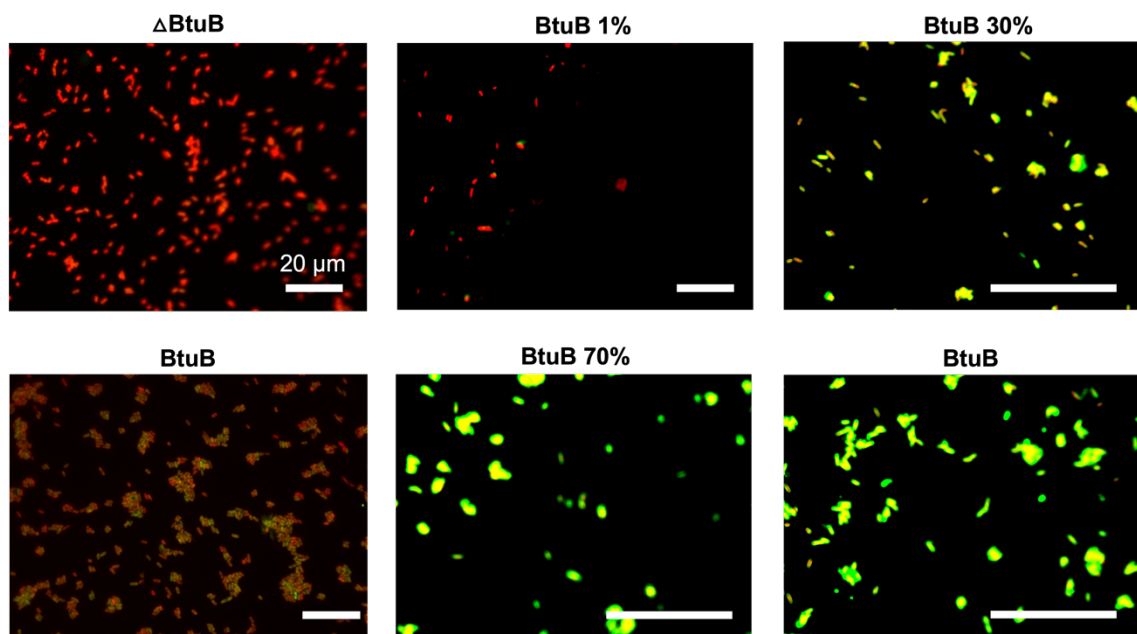


**Figure 6.12.** Co-localization assay of strains containing different BtuB expression profiles with ColE9-GFP.

These results confirm that the expression of BtuB receptor is differential although it could not be quantified through the culture and disk diffusion methodologies used initially.

### 6.2.3.3. *3D printing of bacterial networks*

The ultimate objective of this work is to confirm that patterning affects toxin removal and toxin susceptibility behaviors as it was proposed by the computational model evaluated in this work. In parallel to the obtaining of strains with variable toxin removal states, 3D printing works were performed.

The 3D printer used in this work is a custom-made piezo electric printer previously constructed in the research group for the tailored printing of bioinks containing bacterial cells embedded in molten agarose. Line-by-line printing is used to deposit droplets of around 100  $\mu\text{m}$  forming software-defined 2D or 3D patterns (Figure 6.13.A.). Bioink droplets are ejected over a lipid-in-oil solution what forms a lipid monolayer around the surface of the droplets, forming stable bilayers, named droplet interface bilayers (DIBs), that connect droplets between them<sup>435</sup>. The printer is composed of a water filled piezo ejector to which nozzles are connected. When two different layers with distinct bioink compositions are printed, two nozzles, each connected to a piezo, are used. The cuvette containing the lipid bath is mounted on top of a micromanipulator that it is moved through a custom computer program synchronously with printing (Figure 6.13.B.).

---

<sup>435</sup> M. A. Holden, D. Needham, H. Bayley. *J. Am. Chem. Soc.* (2007), 129, 27, 8650–8655

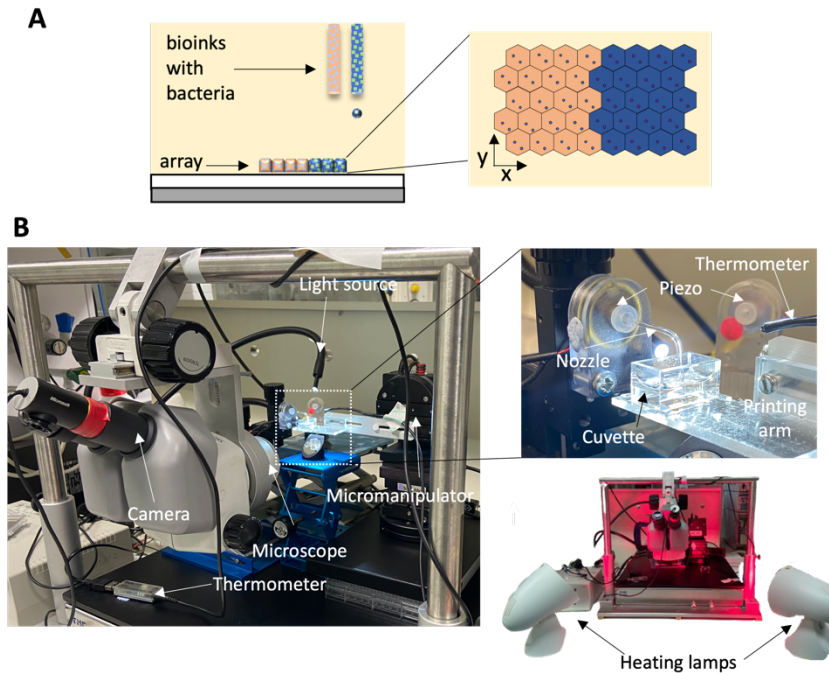


**Figure 6.13.** 3D-printer system used. **A.** Schematic representation of the methodology followed with a droplet 3D-printer. **B.** Images of the real set-up of the droplet 3D printer with a description of their components.

A first approach to printing 3D structures containing *E. coli* strains with variable toxin removal conditions was done in this work. For that purpose, a first initial pattern containing just *E. coli* E2 producer strains labelled with GFP, together with a segregated pattern containing *E. coli* E2 producer strains labelled with GFP (Figure 6.14.A.) and *E. coli*  $\Delta$ BtuB strains labeled with RFP were printed together (Figure 6.14.B.). it could be clearly seen that after incubation at 37°C of the structures for more than 16h, the structures are maintained. No death is apparently observed when producer strains are printed together with  $\Delta$ BtuB strains as it was expected.

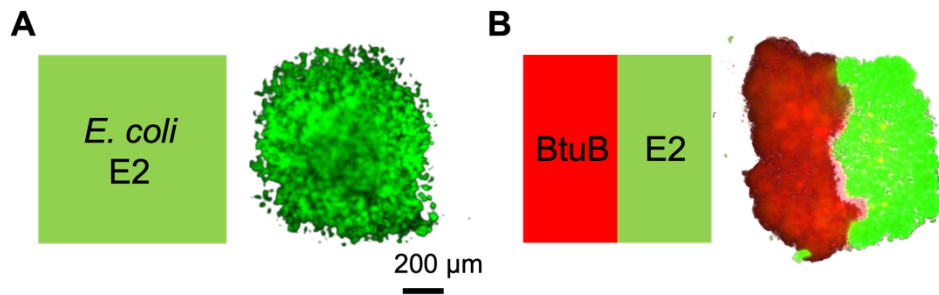


**Figure 6.14.** Results obtained through 3D-printing with A. one strain and B. two strains.

Unfortunately, and due to time limitations, no more trials were done with *E. coli* strains expressing BtuB at different proportions. This part of the project will be continued in the future for publication.

#### 6.2.3.4. Evaluation of bacteria present in chronic wounds

The ultimate goal of this project was to study bacteria interactions between the predominant microorganisms present in chronic wounds, *S. aureus* and *P. aeruginosa*. However, before all the technology described above can be implemented in the study of these strains, it is necessary to carry out optimization work beforehand.

All the previous works performed in the research group used LB medium as part of the bioink components. In this work, we have initially considered the cultivation of *S. aureus* and *P. aeruginosa* in TSB to be consistent with the work carried out at the University of Oviedo (section 6.3.). Therefore, the first approach consisted of forming droplets containing these bacteria cultured in TSB as part of the bioink. In this case, as a first and simpler approach, droplets were formed manually through reverse pipetting instead of using the 3D printer.

Preliminary results showed that the encapsulated strains did not show uniform growth as previously observed for *E. coli* through 3D printing (Figure 6.15.). This could be both due to the change in the culture media or just to experimental errors. Further optimization of this process would be required prior to incorporate *S. aureus* and *P. aeruginosa* to a more sophisticated printing setup.

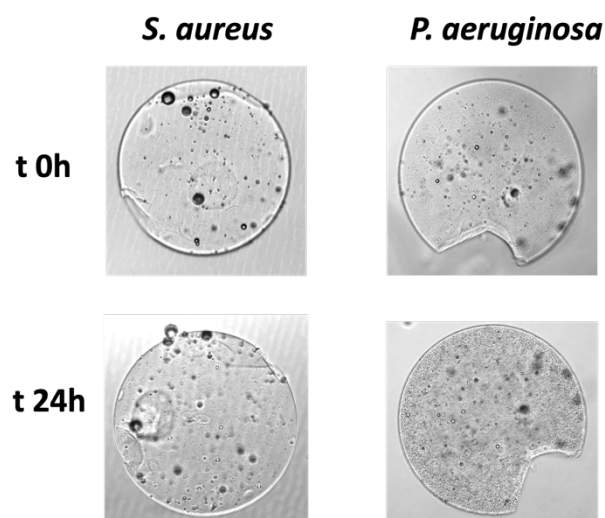


**Figure 6.15.** Encapsulation of *S. aureus* and *P. aeruginosa* in TSB, molten agar droplets.



#### **6.2.4. Conclusions**

In this preliminary work, the correlation between a computational model and an *in vivo* model for the study of bacteria interaction mechanisms was investigated. More particularly, *E. coli* colicin diffusion mechanisms and how they affect survival of *E. coli* susceptible strains was researched. For that purpose, first, *E. coli* strains expressing BtuB, the receptor responsible for colicin internalization, under different proportions were obtained and tested again different colicin concentrations.

Two methodologies were used for the obtaining of these stress, the inducible expression of BtuB under IPTG and Glucose control, and the constitutive expression of the receptor. In the first scenario, it was observed that the addition of IPTG to the *E. coli* strains tested implied a growing burden making unable to differentiate between it and colicin toxicity.

Strains constitutively expressing BtuB were then tested both using MIC and disk diffusion techniques. But both approaches were not sensible enough to differentiate between BtuB expressing strains. Co-localization of a GFP fusion E9 protein over RFP labeled *E. coli* strains was then used as approached, clearly allowing to distinguish between BtuB expressions.

As an initial proof-of- concept of the suitability of 3D printing approaches for bacteria strains involved in chronic wounds, *S. aureus* and *P. aeruginosa* were cultured in 3D TSB droplets, but growth inside bacteria was lower compared to the observed for *E. coli* strains in LB media, requiring further optimization.

## 6.3. Scientific article 10

### Rapid screening of novel antimicrobial compounds with a nanoporous-based electrochemical platform

Under preparation

#### 6.3.1. Introduction

Antimicrobial resistance is an increasing healthcare problem which points to become the next pandemic the world is going to suffer<sup>436</sup>. The increasing tolerance of microorganisms to the currently available antibiotic treatments makes the handling of infectious diseases challenging<sup>437</sup>. To tackle this problem, a fast and accurate detection of infection is mandatory to avoid antibiotic overuse<sup>438</sup>, as, as a result, the emergence of these resistance will continue to occur. However, early detection is of no use if it is not accompanied by effective treatment administration. Developing novel antimicrobial compounds is then a need. But unfortunately, the high cost of development and the long-time required of gold-standard antimicrobial susceptibility tests (AST), has made industries leave the antibiotic innovation race<sup>439</sup>. The development of reproducible and high-throughput AST methods, as electrochemical sensors, stands out as a solution to solve this challenge<sup>440</sup>.

Electrochemical sensors have distinguished themselves as point-of-care (POC) devices owing to their specificity, fast reaction, ease of use, portability, and adaptability<sup>441</sup>. However, there are just a few examples of how electrochemical sensors may be used to test novel drug candidates.

In this work, we have developed an electrochemical sensing platform based on the use of nanoporous alumina membranes for the evaluation of novel antimicrobial

---

<sup>436</sup> C.L. Ventola. *Ther.* 40 (2015) 277–283.

<sup>437</sup> M. Miethke et al. *Nat. Rev. Chem.* 5 (2021) 726–749.

<sup>438</sup> J.-T. Hsu et al. *BMC Med Inform Decis Mak.* 2019, 19:99

<sup>439</sup> The Pew Charitable Trusts., *Tracking the Global Pipeline of Antibiotics in Development*, March 2021, (2021).

<sup>440</sup> C. Toyos-Rodríguez, D. Valero-Calvo, A. de la Escosura-Muñiz. *Anal. Bioanal. Chem.* **2023**, 415, 1107-1121

<sup>441</sup> Ü. Anik, *Electrochemical medical biosensors for POC applications*, in: *Med. Biosens. Point Care POC Appl.*, Roger J. Narayan, Woodhead Publishing, 2017: pp. 275–292.

compounds. Nanoporous alumina membranes are arrays of hundreds of single nanochannels with diameter size, that present low unspecific absorption and high biocompatibility make them suitable platforms for the *in vivo* culture of bacteria<sup>442</sup>. The developed sensor device is meant to be used for the screening of antibiotic compounds against two predominant microorganisms present in chronic wounds, *P. aeruginosa* and *S. aureus*.

The principle of this sensor is based on the modification of the inner walls of the nanochannels with antibodies against two virulence factors released by these two highly virulent bacteria. Virulence factors are then selectively capture inside the nanochannels, blocking the passage of a redox indicator solution, what decreases the electrochemical current recorded. Under the presence of an effective antimicrobial compound, the release of these virulence factors is reduced, generating an unblocking of the nanochannel.

Compared to traditional AST methods, the developed sensor allows the differentiation between the bactericidal and bacteriostatic effects of a novel antimicrobial compound and helps to easily determine the minimum inhibitory concentration required.

The electrochemical platform developed in this work is not only useful for the screening of novel antimicrobial compounds, but also opens the path to a more personalized medicine, allowing an *on-demand* antibiotic administration.

### **6.3.2. Protocols**

#### *6.3.2.1. Bacterial strains*

Bacterial strains used in this work are *P. aeruginosa* (ATCC 10145) and *S. aureus* (ATCC 25923) purchased from American Type Culture Collection (ATCC LGC Standards, Spain). Bacteria were first isolated in tryptic soy agar (TSA) plates using a streaking technique and single colonies were grown in tryptic soy broth (TSB) media at 37°C, 250 rpm overnight. The day after, cells were concentrated and mixed with glycerol 50% for conservation at 4°C over the duration of the experiment.

---

<sup>442</sup> A. de la Escosura-Muñiz, K. Ivanova, T. Tzanov. ACS Appl. Mater. Interfaces. 2019, 11 (14), 13140-13146

#### 6.3.2.2. *Toxicity testing of redox indicators*

A redox indicator solution is required to perform the electrochemical measurements. To make sure that these redox indicator solutions do not have any effect over the normal growth of the bacteria used in this work, first toxicity was evaluated. The redox indicator solutions evaluated were ferrocyanide at 10 mM and hexamine ruthenium at 0.5 mM. These redox indicators were also doped with the salts NaCl, KCl, NaNO<sub>3</sub> and KNO<sub>3</sub> at concentrations of 0.1 and 0.05 M to improve conductivity. Toxicity was evaluated making use of a minimum inhibitory concentration assay using a previously optimized protocol.

First, 10  $\mu$ L of the glycerol cell stock were inoculated on 5 mL of TSB and incubated at 37°C, 250 rpm overnight. After that time, OD<sub>600</sub> was checked, and bacteria concentration was normalized to 1 x10<sup>6</sup> cells/mL. In parallel, in a 96-well plate, dilutions of the different redox indicators in TSB were added. Positive and negative controls were also incorporated to each plate. Plates were incubated at 37°C without shaking overnight, and after that time OD<sub>600</sub> was measured.

#### 6.3.2.3. *Electrochemical measurements*

The developed sensor was constructed using an ITO/PET as working electrode, Ag/AgCl reference electrode and platinum counter electrode using the same methacrylate cell setup explained in Chapter 5. Prior to the integration of the nanoporous alumina membranes, the electrochemical signal provided by the redox indicator solutions tested in the previous section in TSB media was evaluated. For ferrocyanide, DPV at scan was performed from -0.1 V to +1.1 V (step potential: 10 mV, modulation amplitude: 50 mV, and scan rate: 33.5 mV/s). For hexamine ruthenium a DPV was performed with a pre-treatment at +0.20 V applied for 30 s followed by a scan from +0.20 V to -0.40 V (Step potential: -0.01 V; Modulation amplitude: 0.05 V; Modulation time: 0.01 s; Interval time: 0.5 s; Scan rate: 0.02 V/s).

#### 6.3.2.4. *Nanoporous alumina membranes functionalization, antibody immobilization and virulence factor detection*

Nanoporous alumina membranes of 20 nm were functionalized following previously optimized procedures (Chapter 5) and used for the detection of both virulence factors. Anti-enterotoxin B antibody was added to the membranes at a concentration of 2

$\mu\text{g/mL}$ . For pyocyanin detection, anti-pyocyanin monoclonal antibody was added at a concentration of  $100 \mu\text{g/mL}$ . Antibodies were immobilized following the carbodiimide chemistry already explained in this PhD Thesis and left incubate at RT without shaking for 2h. Later, enterotoxin B and pyocyanin were added to the respectively modified membranes at a concentration of  $1000 \text{ ng/mL}$  and left incubating for 1h. The effect of the pH over the detection of both virulence factors was address, using buffer measurement solutions of  $10\text{mM MES (pH 5)}$  and  $0.1 \text{ M Tris-HCl (pH 8.6)}$  for enterotoxin B, and  $0.1 \text{ M NaAc (pH 4.2)}$  and  $0.1 \text{ M Tris-HCl (pH 7.6)}$  for pyocyanin.

### **6.3.3. Results and discussion**

#### *6.3.3.1. Evaluation of the redox properties of different indicator solutions in TSB*

The purpose of this work is the evaluation of novel antimicrobial compounds *in vivo* using an electrochemical sensor for the monitoring of the release of virulence factors. Bacterial cell of the strains against which the antimicrobial compounds are evaluated, are cultured on top of the electrochemical sensor, and the release of virulence factors is monitored by electrochemically recording the passage of a redox indicator solution. As bacteria cells are cultured in TSB media, a redox indicator with adequate properties in this media is needed. To select a proper redox indicator, first the redox pairs  $[\text{Ru}(\text{NH}_3)_6]^{3+}/[\text{Ru}(\text{NH}_3)_6]^{2+}$  and  $[\text{Fe}(\text{CN})_6]^{4-} / [\text{Fe}(\text{CN})_6]^{3-}$  were evaluated alone and in combination with different salt concentrations ( $\text{NaCl}$ ,  $\text{KCl}$ ,  $\text{NaNO}_3$  and  $\text{KNO}_3$  at  $0.05$  and  $0.1 \text{ M}$ ).

For the redox pair  $[\text{Ru}(\text{NH}_3)_6]^{3+}/[\text{Ru}(\text{NH}_3)_6]^{2+}$  (Figure 6.16.A.), the corresponding reduction peak current clearly increases from a solution containing the redox pair alone and solutions dopped by the addition of salts, being between 3 to 6 times higher. Additionally, a clear correlation between salt concentration and pick current recorded is observed for all the conditions texted, being the combination of the redox pair dopped with  $\text{NaCl } 0.1\text{M}$  the one that provides a higher current value (average of  $242 \mu\text{A}$  in absolute value).

In the case of the redox pair  $[\text{Fe}(\text{CN})_6]^{4-} / [\text{Fe}(\text{CN})_6]^{3-}$  (Figure 6.16.B.) the behaviour is equivalent with an increase in the current recorded with the addition of salts compared

to the redox pair alone, and being the condition including NaCl 0.1M the one providing a higher current value (average of 140  $\mu$ A in absolute value).

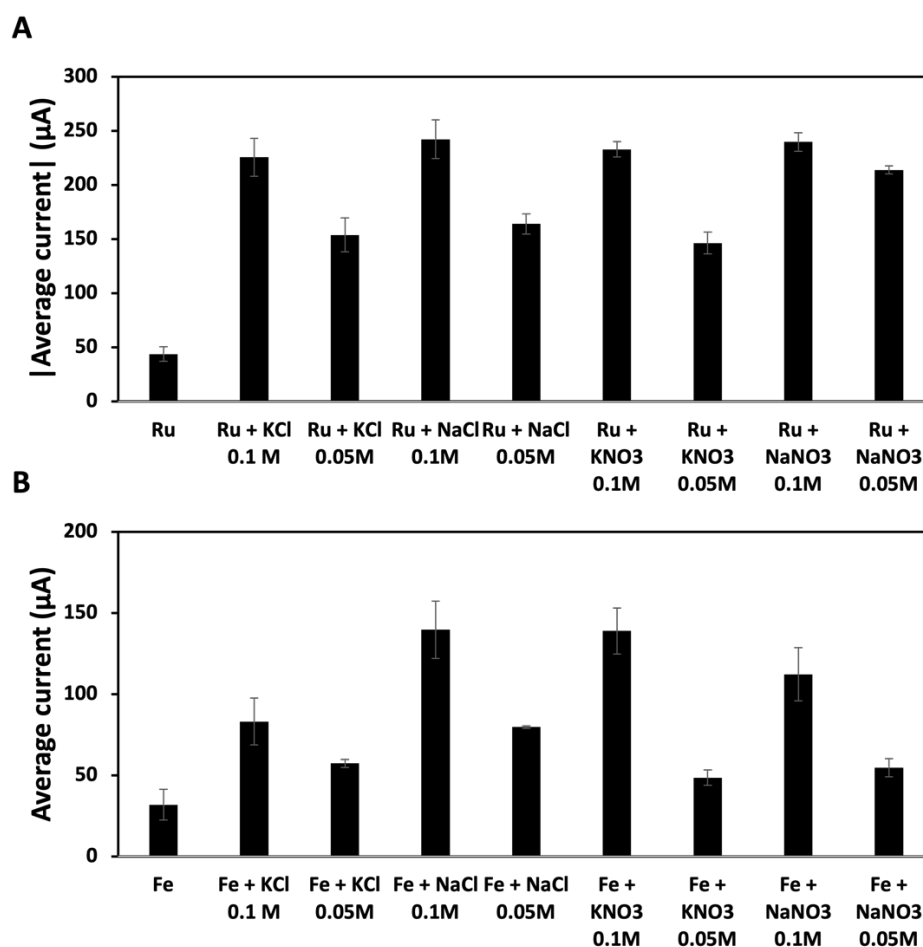


**Figure 6.16.** Comparison of the average current recorded with two redox pairs alone and in combination with different electrolyte salts. **A.** Comparison for the  $[\text{Ru}(\text{NH}_3)_6]^{3+}/[\text{Ru}(\text{NH}_3)_6]^{2+}$  redox pair. **B.** Comparison for the  $[\text{Fe}(\text{CN})_6]^{4-}/[\text{Fe}(\text{CN})_6]^{3-}$  redox pair. Data is given as average ( $n=3$ )  $\pm$  SD.

### 6.3.3.2. Evaluation of the toxicity of redox indicator solutions against *P. aeruginosa* and *S. aureus*

Apart from the electrochemical behavior of redox pairs in TSB media, another important parameter to evaluate is the toxicity that redox solutions have over bacteria cell growth. It is important to address this aspect prior to the selection of a proper redox indicator solution, as it is cell growth and virulency the parameter that will be monitored to evaluate antimicrobial efficacy.

Both  $[\text{Ru}(\text{NH}_3)_6]^{3+}/[\text{Ru}(\text{NH}_3)_6]^{2+}$  and  $[\text{Fe}(\text{CN})_6]^{4-} / [\text{Fe}(\text{CN})_6]^{3-}$  redox pairs, alone and in combination with the same electrolytic salts explained above, were tested over both *S. aureus* and *P. aeruginosa*. Additionally, salts alone, without the addition of a redox indicator, were tested to evaluate the effect that have over cell growth.

For *S. aureus* (Figure 6.17), results show that the redox pair  $[\text{Fe}(\text{CN})_6]^{4-} / [\text{Fe}(\text{CN})_6]^{3-}$  slightly decreases the growth obtained compared to non-treated *S. aureus* and that the growing burden is higher for redox solutions containing  $\text{NO}_3^-$  anion as electrolyte. This same behaviour is also observed for the redox pair  $[\text{Ru}(\text{NH}_3)_6]^{3+}/[\text{Ru}(\text{NH}_3)_6]^{2+}$  although an increase in the growth is observed for certain conditions. When electrolytic salts were evaluated alone, an increase in the growth was obtained for  $\text{Cl}^-$  salts while growth was reduced when  $\text{NO}_3^-$  salts were added.

In the case of *P. aeruginosa* (Figure 6.18.) results are much more relevant, with a notable effect of the addition of redox solutions over the bacterial growth for the redox pair  $[\text{Ru}(\text{NH}_3)_6]^{3+}/[\text{Ru}(\text{NH}_3)_6]^{2+}$ . In this case, there is a clear correlation between the presence of the redox solution and an inhibition of bacteria growth. It is extremely curious that this susceptibility is seen in *P. aeruginosa* bacteria while it is not noticeable for *S. aureus*. The mechanism by which this susceptibility occurs will be studied in further researches.

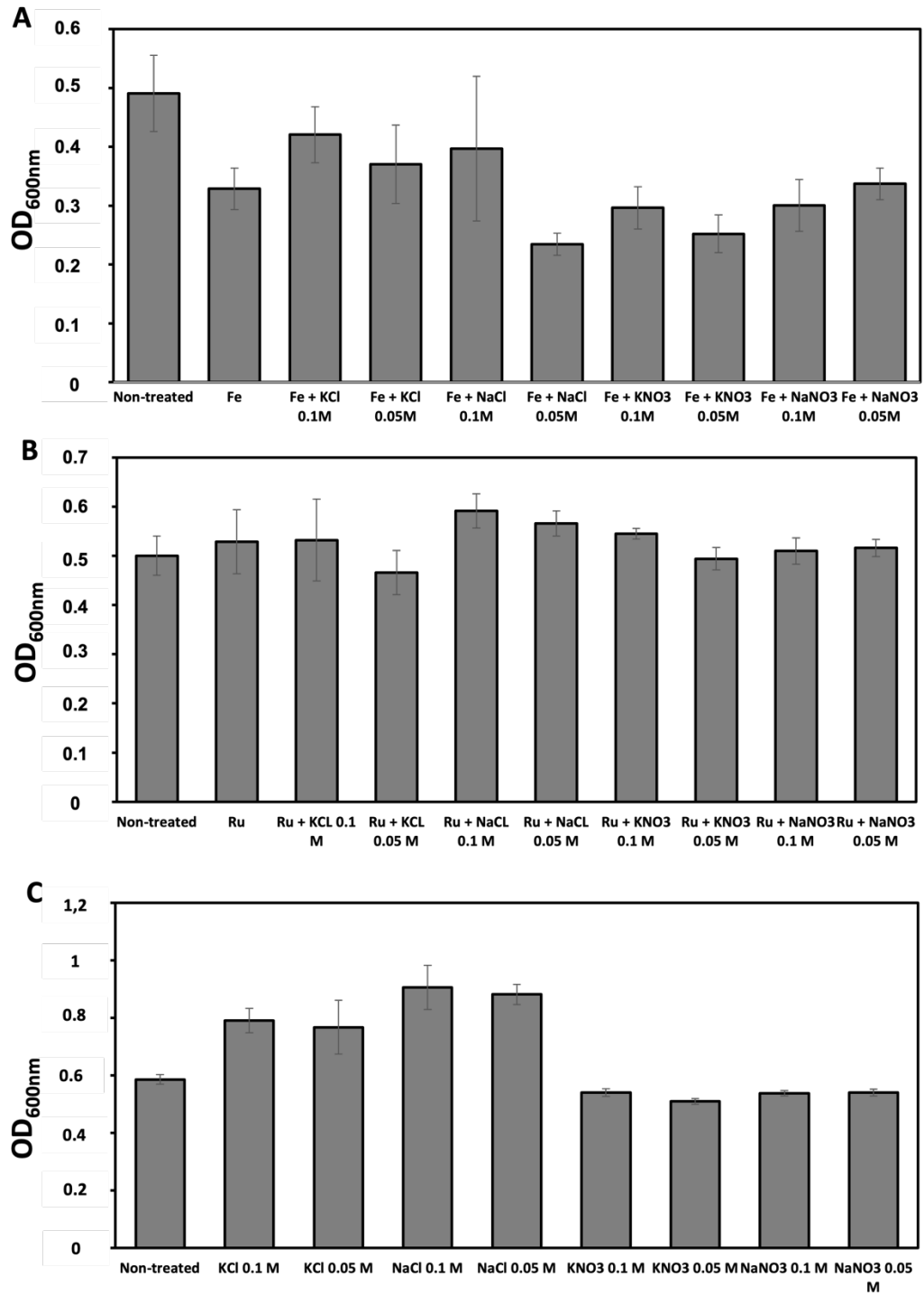


**Figure 6.17.** Comparison of the growth (considered as the OD<sub>600</sub>) for *S. aureus* under different conditions. **A.** Treated with [Fe(CN)<sub>6</sub>]<sup>4-</sup> / [Fe(CN)<sub>6</sub>]<sup>3-</sup> doped with electrolytic salts. **B.** Treated with [Ru(NH<sub>3</sub>)<sub>6</sub>]<sup>3+</sup> / [Ru(NH<sub>3</sub>)<sub>6</sub>]<sup>2+</sup> doped with electrolytic salts. **C.** Salts alone.



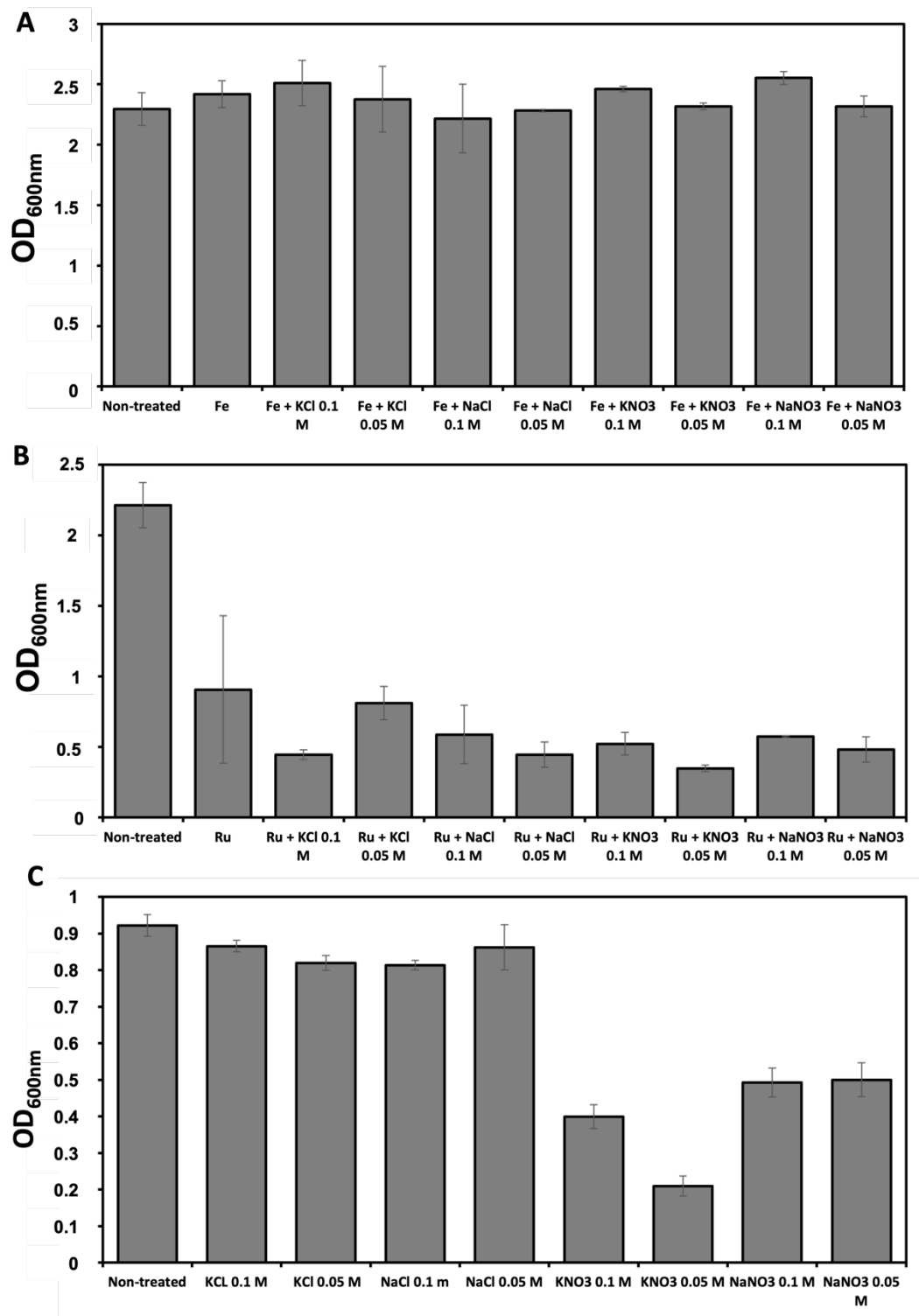


**Figure 6.18.** Comparison of the growth (considered as the OD<sub>600</sub>) for *P. aeruginosa* under different conditions. **A.** Treated with [Fe(CN)<sub>6</sub>]<sup>4-</sup> / [Fe(CN)<sub>6</sub>]<sup>3-</sup> doped with electrolytic salts. **B.** Treated with [Ru(NH<sub>3</sub>)<sub>6</sub>]<sup>3+</sup> / [Ru(NH<sub>3</sub>)<sub>6</sub>]<sup>2+</sup> doped with electrolytic salts. **C.** Salts alone.

### 6.3.3.3. *Detection of enterotoxin B and pyocyanin as virulence factor: optimization of measurement pH*

The pH of the measurement solution is a key parameter that will determine the charges that the different proteins immobilized and captured within the nanochannels will have when the redox indicator ions pass through.

For enterotoxin B, knowing that the isoelectric point (pI) of the anti-enterotoxin B antibody ranges between 5.5-7.5, while that of enterotoxin B is 8.6, redox indicator solutions were prepared in buffers at different pH. Two buffers were chosen: 10mM MES (pH 5) and 0.1 M Tris-HCl (pH 8.6) and in each buffer. Based on the pI values specified above, at pH 5 the antibody is positively charged, which exerts a certain electrostatic blocking effect on the diffusion of  $[\text{Ru}(\text{NH}_3)_6]^{3+}$  ions. This blocking effect is greatly enhanced in the presence of the specifically captured enterotoxin, as the molecule is also positively charged at this pH (Figure 6.19.).

Although this result follows the expected hypothesis for nanochannel blockage observed in previous works, in this case, the change required in the pH used for measuring could have an impact over cell growth, being required a reevaluation of this aspect prior to further optimization procedures.

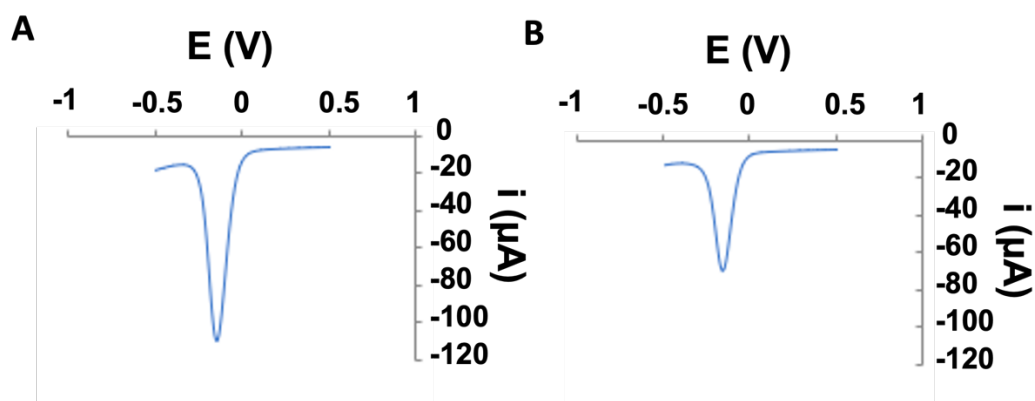


**Figure 6.19.** Voltamperograms corresponding to the evaluation of enterotoxin blockage for A. pH 5 and B. pH 7.2.

For the case of pyocyanin, this virulence factor is a small zwitterion molecule that it is neutrally charged at a pH higher than the pKa of one of its amine groups (pKa 4.9). This means that the charge difference can only be exploited in the positive direction by using a positively charged redox indicator. Considering the toxicity that the positive redox

pair  $[\text{Ru}(\text{NH}_3)_6]^{3+}/[\text{Ru}(\text{NH}_3)_6]^{2+}$  has over *P. aeruginosa*, the bacteria strain responsible of pyocyanin secretion, it is not as relevant to optimize the pH effect than to select a proper non-toxic redox indicator that maximizes blockage as much as possible. Therefore, other redox molecules as ferrocenemethanol will be evaluated. Additionally, nanochannel diameter size will be also optimized to maximize the steric blockage produced by such a small molecule as pyocyanin.

#### 6.3.4. Conclusions

In this work, an electrochemical sensor for the evaluation of novel antimicrobial compounds is being developed. First, the conductance of different redox indicator pairs in the same media as bacteria are cultured was evaluated. The conductance of both  $[\text{Fe}(\text{CN})_6]^{4-} / [\text{Fe}(\text{CN})_6]^{3-}$  and  $[\text{Ru}(\text{NH}_3)_6]^{3+}/[\text{Ru}(\text{NH}_3)_6]^{2+}$  redox pairs decreases as expected in TSB media, requiring the addition of electrolytic salts to increase the conductance obtained.

Moreover, the toxicity effect of these redox pairs over the growth of *P. aeruginosa* and *S. aureus*, the two predominant bacteria in chronic wounds. Although *S. aureus* seemed to be less susceptible to the presence of these redox pairs, for *P. aeruginosa*, they all generate a burden over cell growth, being especially relevant the toxicity displayed by  $[\text{Ru}(\text{NH}_3)_6]^{3+}/[\text{Ru}(\text{NH}_3)_6]^{2+}$  redox pair.

Considering this information, first optimization steps were performed for the identification of both enterotoxin B and pyocyanin using an electrochemical sensor based on nanoporous alumina membranes. These optimization approaches pointed out the importance of the measurement pH used for maximizing the blockage obtained.

The electrochemical platform established in this study is not only valuable for screening novel antimicrobial compounds, but it also paves the way for more customized therapy by permitting antibiotic dosing on-demand.

## **Chapter 7. Conclusions and future perspectives /**

### **Conclusiones y perspectivas de futuro**

---

<b><u>Chapter 7. Conclusions and future perspectives / Conclusiones y perspectivas de futuro</u></b> .....	189
<u>7.1. Conclusions</u> .....	191
<u>7.2. Future Perspectives</u> .....	195
<u>7.3. Conclusiones</u> .....	197
<u>7.4. Perspectivas de futuro</u> .....	201

---



## 7.1. Conclusions

In this Doctoral Thesis, several novel (bio)analytical platforms have been developed using innovative nanomaterials, such as electrocatalytic nanoparticles, magnetic microparticles with high magnetisation or nanoporous membranes. These platforms have not only been used for biomarker detection but have also been studied for the screening of novel antimicrobial compounds. New strategies for the study of microbial interactions have even been explored.

Although the conclusions obtained have been set out in the corresponding Chapters of this Doctoral Thesis, the main contributions derived from this it are summarised below:

- ❖ Bimetallic gold-palladium nanoparticles (Pd-AuNPs) show a high electrocatalytic capacity against the oxygen reduction reaction at neutral pH. This activity is related to the presence of Au in the most reactive positions of the Pd core and is maximal for an Au ratio of 30%. Above this ratio, the electrocatalytic activity decreases. The obtained nanoparticles, whose electrocatalytic capacity was maximal, proved to be excellent marks in an electrochemical immunosensor able to operate at neutral pH, which avoids the use of additional reagents. This immunosensor was applied to the detection of hyaluronidase, an enzyme related to infection processes in chronic wounds, making it possible to differentiate between infected and clean wounds.
- ❖ It was found that the controlled introduction of Zn ions in the synthesis of magnetite nanoparticles (FeNPs), following a thermal decomposition process, increases the magnetism of the resulting nanoparticles. The encapsulation of these nanoparticles in polymeric matrices such as PLGA, allows obtaining microparticles that maintain the superparamagnetic behaviour and, at the same time, are suitable for functionalisation. The microparticles obtained were modified with neutravidin, in order to compare their performance with commercially available microparticles functionalised with the same protein. This aspect was compared by constructing a sandwich-type immunosensor using gold nanoparticles as label, confirming that the reproducibility of the assay was better with the magnetic microparticles developed in this Doctoral Thesis. Finally, these microparticles were used to

detect Tau protein, a biomarker of Alzheimer's disease. Although it is true that the detection limits obtained are high compared to the concentration at which this protein is found in real samples, the magnetic microparticles developed proved to be useful in complex samples, not observing matrix effects.

- ❖ Nanoporous alumina membranes are a suitable sensing platform for the detection of biomarkers without the need of tags. They are also useful in real samples, given their low non-specific adsorptions. Quantification using these nanomembranes is achieved by measuring the blocking (or unblocking) of the nanochannel in terms of the decrease (or increase) in the passage of a redox indicator substance and, therefore, of the analytical signal recorded. Both steric and electrostatic effects within the nanochannel are involved in maximising this blocking/unblocking.
- ❖ The electrostatic effects inside the nanochannels are due to the charge of the molecules immobilised inside them and the charge of the redox indicator used. In this Doctoral Thesis it has been confirmed that, in the case of the detection of an analyte through the formation of an immunocomplex, the charge of both the antibody and the analyte plays a fundamental role in the blockage achieved. Therefore, it is necessary to choose a pH for the measurement solution that ensures that both molecules are equally charged. This has been demonstrated by developing a (bio)analytical platform for the electrochemical detection of Tau protein, allowing its quantification in serum samples without observing matrix effects.
- ❖ Another relevant factor in blocking is steric hindrance, derived from the size that the analyte molecule occupies within the nanochannel. This factor depends on the pore diameter, as was demonstrated for the detection of lysozyme, a marker of infections in chronic wounds. In this case, an unblocking strategy of the nanochannel was studied for the first time, by means of the enzymatic action of lysozyme against its specific substrate, peptidoglycan. In this way, it was possible to develop a simple electrochemical method that does not require the use of tags for the detection of an enzymatic biomarker.
- ❖ In addition to the pore size, this Doctoral Thesis has shown that the thickness of the nanochannels also plays a fundamental role in the steric blocking

achieved. It has been shown that this is even higher than that presented by membranes with smaller pore diameters but greater thickness. Nanoporous alumina membranes with an optimal thickness were used for the detection of catalase related to chronic wound infections.

- ❖ In this Doctoral Thesis, other innovative (bio)analytical strategies have also been studied, such as 3D printing, and whose role may be relevant for the study of microbial interactions, such as those that may occur in chronic wounds. In the preliminary studies carried out in this Doctoral Thesis, it has been observed that traditional techniques, such as solid or liquid detection of the minimum inhibitory concentration, may not be sufficiently sensitive to determine changes in the expression of membrane proteins such as BtuB, which are responsible for the internalisation of toxins such as colicin. Replacing these techniques with more sensitive procedures, such as co-localisation of fluorescently labelled proteins by fluorescence microscopy, allows these changes to be detected. The use of more sensitive 3D printing techniques could help in these studies, allowing to achieve better resolutions.
- ❖ Nanoporous alumina membranes also allow bacterial culture on their surface, given their high biocompatibility, what opens the door to their use for the screening of candidate antimicrobial compounds. The use of redox indicator substances on these platforms can affect bacterial growth, being especially toxic when they contain ammonium salts. Quantification of bacterial virulence factors such as pyocyanin (*P. aeruginosa*) or enterotoxin B (*S. aureus*) can be useful to determine the effect of antimicrobial compounds.





## 7.2. Future Perspectives

The development of newly (bio)analytical instruments useful as POC devices is an increasing necessity in the current healthcare paradigm, that makes fast detection a requirement. Nanomaterials have been included in these (bio)analytical techniques to increase their performance, serving as electrocatalytic tags at neutral pH or low absorption sensing platforms (as MBs or nanoporous membranes). But there is still space for development in the nanomaterials field as it is with the works developed in this PhD Thesis. It is worthy to say that part of the future perspectives derived from this PhD Thesis are already ongoing projects in the NanoBioAnalysis research group at the University of Oviedo.

- ❖ The developed bimetallic nanoparticles are coloured and present intrinsic absorbance, what makes them suitable for lateral flow and electrochemiluminescence applications, as it has been already done with other bimetallic nanoparticles developed in this research group.
- ❖ The integration of the developed bimetallic nanoparticles with the synthesized magnetic microparticles is also a future work that it was not textured in this PhD Thesis due to time limitations.
- ❖ The steric and electrostatic optimizations obtained in this PhD Thesis are being also applied for the detection of other biomarkers related with chronic wounds infection, as myeloperoxidase, matrix metalloproteinases or microRNAs.
- ❖ Integrating theoretical and computational models would be desirable to completely understand the electrostatic effects that govern nanochannel blockage.
- ❖ The development of highly integrated sensing platforms on the electrode surface is still an unfinished research line. During this PhD Thesis, two projects in this line were initiated, consisting on the deposition of Al on top of ITO/PET electrodes for a subsequent anodization, and the use of block co-polymer strategies for nanopore formation onto ITO/glass electrodes. Both research lines are currently being developed in the research group.
- ❖ The electrochemical nanoporous membrane platforms developed could be used for monitoring *in vivo* the release of virulence factors.



## 7.3. Conclusiones

En esta Tesis Doctoral, se han desarrollado diversas plataformas (bio)analíticas novedosas empleando nanomateriales innovadores, como son las nanopartículas electrocatalíticas, las micropartículas magnéticas con alto poder de imanación o las membranas nanoporosas. Estas plataformas, no solo se han utilizado para la detección de biomarcadores, sino también se ha estudiado su uso para el testeo de nuevos antimicrobianos. Incluso, se han explorado nuevas estrategias para el estudio de las interacciones microbianas.

Aunque las conclusiones se han ido exponiendo en los correspondientes capítulos de esta Tesis Doctoral, se resumen a continuación, las principales aportaciones derivadas de esta Tesis Doctoral:

- ❖ Las nanopartículas bimetalicas de oro y paladio (Pd-AuNPs) presentan una alta capacidad electrocatalítica frente a la reacción de reducción del oxígeno a pH neutro. Esta actividad está relacionada con la presencia de Au en las posiciones más reactivas del núcleo de Pd y es máxima para una proporción de Au del 30%. Por encima de esta proporción, la actividad electrocatalítica disminuye. Las nanopartículas obtenidas, cuya capacidad electrocatalítica era máxima, demostraron ser excelentes marcas en un inmunosensor electroquímico capaz de operar a pH neutro, lo que evita el uso de reactivos adicionales. Este inmunosensor se aplicó a la detección de la hialuronidasa, un enzima relacionado con los procesos de infección en heridas crónicas, permitiendo diferenciar entre heridas infectadas y limpias.
- ❖ Se comprobó que la introducción controlada de iones Zn en el proceso de síntesis de nanopartículas de magnetita (FeNPs), siguiendo un proceso de descomposición térmica, aumenta el magnetismo de las nanopartículas resultantes. La encapsulación de estas nanopartículas en matrices poliméricas como el PLGA, permite la obtención de micropartículas que mantienen el comportamiento superparamagnético y a la vez que su funcionalización. Las micropartículas obtenidas fueron modificadas con neutravidina, para así comparar su rendimiento en comparación con micropartículas comerciales

funcionalizadas con esta misma proteína. Esto fue comparado construyendo un inmunosensor de tipo sándwich empleando nanopartículas de oro como marca, comparando que la reproducibilidad del ensayo era mejor con las micropartículas magnéticas desarrolladas en esta Tesis Doctoral. Por último, estas micropartículas se emplearon para la detección de la proteína Tau, biomarcadora de Alzheimer, si bien es cierto que los límites de detección obtenidos son altos en comparación con la concentración en la que esta proteína se encuentra en muestras reales.

- ❖ Las membranas de alúmina nanoporosas constituyen una plataforma sensora adecuada para la detección de biomarcadores, sin necesidad del uso de marcas, en muestras reales, dadas sus bajas absorciones inespecíficas. La cuantificación empleando estas nanomembranas se consigue midiendo el bloqueo (o desbloqueo) del nanocanal en términos de la disminución (o aumento) del paso de una sustancia indicadora redox y, por tanto, de la señal analítica registrada. En la maximización de este bloqueo/desbloqueo, están implicados los efectos tanto estéricos como electrostáticos en el interior del nanocanal.
- ❖ Los efectos electrostáticos en el interior de nanocanales se deben a la carga de las moléculas inmovilizadas en su interior y a la carga del indicador redox empleado. En esta Tesis Doctoral se ha confirmado como, en el caso de la detección de un analito a través de la formación de un inmunocomplejo, la carga tanto del anticuerpo como del analito, juegan un papel fundamental en el bloque conseguido. Por tanto, es necesario escoger un pH para la solución de medida, que asegure que ambas moléculas están cargadas de igual forma. Esto se ha demostrado desarrollando una plataforma (bio)analítica para la detección electroquímica de proteína Tau, permitiendo su cuantificación en muestras de suero sin observarse efectos de matriz.
- ❖ Otro factor relevante en el bloqueo es el estérico, derivado del tamaño que ocupa, en el interior del nanocanal, la molécula analito. Este factor depende del diámetro de poro, como se demostró para la detección de la lisozima, marcador de infecciones en heridas crónicas. En este caso, se estudió por primera vez una estrategia de desbloqueo del nanocanal, mediante la acción enzimática de la lisozima frente a su sustrato específico, el peptidoglicano. De esta forma se consiguió desarrollar un método electroquímico sencillo y

que no precisa del uso de marcas, para la detección de un biomarcador enzimático.

- ❖ Además del tamaño de poro, en esta Tesis Doctoral se ha demostrado que el grosor de los nanocanales empleados también juega un papel fundamental en el bloqueo estérico conseguido. Se ha comprobado como este es incluso superior al presentado por membranas con diámetros de poro inferiores pero mayor grosor. Las membranas de alúmina nanoporosa con un espesor óptimo se emplearon para la detección de la catalasa relacionada con las infecciones en heridas crónicas.
- ❖ En esta Tesis Doctoral, también se han estudiado otras estrategias (bio)analíticas innovadoras, como es la impresión 3D, y cuyo papel puede ser relevante para el estudio de interacciones microbianas, como las que pueden ocurrir en las heridas crónicas. En los estudios preliminares realizados en esta Tesis Doctoral, se ha observado cómo las técnicas tradicionales, como la detección en placa o en medio líquido de la concentración mínima inhibitoria pueden no ser suficientemente sensibles para determinar cambios en la expresión de proteínas de membrana como la BtuB, encargadas de la internalización de toxinas como la colicina. La sustitución de estas técnicas por otras más sensibles, como la co-localización de proteínas marcadas fluorescentemente mediante microscopía de fluorescencia, permite ver estos cambios. El uso de técnicas de impresión 3D, más sensibles, podría ayudar en estos estudios, permitiendo aumentar la sensibilidad conseguida.
- ❖ Las membranas de alúmina nanoporosas, dada su alta biocompatibilidad, también permiten el cultivo bacteriano en su superficie, lo que abre la puerta a su uso para el testeado de nuevos compuestos antimicrobianos. El uso de sustancias indicadoras redox en estas plataformas puede afectar al crecimiento bacteriano, resultando especialmente tóxicas cuando contienen sales de amonio. La cuantificación de factores de virulencia bacteriana como la piocianina (*P. aeruginosa*) o la enterotoxina B (*S. aureus*), puede ser de utilidad para determinar el efecto de compuestos antimicrobianos.



## 7.4. Perspectivas de futuro

El desarrollo de nuevas plataformas (bio)analíticas útiles como dispositivos POC es una necesidad creciente en el paradigma sanitario actual, que hace de la detección rápida un requisito indispensable. Los nanomateriales se han ido incluyendo en estos dispositivos para aumentar su rendimiento, sirviendo como marcas electrocatalíticas a pH neutro o plataformas de detección de baja absorción (como las micropartículas magnéticas o las membranas nanoporosas). Pero el margen de desarrollo en el campo de los nanomateriales es todavía amplio, al igual que ocurre con los trabajos desarrollados en esta Tesis Doctoral. Cabe decir que parte de las líneas derivadas de esta Tesis Doctoral son ya proyectos en marcha en el grupo de investigación NanoBioAnálisis de la Universidad de Oviedo:

- ❖ Las nanopartículas bimetálicas desarrolladas presentan color y absorbancia propias, lo que las hace adecuadas para aplicaciones de flujo lateral y electroquimioluminiscencia, como ya se ha hecho con otras nanopartículas bimetálicas desarrolladas en este grupo de investigación.
- ❖ La integración de las nanopartículas bimetálicas desarrolladas con las micropartículas magnéticas sintetizadas es también un trabajo futuro que no pudo desarrollarse en el marco de esta Tesis Doctoral debido a limitaciones de tiempo.
- ❖ Las optimizaciones estéricas y electrostáticas obtenidas en esta Tesis Doctoral se están aplicando también para la detección de otros biomarcadores relacionados con la infección de heridas crónicas, como son la mieloperoxidasa, las metaloproteinasas de matriz o los microRNAs.
- ❖ La integración de modelos teóricos y computacionales sería deseable para comprender completamente los efectos electrostáticos que gobiernan el bloqueo de nanocanales.
- ❖ El desarrollo de plataformas sensoras altamente integradas en la superficie del electrodo es todavía una línea de investigación en marcha. Durante esta Tesis Doctoral se iniciaron dos proyectos en esta dirección, consistentes en la deposición de Al sobre electrodos de ITO/PET para una posterior anodización, y el uso de copolímeros en bloque para la formación de nanoporos sobre electrodos de ITO/vidrio. Ambos trabajos se están desarrollando actualmente en el grupo de investigación.



- ❖ Las plataformas electroquímicas de membranas nanoporosas desarrolladas podrían utilizarse para monitorizar *in vivo* la liberación de factores de virulencia y el efecto de compuestos antimicrobianos.

## **Annexes**

---



## Annex A. Theoretical concepts

### *A.1. Antibody structure*

Antibodies, also known as immunoglobulins (Igs), are a family of glycoproteins able to specifically bind an antigen molecule. Igs are produced by the mammalian immune system as part of the humoral immune response against an unknown substance. They are produced by B cells in plasma by the binding of an antigen or immunogen with the B-cell receptor (BCR) present in the surface of B-lymphocytes<sup>443</sup>. There are five types of Igs in humans: IgM, IgG, IgA, IgE and IgD, which differ in their structure, specificity, and time of production. IgGs are the most abundant ones, present in a 70-75% of total Igs and in 10-20% of total plasma proteins<sup>444,445</sup>. Hence, IgGs are the predominant antibodies used in biosensing.

IgGs have four polypeptide chains, two identical light chains (L) of 25 kDa; and two heavy chains (H) of around 50 kDa bonded by disulfide bonds. As both L and H chains are identical, Igs have two antigen-binding sites. Every chain is divided into different constant (one for L chains and 3 for H chains) and variable (one per each chain) domains<sup>446</sup>. The variable region has three complementary-determining regions (CDRs) that confer specificity against different antigen regions, with which they interact non-covalently. Preserving this specificity is a major challenge in immunosensors, for what immobilization of the antibodies is the limiting step, as it will be explained below.

---

<sup>443</sup> D.R. Burton. Trends Biochem. Sci. 15 (1990) 64–69.

<sup>444</sup> Vidarsson G, Dekkers G, Rispens T. Front Immunol. 2014 Oct 20;5:520.

<sup>445</sup> T. Azam, S.H. Bukhari, U. Liaqat, W. Miran. Sensors. 23 (2023) 676.

<sup>446</sup> Janeway CA Jr, Travers P, Walport M, Mark J Shlomchik. Immunobiology: The Immune System in Health and Disease. 5th edition. New York: Garland Science; 2001.

## ***A.2. Electrochemical techniques***

### **❖ Amperometric techniques**

Amperometric techniques are based on the application of a controlled potential to record the current generated by a redox reaction occurring in the electrode. The applied potential is normally characteristic of the redox reaction studied, what increases the selectivity of the process. The intensity of the current is then directly related with the concentration of the redox species in contact with the electrode.

In chronoamperometry, changes in the current intensity from faradaic processes occurring in the electrode are recorded among time. During a chronoamperometric recording, a step potential from  $E_i$ , where any reaction takes place, to an  $E_f$ , where the redox reaction occurs, is applied. This potential promotes the electron exchange between the electrode and the redox species in the surface. The current intensity measured is then proportional to the concentration of the analyte of interest according to Faraday equation (equation 1):

$$Q = \frac{nFm}{M} \quad (1)$$

where  $Q$  is the electrical charge transferred,  $n$  is the number of electrons exchanged,  $F$  is Faraday constant,  $m$  is the quantity (in mass) of the transformed specie and  $M$  the molarity of that specie.

### **❖ Voltammetric techniques**

In voltammetric techniques, potential ( $E$ ) (or a potential range) is applied as excitation signal, producing a change in the current intensity ( $i$ ) that it is registered ( $i$  vs  $E$  voltammogram) among time. The resulting current is proportional to the concentration of the electroactive species present in the electrode-solution interface. According on how the excitation signal is applied, different voltamperometric techniques could be distinguished.

#### **i) Linear and cyclic voltammetry**

Cyclic voltammetry (CV) is the most used electrochemical technique, as provides qualitative and quantitative information of the electrochemical reactions that occur in the electrode surface. CV registers current changes as a function of a triangle potential

waveform applied. Measurements are recorded with the addition of a highly concentrated background electrolyte, to increase conductivity and decrease resistance of the solution.

An initial potential ( $E_i$ ) that does not alter the electrochemical reaction is initially applied. Then, the potential is scanned from  $E_i$  to an end potential  $E_f$ , that it is greater than the equilibrium potential of the target redox compound. The potential scan in this direction is known as direct scan. The returning potential scanning from  $E_f$  to a potential that it is normally equal to  $E_i$  is called inverse scanning.

In CV, the parameters that need to be fixed are: i) the anodic and cathodic peak currents ( $i_{p_a}$ ,  $i_{p_c}$ ), ii) the peak potentials ( $E_p$ ) and iii) the scan rate ( $v$ ). This technique is mainly selected to study the reversibility of an electrochemical process. This is done by checking the difference between the anodic and cathodic  $E_p$  ( $\Delta E_p = E_{p_a} - E_{p_c}$ ). For an ideal reversible electron transfer, the value of  $\Delta E_p$  is independent of the scan rate and will satisfy the Nernst equation (equation 2):

$$\Delta E_p = \frac{59}{n} \text{ mV} \quad (\text{a } 25^\circ\text{C}) \quad (2)$$

where  $n$  is the number of electrons involved in the reaction. Another way to estimate the reversibility of an electrochemical reaction is by the ratio between  $i_{p_a}/i_{p_c}$ . If this ratio has a value of 1, that means the reaction is stable, as the species formed in the direct reaction are present in the same concentration during the reverse reaction.

In contrast, linear sweep voltammetry (LSV) consists of applying a potential that varies linearly with time at a fixed scan rate. This potential is applied linearly just in one direction.

## ii) Differential pulse voltammetry

Pulse voltammetry techniques were introduced to increase sensitivity over traditional sweep techniques. These techniques consist of applying a pulse potential and registering the current intensity at the end of the pulse. This end time-point is chosen as it is where the faradaic current is significantly higher compared to non-faradaic current.

Differential pulse voltammetry (DPV), consist of applying sequential and pulses of fixed amplitude ( $\Delta E$ ). Current intensity is measured at the beginning ( $\tau$ ) and the end ( $\tau'$ ) of the pulse, and the response is represented as the peak corresponding to the difference of intensity vs pulse potential.

### ***A.3. Immobilization techniques***

#### **❖ Immobilization of the biological recognition element in the surface of micro and nanomaterials**

The bioreceptor is, together with the transducer, a basic component of biosensors and its immobilization is a determining factor in the overall performance of the device. A proper immobilization should ensure the accessibility by the analyte to the active sites, retaining their activity and making sure the complex formation<sup>447</sup>.

Strictly speaking, immobilization of a bioreceptor in a (bio)sensor should be performed directly on the electrode surface. However, there is an increasing tendency in (bio)analytical applications to incorporate sensing platforms, as MBs or nanoporous membranes, to which biorecognition elements are immobilized. Additionally, in sandwich-based assays where a label is needed, the immobilization of a recognition element on it is also mandatory. In this Thesis, immobilization of recognition elements has been done in the surface of the nanomaterials above described and not directly to the electrode surface. In any case, the immobilization mechanisms used are equal between sensing platforms or labels and the electrode surface, so that the information that is explained in this section is shared between surfaces.

Immobilization could be done following two processes: reversible, if the support could be regenerated, and irreversible immobilization, if not. The first one englobes adsorption, affinity, chelating binding, or disulfide bonding. Irreversible methods include covalent binding, cross-linking or entrapment<sup>448</sup>. In this Thesis, both group of methods have been employed (strept(avidin)-biotin binding, disulfide bonding or EDC/NHS chemistry). Below, the used immobilization methods will be widely explained.

#### **❖ Biotin-Avidin binding**

Biotin-strep(avidin) binding is a reversible bioaffinity immobilization strategy, widely spread in biosensing due to its easiness. Biotin, also known as vitamin H, is a low molecular weight (244.3 Da) protein present in all living cells. Avidin is a basic (pI of 10) tetrameric glycoprotein contains one binding site for biotin on each subunit. This

---

<sup>447</sup> Gubala, V., Klein, R., Templeton, D. M., & Schwenk, M. (2014). *Pure and Applied Chemistry*, 86(10), 1539-1571.

<sup>448</sup> S. Liébana, G.A. Drago. *Essays Biochem.* 60 (2016) 59–68

allows the binding of four biotins per each avidin, what helps to increase sensitivity. Streptavidin is, in contrast, an acidic protein (pI of around 5-6) obtained from the bacteria *Streptomyces avidinii* has the lowest nonspecific binding tendency. NeutrAvidin is also a deglycosylate version of avidin with a molecular weight of 60 kDa and a neutral isoelectric point of 6.3. The absence of oligosaccharides of this protein increases binding specificity. Despite the difference in structure of avidin/ neutravidin and streptavidin, all proteins have a strong non-covalent affinity for biotin, with an equilibrium dissociation constants ( $K_D$ ) of  $1.3 \times 10^{-15}$  M<sup>449</sup> [23] and  $4 \times 10^{-14}$  M<sup>450</sup> respectively. The resistance and strength of this interaction makes it remarkably useful in bioconjugation.

#### ❖ Au-S bonding

This bioconjugation method is based on the affinity of thiol (-SH) groups by gold surfaces forming gold-sulfur bond. The mechanism of this covalent interaction is mediated by the formation of i) a thiol radical ( $RS\cdot$ ) by deprotonation of sulfhydryl groups and ii) the formation of a gold-thiolated bonds<sup>451</sup>. This interaction has been deeply used in biosensing for the formation of self-assembled monolayers (SAMs)<sup>452</sup> and for the binding of biomolecules to gold nanoparticles<sup>453</sup>.

#### ❖ Carbodiimide/N-hydroxysuccinimide (EDC/NHS) chemistry

Another bioconjugation strategy is based on the irreversible formation of an amide bond between the carboxyl (-COOH) and primary amine (-NH<sub>2</sub>) groups of a biological recognition molecules and a determine surface (e.g., the transducer or a nanomaterial). This binding is achieved by using (1-Ethyl-3-[3-dimethylaminopropyl]-carbodiimide hydrochloride) (EDC) as a crosslinker agent. First, EDC reacts with -COOH group forming an amine-reactive O-acyl isourea intermediate. This intermediate is unstable, thus, in the absence of an amine group, it hydrolyzes going back to the carboxylic group. To avoid this, N-hydroxy succinimide (NHS) or its water-soluble equivalent (Sulfo-NHS)

---

<sup>449</sup> R.P. Haugland, W.W. You.. *Protoc.*, Humana Press, New Jersey, 1998: pp. 173–184.

<sup>450</sup> J.M. Marangoni, S.-C. Wu, D. Fogen, S.-L. Wong, K.K.S. Ng. *Sci. Rep.* 10 (2020) 12483.

<sup>451</sup> H. Häkkinen. *Nat. Chem.* 4 (2012) 443–455.

<sup>452</sup> Y. Xue, X. Li, H. Li, W. Zhang. *Nat. Commun.* 5 (2014) 4348.

<sup>453</sup> C. Parolo, A. de la Escosura-Muñiz, E. Polo, V. Grazú, J.M. de la Fuente, A. Merkoçi. *ACS Appl. Mater. Interfaces.* 5 (2013) 10753–10759.



is often added and reacts with O-acyl isourea forming a stable amine-reactive ester. This intermediate reacts then with a primary amine forming the final amide conjugate<sup>454</sup>.

#### ❖ Glutaraldehyde cross-linking

Glutaraldehyde is a dialdehyde that can covalently bond amines, hydroxyls, thiols, phenols and imidazoles. The use of GA as a cross-linker in biosensing and biomedical applications is extended, due to its versatility, low-cost and binding strength. GA can react with compounds containing amine or hydroxyl groups<sup>455</sup>. In this Thesis, GA has been used for the cross-linking of amine groups in polyethyleneimine and NeutrAvidin in the surface of magnetic microparticles (Chapter 4). GA binding mechanisms is still not completely understood. What it is known is that reaction with amine groups is kinetically favored under neutral or basic conditions<sup>456</sup>.

---

<sup>454</sup> N.J. Mol, M.J.E. Fischer, eds., *Amine Coupling Through EDC/NHS: A Practical Approach*, in: *Surf. Plasmon Reson.*, Humana Press, Totowa, NJ, 2010: pp. 55–73.

<sup>455</sup> K. Pal, A.T. Paulson, D. Rousseau. *Biodegrad. Plast.*, Elsevier, 2013: pp. 329–363.

<sup>456</sup> A.V. Bounegru, C. Apetrei. *Nanomaterials*. 13 (2023) 760.

## Annex B. Scientific production

The research work performed over this PhD Thesis has been undergone in the NanoBioAnalysis research group at the University of Oviedo. This PhD Thesis is presented as a compendium of publications with the approval of the Doctoral Program in Chemical, Biochemical and Structural Analysis and Computational Modeling.

### B.1. List of scientific articles included in this PhD Thesis

The work performed in this PhD Thesis, both research and review work, has led to the publication of six publications in scientific journals included in the Journal Citation Reports (JCR) and four more under preparation or submitted.

- **Scientific article 1.** Toyos-Rodríguez C., García-Alonso F.J. De la Escosura-Muñiz A. “*Electrochemical biosensors based on nanomaterials for early detection of Alzheimer’s Disease.*” *Sensors*, **2020**, 20 (17), 4748
- **Scientific article 2.** Toyos-Rodríguez C., Valero-Calvo D., De la Escosura-Muñiz A. “*Advances in the screening of antimicrobial compounds using electrochemical biosensors. Is there room for nanomaterials?*” *Analytical and Bioanalytical Chemistry*, **2023**, 415 (6), 1107-1121
- **Scientific article 4.** Toyos-Rodríguez C., Adawy A., García-Alonso F.J. De la Escosura-Muñiz A. “*Enhancing the electrocatalytic activity of palladium nanocluster tags by selective introduction of gold atoms: Application for a wound infection biomarker detection.*” *Biosensors and Bioelectronics*, **2022**, 200, 113926
- **Scientific article 5.** Toyos-Rodríguez C., Llamedo-González A., Pando D., García S., García J.A., García-Alonso F.J. De la Escosura-Muñiz A. “*Novel magnetic beads with improved performance for Alzheimer’s Disease biomarker detection*” *Microchemical Journal*, **2022**, 175, 107211
- **Scientific article 6.** Toyos-Rodríguez C., García-Alonso F.J. De la Escosura-Muñiz A. “*Towards the maximization of nanochannels blockage through antibody-antigen charge control: application for the detection of an Alzheimer’s disease biomarker.*” *Sensors and Actuators B Chemical*, **2023** 133394
- **Scientific article 7.** Iglesias- Mayor A., Amor-Gutiérrez O., Toyos-Rodríguez C., Bassegoda A., Tzanov T., De la Escosura-Muñiz A. “*Electrical monitoring of*

*infection biomarkers in chronic wounds using nanochannels.” Biosensors and Bioelectronics, 2022, 209, 114243*

### List of articles in preparation

- **Scientific article 3.** Toyos-Rodríguez C., Valero-Calvo D., García-Alonso F.J., De la Escosura-Muñiz A. “*Nanomaterial-based electrochemical platforms for the monitoring of chronic wounds.*” Under preparation.
- **Scientific article 8.** Toyos-Rodríguez C., Valero-Calvo D., Iglesias- Mayor A., Vega-Martínez V., De la Escosura-Muñiz A. “*Modifying thickness of nanoporous membranes reduces limit of detection: Application in an electrochemical sensor for chronic wound infection*”. Invited contribution to *Frontiers in Bioengineering and Biotechnology*.

The Impact Factor, and the position of the journals in their corresponding field, of the articles already published, are summarized in the following Table.

Journal	Year	IF	IF of the last 5 years	Field	Ranking	Publication state
Sensors	2020	3.576	4.050	Chemistry, Analytical	26/87 (Q2)	Published
Analytical and Bioanalytical Chemistry	2022	4.478	4.290	Chemistry, Analytical	22/87 (Q2)	Published
Biosensors and Bioelectronics	2022	12.545	10.722	Chemistry, Analytical	3/87 (Q1)	Published
Microchemical Journal	2022	5.304	4.723	Chemistry, Analytical	17/87 (Q1)	Published
Sensos and Actuators B: Chemical	2023	9.221	7.676	Chemistry, Analytical	6/87 (Q1)	Published
Frontiers in Bioengineering and Biotechnology	2023	6.064	5.497	Multidisciplinary Sciences	16/74 (Q1)	Invited contribution

## B.2. List of communications in scientific conferences

Additionally, the author of this PhD Thesis has participated in the following scientific conferences throughout this Thesis.

### Oral Communications

- **Junior Oral Communication:** Toyos-Rodríguez C., Valero-Calvo D., Ivanova K., Tzanov T., Vilaplana L., Pilar-Marco M., de la Escosura-Muñiz A. “*Rapid screening of novel antimicrobial compounds with a nanoporous-based electrochemical platform*”. II Reunión Científica del GCTbA. 27-28 June 2023, Zaragoza, Spain
- Toyos-Rodríguez C., Valero-Calvo D., Iglesias-Mayor A., Amor-Gutiérrez O., Bassegoda A., Tzanov T., De la Escosura-Muñiz A. “*Blocking and unblocking strategies in electrical nanochannel sensors for tackling chronic wound infection*” 33<sup>rd</sup> World Congress on Biosensors. 5-8 June 2023, Busan, South Korea
- Toyos-Rodríguez C., Iglesias-Mayor A., Amor-Gutiérrez O., Bassegoda A., Tzanov T., De la Escosura-Muñiz A. “*Lysozyme detection using a nanochannel array-based sensor for chronic wound infection monitoring*” 73<sup>rd</sup> Annual Meeting of the International Society of Electrochemistry. 16 September 2022. Online
- Toyos-Rodríguez C., Adawy A., García-Alonso F.J., De la Escosura-Muñiz A. “*Electrocatalytically highly active PdAuNPs as tags in a biosensor for the detection of chronic wound infection*” X International Congress on Analytical Nanoscience and Nanotechnology. 5-8 September 2022. Ciudad Real, Spain. Best Oral Communication Award
- Toyos-Rodríguez C., Iglesias-Mayor A., Amor-Gutiérrez O., Bassegoda A., Tzanov T., De la Escosura-Muñiz A. “*Early diagnosis of infections in chronic wounds using an electrochemical biosensor based on nanoporous membranes*”. XXIII Meeting of the Spanish Society of Analytical Chemistry (SEQA). 12-14 July 2022. Oviedo, Spain. Best Oral Communication Award
- Toyos-Rodríguez C., Adawy A., García-Alonso F.J. De la Escosura-Muñiz A. “*Gold-palladium bimetallic nanoparticles with enhanced electrocatalytic activity as tags for wound infection diagnosis*”. 3<sup>rd</sup> Workshop ELECTROBIONET “Electrochemical Sensors and Biosensors”. 23-24 June 2022. Madrid, Spain.

- Toyos-Rodríguez C., García-Alonso F.J. De la Escosura-Muñiz A. “*Detection of Alzheimer’s Disease biomarkers using an electrochemical immunosensor based on nanomaterials*”. XIV Annual Congress of Biotechnology. 8-9 July 2021. Online. Best Oral Communication Award.
- Toyos-Rodríguez C., García-Alonso F.J. De la Escosura-Muñiz A. “*Polymeric Magnetic Microparticles as Electrochemical Immunosensing Platforms*” 1st International Electronic Conference in Biosensors. 2-17 November 2020. Online

### Poster Communications

- Toyos-Rodríguez C., Valero-Calvo D., Iglesias- Mayor A., Vega-Martínez V., De la Escosura-Muñiz A. “*Effect of membrane thickness in the sensitivity of a solid-state nanoporous-based biosensing system for infection diagnosis*”. XXIX Reunión Bienal de Química. 25-29 June 2023, Zaragoza, Spain
- Toyos-Rodríguez C., Valero-Calvo D., Iglesias- Mayor A., Vega-Martínez V., De la Escosura-Muñiz A. “*Modifying thickness of nanoporous membranes reduces limit of detection: Application in an electrochemical sensor for chronic wound infection*”. 33<sup>rd</sup> World Congress on Biosensors. 5-8 June 2023, Busan, South Korea
- Toyos-Rodríguez C., Adawy A., García-Alonso F.J., .De la Escosura-Muñiz A. “*Electrocatalytic bimetallic PdAuNPs tags for the detection of hyaluronidase biomarker in infected chronic wound exudates*”. 73<sup>rd</sup> Annual Meeting of the International Society of Electrochemistry. 16 September 2022. Online
- Toyos-Rodríguez C., Llamedo-González A., Pando D., García S., García J.A., García-Alonso F.J. De la Escosura-Muñiz A. “*Alzheimer’s disease biomarkers detection using a biosensor based on novel magnetic beads*”. X International Congress on Analytical Nanoscience and Nanotechnology. 5-8 September 2022. Ciudad Real, Spain.
- Iglesias-Mayor A., Amor-Gutiérrez O., Toyos-Rodríguez C., Bassegoda A., Tzanov T., De la Escosura-Muñiz A. “*Electrochemical nanochannel array-based sensor for monitoring infection biomarkers in chronic wounds*”. 7<sup>th</sup> International Conference on Bio-sensing Technology. 22-25 May 2022. Sitges, Spain. Best Poster Award

- Toyos-Rodríguez C., García-Alonso F.J. De la Escosura-Muñiz A. “*Selective introduction of gold atoms on palladium nanocluster tags for an enhanced electrocatalytic activity: application in wound infection detection*”. 7th International Conference on Bio-sensing Technology. 22-25 May 2022. Sitges, Spain.
- **Flash poster:** Toyos-Rodríguez C., Adawy A., García-Alonso F.J. De la Escosura-Muñiz A. “*Highly electrocatalytic gold-palladium bimetallic nanoparticles as effective tags for wound infection diagnosis*” 3rd International Conference on Nanomaterials Applied to Life Sciences. 27-29 April 2022. Santander, Spain.
- Toyos-Rodríguez C., García-Alonso F.J. De la Escosura-Muñiz A. “*Enhancing the electrocatalytic activity of palladium nanocluster tags by selective introduction of gold atoms: application in immunosensing*”. 31st World Congress on Biosensors. 26-29 July 2021. Online

### B.3. Additional publications

Apart from the publications included in this PhD Thesis, the Doctoral candidate has also co-authored the following publications during her PhD period:



- Toyos-Rodríguez C., Calleja-García J., Torres-Sánchez L., López A., Abu-Dief A.M., Costa A., Elbaile L., Crespo R.D., Garitaonandia J.S., Lastra E., García J.A\*. García-Alonso F.J. “*A simple and reliable synthesis of superparamagnetic magnetite nanoparticles by thermal decomposition of Fe(acac)<sub>3</sub>*.” Journal of Nanomaterials, 2019, 2464010
- Toyos-Rodríguez C., García-Alonso F.J. De la Escosura-Muñiz A. “*Polymeric magnetic microparticles as electrochemical immunosensing platforms*”. Proceedings, 2020, 60(1), 21
- Valero-Calvo D., Toyos-Rodríguez C., García-Alonso F.J, De la Escosura-Muñiz A “*Electrochemical monitoring of enzymatic cleavage in nanochannels with nanoparticle-based enhancement: determination of MMP-9 biomarker.*” Accepted in Microchimica Acta.
- Villa-Manso, A. M., Guerrero-Esteban, T., Pariente, F., Toyos-Rodríguez, C., de la Escosura-Muñiz, A., Revenga-Parra, M., Lorenzo, E. “*Bifunctional Au@Pt/Au*

*nanoparticles as electrochemiluminescence signaling probes for SARS-CoV-2 detection.*” Talanta, 260, 124614

- García S., Amor-Gutiérrez O., Palomares-Albarrán M., Toyos-Rodríguez C., Cuetos F., Martínez C., Costa-García A., Fernández-Sánchez M.T., de la Escosura-Muñiz A., Novelli A. “*Unfolded p53 as a biomarker of oxidative stress in Mild Cognitive Impairment, Alzheimer’s and Parkinson Diseases*” Current Alzheimer Research, 2021, 18(9), 695-700
- Fernandez-Sanjurjo M., Pinto-Hernández P., Davalos A., Díaz-Martínez A.E., Martín-Hernández R., Castilla-Silgado J., Toyos-Rodríguez C., Whitham M., Amado-Rodríguez L., Albaiceta G. M., Terrados N., Fernández-García B., Iglesias-Gutierrez E. “*miR-16-5p, miR-19a-3p, miR-451a, and miR-25-3p cargo in extracellular vesicles as sedentarism biomarkers in young males.*” Under revision in European Journal of Sport Science.

Review

# Electrochemical Biosensors Based on Nanomaterials for Early Detection of Alzheimer's Disease

Celia Toyos-Rodríguez <sup>1,2</sup> , Francisco Javier García-Alonso <sup>2,3</sup> and Alfredo de la Escosura-Muñiz <sup>1,2,\*</sup> 

<sup>1</sup> NanoBioAnalysis Group-Department of Physical and Analytical Chemistry, University of Oviedo, Julián Clavería 8, 33006 Oviedo, Spain; toyoscelia@uniovi.es

<sup>2</sup> Biotechnology Institute of Asturias, University of Oviedo, Santiago Gascon Building, 33006 Oviedo, Spain; fjga@uniovi.es

<sup>3</sup> NanoBioAnalysis Group-Department of Organic and Inorganic Chemistry, University of Oviedo, Julián Clavería 8, 33006 Oviedo, Spain

\* Correspondence: alfredo.escosura@uniovi.es; Tel.: +34-985103521

Received: 31 July 2020; Accepted: 19 August 2020; Published: 22 August 2020



**Abstract:** Alzheimer's disease (AD) is an untreatable neurodegenerative disease that initially manifests as difficulty to remember recent events and gradually progresses to cognitive impairment. The incidence of AD is growing yearly as life expectancy increases, thus early detection is essential to ensure a better quality of life for diagnosed patients. To reach that purpose, electrochemical biosensing has emerged as a cost-effective alternative to traditional diagnostic techniques, due to its high sensitivity and selectivity. Of special relevance is the incorporation of nanomaterials in biosensors, as they contribute to enhance electron transfer while promoting the immobilization of biological recognition elements. Moreover, nanomaterials have also been employed as labels, due to their unique electroactive and electrocatalytic properties. The aim of this review is to add value in the advances achieved in the detection of AD biomarkers, the strategies followed for the incorporation of nanomaterials and its effect in biosensors performance.

**Keywords:** Alzheimer's disease; neurodegenerative diseases; nanoparticles; labels; electroactivity; electrocatalysis; electrochemistry; immunosensors; biosensors; nanomaterials

## 1. Introduction

Alzheimer's disease (AD) is a debilitating neurodegenerative disorder and the current main cause of dementia [1]. This untreatable disease affected more than 50 million people in 2019 and this number is estimated to increase to 152 million by 2050 according to Alzheimer's disease international (ADI) and the World health organization (WHO) [2]. Even though AD affects mainly older people, it is considered a multifactorial disease that appears before 65 years in 4% of cases. Commonly, AD starts with an initial phase, known as mild cognitive impairment (MCI), characterized by unclear episodes of memory and non-memory related impairments, that evolves to symptoms of dementia, implying deterioration of cognitive functions, memory loss, inability to perform daily tasks or time and space disorientation [3,4]. Cognitive decline associated with AD has a significant impact not only in patients, but also in families and careers, affecting them both emotionally and economically. In 2015, the Global Economic Impact of AD was of 818 billion US dollars, nearly 1.1% of the Gross Domestic Product (GDP) and it is expected to grow to two trillion US dollars by 2030 [5].

Due to its socio-economic effect, the Group of eight (G8) inter-governmental political forum stated in 2013 that discovering a therapy before 2025 was a global priority [1]. Unfortunately, there is still no treatment for AD, although recent research has been focused on disease-modifying drugs for early



stages of the disease owing to its increased efficiency [1,6], what highlights the importance of an early detection. The diagnose of AD can be performed by conducting cognitive tests and by imaging techniques, mainly magnetic resonance imaging (MRI), positron emission tomography (PET) and near infrared (NIR), used to detect abnormalities in patient brains [7]. The analysis of cerebrospinal fluid (CSF) and blood plasma biomarkers by immunohistochemistry and enzyme linked immunosorbent assay (ELISA) have also been used [8]. These techniques are time-consuming, expensive and invasive and do not constitute a generalize method for an early detection of AD. Due to that, there is a still a need to develop easy-to-use, low-cost, sensitive methods to facilitate the detection of AD and that require less amount of sample to minimize the extraction procedures performed on patients, as it is the case of electrochemical biosensors. In this review, electrochemical biosensors for the detection of AD are revised, according to the biomarkers detected and focusing on the use of nanomaterials in these analytical devices to improve biosensors performance.

## 2. Biomarkers for Alzheimer's Disease

AD is a multifactorial disease that evolves progressively until the first symptoms of dementia appear with variable clinical among patients. This fluidity difficulties detection only by cognitive tests, favoring misdiagnosis and delaying medication administration [8]. Due to that, biomarkers have gained importance for an early diagnosis of AD.

Even though molecular bases of AD are not well established, amyloid beta ( $A\beta$ ) peptides plaques and intracellular neurofibrillary tangles (NFTs) of hyperphosphorylated microtubule-associated protein tau (MAPT) are the most accepted pathological hallmarks of the disease.

$A\beta$  plaques are composed by aggregated  $A\beta$  peptides, generated by the proteolysis of amyloid precursor protein (APP), a transmembrane type I glycoprotein that is present in almost all tissues and whose physiological function is still unknown [9]. The cleavage of APP occurs by two different pathways: amyloidogenic, which is the causative of amyloidogenic diseases, including AD, and non-amyloidogenic [10]. In the amyloidogenic pathway, APP is cleaved by  $\beta$ -secretase (identified as BACE1) and  $\gamma$ -secretase (composed of four proteins including presenilin protein) on the N- and C-terminal ends, generating peptides of 39–43 amino acids [11,12],  $A\beta(1-40)$  and  $A\beta(1-42)$  being predominant. However, this cleavage occurs only in 10–20% of cases, as the predominant cleavage pathway (non-amyloidogenic) is performed by  $\alpha$ -secretase between 16 and 17 residues [13], generating non-amyloidogenic peptides. Any imbalance in the generation or clearance of amyloidogenic  $A\beta$  peptides leads to  $A\beta$  accumulation and constitutes a risk factor for AD development. Mutations in the APP gene and in presenilin gene have been related with an increased  $A\beta$  production and are associated with familial AD, the main cause of early onset dementia [14,15].

After  $A\beta$  peptide generation,  $A\beta$  monomers tend to form aggregates first in the form of oligomers ( $A\beta_o$ ), protofibrils and then fibrils ( $A\beta_f$ ) that accumulate extracellularly in neuron cell surfaces forming senile plaques. According to the “amyloid-cascade hypothesis” postulated by Hardy and Higgins in 1992 [16] the accumulation of  $A\beta$  forming plaques was the main cause of neurotoxicity and dementia. However, later studies have reported that some normal cognitive patients also possessed senile plaques [17,18], suggesting that there are other components involved in the onset of AD. Free soluble  $A\beta_o$  have been detected in CSF samples of AD patients [19] and have been found to produce cognitive impairments in patients without plaques [20]. The toxicity of  $A\beta_o$  has been related with the capacity of these molecules to cross the lipid bilayer of neuronal cells, inducing the depolarization of neurons' membranes by an allowable influx of  $Ca^{2+}$  ions leading to synaptic failure [21–23].

Another important hallmark is NFTs of MAPT, that are generated by the hyperphosphorylation of tau protein [24]. Tau protein is the main microtubule-associated protein of neurons involved in the assembly of tubulin. Normal phosphorylation of tau protein regulates axonal growth, transport and neuronal polarity. In several neurodegenerative diseases, tau is hyperphosphorylated and tends to aggregate forming pair helical filaments (PHFs), that form intracellular NFTs, neuropil threads and dystrophic neurons extracellularly accumulated near  $A\beta$  plaques [24–28].

A $\beta$  and fibrillary tangles are not the only biomarkers currently object of study. ApoE4 has been postulated for an early detection of AD as it is considered the major genetic risk factor for AD. ApoE is a glycoprotein that acts as a ligand in mediated endocytosis of lipoprotein particles and it is mainly expressed in the brain in astrocytes and microglia [29]. Human ApoE has three isoforms (ApoE2, ApoE3 and ApoE4) that differ in the presence of arginine or cysteine amino acids at positions 112 and 158 [30], being E4 directly associated with AD, especially with an earlier age onset [31]. ApoE4 in AD is considered to act as a binding protein for A $\beta$ , inducing the formation of pathological  $\beta$ -sheets [32]. A $\beta$ , hyperphosphorylated Tau and ApoE4 have all been found in CSF samples of AD patients [33] constituting reliable biomarkers of the disease with a sensitivity of 85–90% in early onset AD.

AD pathogenesis has also been related with novel biomarkers as p53 protein, since Lanni et al. [34] observed in 2007 that unfolded p53 peptide is highly expressed in fibroblast of non-AD patients in the presence of nanomolar concentrations of A $\beta$  peptide, suggesting that the presence of low and non-toxic levels of this biomarker could induce cell changes, including the formation of an abnormal tertiary conformation of p53 which must appear before the start of amyloidogenic cascade. In its normal conformation, p53 is considered as the “guardian of the genome” as it is a multifunctional protein with antioxidant activity involved in tumoral growth suppression [35], while its unfolded conformation has been studied owing to its pathogenicity [36–38].

Moreover, neurotransmitters have also been related with the development of neurodegenerative diseases, including AD, as they may interact with A $\beta$  [39]. Acetylcholine (Ach), dopamine (DA) and norepinephrine (NE) have been studied as potential biomarkers for the evaluation of neurodegenerative diseases, not only for an early detection but also to evaluate potential drug candidates [40–42].

Oxidative stress has also been proposed as hallmark since inflammation, A $\beta$  accumulation or hyperphosphorylated tau could induce the process [43]. When this happens, an increase in oxidative stress biomarkers (H<sub>2</sub>O<sub>2</sub> or superoxide dismutase (SOD) among others) in blood is reported [44].

All the above mentioned biomarkers have been summarized in Table 1, as well as less extended AD biomarkers as microRNAs (miRNAs), BACE1 [45] or  $\alpha$ -1-antitripsine [46], a protein related with A $\beta$  peptide fibril formation [47], that have also been investigated by electrochemical means.

With regard to the samples measured, most of the biomarkers studied so far are present in CSF and blood samples, as has been stated above, but there is an increasing tendency to use salivary samples, both to detect conventional biomarkers and others like lactoferrin specific for this type of samples [48]. However, it is still needed further investigation before their application in biosensing.

**Table 1.** AD biomarkers accepted and the role that they have in AD pathogenesis.

Biomarker	Pathogenicity in AD	Reference
A $\beta$ peptide	Forms aggregates that accumulate extracellularly around neurons forming senile plaques, causing neurotoxicity and dementia.	[17,18]
A $\beta$ o	Aggregated form of A $\beta$ peptide, present in CSF samples that produces cognitive impairment by inducing the depolarization of neurons' membranes	[19–21]
Hyperphosphorylated tau	The abnormality phosphorylation of tau promotes its aggregation forming PHF, that form intracellular NFTs, neuropil threads and dystrophic neurons extracellularly accumulated near A $\beta$ plaques.	[24–28]
ApoE4	Acts as a binding protein for A $\beta$ , promoting the formation of $\beta$ -sheets. It is the main biomarker related with early onset dementia.	[31,32]
Unfolded p53	It is present at nanomolar concentrations of A $\beta$ peptide as a consequence of it but previously to the formation of notable A $\beta$ plaques.	[36–38]

Table 1. Cont.

Biomarker	Pathogenicity in AD	Reference
Neurotransmitters	They could interact with A $\beta$ and minor changes on its synthesis and release could be associated to neurodegenerative diseases.	[39,49]
Oxidative stress	Induce by inflammation, A $\beta$ formation and hyperphosphorylation of tau. Little changes in the brain could induce a disbalance in blood samples.	[43,50]
miRNAs	Short oligonucleotides that regulate the translation of mRNA of presenilins and APP genes.	[51,52]
BACE-1	$\beta$ -secretase that cleaves APP gene in its amyloidogenic pathway.	[45]
$\alpha$ -1-antitripsine	Related with the formation of fibrils of A $\beta$ peptide.	[46]

A $\beta$ : A $\beta$  oligomers; APP: amyloid precursor protein; CSF: cerebrospinal fluid; mRNA: messenger RNA; NFTs: neurofibrillary tangles; PHF: pair helical filaments.

Although the identification of AD biomarkers is a complex and extensive field, diagnosis criteria vary as further as investigations are performed. What is clear is that as important as knowing the appropriate biomarkers is being able to identify them, for what electrochemical biosensors emerge as outstanding tools.

### 3. Electrochemical Biosensors: The Role of Nanomaterials

#### 3.1. General Overview

Electrochemistry is defined as the branch of chemistry implicated in the interrelation between electrical and chemical effects [53], which includes the study of the production of electricity by chemical reactions and the chemical changes generated by the passage of an electrical current. Both these phenomena are used in biosensors development. On the other hand, a biosensor is defined as a device that converts biological information into measurable analytical signals [54]. Biosensors are composed of a molecular recognition element (receptor) and a physicochemical transducer, that in the case of electrochemical biosensors is an electronic conducting, semi-conducting or ionic conducting material, that allows measuring analytical samples by different techniques including potentiometry, amperometry, conductometry and field-effect.

With regard to the electrochemical recognition process employed, biosensors may be classified in two groups, those that use a biocatalytic recognition element, namely enzymes, cells and tissues, and those based on bioaffinity reactions, which includes immunosensors (using antigen-antibody interactions), genosensors (employing nucleic acids as recognition element) and aptamer-based biosensors (sequence of synthetic oligonucleotides as biological recognition element) [54–56]. Electrochemical immunosensors have been widely studied as the high affinity reached by antigen-antibody interactions improves specificity and allows the detection of trace amounts of biomarkers. Deoxyribonucleic acid (DNA) and ribonucleic acid (RNA) sensors, in contrast, are characterized by having a sequence of oligonucleotides (probe) as biological recognition element [55,57]. The principle of these sensors is based on the specific hybridization between the oligonucleotides immobilized in the transducer and the complementary analyte in such a way that they could be applied for the detection of polymorphisms in the DNA and RNA associated with genetic-related diseases. Compared to traditional techniques for the detection of DNA and RNA sequences that include polymerase chain reaction (PCR) [58] or fluorescence in situ hybridization (FISH) [59], biosensors are simpler, less time-consuming and more sensible. Due to that, they have gained attention for the detection of circulating biomarkers, including those related to AD disease.

Among bioaffinity sensors, aptamer-based ones have gained special interest as they have an enhanced efficiency in contrast to antibodies, as they are more stable, easier to bioconjugate and less toxic [60,61]. However, selection process of aptamers is slightly more tedious as selective evolution of ligands by exponential enrichment (SELEX) has to be performed, so that antibodies are still the most chosen option.

An appropriate immobilization of biological recognition elements on the transducer is a key aspect in bioaffinity sensors, as the performance is dependent on the coating obtained. With the aim of improving this aspect, nanomaterials have been extensively used.

Overall, due to their reduced size, fast operation, sensitivity and low cost, electrochemical biosensors are point-of-care (POC) devices suitable for replacing currently used laboratory analysis [62]. It is also worthy to highlight the low sample volume required by most of the electrochemical biosensing configurations (typically around 10  $\mu$ L). This is of special relevance for the analysis of samples like blood and CSF which require invasive extraction.

### 3.2. The Role of Nanomaterials

Although electrochemical biosensors have gained importance as POC devices over the past few years, it is still necessary to enhance biosensors performance in order to lower detection limits. For that purpose, nanomaterials have been proved to be useful [63] both as electrode modifiers and as labels, due to their high electron transfer, biocompatibility and electrocatalytic activity, among other properties.

In the last decades, significant progress has been made in the synthesis of nanomaterials with tailored characteristics (size, shape or surface charge) and on their functionalization and combination with other nanomaterials, polymers or biomolecules [64].

As electrode modifiers, nanomaterials have mainly been incorporated following two objectives: improving the electronic transference and anchoring biological recognition elements.

The immobilization of biomolecules in nanomaterials has a huge impact on the reproducibility, robustness of the assay and increased time stability, owing to its strong absorption capacity and its biocompatibility compared to bulk materials.

Coating the transducer with nanomaterials functionalized with biomolecules allows an appropriate orientation of the biological recognition elements, which is of key relevance for ensuring that the binding sites are accessible and that the redox-active sites in the biomolecule are in contact with the transducer [65–68].

Additionally, nanomaterials have also been used as labels, including metal nanoparticles, carbon-based nanomaterials or electroactive nanovesicles, due to their electrochemical and electrocatalytic properties [69,70]. Even though enzyme-based labels are most common, their low thermal stability and non-conductivity have favored its substitution by nanomaterials. In comparison, nanomaterials have higher stability, signal amplification capacity and sensitive electrochemical response than traditional enzymes or metal ion probes [71,72]. Their particular characteristics compared to those of the bulk materials have raised them as fundamental parts of electrochemical biosensors as they are ideal tools for improving sensitivity, time stability and lower limits of detection (LOD). In Figure 1, nanomaterials mostly used in AD biosensors, both as electrode modifiers and as labels, have been represented, thereby AD biomarkers detected through electrochemical biosensors. Principal strategies followed for the detection of AD biomarkers are also outlined, including the use of antibodies, DNA probes, aptamers and proteins as recognition elements.

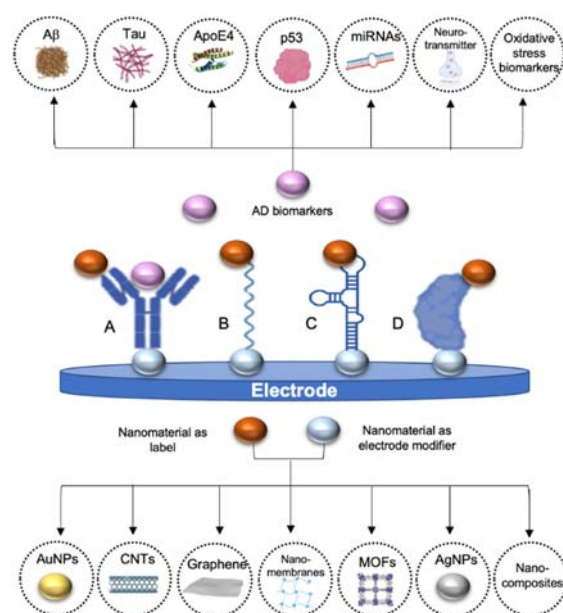


**Figure 1.** Schematic representation of the main AD biomarkers and the typical nanomaterials used in electrochemical biosensors for AD detection (gold nanoparticles (AuNPs), carbon nanotubes (CNTs), graphene, nanomembranes, metal-organic frameworks, silver nanoparticles (AgNPs) and nanocomposites). A. Using antibodies as recognition element, B. using oligonucleotides as recognition element, C. using aptamers as recognition element and D. using affinity proteins as recognition elements. In all cases nanomaterials may be used both to modify the electrode and as label, not being necessary the use of both nanomaterials at the same time in all the detection strategies.

#### 4. Electrochemical Biosensors for Alzheimer's Disease Diagnostics

The increasing incidence of AD has turned it into the most studied neurodegenerative disease. The presence of AD biomarkers in blood and CSF has promoted the development of electrochemical biosensors for their detection, as they allow the obtention of quantitative results in five minutes to two hours [48]. However, reaching the low cut-off values of the main AD biomarkers in human samples and improving selectivity and time-stability of biosensors are the heading challenges here [73]. For that purpose, nanomaterials have been introduced in biosensors either as labels or electrode modifiers.

As it can be deduced from the works revised in this review, peptides are, by far, the most widely detected biomarkers followed by proteins, as Aβ peptide is, till now, the mainly accepted biomarker. With regard to biological recognition elements, antibodies are predominant even though the use of aptamers is remarkable as well as the combination of these two elements in sandwich type biosensors. From nanomaterials, AuNPs are, without no doubt, the most frequently used materials, both as electrode modifiers and as labels, followed by carbon-based nanomaterials. It is worth remarking that the use of combinations of different nanomaterials, known as nanocomposites, is increasing as in the majority of cases they present a synergistic effect.

Below are described the most representative electrochemical biosensors for the detection of AD biomarkers in which nanomaterials are involved, classified according to the analyte measured: DNA or RNA, peptides, proteins, neurotransmitters and oxidative stress biomarkers, and attending to the nanomaterials used and the contribution they made to biosensors performance.

##### 4.1. DNA and RNA Biomarkers

DNA is the carrier of genetic information, that differs in every single organism making it unique. During cells life cycle many mutations can occur, having a severe impact in humans health in a hereditary way [74]. Since the discovery of DNA double helix structure [75], the identification and sequencing of this genetic information have been of top interest to both understand and diagnose



genetic diseases. In the case of AD, ApoE4 gene is the main genetic biomarker, as it has been related to late-onset familial AD [76]. Moreover, not only DNA sequences have been used as nucleic acid biomarkers. MicroRNAs (miRNAs) have been a hot topic since their identification in plasma and serum human samples in 2008 [77]. MiRNAs are single-stranded, non-coding short oligonucleotides (~22 nucleotides) that regulate the translational expression of their complementary target messenger RNA (mRNA) by specifically binding to them on the 3' untranslated regions (UTRs) [78]. An aberrant expression of miRNAs can lead to the appearance of various diseases, including AD, in which it has been hypothesized that the downregulation of these sequences could be related with a pathological regulation of APP and presenilins 1 and 2 genes [51,52]. Owing to the great potential of miRNAs, the development of electrochemical biosensors for their detection have increased in recent years [79].

#### 4.1.1. Nanomaterials as Electrode Modifiers

Graphene and its derivatives have been the most extensively used nanomaterials to modify the electrode in AD immunosensors. Graphene is a two-dimensional (2D) sheet of carbon atoms with sp<sup>2</sup> hybridization which has gained importance since its isolation in 2004 due to its mechanical strength and thermal and electrical conductivity [80]. Since its discovery, it has been investigated for a wide range of applications including biosensors development.

Graphene oxide (GO), a derivative of graphene, is obtained by the functionalization of graphene with oxygen groups (hydroxyl, carboxyl and epoxide) and presents good solubility although it has a reduced electron transfer capacity [81]. This functionalization enhances graphene selectivity towards anchoring biological recognition elements. In electrochemical biosensors, reduced GO (rGO), a derivative of GO, was firstly reported as electrode modifier by Zhou et al. in 2009 [82] for the sensing of DNA, showing increased electrochemical activity compared to graphite electrode. Since then, graphene and its derivatives have been incorporated into different types of biosensors, including AD biosensors. ApoE4 gene biomarker was detected taking advantage of curcumin-graphene quantum dots (QDs) as dual electrochemical and fluorescence platform for the modification of indium tin oxide (ITO) electrodes [83]. Curcumin, also known as Diferuloylmethane (C<sub>21</sub>H<sub>20</sub>O<sub>6</sub>) is an antioxidant polyphenol that has been used for clinical purposes due to its anti-inflammatory, antibacterial and anti-cancer activity among other properties. In that work, curcumin coated graphene QDs were used as electrode modifiers (Figure 2A). More precisely, a transparent ITO electrode was coated successively with graphene quantum dots (GQD) and electro-polymerized curcumin and then, the probe DNA was immobilized upon the resultant CU-GQD-ITO platform by means of malonic acid and 1-ethyl-3-(3-dimethylaminopropyl) carbodiimide (EDC)/N-hydroxysuccinimide (NHS) chemistry. As curcumin is a fluorescence and electroactive molecule, the functionalization of the electrode with this substance was confirmed by recording the corresponding oxidation current, what facilitates the characterization of the sensor constructed. Finally, ApoE4 gene was added to test biosensors performance, showing a linear decrease in the amperometric response recorded after hybridization and quenching of curcumin signals, with a LOD of 16.7 fM. The incorporation of curcumin to this sensor is of great relevance since it facilitates the anchoring of recognition elements while providing a double recognition tool due to fluorescence capacity of this molecule.

Wu et al. [84] used a graphene-mesoporous silica hybrid (GSH) nanomaterial as electrochemical platform also for the detection of ApoE4 gene. Silicon-derived nanomaterials have gained attention as potential components for energetic or catalytic applications due to their biocompatibility, facile surface modification and electronic properties among others, been widely used in biosensing for increasing sensitivity, selectivity and detection capacity [85]. In that work, GSH generated by soft template-assisted reducing process, acted as reservoir for the accumulation of methylene blue, added to the electrode as electroactive reporter. Moreover, ferrocenecarboxylic acid was conjugated to the nanomaterial as built-in control molecule and probe DNA was also immobilized by a bifunctional cross-linker 4-Maleimidobutyric acid and N-hydroxysuccinimide ester onto the electrode. The "on-off" biosensor worked as follows: first, an assistant probe DNA, only partly complementary to the long DNA

probe immobilized onto the electrode was hybridized, preventing the leakage of methylene blue. Then, the analyte (the full complemented DNA sequence) was added, competing with the assistant probe DNA for the binding to the DNA probe, destroying the double structure and facilitating the release of methylene blue and the consequent decrease in the differential pulse voltammetric (DPV) current measured. Even though this sensor does not provide a lower LOD (down to 10 fM) than that of previous works [83], the use of this “on-off” strategy seems to reduce systematic errors and to increase reproducibility.

With regard to AD related miRNAs, Congur et al. [86] used GO as electrode modifier to develop a RNA biosensor for the detection of miRNA-34a, a biomarker of AD and various types of cancers. Firstly, they let react electrochemically activated pencil graphite electrodes with EDC/NHS and then with GO for increasing surface area of the electrode and favoring immobilization of miRNA, generating single use GO sensors. This strategy provides a cost-effective and easy to use sensor device that requires the use of less chemical reagents, all important qualities for the transferability of the device. Concentration of miRNA-34a was measured by electrochemical impedance spectroscopy (EIS) on phosphate buffer saline (PBS), showing a LOD of 261.7 nM.

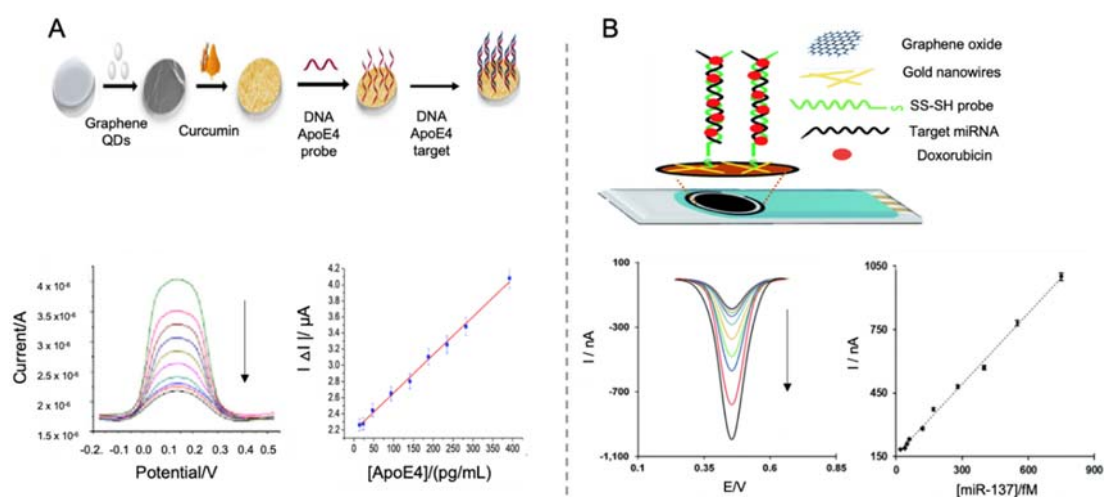


**Figure 2.** Electrochemical biosensors for the detection of DNA and RNA biomarkers of AD. (A). Schematic representation of a ITO electrode modified with graphene QDs, electropolymerized curcumin as reporter signal and DNA ApoE4 probe for the detection of ApoE4 gene using a DNA probe as recognition element (top) and differential pulse voltammetric (DPV) curves of the detected ApoE4 at different concentrations, representing an increase in the resistance with higher concentrations of ApoE4 and the corresponding calibration curve (bottom). Reprinted from [83]. Copyright (2018) with permission from Elsevier. (B). Schematic representation of miRNA biosensor based on the modification of a SPCE using GO, gold nanowires, thiolated RNA probe as recognition element and doxorubicin as reporter signal due to its intercalating capacity (top) and DPV curves of decreasing concentrations of target miRNA and the corresponding calibration curve (bottom). Reproduced from [87]—Published by The Royal Society of Chemistry.

Another example of miRNA detection is the work performed by Azimzaeh et al. [87] for the detection of miRNA-137 using a screen-printed carbon electrode (SPCE) modified with electrochemically-reduced GO and gold nanowires for enhancing the sensitivity of the biosensor and facilitating the immobilization of single stranded DNA (ssDNA) probe (Figure 2B). As electrochemical tag, doxorubicin was employed, due to its capacity to get intercalated in double stranded oligonucleotides [88] and also its electroactive properties, so that correlating directly to the concentration of hybridized biomarker. Doxorubicin concentration was recorded by DPV showing a detection limit of 1.7 fM and a good selectivity in human serum samples, which represents a notable increase compared

to similar works [86], what seems to indicate that the use of doxorubicin as reporting signal helps to increase sensitivity.

Further studies for the detection of DNA and RNA AD biomarkers by using other nanomaterials are gathered at Table 2 [89].

**Table 2.** Electrochemical biosensors for the detection of DNA and RNA AD biomarkers using nanomaterials as electrode modifiers or as labels published over the last ten years.

Nanomaterial	Role	Biomarker	LOD	Linear Range	Selectivity Tested	Real Sample Tested	Ref
CM-GQDs	Electrode modifier	ApoE4 gene	16.7 fM	1.54–30.73 pM	Presence of 100-fold of non-complementary DNA, IgG, cholesterol and glucose oxidase	Human blood plasma	[83]
MB/Fc-GSHs	Electrode modifier	ApoE4 gene	10 fM	$10^{-8}$ – $10^{-14}$ M	Non-complementary DNA and one mismatched DNA	Not tested	[84]
GO-CA-PGE	Electrode modifier	miRNA-34a	261.7 nM	0–1.45 $\mu$ M	Other miRNAs	Not tested	[86]
ERGO/AuNWs	Electrode modifier	miRNA-137	1.7 fM	5.0–750.0 fM	Non-specific oligonucleotides	Human serum with the addition of miRNA	[87]
AuNPs	Electrode modifier	ApoE4 gene	286 nM	10 $\mu$ M–250 nM	Not tested	Not tested	[89]
Fc-capped AuNPs	Label	ApoE4 gene	0.1 pM	0.1–5 pM	ApoE2/3 with a single base mismatch	DNA extracts from serum samples	[90]

AuNPs: gold nanoparticles; CM-GQDs: curcumin modified graphene quantum dots; ERGO/AuNWs: electrochemically-reduced graphene oxide (ERGO) combined with gold nanowires (AuNWs); Fc-capped AuNPs: ferrocene capped gold nanoparticles modified with streptavidine; GO-CA-PGE: graphene oxide (GO) chemical activated (CA) pencil graphite electrode (PGE); MB/Fc-GSHs: Methylene blue (MB) loaded ferrocenecarboxylic acid (Fc) conjugated graphene @ mesoporous silica hybrids (GSH).

#### 4.1.2. Nanomaterials as Labels

Some nanomaterials have intrinsic properties that facilitate their use as electrochemical labels, which is a desirable characteristic for reducing time and complexity of measurements. Among all the nanomaterials, AuNPs have been the most extensively studied, as they are easy to synthesize and bioconjugate with antibodies [91]. Owing to their high surface-to-volume ratio in particles between 1–100 nm and high surface energy, they favor the immobilization of biological recognition elements [92].

AuNPs, alone or in combination with other molecules, have been extensively used as signal reporters for AD biomarkers detection, thanks to their facility for anchoring biological elements and their electroactive and electrocatalytic properties.

Lu et al. [90] developed a sensitive DNA sensor for the detection of ApoE4 gene using streptavidin-modified ferrocene capped AuNPs (Fc-AuNPs) as labels (Figure 3). By using a gold electrode modified with biotinylated specific oligonucleotides, ApoE4 gene was specifically trapped, generating a double chain DNA helix with the sequence of nucleotides GCGC. Such specific sequence is the cleavage site of the enzyme HhaI, a restriction enzyme that was used for increasing the specificity of the biosensor. Therefore, if the immobilized oligonucleotides hybridize with ApoE4 gene, GCGC sequence was generated in the middle of the double helix and by the addition of HhaI, the biotinylated fraction of the double stranded DNA was released, preventing the binding of Fc-AuNPs. Thus, the ApoE4 sequence could be discriminated against other ApoE sequences by EIS measurement with a LOD of 0.1 pM, which, although being low value, does not improve the LODs obtained with previous strategies.



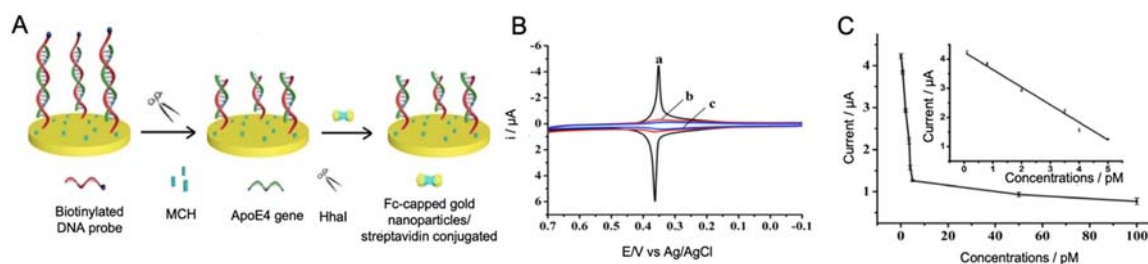


**Figure 3.** (A) Schematic representation of an electrochemical biosensor for the detection of ApoE4 gene using Fc-capped gold nanoparticles conjugated with streptavidin as labels and biotinylated DNA as capture probe. The biosensor principle is based on the specific cleavage of HhaI to double stranded DNA helix. 6-mercaptohexanol (MCH) is added as blocking agent. (B) CV responses of (a) biotinylated probe after hybridization with 50 pM ApoE4 gene, (b) same biotinylated probe after the addition of HhaI restriction enzyme and (c) unbiotinylated probe after hybridization with 50 pM ApoE4 gene; and (C) representation of the dependence between current ( $\mu\text{A}$ ) and different concentrations of ApoE4 gene, where the insert represents the linear part between 0.1 and 5 pM. Reprinted by permission from: Springer Nature, *Microchimica Acta*, [90], 2018.

#### 4.2. Peptide Biomarkers

A $\beta$  peptides and their different aggregated forms (oligomers, fibrils or plaques) are considered the main pathological hallmark of AD. From all A $\beta$  peptides, A $\beta$ (1-42) has been deeply investigated as it is more prone to aggregate thus being an important biomarker. For that reason, peptides are without no doubt the most investigated AD analytes in electrochemical biosensors. Below are described the main electrochemical biosensors for the detection of AD related peptides.

##### 4.2.1. Nanomaterials as Electrode Modifiers

- Gold nanoparticles

A $\beta$ (1-42) peptide was detected by Wu et al. [93] using an EIS immunosensor based on an anodic aluminum oxide layer with a honeycomb-like surface as template for the electrodeposition of a gold film and over it AuNPs, used for the immobilization of monoclonal antibodies, specific only for the C-terminal end of A $\beta$ (1-42) peptide, via 11-mercaptoundecanoic acid and EDC/NHS. The use of this nanomaterial may notably increase the surface area of the biosensor, so that increasing the amount of analyte captured. EIS was performed using  $\text{Fe}(\text{CN})_6^{3-/4-}$  as electroactive indicator for the determination of A $\beta$ (1-42) peptide at different concentrations in buffer solution, obtaining a LOD of 22.2 fM. Increasing concentrations of A $\beta$ (1-42) peptide revealed the appearance of aggregates examined by scanning electron microscopy (SEM) and atomic force microscopy (AFM).

Using a similar approximation Carneiro et al. [94] developed a label-free immunosensor for the detection of A $\beta$ (1-42) peptide by using in this case a gold electrode modified with a mercaptopropionic acid monolayer and electrodeposited AuNPs. By square-wave voltammetry (SWV) and EIS using  $\text{Fe}(\text{CN})_6^{3-/4-}$  as electroactive indicator, the biosensor showed a LOD of 1.15 pM, although sensor selectivity and performance in real samples were not tested. LOD reached by this sensor is lower than the one exposed by Wu et al. [93], what may suggest that the use of a mercaptopropionic acid monolayer is not as effective as a gold film for the immobilization of AuNPs, although the selected electrode should also have an influence in the overall performance.

Amor-Gutiérrez et al. [95] developed an immunosensor for the detection of unfolded p53 in blood samples (Figure 4A). Using a SPCEs modified with AuNPs for the immobilization of monoclonal antibodies against p53, they developed a competitive biosensor able to detect unfolded p53 by linear sweep voltammetry (LSV), with a LOD of 0.05 nM. The competitive assay consisted in the incorporation on the biosensor of biotinylated and non-biotinylated p53 for its specific detection by the immobilized antibodies. After that, streptavidin labelled with alkaline phosphatase was first added to

the electrode for the binding to only biotinylated p53. By adding 3-indoxyl phosphate and, afterwards, silver nitrate solution, alkaline phosphatase catalyzed the enzymatic reduction of silver and generated the electrochemical signal by the anodic stripping of the produced  $\text{Ag}^0$ . One of the main strengths of this work is the evaluation of the performance of the biosensor generated in real blood samples of patients with MCI and AD, showing no significant differences with ELISA results.

AuNPs or derivatives have also been widely used in sandwich immunoassays, that allow a double recognition of the biomarker detected. For AD biomarkers identification, several sandwich-type immunosensors using AuNPs are reported in Table 3 [96,97]. It is worthy to highlight that selectivity studies are missing in some of these works, although it is countered by the analysis of real samples.

But sandwich-type sensors not necessarily use only antibodies, since aptamer-based sandwich biosensors are also employed. Zhou et al. [98] built an aptamer-based biosensor for the detection of  $\text{A}\beta$  using AuNPs and Cu-MOFs (AuNPs/Cu-MOFs) nanocomposites as labels and gold nanoflowers (AuNFs) as electrode modifiers. AuNFs acted as immobilization platform for the primary aptamer while increasing the sensitivity of a glassy carbon electrode (GCE), reaching a LOD of 0.45 nM. Even though the flower-like structure of AuNFs should seem an advantage as it increases surface area, it does not represent an improvement in the LOD compared to previous works [93].

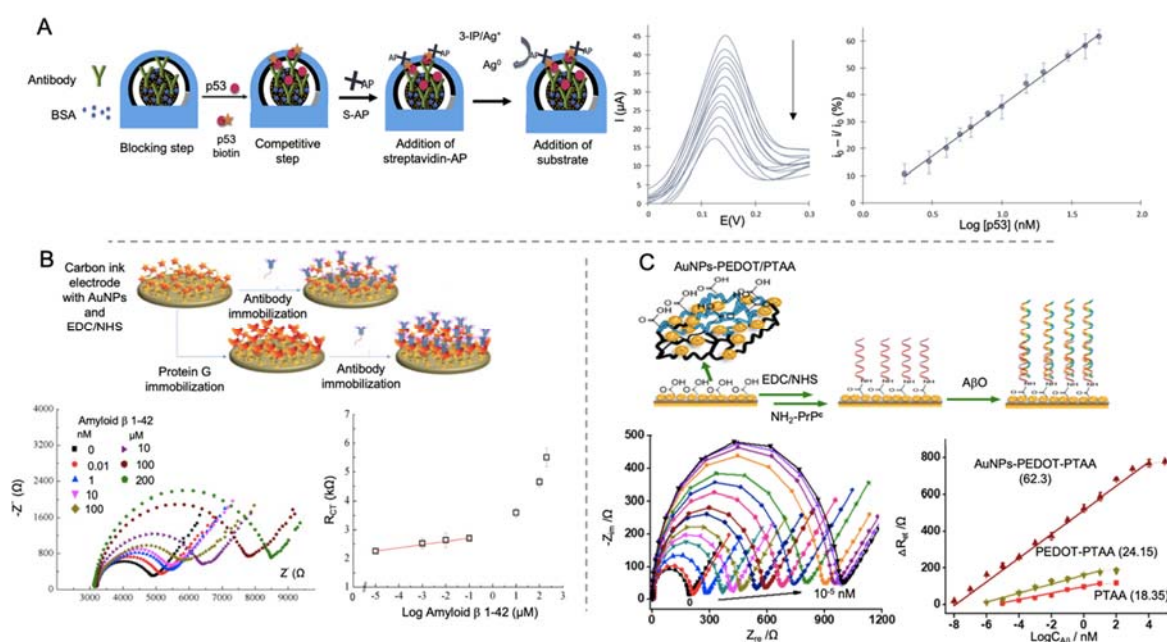


**Figure 4.** Electrochemical biosensors for the detection of AD peptides using AuNPs as electrode modifier. (A) Schematic representation of a competitive immunosensor for the detection of p53 peptide using streptavidin labelled alkaline phosphatase (S-AP) as electrochemical signal (left), accompanied by LSV voltammograms of different p53 concentrations and the corresponding calibration curve (right). Reprinted from [95]. Copyright (2020) with permission from Elsevier. (B) Schematic diagram of an immunosensor for the detection of  $\text{A}\beta$  peptide using different strategies; anchoring antibodies directly to the electrode by EDC/NHS or using protein G for the immobilization (top) and impedance curve of different concentrations of  $\text{A}\beta$  detected using antibodies immobilized by protein G and the associated calibration curve representing electron transfer resistance ( $R_{CT}$ ) vs log  $\text{A}\beta$  concentration (bottom). Reprinted from [99]. Copyright (2015) with permission from Elsevier. (C) Representation of a biosensor construction for the detection of  $\text{A}\beta_0$  using AuNPs and poly(thiophene-3-acetic acid) (PTAA) for the immobilization of PrPc receptor (top) and the Nyquist plot of different concentration of  $\text{A}\beta_0$  and the corresponding calibration curves (bottom). Adapted with permission from [100]. Copyright (2019) American Chemical Society.

**Table 3.** Electrochemical biosensors for the detection of AD peptide biomarkers using nanomaterials as electrode modifiers or as labels published over the last ten years.

Nanomaterial	Role	Biomarker	LOD	Linear Range	Selectivity Tested	Real Sample Tested	Ref
AuNPs	Electrode modifier	A $\beta$	22 fM	0.22 pM–2.22 nM	Not tested	Serum samples	[93]
AuNPs	Electrode modifier	A $\beta$	1.15 pM	2.22–221.6 pM	Not tested	Not tested	[94]
AuNPs	Electrode modifier	p53	0.05 nM	2–50 nM	Not tested	Real plasma samples of MCI and AD patients	[95]
AuNPs	Electrode modifier	A $\beta$	22.2 pM	111 pM–111 nM	Not tested	Not tested	[96]
AuNPs	Electrode modifier	A $\beta$	100 fM	100 fM–25 pM.	HSA, IgG and other AD proteins	Serum and plasma samples	[97]
AuNFs AuNPs/Cu-MOFs	Electrode modifier Label	A $\beta$ o	0.45 nM	1 nM–2 $\mu$ M	A $\beta$ 40, 42 monomers and A $\beta$ (40–42)f	Not tested	[98]
AuNPs	Electrode modifier	A $\beta$	0.57 nM	10 pM–100 nM	BSA	Not tested	[99]
AuNPs-PEDOT	Electrode modifier	A $\beta$ o	10 <sup>-2</sup> fM	10 <sup>-8</sup> –10 <sup>4</sup> nM	A $\beta$ f and monomers	AD mice tissue	[100]
rGO	Electrode modifier	A $\beta$	2.398 pM	11 pM–55 nM	A $\beta$ 40 and ApoE4	Mice and human plasma	[101]
CNT-CuO	Electrode modifier	A $\beta$ o	88.6 fM	22 pM–14.6 nM	Not tested	Serum samples	[102]
PS-b-P4VP-CR	Electrode modifier	A $\beta$	2.21 pM	2.21 pM–221 nM.	A $\beta$ monomers, peptides and complex media with other proteins	Human blood serum	[103]
Au/NiFe <sub>2</sub> O <sub>4</sub> @GO-Ch	Electrode modifier	A $\beta$	0.66 pM	0.22 pM–222 pM	A $\beta$ 1–40, prostate specific antigens, cortisol and thrombin.	CSF	[104]
A $\beta$ (1–16)-heme-AuNPs	Label	A $\beta$	10 pM	0.02–1.50 nM	Artificial CSF	Not tested	[105]
AuNPs	Label	A $\beta$	22.15 fM	0.02–22.2 pM	Brain-derived neurotrophic factor and prostate-specific antigen	Mouse plasma sample	[106]
MB Au@Pt/Au	Electrode modifier Label	p53	66 nM	50–1000 nM.	Not tested	Human plasma samples	[107]

Table 3. Cont.

Nanomaterial	Role	Biomarker	LOD	Linear Range	Selectivity Tested	Real Sample Tested	Ref
AuNPs	Label	A $\beta$ o	100 pM	0.5–30 nM	A $\beta$ 40–42 monomers, A $\beta$ (40–42)o, A $\beta$ (40–42)f	CSF	[108]
AuNPs	Label	A $\beta$	28 pM	0.1–50 nM	Not tested	CSF and rat brain tissues	[109]
Cu <sup>2+</sup> -PEI/AuNPs-hemin	Label	A $\beta$ aggregation	0.2 pM	1 pM–50 nM	Endogenous proteins, A $\beta$ oligomers, metal ions, amino acids and other biological species	CSF of normal and AD mice	[110]
AuNPs	Label	A $\beta$ o	45 pM	0.1 nM–0.2 $\mu$ M	A $\beta$ f and monomers, IgG and thrombin	Blood serum	[111]
AgNPs	Label	A $\beta$ o	8 pM	20 pM–100 nM.	A $\beta$ f and monomers, IgG, BSA, thrombin and $\alpha$ -synudein	Serum samples	[112]
AuNPs SiO <sub>2</sub> @AgNPs	Electrode modifier Label	A $\beta$ o	0.27 pM	1.1 pM–2.2 nM	A $\beta$ 40–42 monomers, A $\beta$ (40–42)o, A $\beta$ (40–42)f	Human serum samples	[113]
ZIF-8/Fer	Label	A $\beta$ o	10 <sup>-5</sup> $\mu$ M	10 <sup>-5</sup> –10 <sup>2</sup> $\mu$ M	A $\beta$ f and monomers and artificial CSF	Not tested	[114]

A $\beta$ (1–16)-heme-AuNPs: gold nanoparticles conjugated with A $\beta$ (1–16)-heme; Au@Fc-Zn-MOF: gold nanoparticles combined with ferrocene confined in metal-organic framework (Fc-Zn-MOF); AuNFs: gold nanoflowers; Au/NiFe<sub>2</sub>O<sub>4</sub>@GO-Ch: gold nanoparticle/nickel ferrite decorated graphene oxide-chitosan nanocomposite; AuNPs: gold nanoparticles; AuNPs/Cu-MOFs: gold nanoparticles combined with copper metal-organic frameworks; AuNPs-PEDOT: AuNPs embedded in a layer of poly(3,4-ethylene dioxythiophene); Au@Pt/Au: core@shell gold platinum nanoparticles; CNT-CuO: carbon nanotubes combined with copper oxide; CNT-PIL: carbon nanotubes combined with polymer ion liquid; Cu<sup>2+</sup>-PEI/AuNPs-hemin: Polyethyleneimine (PEI) covered AuNPs were used as labels by functionalization of hemin and Cu<sup>2+</sup>; HSA: human serum albumin; MB: magnetic beads; NLC: nanostructure lipid carrier; PS-b-P4VP-CR: nanostructured isoporous poly(styrene-b-4-vinylpyridine) membrane conjugated with congo red; rGO: reduced graphene oxide; SiO<sub>2</sub>@AgNPs: silver nanoparticles and silica nanoparticles; ZIF-8/Fer: Zn zeolite imidazole framework with ferrocene.

Affinity proteins, considered as noncatalytic and nonimmune generated proteins, are also used as recognition element, as they are able to interact with some molecules in a similar way that antibodies or enzymes do [115,116]. Lien and co-workers [99] developed an impedimetric immunosensor for the detection of A $\beta$  peptides using carbon printed electrodes modified with protein G. For evaluating the effect of the electrode modification, they proposed a three-electrode immunosensor, each one with a different surface chemical modification (Figure 4B). First of them was the bare electrode functionalized by the monoclonal antibody against A $\beta$  peptide by means of 1-pyrenebutanoic acid succinimidyl ester. For the second and third ones, they modified the electrode successively with AuNPs, generated by electrodeposition and then with a self-assemble monolayer (SAM) of 16-mercaptohexadecanoic acid (MHDA) for the further attachment of monoclonal antibodies. In the third electrode, protein G was immobilized on the surface before the addition of the antibody in order to orientate the latter. This modification helped to lower the LOD to 0.57 nM which is a notable reduction compared to bare electrode (2.04  $\mu$ M) and protein G free electrode (2.65 nM) but not enough for reaching the lowest values seen in A $\beta$  peptides detection.

Qin et al. [100] developed an impedance biosensor for the detection of A $\beta$  by using cellular prion protein (PrPc) peptide as bioreceptor immobilized on to a gold electrode (Figure 4C). PrPc is a cell-surface glycoprotein that its conversion in an altered isoform is related with neurodegenerative infectious prion disease and it has been also postulated as receptor for A $\beta$  [117]. In this biosensor, AuNPs embedded in a layer of poly (3,4-ethylene dioxythiophene) (AuNPs-PEDOT) and poly(thiophene-3-acetic acid) were successively electrodeposited onto for further anchoring of PrPc by EDC/NHS chemistry. A $\beta$  was detected by EIS measurement in A $\beta$  solutions and animal real samples, showing a LOD of 10<sup>-2</sup> fM. This value is the lowest collected in this review for A $\beta$  detection. This could indicate that the use of specific proteins, like PrPc could be an advantageous strategy for improving the detection of biomolecules with a high sensitivity and selectivity.

- Carbon nanotubes

CNTs are nanowires constituted by sp<sup>2</sup> carbon atoms arranged in hexagons that were first observed in 1952 by Radushkevich and Lukyanovich [118]. Physical and chemical conditions during chemical synthesis lead to the formation of different types of CNTs listed by the number of walls they have, going from one (single-walled carbon nanotubes (SWCNTs)) to multiple walls (multi-walled carbon nanotubes (MWCNTs)) [119]. CNTs have been acknowledge for their electrochemical properties, including an enhanced electron transfer capacity, and also for their outstanding physical properties, making them ideal materials for biosensing [120]. In this context, Moreira et al. developed a biosensor for the detection of A $\beta$  using CNTs and molecular imprinted polymers (MIPs) [102].

In general, biomarkers may be detected by the use of biological recognition elements as antibodies, aptamers or specific proteins. Alternatively, these recognition elements could be created artificially for mimicking these molecules with a high selectivity and versatility. MIPs, defined as synthetic polymers generated by polymerization in the presence of a template, have been thoroughly used in biosensing due to its engineerability [121,122].

In AD biomarkers detection, MIPs were first used for the detection of A $\beta$  by Moreira et al. [123] using  $\alpha$ -cyclodextrin as polymeric matrix, achieving a LOD of 44 pM. In a subsequent study [102], the same group improved the performance of the biosensor by using aniline as polymeric matrix and CNTs modified with copper oxide nanoparticles as conductive substrate for improving electrocatalytic activity and electron transferability (Figure 5). A $\beta$  detection was performed by cyclic voltammetry (CV) and SWV in artificial serum samples with a notable improvement in the performance compared to its previous work, reaching a LOD of 88.6 fM.



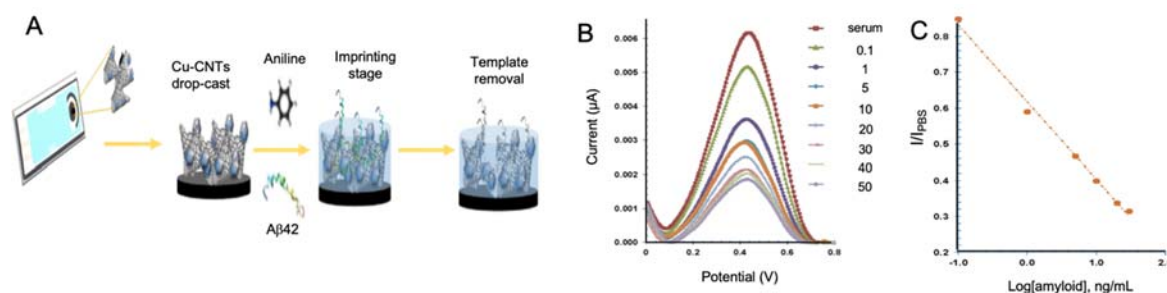


**Figure 5.** Electrochemical biosensors for the detection of AD peptides using CNTs as electrode modifier. (A) Representation of the generation of a MIPs for the detection of A $\beta$  peptide using electropolymerized aniline and Cu-CNTs as electrode modifier, (B) SWV measurements of the modified electrode at different A $\beta$  concentrations in human serum samples and (C) the corresponding calibration curve. Reprinted from [102]. Copyright (2018) with permission from Elsevier.

- Nanomembranes

Nanomembranes are structures of 1–100 nm thickness and a large of at least two magnitude orders more than their thickness. They have been implemented as scaffolds for nanoparticle synthesis or used in electrochemical devices as they endure repeated elastic deformation [124]. Nanomembranes are commonly made from organic polymers, like cellulose nitrate, polyacrylonitrile or polyvinyl as they offer a high selectivity and high fluxes [125]. They are often used forming nanocomposites, introducing two or more phases that contribute to enhance the functionality of the final structure, achieved by lamination, patterning, surface sculpting or introduction of nanoparticles [126].

Nanomembranes have been used for AD biosensing by Wustoni et al. [103] who implemented for the first time the combination of pristine isoporous membranes from the block copolymer poly(styrene-*b*-4-vinylpyridine) and organic electrochemical transistors (OECT) for the building of an immunosensor, in this case for the detection of A $\beta$  peptide aggregates. OECTs are a type of transistor composed of a channel of an ion-permeable organic material through which an electrolyte solution is injected by the application of a voltage to the gate electrode [127]. By the immobilization of a biological recognition element inside the channel or the electrode gate, it is achieved the detection of specific proteins as its binding inside the channel partially blocks the ionic current, reducing the electrochemical signal recorded. However, the main drawback of this technology is that the immobilization of biological recognition elements may change the channel surface or even lead to electronic material degradation. To overcome this issue, Wustoni and coworkers placed, between the channel and the electrolyte solution, a 50 nm pore size pristine nanomembrane functionalized with Congo red as it has a strong affinity to a cross- $\beta$  structure of A $\beta$  aggregates, conferring the biosensor with a high specificity. As A $\beta$  aggregates are bigger than the pore size of the membrane they block the ion transport in a concentration dependent manner, thus constituting a novel design of electrochemical immunosensors. The nanomembrane-based sensor detected A $\beta$  aggregates with a LOD of 2.21 pM. Even though this value is not sufficiently low compared to other works, the implementation of nanomembranes in biosensing opens the way to its use in multianalyte detection.

- Nickel ferrite nanoparticles (NiFe<sub>2</sub>O<sub>4</sub>)

Nickel ferrite nanoparticles (NiFe<sub>2</sub>O<sub>4</sub> NPs) are magnetic materials with a high resistance, permeability and saturation magnetization that have been highly implemented as gas sensors [128].

In the work performed by Devi et al. [104], NiFe<sub>2</sub>O<sub>4</sub> NPs were used to develop a label-free immunosensor for the detection of A $\beta$  peptide by using a GCE in combination with GO, chitosan and AuNPs (Au/NiFe<sub>2</sub>O<sub>4</sub> NPs) (Figure 6). CV was used to evaluate the effect of the Au/NiFe<sub>2</sub>O<sub>4</sub> NPs incorporation, showing an increased surface area and conductivity, while performance of the biosensor was evaluated in real CSF samples by DPV and EIS measurements, revealing a LOD of 0.66 pM.

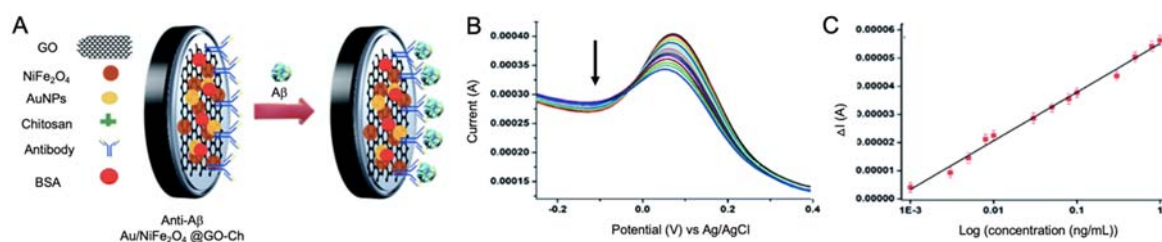


**Figure 6.** (A) Schematic representation of an immunosensor for the detection of A $\beta$  peptide using GO, chitosan, AuNPs and NiFe<sub>2</sub>O<sub>4</sub> NPs as electrode modifiers for the immobilization of antibodies and improving sensitivity; (B) DPV response of the biosensor at different A $\beta$  peptide concentrations, revealing the decrease in the signal recorded while concentration is increased and (C) calibration curve showing linearity. Reproduced from [104]—Published by The Royal Society of Chemistry.

#### 4.2.2. Nanomaterials as Labels

- Gold nanoparticles

AuNPs have also been used as labels for AD peptide biomarkers sensing [105–111]. Yoo et al. [106] designed a sandwich-type immunosensor for the detection of A $\beta$  peptide by using an antibody-modified interdigitated microelectrode and AuNPs conjugated with antibodies as labels for signal amplification (Figure 7A). By measuring impedance changes in the presence of A $\beta$  peptides, they obtained a LOD of 22.15 fM, what indicates that the use of AuNPs as labels for A $\beta$  peptide is as valid as the use of AuNPs as electrode modifiers [94].

AuNP tags in combination with the use of magnetic bead platforms have also been employed for AD biomarkers detection. Magnetic micro- and nano-particles have been notably used for biomedical purposes, as drug delivery or hyperthermia, due to their unique properties, which include biocompatibility and superparamagnetic behavior of small magnetic nanoparticles [129,130]. In biosensing field, magnetic particles have become interesting tools especially as platforms for the immobilization of biological recognition elements, as their magnetic behavior allows the analyte pre-concentration and separation from complex samples, minimizing matrix effects. Taking advantage of magnetic bead platforms, Iglesias-Mayor et al. [107] proposed an immunosensor for the detection of unfolded p53 peptide using bifunctional core@shell Au@Pt/Au NPs as labels (Figure 7B). Au@Pt/Au NPs were synthesized by Pt deposition on AuNPs surface and the subsequent galvanic replacement reaction for the substitution of some of the Pt atoms by Au. These Au protuberances were used as anchoring element for the immobilization of antibodies. The electrocatalytic activity of Au@Pt/Au NPs toward the water oxidation reaction (WOR) allowed their sensitive chronoamperometric detection at neutral pH. This represented a high advance beyond the state of the art, since the measurements are performed in the same medium of the immunoassay, without the need of additional reagents. The immunosensor presented a LOD of 66 nM and was able to detect unfolded p53 in cognitively healthy subjects.

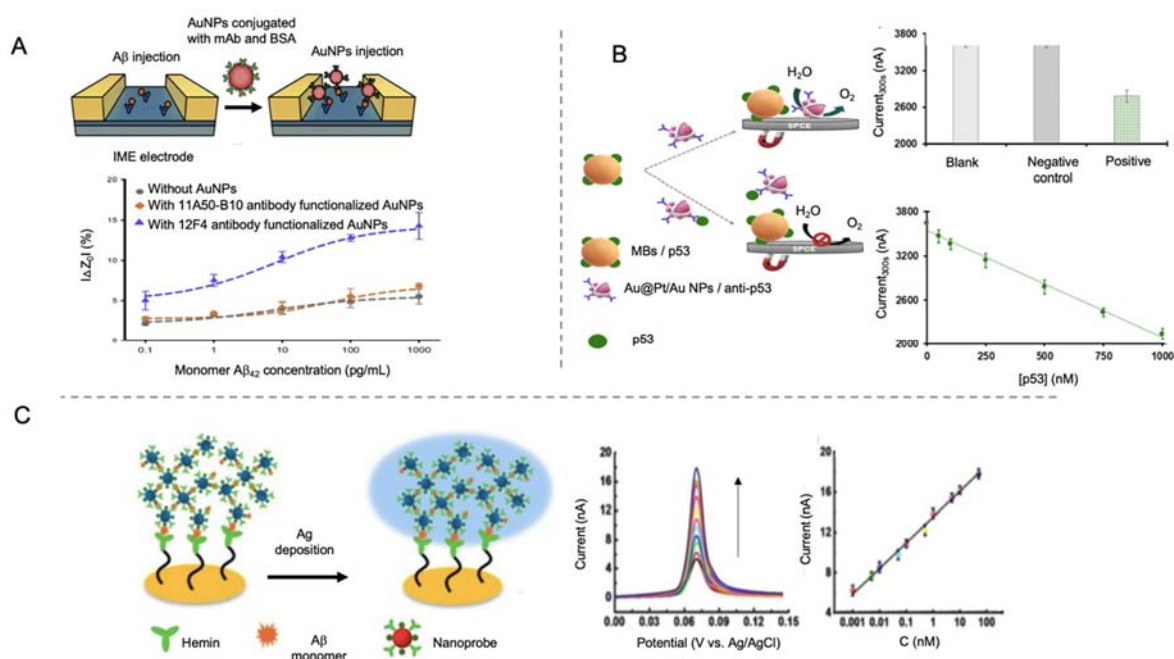


**Figure 7.** Electrochemical biosensors for the detection of AD peptides using AuNPs as labels. (A) Schematic representation of interdigitated microelectrode (IME) for the impedance detection of Aβ using AuNPs as labels (top) and the impedance curve with and without AuNPs and with different antibodies (bottom). Reprinted from [106]. Copyright (2020) with permission of Elsevier. (B) Schematic representation of a competitive immunosensor for the detection of unfolded p53 using core@shell Au@Pt/AuNPs for the catalysis of WOR and magnetic beads as immobilization platform. At the right, the analytical signal recorded for solutions without protein (blank), containing human IgG (negative control) and containing p53 peptide (positive); and the calibration curve for p53 concentrations between 50 nM to 1000 nM (bottom). Adapted with permission from [107]. Copyright (2020) American Chemical Society. (C) Schematic representation of a biosensor for the detection of Aβ monomer using hemin as bioreceptor and AuNPs and Ag deposition as electrochemical signal. At the right side the LSV curves of the biosensor performance at different Aβ monomer concentrations and the corresponding calibration curve. Republished with permission of Royal Society of Chemistry, from [110]; permission conveyed through Copyright Clearance Center, Inc.

Aptamer-antibody sandwich sensors have also been investigated in order to overcome the lack of sensitivity and transferability to commercial products of aptamer-based biosensors alone, exhibiting an improved sensitivity and specificity compared to the latter [131]. This is the case of Zhou et al. [108] that used carboxyl graphene as electrode modifier for the immobilization of an antibody against Aβ oligomers using EDC/NHS chemistry and AuNPs functionalized with thionine as labels. The reduction process of thionine was electrochemically monitored for amplifying the signal recorded by DPV, providing a LOD of 100 pM. The use of thionine as electrochemical target seems to be less effective than AuNPs alone, as it was the case of Yoo et al. [106]. In this case, the difference between the analytical methods followed (impedance changes and DPV) may also be a determining factor that should be taken into consideration.

Moreover, affinity proteins were evaluated as recognition element in AD peptide detection. This is the case of gelsolin, a secretory protein present intracellularly and in CSF or plasma, that interacts with Aβ monomers extracellularly [132]. Yu et al. [109] developed a sandwich type biosensor using gelsolin as recognition element and AuNPs functionalized with gelsolin and horseradish peroxidase (HRP) as labels. The sensing principle was based on the recognition of Aβ(1-40) and Aβ(1-42) peptides by gelsolin that was both bonded to the electrode and to the label. The HRP incorporated to the label catalyzed the oxidation of 3,3',5,5'-tetramethylbenzidine in the presence of H<sub>2</sub>O<sub>2</sub>, generating



a electrochemical signal measured by DPV. The use of gelsolin instead of other recognition element displayed satisfactory sensitivity in normal and AD rat brains even though the LOD was lower than previous revised studies (28 pM).

In a different approach, Ding et al. [110] used hemin as biological recognition element, taking advantage of its affinity to A $\beta$  peptides. In this work, a gold microelectrode was used as template for the immobilization of hemin through cysteamine and EDC/NHS (Figure 7C). Polyethyleneimine (PEI) covered AuNPs were used as labels by functionalization of hemin and Cu<sup>2+</sup> (Cu<sup>2+</sup>-PEI/AuNPs-hemin). The presence of A $\beta$  peptides produced an aggregation network of Cu<sup>2+</sup>-PEI/AuNPs-hemin nanoprobe through specific Cu<sup>2+</sup>-A $\beta$ -hemin coordination. Such aggregates were deposited on the microelectrode by joining their copper ions to the hemin groups of the electrode, and then generating active sites for the deposition of silver, which was finally detected by the well-known anodic stripping analysis. The main objective of depositing silver instead of using AuNPs directly was to amplify the signal, a purpose that, considering that the LOD obtained in this work was of 0.2 pM, was not completely reached compared to other works.

In a different approach, Xia et al. [111] developed a biosensor for the detection of A $\beta$  based on the use of PrPc peptide as recognition element and AuNPs as labels. In this case, the affinity of AuNPs to peptides was explored, as they tend to form aggregates with free peptides, increasing the EIS signal detected. Once A $\beta$  peptide was anchored to PrPc, AuNPs were added, so that they formed aggregates with free peptides anchored to the gold electrode through MCH. Performance of the biosensor was first evaluated using human chronic gonadotropin as model analyte and then implemented for blood serum to test sensitivity and selectivity against AD biomarkers, showing an extreme selectivity to A $\beta$  even in the presence of A $\beta$ f and A $\beta$  monomers and a LOD of 45 pM. If we compare this sensor with the one developed by Qin et al. [100], the LOD obtained is higher even though in both cases PrPc is used as recognition element. This shows that the detection strategy chosen, and the role of the nanomaterials are a fundamental part of the device generated.

- Silver nanoparticles

In a minor extent, AgNPs have also been used as tags in electrochemical biosensing [133]. AgNPs have marked properties, including catalytical activity and large surface area, like AuNPs have, but, in comparison, they have easier electrochemical oxidation capacity and higher extinction coefficient. However, they are instable and difficult to be functionalized, thus they have been rarely used for biosensing.

In AD, Xia et al. [112] proposed a biosensor for the detection of A $\beta$  using the same principle than in their previous work with AuNPs [111] but in this case employing AgNPs modified with adamantine (for colorimetric testing) as labels. The AgNPs detection through the solid-state Ag/AgCl reaction allowed to achieve a LOD of 8 pM, lower than the reported for AuNPs.

You et al. [113] developed a sandwich-type aptamer-based biosensor for the detection of A $\beta$  using a nanocomposite of AgNPs and silica nanoparticles (SiO<sub>2</sub>@AgNPs) as label. Detection of A $\beta$  was performed by using MIPs, generated over a GCE functionalized with GO and AuNPs for improving electrical conductivity and surface-area rate, by using a polymer precursor solution composed of methacrylic acid, 1,3-diallylurea, divinylbenzene and N, N'- azo-bis-(2,4-dimethyl)valeronitrile. The voltammetric detection of AgNPs, amplified by the nanocomposite, allowed the determination of the biomarker in human samples with acceptable relative standard deviation (RSD) (2.5–9.8%) and a LOD of 0.27 pM.

- Metal-organic frameworks (MOFs)

MOFs are three-dimensional (3D) porous coordination polymers formed by the bridging of inorganic components with organic ligands [134], and have deeply been used in gas storage, chemical sensing, catalysis or drug delivery among other applications [135]. Even though the vast majority of MOF investigations have been focused on bulk systems, more recently, MOF nanoparticles have

started to be synthesized as they have an improved bioavailability compared to bulk materials [136]. In electrochemical sensing, MOFs have been postulated as labels, as some of them exhibit a good electrochemical activity and high number of surface-active sites with enhanced enzyme-like catalytic activity [137]. However, they lack from a good electronic conductivity and electrocatalytic ability, so that they have been used in combination with other nanomaterials forming nanocomposites [138] or as electrochemical signal carriers.

In this line, Qin et al. [114] developed a biosensor for A $\beta$  detection using Zn zeolite imidazole framework (ZIF-8) with ferrocene encapsulated as electrochemical signal (Figure 8). This biosensor was based on the contacting of ferrocene—ZIF-8 with A $\beta$ , in a way that Zn ions of ZIF-8 tended to coordinate with A $\beta$  causing the breakup of the ZIF-8 structure and the release of ferrocene. The supernatant of the solution was measured by CV to determine A $\beta$  concentration with a LOD of  $10^{-5}$   $\mu$ M, much higher than that of the rest of the works revised for A $\beta$  detection, what agrees with the lack of electronic conductivity of MOFs.

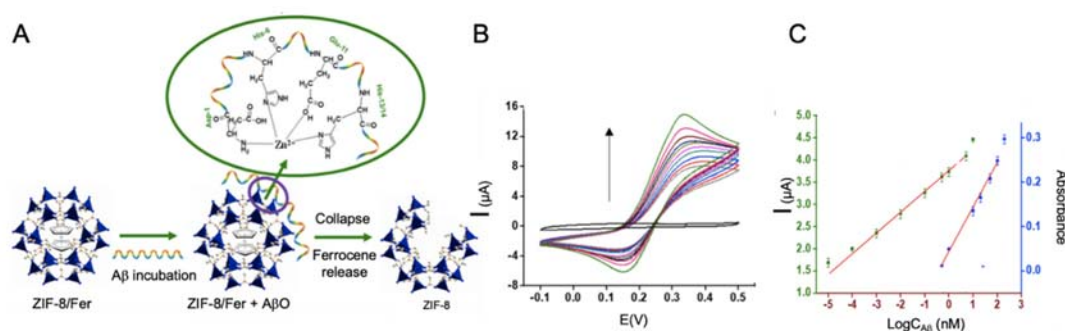


**Figure 8.** (A) Schematic representation of A $\beta$  detection biosensor using ZIF-8 with ferrocene encapsulated as reporter, as it is able to release ferrocene specifically when A $\beta$  is present due to its tendency to coordinate with Zn ions from ZIF-8. (B) CV curve of different concentrations of A $\beta$  peptide and (C) the corresponding calibration curve. The biosensor is based on the aggregation capacity of A $\beta$  peptide with Zn ions and the consequent destruction of ZIF-8 structure and the release of ferrocene. Adapted with permission from [114]. Copyright (2019) American Chemical Society.

#### 4.3. Protein Biomarkers

AD protein biomarkers are a spare target of investigation in early detection of this devastating disease. It is remarkable the earmarking of ApoE4 and tau protein in these sensors, without forgetting A $\beta$  detection in its protein conformation. Minority biomarkers, as BACE-1 and  $\alpha$ -1 antitrypsin have also been subject of study.

##### 4.3.1. Nanomaterials as Electrode Modifiers

- Gold nanoparticles

Liu et al. [139] proposed a sandwich-type electrochemical immunosensor for the detection of ApoE4, using an ITO electrode. For the modification of the ITO electrode they used a fractal gold nanostructure generated by electrodeposition, which due to its ramified conformation, it has a high surface-to-volume rate allowing the binding of a greater number of monoclonal antibodies against ApoE4. As label, in this case they used the enzyme HRP that catalyzes the oxidation of hydroquinone into quinone in the presence of H $_2$ O $_2$ . The reductive current generated was recorded by amperometry showing a detection limit of 8.78 pM.

In a further work, the same group [140] developed also a sandwich-type biosensor for the detection of ApoE4 but in this occasion, using gold nanobipyramids coated with Pt nanoparticles deposited on a GCE/Au electrode for increasing conductivity and electroactive area (Figure 9A). After that, primary antibodies were self-assembled onto the transducer, obtaining a LOD of 0.45 pM, lower than

the obtained in their previous work, what clarifies that the structure of the selected nanomaterial is important for the immobilization of biological recognition elements. Polydopamine nanotubes doped with AuPd were used as labels.

Negahdary et al. [141] explored an aptamer-based biosensor based on the electrodeposition of fern leaves-like gold nanostructures onto a gold electrode in the presence of polyethylene glycol 6000. Fern leaves-like gold nanostructures provided the electrode with a high surface area for the concentration and immobilization of the RNA aptamer, meanwhile polyethylene glycol 6000 was used for controlling size and shape of the nanomaterial. Detection of A $\beta$  was performed by DPV using ferro/ferricyanide redox probe showing a LOD of 88.6 fM. In a subsequent work [142], the same group developed a biosensor also for the detection of A $\beta$  using microporous gold nanostructures and A $\beta$  peptide as bioreceptor (Figure 9B). In this case, the LOD was lowered to 44 fM, as the nanostructure allowed a good immobilization of A $\beta$  peptide and the enhancement of the label diffusion.

Taking advantage of the combination of AuNPs and MOFs, Hang et al. [143] developed a biosensor for the detection of A $\beta$  peptide using AuNPs for modifying the electrode and a flower-like zinc metal-organic framework (Zn-MOF) as label. AuNPs were incorporated both in the electrode and in the Zn-MOF to serve as anchoring platform for antibodies. The use of MOF nanomaterials as labels is revised in the corresponding section.

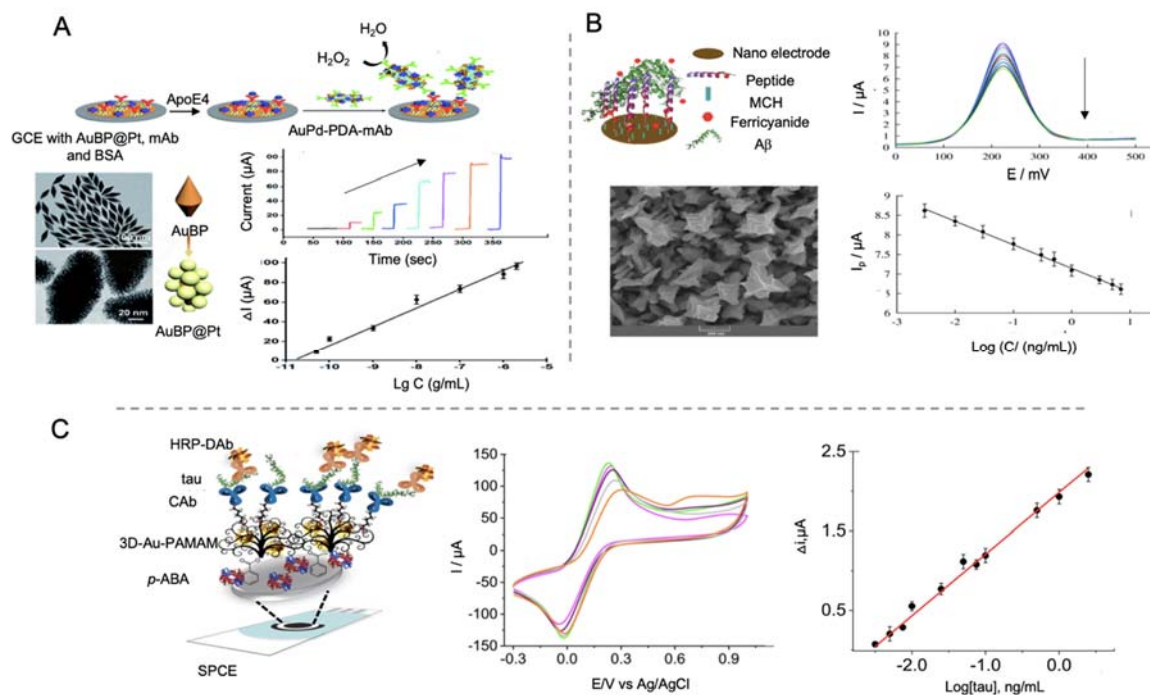


**Figure 9.** Electrochemical biosensors for the detection of AD proteins using AuNPs as electrode modifiers. (A) Schematic representation of a sandwich type immunosensor for the detection of ApoE4 using gold bipyramids coated with platinum as electrode modifier and polydopamine nanotubes doped with AuPd as labels (top), micrographs of SEM of AuBP, micrographs of TEM of AuBP@Pt, amperometric curves at different concentrations of ApoE4 protein and the corresponding calibration curve (bottom). Reproduced from [140] Published by The Royal Society of Chemistry. (B) Schematic representation of a biosensor for the detection of A $\beta$  using a gold nanostructured electrode and ferrocene as reporter (top) and field-emission scanning electron microscopy (FESEM) of the gold nanostructures, DPV curves at different concentrations of A $\beta$  protein and the corresponding calibration curve (bottom). Reprinted by permission from Springer Nature, *Microchimica Acta* [142]. Copyright (2019). (C) Schematic representation of a biosensor for the detection of tau protein using SPCEs modified

with 3D-Au-PAMAM nanocomposites and using HRP enzyme as signal generator (left). At the right side CV curves at different stages of the functionalization process: 3D-Au-PAMAM-*p*-ABA-SPCE (magenta), GA-3D-Au-PAMAM-*p*-ABA-SPCE (green), CAb-3D-Au-PAMAM-*p*-ABA-SPCE (purple), blocked CAb-3D-Au-PAMAM-*p*-ABA-SPCE (grey) and HRP-DAb-tau-CAb-3D-Au-PAMAM-*p*-ABA-SPCE (orange) and calibration curve at different tau protein concentrations. Reprinted from [144]. Copyright (2020) with permission from Elsevier.

Tau protein has also been detected by Prof. Pingarrón group's using AuNPs—poly(amidoamine) (PAMAM) dendrimer nanocomposite as electrode modifier [144]. In this work, first SPCEs were modified with AuNPs-PAMAM and electrografted *p*-aminobenzoic acid for the ulterior anchoring of antibodies through glutaraldehyde. HRP functionalized with specific antibodies was used for the electrochemical signal generation, upon de addition of hydroquinone and H<sub>2</sub>O<sub>2</sub>, recorded by amperometric detection with a LOD of 0.031 pM (Figure 9C). Biosensors performance was evaluated in human plasma samples and in brain tissue of healthy and AD diagnosed patients, what represents the main input of this work.

- Carbon nanotubes

MWCNTs have been used by Özcan et al. [145] in the development of a biosensor for the detection of A $\beta$  protein using a combination of delaminated titanium carbamide MXene (d-Ti<sub>3</sub>C<sub>2</sub>T<sub>x</sub>MXene) and MWCNTs to modify a GCE electrode (Figure 10A). MXene are 2D materials formed by early transition metal carbides and/or carbonitrides generated by etching of A elements of MAX phases (M = Ti, V, Nb; A = elements from IIA and IVA; X = N and/or C). These materials are easy to fabricate and have a good electrical conductivity, so they are widely used as electrode materials [146]. In this work, d-Ti<sub>3</sub>C<sub>2</sub>T<sub>x</sub>MXene was combined with MWCNTs as they prevented the aggregation of Mxene. MIPs of pyrrole were generated as template for the detection of A $\beta$  by DPV with a LOD of 44 aM, the lowest found in all the works revised in this review paper. This value seems to highlight, both the important role of CNTs as electrode modifiers and the utility of MXene as electrode construction material. This last point, as well as its ease of manufacturing, are of special concern with regard to commercialization of AD biomarker detection biosensors.

Tau-441 protein was detected by Li et al. [147] using MWCNTs and rGO as electrode modifiers and AuNPs for signal amplification (Figure 10B). The synergistic effect of MWCNTs and rGO provided a better electron transfer than with both nanomaterials alone and the binding of chitosan to MWCNTs by electrostatic forces allowed the anchoring through glutaraldehyde of the capturing antibodies. Tau-441 was conjugated to AuNPs through cysteamine for its capturing by the antibodies immobilized onto the electrode. When affinity recognition occurred, electron transfer of [Fe(CN)<sub>6</sub>]<sup>3-/4-</sup> was blocked, reducing the electron transfer process measured by DPV, providing a LOD of 0.46 fM.

#### 4.3.2. Nanomaterials as Labels

- Gold nanoparticles

Shui et al. [148] developed a biosensor for the detection of tau-381 protein biomarker in human serum, using an antibody-aptamer based biosensor. In this case, cysteamine-stabilized AuNPs were used as probe for the amplification of the electrochemical signal recorded by DPV. Cysteamine is a stable aminothiols used in nanoparticles synthesis since, due to its -NH<sup>3+</sup> terminus, provides nanoparticles with an external positive charge, preventing aggregation and facilitating the interaction with negatively charged oligonucleotides [149]. The use of AuNPs as signal amplifiers allowed a LOD of 0.42 pM. Human serum of AD patients was tested verifying the feasibility of the biosensor and its potential use as clinical test.

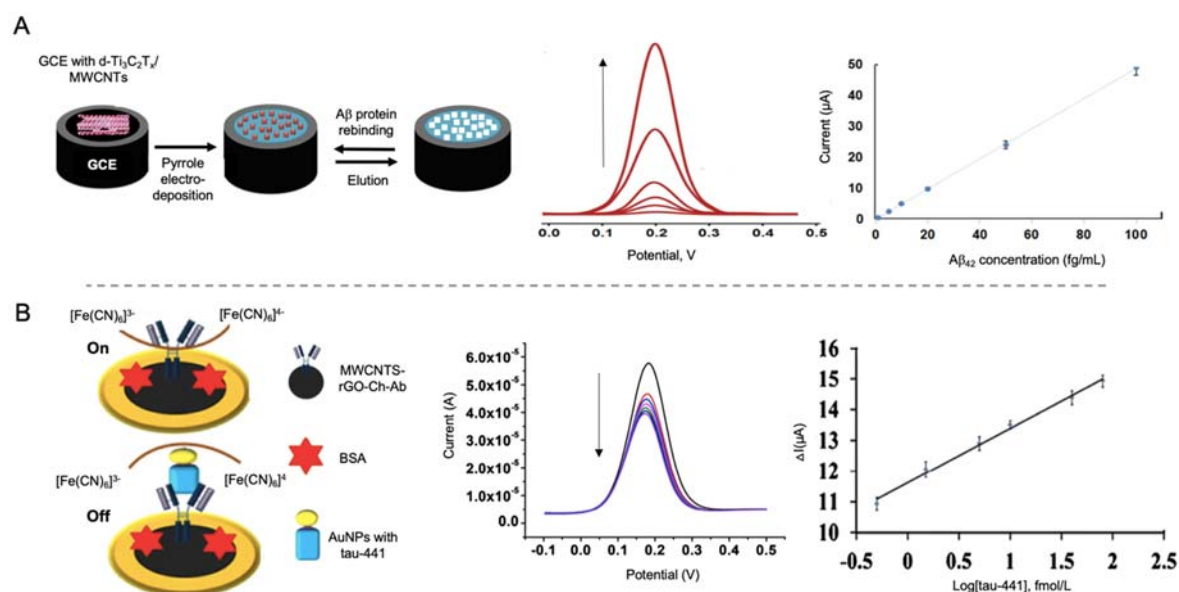


**Figure 10.** (A) Schematic representation of a MWCNTs modified electrode combined with MXene for the detection of  $\text{A}\beta$  protein using pyrrole as template for the generation of a MIPs as recognition platform (left) and the DPV curves at different concentrations of  $\text{A}\beta$  protein and the corresponding calibration curve (right). Reprinted from [145]. Copyright (2020), with permission from Elsevier. (B) Biosensor for the detection of tau-441 using MWCNTs-rGO with chitosan as electrode modifiers for the immobilization of antibodies and AuNPs conjugated with tau-441 for signal amplification. The biosensor works with an on/off system based on the blocking of electron transference of  $[\text{Fe}(\text{CN})_6]^{3-/4-}$  in the presence of tau-441. At the right side the DPV curves of growing concentrations of tau-441 and the corresponding calibration curve. Reprinted by permission from Springer Nature, *Microchimica Acta* [147]. Copyright (2020).

Using a bimetallic nanocomposite of polydopamine nanotubes doped with AuPd alloy, Liu et al. [140] developed an immunosensor for the detection of ApoE4, deeply described above. AuPd alloys were bio-conjugated with secondary antibodies and used as labels for catalyzing the reduction of  $\text{H}_2\text{O}_2$  as electrochemical signal, although they achieved a LOD of only 0.45 pM. Even though the LOD may be improved, the use of AuPd alloys as catalytical labels favors its use directly in the same media as immunoreaction takes place, as it has been highlighted in above mentioned works [107], what reduces the analysis time.

- Metal-organic frameworks

MOFs have also been used as labels for the detection of AD proteins due to their good electrochemical and catalytic activity. In the work performed by Hang et al. [143] Zn-MOF, functionalized with ferrocene and with AuNPs for the immobilization of antibodies, were used as labels for the detection of  $\text{A}\beta$  (Figure 11). The flower like structure of Zn-MOF allowed an enhanced electrochemical signal and allowed an upgraded immobilization of antibodies, which increased the performance of the biosensor, reaching a LOD of 6.6 fM.



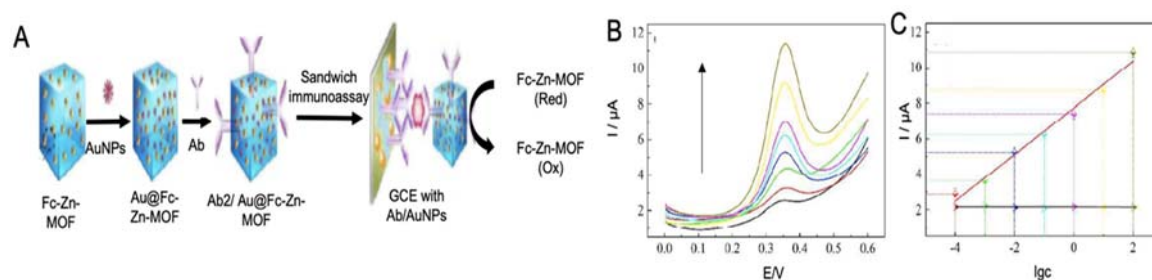


**Figure 11.** (A) Schematic representation of a sandwich type immunosensor for the detection of A $\beta$  protein using AuNPs as electrode modifiers and Zn-MOF with ferrocene encapsulated as electrochemical signal and AuNPs conjugated for the immobilization of antibodies. The analytical signal was obtained by the oxidation of ferrocene, (B) the SWV curves at different A $\beta$  protein concentrations and. (C) the corresponding calibration curve. Reproduced from [143]-Published by The Royal Society of Chemistry.

- Cerium oxide nanoparticles

Cerium oxide nanoparticles (CeNPs) have interesting catalytic and electrochemical properties that make them a valuable tool for biosensing [150]. Moreover, their high electron-transfer rate and surface coverage make them an excellent co-immobilization material [151].

Gao et al. [152] proposed an immunosensor for the detection of A $\beta$  using a AuCu<sub>x</sub>O-embedded mesoporous CeO<sub>2</sub> (AuCu<sub>x</sub>O@m-CeO<sub>2</sub>) nanocomposites as electrocatalytic label and AuNPs-functionalized with GO as electrode modifier (Figure 12). The role of m-CeO<sub>2</sub> in the nanocomposite was serving as immobilization platform for the antibodies, as it tends to form bonds with carboxyl functional groups of the latter. In a complementary way AuCu<sub>x</sub>O served as catalytic platform, as Cu<sub>x</sub>O has a tendency for the reduction of H<sub>2</sub>O<sub>2</sub> to H<sub>2</sub>O while Au decreases the activation energy required for the reaction. By measuring this process, A $\beta$  protein was successfully detected with a LOD of 7.97 fM.

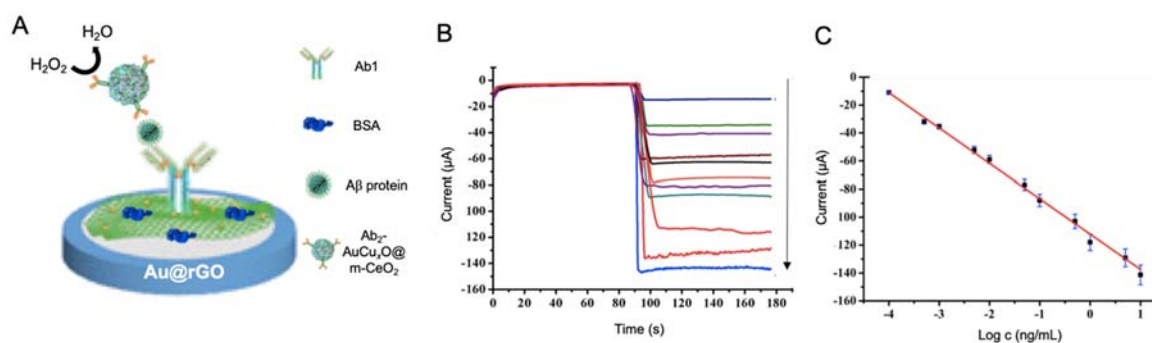


**Figure 12.** (A) Schematic representation of a biosensor for the detection of A $\beta$  protein using Au@rGO as electrode modifier and anchoring platform of antibodies (Ab1) and Ab-AuCu<sub>x</sub>O@m-CeO<sub>2</sub> as labels for the reduction of H<sub>2</sub>O<sub>2</sub>. BSA was incorporated as blocking agent. At the right, (B) current response curves of the biosensor and (C) the calibration curve at different A $\beta$  protein concentrations. Adapted with permission from [152]. Copyright (2019) American Chemical Society.

- Quantum dots

QDs are inorganic semiconductor nanocrystals extensively used in optoelectronics. Nonetheless they are also exploited as electrochemical labels thanks to the presence of electroactive metals on their composition [153].

Medina-Sánchez et al. [154] developed a sandwich immunosensor for the detection of ApoE by using QDs as labels. In this work, cadmium-selenide/zinc-sulfide (CdSe@ZnS) QDs were used as labels while tosylactivated magnetic beads were used to modify polydimethylsiloxane (PDMS)-polycarbonate

(PC) microfluidic chip integrated into screen-printed electrodes. Firstly, magnetic beads were functionalized with antibodies and anchored to the electrode by using a neodymium magnet. Then, ApoE in different concentrations was incorporated followed by the addition of biotinylated antibodies. Streptavidin modified QDs were then flushed and used for the electrochemical measurement of  $\text{Cd}^{2+}$  reduction and re-oxidation by SWV, providing the determination of ApoE in a LOD of 0.37 nM, higher than values reported in previous works. Selectivity and performance in real samples were also evaluated showing a good correlation between the results by the biosensor and standard techniques, what it is a valuable probe of the viability of the device.

- Iridium oxide nanoparticles ( $\text{IrO}_2$  NPs)

$\text{IrO}_2$  NPs have been applied in biosensing due to their excellent catalytic activity toward WOR and  $\text{H}_2\text{O}_2$  reduction, what makes them suitable labels for detection at neutral pH [155]. Moreover, they present wide surface specificity for the immobilization of biological recognition elements [156] and a high biocompatibility [157].

ApoE was electrocatalytically detected by Rivas et al. [158] by using carboxylated magnetic microbeads as anchoring platform for the immobilization of antibodies and  $\text{IrO}_2$  NPs as labels (Figure 13). ApoE was detected by following the catalytic effect of  $\text{IrO}_2$  NPs toward the WOR in chronoamperometric mode, with a LOD of 1.99 nM, with reproducible results in human plasma samples. As it happens with the work developed by Liu et al. [140], the use of this kind of labels does not allow reaching low LODs, but the electrocatalytic properties of the nanomaterials help to simplify the measurement procedure.

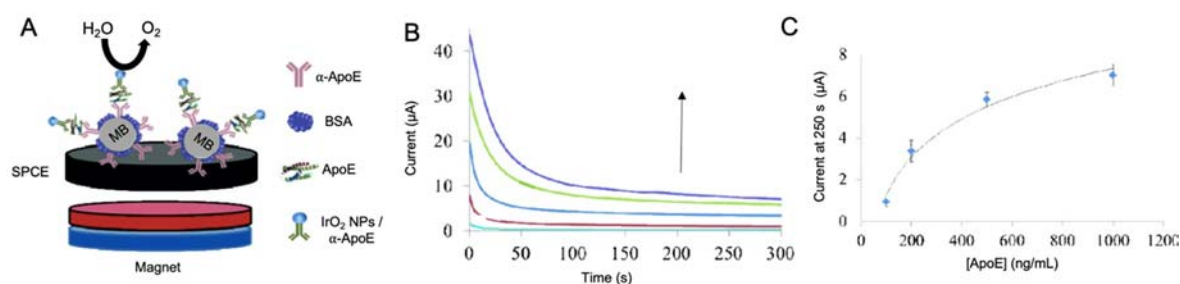


**Figure 13.** (A) Schematic representation of a sandwich type immunosensor for the detection of ApoE4 based on the use of magnetic beads platforms and  $\text{IrO}_2$  NP as labels for the catalysis of WOR. The use of MB allows the separation and purification of the process by the use of an external magnetic field. At the right, (B) chronoamperograms at different ApoE4 concentrations and (C) its corresponding calibration curve. Adapted with permission from [158].

Further examples of the use of other nanomaterials as labels for AD protein sensing are revised in Table 4 [45,46].

**Table 4.** Electrochemical biosensors for the detection of AD protein biomarkers using nanomaterials as electrode modifiers or as labels published over the last ten years.

Nanomaterial	Role	Biomarker	LOD	Linear Range	Selectivity Tested	Real Sample Tested	Ref
FracAu	Electrode modifier	ApoE4	8.78 pM	23.9 pM–293 nM	BSA, human ApoE2 and ApoE3	Not tested	[139]
AuBP@Pt AuPd-PDA	Electrode modifier Label	ApoE4	0.45 pM	1.46 pM–58.6 nM	BSA, human ApoE2 and ApoE3	Not tested	[140]
Au-FLGN	Electrode modifier	A $\beta$ protein	88.6 fM	0.44–284 pM	Hb, heparin, HSA and bilirubin	Serum and CSF	[141]
Microporous gold nanostructure	Electrode modifier	A $\beta$ protein	44.3 fM	0.7 pM–1.6 nM	Hb, heparin, HSA and bilirubin	Plasma and CSF in AD and elderly normal controls	[142]
AuNPs Au@Fc-Zn-MOF	Electrode modifier Label	A $\beta$ protein	6.6 fM	22.2 fM–22.2 nM	HSA, thrombin, BSA, IgG, A $\beta$ <sub>o</sub> , A $\beta$ <sub>f</sub> and monomers	Human serum samples	[143]
3D-Au-PAMAM	Electrode modifier	Tau	0.031 pM	~0.11–91 pM	IgG, Hb, HSA and BSA	Plasma and tissue extract samples	[144]
MWCNTs	Electrode modifier	A $\beta$ protein	44 aM	0.22–22.2 fM	A $\beta$ <sub>42</sub> , Hb, heparin and bilirubin	Not tested	[145]
MWCNTs@rGO AuNPs	Electrode modifier Label	Tau-441	0.46 fM	0.5–80 fM	Glucose, AA, L-cysteine, HSA	Normal people and MCI patients	[147]
AuNPs	Label	Tau-381	0.42 pM	2.52–25.2 nM	Not tested	Human plasma samples	[148]
Au@rGO AuCu <sub>x</sub> O@m-CeO <sub>2</sub>	Electrode modifier Label	A $\beta$ protein	7.97 fM	22.2 fM–2.2 nM	Insulin, prostate-specific antigen and alpha fetal protein	Not tested	[152]
MB CdSe@ZnS QDs	Electrode modifier Label	ApoE4	0.37 nM	0.29–5.86 nM	Not tested	Human plasma samples	[154]
MB IrO <sub>2</sub> NPs	Electrode modifier Label	ApoE4	nM	100–500 nM	Not tested	Ex-vivo AD-induced rat brain samples	[158]
HAP NPs	Label	BACE-1	0.1 U/mL	0.25 to 100 U/mL.	Protein kinase A, alkaline phosphatase, glucose oxidase and alcohol dehydrogenase	Serum samples	[45]
PTCA-CNTs ALP-AAT Ab-Ag NPs	Electrode modifier Label	$\alpha$ -1 antitrypsin	0.01 pM	0.05–20.0 pM	IgG and IgE	Serum samples	[46]

3D-Au-PAMAM: AuNPs-poly(amidoamine) (PAMAM) dendrimer nanocomposite; AA: ascorbic acid; ALP-AAT Ab-Ag NPs: alkaline phosphatase-labeled AAT antibody functionalized silver nanoparticles; AuBP@Pt: gold nanobipyramids coated with Pt; AuCu<sub>x</sub>O@m-CeO<sub>2</sub>: AuCu<sub>x</sub>O- embedded mesoporous CeO<sub>2</sub> Au-FLGN: fern-leaves like gold nanostructured covered with gold; AuNPs: gold nanoparticles; AuPd-PDA: polydopamine nanotubes doped with AuPd; Au@rGO: gold nanoparticles functionalized with reduced graphene oxide; CdSe@ZnS QDs: cadmium-selenide/zinc-sulfide quantum dots; FracAu: fractal gold nanostructures; HAP NPs: hydroxyapatite nanoparticles; Hb: hemoglobin; HSA: human serum albumin; MB: magnetic beads; MWCNTs: multi-walled carbon nanotubes; MWCNTs@rGO: multi-walled carbon nanotubes and reduced graphene oxide; PTCA-CNTs: 3,4,9,10-perylene tetracarboxylic acid/carbon nanotubes.



#### 4.4. Neurotransmitter Biomarkers

Neurotransmitters are endogenous neurochemicals that enable neuron communication in order to maintain synaptic and cognitive function [159]. Minor changes in the synthesis or release of neurotransmitters have been related with neurological disorders like AD or Parkinson's Disease, so that they have been proposed as suitable biomarkers for the detection and treatment of neurodegenerative disorders [49].

Recently, liquid chromatography, microdialysis or capillary electrophoresis, among others, have been used for neurotransmitter detection. However, these techniques are time-consuming, so they do not constitute an adequate screening method. Therefore, optical and electrochemical sensing have emerged as an alternative. But, even though a great number of biosensors have been developed for neurotransmitter detection, they have not only been applied to AD, being mainly focused on water and food safety purposes [160,161].

For AD detection, Shin et al. [41] proposed a biosensor for the detection of DA, a neurotransmitter responsible for memory, behavior and movement. By using an ITO working electrode modified with GO and AgNPs (Figure 14A), they achieved a lower LOD compared to previous works that employed gold or carbon-based nanomaterials [162,163], improving biosensing performance at low DA levels. The electrochemical detection of DA was performed by direct detection of the oxidation process of this molecule by CV, DPV and amperometry. Ascorbic acid (AA) and uric acid (UA) were used for the evaluation of the biosensor selectivity, as they have similar oxidative potentials than DA and other neurotransmitters and is present in blood samples at higher concentrations [164]. The biosensor showed a specific response to DA at 0.2  $\mu\text{M}$  levels.

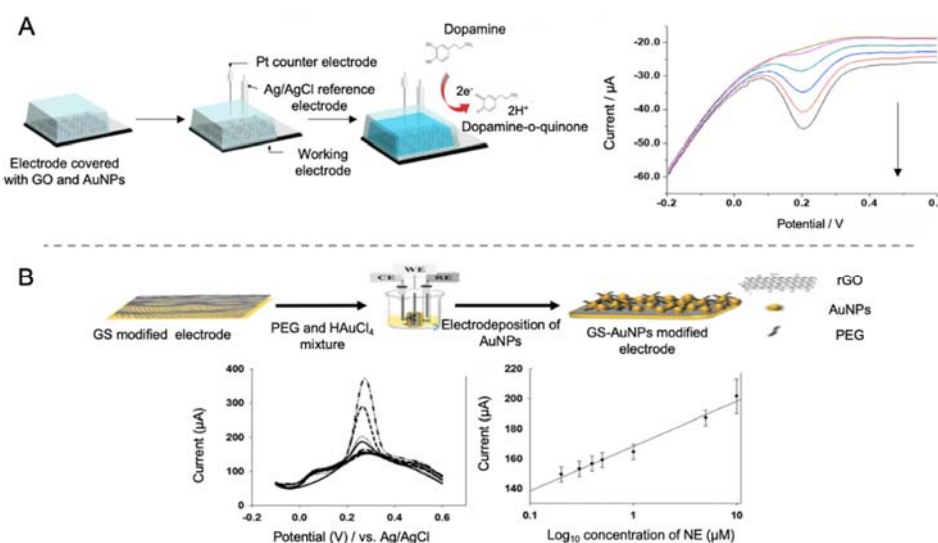


**Figure 14.** Biosensors for the detection of neurotransmitters. (A) Schematic representation of a biosensor for the direct detection of DA using GO and AgNPs by direct detection of the oxidation process of this molecule. At the right side, the DPV curves at different concentrations of DA. Reproduced with permission from [41]. (B) Schematic representation of a biosensor for the direct detection of NE by using a rGO and electrodeposited AuNPs modified electrode (top), accompanied with the DPV curves at different concentrations of norepinephrine and the corresponding calibration curve (bottom). Reprinted by permission from Springer Nature, Korean Journal of Chemical Engineering [42]. Copyright (2017).

DA has also been detected by Park et al. [165] using a gold electrode modified with a nanocomposite of rGO sheets and AuNPs. rGO sheets were used to improve the sensitivity of the biosensor due to their great conductivity while AuNPs were incorporated for improving electrocatalytic activity. Selectivity was achieved as  $\pi$  electron of rGO sheets tend to form  $\pi$ - $\pi$  bonds with benzene rings of aromatic compounds as DA. However, other molecules with a similar structure as DA, like AA, may

affect the selectivity of the biosensor. For that reason, the assay was performed at pH 7.4 at which AA exists as an anion while DA as a cation, thus facilitating the electrostatic interaction of DA with the electrode surface. DA was detected with a LOD of 0.098  $\mu\text{M}$  in the presence of AA 400  $\mu\text{M}$ .

Using a similar approach, Lee et al. [42] developed a biosensor for the detection of NE using rGO and AuNPs as electrode modifiers (Figure 14B). NE is a monoamine neurotransmitter highly related with neural diseases. However, the main drawback of NE detection is its similarity with AA and UA, as they have similar electrochemical oxidation potentials. In the biosensor developed in this case, detection of NE was achieved with a LOD of 200 nM in the presence of a concentration of AA 2000 times higher.

Another neurotransmitter highly studied for its relationship with AD is ACh. ACh is a neurochemical molecule used by cholinergic neurons, present in peripheral and central nervous system. It is involved in cognition, memory and movement, so it constitutes an important modulator of AD dysfunction [166].

Da Silva et al. [167] developed a biosensor for the detection of ACh using the enzyme acetylcholinesterase as receptor. To increase surface-to-volume rate and provide the biosensor with an appropriate immobilization matrix, they used  $\text{Fe}_2\text{O}_3$  nanoparticles due to its strong absorption properties and electron-transfer capacity. In order to have an enhanced applicability,  $\text{Fe}_2\text{O}_3$  nanoparticles were modified with films of poly (neutral red) generated by electropolymerization in the presence of ethaline deep eutectic solvents (DES) with the addition of acid dopants. Acetylcholinesterase was further immobilized by glutaraldehyde cross-linking. The feasibility of the biosensor was evaluated in synthetic urine samples by amperometric measurement showing a LOD of 1.04  $\mu\text{M}$ . Further examples of biosensors for the detection of neurotransmitters using nanomaterials and developed in the last ten years are collected in Table 5 [168–170].

**Table 5.** Electrochemical biosensors for the detection of neurotransmitters using nanomaterials published over the last ten years.

Nanomaterial	Role	Biomarker	LOD	Linear Range	Selectivity Tested	Real Sample Tested	Ref
SNPs@GO	Electrode modifier	DA	0.2 $\mu\text{M}$	0.1–100 $\mu\text{M}$	UA and AA	Not tested	[41]
pGO-GNPs	Electrode modifier	DA	1.28 $\mu\text{M}$	0.1–30 $\mu\text{M}$	AA and glucose	Not tested	[162]
Pdop@GR-MWCNTs	Electrode modifier	DA	1 $\mu\text{M}$	7–297 $\mu\text{M}$	AA, glucose and different ions	Human serum	[163]
rGS-GNPs	Electrode modifier	DA	0.098 $\mu\text{M}$	0.1–100 $\mu\text{M}$	AA	Not tested	[165]
rGS-GNPs	Electrode modifier	NE	200 nM	0.2–10 $\mu\text{M}$	AA	Not tested	[42]
$\text{Fe}_2\text{O}_3$ NPs	Electrode modifier	ACh	1.04 $\mu\text{M}$	2.5–60 $\mu\text{M}$	Glucose, albumin, DA, NE and AA	Not tested	[167]
Pd/NPG	Electrode modifier	DA	1 $\mu\text{M}$	1–220 $\mu\text{M}$	AA, UA, NE, epinephrine and catechol	Not tested	[168]
CHIT/Fe@AuNPs	Electrode modifier	ACh	0.005 $\mu\text{M}$	0.005–400 $\mu\text{M}$	AA, UA, DA, lactic acid, heparin sodium, $\text{CuSO}_4$ , KCl, NaCl and $\text{MgCl}_2$	Healthy and AD plasma samples	[169]
$\text{Fe}_2\text{O}_3$ /rGO-PEDOT	Electrode modifier	ACh	4 nM	4 nM–800 $\mu\text{M}$	AA, bilirubin, urea, UA, 4-acetamidophenol and glucose	Healthy and AD serum samples	[170]

AA: ascorbic acid; ACh: acetylcholine; CHIT/Fe@AuNPs: nanocomposite of chitosan (CHIT)/gold-coated ferric oxide nanoparticles (Fe@AuNPs); DA: dopamine;  $\text{Fe}_2\text{O}_3$  NPs: magnetic nanoparticles;  $\text{Fe}_2\text{O}_3$ /rGO-PEDOT: iron oxide nanoparticles ( $\text{Fe}_2\text{O}_3$  NPs) combined with poly(3,4-ethylenedioxythiophene) (PEDOT)—reduced graphene oxide (rGO) nanocomposite; MWCNTs: multi-walled carbon nanotubes; NE: norepinephrine; Pd/NPG: palladium nanoparticles (Pd) onto a self-supporting nanoporous gold (NPG) wire; Pdop@GR: polydopamine functionalized with graphene; pGO: porous GO; rGS-GNPs: reduced graphene oxide sheets with gold nanoparticles; SNPs@GO: silver nanoparticles covered with graphene oxide; UA: uric acid.

While it is true that neurotransmitters detection is an important parameter for AD detection, their use as biomarkers it is still not widespread, what is reflected in the number of biosensors that test neurotransmitters detection in real samples. Moreover, of special interest are the interferences with other substances as UA or AA, for what the approximation followed by Lee et al. [42] is the most promising for increasing selectivity. Regarding LOD, it should be highlighted that the obtained values are lower than those reported for other AD biomarkers. Regarding the nanomaterials, the use of graphene derivatives is much more widespread than for other AD biomarkers, what may be due to its tendency to form  $\pi$ - $\pi$  bonds with aromatic compounds.

#### 4.5. Oxidative Stress Biomarkers

The imbalance between free radicals' generation and degradation in the body plays a significant role in the pathogenesis of cancer, autoimmune diseases and neurodegenerative diseases, including AD [43]. Most of the biological molecules that compose neurons can be oxidized due to mitochondrial dysfunction or inflammation, being both processes that occur during AD. As a consequence of an increase in the presence of reactive oxygen species (ROS) or other oxidative stress biomarkers [171] A $\beta$  deposition and tau hyperphosphorylation are enhanced. When the levels of oxidative stress biomarkers are disbalanced in the brain, values in blood are also increased, facilitating their detection [50] and serving as early indicator of health issue. The main drawback of this biomarkers is the lack of specificity, as oxidative stress is associated to a wide variety of health issues.

Wang et al. [172] developed a biosensor for the detection of H<sub>2</sub>O<sub>2</sub> as a potential oxidative stress biomarker (Figure 15). This biosensor was based on the use of a GCE functionalized with rGO blended with Au, Fe<sub>3</sub>O<sub>4</sub> and platinum nanoparticles generated by electrodeposition. For in vitro detection, working electrode was introduced in cellular culture media, in which H<sub>2</sub>O<sub>2</sub> was present as it was liberated by cells under oxidative stress conditions, provoked by the injection of AA. Reduction of H<sub>2</sub>O<sub>2</sub> was measured by CV, providing a LOD of 0.1  $\mu$ M, without the need of enzymatic labels, what notably reduced the analysis time.

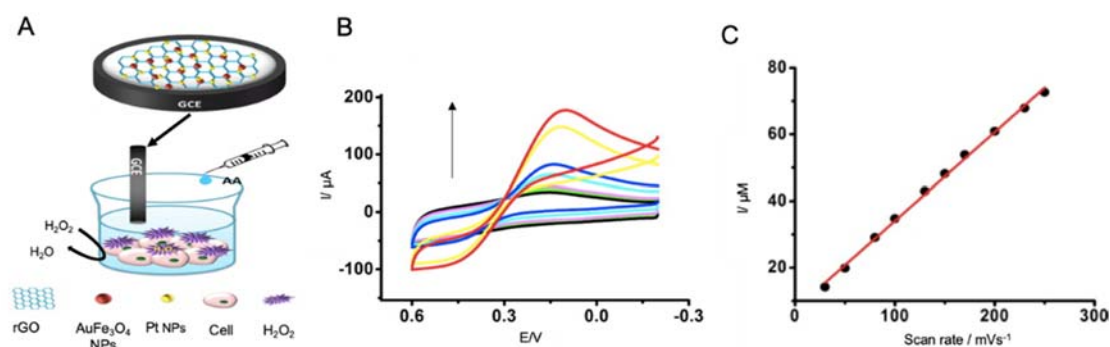


**Figure 15.** Electrochemical biosensors for the detection of oxidative stress biomarkers. (A) Schematic representation of a biosensor for the detection of H<sub>2</sub>O<sub>2</sub> in culture media using a GCE modified with rGO, AuFe<sub>3</sub>O<sub>4</sub> NPs and PtNPs, that is introduced in a cell culture under oxidative stress conditions provoked by the addition of AA to culture media. These conditions promote the release of H<sub>2</sub>O<sub>2</sub> by the cells, indicating the oxidative stress suffered. (B) CV curves of different H<sub>2</sub>O<sub>2</sub> concentrations and (C) the corresponding calibration curve. Adapted with permission from [172]. Copyright (2015) American Chemical Society.

Sekar et al. [173] developed a biosensor for the detection of H<sub>2</sub>O<sub>2</sub> in human blood using zinc oxide-polyvinyl alcohol (ZnO-PVA) nanocomposites as electrode modifiers. ZnO was selected in this work as it has a high electronic conductivity and high catalytic activity. Functionalization with PVA provided a higher electrical conductivity compared to bare ZnO and the presence of -OH groups facilitated electron density on the biosensors surface. For the specific catalysis of H<sub>2</sub>O<sub>2</sub> into H<sub>2</sub>O and O<sub>2</sub>, the enzyme catalase was immobilized in the electrode surface and the process was recorded by CV,

allowing to reach a LOD of 9.13 nM. Following a similar approach, other studies have been developed for the detection of H<sub>2</sub>O<sub>2</sub> and are revised in Table 6 [174–176].

**Table 6.** Electrochemical biosensors for the detection of oxidative stress biomarkers using nanomaterials published over the last ten years and focused on its application for AD detection.

Nanomaterial	Role	Biomarker	LOD	Linear Range	Selectivity Tested	Real Sample Tested	Ref
RGO/AuFe <sub>3</sub> O <sub>4</sub> /Pt	Electrode modifier	H <sub>2</sub> O <sub>2</sub>	0.1 μM	0.5 μM–11.5 mM	UA, AA and glucose	Living cells	[172]
ZnO-PVA	Electrode modifier	H <sub>2</sub> O <sub>2</sub>	9.13 nM	1–17 μM	AA, lactic acid, urea and glucose	Human blood serum samples	[173]
CuS/RGO	Electrode modifier	H <sub>2</sub> O <sub>2</sub>	0.27 μM	5–1500 μM	AA, UA, DA, acetaminophen, citric acid and glucose	Human serum and urine samples	[174]
CNPs	Electrode modifier	H <sub>2</sub> O <sub>2</sub>	0.1 pM	0.1 pM–0.1 μM	Glucose, sodium nitrite and UA	Not tested	[175]
PIL/PB/CNT	Electrode modifier	Superoxide anion	0.42 μM	1–228 μM	O <sub>2</sub> , tertbutylhydroperoxide, –OCl, OH, OtBu, ONOO–	Living cells	[176]

AA: ascorbic acid; CNPs: ceria nanoparticles; CuS/RGO: copper sulfide-decorated reduced graphene oxide composites; DA: dopamine; PIL/PB/CNT: ionic liquid polymer (PIL) onto PB nanoparticles (PBNPs) and carbon nanotubes (CNT); RGO/AuFe<sub>3</sub>O<sub>4</sub>/Pt: reduced graphene oxide (RGO) nanocomposites decorated with Au, Fe<sub>3</sub>O<sub>4</sub>, and Pt nanoparticles; UA: uric acid; ZnO-PVA: zinc oxide-polyvinyl alcohol nanocomposites.

H<sub>2</sub>O<sub>2</sub> detection constitutes an interesting way of monitoring oxidative stress, what is nowadays of special concern specially for the study of AD disease as reflected in the application of the sensors described above in in vitro cell cultures. In any case, it is required further investigation on the clinical parameters of oxidative stress in AD patients before the implementation of this biosensors. However, the development of this technology and its study focused on AD is a sign of progress in this field.

#### 4.6. Multianalyte Detection

The multifactorial profile of AD implies the contribution of proteins and genetic biomarkers to its etiology that conditions the development of the disease. All the above revised biomarkers contribute to the development of AD so that the evaluation of one biomarker alone do not constitute an accurate diagnosing tool. Moreover, there are at least five different subgroups of AD patients differentiated by the concentration of Aβ and tau levels in CSF, what affects the efficiency of medical treatments [177]. For that reason, the development of multianalyte biosensors has emerged as a prosper alternative for AD detection, as summarized in Table 7.

An initial approximation for this purpose is the identification, using the same biosensor, of different biomarkers. This is the case of de la Escosura-Muñiz et al. [178], that explored the detection of ApoE and Aβ peptide using magnetic beads as platforms of the immunoreaction and AuNPs tags. The electrocatalytic activity of AuNPs toward the hydrogen evolution reaction (HER) allowed the chronoamperometric detection of such biomarkers at clinically relevant levels in CSF, serum and plasma samples of patients suffering from AD. The performance of the biosensor was successfully evaluated, showing a LOD of 4.21 pM for Aβ peptide and 2.34 pM for ApoE.

In a similar approximation, Tau protein was detected by Serafin et al. [179] in combination with TAR DNA binding protein 43 (TDP-43), a protein involved in the evolution of several neurodegenerative diseases that has been found to form deposits in AD [180]. In this biosensor, AuNPs combined with PAMAM were used as scaffolds for the immobilization of antibodies to dual SPCEs, while HRP functionalized with antibodies was used for the amperometric detection of AD biomarkers using H<sub>2</sub>O<sub>2</sub> / hydroquinone system as reporter, providing a LOD of 50 fM for tau-441 and 0.287 pM for TDP-43.

**Table 7.** Electrochemical biosensors for the multi-detection of AD biomarkers reported during the last ten years.

Nanomaterial	Role	Biomarker	LOD	Linear Range	Selectivity Tested	Real Sample Tested	Ref
MB	Electrode modifier	ApoE4	2.34 pM	2.93–366 pM	Not tested	CSF, serum and plasma	[178]
AuNPs	Label	A $\beta$	4.21 pM	4.43–2.77 nM			
3D-Au-PAMAM	Electrode modifier	Tau-441	50 fM	0.18–109 pM	BSA, HSA, IgG and Hb	Plasma and tissue samples	[179]
		TDP-43	0.287 pM	1–349 pM			
ABTS-PDDA/CNTs	Electrode modifier	A $\beta$	0.11 nM	22.2–842 nM	Metal ions, amino acids, AA, DA, UA, lactic acid and glucose	Plasma and hippocampus of normal and AD rats	[181]
		Cu <sup>2+</sup>	0.04 $\mu$ M	0.1–10 $\mu$ M			
CNT-PIL NLC	Electrode modifier Label	A $\beta$ <sub>o</sub>	2.2 pM	0.04–8.86 nM	Metal ions, amino acids, other isoforms of A $\beta$	AD rat brain	[182]
		A $\beta$ <sub>f</sub>	4.4 pM				
Au nanodendrites	Electrode modifier	miRNA-101	91.4 pM	0.1 pM–100 pM	BSA other miRNAs	Serum samples	[183]
		ApoE4	2.09 fM	2.93 fM–2.93 pM			
		Tau	1.29 fM	2.18 fM–2.18 pM			
		A $\beta$	1.9 fM	22.2 fM–22.2 pM			

3D-Au-PAMAM: AuNPs-poly(amidoamine) (PAMAM) dendrimer nanocomposite; AA: ascorbic acid; ABTS-PDDA/CNTs: 2,2-azinobis-(3-ethylbenzthiazoline-6-sulphonate) (ABTS)- poly(diallyldimethylammonium chloride) (PDDA)/single-walled carbon nanotubes; AuNPs: gold nanoparticles; CNT-PIL: carbon nanotubes combined with polymer ion liquid; DA: dopamine; Hb: hemoglobin; HSA: human serum albumin; MB: magnetic beads; NLC: nanostructure lipid carrier; UA: uric acid.

CNTs have been used by Yu et al. [181] for the identification of Cu<sup>2+</sup> and A $\beta$  monomers taking advantage of the affinity protein neurokinin B (NKB), that enhances A $\beta$  aggregation capacity. In this competitive biosensor, Cu<sup>2+</sup> and A $\beta$  monomers were detected by using the specificity of NKB to Cu<sup>2+</sup> and the Cu<sup>2+</sup> tendency to form aggregates with A $\beta$ , obtaining a more complete detection tool. First, a GCE was modified with SWCNTs functionalized with poly (diallyldimethylammonium chloride) (PDDA) and 2,2-azinobis-(3-ethylbenzthiazoline-6-sulphonate) (ABTS), as inner reference molecule and as sensitivity enlarger. NKB was coated on the ABTS-PDDA/CNTs electrode surface to form the complex [CuII(NKB)<sub>2</sub>]. After that, certain amounts of A $\beta$  dispersed in Cu<sup>2+</sup> containing PBS were added, promoting the generation of aggregates and the release of Cu<sup>2+</sup> from NKB. Quantification of Cu<sup>2+</sup> and A $\beta$ (1-42) was performed by comparing the reduction peaks at -0.12 V of Cu<sup>2+</sup> and A $\beta$  and at 0.58 V of the ABTS, obtaining a LOD of 0.04  $\mu$ M for Cu<sup>2+</sup> and 0.11 nM for A $\beta$ . In a subsequent work, the same group [182] developed an immunosensor for the detection of A $\beta$ <sub>o</sub> and A $\beta$ <sub>f</sub> while monitoring the aggregation process (Figure 16A). For that purpose, a two-channel electrochemical system was constructed, with a specific antibody (against oligomers or fibrils) in each channel. Electrodes were functionalized with CNTs and polymer ion liquid to facilitate the electron transfer and the immobilization of the antibodies. Nanostructure lipid carriers made of poloxamer and functionalized with antibodies and thionine were used as labels, taking advantage of thionine as signal reporter. The principle of the sensor is based on the aggregation of A $\beta$ <sub>o</sub> into fibrils among time, as A $\beta$ <sub>o</sub> tends to get converted into A $\beta$ <sub>f</sub> reducing the signal corresponding to A $\beta$ <sub>o</sub>. The biosensor was tested in CSF and tissue samples of AD rats, constituting the first biosensors for the monitoring of A $\beta$  aggregation among time. Yu and co-workers achieved in this case a LOD for A $\beta$  detection of 2.2 pM for A $\beta$ <sub>o</sub> and 4.4 pM for A $\beta$ <sub>f</sub>.



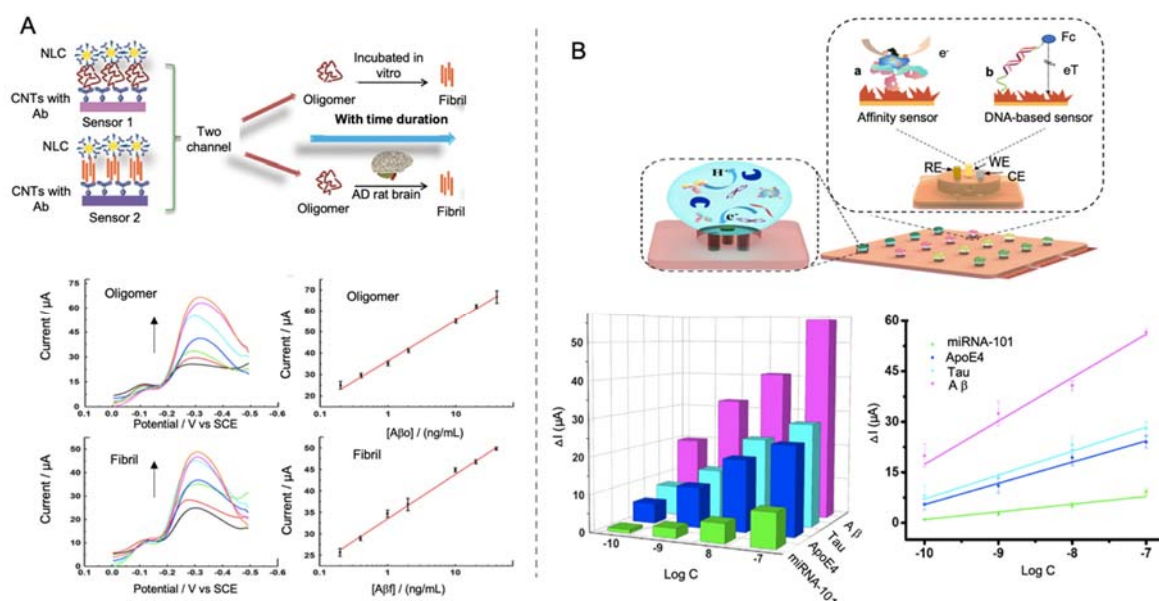


**Figure 16.** (A) Schematic representation of a biosensor for the combined detection of A $\beta$  and A $\beta$  in a two-channel system for monitoring A $\beta$  aggregation among time using CNTs with antibodies as electrode modifiers and Poloxamer nanocarriers (NLC) as labels (top). DPV curves for different concentrations of oligomers and fibrils and the corresponding calibration curves (bottom). Adapted with permission from [182]. Copyright (2019) American Chemical Society. (B) Mini-pillar sensor of polydimethylsiloxane and gold nanodendrites for the detection of multiple AD biomarkers at the same time. Each hole of the biosensor constitutes a reservoir in which biomarkers interact with the recognition element producing an increase in the surface resistance in the case of affinity biomarkers (Tau, ApoE4 and A $\beta$ ) and reducing the electrochemical signal reported by ferrocene (Fc) in the case of DNA probes for miRNA-101 detection. At the bottom, the electrochemical response of different concentration of the AD biomarkers measured and the corresponding calibration curve (green: miRNA-101, blue: ApoE4, cyan: Tau, magenta: A $\beta$ ). Reprinted from [183]. Copyright (2020) with permission from Elsevier.

In a more complete approximation, Song et al. [183] were able to detect four different AD biomarkers in the same platform (Tau, ApoE4, A $\beta$  and miRNA-101) by using a mini-pillar sensor modified with gold nanodendrites (Figure 16B). This sensor was constructed by using polydimethylsiloxane as prepolymer and a template of polytetrafluoroethylene with holes of  $\sim 5$  mm of diameter and  $\sim 1.65$  mm of height. On each hole of the array they were embedded an Au working electrode, a Pt counter electrode and a reference electrode of Ag. After the construction of the mini-pillar polydimethylsiloxane electrode, gold nanodendrites were electrodeposited onto the working electrode for favoring the immobilization of both specific antibodies and DNA probes. This open-channel biosensor allowed the simultaneous sensing of trace amounts of different biomarkers, reaching LODs of 91.4 pM for miRNA-101, 1.29 fM for tau, 2.09 fM for ApoE4 and 1.9 fM for A $\beta$ .

Even though LOD values are in some cases higher than the ones reached by other individual sensors, the ability to monitor the amount of different biomarkers in a single analysis is crucial for providing a more complete diagnosis and to reduce the measurement time and the number of samples required. This would reduce the number of invasive extractions needed to be performed on the patient. All of this constitute the way to obtain biosensor AD diagnostics close to the market requirements.

## 5. Conclusions

AD incidence is growing each day, and with it grows the social and economic burden associated to this devastating disease. Although there is not still a cure, an early detection of AD is crucial to delay as much as possible the appearance of degenerative effects and to allow family and carers to prepare themselves for the changes associated to it. Therefore, the development of an analytical device

for the detection of early biomarkers of AD is required. In this context, the main obstacle to overcome is achieving good sensitivity and selectivity, as CSF and blood serum are complex samples that could interfere in the outcome of measurements. In this field, notably most of the biosensors revised in this work have evaluated the selectivity of the sensor against other widely spread biomolecules such as HSA, BSA or glucose. Those that do not separately evaluate selectivity against concrete biomolecules, mostly test biosensors performance in real samples.

Furthermore, efficiency and long-term stability need also to be evaluated as they are essential for the use of biosensors as screening methods. For that purpose, nanomaterials have been implemented in biosensing, in association with the outstanding progress made in nanomaterials synthesis and functionalization. Within this framework, nanomaterials have been implemented in biosensors as electrode modifiers, being gold and carbon-based nanomaterials the most widespread, specially MWCNTs that have allowed to achieve the lowest LOD found in the biosensors included in this review ( $10^{-2}$  fM). The modification of transducers with these nanostructures let a better electrochemical performance as its use improves conductivity, while favoring immobilization and orientation of biological recognition elements. In addition, the use of nanomaterials as labels, has provided an amplification of the signal, due to their electroactivity and electrocatalytic properties, that even though its use is more complicated, enables a higher sensitivity. In this field, again, the use of gold nanomaterials, alone or in combination with others, is massive, followed by the use of MOFs as reporter carriers. The use of electrocatalytic labels has also been a valuable improvement as it facilitates the detection of biomolecules at neutral pH, offering a more integrated sensing systems, also reducing the time of analysis which is of key relevance for meeting the market needs.

According to this, it should be noted that, in terms of LOD, the use of labels has not supposed an increased advantage in the amplification of the signal compared to the use of nanomaterials as electrode modifiers. Neither the use of nanomaterials as both electrode modifiers and labels has allowed to reach the lowest LODs. This highlights that there is much room for improvement in the implementation of combinations of nanomaterials for biosensing.

Surprisingly, lowest LODs have been achieved in biosensors using MIPs or recognition proteins, what suggests that the biological recognition element employed should be another parameter that should be taken into consideration.

Regarding the applicability of these biosensors for the detection of AD biomarkers highlights the great number of investigations related with the detection of A $\beta$  peptide and its different aggregated forms, as it is still considered the main pathological hallmark of AD. However, it is interesting the increase in the detection of other biomarkers, such as ApoE4 and unfolded p53, that can shed light in the early diagnosis of AD. Moreover, the increased development of biosensor for the detection of multiple analytes is encouraging, as it supposes an advanced in the obtention of more complete diagnostic tools. However, many of the revised works do not evaluate final sensors performance in real human plasma or CSF samples of AD patients and even less compare the results with those provided by traditional techniques as ELISA. This point should be of special relevance to validate the applicability of the biosensors developed.

In any case, even though sensitivity and selectivity issues seem to be overcome, as fM and pM detection limits are reached, efficiency and long-term stability are not taken into account in many works, which is a problem for the transferability of the biosensors created. It is also a drawback the lack of evaluation of biosensors performance in real samples, that it is definitely necessary for evaluating biosensors effectiveness.

All these challenges need to be overcome if a commercial AD biosensor wants to be developed, and for that purpose these parameters should be assessed if we want AD early detection to become a reality.

**Author Contributions:** C.T.-R.; writing—review and editing; F.J.G.-A. writing—review and editing; A.d.l.E.-M.; writing—review and editing and funding acquisition. All authors have read and agreed to the published version of the manuscript.

**Funding:** This research was funded by the FC-GRUPIN-ID/2018/000166 project from the Asturias Regional Government and the CTQ2017-86994-R project from the Spanish Ministry Economy and Competitiveness (MINECO).

**Acknowledgments:** C. Toyos-Rodríguez thanks the MICINN (Spain) for the award of a FPI Grant (PRE2018-084853). A. de la Escosura-Muñiz acknowledges the MICINN (Spain) for the “Ramón y Cajal” Research Fellow (RyC-2016-20299).

**Conflicts of Interest:** The authors declare no conflict of interest.

## Abbreviations

2D	Two-dimensional
3D	Three-dimensional
AA	Ascorbic acid
A $\beta$	Amyloid $\beta$
A $\beta$ f	Amyloid $\beta$ fibrils
A $\beta$ o	Amyloid $\beta$ oligomers
Ach	Acetylcholine
AD	Alzheimer’s disease
ADI	Alzheimer’s disease international
AFM	Atomic force microscopy
AgNPs	Silver nanoparticles
APP	Amyloid precursor protein
AuNPs	Gold nanoparticles
CA	Chronoamperometry
CeNPs	Cerium oxide nanoparticles
CNTs	Carbon nanotubes
CSF	Cerebrospinal fluid
CV	Cyclic voltammetry
DA	Dopamine
DES	Deep eutectic solvents
DNA	Deoxyribonucleic acid
DPV	Differential pulse voltammetry
EDC	1-ethyl-3-(3-dimethylaminopropyl) carbodiimide
ELISA	Enzyme linked immunosorbent assay
FBS	Fetal bovine serum
FISH	Fluorescence in situ hybridization
G8	Group of eight inter-governmental political forum
GCE	Glassy carbon electrode
GDP	Gross domestic product
GO	Graphene oxide
HER	Hydrogen evolution reaction
HRP	Horseradish peroxidase
IrO <sub>2</sub> NPs	Iridium oxide nanoparticles
ITO	Indium tin oxide
LOD	Limit of detection
LSV	Linear sweep voltammetry
MAPT	Microtubule-associated protein Tau
MCH	6-mercapto-1-hexanol
MCI	Mild cognitive impairment
MIPs	Molecular imprinted polymer
miRNAs	microRNAs
MHDA	16-mercaptohexadecanoic acid
MOFs	Metal-organic frameworks
MRI	Magnetic resonance imaging
mRNA	Messenger RNA



MWCNTs	Multi-walled carbon nanotubes
NE	Norepinephrine
NFTs	Neurofibrillary tangles
NiFe <sub>2</sub> O <sub>4</sub>	Nickel ferrites
NIR	Near infrared
NKB	Neurokinin B
NHS	N-hydroxysuccinimide
OECT	Organic electrochemical transistors
PBS	Phosphate buffer saline
PCR	Polymerase chain reaction
PEI	Polyethyleneimine
PET	Positron emission tomography
PHFs	Pair helical filaments
POC	Point-of-care
PrPc	Cellular prion protein
QDs	Quantum dots
rGO	Reduced graphene oxide
RNA	Ribonucleic acid
ROS	Reactive oxygen species
RSD	Relative standard deviation
SAM	Self-assembled monolayer
SELEX	Selective evolution of ligands by exponential enrichment
SEM	Scanning electron microscopy
SPCEs	Screen-printed carbon electrodes
ssDNA	Single-stranded DNA
SWCNTs	Single-walled carbon nanotubes
SWV	Square wave voltammetry
TDP-43	TAR DNA-binding protein 43
UA	Uric acid
WHO	World health organization
WOR	Water oxidation reaction

## References

- Scheltens, P.; Blennow, K.; Breteler, M.M.B.; de Strooper, B.; Frisoni, G.B.; Salloway, S.; Van der Flier, W.M. Alzheimer's disease. *Lancet* **2016**, *388*, 505–517. [[CrossRef](#)]
- Alzheimer's Disease International. *World Alzheimer Report 2019: Attitudes to Dementia*; Alzheimer's Disease International: London, UK, 2019; p. 160.
- Alzheimer Association. *2018 Alzheimer's Disease Facts and Figures*; Alzheimer Association: Chicago, IL, USA, 2019; pp. 1–88.
- Joe, E.; Ringman, J.M. Cognitive symptoms of Alzheimer's disease: Clinical management and prevention. *BMJ* **2019**, *367*, l6217. [[CrossRef](#)]
- Prince, M.; Wimo, A.; Guerchet, M.; Ali, G.-C.; Wu, Y.-T.; Prina, M. *World Alzheimer Report 2015. The Global Impact of Dementia, an Analysis of Prevalence, Incidence, Cost and Trends*; Alzheimer's Disease International: London, UK, 2015; p. 87.
- Hansson, O.; Seibyl, J.; Stomrud, E.; Zetterberg, H.; Trojanowski, J.Q.; Bittner, T.; Lifke, V.; Corradini, V.; Eichenlaub, U.; Batrla, R.; et al. CSF biomarkers of Alzheimer's disease concord with amyloid- $\beta$  PET and predict clinical progression: A study of fully automated immunoassays in BioFINDER and ADNI cohorts. *Alzheimer's Dement.* **2018**, *14*, 1470–1481. [[CrossRef](#)] [[PubMed](#)]
- Kaushik, A.; Jayant, R.D.; Tiwari, S.; Vashist, A.; Nair, M. Nano-biosensors to detect beta-amyloid for Alzheimer's disease management. *Biosens. Bioelectron.* **2016**, *80*, 273–287. [[CrossRef](#)] [[PubMed](#)]
- Shui, B.; Tao, D.; Florea, A.; Cheng, J.; Zhao, Q.; Gu, Y.; Li, W.; Jaffrezic-Renault, N.; Mei, Y.; Guo, Z. Biosensors for Alzheimer's disease biomarker detection: A review. *Biochimie* **2018**, *147*, 13–24. [[CrossRef](#)] [[PubMed](#)]

9. O'Brien, R.J.; Wong, P.C. Amyloid Precursor Protein Processing and Alzheimer's Disease. *Annu. Rev. Neurosci.* **2011**, *34*, 185–204. [[CrossRef](#)] [[PubMed](#)]
10. Chen, G.; Xu, T.; Yan, Y.; Zhou, Y.; Jiang, Y.; Melcher, K.; Xu, H.E. Amyloid beta: Structure, biology and structure-based therapeutic development. *Acta Pharmacol. Sin.* **2017**, *38*, 1205–1235. [[CrossRef](#)]
11. Brazaca, L.C.; Sampaio, I.; Zucolotto, V.; Janegitz, B.C. Applications of biosensors in Alzheimer's disease diagnosis. *Talanta* **2020**, *210*, 120644. [[CrossRef](#)]
12. Nunan, J.; Small, D.H. Regulation of APP cleavage by K-, L- and Q-secretases. *FEBS Lett.* **2000**, *483*, 6–10. [[CrossRef](#)]
13. Baranello, R.; Bharani, K.; Padmaraju, V.; Chopra, N.; Lahiri, D.; Greig, N.; Pappolla, M.; Sambamurti, K. Amyloid-Beta Protein Clearance and Degradation (ABCD) Pathways and their Role in Alzheimer's Disease. *CAR* **2015**, *12*, 32–46. [[CrossRef](#)]
14. Weggen, S.; Behr, D. Molecular consequences of amyloid precursor protein and presenilin mutations causing autosomal-dominant Alzheimer's disease. *Alzheimers Res. Ther.* **2012**, *4*, 9. [[CrossRef](#)] [[PubMed](#)]
15. Selkoe, D.J. Alzheimer's Disease: Genes, Proteins, and Therapy. *Physiol. Rev.* **2001**, *81*, 741–766. [[CrossRef](#)] [[PubMed](#)]
16. Hardy, J.A.; Giggins, G.A. Alzheimer's disease: The amyloid cascade hypothesis. *Science* **1992**, *256*, 184–185. [[CrossRef](#)] [[PubMed](#)]
17. Erten-Lyons, D.; Woltjer, R.L.; Dodge, H.; Nixon, R.; Vorobik, R.; Calvert, J.F.; Leahy, M.; Montine, T.; Kaye, J. Factors associated with resistance to dementia despite high Alzheimer disease pathology. *Neurology* **2009**, *72*, 354–360. [[CrossRef](#)] [[PubMed](#)]
18. Sengupta, U.; Nilson, A.N.; Kaye, R. The Role of Amyloid- $\beta$  Oligomers in Toxicity, Propagation, and Immunotherapy. *EBioMedicine* **2016**, *6*, 42–49. [[CrossRef](#)]
19. Yang, T.; Hong, S.; O'Malley, T.; Sperling, R.A.; Walsh, D.M.; Selkoe, D.J. New ELISAs with high specificity for soluble oligomers of amyloid  $\beta$ -protein detect natural A $\beta$  oligomers in human brain but not CSF. *Alzheimer's Dement.* **2013**, *9*, 99–112. [[CrossRef](#)]
20. Gandy, S.; Simon, A.J.; Steele, J.W.; Lublin, A.L.; Lah, J.J.; Walker, L.C.; Levey, A.I.; Krafft, G.A.; Levy, E.; Checler, F.; et al. Days to criterion as an indicator of toxicity associated with human Alzheimer amyloid- $\beta$  oligomers. *Ann. Neurol.* **2010**, *68*, 220–230. [[CrossRef](#)]
21. Chakroborty, S.; Stutzmann, G.E. Calcium channelopathies and Alzheimer's disease: Insight into therapeutic success and failures. *Eur. J. Pharmacol.* **2014**, *739*, 83–95. [[CrossRef](#)]
22. Disterhoft, J.F.; Moyer, J.R.; Thompson, L.T. The Calcium Rationale in Aging and Alzheimer's Disease: Evidence from an Animal Model of Normal Aging. *Ann. N. Y. Acad. Sci.* **2006**, *747*, 382–406. [[CrossRef](#)]
23. Lambert, M.P.; Barlow, A.K.; Chromy, B.A.; Edwards, C.; Freed, R.; Liosatos, M.; Morgan, T.E.; Rozovsky, I.; Trommer, B.; Viola, K.L.; et al. Diffusible, nonfibrillar ligands derived from A 1-42 are potent central nervous system neurotoxins. *Proc. Natl. Acad. Sci. USA* **1998**, *95*, 6448–6453. [[CrossRef](#)]
24. Iqbal, K.; Liu, F.; Gong, C.-X.; Grundke-Iqbal, I. Tau in Alzheimer Disease and Related Tauopathies. *CAR* **2010**, *7*, 656–664. [[CrossRef](#)] [[PubMed](#)]
25. Iqbal, K.; Alonso, A.d.C.; Gong, C.-X.; Khatoon, S.; Pei, J.-J.; Wang, J.Z.; Grundke-Iqbal, I. Mechanisms of neurofibrillary degeneration and the formation of neurofibrillary tangles. In *Ageing and Dementia*; Jellinger, K., Fazekas, F., Windisch, M., Eds.; Journal of Neural Transmission. Supplementa; Springer: Vienna, Austria, 1998; Volume 53, pp. 169–180. ISBN 978-3-211-83114-4.
26. Iqbal, K.; Zaidi, T.; Wen, G.Y.; Grundke-Iqbal, I.; Merz, P.A.; Shaikh, S.S.; Wisniewski, H.M.; Alafuzoff, I.; Winblad, B. Defective brain microtubule assembly in Alzheimer's disease. *Lancet* **1986**, *2*, 421–426. [[CrossRef](#)]
27. Zhou, Y.; Shi, J.; Chu, D.; Hu, W.; Guan, Z.; Gong, C.-X.; Iqbal, K.; Liu, F. Relevance of Phosphorylation and Truncation of Tau to the Etiopathogenesis of Alzheimer's Disease. *Front. Aging Neurosci.* **2018**, *10*, 27. [[CrossRef](#)] [[PubMed](#)]
28. Braak, H.; Braak, E.; Grundke-Iqbal, I.; Iqbal, K. Occurrence of neuropil threads in the senile human brain and in Alzheimer's disease: A third location of paired helical filaments outside of neurofibrillary tangles and neuritic plaques. *Neurosci. Lett.* **1986**, *65*, 351–355. [[CrossRef](#)]
29. Grehan, S.; Tse, E.; Taylor, J.M. Two Distal Downstream Enhancers Direct Expression of the Human Apolipoprotein E Gene to Astrocytes in the Brain. *J. Neurosci. Res.* **2001**, *21*, 812–822. [[CrossRef](#)]
30. Rall, J.S.; Weisgraber, K.; Mahley, R. Human Apolipoprotein E: The complete amino acid sequence. *Int. J. Biol. Chem.* **1982**, *257*, 4171–4178.

31. Kim, J.; Basak, J.M.; Holtzman, D.M. The Role of Apolipoprotein E in Alzheimer's Disease. *Neuron* **2009**, *63*, 287–303. [[CrossRef](#)]
32. Wisniewski, T.; Frangione, B. Apolipoprotein E: A pathological chaperone protein in patients with cerebral and systemic amyloid. *Neurosci. Lett.* **1992**, *135*, 235–238. [[CrossRef](#)]
33. Blennow, K.; Hampel, H.; Weiner, M.; Zetterberg, H. Cerebrospinal fluid and plasma biomarkers in Alzheimer disease. *Nat. Rev. Neurol.* **2010**, *6*, 131–144. [[CrossRef](#)]
34. Lanni, C.; Uberti, D.; Racchi, M.; Govoni, S.; Memo, M. Unfolded p53: A Potential Biomarker for Alzheimer's Disease. *JAD* **2007**, *12*, 93–99. [[CrossRef](#)]
35. Lane, D.P. Cancer. p53, guardian of the genome. *Nature* **1992**, *358*, 15–16. [[CrossRef](#)] [[PubMed](#)]
36. Lanni, C.; Racchi, M.; Stanga, S.; Mazzini, G.; Ranzenigo, A.; Polotti, R.; Memo, M.; Govoni, S.; Uberti, D. Unfolded p53 in Blood as a Predictive Signature of the Transition from Mild Cognitive Impairment to Alzheimer's Disease. *JAD* **2010**, *20*, 97–104. [[CrossRef](#)] [[PubMed](#)]
37. Uberti, D.; Ferrari-Torinelli, G.; Bonini, S.A.; Sarnico, L.; Benarese, M.; Pizzi, M.; Benussi, L.; Ghidoni, R.; Binetti, G.; Spano, P.; et al. Blockade of the Tumor Necrosis Factor-Related Apoptosis Inducing Ligand Death Receptor DR5 Prevents b-Amyloid Neurotoxicity. *Neuropsychopharmacology* **2007**, *32*, 872–880. [[CrossRef](#)] [[PubMed](#)]
38. Lanni, C.; Racchi, M.; Mazzini, G.; Ranzenigo, A.; Polotti, R.; Sinfioriani, E.; Olivari, L.; Barcikowska, M.; Styczynska, M.; Kuznicki, J.; et al. Conformationally altered p53: A novel Alzheimer's disease marker? *Mol. Psychiatry* **2008**, *13*, 641–647. [[CrossRef](#)]
39. Martorana, A. Is dopamine involved in Alzheimer's disease? *Front. Aging Neurosci.* **2014**, *6*, 252. [[CrossRef](#)]
40. Karami, A.; Eyjolfsson, H.; Vijayaraghavan, S.; Lind, G.; Almqvist, P.; Kadir, A.; Linderöth, B.; Andreasen, N.; Blennow, K.; Wall, A.; et al. Changes in CSF cholinergic biomarkers in response to cell therapy with NGF in patients with Alzheimer's disease. *Alzheimer's Dement.* **2015**, *11*, 1316–1328. [[CrossRef](#)]
41. Shin, J.-W.; Kim, K.-J.; Yoon, J.; Jo, J.; El-Said, W.A.; Choi, J.-W. Silver Nanoparticle Modified Electrode Covered by Graphene Oxide for the Enhanced Electrochemical Detection of Dopamine. *Sensors* **2017**, *17*, 2771. [[CrossRef](#)]
42. Lee, E.J.; Choi, J.-H.; Um, S.H.; Oh, B.-K. Electrochemical sensor for selective detection of norepinephrine using graphene sheets-gold nanoparticle complex modified electrode. *Korean J. Chem. Eng.* **2017**, *34*, 1129–1132. [[CrossRef](#)]
43. Chen, Z.; Zhong, C. Oxidative stress in Alzheimer's disease. *Neurosci. Bull.* **2014**, *30*, 271–281. [[CrossRef](#)]
44. Zhao, Y.; Zhao, B. Oxidative Stress and the Pathogenesis of Alzheimer's Disease. *Oxid. Med. Cell. Longev.* **2013**, *2013*, 1–10. [[CrossRef](#)]
45. Qu, F.; Yang, M.; Rasooly, A. Dual Signal Amplification Electrochemical Biosensor for Monitoring the Activity and Inhibition of the Alzheimer's Related Protease  $\beta$ -Secretase. *Anal. Chem.* **2016**, *88*, 10559–10565. [[CrossRef](#)] [[PubMed](#)]
46. Zhu, G.; Lee, H.J. Electrochemical sandwich-type biosensors for  $\alpha$ -1 antitrypsin with carbon nanotubes and alkaline phosphatase labeled antibody-silver nanoparticles. *Biosens. Bioelectron.* **2017**, *89*, 959–963. [[CrossRef](#)] [[PubMed](#)]
47. Eriksson, S.; Janciauskiene, S.; Lannfelt, L. Alpha1-Antichymotrypsin regulates Alzheimer beta-amyloid peptide fibril formation. *Proc. Natl. Acad. Sci. USA* **1995**, *92*, 2313–2317. [[CrossRef](#)] [[PubMed](#)]
48. Serafín, V.; Gamella, M.; Pedrero, M.; Montero-Calle, A.; Razzino, C.A.; Yáñez-Sedeño, P.; Barderas, R.; Campuzano, S.; Pingarrón, J.M. Enlightening the advancements in electrochemical bioanalysis for the diagnosis of Alzheimer's disease and other neurodegenerative disorders. *J. Pharmaceut. Biomed.* **2020**, *189*, 113437. [[CrossRef](#)]
49. Sanguotla, R.; Kim, J. Recent trends in analytical approaches for detecting neurotransmitters in Alzheimer's disease. *TrAC* **2018**, *105*, 240–250. [[CrossRef](#)]
50. Beal, M.F. Oxidative damage as an early marker of Alzheimer's disease and mild cognitive impairment. *Neurobiol. Aging* **2005**, *26*, 585–586. [[CrossRef](#)]
51. Wu, H.Z.Y.; Ong, K.L.; Seeher, K.; Armstrong, N.J.; Thalamuthu, A.; Brodaty, H.; Sachdev, P.; Mather, K. Circulating microRNAs as Biomarkers of Alzheimer's Disease: A Systematic Review. *JAD* **2016**, *49*, 755–766. [[CrossRef](#)]

52. Bekris, L.M.; Lutz, F.; Montine, T.J.; Yu, C.E.; Tsuang, D.; Peskind, E.R.; Leverenz, J.B. MicroRNA in Alzheimer's disease: An exploratory study in brain, cerebrospinal fluid and plasma. *Biomarkers* **2013**, *18*, 455–466. [[CrossRef](#)]
53. Bard, A.J.; Faulkner, L.R. *Electrochemical Methods: Fundamentals and Applications*, 2nd ed.; Wiley: New York, NY, USA, 2001; ISBN 978-0-471-04372-0.
54. Thévenot, D.R.; Toth, K.; Durst, R.D.; Wilson, G.S. Electrochemical biosensors: Recommended definitions and classification. *Pure Appl. Chem.* **1999**, *71*, 2333–2348. [[CrossRef](#)]
55. Goumi, Y.E. Electrochemical Genosensors: Definition and Fields of Application. *Int. J. Biosens.* **2017**, *3*, 353–355. [[CrossRef](#)]
56. Monošík, R.; Stred'anský, M.; Šturdík, E. Biosensors-classification, characterization and new trends. *Acta Chim. Slov.* **2012**, *5*, 109–120. [[CrossRef](#)]
57. Pividori, M. Electrochemical genosensor design: Immobilisation of oligonucleotides onto transducer surfaces and detection methods. *Biosens. Bioelectron.* **2000**, *15*, 291–303. [[CrossRef](#)]
58. Campuzano, S.; Yáñez-Sedeño, P.; Pingarrón, J. Electrochemical Genosensing of Circulating Biomarkers. *Sensors* **2017**, *17*, 866. [[CrossRef](#)] [[PubMed](#)]
59. Bauman, J.G.J.; Weigant, J.; Borst, P.; van Duijn, P. A new method for fluorescence microscopical localization of specific DNA sequences by in situ hybridization of fluorochrome-labelled RNA. *Exp. Cell Res.* **1980**, *128*, 485–490. [[CrossRef](#)]
60. Ellington, A.D.; Szostak, J.W. In vitro selection of RNA molecules that bind specific ligands. *Nature* **1990**, *346*, 818–822. [[CrossRef](#)]
61. Odeh, F.; Nsairat, H.; Alshaer, W.; Ismail, M.A.; Esawi, E.; Qaqish, B.; Bawab, A.A.; Ismail, S.I. Aptamers Chemistry: Chemical Modifications and Conjugation Strategies. *Molecules* **2019**, *25*, 3. [[CrossRef](#)]
62. Anik, Ü. Electrochemical medical biosensors for POC applications. In *Medical Biosensors for Point of Care (POC) Applications*; Elsevier: Amsterdam, The Netherlands, 2017; pp. 275–292. ISBN 978-0-08-100072-4.
63. Carneiro, P.; Morais, S.; Pereira, M.C. Nanomaterials towards Biosensing of Alzheimer's Disease Biomarkers. *Nanomaterials* **2019**, *9*, 1663. [[CrossRef](#)]
64. Hayat, A.; Catanante, G.; Marty, J. Current Trends in Nanomaterial-Based Amperometric Biosens. *Sensors* **2014**, *14*, 23439–23461. [[CrossRef](#)]
65. Holzinger, M.; Le Goff, A.; Cosnier, S. Nanomaterials for biosensing applications: A review. *Front. Chem.* **2014**, *2*, 63. [[CrossRef](#)]
66. Walcarius, A.; Minteer, S.D.; Wang, J.; Lin, Y.; Merkoçi, A. Nanomaterials for bio-functionalized electrodes: Recent trends. *J. Mater. Chem. B* **2013**, *1*, 4878–4908. [[CrossRef](#)]
67. Mansuriya, B.D.; Altintas, Z. Applications of Graphene Quantum Dots in Biomedical Sensors. *Sensors* **2020**, *20*, 1072. [[CrossRef](#)] [[PubMed](#)]
68. Malhotra, B.D.; Ali, M.A. Nanomaterials in Biosensors. In *Nanomaterials for Biosensors*; Elsevier: Amsterdam, The Netherlands, 2018; pp. 1–74. ISBN 978-0-323-44923-6.
69. De la Escosura-Muñiz, A.; Ambrosi, A.; Merkoçi, A. Electrochemical analysis with nanoparticle-based biosystems. *TrAC* **2008**, *27*, 568–584.
70. Liu, G.; Lin, Y. Nanomaterial labels in electrochemical immunosensors and immunoassays. *Talanta* **2007**, *74*, 308–317. [[CrossRef](#)] [[PubMed](#)]
71. Zhang, Y.; Wei, Q. The role of nanomaterials in electroanalytical biosensors: A mini review. *J. Electroanal. Chem.* **2016**, *781*, 401–409. [[CrossRef](#)]
72. Iglesias-Mayor, A.; Amor-Gutiérrez, O.; Costa-García, A.; de la Escosura-Muñiz, A. Nanoparticles as Emerging Labels in Electrochemical Immunosensors. *Sensors* **2019**, *19*, 5137. [[CrossRef](#)]
73. Forlenza, O.V.; Radanovic, M.; Talib, L.L.; Aprahamian, I.; Diniz, B.S.; Zetterberg, H.; Gattaz, W.F. Cerebrospinal fluid biomarkers in Alzheimer's disease: Diagnostic accuracy and prediction of dementia. *Alzheimer's Dement. Diagn. Assess. Dis. Monit.* **2015**, *1*, 455–463. [[CrossRef](#)]
74. Sohrabi, N.; Valizadeh, A.; Farkhani, S.M.; Akbarzadeh, A. Basics of DNA biosensors and cancer diagnosis. *Artif. Cells Nanomed. Biotechnol.* **2016**, *44*, 654–663. [[CrossRef](#)]
75. Crick, F.H.C.; Watson, J.D. The complementary structure of deoxyribonucleic acid. *Proc. Math. Phys. Eng. Sci.* **1954**, *223*, 80–96.

76. Saunders, A.M.; Strittmatter, W.J.; Schmechel, D.; George-Hyslop, P.H.S.; Pericak-Vance, M.A.; Joo, S.H.; Rosi, B.L.; Gusella, J.F.; Crapper-MacLachlan, D.R.; Alberts, M.J.; et al. Association of apolipoprotein E allele E4 with late-onset familial and sporadic Alzheimer's disease. *Neurology* **1993**, *43*, 1467. [[CrossRef](#)]
77. Chen, X.; Ba, Y.; Ma, L.; Cai, X.; Yin, Y.; Wang, K.; Guo, J.; Zhang, Y.; Chen, J.; Guo, X.; et al. Characterization of microRNAs in serum: A novel class of biomarkers for diagnosis of cancer and other diseases. *Cell Res.* **2008**, *18*, 997–1006. [[CrossRef](#)]
78. Bartel, D.P. MicroRNAs: Target Recognition and Regulatory Functions. *Cell* **2009**, *136*, 215–233. [[CrossRef](#)] [[PubMed](#)]
79. Azimzadeh, M.; Rahaie, M.; Nasirizadeh, N.; Daneshpour, M.; Naderi, H. Electrochemical miRNA Biosensors: The Benefits of Nanotechnology. *Nanomed. Res. J.* **2017**, *2*, 36–48.
80. Novoselov, K.S. Electric Field Effect in Atomically Thin Carbon Films. *Science* **2004**, *306*, 666–669. [[CrossRef](#)] [[PubMed](#)]
81. Wang, Y.; Li, Z.; Wang, J.; Li, J.; Lin, Y. Graphene and graphene oxide: Biofunctionalization and applications in biotechnology. *Trends Biotechnol.* **2011**, *29*, 205–212. [[CrossRef](#)]
82. Zhou, M.; Zhai, Y.; Dong, S. Electrochemical Sensing and Biosensing Platform Based on Chemically Reduced Graphene Oxide. *Anal. Chem.* **2009**, *81*, 5603–5613. [[CrossRef](#)]
83. Mars, A.; Hamami, M.; Bechnak, L.; Patra, D.; Raouafi, N. Curcumin-graphene quantum dots for dual mode sensing platform: Electrochemical and fluorescence detection of APOe4, responsible of Alzheimer's disease. *Anal. Chim. Acta* **2018**, *1036*, 141–146. [[CrossRef](#)]
84. Wu, L.; Ji, H.; Sun, H.; Ding, C.; Ren, J.; Qu, X. Label-free ratiometric electrochemical detection of the mutated apolipoprotein E gene associated with Alzheimer's disease. *Chem. Commun.* **2016**, *52*, 12080–12083. [[CrossRef](#)]
85. Peng, F.; Su, Y.; Zhong, Y.; Fan, C.; Lee, S.-T.; He, Y. Silicon Nanomaterials Platform for Bioimaging, Biosensing, and Cancer Therapy. *Acc. Chem. Res.* **2014**, *47*, 612–623. [[CrossRef](#)]
86. Congur, G.; Eksin, E.; Erdem, A. Impedimetric detection of miRNA-34a using graphene oxide modified chemically activated graphite electrodes. *Sens. Actuators A Phys.* **2018**, *279*, 493–500. [[CrossRef](#)]
87. Azimzadeh, M.; Nasirizadeh, N.; Rahaie, M.; Naderi-Manesh, H. Early detection of Alzheimer's disease using a biosensor based on electrochemically-reduced graphene oxide and gold nanowires for the quantification of serum microRNA-137. *RSC Adv.* **2017**, *7*, 55709–55719. [[CrossRef](#)]
88. Zunino, F.; Di Marco, A.; Zaccara, A.; Gambetta, R.A. The interaction of daunorubicin and doxorubicin with DNA and chromatin. *Biochim. Biophys. Acta (BBA)-Nucleic Acids Protein Synth.* **1980**, *607*, 206–214. [[CrossRef](#)]
89. Cheng, X.R.; Hau, B.Y.H.; Endo, T.; Kerman, K. Au nanoparticle-modified DNA sensor based on simultaneous electrochemical impedance spectroscopy and localized surface plasmon resonance. *Biosens. Bioelectron.* **2014**, *53*, 513–518. [[CrossRef](#)] [[PubMed](#)]
90. Lu, H.; Wu, L.; Wang, J.; Wang, Z.; Yi, X.; Wang, J.; Wang, N. Voltammetric determination of the Alzheimer's disease-related ApoE 4 gene from unamplified genomic DNA extracts by ferrocene-capped gold nanoparticles. *Microchim. Acta* **2018**, *185*, 549. [[CrossRef](#)] [[PubMed](#)]
91. Jiang, P.; Wang, Y.; Zhao, L.; Ji, C.; Chen, D.; Nie, L. Applications of Gold Nanoparticles in Non-Optical Biosensors. *Nanomaterials* **2018**, *8*, 977. [[CrossRef](#)]
92. Li, Y.; Schluesener, H.J.; Xu, S. Gold nanoparticle-based biosensors. *Gold Bull.* **2010**, *43*, 29–41. [[CrossRef](#)]
93. Wu, C.-C.; Ku, B.-C.; Ko, C.-H.; Chiu, C.-C.; Wang, G.-J.; Yang, Y.-H.; Wu, S.-J. Electrochemical impedance spectroscopy analysis of A-beta (1–42) peptide using a nanostructured biochip. *Electrochim. Acta* **2014**, *134*, 249–257. [[CrossRef](#)]
94. Carneiro, P.; Loureiro, J.; Delerue-Matos, C.; Morais, S.; do Carmo Pereira, M. Alzheimer's disease: Development of a sensitive label-free electrochemical immunosensor for detection of amyloid beta peptide. *Sensor. Actuat. B Chem.* **2017**, *239*, 157–165. [[CrossRef](#)]
95. Amor-Gutiérrez, O.; Costa-Rama, E.; Arce-Varas, N.; Martínez-Rodríguez, C.; Novelli, A.; Fernández-Sánchez, M.T.; Costa-García, A. Competitive electrochemical immunosensor for the detection of unfolded p53 protein in blood as biomarker for Alzheimer's disease. *Anal. Chim. Acta* **2020**, *1093*, 28–34. [[CrossRef](#)]
96. Rama, E.C.; González-García, M.B.; Costa-García, A. Competitive electrochemical immunosensor for amyloid-beta 1–42 detection based on gold nanostructured Screen-Printed Carbon Electrodes. *Sensor. Actuat. B Chem.* **2014**, *201*, 567–571. [[CrossRef](#)]



97. Diba, F.S.; Kim, S.; Lee, H.J. Electrochemical immunoassay for amyloid-beta 1–42 peptide in biological fluids interfacing with a gold nanoparticle modified carbon surface. *Catal. Today* **2017**, *295*, 41–47. [[CrossRef](#)]
98. Zhou, Y.; Li, C.; Li, X.; Zhu, X.; Ye, B.; Xu, M. A sensitive aptasensor for the detection of  $\beta$ -amyloid oligomers based on metal–organic frameworks as electrochemical signal probes. *Anal. Methods* **2018**, *10*, 4430–4437. [[CrossRef](#)]
99. Lien, T.T.N.; Takamura, Y.; Tamiya, E.; Vestergaard, M.C. Modified screen printed electrode for development of a highly sensitive label-free impedimetric immunosensor to detect amyloid beta peptides. *Anal. Chim. Acta* **2015**, *892*, 69–76. [[CrossRef](#)] [[PubMed](#)]
100. Qin, J.; Cho, M.; Lee, Y. Ultrasensitive Detection of Amyloid- $\beta$  Using Cellular Prion Protein on the Highly Conductive Au Nanoparticles–Poly (3,4-ethylene dioxythiophene)–Poly(thiophene-3-acetic acid) Composite Electrode. *Anal. Chem.* **2019**, *91*, 11259–11265. [[CrossRef](#)]
101. Sethi, J.; Van Bulck, M.; Suhail, A.; Safarzadeh, M.; Perez-Castillo, A.; Pan, G. A label-free biosensor based on graphene and reduced graphene oxide dual-layer for electrochemical determination of beta-amyloid biomarkers. *Microchim. Acta* **2020**, *187*, 288. [[CrossRef](#)] [[PubMed](#)]
102. Moreira, F.T.C.; Rodriguez, B.A.G.; Dutra, R.A.F.; Sales, M.G.F. Redox probe-free readings of a  $\beta$ -amyloid-42 plastic antibody sensory material assembled on copper@carbon nanotubes. *Sensor. Actuat. B Chem.* **2018**, *264*, 1–9. [[CrossRef](#)]
103. Wustoni, S.; Wang, S.; Alvarez, J.R.; Hidalgo, T.C.; Nunes, S.P.; Inal, S. An organic electrochemical transistor integrated with a molecularly selective isoporous membrane for amyloid- $\beta$  detection. *Biosens. Bioelectron.* **2019**, *143*, 111561. [[CrossRef](#)] [[PubMed](#)]
104. Devi, R.; Gogoi, S.; Dutta, H.S.; Bordoloi, M.; Sanghi, S.K.; Khan, R. Au/NiFe<sub>2</sub>O<sub>4</sub> nanoparticle-decorated graphene oxide nanosheets for electrochemical immunosensing of amyloid beta peptide. *Nanoscale Adv.* **2020**, *2*, 239–248. [[CrossRef](#)]
105. Liu, L.; Zhao, F.; Ma, F.; Zhang, L.; Yang, S.; Xia, N. Electrochemical detection of  $\beta$ -amyloid peptides on electrode covered with N-terminus-specific antibody based on electrocatalytic O<sub>2</sub> reduction by A $\beta$ (1–16)-heme-modified gold nanoparticles. *Biosens. Bioelectron.* **2013**, *49*, 231–235. [[CrossRef](#)]
106. Yoo, Y.K.; Kim, G.; Park, D.; Kim, J.; Kim, Y.; Yun Kim, H.; Yang, S.H.; Lee, J.H.; Hwang, K.S. Gold nanoparticles assisted sensitivity improvement of interdigitated microelectrodes biosensor for amyloid- $\beta$  detection in plasma sample. *Sensor. Actuat. B Chem.* **2020**, *308*, 127710. [[CrossRef](#)]
107. Iglesias-Mayor, A.; Amor-Gutiérrez, O.; Novelli, A.; Fernández-Sánchez, M.-T.; Costa-García, A.; de la Escosura-Muñiz, A. Bifunctional Au@Pt/Au core@shell Nanoparticles As Novel Electrocatalytic Tags in Immunosensing: Application for Alzheimer’s Disease Biomarker Detection. *Anal. Chem.* **2020**, *92*, 7209–7217. [[CrossRef](#)]
108. Zhou, Y.; Zhang, H.; Liu, L.; Li, C.; Chang, Z.; Zhu, X.; Ye, B.; Xu, M. Fabrication of an antibody-aptamer sandwich assay for electrochemical evaluation of levels of  $\beta$ -amyloid oligomers. *Sci. Rep.* **2016**, *6*, 35186. [[CrossRef](#)] [[PubMed](#)]
109. Yu, Y.; Sun, X.; Tang, D.; Li, C.; Zhang, L.; Nie, D.; Yin, X.; Shi, G. Gelsolin bound  $\beta$ -amyloid peptides (1–40/1–42): Electrochemical evaluation of levels of soluble peptide associated with Alzheimer’s disease. *Biosens. Bioelectron.* **2015**, *68*, 115–121. [[CrossRef](#)] [[PubMed](#)]
110. Ding, S.; Xu, Y.; Llu, Q.; Gu, H.; Zhu, X.; Shi, G. Interface engineering of microelectrodes toward ultrasensitive monitoring of  $\beta$ -amyloid peptides in cerebrospinal fluid in Alzheimer’s disease. *Analyst* **2020**, *145*, 2331–2338. [[CrossRef](#)] [[PubMed](#)]
111. Xia, N.; Wang, X.; Yu, J.; Wu, Y.; Cheng, S.; Xing, Y.; Liu, L. Design of electrochemical biosensors with peptide probes as the receptors of targets and the inducers of gold nanoparticles assembly on electrode surface. *Sensor. Actuat. B Chem.* **2017**, *239*, 834–840. [[CrossRef](#)]
112. Xia, N.; Wang, X.; Zhou, B.; Wu, Y.; Mao, W.; Liu, L. Electrochemical Detection of Amyloid- $\beta$  Oligomers Based on the Signal Amplification of a Network of Silver Nanoparticles. *ACS Appl. Mater. Interfaces* **2016**, *8*, 19303–19311. [[CrossRef](#)]
113. You, M.; Yang, S.; An, Y.; Zhang, F.; He, P. A novel electrochemical biosensor with molecularly imprinted polymers and aptamer-based sandwich assay for determining amyloid- $\beta$  oligomer. *J. Electroanal. Chem.* **2020**, *862*, 114017. [[CrossRef](#)]

114. Qin, J.; Cho, M.; Lee, Y. Ferrocene-Encapsulated Zn Zeolitic Imidazole Framework (ZIF-8) for Optical and Electrochemical Sensing of Amyloid- $\beta$  Oligomers and for the Early Diagnosis of Alzheimer's Disease. *ACS Appl. Mater. Interfaces* **2019**, *11*, 11743–11748. [[CrossRef](#)]
115. Rogers, K.R. Principles of affinity-based biosensors. *Mol. Biotechnol.* **2000**, *14*, 109–129. [[CrossRef](#)]
116. Grönwall, C.; Ståhl, S. Engineered affinity proteins—Generation and applications. *J. Biotechnol.* **2009**, *140*, 254–269. [[CrossRef](#)]
117. Gunther, E.C.; Strittmatter, S.M.  $\beta$ -amyloid oligomers and cellular prion protein in Alzheimer's disease. *J. Mol. Med.* **2010**, *88*, 331–338. [[CrossRef](#)]
118. Radushkevich, L.V.; Lukyanovich, V.M. The structure of carbon forming in thermal decomposition of carbon monoxide on an iron catalyst. *Russ. J. Phys. Chem.* **1952**, *26*, 88–95.
119. Herlem, G.; Picaud, F.; Girardet, C.; Micheau, O. Carbon Nanotubes: Synthesis, Characterization, and Applications in Drug-Delivery Systems. In *Nanocarriers for Drug Delivery. Nanoscience and Nanotechnology in Drug Delivery. A Volume in Micro and Nano Technologies*; Elsevier: Amsterdam, The Netherlands, 2019; pp. 469–529. ISBN 978-0-12-814033-8.
120. Tîlmaciu, C.-M.; Morris, M.C. Carbon nanotube biosensors. *Front. Chem.* **2015**, *3*, 59. [[CrossRef](#)] [[PubMed](#)]
121. Scriba, G.K.E. Chiral recognition in separation science—an update. *J. Chromatogr. A* **2016**, *1467*, 56–78. [[CrossRef](#)] [[PubMed](#)]
122. Hillberg, A.; Brain, K.; Allender, C. Molecular imprinted polymer sensors: Implications for therapeutics. *Adv. Drug Deliv. Rev.* **2005**, *57*, 1875–1889. [[CrossRef](#)] [[PubMed](#)]
123. Moreira, F.T.C.; Sales, M.G.F. Smart naturally plastic antibody based on poly ( $\alpha$ -cyclodextrin) polymer for  $\beta$ -amyloid-42 soluble oligomer detection. *Sensor. Actuat. B Chem.* **2017**, *240*, 229–238. [[CrossRef](#)]
124. Vendamme, R.; Onoue, S.-Y.; Nakao, A.; Kunitake, T. Robust free-standing nanomembranes of organic/inorganic interpenetrating networks. *Nat. Mater.* **2006**, *5*, 494–501. [[CrossRef](#)]
125. Agboola, O.; Sadiku, E.R.; Mokrani, T. Nanomembrane Materials Based on Polymer Blends. In *Design and Applications of Nanostructured Polymer Blends and Nanocomposite Systems*; Elsevier: Amsterdam, The Netherlands, 2016; pp. 101–123. ISBN 978-0-323-39408-6.
126. Jakšić, Z.; Matovic, J. Functionalization of Artificial Freestanding Composite Nanomembranes. *Materials* **2010**, *3*, 165–200. [[CrossRef](#)]
127. Rivnay, J.; Inal, S.; Salleo, A.; Owens, R.M.; Berggren, M.; Malliaras, G.G. Organic electrochemical transistors. *Nat. Rev. Mater.* **2018**, *3*, 17086. [[CrossRef](#)]
128. Singh, P.; Rathore, D. A biosensor system using nickel ferrite nanoparticles. *AIP Conf. Proc.* **2016**, *1728*, 020259.
129. Rocha-Santos, T.A.P. Sensors and biosensors based on magnetic nanoparticles. *TrAC* **2014**, *62*, 28–36. [[CrossRef](#)]
130. Pansieri, J.; Gerstenmayer, M.; Lux, F.; Mériaux, S.; Tillement, O.; Forge, V.; Larrat, B.; Marquette, C. Magnetic Nanoparticles Applications for Amyloidosis Study and Detection: A Review. *Nanomaterials* **2018**, *8*, 740. [[CrossRef](#)] [[PubMed](#)]
131. Seo, H.B.; Gu, M.B. Aptamer-based sandwich-type biosensors. *J. Biol. Eng.* **2017**, *11*, 11. [[CrossRef](#)] [[PubMed](#)]
132. Chauhan, V.P.S.; Ray, I.; Chauhan, A.; Wisniewski, H.M. Binding of Gelsolin, a Secretory Protein, to Amyloid Protein. *Biochem. Biophys. Res. Commun.* **1999**, *258*, 241–246. [[CrossRef](#)] [[PubMed](#)]
133. Li, H.; Xu, D. Silver nanoparticles as labels for applications in bioassays. *TrAC* **2014**, *61*, 67–73. [[CrossRef](#)]
134. Yaghi, O.M.; O'Keeffe, M.; Ockwig, N.W.; Chae, H.K.; Eddaoudi, M.; Kim, J. Reticular synthesis and the design of new materials. *Nature* **2003**, *423*, 705–714. [[CrossRef](#)]
135. Wang, S.; McGuirk, C.M.; d'Aquino, A.; Mason, J.A.; Mirkin, C.A. Metal-Organic Framework Nanoparticles. *Adv. Mater.* **2018**, *30*, 1800202. [[CrossRef](#)] [[PubMed](#)]
136. Sakata, Y.; Furukawa, S.; Kondo, M.; Hirai, K.; Horike, N.; Takashima, Y.; Uehara, H.; Louvain, N.; Meilikhov, M.; Tsuruoka, T.; et al. Shape-Memory Nanopores Induced in Coordination Frameworks by Crystal Downsizing. *Science* **2013**, *339*, 193–196. [[CrossRef](#)]
137. Zhao, F.; Geng, F.; Chen, P.; Gao, Y. Metal-Organic Frameworks-Based Electrochemical Sensors and Biosensors. *Int. J. Electrochem. Sci.* **2019**, *14*, 5287–5304. [[CrossRef](#)]
138. Doherty, C.M.; Buso, D.; Hill, A.J.; Furukawa, S.; Kitagawa, S.; Falcaro, P. Using Functional Nano- and Microparticles for the Preparation of Metal–Organic Framework Composites with Novel Properties. *Acc. Chem. Res.* **2014**, *47*, 396–405. [[CrossRef](#)]

139. Liu, Y.; Xu, L.-P.; Wang, S.; Yang, W.; Wen, Y.; Zhang, X. An ultrasensitive electrochemical immunosensor for apolipoprotein E4 based on fractal nanostructures and enzyme amplification. *Biosens. Bioelectron.* **2015**, *71*, 396–400. [[CrossRef](#)]
140. Liu, Y.; He, G.; Liu, H.; Yin, H.; Gao, F.; Chen, J.; Zhang, S.; Yang, B. Electrochemical immunosensor based on AuBP@Pt nanostructure and AuPd-PDA nanozyme for ultrasensitive detection of APOE4. *RSC Adv.* **2020**, *10*, 7912–7917. [[CrossRef](#)]
141. Negahdary, M.; Heli, H. An ultrasensitive electrochemical aptasensor for early diagnosis of Alzheimer's disease, using a fern leaves-like gold nanostructure. *Talanta* **2019**, *198*, 510–517. [[CrossRef](#)] [[PubMed](#)]
142. Negahdary, M.; Heli, H. An electrochemical peptide-based biosensor for the Alzheimer biomarker amyloid- $\beta$  (1–42) using a microporous gold nanostructure. *Microchim. Acta* **2019**, *186*, 766. [[CrossRef](#)] [[PubMed](#)]
143. Hang, J.; Zhang, M.; Chen, G.; Zhang, Y.; Wei, Q.; Zhuo, Y.; Xie, G.; Yuan, R.; Chen, S. Ferrocene covalent-confined in porous MOF as signal tags for highly sensitive electrochemical immunoassay of amyloid- $\beta$ . *J. Mater. Chem. B* **2017**, *5*, 8330–8336.
144. Razzino, C.A.; Serafín, V.; Gamella, M.; Pedrero, M.; Montero-Calle, A.; Barderas, R.; Calero, M.; Lobo, A.O.; Yáñez-Sedeño, P.; Campuzano, S.; et al. An electrochemical immunosensor using gold nanoparticles-PAMAM-nanostructured screen-printed carbon electrodes for tau protein determination in plasma and brain tissues from Alzheimer patients. *Biosens. Bioelectron.* **2020**, *163*, 112238. [[CrossRef](#)]
145. Özcan, N.; Medetalibeyoglu, H.; Akyıldırım, O.; Atar, N.; Yola, M.L. Electrochemical detection of amyloid- $\beta$  protein by delaminated titanium carbide MXene/multi-walled carbon nanotubes composite with molecularly imprinted polymer. *Mater. Today Commun.* **2020**, *23*, 101097. [[CrossRef](#)]
146. Naguib, M.; Mashtalir, O.; Carle, J.; Presser, V.; Lu, J.; Hultman, L.; Gogotsi, Y.; Barsoum, M.W. Two-Dimensional Transition Metal Carbides. *ACS Nano* **2012**, *6*, 1322–1331. [[CrossRef](#)]
147. Li, X.; Jiang, M.; Cheng, J.; Ye, M.; Zhang, W.; Jaffrezic-Renault, N.; Guo, Z. Signal multi-amplified electrochemical biosensor for voltammetric determination of tau-441 protein in biological samples using carbon nanomaterials and gold nanoparticles to hint dementia. *Microchim. Acta* **2020**, *187*, 302. [[CrossRef](#)]
148. Tao, D.; Shui, B.; Gu, Y.; Cheng, J.; Zhang, W.; Jaffrezic-Renault, N.; Song, S.; Guo, Z. Development of a Label-Free Electrochemical Aptasensor for the Detection of Tau381 and its Preliminary Application in AD and Non-AD Patients' Sera. *Biosensors* **2019**, *9*, 84. [[CrossRef](#)]
149. Wai, J.L.; New, S.Y. Cysteamine-coated gold nanoparticles for bimodal colorimetric detection with inverse sensitivity: A proof-of-concept with lysozyme. *RSC Adv.* **2020**, *10*, 1088–1094. [[CrossRef](#)]
150. Charbgo, F.; Ramezani, M.; Darroudi, M. Bio-sensing applications of cerium oxide nanoparticles: Advantages and disadvantages. *Biosens. Bioelectron.* **2017**, *96*, 33–43. [[CrossRef](#)] [[PubMed](#)]
151. Solanki, P.R.; Kaushik, A.; Agrawal, V.V.; Malhotra, B.D. Nanostructured metal oxide-based biosensors. *NPG Asia Mater.* **2011**, *3*, 17–24. [[CrossRef](#)]
152. Gao, Z.; Li, Y.; Zhang, C.; Zhang, S.; Jia, Y.; Li, F.; Ding, H.; Li, X.; Chen, Z.; Wei, Q. AuCu<sub>x</sub>O-Embedded Mesoporous CeO<sub>2</sub> Nanocomposites as a Signal Probe for Electrochemical Sensitive Detection of Amyloid-Beta Protein. *ACS Appl. Mater. Interfaces* **2019**, *11*, 12335–12341. [[CrossRef](#)] [[PubMed](#)]
153. Díaz-González, M.; de la Escosura-Muñiz, A.; Fernandez-Argüelles, M.T.; García Alonso, F.J.; Costa-Fernandez, J.M. Quantum Dot Bioconjugates for Diagnostic Applications. *Top. Curr. Chem. Z* **2020**, *378*, 1–44. [[CrossRef](#)] [[PubMed](#)]
154. Medina-Sánchez, M.; Miserere, S.; Morales-Narváez, E.; Merkoçi, A. On-chip magneto-immunoassay for Alzheimer's biomarker electrochemical detection by using quantum dots as labels. *Biosens. Bioelectron.* **2014**, *54*, 279–284. [[CrossRef](#)]
155. Hara, M.; Mallouk, T.E. Photocatalytic water oxidation by Nafion-stabilized iridium oxide colloids. *Chem. Commun.* **2000**, 1903–1904. [[CrossRef](#)]
156. Finkelstein-Shapiro, D.; Fournier, M.; Méndez-Hernández, D.D.; Guo, C.; Calatayud, M.; Moore, T.A.; Moore, A.L.; Gust, D.; Yarger, J.L. Understanding iridium oxide nanoparticle surface sites by their interaction with catechol. *Phys. Chem. Chem. Phys.* **2017**, *19*, 16151–16158. [[CrossRef](#)]
157. Quesada-González, D.; Baiocco, A.; Martos, A.A.; de la Escosura-Muñiz, A.; Palleschi, G.; Merkoçi, A. Iridium oxide (IV) nanoparticle-based electrocatalytic detection of PBDE. *Biosens. Bioelectron.* **2019**, *127*, 150–154. [[CrossRef](#)]



158. Rivas, L.; de la Escosura-Muñiz, A.; Pons, J.; Merkoçi, A. Alzheimer Disease Biomarker Detection Through Electrocatalytic Water Oxidation Induced by Iridium Oxide Nanoparticles. *Electroanalysis* **2014**, *26*, 1287–1294. [[CrossRef](#)]
159. Kandimalla, R.; Reddy, P.H. Therapeutics of Neurotransmitters in Alzheimer's Disease. *J. Alzheimers Dis.* **2017**, *57*, 1049–1069. [[CrossRef](#)]
160. Hughes, G.; Pemberton, R.M.; Fielden, P.R.; Hart, J.P. The design, development and application of electrochemical glutamate biosensors. *TrAC* **2016**, *79*, 106–113. [[CrossRef](#)]
161. Kwong, A.W.K.; Gründig, B.; Hu, J.; Renneberg, R. Comparative study of hydrogel-immobilized l-glutamate oxidases for a novel thick-film biosensor and its application in food samples. *Biotechnol. Lett.* **2000**, *22*, 267–272. [[CrossRef](#)]
162. Choo, S.-S.; Kang, E.-S.; Song, I.; Lee, D.; Choi, J.-W.; Kim, T.-H. Electrochemical Detection of Dopamine Using 3D Porous Graphene Oxide/Gold Nanoparticle Composites. *Sensors* **2017**, *17*, 861. [[CrossRef](#)] [[PubMed](#)]
163. Wang, C.; Li, J.; Shi, K.; Wang, Q.; Zhao, X.; Xiong, Z.; Zou, X.; Wang, Y. Graphene coated by polydopamine/multi-walled carbon nanotubes modified electrode for highly selective detection of dopamine and uric acid in the presence of ascorbic acid. *J. Electroanal. Chem.* **2016**, *770*, 56–61. [[CrossRef](#)]
164. Deletioğlu, D.; Hasdemir, E.; O Solak, A. Simultaneous Determination of Dopamine and Uric Acid in the Presence of Ascorbic Acid at the Indole-3-Carboxaldehyde Modified Glassy Carbon Electrode. *Curr. Anal. Chem.* **2010**, *6*, 203–208. [[CrossRef](#)]
165. Park, D.-J.; Choi, J.-H.; Lee, W.-J.; Um, S.H.; Oh, B.-K. Selective Electrochemical Detection of Dopamine Using Reduced Graphene Oxide Sheets-Gold Nanoparticles Modified Electrode. *J. Nanosci. Nanotechnol.* **2017**, *17*, 8012–8018. [[CrossRef](#)]
166. Van der Zee, E.A.; Luiten, P.G.M. Muscarinic acetylcholine receptors in the hippocampus, neocortex and amygdala: A review of immunocytochemical localization in relation to learning and memory. *Prog. Neurobiol.* **1999**, *58*, 409–471. [[CrossRef](#)]
167. Da Silva, W.; Brett, C.M.A. Novel biosensor for acetylcholine based on acetylcholinesterase/poly(neutral red)–Deep eutectic solvent/Fe<sub>2</sub>O<sub>3</sub> nanoparticle modified electrode. *J. Electroanal. Chem.* **2020**, *862*, 114050. [[CrossRef](#)]
168. Yi, X.; Wu, Y.; Tan, G.; Yu, P.; Zhou, L.; Zhou, Z.; Chen, J.; Wang, Z.; Pang, J.; Ning, C. Palladium nanoparticles entrapped in a self-supporting nanoporous gold wire as sensitive dopamine biosensor. *Sci. Rep.* **2017**, *7*, 7941. [[CrossRef](#)]
169. Chauhan, N.; Pundir, C.S. Amperometric determination of acetylcholine—A neurotransmitter, by chitosan/gold-coated ferric oxide nanoparticles modified gold electrode. *Biosens. Bioelectron.* **2014**, *61*, 1–8. [[CrossRef](#)]
170. Chauhan, N.; Chawla, S.; Pundir, C.S.; Jain, U. An electrochemical sensor for detection of neurotransmitter-acetylcholine using metal nanoparticles, 2D material and conducting polymer modified electrode. *Biosens. Bioelectron.* **2017**, *89*, 377–383. [[CrossRef](#)] [[PubMed](#)]
171. Nunomura, A.; Castellani, R.J.; Zhu, X.; Moreira, P.I.; Perry, G.; Smith, M.A. Involvement of Oxidative Stress in Alzheimer Disease. *J. Neuropathol. Exp. Neurol.* **2006**, *65*, 631–641. [[CrossRef](#)] [[PubMed](#)]
172. Wang, L.; Zhang, Y.; Cheng, C.; Liu, X.; Jiang, H.; Wang, X. Highly Sensitive Electrochemical Biosensor for Evaluation of Oxidative Stress Based on the Nanointerface of Graphene Nanocomposites Blended with Gold, Fe<sub>3</sub>O<sub>4</sub>, and Platinum Nanoparticles. *ACS Appl. Mater. Interfaces* **2015**, *7*, 18441–18449. [[CrossRef](#)] [[PubMed](#)]
173. Sekar, N.K.; Gumpu, M.B.; Ramachandra, B.L.; Nesakumar, N.; Sankar, P.; Babu, K.J.; Krishnan, U.M.; Rayappan, J.B.B. Fabrication of Electrochemical Biosensor with ZnO-PVA Nanocomposite Interface for the Detection of Hydrogen Peroxide. *J. Nanosci. Nanotechnol.* **2018**, *18*, 4371–4379. [[CrossRef](#)]
174. Bai, J.; Jiang, X. A Facile One-Pot Synthesis of Copper Sulfide-Decorated Reduced Graphene Oxide Composites for Enhanced Detecting of H<sub>2</sub>O<sub>2</sub> in Biological Environments. *Anal. Chem.* **2013**, *85*, 8095–8101. [[CrossRef](#)]
175. Neal, C.J.; Gupta, A.; Barkam, S.; Saraf, S.; Das, S.; Cho, H.J.; Seal, S. Picomolar Detection of Hydrogen Peroxide using Enzyme-free Inorganic Nanoparticle-based Sensor. *Sci. Rep.* **2017**, *7*, 1–10. [[CrossRef](#)]
176. Peng, Q.; Yan, X.; Shi, X.; Ou, S.; Gu, H.; Yin, X.; Shi, G.; Yu, Y. In vivo monitoring of superoxide anion from Alzheimer's rat brains with functionalized ionic liquid polymer decorated microsensor. *Biosens. Bioelectron.* **2019**, *144*, 111665. [[CrossRef](#)]
177. Iqbal, K.; Grundke-Iqbal, I. Alzheimer's disease, a multifactorial disorder seeking multitherapies. *Alzheimers Dement.* **2010**, *6*, 420–424. [[CrossRef](#)]

178. De la Escosura-Muñiz, A.; Plichta, Z.; Horák, D.; Merkoçi, A. Alzheimer's disease biomarkers detection in human samples by efficient capturing through porous magnetic microspheres and labelling with electrocatalytic gold nanoparticles. *Biosens. Bioelectron.* **2015**, *67*, 162–169. [[CrossRef](#)]
179. Serafín, V.; Razzino, C.A.; Gamella, M.; Pedrero, M.; Povedano, E.; Montero-Calle, A.; Barderas, R.; Calero, M.; Lobo, A.O.; Yáñez-Sedeño, P.; et al. Disposable immunoplatfroms for the simultaneous determination of biomarkers for neurodegenerative disorders using poly(amidoamine) dendrimer/gold nanoparticle nanocomposite. *Anal. Bioanal. Chem.* **2020**. [[CrossRef](#)]
180. Chang, X.-L.; Tan, M.-S.; Tan, L.; Yu, J.-T. The Role of TDP-43 in Alzheimer's Disease. *Mol. Neurobiol.* **2016**, *53*, 3349–3359. [[CrossRef](#)] [[PubMed](#)]
181. Yu, Y.; Wang, P.; Zhu, X.; Peng, Q.; Zhou, Y.; Yin, T.; Liang, Y.; Yin, X. Combined determination of copper ion and  $\beta$ -amyloid peptide by a single ratiometric electrochemical biosensor. *Analyst* **2018**, *143*, 323–331. [[CrossRef](#)] [[PubMed](#)]
182. Yu, Y.; Yin, T.; Peng, Q.; Kong, L.; Li, C.; Tang, D.; Yin, X. Simultaneous Monitoring of Amyloid- $\beta$  ( $A\beta$ ) Oligomers and Fibrils for Effectively Evaluating the Dynamic Process of  $A\beta$  Aggregation. *ACS Sens.* **2019**, *4*, 471–478. [[CrossRef](#)] [[PubMed](#)]
183. Song, Y.; Xu, T.; Zhu, Q.; Zhang, X. Integrated individually electrochemical array for simultaneously detecting multiple Alzheimer's biomarkers. *Biosens. Bioelectron.* **2020**, *162*, 112253. [[CrossRef](#)]



© 2020 by the authors. Licensee MDPI, Basel, Switzerland. This article is an open access article distributed under the terms and conditions of the Creative Commons Attribution (CC BY) license (<http://creativecommons.org/licenses/by/4.0/>).



# Advances in the screening of antimicrobial compounds using electrochemical biosensors: is there room for nanomaterials?

Celia Toyos-Rodríguez<sup>1,2</sup> · David Valero-Calvo<sup>1,2</sup> · Alfredo de la Escosura-Muñoz<sup>1,2</sup>

Received: 30 September 2022 / Revised: 11 November 2022 / Accepted: 17 November 2022 / Published online: 29 November 2022  
© Springer-Verlag GmbH Germany, part of Springer Nature 2022

## Abstract

The abusive use of antimicrobial compounds and the associated appearance of antimicrobial resistant strains are a major threat to human health. An improved antimicrobial administration involves a faster diagnosis and detection of resistances. Antimicrobial susceptibility testing (AST) are the reference techniques for this purpose, relying mainly in the use of culture techniques. The long time required for analysis and the lack of reproducibility of these techniques have fostered the development of high-throughput AST methods, including electrochemical biosensors. In this review, recent electrochemical methods used in AST have been revised, with particular attention on those used for the evaluation of new drug candidates. The role of nanomaterials in these biosensing platforms has also been questioned, inferring that it is of minor importance compared to other applications.

**Keywords** Electrochemical biosensors · Antimicrobial compounds · Antimicrobial susceptibility testing (AST) · Nanomaterials · Screening methods

## Introduction

The abuse in the use of antibiotic treatments both in the livestock and agricultural sectors and in human healthcare, together with a deficient treatment of antibiotic waste, has enhanced the problem of antimicrobial resistance (AMR) [1, 2]. This worldwide challenge translates into an increase in the minimal inhibitory concentrations (MIC) bacteria could tolerate, leading to an enlarged mortality and morbidity due to the prevalence of AMR superbugs. According to the European Centre for Disease Prevention and Control (ECDC), each year, more than 670,000 infections are initiated by AMR bacteria, leading to the death of over 33,000 person each year just in the European Union/European Economic

Area [3] and around 700,000 worldwide. Without action, this value is expected to increase to over 10 million deaths per year by 2050 [4].

The current pandemic situation due to the SARS-CoV-2 (COVID-19 disease) has required the use of antibiotics as co-adjuvant treatments to stop more severe symptoms of this disease, what has just aggravated the AMR problem [5–8].

Resistance of bacteria against traditional antibiotic treatments (e.g., broad-spectrum  $\beta$ -lactam antibiotics) is generated by two main genetic mechanisms: gene mutations and horizontal gene transfer [9]. These mechanisms lead to the production of enzymes or modification in the bacteria characteristics that do not allow drug penetration, modify the antimicrobial target, or generate global changes in metabolic pathways. Hydrolytic extensive spectrum  $\beta$ -lactamase enzyme is an example of these resistance mechanisms. By hydrolyzing the  $\beta$ -lactam ring of the broad-spectrum  $\beta$ -lactam antibiotics, bacteria inhibit antibiotic effect by avoiding the incorporation of the  $\beta$ -lactam ring to bacteria cell walls through penicillin-binding proteins (PBPs), thus stopping the mechanism of action of these drugs, avoiding bacteria growth [10].

Developing resistance mechanisms is the expected consequence of the remarkable genetic plasticity of bacteria and the co-evolution of bacteria and antimicrobial compounds present in nature. However, the misuse of clinical antibiotic

---

Published in the topical collection *Electrochemical Biosensors – Driving Personalized Medicine* with guest editors Susana Campuzano Ruiz and Maria Jesus Lobo-Castañón.

---

✉ Alfredo de la Escosura-Muñoz  
alfredo.escosura@uniovi.es

<sup>1</sup> NanoBioAnalysis Group, Department of Physical and Analytical Chemistry, University of Oviedo, Julián Clavería 8, 33006 Oviedo, Spain

<sup>2</sup> Biotechnology Institute of Asturias, University of Oviedo, Santiago Gascon Building, 33006 Oviedo, Spain

treatments since their discovery has favored the scaling up of acquired resistance.

But, although bacteria adaptability to antibiotics is an aspect we could not modulate, there are two features on antibiotic usage in which mankind could definitively make things better. Antibiotic release to the environment is one of them [11]. Through human and domestic animal excretion, production or excess drug waste handling, or direct rivers and sea contamination, antibiotics reach the environment, favoring environmental selection [12–16]. A proper identification of contaminated environments by antibiotics is fundamental to address this problem, and in this sense, biosensing approaches, specially electrochemical biosensors, have been deeply studied as useful tools for point-of-care, rapid, and low-cost detection of antibiotics in complex samples [17–19].

However, even antibiotic detection in complex environmental samples is helpful, what it is really a challenge is to provide valuable knowledge on both the effect and the dose required of antimicrobial compounds to fight infection. Antibiotic screening approaches are used in this sense, and in this field of research, electrochemical biosensors have also played their role. However, their use specially for screening new antibiotic compounds is far to be completely exploited.

In this review, a revision onto the electrochemically based antibiotic screening methods has been done, focusing on personalize medicine and those that have potential as screening platforms for new antibiotic development. A special consideration will have electrochemical sensors incorporating nanomaterials, which purpose and need will be critically evaluated.

## Antibiotic screening in the clinical practice

Antibiotic screening is divided in two purposes, the selection of suitable treatments for antimicrobial resistant organisms and the identification of new antibiotic compounds. The first one has extended application in the clinical practice and relies on the use of antimicrobial susceptibility testing (AST). AST is defined as the identification of the susceptibility of a microorganism against a determined drug to search for resistance and provide information on the suitability of a treatment [20]. The use of AST is intended to warrant that antibiotics are prescribed properly and to construct patterned roadmaps of the antimicrobial resistant organisms present in a local area [21]. AST methods are standardized by the European Committee on Antimicrobial Susceptibility Testing (EUCAST) and the Clinical Laboratory Standards Institute (CLSI), being necessary for a new AST method to be tested against standardized ones to be validated [22].

Main AST techniques are based on bacterial growth in solid or liquid media and rely on the diffusion or dilution of

antibiotics across the media [23]. From diffusion test, disk diffusion method is the gold standard technique used in clinical microbiology laboratories. This test consists in placing a permeable disk impregnated with antibiotics on top of an agar plate seeded with the bacteria wanted to be tested [24]. After overnight inoculation, a bright clear ring is formed around the disk if the antibiotic is effective, being the diameter directly related to the bacteria susceptibility against the compound. However, a direct quantification of the MIC is just suitable for certain types of bacteria and antibiotics and implies the use of complex algorithms [25]. Differentiation between bactericidal (kills the bacteria) and bacteriostatic (suppresses the growth) effect is not possible also, as only growth inhibition is recorded [26]. Although this method is simple and cost-effective, the time required and the lack of information make it clearly improvable. However, it is still the reference technique not only in a clinical scenario but also in drug discovery [27–29].

Dilution methods in contrast are the more reliable techniques for MIC determination. Both in agar and in broth, the method consists in adding increasing and known concentrations of antibiotic to a fix concentration of inoculum, thus considering as the MIC the lowest concentration at which growth is completely inhibited by naked eye [30]. Although the simplicity of the method allows its use as antimicrobial screening platform, the irreproducibility of this quantification approach has led to a deep research on visual and colorimetric techniques that allow a more accurate MIC quantification, especially in broth dilution methods [31–34].

A combination of agar dilution and disk diffusion known as the antimicrobial gradient method is commercially available under the name Etest® and allows to determine the MIC of a compound using diffusion techniques. By impregnating a strip with different concentrations of an antimicrobial compound, the MIC could be extrapolated, in an easy-to-use approach that combines the simplicity of disk diffusion and the quantification of agar dilution. However, the cost per strip (between \$2 and 3) makes their use as screening platform less cost-effective [23, 35].

Another drawback of the currently available AST methods is the lack of appropriateness for complex human samples such as blood. In this sense, EUCAST has recently moved research closer to a solution by developing a rapid antimicrobial susceptibility testing (RAST) able to detect infections in the bloodstream [36].

Moreover, four automatized equipment for AST are also approved by the FDA and available in the market: VITEK2 (bioMérieux), MicroScan WalkAway (Siemens Healthcare Diagnostics), BD Phoenix (BD Diagnostics), and Sensititre ARIS 2× (Trek Diagnostic Systems). All of them require between 3.5 and 16 h for giving a result, apart from the time needed for pre-incubating the samples, which could last between 24 and 48 h [37].

But the use of AST methods is not limited to the identification of resistance and suitable treatments in a clinical scenario. They are also powerful tools to help in the development of alternative antibiotic compounds to substitute traditional ones, a real challenge that has been scarcely dealt. With only 43 new antibiotic compounds in development, a value that is comparably reduced considering the more than 4000 immuno-oncology drugs being researched [38], antibiotic development is the problem that pharmaceutical industry is trying to avoid. The high cost of development and reduced revenue of antibiotic commercialization has made big pharmaceutical industries leave the antibiotic development race, with only 4 top companies still in the lead.

Approximately, 45% of the costs associated to antibiotic development are expended in preclinical stages, also the more risky ones [39]. Novel approximations to faster antimicrobial development pipeline have emerged to help reduce the cost associated to these initial steps. This is the case of artificial intelligence (AI), a resource deeply needed for going through the more than  $10^{30}$  drug-like compounds that it is estimated that still could be discovered [40, 41]. But once synthetically discovered, the efficacy of the compounds must be evaluated, for what AST are the preferred choice. However, although there is a deep investigation on new natural and synthetic antimicrobial compounds, the need to modify the characteristic of AST assays (e.g., inoculum size, medium, and growth conditions) to achieve a proper result hinders comparison between different research works [23].

## Antibiotic screening through electrochemical means

The limitations of the traditional AST methods, such as the long time required or the standardization, have prompted the development of alternative screening methods that allow not only to identify resistant bacteria but also to serve as platform for new drug screening.

Sensors and biosensors have stood out due to their specificity, rapid response, easy to use, portability, low cost, and suitability as point-of-care (POC) devices [42]. Biosensors are formed by two main components: a versatile recognition element (e.g., antibodies and aptamers) and the transducer that detects the recognition event and converts it in a measurable signal (e.g., electrochemical, magnetic, surface plasmon resonance, and optical) [43]. Electrochemical transduction systems have gained attention due to their simplicity, affordability, and portability, bringing POC testing to a reality [44].

Their usefulness as simple platforms have been applied to several applications including AST, ranging from the use of different types of electrodes to a variety of electrochemical techniques (Table 1). The choice of a direct or indirect

detection approach for bacteria cell viability testing is one of the points that differentiate the electrochemical AST methods developed until this moment. The evaluation of AST methods in complex samples has been pointed out in those works intended to be used for resistance detection, although many works meant to be used as antibiotic screening platforms do not consider this parameter.

## Electrochemical AST methods using redox dye labels

The use of redox active dye labels to provide an indirect analytical signal has been extensive in electrochemical sensing, including, unsurprisingly, AST sensors.

Using a conventional three-electrode setup, fluorescein diacetate was used as a label [45] to evaluate the susceptibility of *E. coli* against penicillin and streptomycin. In the presence of active bacteria, fluorescein diacetate is hydrolysed by the enzymes secreted by *E. coli*. The oxidation of this product is monitored through voltammetric scans, being an increase in the current associated to an increase in the bacteria growth.

Using a conventional three-electrode setup, Mishra et al. [46] presented a fast-screening method to evaluate the response of bacteria to antibiotics. Using a Pt modified glass substrate as working electrode, they measured bacterial cell metabolic activity via the use of resazurin. Resazurin is a blue-colored, electroactive redox dye [59] able to penetrate bacteria cell walls and be oxidized by bacteria metabolic enzymes into a pink fluorescence resorufin product [60]. The methodology of this work is based on the incubation separately of the dye with bacteria *Klebsiella pneumoniae* and *E. coli*, reducing the dye and consequently lowering the current peak recorded through differential pulse voltammetry (DPV). However, when antibiotics such as ampicillin, kanamycin, and tetracycline are present, the reduction is inhibited due to the bacterial cell death.

The use of resazurin as dye in AST methodologies is extensive. Combining resazurin with screen-printed electrodes, a platform for the electrochemical antibiotic susceptibility testing of *E. coli* against gentamicin sulfate was developed [47]. DPV was also used allowing the determination of antibiotic susceptibility after 90 min, including the steps of inoculation, pre-incubation, and testing. This is a considerable reduction of the assay time required compared to previous resazurin-based biosensors, and a costless and easy-to-use AST methodology that can be easily implemented in a clinical scenario. As the developed biosensor was intended to be used for the detection of urinary tract infections, artificial urine samples were used during antibiotic testing; however, no thorough matrix effects and selectivity experiments were undergone.

Metabolic activity of bacteria has been used in combination with dyes attending to different parameters. A recent work by Bolotsky et al. [48] proposed a different approach



**Table 1** Current electrochemistry methods for AST detection according to the electrochemical technique used. Bacteria used, antibiotic detected, and time required are summarized in this table as the most relevant parameters in an AST sensor

Electrochemical technique	Bacteria	Antibiotic	Concentrations tested	Detection time	Reference
LSV	<i>E. coli</i>	Penicillin and streptomycin	Not specified	2 h	[45]
DPV	<i>E. coli</i> and <i>K. pneumoniae</i>	Ampicillin, kanamycin, and tetracycline	10 µg/mL	1 h	[46]
DPV	<i>E. coli</i>	Gentamicin sulfate	1.55 µM	90 min	[47]
CV	<i>E. coli</i>	Ampicillin and kanamycin	0–16 µg/mL and 0–64 µg/mL, respectively	1 h	[48]
Amperometric oxygen sensor	<i>E. coli</i> , <i>E. adecarboxylata</i> , <i>C. acidovorans</i> , <i>C. glutamicum</i> , and <i>S. epidermidis</i>	Tetracycline, ampicillin, and chloramphenicol	1 µg/mL, 5 µg/mL, and 5 µg/mL, respectively	8 h	[49]
SWV	<i>E. coli</i>	Erythromycin, amikacin, ampicillin, and cefepime	13.6 µM, 0.852 mM, 1.43 mM, and 1.04 mM, respectively	2–5 h	[50]
EIS and DPV	<i>S. aureus</i> and methicillin-resistant <i>S. aureus</i>	Amoxicillin and oxacillin	8 µg/mL	< 45 min	[51]
EIS	<i>E. coli</i>	Streptomycin	4 µg/mL	2.5 h	[52]
Impedance	<i>E. coli</i>	Ampicillin	10 mg/L	1–2 h	[53]
EIS	<i>S. aureus</i>	Flucloxacillin	300 mg/mL	2 h	[54]
Impedance	<i>E. coli</i> , <i>S. aureus</i> , and <i>P. aeruginosa</i>	Ampicillin, chloramphenicol, gentamicin, and amikacin	0–128 mg/mL	4 h	[55]
Impedance	<i>E. coli</i> and methicillin-resistant <i>S. aureus</i>	Ampicillin, ciprofloxacin, erythromycin, daptomycin, gentamicin, and methicillin	0.1–100 µg/mL	< 90 min	[56]
Capacitance	<i>E. coli</i> and <i>S. aureus</i>	Gentamicin, tetracycline, and ampicillin	0–50 µg/mL, 2 µg/mL, and 8 µg/mL, respectively	Not specified	[57]
Electrical resistance	<i>E. coli</i> , <i>K. pneumoniae</i> , and <i>S. saprophyticus</i>	Ampicillin and nalidixic acid	10 mg/L and 20 mg/L, respectively	2 h	[58]

CV, cyclic voltammetry; DPV, differential pulse voltammetry; EIS, electrochemical impedance spectroscopy; LSV, linear sweep voltammetry; SWV, square wave voltammetry

for a rapid antibiotic susceptibility testing using bacteria pH changes as signal generator (Fig. 1A). Electrodeposition was performed to create a redox-active organic crystalline layer (RZx) on pyrolytic graphite sheets (PGS), used to monitor the bacterial metabolic activity. The sensors were proved with *E. coli* K-12 incubated with two different antibiotics: ampicillin and kanamycin. The principle relies in the fact that the RZx creates responses to the bacterial metabolism by monitoring the pH change with the cell proliferation. One of the main advantages of the sensor is that it is highly stable, being viable after 60 days storage, which can be of great interest for the point-of-care antibiotic susceptibility testing. Moreover, detection of bacterial viability has been demonstrated in spiked human blood and low-fat milk as complex solutions, with no matrix effects observed. Additionally, measurement in complex samples was compared to traditional AST methods as optical density at 600 nm measurement, for which the opacity of complex samples makes measurement impossible.

### Label-free AST methods

Although labels are widely used in biosensing applications, there is an increasing interest in developing label-free biosensors. These devices are more point-of-care orientated as they involve less steps and reagents during measurement process [61].

Equally to label-based sensors, some label-free ones also rely on bacteria metabolic changes as signal generators. As example, Karasinski et al. [49] proposed the use of amperometric signals with a multi-array dissolved oxygen electrochemical sensor to monitor bacteria susceptibility. The effects of different antibiotics on the bacterial growth and their respiratory activity over time were studied. The approach is based on the addition of small concentrations of antibiotics to the bacterial medium. The presence of increasing antibiotic concentrations is directly related to the consumption of oxygen performed by the bacteria, creating a unique fingerprint for each species. Tetracycline,

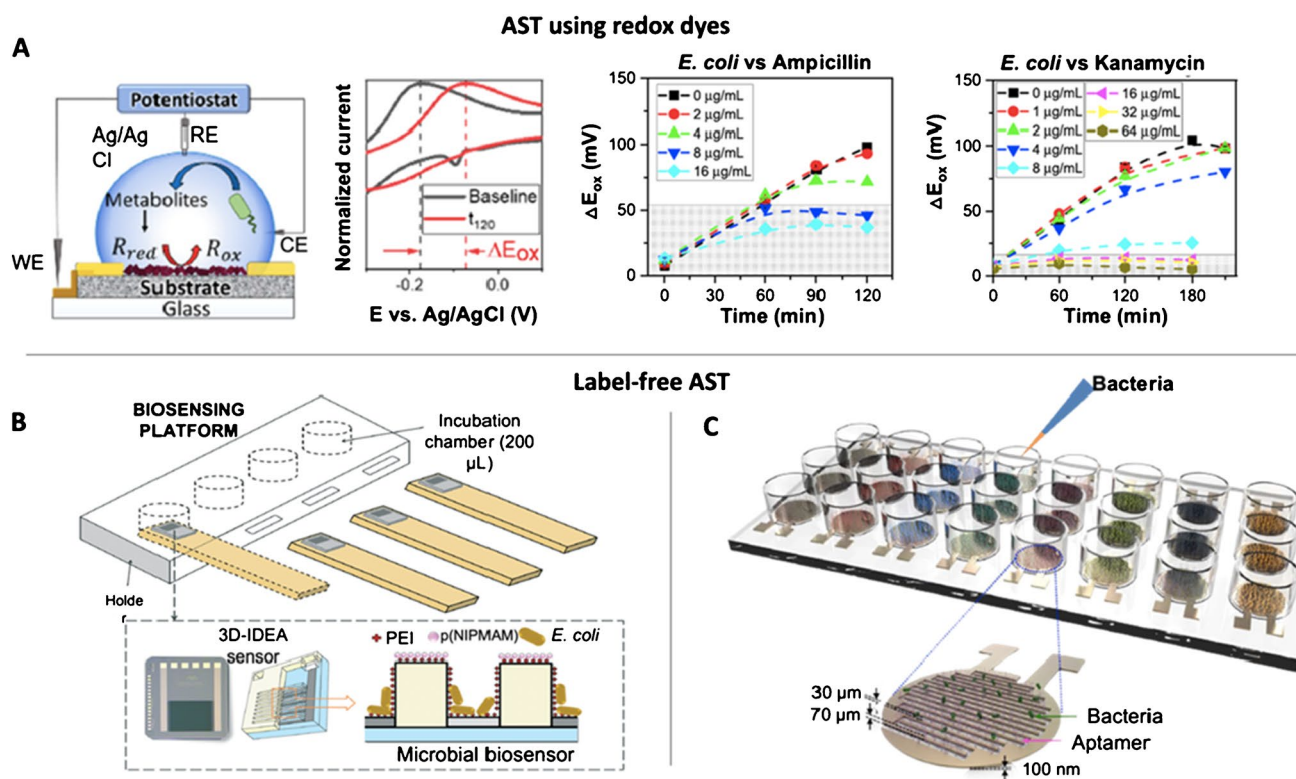


**Fig. 1** AST electrochemical sensors using redox dyes (**A**) and label-free (**B**, **C**). **A** Test of ampicillin and kanamycin against *E. coli* using a redox-active crystalline layer on pyrolytic graphite sheets (RZX-PGS) electrode. Reprinted from [48] with permission of Elsevier. **B** Biosensing platform with a PDMS impedimetric transducer functionalized with polyethyleneimine (PEI), poly(N-isopropylmethacrylamide) (pNIPAM), and *E. coli* for the susceptibility testing

of ampicillin. Used with permission of the Royal Society of Chemistry from [53]; permission conveyed through Copyright Clearance Center, Inc. **C** Capacitance AST array with aptamers as recognition elements immobilized in between electrodes. Bacteria are recognized by aptamers increasing the capacitance recorded. In the presence of an antibiotic, this capacitance is decreased. Reprinted from [57] with permission of Elsevier

ampicillin, and chloramphenicol were tested by measuring the level change of oxygen against five species of bacteria: *E. coli*, *E. adecarboxylata*, *Comamonas acidovorans*, *Corynebacterium glutamicum*, and *Staphylococcus epidermidis*. A pattern recognition was applied using a principal component analysis (PCA), generating a template that can be used to select specific combinations and concentrations of cell/antibiotics.

The direct electron transfer capacity that bacteria intrinsically present has also been exploited for cell growth viability testing in AST sensors [62]. Disposable screen-printed electrodes, modified with membranous didodecylmethylammonium bromide (DDAB), were used to estimate the susceptibility of Gram-negative *Escherichia coli* JM109 against well-known antibiotics such as erythromycin, amikacin, ampicillin, and cefepime [50]. The dynamic direct electron transfer capacities of *E. coli* were used in this work as a label-free way to monitor cell growth through cyclic voltammetry and square wave voltammetry. DDAB/*E. coli* biofilms, deposited on the surface of the electrode, promoted conductivity without affecting bacteria viability. In less than

5 h, they were able to confirm that cefepime, amikacin, and ampicillin inhibited cell growth while erythromycin had any effect.

Alternatively, Hannah et al. [51] modified screen-printed gold electrodes with a hydrogel of agarose for bacterial growth monitoring through electrochemical impedance spectroscopy (EIS) and DPV. Drug-resistant *Staphylococcus aureus* was deposited on top of the hydrogel to monitor the influence of the antibiotic's amoxicillin and oxacillin in less than 45 min, taking measurements in periods of 5 min. The electrodes showed a good resolution, being able to differentiate between bacteria growth in absence of antibiotic and under low antibiotic concentrations. In a later work [52], the same methodology was used to monitor the electrochemical growth profiles of *E. coli* against streptomycin, throwing differences in approximately 2.5 h. The main difference between these two protocols is the enlarged growing of bacteria among time obtained with the second method due to the prolonged integrity of the gel-modified electrode compared to the hydrogel used in the previous work. The bacterial growth profiles were monitored by EIS.

EIS was also used by Brosel-Uliu et al. [53] by the immobilization of the bacteria *E. coli* in a three-dimensional interdigitated electrode array (3D-IDEA) modified with microgels to prevent bacteria deposition and increase reproducibility and sensitivity (Fig. 1B). This microbial sensor allows to monitor bacterial response to ampicillin by monitoring impedance fluctuations for 24 h. The 3D-IDEA sensor showed a large decrease in  $R_s$  in the first 2 h, while after the fourth hour, it remained quite stable.

Abeyrathne et al. [54] used also EIS technique in a non-faradic approach for detecting the antibiotic susceptibility of *S. aureus* against flucloxacillin in less than 2 h using interdigitated electrodes as platforms. Electrodes were SiO<sub>2</sub> passivated and functionalized with antibodies as recognition element. Through EIS measurements, they were able to differentiate live and dead bacteria cells while they were exposed to antibiotics due to the change of the medium conductivity as a result of the bacteria metabolic process. As next step, the modifying of the sensor for the detection of *S. aureus* in whole blood must be studied. For that purpose, addition of a filter paper to the proposed sensor that remove erythrocytes and neutrophils (bigger diameters respect to the bacteria) and a subsequent wash step to remove unbound cells will be investigated.

Puttaswamy et al. [55] presented a rapid electrical method to determine the effect of antibiotics on bacteria using a different type of “impedance microbiology.” The bacterial metabolism shows the conductance/impedance at a single frequency since this method uses measurements at 500 different frequencies to estimate the electric charge that is stored due to the charge polarization at cell membranes of the living bacteria. It allows to track the number of living bacteria every 1 h that the measure is taken. So, the decrease in the number of bacteria that are proliferating in presence of antibiotic can be determined. For the study, different strains such as *E. coli* and *S. aureus* were tested against ampicillin and chloramphenicol while *P. aeruginosa* was exposed against gentamicin and amikacin in about 4 h.

By taking advantage of the use of printed electrodes and impedance electrochemical measurements, Safavieh et al. [56] reported a biosensor that allows the detection of pathogens, the identification of the correct antibiotics through antibiotic susceptibility testing, and the monitoring of mutations that help to adjust the correct therapy. The biosensor presents a rapid (<90 min), label-free, and real-time analysis via capturing the target bacteria on flexible plastic-based microchips using electrodes modified with antibodies and monitoring the impedimetric response in the presence and absence of the antibiotics after incubation for 1 h. The microchip was evaluated with *E. coli* and methicillin-resistant *Staphylococcus aureus* (MRSA) for different antibiotics such as ampicillin, erythromycin, daptomycin, ciprofloxacin, daptomycin, methicillin, and gentamicin. Also, the ability of

the microchip was demonstrated with MRSA-spiked whole blood with different clinically relevant concentrations of bacteria, being able to be used in urine samples too.

Another common recognition element used in biosensing to increase selectivity are aptamers [63]. The use of aptamers in AST was reported by Jo et al. [57] in a functionalized capacitance sensor that allows the monitoring of antibiotic susceptibility and the bacterial growth in real time (Fig. 1C). Due to the intrinsic high selectivity of aptamers, the bacteria can be identified within 1 h using this sensor. The combination in the use of aptamers and electrical sensors allows the direct and rapid identification of the bacteria and the evaluation of their resistance against different antibiotics with high accuracy, sensitivity, and selectivity. In this sensor, bacteria are bounded over the sensor surface via aptamers between electrodes, acting as capacitors that are connected between parallel electrodes. For the antimicrobial susceptibility tests, different antibiotics such as gentamicin, tetracycline, and ampicillin were tested. For the culture of *E. coli* and *S. aureus*, the bacteria death is monitored by the change of capacitance when treated with antibiotics demonstrating the applicability of this sensor for rapid AST.

The use of microfluidics to perform rapid drug testing has also been exploited in AST. Their feasibility and use as organ-on-a-chip platforms has facilitated their implementation in AST screening [64]. Using microfluidics, Yang et al. [58] described an ultrasensitive all-electrical measurement constituted by a set of microfluidic channels that allows the flow of a liquid bacteria sample in the device for the subsequent incubation with different antibiotics. The signal measured is the electrical resistance of the microchannels that changes in proportion to the cell viability, allowing a rapid AST within 2 h. In addition, the constant fluctuations due to the antibiotics in the electrical resistance can be related to morphological changes of the bacteria. Ampicillin and nalidixic acid, antibiotics with different action mechanisms, were evaluated against *E. coli*, *K. pneumoniae*, and *S. saprophyticus*. Interestingly, the electrical measurement developed in this work is suitable for a multiplexed analysis desirable for a large antibiotic screening testing. As a drawback, application in clinical test could be limited in patients with complex urine matrices, not being able to be tested in the proposed device.

### AST in drug screening

Although AST techniques are also used for drug screening purposes, the electrochemical AST sensors developed have been predominantly focused on addressing antimicrobial resistance. However, there are just a few examples that exploit the potential of electrochemical sensors for a faster and simple screening of new drug candidates (Table 2).

Combining the use of a disposable screen-printed electrode coupled to a microfluidic chamber, Webster et al. [65] monitored the antibiotic susceptibility of *P.*



**Table 2** Potential electrochemical AST sensors for screening new drug candidates classified according to their most relevant parameters: electrochemical technique used, bacteria detected, antibiotic tested (both type and concentration), and time required for performing the measurement

Electrochemical technique	Bacteria	Antibiotic	Concentrations tested	Detection time	Ref
SWV	<i>P. aeruginosa</i>	Colistin sulfate	4, 16, and 100 mg/L	45 h	[65]
SWV	<i>P. aeruginosa</i>	Antimicrobial peptides	5–50 $\mu$ M	300 s	[66]
SWV	<i>P. aeruginosa</i>	RA13	5–50 $\mu$ M	300 s	[67]

RA13, reverse amide 2-aminoimidazole derivative; SWV, square wave voltammetry

*aeruginosa* via electrochemical detection of the virulence factor pyocyanin (Fig. 2A). Bacteria was exposed to different concentrations of colistin sulfate as antibiotic. For the electrochemical measurement, square wave voltammetry was used as technique due to its increased sensitivity and ability to monitor the reduction peak corresponding to pyocyanin, directly correlated with a decrease in cell growth. The main disadvantage of this methodology is that the time required for completing measurements is of 45 h, comparable with the standard techniques currently used.

Antibiotic compounds are not the only therapeutic target in antimicrobial research. Anti-biofilms have been subject of study for many pathological microorganisms as the formation of biofilms enhances multidrug tolerance. Besides, the incorporation of electrochemical scaffolds together with anti-biofilm compounds has also been confirmed to have a co-adjuvant effect in antimicrobial treatment [68].

Evaluation of new anti-biofilm forming compounds has also been done using an electrochemical sensor using ferricyanide as redox indicator. In this case, alginate, one of the main components of mucoid *P.*

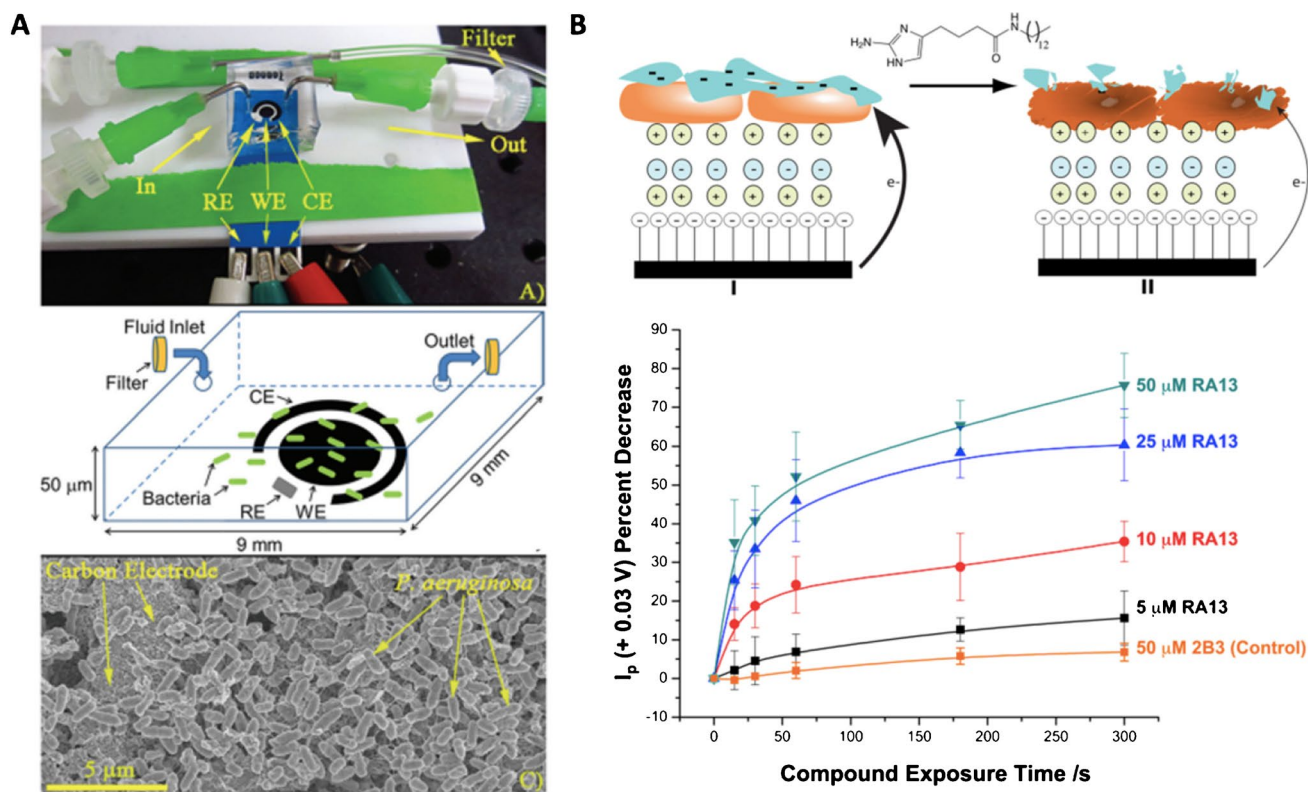


**Fig. 2** AST methods for the screening of new drug candidates. **A** Screen-printed electrode-based sensor covered with a microfluidic chamber with bacteria trapped on the inside. Reproduced from [65] with permission from the Royal Society of Chemistry. **B** Electrode based on the formation of cationic (green) and anionic (blue) polymers and *P. aeruginosa* bio-

film (orange). After anti-biofilm exposure, the structure is compromised reducing the current recorded due to the electroactive phenazines produced by *P. aeruginosa*. Reprinted from [67] with permission of Elsevier

*aeruginosa* strain biofilms [69], was immobilized on top of a pyrolytic graphite electrode modified layer-by-layer with poly(diallyldimethylammonium) chloride and polystyrene sulfonate. Both polymers have opposite charge, which allows the retaining of alginate in the upper electrode layer [66]. By the addition of antimicrobial peptides, the alginate was broken and ferricyanide was able to go through the layers and reach the electrode, providing an increase in the oxidation current recorded. In a later work, the same group used the same type of electrodes but in this case with the immobilization of *P. aeruginosa* on the upper layer (Fig. 2B). Direct electrochemical reduction of phenazine compounds produced by *P. aeruginosa* was recorded through SWV in a label-free sensor. With this sensor, the establishment of the half maximal inhibition concentration ( $IC_{50}$ ) and half maximal effective concentration ( $EC_{50}$ ) of an anti-biofilm compound was possible in just a few minutes [67].

### Nanomaterials in the screening of antibiotic compounds: are they really needed?

Nanomaterials are defined as those materials that present at least one dimension in the range of 1–100 nm. Their small size provides them with outstanding properties not presented by their counterpart bulk materials [70].

In the last decades, nanomaterials have gained significant importance in multiple applications, going from medical imaging, drug delivery, food technology, cosmetics, and biomolecular electronic devices [71]. Nanomaterials have been incorporated in biosensing as they present enhanced electrical conductivity, improved biological sensing accuracy, and biocompatibility, what allows to increase sensitivities and decrease detection limits. Besides this, their high surface area also facilitates the immobilization of increased amounts of different bioreceptors [72] through an extended range of chemical reactions [73].

Nanomaterials are typically incorporated in electrochemical biosensing either as electrode modifiers or as detection labels [74]. The incorporation of nanomaterials, such as carbon-based nanomaterials, quantum dots, or metallic nanoparticles, has helped to overcome the slack electrode surface kinetics, acting as electrocatalysts or transduction systems [75]. However, the immobilization of these nanomaterials on the electrode surface is still a challenge to overcome [76].

As detection labels, nanomaterials have been explored as substitutes to traditional enzymatic labels that, although sensitive, require harsh conditions and present a low thermal stability, hindering their integration into commercial devices. To overcome these problems, nanomaterials have emerged as alternative, both alone or in combination with enzymes [77]. Again, metallic nanoparticles such as silver nanoparticles, gold nanoparticles, bimetallic nanoparticles,

or zinc or cerium oxide nanoparticles stand out for their redox properties and electrocatalytic activities [78–80].

Their superior qualities have also made them ideal candidates as promising antimicrobial drugs [81, 82]. With silver nanoparticles (AgNPs) showing up for their intrinsic antimicrobial properties against known bacterial strains such as *E. coli*, *S. aureus*, or *P. aeruginosa*, multimetallic nanoparticles have also seem to be effective [83].

Although their use is extended in electrochemical biosensors, even for the detection of antibiotic residues [17], their application on AST is scant, being introduced in a reduced number of recent works (Table 3). The toxicity of some of these nanomaterials against microorganisms could be one of the reasons why their use is not as spread compared to other fields of research [74, 77]. However, their potential deserves a wider look onto their implementation in AST electrochemical sensing.

As example, cerium oxide nanoparticles (CeNPs) have been used in an electrochemical AST as ITO electrode modifiers [84] allowing the monitoring within 15 min by time-lapse microscopy video and electrochemistry of the susceptibility of Gram-positive *Bacillus subtilis* and Gram-negative *E. coli* against the antibiotics ciprofloxacin, cefixime, and amoxicillin. In this work, the toxicity of CeNPs against *E. coli* has also been considered and explored as a relevant parameter in the antimicrobial screening biosensor developed. For that purpose, bulk CeNPs, CeNPs functionalized with L-lysine (L-CeNPs), and with pluronic acid (P-CeNPs) were compared, observing that L-lysine presents a protective effect against the antimicrobial activity, allowing their use in an AST sensor. In terms of conductivity, the modification of the ITO electrode with L-CeNPs significantly increased the conductivity obtained.

Carbon nanotubes (MWCNTs) and gold nanoparticles (AuNPs) have also been used as electrode modifiers in combination with resazurin as label [85]. The incorporation of these two nanomaterials combined into screen-printed carbon electrodes (SPCEs) increased the peak current recorded, what it is in correlation with the enhanced conductivity and electropolymerization that these nanomaterials present. Ofloxacin and penicillin antibiotics were tested against *Salmonella gallinarum* isolates by mixing bacteria, resazurin, and different concentrations of the antibiotics. DPV was selected for the detection of viable bacteria, been able to detect them above  $10^2$  CFU/mL after 1 h of incubation. The methodology was also applied in egg liquid sample obtaining a decrease of the signal sensor due to the change of the resistance of the medium, although the absolute change of current was maintained.

Taking advantage of the acidification properties of bacteria while growing, an ion-selective silicon nanowire field-effect transistor (SiNWFET) sensor [86] was developed. *E. coli* and other pathogen species such as *S. aureus*

**Table 3** Nanomaterial-based electrochemical biosensors for AST classified according to the nanomaterial used and their function, the electrochemical technique used, bacteria detected, antibiotic tested and their concentration, and the time required for performing the analysis

Nanomaterial	Nanomaterial function	Electrochemical technique	Bacteria	Antibiotics	Concentrations tested	Detection time	Ref
L-CeONP/ITO	Working electrode	CV	<i>Bacillus subtilis</i> , <i>Escherichia coli</i>	Ciprofloxacin, cefixime, and amoxicillin	2 µg/µL	15 min	[84]
MWCNTs and AuNPs	Enhance the sensitivity of SPCEs	DPV	<i>Salmonella gallinarum</i>	Ofloxacin and penicillin	0.0625–256 µg/mL	4 h	[85]
Silicon nano transistors	Sensor design	SiNWFETs	<i>E. coli</i> , <i>S. saprophyticus</i> , and <i>S. aureus</i>	Ampicillin, cefotaxime, and ciprofloxacin	100 mg/L, 20 mg/L, and 1–4 mg/L, respectively	30 min	[86]
CDs	Bacterial growth-monitoring sensor	CV	<i>E. coli</i> and ampicillin resistant <i>E. coli</i>	Ampicillin	100 µg/mL	20 min	[87]
AgNPs-invertase complexes	Inhibition of enzymatic activity	PGM	<i>E. coli</i>	Colistin, spectinomycin, streptomycin, and tetracycline	0–65 µg/mL	4 h	[88]
Nanochannels	Sensing platforms	DPV	<i>S. aureus</i>	RIP, YSPWTNF-NH2	50 µg/mL	24 h	[89]

Nanomaterials: *AgNPs-invertase complexes*, silver nanoparticles-invertase complexes; *CDs*, carbon nanodots; *L-CeONP/ITO*, L-lysine-functionalized cerium oxide nanoparticle coated indium tin oxide; *MWCNTs and AuNPs*, multiwalled carbon nanotubes and gold nanoparticles; *RIP*, RNAlII-inhibiting peptide. Electrochemical methods: *CV*, cyclic voltammetry; *DPV*, differential pulse voltammetry; *EIS*, electrochemical impedance spectroscopy; *LSV*, linear sweep voltammetry; *SWV*, square wave voltammetry

and *S. saprophyticus* were tested in presence and absence of different antibiotics in less than 30 min. SiNWFET used in this work contained a H<sup>+</sup>-selective sensing oxide layer for a specific detection of pH changes even in media with a high ionic concentration that increase background signal. Moreover, the use of this technology also minimizes variation between sensors, what it is desirable both to perform parallel AST screening and for research transference purposes. Largely, the use of this SiNWFET allowed the detection of tiny changes on the pH even under high ionic background concentrations, providing a better sensitivity. In addition, the proposed sensor could be modified to add a pre-filtering system that allows the detection of real samples without any preparation step as pre-cultivation.

In a different approach, but also considering bacteria acidification, carbon nanodots (CDs) have been used as electrochemical labels in an AST method [87] able to detect antibiotic susceptibility in 20 min (Fig. 3A). CDs have many advantages such as small size, good conductivity, low toxicity, and high solubility. Also, the economical and one-step synthesis of CDs makes them interesting materials for applications in biosensing. The sensor consisted in the encapsulation of CDs in alginate microspheres, together with *E. coli* (non-resistant) and *E. coli + pET32* (resistant) and antibiotic concentrations. The presence of the alginate microspheres allows an enhanced 3D growing of the

bacteria, better mimicking a real-case scenario. The change in the redox potential over time of the CDs due to the pH changes generated by the bacteria metabolism was recorded by cyclic voltammetry at 0 and 20 min, showing a discrimination between low bacterial counts of < 10<sup>3</sup> CFU/mL. The biocompatibility of the used microspheres with the bacteria tested was also evaluated, confirming that the bacteria growing rate was not affected by the presence of these nanomaterials in the microenvironment.

Nanoparticles can also be used as encapsulating agents as they improve availability of active compounds [90]. In this line, Laibao et al. [88] proposed the use of a modified personal glucometer as a biosensor for rapid (withing 4 h) and reliable antimicrobial susceptibility testing using polyethyleneimine AgNPs (PEI-AgNPs) to encapsulate invertase complexes. Cationic PEI-AgNPs could reversibly bind the anionic enzyme invertase, inhibiting the catalytic activity by forming an electrostatic interaction between both of them. In the presence of bacteria, invertase is released from the complex, as the cationic PEI-AgNPs bind to the anionic surface of bacteria, thus releasing invertase. The enzyme is then active to convert sucrose into glucose, a change that is recorded by the glucometer. The AST of *E. coli* was tested with four different antibiotics (colistin, spectinomycin, streptomycin, and tetracycline) within 5 h. The PEI-AgNPs used in this case act as a detection mechanism for bacteria identification. However,

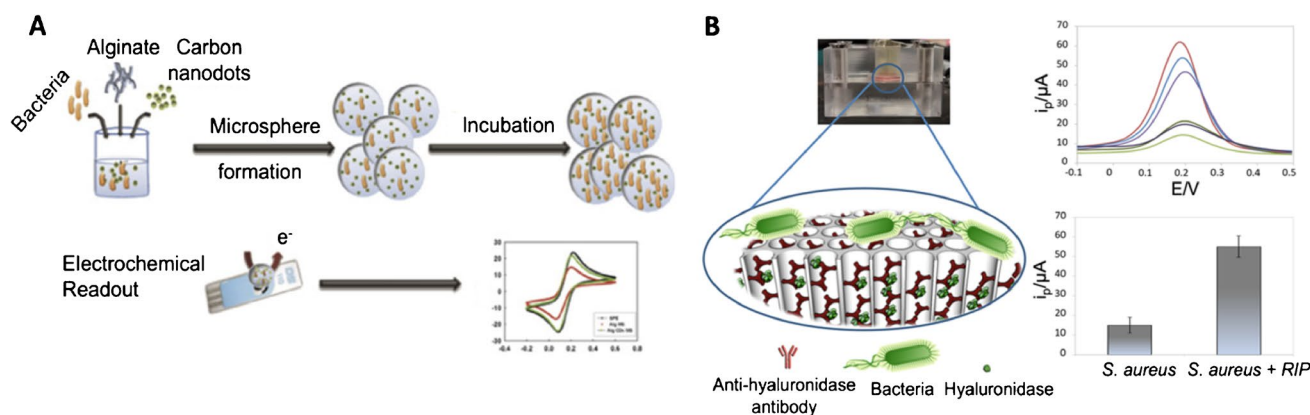


**Fig. 3** Nanomaterial-based AST sensors. **A** Using carbon nanodots as pH sensitive labels encapsulated in alginate microspheres for a better 3D bacterium growing. Reprinted from [87] with permission from Elsevier. **B** Using a nanochannel-based immunosensor for the detec-

tion of hyaluronidase, a virulence factor of Gram-positive bacteria, and the evaluation of a quorum sensing inhibitor (RIP). Adapted with permission from [89]. Copyright 2022 American Chemical Society

a main drawback of the work is the lack of specificity of the proposed biosensor, as it responds to different bacteria which can be an issue for application in real samples.

Nanopore/nanochannel-based materials have also been shown as outstanding tools for electrochemical biosensing [91, 92]. Regarding antibiotic screening, an innovative approach to monitor the effect of new quorum sensing inhibitors against *S. aureus* using a nanochannel-based electrochemical immunosensor has been recently reported [89]. The sensor was able to differentiate between *S. aureus* and *P. aeruginosa* by monitoring hyaluronidase detection, a virulence factor primarily secreted by Gram-positive bacteria. Additionally, the effect of anti-infective RNAIII-inhibiting peptide (RIP, YSPWTNF-NH<sub>2</sub>), a quorum sensing inhibitor, as suppressor of bacterial growth and virulence was evaluated using the developed sensor, by monitoring the decrease in the hyaluronidase secreted levels (Fig. 3B). The use of nanochannel membranes in this work facilitates the identification of biomarkers in complex samples due to their intrinsic filtering properties. Moreover, nanochannel membranes serve as platform for the immobilization of biorecognition elements, what leads to a label-free identification of the analytes of interest.

In general terms, the nanomaterials used in AST methods covered both the implementation such as electrode modifiers, labels, or even encapsulating agents. And although their use is relevant in terms of the bacteria concentration that could be detected, with a low CFU/mL counting in many of the works revised, this is not translated in lower antibiotic concentrations that could be tested or even the time required for obtaining a result. It is worthy to mention that the potential toxicity of these materials and how it could affect bacterial growth is not considered in many of the works, being a parameter of paramount importance for AST methods.

All considered, although the use of nanomaterials seems promising for increasing conductivity and lowering limits of detection, it is not translated into improved results for antibiotic resistance identification. However, the intrinsic characteristics of nanomaterials could be more interestingly exploited in the screening of new antimicrobial compounds and in the identification of MIC concentrations, for which reaching a lower CFU/mL count is more relevant.

### Commercial potential of electrochemical AST methods: barriers to overcome

Antimicrobial resistance is a health challenge that research, industry, and policymakers should stop ignoring. With an increasing tendency of superbugs becoming more deadly than cancer, the need to find solutions to this problem is increasingly imminent. And these solutions go through both a control administration of existent antimicrobial drugs and the development of new ones. But the lack of fast, accurate, and easy-to-use diagnosis devices complicates them. Thus, the development of specific and rapid point-of-care devices can assist in managing this global health crisis, preventing unnecessary antibiotic administration [93]. Although some rapid infection testing are out on the market, they still lack from integration and require the extraction of invasive samples [94].

For that reason, the use of electrochemical biosensors both for the identification of antimicrobial resistance and for the development of new drugs seems to be a promising approach, and it has been seen like that by the research community. But still, the commercialization of these type of devices is far to become a reality.



Technical parameters such as long-term stability of the sensors developed, matrix effects, cost, or feasibility of their use by non-specialized personnel are scarcely evaluated by research works on electrochemical sensors [63] and are also lacking in the works revised in this review. Although LOD, sensitivity, and specificity have been clearly adopted as parameters that should be optimized in biosensing, it is also important to keep in mind the above-mentioned characteristics. Moreover, cost-effectivity is also an important criterion to consider, being the low profit rate the main reason for the reduced investment of pharmaceutical industry in antibiotic development [39].

Thus, the inclusion of a deeper evaluation of these and other parameter should be promoted in research works if we want to be able to transmute laboratory results into real clinically relevant devices.

Moreover, the development of multiplexed systems able to identify or evaluate more than one superbug is also desirable, as these complex infections are worsened by the presence of polymicrobial interactions [95]. This is especially relevant in the development of new antimicrobial compounds as polymicrobial infections have been directly related with an enhanced antimicrobial resistance [96].

Despite some promising leads, the way electrochemical AST methods have been developed needs to be revisited to really address market needs.

## Outlook

The implementation of new AST methods is constantly evolving given the increasingly worrying incidence of antimicrobial resistances. However, traditional AST methods still do not solve this issue, which leads to increased research in alternative high-throughput screening strategies such as biosensors. Biosensing field has proved to be relevant in reducing antimicrobial resistance through environmental monitoring of antibiotics, with many biosensors developed in this field. The reduced complexity of environmental samples could be a fundamental factor to explain this difference. Detection of antimicrobial resistance through electrochemical means in human samples is a different matter. Although promising, as they help to reduce time and increase sensitivity compared to traditional AST methods, they still not accomplish all what it is claimed to AST methods. Cost of the final assay is not even considered in research works revised and is one of the main arguments that must be revised to point out biosensors as alternative to AST methods. This cost reduction is fundamental to improve antimicrobial screening research, being the main

obstacle to overcome for pharmaceutical industry. It is also noticeable the scarcity of bacteria tested with these sensors, using *E. coli* as preferred choice as it is an easy-to-use bacterial model. But the reality is that genders of bacteria such as *Klebsiella pneumoniae*, *Acinetobacter baumannii*, and MRSA are predominantly associated to nosocomial infections and represent a larger burden for healthcare systems [97]. Bactericidal and bacteriostatic effects are lacked also in these works, and it is one of the main demands done to traditional AST methods. This aspect is less relevant in the identification of antibiotic resistance, but it is definitively a concern in the screening of new drug candidates. In this last field, it is surprising that the low number of electrochemical biosensors was developed. Although they have a greater potential, antimicrobial screening electrochemical sensors focused on the activity testing of new antimicrobial compounds are scarce. The lack of standardization of these methods compared to the AST techniques approved by the EUCAST and CLSI could be one of the reasons. Potentiating communication between electrochemical groups and microbiology research groups in charge of discovering new antibiotic compounds is a suitable way to promote this synergy and favor antimicrobial compounds development.

Regarding the use of nanomaterials, although promising, it is still not relevant enough to make a significant difference compared to non-nanomaterial-based biosensors. However, the low CFU/mL that these methodologies can reach, open the path to their use for MIC determination. That is why their use is not unjustified, but the type of analysis to be carried out with these instruments must be modified.

As we have outlined in this review, electrochemical biosensors are promising AST methods to both detect resistance in the clinical setting and to serve as screening platforms for new drug candidates, but further improvements are still required to be relevant in the combat against antimicrobial resistance.

**Acknowledgements** C. Toyos-Rodríguez and D. Valero-Calvo thank the Spanish Ministry of Science and Innovation (MICINN) for the award of the FPI Grants PRE2018-084953 and PRE2021-097567, respectively. A. de la Escosura-Muñiz also acknowledges the MICINN for the “Ramón y Cajal” Research Fellow (RyC-2016-20299).

**Funding** This work has been supported by the MCI-21-PID2020-115204RB100 project from the Spanish Ministry of Science and Innovation (MICINN) and the SV-PA-21-AYUD/2021/51323 project from the Asturias Regional Government.

## Declarations

**Conflict of interest** The authors declare no competing interests.

## References

- Miethke M, Pieroni M, Weber T, Brönstrup M, Hammann P, Halby L, Arimondo PB, Glaser P, Aigle B, Bode HB, Moreira R, Li Y, Luzhetskyy A, Medema MH, Pernodet J-L, Stadler M, Tormo JR, Genilloud O, Truman AW, Weissman KJ, Takano E, Sabatini S, Stegmann E, Brötz-Oesterhelt H, Wohlleben W, Seemann M, Empting M, Hirsch AKH, Loretz B, Lehr C-M, Titz A, Herrmann J, Jaeger T, Alt S, Hestekamp T, Winterhalter M, Schiefer A, Pfarr K, Hoerauf A, Graz H, Graz M, Lindvall M, Ramurthy S, Karlén A, van Dongen M, Petkovic H, Keller A, Peyrane F, Donadio S, Fraisse L, Piddock LJV, Gilbert IH, Moser HE, Müller R. Towards the sustainable discovery and development of new antibiotics. *Nat Rev Chem*. 2021;5:726–49. <https://doi.org/10.1038/s41570-021-00313-1>.
- Ventola CL. The antibiotic resistance crisis P&T. 2015;40:277–83.
- WHO Regional Office for Europe/European Centre for Disease Prevention and Control (2022) Antimicrobial resistance surveillance in Europe 2022–2020 data. In: Copenhagen: WHO Regional Office for Europe; 2022. [https://www.ecdc.europa.eu/en/publications-data/antimicrobial-resistance-surveillance-europe-2022-2020-data#:~:text=Antimicrobial%20resistance%20\(AMR\)%20remains%20a,people%20die%20as%20a%20direct](https://www.ecdc.europa.eu/en/publications-data/antimicrobial-resistance-surveillance-europe-2022-2020-data#:~:text=Antimicrobial%20resistance%20(AMR)%20remains%20a,people%20die%20as%20a%20direct). Accessed 29 Aug 2022.
- O'Neill J. Tackling drug-resistant infections globally: final report and recommendations. 2016. [https://amrreview.org/sites/default/files/160525\\_Final%20paper\\_with%20cover.pdf](https://amrreview.org/sites/default/files/160525_Final%20paper_with%20cover.pdf). Accessed 29 Aug 2022.
- Vaughn VM, Gandhi TN, Petty LA, Patel PK, Prescott HC, Malani AN, Ratz D, McLaughlin E, Chopra V, Flanders SA. Empiric antibacterial therapy and community-onset bacterial coinfection in patients hospitalized with coronavirus disease 2019 (COVID-19): a multi-hospital cohort study. *Clin Infect Dis*. 2021;72:e533–41. <https://doi.org/10.1093/cid/ciaa1239>.
- Sharifipour E, Shams S, Esmkhani M, Khodadadi J, Fotouhi-Ardakani R, Koohpaei A, Doosti Z, Golzari EJ, S., Evaluation of bacterial co-infections of the respiratory tract in COVID-19 patients admitted to ICU. *BMC Infect Dis*. 2020;20:646. <https://doi.org/10.1186/s12879-020-05374-z>.
- Nori P, Szymczak W, Puius Y, Sharma A, Cowman K, Gialanella P, Fleischner Z, Corpuz M, Torres-Isasiga J, Bartash R, Felsen U, Chen V, Guo Y. Emerging co-pathogens: New Delhi metallo-beta-lactamase producing Enterobacterales infections in New York City COVID-19 patients. *Int J Antimicrob Agents*. 2020;56:106179. <https://doi.org/10.1016/j.ijantimicag.2020.106179>.
- Getahun H, Smith I, Trivedi K, Paulin S, Balkhy HH. Tackling antimicrobial resistance in the COVID-19 pandemic. *Bull World Health Organ*. 2020;98:442–442A. <https://doi.org/10.2471/BLT.20.268573>.
- Munita JM, Arias CA (2016) Mechanisms of antibiotic resistance. *Microbiol Spectr* 4:4.2.15. <https://doi.org/10.1128/microbiolspec.VMBF-0016-2015>
- Rice LB. Mechanisms of resistance and clinical relevance of resistance to  $\beta$ -lactams, glycopeptides, and fluoroquinolones. *Mayo Clin Proc*. 2012;87:198–208. <https://doi.org/10.1016/j.mayocp.2011.12.003>.
- Larsson DGJ, Flach C-F. Antibiotic resistance in the environment. *Nat Rev Microbiol*. 2022;20:257–69. <https://doi.org/10.1038/s41579-021-00649-x>.
- Milaković M, Vestergaard G, González-Plaza JJ, Petrić I, Šimatović A, Senta I, Kublik S, Schloter M, Smalla K, Udiković-Kolić N. Pollution from azithromycin-manufacturing promotes macrolide-resistance gene propagation and induces spatial and seasonal bacterial community shifts in receiving river sediments. *Environ Int*. 2019;123:501–11. <https://doi.org/10.1016/j.envint.2018.12.050>.
- Taylor P, Reeder R. Antibiotic use on crops in low and middle-income countries based on recommendations made by agricultural advisors. *CABI Agric Biosci*. 2020;1:1. <https://doi.org/10.1186/s43170-020-00001-y>.
- Cabello FC, Godfrey HP, Buschmann AH, Dölz HJ. Aquaculture as yet another environmental gateway to the development and globalisation of antimicrobial resistance. *Lancet Infect Dis*. 2016;16:e127–33. [https://doi.org/10.1016/S1473-3099\(16\)00100-6](https://doi.org/10.1016/S1473-3099(16)00100-6).
- Anwar M, Iqbal Q, Saleem F. Improper disposal of unused antibiotics: an often overlooked driver of antimicrobial resistance. *ERATCK*. 2020;18:697–9. <https://doi.org/10.1080/14787210.2020.1754797>.
- Wang J, Chu L, Wojnárovits L, Takács E. Occurrence and fate of antibiotics, antibiotic resistant genes (ARGs) and antibiotic resistant bacteria (ARB) in municipal wastewater treatment plant: an overview. *Sci Total Environ*. 2020;744:140997. <https://doi.org/10.1016/j.scitotenv.2020.140997>.
- Sun Y, Zhao J, Liang L. Recent development of antibiotic detection in food and environment: the combination of sensors and nanomaterials. *Microchim Acta*. 2021;188:21. <https://doi.org/10.1007/s00604-020-04671-3>.
- Joshi A, Kim K-H. Recent advances in nanomaterial-based electrochemical detection of antibiotics: challenges and future perspectives. *Biosens Bioelectron*. 2020;153:112046. <https://doi.org/10.1016/j.bios.2020.112046>.
- Hermouche L, Bendany M, Abbi K, El Hamdouni Y, Labjar N, El Mahi M, Lotfi E mostapha, Dalimi M, Dhiba D, El Hajjaji S (2021) Electrochemical sensors for tetracycline antibiotics detection based on carbon electrode materials modified by biological and chemical compounds: a review. *J Environ Anal Chem* 1–23 <https://doi.org/10.1080/03067319.2021.1946525>
- Giske CG, Turnidge J, Cantón R, Kahlmeter G. Update from the European Committee on Antimicrobial Susceptibility Testing (EUCAST). *JCM*. 2022;60:e00276–e321. <https://doi.org/10.1128/jcm.00276-21>.
- van Belkum A, Bachmann TT, Lüdke G, Lisby JG, Kahlmeter G, Mohess A, Becker K, Hays JP, Woodford N, Mitsakakis K, Moran-Gilad J, Vila J, Peter H, Rex JH, WmM D. Developmental roadmap for antimicrobial susceptibility testing systems. *Nat Rev Microbiol*. 2019;17:51–62. <https://doi.org/10.1038/s41579-018-0098-9>.
- Vasala A, Hytönen VP, Laitinen OH. Modern tools for rapid diagnostics of antimicrobial resistance. *Front Cell Infect Microbiol*. 2020;10:308. <https://doi.org/10.3389/fcimb.2020.00308>.
- Balouiri M, Sadiki M, Ibsouda SK. Methods for in vitro evaluating antimicrobial activity: a review. *J Pharm Anal*. 2016;6:71–9. <https://doi.org/10.1016/j.jpha.2015.11.005>.
- Jorgensen JH, Ferraro MJ. Antimicrobial susceptibility testing: a review of general principles and contemporary practices. *CLIN INFECT DIS*. 2009;49:1749–55. <https://doi.org/10.1086/647952>.
- Nijs A, Cartuyvels R, Mewis A, Peeters V, Rummens JL, Magerman K. Comparison and evaluation of Osiris and Sirscan 2000 antimicrobial susceptibility systems in the clinical microbiology laboratory. *J Clin Microbiol*. 2003;41:3627–30. <https://doi.org/10.1128/JCM.41.8.3627-3630.2003>.
- Bernatová S, Samek O, Pilát Z, Šerý M, Ježek J, Ják P, Šiler M, Krzyžánek V, Zemánek P, Holá V, Dvořáčková M, Růžička F. Following the mechanisms of bacteriostatic versus bactericidal action using Raman spectroscopy. *Molecules*. 2013;18:13188–99. <https://doi.org/10.3390/molecules181113188>.
- Das K, Tiwari RKS, Shrivastava DK. Techniques for evaluation of medicinal plant products as antimicrobial agent: current methods and future trends. *J Med Plant Res*. 2010;4:104–11. <https://doi.org/10.5897/JMPR09.030>.
- Lage O, Ramos M, Calisto R, Almeida E, Vasconcelos V, Vicente F. Current screening methodologies in drug discovery for selected

- human diseases. *Mar Drugs*. 2018;16:279. <https://doi.org/10.3390/md16080279>.
29. Sani I, Ukwuani-Kwaja AN, Abdulkadir D (2022) Antibacterial activities of plant-derived metallic nanoparticles on some selected multidrug-resistant clinical isolates. *Asian J Biol Sci* 15:15–26. <https://doi.org/10.17311/ajbs.2022.15.26>
  30. Humphries RM, Ambler J, Mitchell SL, Castanheira M, Dingle T, Hindler JA, Koeth L, Sei K, Hardy D, Zimmer B, Butler-Wu S, Dien Bard J, Brasso B, Shawar R, Dingle T, Humphries R, Sei K, Koeth L. CLSI methods development and standardization working group best practices for evaluation of antimicrobial susceptibility tests. *J Clin Microbiol*. 2018;56:e01934–e2017. <https://doi.org/10.1128/JCM.01934-17>.
  31. Vanegas D, Abril-Novillo A, Khachatryan A, Jerves-Andrade L, Peñaherrera E, Cuzco N, Wilches I, Calle J, León-Tamariz F. Validation of a method of broth microdilution for the determination of antibacterial activity of essential oils. *BMC Res Notes*. 2021;14:439. <https://doi.org/10.1186/s13104-021-05838-8>.
  32. Gun MA, TanriverdiCayci Y, Durupinar B, Coban AY. A new colorimetric method for rapid detection of antibiotic resistance in *Escherichia coli* isolates. *Jundishapur J Microbiol*. 2022;14:e119858. <https://doi.org/10.5812/jjm.119858>.
  33. Philips S, Van Hoecke F, De Laere E, Vervaeke S, De Smedt R, Boelens J, De Geyter D, Piérard D, Lagrou K. Comparison of two commercial colorimetric broth microdilution tests for *Candida* susceptibility testing: Sensititre YeastOne versus MICRONAUT-AM. *JoF*. 2021;7:356. <https://doi.org/10.3390/jof7050356>.
  34. Gutiérrez-del-Río I, López-Ibáñez S, Magadán-Corpas P, Fernández-Calleja L, Pérez-Valero Á, Tuñón-Granda M, Miguélez EM, Villar CJ, Lombó F. Terpenoids and polyphenols as natural antioxidant agents in food preservation. *Antioxidants*. 2021;10:1264. <https://doi.org/10.3390/antiox10081264>.
  35. Hoffner SE, Klintz L, Olsson-Liljequist B, Bolmström A. Evaluation of Etest for rapid susceptibility testing of *Mycobacterium chelonae* and *M. fortuitum*. *J Clin Microbiol*. 1994;32:1846–9. <https://doi.org/10.1128/jcm.32.8.1846-1849.1994>.
  36. Åkerlund A, Jonasson E, Matuschek E, Serrander L, Sundqvist M, Kahlmeter G, the RAST Study Group, Dzajic E, Hansen DS, Agergaard harlotte N, Pätäri-Sampo A, Manninen R, Grönroos JO, Rasigade J-P, Salka W, Boyer PH, Lebessi E, Zapaniotis N, Petinaki E, Spiliopoulou I, Kolonitsiou F, Helgason KO, Brazil J, Riccobono E, Lo Cascio G, Maccacaro L, Kolstad H, Haukeland TS, Kellokumpu P-L, Fossum Mjøen A, Tofteland S, Harbak B, Hartzen SH, Haug Hånsen S, Gammelsrud KW, Skolbekken U, Michalsen N, Brekken AL, Pedersen B, Guenigsman B, Lia A, Berg AK, Marco F, Pitart C, Egea P, Cortes-Cuevas JL, Machuca J, Wietzke M, Dammström M, Granström R, Corneliussen M, Skarstedt M, Frykfeldt K, Ivarsson CL, Sergejev A, Hagström S, Lidén U, Rydberg J, Ramström H, Fröding I, Petropoulos EA, Ininbergs K, Jalal S, Persson A-LS, Kamenska N, Granlund K, Smekal A-K, Hill A, Rådberg G, Heyman G, Rodriguez L, Vennberg L, Hazirolan G, Akyar I, Gülşen Altınkanat G, Kaygisiz ANS, Dzajic E, Hansen DS, Agergaard harlotte N, Pätäri-Sampo A, Manninen R, Grönroos JO, Rasigade J-P, Salka W, Boyer PH, Lebessi E, Zapaniotis N, Petinaki E, Spiliopoulou I, Kolonitsiou F, Helgason KO, Brazil J, Riccobono E, Lo Cascio G, Maccacaro L, Kolstad H, Haukeland TS, Kellokumpu P-L, Fossum Mjøen A, Tofteland S, Harbak B, Hartzen SH, Haug Hånsen S, Gammelsrud KW, Skolbekken U, Michalsen N, Brekken AL, Pedersen B, Guenigsman B, Lia A, Berg AK, Marco F, Pitart C, Egea P, Cortes-Cuevas JL, Machuca J, Wietzke M, Dammström M, Granström R, Corneliussen M, Skarstedt M, Frykfeldt K, Ivarsson CL, Sergejev A, Hagström S, Lidén U, Rydberg J, Ramström H, Fröding I, Petropoulos EA, Ininbergs K, Jalal S, Persson A-LS, Kamenska N, Granlund K, Smekal A-K, Hill A, Rådberg G, Heyman G, Rodriguez L, Vennberg L, Hazirolan G, Akyar I, Gülşen Altınkanat G, Kaygisiz ANS (2020) EUCAST rapid antimicrobial susceptibility testing (RAST) in blood cultures: validation in 55 European laboratories. *J Antimicrob Chemother* 75:3230–3238 <https://doi.org/10.1093/jac/dkaa333>
  37. van Belkum A, Burnham C-AD, Rossen JWA, Mallard F, Rochas O, Dunne WM. Innovative and rapid antimicrobial susceptibility testing systems. *Nat Rev Microbiol*. 2020;18:299–311. <https://doi.org/10.1038/s41579-020-0327-x>.
  38. The Pew Charitable Trusts. (2021) Tracking the global pipeline of antibiotics in development, March 2021. <https://www.pewtrusts.org/en/research-and-analysis/issue-briefs/2021/03/tracking-the-global-pipeline-of-antibiotics-in-development>. Accessed 2 Sept 2022.
  39. Plackett B. Why big pharma has abandoned antibiotics. *Nature*. 2020;586:S50–S50. <https://doi.org/10.1038/d41586-020-02884-3>.
  40. Melo MCR, Maasch JRMA, de la Fuente-Nunez C. Accelerating antibiotic discovery through artificial intelligence. *Commun Biol*. 2021;4:1050. <https://doi.org/10.1038/s42003-021-02586-0>.
  41. Schneider G. Automating drug discovery. *Nat Rev Drug Discov*. 2018;17:97–113. <https://doi.org/10.1038/nrd.2017.232>.
  42. Anik Ü (2017) Electrochemical medical biosensors for POC applications. In: RJ Narayan (ed.), *Medical biosensors for point of care (POC) applications*. Duxford: Woodhead Publishing, pp 275–292.
  43. Ahmadian E, Samiei M, Hasanzadeh A, Kavetsky T, Jafari S, Alipour M, Salatin S, Rameshrad M, Sharifi S, Eftekhari A, Hasanzadeh M. Monitoring of drug resistance towards reducing the toxicity of pharmaceutical compounds: past, present and future. *J Pharm Biomed*. 2020;186:113265. <https://doi.org/10.1016/j.jpba.2020.113265>.
  44. Hayat A, Catanante G, Marty JL. Current trends in nanomaterial-based amperometric biosensors. *Sensors (Switzerland)*. 2014;14:23439–61. <https://doi.org/10.3390/s141223439>.
  45. Menon S, Vishnu N, Panchapakesan SSS, Kumar AS, Sankaran K, Unrau P, Parameswaran MA. Electrochemical sensing methodology for antibiogram assays. *J Electrochem Soc*. 2014;161:B3061–3. <https://doi.org/10.1149/2.011402jes>.
  46. Mishra P, Singh D, Mishra KP, Kaur G, Dhull N, Tomar M, Gupta V, Kumar B, Ganju L. Rapid antibiotic susceptibility testing by resazurin using thin film platinum as a bio-electrode. *J Microbiol Methods*. 2019;162:69–76. <https://doi.org/10.1016/j.mimet.2019.05.009>.
  47. Crane B, Hughes JP, Rowley Neale SJ, Rashid M, Linton PE, Banks CE, Shaw KJ. Rapid antibiotic susceptibility testing using resazurin bulk modified screen-printed electrochemical sensing platforms. *Analyst*. 2021;146:5574–83. <https://doi.org/10.1039/d1an00850a>.
  48. Bolotsky A, Muralidharan R, Butler D, Root K, Murray W, Liu Z, Ebrahimi A. Organic redox-active crystalline layers for reagent-free electrochemical antibiotic susceptibility testing (ORACLE-AST). *Biosens Bioelectron*. 2021;172:112615. <https://doi.org/10.1016/j.bios.2020.112615>.
  49. Karasinski J, White L, Zhang Y, Wang E, Andreescu S, Sadik OA, Lavine BK, Vora M. Detection and identification of bacteria using antibiotic susceptibility and a multi-array electrochemical sensor with pattern recognition. *Biosens Bioelectron*. 2007;22:2643–9. <https://doi.org/10.1016/j.bios.2006.10.037>.
  50. Chalenko Y, Shumyantseva V, Ermolaeva S, Archakov A. Electrochemistry of *Escherichia coli* JM109: direct electron transfer and antibiotic resistance. *Biosens Bioelectron*. 2012;32:219–23. <https://doi.org/10.1016/j.bios.2011.12.015>.
  51. Hannah S, Addington E, Alcorn D, Shu W, Hoskisson PA, Corrigan DK. Rapid antibiotic susceptibility testing using low-cost, commercially available screen-printed electrodes. *Biosens Bioelectron*. 2019;145:111696. <https://doi.org/10.1016/j.bios.2019.111696>.
  52. Hannah S, Dobrea A, Lasserre P, Blair EO, Alcorn D, Hoskisson PA, Corrigan DK. Development of a rapid, antimicrobial



- susceptibility test for *E. coli* based on low-cost, screen-printed electrodes. *Biosensors*. 2020;10:153. <https://doi.org/10.3390/bios10110153>.
53. Brosel-Oliu S, Mergel O, Uria N, Abramova N, van Rijn P, Bratov A. 3D impedimetric sensors as a tool for monitoring bacterial response to antibiotics. *Lab Chip*. 2019;19:1436–47. <https://doi.org/10.1039/C8LC01220B>.
  54. Abeyrathne C, Huynh D, McIntire T, Nguyen T, Nasr B, Zantomio D, Chana G, Abbot I, Choong P, Catton M, Skafidas E. Lab on a chip sensor for rapid detection and antibiotic resistance determination of *Staphylococcus aureus*. *Analyst*. 2016;21:1922–9. <https://doi.org/10.1039/c5an02301g>.
  55. Puttaswamy S (2013) Novel electrical method for the rapid determination of minimum inhibitory concentration (MIC) and assay of bactericidal/bacteriostatic activity. *J Biosens Bioelectron* 2 <https://doi.org/10.4172/2155-6210.S2-003>
  56. Safavieh M, Pandya HJ, Venkataraman M, Thirumalaraju P, Kanakasabapathy MK, Singh A, Prabhakar D, Chug MK, Shafiee H. Rapid real-time antimicrobial susceptibility testing with electrical sensing on plastic microchips with printed electrodes. *ACS Appl Mater Interfaces*. 2017;9:12832–40. <https://doi.org/10.1021/acsami.6b16571>.
  57. Jo N, Kim B, Lee S-M, Oh J, Park IH, Jin Lim K, Shin J-S, Yoo K-H. Aptamer-functionalized capacitance sensors for real-time monitoring of bacterial growth and antibiotic susceptibility. *Biosens Bioelectron*. 2018;102:164–70. <https://doi.org/10.1016/j.bios.2017.11.010>.
  58. Yang Y, Gupta K, Ekinici KL. All-electrical monitoring of bacterial antibiotic susceptibility in a microfluidic device. *Proc Natl Acad Sci USA*. 2020;117:10639–44. <https://doi.org/10.1073/pnas.1922172117>.
  59. Rampersad SN. Multiple applications of Alamar Blue as an indicator of metabolic function and cellular health in cell viability bioassays. *Sensors*. 2012;12:12347–60. <https://doi.org/10.3390/s120912347>.
  60. McGaw LJ, Elgorashi EE, Eloff JN (2014) Cytotoxicity of African medicinal plants against normal animal and human cells. In: *Toxicological survey of African medicinal plants*. Elsevier, pp 181–233.
  61. Kanagavalli P, Andrew C, Veerapandian M, Jayakumar M. In-situ redox-active hybrid graphene platform for label-free electrochemical biosensor: insights from electrodeposition and electroless deposition. *TrAC*. 2021;143:116413. <https://doi.org/10.1016/j.trac.2021.116413>.
  62. Yang Y, Xu M, Guo J, Sun G. Bacterial extracellular electron transfer in bioelectrochemical systems. *Process Biochem*. 2012;47:1707–14. <https://doi.org/10.1016/j.procbio.2012.07.032>.
  63. Al Mamun M, Wahab YA, Hossain MAM, Hashem A, Johan MR. Electrochemical biosensors with aptamer recognition layer for the diagnosis of pathogenic bacteria: barriers to commercialization and remediation. *TrAC*. 2021;145:116458. <https://doi.org/10.1016/j.trac.2021.116458>.
  64. Dai J, Hamon M, Jambovane S. Microfluidics for antibiotic susceptibility and toxicity testing. *Bioengineering*. 2016;3:25. <https://doi.org/10.3390/bioengineering3040025>.
  65. Webster TA, Sismaet HJ, Chan IJ, Goluch ED. Electrochemically monitoring the antibiotic susceptibility of *Pseudomonas aeruginosa* biofilms. *Analyst*. 2015;140:7195–201. <https://doi.org/10.1039/C5AN01358E>.
  66. Vinogradov SM, Satterwhite-Warden JE, Hicks RP, Anderson E, Hvastkovs EG. Electrochemical detection of alginate penetration in immobilized layer-by-layer films by unnatural amino acid containing antimicrobial peptides. *Electrochim Acta*. 2015;186:245–52. <https://doi.org/10.1016/j.electacta.2015.10.051>.
  67. Robb AJ, Vinogradov S, Danell AS, Anderson E, Blackledge MS, Melander C, Hvastkovs EG. Electrochemical detection of small molecule induced *Pseudomonas aeruginosa* biofilm dispersion. *Electrochim Acta*. 2018;268:276–82. <https://doi.org/10.1016/j.electacta.2018.02.113>.
  68. Sultana ST, Call DR, Beyenal H. Eradication of *Pseudomonas aeruginosa* biofilms and persister cells using an electrochemical scaffold and enhanced antibiotic susceptibility. *NPJ Biofilms Microbiomes*. 2016;2:2. <https://doi.org/10.1038/s41522-016-0003-0>.
  69. Ramsey DM, Wozniak DJ. Understanding the control of *Pseudomonas aeruginosa* alginate synthesis and the prospects for management of chronic infections in cystic fibrosis: *P. aeruginosa* pathogenesis. *Mol Microbiol*. 2005;56:309–22. <https://doi.org/10.1111/j.1365-2958.2005.04552.x>.
  70. Malhotra BD, Ali MA. Nanomaterials in biosensors: fundamentals and applications. *Nanomaterials for Biosensors*. 2018;1:1–74. <https://doi.org/10.1016/B978-0-323-44923-6.00001-7>.
  71. Anjum S, Ishaque S, Fatima H, Farooq W, Hano C, Abbasi BH, Anjum I. Emerging applications of nanotechnology in healthcare systems: grand challenges and perspectives. *Pharmaceuticals*. 2021;14:707. <https://doi.org/10.3390/ph14080707>.
  72. Holzinger M, Le Goff A, Cosnier S (2014) Nanomaterials for biosensing applications: a review. *Front Chem* 2. <https://doi.org/10.3389/fchem.2014.00063>
  73. Malik P, Gupta R, Malik V, Ameta RK. Emerging nanomaterials for improved biosensing. *Meas Sensors*. 2021;16:100050. <https://doi.org/10.1016/j.measen.2021.100050>.
  74. Toyos-Rodríguez C, García-Alonso FJ, de la Escosura-Muñiz A. Electrochemical biosensors based on nanomaterials for early detection of Alzheimer's disease. *Sensors*. 2020;20:4748. <https://doi.org/10.3390/s20174748>.
  75. Baig N, Sajid M, Saleh TA. Recent trends in nanomaterial-modified electrodes for electroanalytical applications. *TrAC*. 2019;111:47–61. <https://doi.org/10.1016/j.trac.2018.11.044>.
  76. Ahmad R, Wolfbeis OS, Hahn Y-B, Alshareef HN, Torsi L, Salama KN. Deposition of nanomaterials: a crucial step in biosensor fabrication. *Materials Today Communications*. 2018;17:289–321. <https://doi.org/10.1016/j.mtcomm.2018.09.024>.
  77. Iglesias-Mayor A, Amor-Gutiérrez O, Costa-García A, de la Escosura-Muñiz A. Nanoparticles as emerging labels in electrochemical immunosensors. *Sensors*. 2019;19:5137. <https://doi.org/10.3390/s19235137>.
  78. Malathi S, Pakrudheen I, Kalkura SN, Webster TJ, Balasubramanian S. Disposable biosensors based on metal nanoparticles. *Sensors International*. 2022;3:100169. <https://doi.org/10.1016/j.sintl.2022.100169>.
  79. Kaushal S, Nanda SS, Samal S, Yi DK. Strategies for the development of metallic-nanoparticle-based label-free biosensors and their biomedical applications. *ChemBioChem*. 2020;21:576–600. <https://doi.org/10.1002/cbic.201900566>.
  80. Toyos-Rodríguez C, Adawy A, García-Alonso FJ, de la Escosura-Muñiz A. Enhancing the electrocatalytic activity of palladium nanocluster tags by selective introduction of gold atoms: application for a wound infection biomarker detection. *Biosens Bioelectron*. 2022;200:113926. <https://doi.org/10.1016/j.bios.2021.113926>.
  81. Makabenta JMV, Nabawy A, Li C-H, Schmidt-Malan S, Patel R, Rotello VM. Nanomaterial-based therapeutics for antibiotic-resistant bacterial infections. *Nat Rev Microbiol*. 2021;19:23–36. <https://doi.org/10.1038/s41579-020-0420-1>.
  82. Morena AG, Bassegoda A, Natan M, Jacobi G, Banin E, Tzanov T. Antibacterial properties and mechanisms of action of sonoenzymatically synthesized lignin-based nanoparticles. *ACS Appl Mater Interfaces*. 2022;14:37270–9. <https://doi.org/10.1021/acsami.2c05443>.
  83. Basavegowda N, Baek K-H. Multimetallic nanoparticles as alternative antimicrobial agents: challenges and perspectives. *Molecules*. 2021;26:912. <https://doi.org/10.3390/molecules26040912>.



84. Rao RP, Sharma S, Mehrotra T, Das R, Kumar R, Singh R, Roy I, Basu T. Rapid electrochemical monitoring of bacterial respiration for Gram-positive and Gram-negative microbes: potential application in antimicrobial susceptibility testing. *Anal Chem.* 2020;92:4266–74. <https://doi.org/10.1021/acs.analchem.9b04810>.
85. Ren Y, Ji J, Sun J, Pi F, Zhang Y, Sun X. Rapid detection of antibiotic resistance in Salmonella with screen printed carbon electrodes. *J Solid State Electrochem.* 2020;24:1539–49. <https://doi.org/10.1007/s10008-020-04645-8>.
86. Xu X, Chen S, Yu Y, Virtanen P, Wu J, Hu Q, Koskineniemi S, Zhang Z. All-electrical antibiotic susceptibility testing within 30 min using silicon nano transistors. *Sens Actuators, B: Chemical.* 2022;357:131458. <https://doi.org/10.1016/j.snb.2022.131458>.
87. Das R, Singh N. Exploring electrochemistry of carbon nanodots and its application in noninvasive bacterial growth monitoring. *Biosens Bioelectron.* 2019;144:111640. <https://doi.org/10.1016/j.bios.2019.111640>.
88. Zheng L, Shen Y, Dong W, Zheng C, Zhou R, Lou Y-L. Rapid detection and antimicrobial susceptibility testing of pathogens using AgNPs-invertase complexes and the personal glucose meter. *Front Bioeng Biotechnol.* 2022;9:795415. <https://doi.org/10.3389/fbioe.2021.795415>.
89. de la Escosura-Muñiz A, de la, Ivanova K, Tzanov T. Electrical evaluation of bacterial virulence factors using nanopores. *ACS Appl Mater Interfaces.* 2019;11:13140–6. <https://doi.org/10.1021/acsami.9b02382>.
90. Olivieri F, Castaldo R, Cocca M, Gentile G, Lavorgna M. Mesoporous silica nanoparticles as carriers of active agents for smart anticorrosive organic coatings: a critical review. *Nanoscale.* 2021;13:9091–111. <https://doi.org/10.1039/D1NR01899J>.
91. de la Escosura-Muñiz A, Merkoçi A. Nanochannels for electrical biosensing *TrAC.* 2016;79:134–50. <https://doi.org/10.1016/j.trac.2015.12.003>.
92. de la Escosura-Muñiz A, Merkoçi A. Nanochannels preparation and application in biosensing. *ACS Nano.* 2012;6:7556–83. <https://doi.org/10.1021/nn301368z>.
93. Burnham C-AD, Leeds J, Nordmann P, O'Grady J, Patel J. Diagnosing antimicrobial resistance. *Nat Rev Microbiol.* 2017;15:697–703. <https://doi.org/10.1038/nrmicro.2017.103>.
94. Lebovitz EE, Burbelo PD. Commercial multiplex technologies for the microbiological diagnosis of sepsis. *Mol Diagn Ther.* 2013;17:221–31. <https://doi.org/10.1007/s40291-013-0037-4>.
95. Azimi S, Lewin GR, Whiteley M (2022) The biogeography of infection revisited. *Nat Rev Microbiol.* <https://doi.org/10.1038/s41579-022-00683-3>
96. Yung DBY, Sircombe KJ, Pletzer D. Friends or enemies? The complicated relationship between *Pseudomonas aeruginosa* and *Staphylococcus aureus*. *Mol Microbiol.* 2021;116:1–15. <https://doi.org/10.1111/mmi.14699>.
97. Christaki E, Marcou M, Tofarides A. Antimicrobial resistance in bacteria: mechanisms, evolution, and persistence. *J Mol Evol.* 2020;88:26–40. <https://doi.org/10.1007/s00239-019-09914-3>.

**Publisher's note** Springer Nature remains neutral with regard to jurisdictional claims in published maps and institutional affiliations.

Springer Nature or its licensor (e.g. a society or other partner) holds exclusive rights to this article under a publishing agreement with the author(s) or other rightsholder(s); author self-archiving of the accepted manuscript version of this article is solely governed by the terms of such publishing agreement and applicable law.



## Enhancing the electrocatalytic activity of palladium nanocluster tags by selective introduction of gold atoms: Application for a wound infection biomarker detection

Celia Toyos-Rodríguez<sup>a,b</sup>, Alaa Adawy<sup>c</sup>, Francisco Javier García-Alonso<sup>b,d</sup>, Alfredo de la Escosura-Muñiz<sup>a,b,\*</sup>

<sup>a</sup> NanoBioAnalysis Group-Department of Physical and Analytical Chemistry, University of Oviedo, Julián Clavería 8, 33006, Oviedo, Spain

<sup>b</sup> Biotechnology Institute of Asturias, University of Oviedo, Santiago Gascon Building, 33006, Oviedo, Spain

<sup>c</sup> Unit of Electron Microscopy and Nanotechnology, Institute for Scientific and Technological Resources (SCTs), Edificio Severo Ochoa S/n, Campus de El Cristo, 33006, Oviedo, Spain

<sup>d</sup> NanoBioAnalysis Group-Department of Organic and Inorganic Chemistry, University of Oviedo, Julián Clavería 8, 33006, Oviedo, Spain

### ARTICLE INFO

#### Keywords:

Palladium nanocluster  
Electrocatalysis  
Bimetallic nanoparticles  
Immunosensor  
Wound infection  
Biomarker

### ABSTRACT

In this work, an unprecedented study exploring the role that slight changes into the Pd/Au proportion have in the electrocatalytic activity of bimetallic Pd-AuNPs toward the oxygen reduction reaction (ORR) is conducted. In particular, a careful control of the amount of Au atoms introduced in the cluster and the evaluation of the optimum Pd:Au ratio for getting the maximum catalytic activity is performed for the first time.

First, PdNPs are synthesized by alcohol reduction in the presence of polyvinylpyrrolidone, and gold atoms are selectively introduced on vertex or corner positions of the cluster in different amounts following a galvanic substitution procedure. Average elemental analysis done relying on EDX spectroscopy allows to evaluate the Pd:Au ratio in the Pd-AuNPs obtained. Lineal sweep voltammetry and chronoamperometry are used for the evaluation of the Pd-AuNPs electrocatalytic activity toward ORR at a neutral pH compared to PdNPs and AuNPs alone. Our results indicate that, the synergy between both metals is strongly enhanced when the amount of gold is controlled and occupies the more reactive positions of the cluster, reaching a maximum activity for the NPs containing a 30% of gold, while an excess of this metal leads to a decrease in such activity, as a shelter of the PdNPs is achieved. Chronoamperometric analysis allows the quantification of the optimal Pd-AuNPs at over  $6 \times 10^9$  NPs/mL levels.

Such optimal Pd-AuNPs were used as tags, taking advantage of the bio-functionalities of gold present in the cluster, in a proof-of-concept electrochemical immunosensor for the detection of hyaluronidase wound infection biomarker, using magnetic beads as platforms. Hyaluronidase was detected at levels as low as 50 ng/mL (0.02 U/mL; 437 U/mg) with good reproducibility (RSD below 8%) and selectivity (evaluated against bovine serum albumin, immunoglobulin G and lysozyme). The low matrix effects inherent to the use of magnetic bead platforms allowed us to discriminate between wound exudates with both sterile and infected ulcers without sample pre-treatment. This novel electrocatalytic immunoassay has the advantage, over common methods for NP tags electrochemical detection, of the signal generation in the same neutral medium where the immunoassay takes place (10 mM PBS pH 7.4), avoiding the use of additional and hazardous reagents, bringing it closer to their use as point-of-care devices.

Overall, our findings may be of great interest not only for biosensing, but also for applications such as energy converting on fuel cells, in which the ORR has a pivotal role.

\* Corresponding author. NanoBioAnalysis Group-Department of Physical and Analytical Chemistry, University of Oviedo, Julián Clavería 8, 33006, Oviedo, Spain.  
E-mail address: [alfredo.escosura@uniovi.es](mailto:alfredo.escosura@uniovi.es) (A. de la Escosura-Muñiz).

## 1. Introduction

The use of nanomaterials has been a breakthrough since they were first synthesized and implemented into different research topics with continuous progress (Bayda et al., 2020; Welch and Compton, 2006). Biosensing is among the main areas of application of these materials, in which the usage of nanomaterials, both as electrode modifiers and as labels has implied a significant improvement. Their unique properties, including electron transfer, biocompatibility and electroactive and electrocatalytic activity, among others, has enabled decreasing detection limits and increasing sensitivity, selectivity and reproducibility of the assays (Carneiro et al., 2019; Holzinger et al., 2014; Huizhi et al., 2008; Iglesias-Mayor et al., 2019; Toyos-Rodríguez et al., 2020). Their use as labels in immunosensing has been deeply studied, constituting an outstanding alternative to traditionally used enzymes (de la Escosura-Muñiz et al., 2008, 2010a; de la Escosura-Muñiz and Merkoçi, 2010; Lara and Pérez-Potti, 2018).

In this context, metal nanoparticles have emerged due to their catalytic potential, making them reporters with an outsized sensitivity that is associated with their high surface-to-volume ratios, high mechanical strength and ease of functionalization (Doria et al., 2012; Wittenberg and Haynes, 2009). From all metal nanoparticles, gold nanoparticles are chiefly used. However, in most cases their detection requires the use of highly acidic media, as it is the case of their use as catalysts of hydrogen evolution reaction (HER) (Baptista-Pires et al., 2019; de la Escosura-Muñiz et al., 2015, 2010b; Hassan et al., 2015; Maltez-da Costa et al., 2012, 2010). However, this extra requisite results the incorporation of additional steps that increase the time of analysis. For this, the use of alternative nanoparticles capable of acting as catalysts at neutral pH has been recently explored (Cao et al., 2020; Iglesias-Mayor et al., 2020; Rivas et al., 2014).

The use of alternative nanoparticles is based on the catalysis of reactions that naturally take place at neutral pH, as water oxidation reaction (WOR) or oxygen reduction reaction (ORR). ORR is one of the most studied electrocatalytic reactions as it plays a pivotal role in the electrochemical energy conversion (Maduraiveeran, 2021; Rahman et al., 2021; Rößner and Armbrüster, 2019; Tian et al., 2020). This cathodic electrode reaction is a complicated and slow process in which various reaction intermediates are embedded. Thus, the reduction of O<sub>2</sub> has been proposed to take place following two different pathways: a straightforward four electron reaction (1) or an indirect process called the two electron process (2) (Han et al., 2009; Lim and Wilcox, 2012; Tammeveski et al., 2012; Wang et al., 2021).



The role of metals such as palladium, platinum or silver has been related to the formation first of a superoxide ion (O<sub>2</sub> + e<sup>-</sup> = O<sub>2</sub><sup>•-</sup>) (Kusunoki et al., 2021; Singh and Buttry, 2012; Spendelow and Wieckowski, 2007).

Platinum (Pt) catalysts have been the benchmark in the ORR catalysis owing to their durability in acidic media and their high activity (Nørskov et al., 2004). However, their high cost is their main drawback. Therefore, the use of other metals has been postulated as an alternatively cheaper catalyst that also boosts ORR activation (Tian et al., 2020).

In this context, palladium (Pd) as a metal has been proven to be as promising as Pt alloy (Wang et al., 2015a, 2015b; Wu et al., 2021) or in combination with other metals. Zhang et al. (2012), described the combination of Pd and Au in a crown-jewel structure with a hexagonal Pd core decorated with upper Au atoms mimicking the disposition of a crown. The selective introduction of upper Au atoms in the vertex and corners of the Pd core, provided a synergistic effect increasing the intrinsic catalytic activity of Pd, as shown toward the glucose oxidation and H<sub>2</sub>O<sub>2</sub> decomposition reactions.

In this context, the objective of this work is to explore for the first

time the role that the introduction of increasing concentrations of Au into Pd nanoclusters have in their electrocatalytic activity toward the oxygen reduction reaction (ORR). A careful control of the amount of Au atoms introduced in the cluster and the evaluation of the optimum Pd: Au ratio for getting the maximum catalytic activity is a key study, missing in the bibliography. This may be of great interest not only for biosensing, but also for applications such as energy converting on fuel cells.

As a proof-of-concept of application in biosensing, the synthesized Pd-AuNPs prepared with an optimum Pd/Au rate have been used as tags in a magnetic bead-based immunoassay for the detection of hyaluronidase, a chronic wound infection biomarker. Chronic wounds represent an important healthcare challenge that affects 1–2% of population in developed countries, a number that it is expected to increase in association to the rise in life expectancy and the establishment of a more sedentary lifestyle (Clinton and Carter, 2015; Järbrink et al., 2016). Chronic wounds lack from healing and infection is a common complication that worsens the situation, prolonging pain and morbidity in patients and requiring long hospitalization periods (Han and Ceilley, 2017; Verbanic et al., 2020). Nosocomial pathogens as Gram-positive *Staphylococcus aureus* or *Enterococcus faecium* and Gram-negative *Pseudomonas aeruginosa* proliferate in chronic wounds, so that their identification to certain stain is required for antibiotic administration (Han et al., 2011; Schmidtchen, Helene Wolff, Carita H, 2001; Serra et al., 2015; Zhou et al., 2020). However, actual identification of infection is based on culture techniques and gold-standard biopsy, both invasive and time-consuming procedures, so as the development of alternative tools for a rapid diagnosis is desirable (de la Escosura-Muñiz et al., 2019; Han et al., 2011; Mahnic et al., 2021; Melendez et al., 2010). In this context, several biomarkers such as hyaluronidase have been identified as virulence factors. Hyaluronidase is produced by the main pathogenic Gram-positive bacteria that colonize mucosal surfaces and skin, although its role is still being investigated (Hynes and Walton, 2000). Even though there are human hyaluronidases, bacterial ones (EC 4.2.2.1 or EC 4.2.99.1) are characterized by producing unsaturated disaccharides through endo-N-acetylhexosaminidase activity (Stern and Jedrzejewski, 2006). This bacterial specificity makes hyaluronidase a potential biomarker of infection in chronic wounds, also allowing to discern between bacterial genders.

In addition to the unprecedented study related to the effect of the Pd: Au ratio on the electrocatalytic activity toward the ORR, to the best of our knowledge, this is the first time that this type of bimetallic NPs are used as tags in biosensing, taking advantage of such property.

## 2. Experimental

### 2.1. Reagents and equipment

Palladium (II) chloride ≥ 99.9%, polyvinylpyrrolidone mol wt 40.000, gold (III) chloride trihydrate 99.9%, gold nanoparticles (5 nm diameter), albumin from bovine serum (BSA), human IgG and lysozyme from chicken egg white were purchased from Sigma-Aldrich (Spain). Ethanol dried (max 0.01% H<sub>2</sub>O), tri-sodium citrate trihydrate and Tween-20 detergent were supplied by Merk Millipore (Spain).

Hyaluronidase recombinant protein, monoclonal biotin-linked antibody to hyaluronidase (epitope aa60-159) and polyclonal antibody to hyaluronidase (epitope N-terminal region) were supplied by MyBioSource (USA). As described, both antibodies are able to recognize different epitopes of the hyaluronidase protein.

Streptavidin-modified magnetic beads (M-280) were obtained from Thermo Fisher Scientific (Spain).

Ultrapure water (18.2 MΩ cm @ 25 °C) taken from a Millipore Direct-Q 3 UV purification system purchased from Millipore Ibérica S.A. (Spain) was used for the preparation of the solutions, unless otherwise stated.

Phosphate buffer electrolyte solutions used for the immunoassay

were composed of sodium chloride, potassium chloride, disodium hydrogen phosphate and potassium dihydrogen phosphate all provided by Merck (Germany).

For the immunoassay, two main buffers were used: binding and washing (B&W) buffer (0.1 M PBS pH 7.2 with 0.05% (v/v) Tween-20) and blocking buffer (BB) (0.1 M PBS pH 7.2 with 5% (w/v) BSA).

## 2.2. Instrumentation

High-resolution transmission electron microscopy (HRTEM) analysis was performed using a JEOL-JEM 2100f operated at 200 kV with a resolution of 1.9 Å between points and 1.0 Å between lines to determine the particle size distribution of the synthesized NPs. Elemental analysis of the corresponding NPs was performed relying on an energy-dispersive X-ray microanalyzer EDX (X-max, Oxford Instruments, Abingdon, UK) coupled to a bright-field detector (EM24541SIOD, JEOL) for use in the STEM mode, together with the use of INCA software (ETAS S.A.S., Saint-Ouen, France).

For the immunoassay, a MagRack® 6 from Sigma-Aldrich (Spain), a MSC-100 cooling thermo shaker from Labolan (Spain) and a thermostatic centrifuge (Rotanta 460 R) from Hettich (Germany) were used.

For the electrochemical characterization, a  $\mu$ Autolab type II with Autolab GPES software from Metrohm (Switzerland) was used. As electrodes, screen-printed carbon electrodes (SPCEs, ref DRP-110) with a working and counter carbon electrode and a silver pseudoreference electrode were used and they were connected to the potentiostat by a specific connector (ref. DRP-DSC) provided by Metrohm DropSens S.L. (Spain). For measuring the immunosandwich assay, a magnetic support for SPEs (DRP-MAGNET-700) (Metrohm DropSens S.L. (Spain)) was used.

## 2.3. Synthesis, bioconjugation and characterization of Pd-AuNPs

The synthesis of Pd nanoclusters was performed following a previously reported procedure with some modifications (Zhang et al., 2012). Briefly, 50 mL of a suspension of 0.66 mM palladium (II) chloride prepared in ethanol: water (1:3) were vigorously stirred in a round bottom flask at room temperature for 15 min. Then, 50 mL of a PVP 66 mM solution in ethanol: water (1:3) were added, and the suspension was again stirred at room temperature for additional 15 min. Afterwards, the suspension was heated at 100 °C for 2h under reflux and inert atmosphere (Ar, Ar  $\geq$  99,999, ALPHAGAZ™ 1, from AirLiquid, Spain). The final product was purified with centrifugation at 4000g, 20 °C for 30 min using Amicons® with a cut-off value of 10.000 molecular weight. Three washing steps with water and one with ethanol, using the same Amicons® were also done. Then, the remaining ethanol was evaporated, and the final product was resuspended in a 1:3 ethanol: water solution to a final concentration of 0.66 mM Pd.

For the selective introduction of gold, 20 mL of a gold (III) chloride trihydrate solution (0.135 mM, 0.735 mM, 0.835 mM, 0.935 mM or 1.135 mM) were poured into a round bottom flask containing the obtained Pd nanoclusters. The solution was heated for 30 min at 100 °C under reflux and inert atmosphere. In order to reduce aggregation, 2 mL of tri-sodium citrate in a concentration of 0.17 M were introduced in the flask and the solution was purified by centrifugation at 8000g, 4 °C for 45 min using LoBind tubes. Then, the remaining pellet was washed three times with water by centrifuging at 8000 g, 20 °C during 30 min.

The final product was resuspended to a final concentration of  $1.45 \times 10^{12}$  NPs/mL according to Nanoparticle tracking analysis (NTA) measurements.

Meanwhile, 690  $\mu$ L of the Pd-AuNPs suspension were transferred into a 1.5 mL LoBind Eppendorf® tube and centrifuged at 7500 g, 20 °C for 20 min with the addition of 10  $\mu$ L of 1.75% Tween-20. After centrifugation, the pellet was resuspended in 700  $\mu$ L of 2 mM trisodium citrate pH 7.4 solution. Then, 57.5  $\mu$ L of 50  $\mu$ g/mL solution of a polyclonal antibody anti-hyaluronidase were added and incubated for 1 h at 650

rpm, 25 °C. For purification, the solution was centrifuged at 7500 g, 4 °C for 15 min, the supernatant was removed, and the pellet resuspended in 0.1M PBS pH 7.2 with 1% BSA.

## 2.4. Electrochemical measurements

The electrocatalytic activity of the obtained Pd and Pd-AuNPs toward the ORR was electrochemically evaluated by dropping 10  $\mu$ L of the NP suspension onto the working electrode of an SPCE. Then, the solution was kept until complete absorption, when 40  $\mu$ L of 10 mM PBS pH 7.4 were added. For obtaining the background signals, 50  $\mu$ L of a 10 mM PBS pH 7.4 solution were used. Linear sweep voltammogram (LSV) scans were recorded in the range from 0 V to  $-0.8$  V at a scan rate of 0.1 V/s.

Chronoamperometric scans were obtained maintaining a fixed potential of  $-0.45$  V for 50s. Signal at 5s was selected as analytical signal for the evaluation of the electrocatalytic activity of the different Pd-AuNPs toward the ORR and for the quantitative studies.

In all the experiments, measurements were performed by triplicate at room temperature, using a different SPCE.

## 2.5. Immunoassay for the detection of hyaluronidase wound infection biomarker

Hyaluronidase was detected using magnetic bead (MB) platforms and Pd-AuNPs tags, adapting a previously reported immunoassay format (Iglesias-Mayor et al., 2020). Briefly, 15  $\mu$ L (10 mg/mL) of commercially available streptavidin-modified MBs were conveyed to a 0.5 mL LoBind Eppendorf tube, and washed three times with B&W buffer. Then, MBs were resuspended in 135  $\mu$ L of B&W buffer and 15  $\mu$ L of 15  $\mu$ g/mL biotin-linked monoclonal anti-hyaluronidase antibody were added, and the solution was incubated for 30 min at 25 °C, 650 rpm in a thermo shaker incubator. Past this time, the excess of biotin-linked monoclonal anti-hyaluronidase antibody was removed with the help of a MagRack®, and the solution was washed three-times with B&W buffer. Then, 150  $\mu$ L of blocking buffer (PBS 0.1 M pH 7.2 with 5% BSA) were added to each tube and incubated for 1 h at the same heating and stirring conditions to minimize unspecific absorptions.

Once the MBs-anti hyaluronidase conjugate was obtained, 100  $\mu$ L of hyaluronidase solutions ranging from 0 to 4600 ng/mL were added and incubated for 30 min at 25 °C, 650 rpm. The final product was washed three times with B&W buffer.

Then, 150  $\mu$ L of the Pd-AuNP conjugate were added to with the MBs final conjugate and incubated for 1h at 25 °C and 650 rpm. The resulting immunocomplex was washed twice with B&W buffer and twice with 10 mM PBS pH 7.4 and reconstituted in 150  $\mu$ L of this buffer. The final conjugate was chronoamperometrically measured by placing 40  $\mu$ L of the final solution on the working area of a SPCEs (with a magnetic support on the reverse side) and applying a voltage of  $-0.45$  V for 50 s, being the value of the current recorded at 5 s selected as analytical signal.

Selectivity was evaluated following the above detailed procedure but with the addition of solutions at 750 ng/mL of albumin from bovine serum (BSA), immunoglobulin G (IgG) or lysozyme (Lys) instead of 750 ng/mL hyaluronidase. Exudates from patients with both sterile and infected ulcers were also measured following the same immunoassay procedure than the detailed for the hyaluronidase standard solutions. Both control and infected swabs were provided by the Chronic Ulcers Unit of the Hospital Universitario Central de Asturias (HUCA), where they were analyzed by traditional culture techniques in order to corroborate the presence of bacterial infection in the infected swab.



### 3. Results and discussion

#### 3.1. Characterization of the PdNPs and Pd-AuNPs with different Pd/Au content

Pd-AuNPs were prepared adapting a previously described procedure consisting in the selective introduction of Au atoms on vertex or corner positions of Pd nanocluster, following a galvanic replacement reaction (Fig. 1). The obtained PdNPs follow a “crown-jewel” model that was first described by Zhang et al. (2012), being this name related to the decoration that Au atoms do in the PdNPs, acting as jewels decorating a crown. This method is based on the synthesis of PdNPs, prepared by alcohol reduction in the presence of polyvinylpyrrolidone, and the subsequent introduction of Au atoms on top positions rather than sheltering the PdNPs. The introduction of Au atoms in these positions has been previously attributed to the difference in free energies associated to top, edges and face atoms of a cluster, that affect the preference of Au atoms to occupy first top positions (Campbell, 2004; Toshima et al., 2005; Zhang et al., 2012).

The presence of both metals has a synergistic effect that increases their electrocatalytic activity. Moreover, the presence of external Au atoms facilitates the further conjugation of the obtained Pd-AuNPs with antibodies, owing to the Au affinity to the cysteine groups that are present in the immunoglobulin structure (Ambrosi et al., 2007; Brust et al., 1994).

Pd-AuNPs prepared with 0.835 mM HAuCl<sub>4</sub> were selected as representative for their comparison with the starting PdNPs. High resolution-transmission electron microscopy (HRTEM) (Fig. 2A and B) characterization showed spherical nanoparticles with a diameter of  $4 \pm 1$  nm for the PdNPs, while a slight increase in the size to  $5 \pm 1$  nm was noticed for Pd-AuNPs. It is worthy to mention that a slight aggregation is observed compared to initial PdNPs, probably due to the introduction of Au. Nevertheless, we observed that the introduction of tri-sodium citrate after the synthesis seems to regulate this effect. Moreover, STEM-TEM mode EDX analysis demonstrated the presence of both Pd and Au in the Pd-AuNPs structure, as expected (Fig. 2C-D-E).

The selective introduction of increasing amounts of Au slightly leads to the galvanic replacement of Pd surface atoms by Au atoms, leading to a higher covering and affecting the electrocatalytic activity of the final NPs. So bimetallic Pd-AuNPs were prepared by adding HAuCl<sub>4</sub> solutions at different concentrations ranging from 0.135 mM to 1.135 mM to the Pd nanocluster. The average elemental analysis done relying on EDX spectroscopy of the obtained Pd-AuNPs confirmed the presence of increasing proportions of Au on the NPs with increasing the incorporated Au concentration in the reaction (Table 1). This continued to be the case until reaching equal proportions of Pd and Au.

#### 3.2. Evaluation of the electrocatalytic activity of Pd-AuNPs toward the oxygen reduction reaction (ORR): effect of the selective introduction of Au atoms in the Pd nanocluster

The electrocatalytic activity of the synthesized Pd-AuNPs toward the

oxygen reduction reaction (ORR) was first evaluated by lineal sweep voltammetry (LSV) on SPCEs. LSV scans were recorded from 0 to  $-0.8$  V in PBS 10 mM pH 7.4 at a scan rate of 0.1 V/s. Pd-AuNP-3 (as described in Table 1) were chosen for this study, being the results compared with those obtained for the unmodified PdNPs. Commercial AuNPs of 5 nm in diameter were also evaluated for comparison purposes (Fig. 3). NPs concentration was  $1.45 \times 10^{12}$  NPs/mL in all cases.

The background (curve a) reveals that the oxygen reduction starts at approximately  $-0.70$  V, and this value slightly shifts to  $-0.55$  V in the presence of AuNPs (curve b). A notable shift of the half-wave potential to around  $-0.47$  V is noticed for PdNPs, also noticing an increase in the associated current. Interestingly, this effect is dramatically enhanced for the Pd-AuNP-3, where the potential shifts to around  $-0.18$  V, accompanied with a high increase in the associated current. This behaviour is in agreement with what was expected, due to the synergy in the catalytic activity of bimetallic NPs (Sha et al., 2019; Tang and Tang, 2015; Wang et al., 2013; Zhao and Xu, 2006), which assist on the cleavage of the O=O bond, lowering the energy barrier (Ma et al., 2019) of such intermediate.

Once corroborated the higher electrocatalytic activity of the bimetallic Pd-AuNPs compared with the individual PdNPs and AuNPs, the effect of the selective introduction of Au atoms in the Pd nanocluster was studied, taking advantage of the chronoamperometric mode due to its high sensitivity, simplicity and speed. In agreement, with what was observed in the LSV study, a fix potential of  $-0.45$  V was selected for the chronoamperometric measurements, being it applied for 50 s (Fig. 4A). The absolute value of the current generated at 5 s (response time of the sensor; current profiles were not stable for shorter times) was chosen as the analytical signal used for the comparison between the different Pd-AuNPs prepared (Fig. 4B). As observed, the NPs with only a 12% of Au (Pd-AuNP-1), give an absolute electrocatalytic current similar to that of the PdNPs cluster (around 11  $\mu$ A). This suggests that although Au atoms are first introduced in the more reactive top positions (vertex and corner) of the cluster, due to the lower free energies of such atoms, this small amount is not enough to significantly enhance the catalytic activity of the Pd nanocluster. However, a dramatic increase in the absolute signal (to approx. 34  $\mu$ A) is observed for the NPs with a 21% of Au (Pd-AuNP-2). A slight increase in the signal (to approx. 38  $\mu$ A) is then observed when increasing the Au content to 30% (Pd-AuNP-3). Interestingly, increasing amounts of Au in the nanocluster (44% for Pd-AuNP-4 and 54% for Pd-AuNP-5) exert the opposite effect. These results indicate that the maximum synergy between both metals is reached for a Pd:Au ratio of approximately 2.3:1. The majority presence of the Au atoms in the vertex and corner positions of the cluster, with a high degree of coordinative unsaturation, makes them available for participating in the ORR reaction, also being responsible of such effect. In such positions of the cluster. However, for increasing amounts of Au synergy begins to lose, dominating the presence of Au, which is a worse catalyst than Pd, as corroborated by the small current (1.54  $\mu$ A) recorded for AuNPs.

According to these results, Pd-AuNP-3 were selected for their further use as electrocatalytic labels in biosensing. Before that, the ability of our

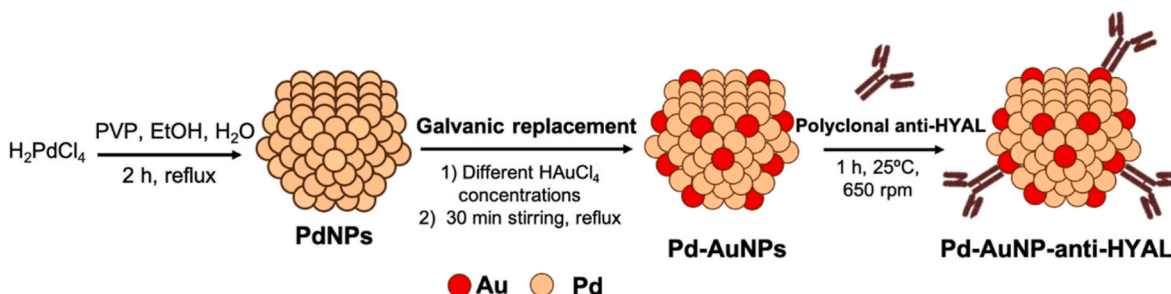
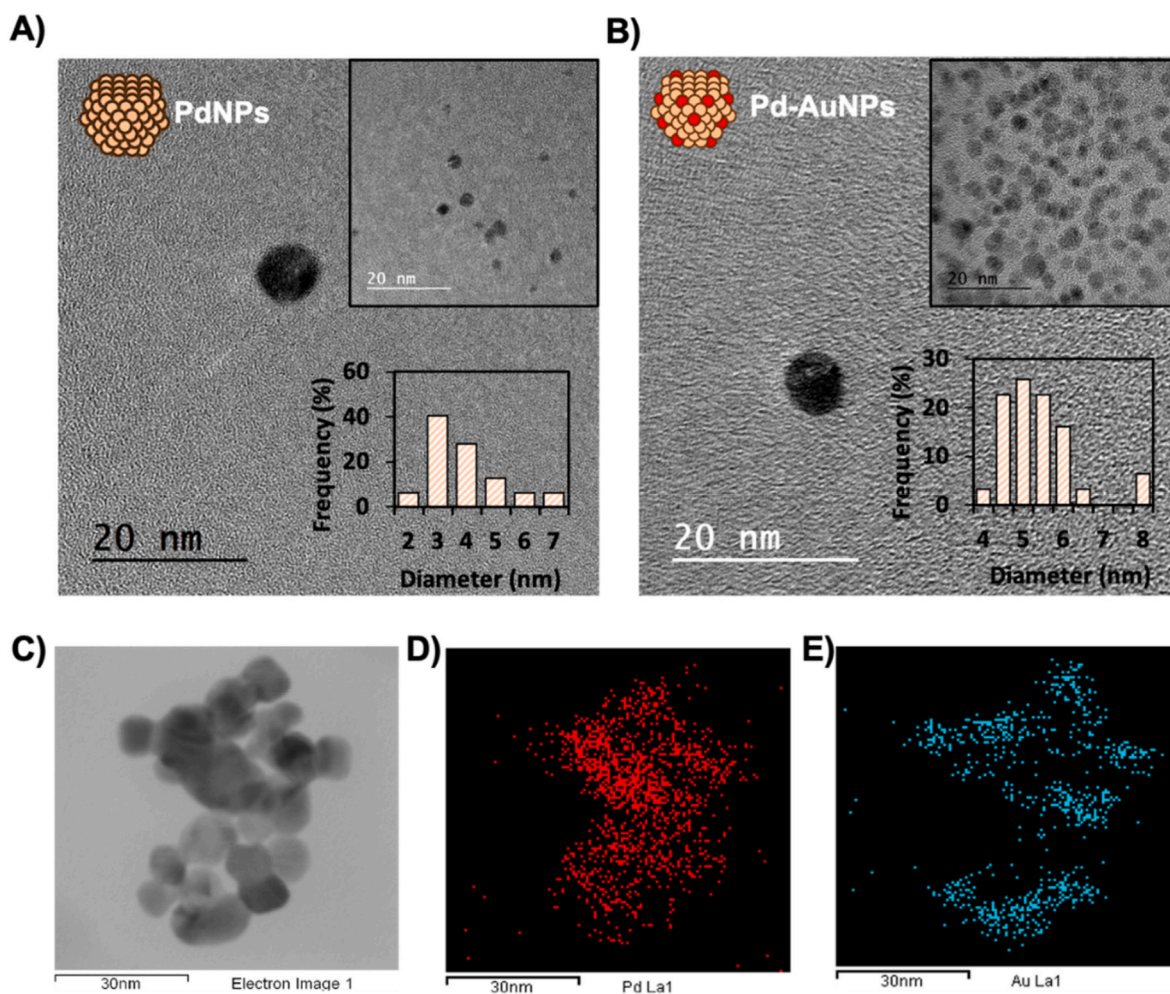


Fig. 1. Schematic representation of PdNPs and Pd-AuNPs synthesis and further conjugation with polyclonal anti-hyaluronidase (HYAL) antibodies.



**Fig. 2.** HRTEM micrographs for PdNPs (A) and Pd-AuNP (B) (prepared with 0.835 mM HAuCl<sub>4</sub>) and their particle size distribution analysis (insets); The difference in the particle density observed in both pictures is due to the different samples dilution used for the analysis. C. Bright-field STEM micrograph showing Pd-AuNPs with the performed EDX area maps showing the presence of Pd elements (D) and Au elements (E).

**Table 1**

Summary of the different synthesized Pd-AuNPs and characterization in terms of their Pd and Au average composition obtained through STEM-EDX analysis. Data are given as average  $\pm$  SD (n = 5).

Sample	[HAuCl <sub>4</sub> ] (mM)	STEM-EDX analysis	
		% Pd atom	% Au atom
Pd-AuNP-1	0.135	97 $\pm$ 1	3 $\pm$ 1
Pd-AuNP-2	0.735	83 $\pm$ 6	17 $\pm$ 3
Pd-AuNP-3	0.835	70 $\pm$ 3	30 $\pm$ 3
Pd-AuNP-4	0.935	56 $\pm$ 16	44 $\pm$ 16
Pd-AuNP-5	1.135	48 $\pm$ 3	52 $\pm$ 3

electroanalytical method to quantify small amounts of such NPs was evaluated. Chronoamperometry, under the same conditions than the described above, was also selected for such quantitative studies. As observed in Fig. 5A, a proportional increase of catalytic cathodic current was observed with corresponding increases in the concentration of Pd-AuNP-3. As shown in Fig. 5B, a linear relationship between the analytical signal (current recorded at 5 s) and the Pd-AuNP-3 concentration was found in the range between  $1 \times 10^{10}$  and  $1.2 \times 10^{11}$  NPs/mL, adjusted to the following equation:

$$I_{\text{Current}_5 \text{ s}} (\mu\text{A}) = 1.63 \times 10^{-10} [\text{Pd-AuNP-3}] (\text{NPs/mL}) - 0.05$$

The calibration curve presented a good correlation coefficient (*r*) of

0.9985 and reproducibility, with a standard deviation below 8.0% (n = 3). The limit of detection (LOD), calculated as three times the standard deviation of the intercepted divided by the slope, was of  $5.97 \times 10^9$  NPs/mL.

### 3.3. Electrocatalytic detection of hyaluronidase wound infection biomarker using Pd-AuNP tags

Hyaluronidase is an enzyme secreted as virulence factor by Gram-positive bacteria during a chronic wound infection. Hyaluronidase detection is useful for the identification of bacterial infection to provide the patients with the correct antibiotic treatment and thus reducing any bacterial antibiotic resistances. As a proof-of-concept of the suitability of the high electrocatalytically active Pd-AuNP-3 as labels, an immunosensor for the detection of hyaluronidase was developed. In this context, the evaluation of the Pd-AuNP-3 activity after conjugation with antibodies is of key relevance for the further biosensing application. As observed in Fig. 6A, such Pd-AuNP-3/antibody conjugate retained most of the catalytic activity, allowing for its use as an electrochemical tag. The little decrease in activity compared with bare Pd-AuNP-3 could be attributed to a partial blocking of the Au surface by the antibodies, which might somehow affect the synergy between both metals. This behavior was previously observed for other metallic and bimetallic NPs catalyzing different reactions (i.e. de la Escosura-Muñoz et al., 2009; Iglesias-Mayor et al., 2020).

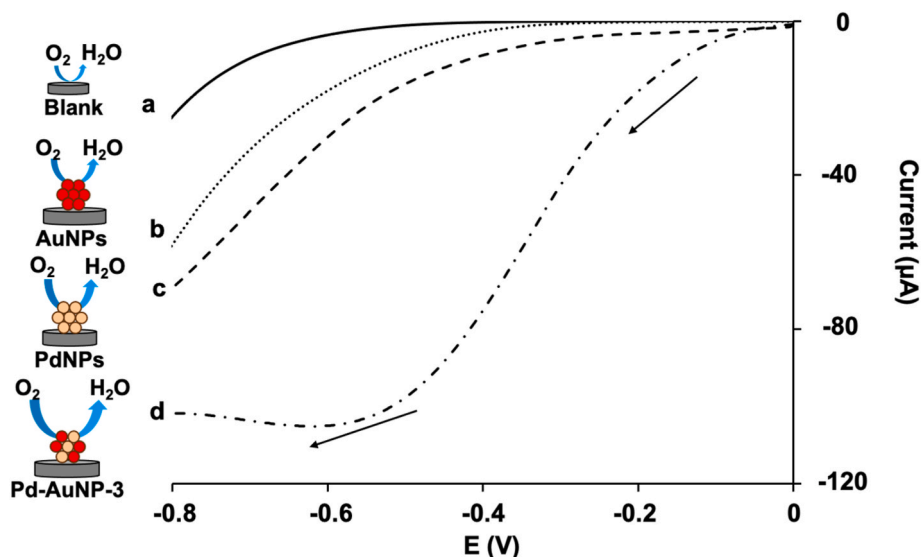


Fig. 3. Lineal sweep voltammograms (LSV) recorded from 0 to  $-0.8$  V at a scan rate of  $0.1$  V/s in  $10$  mM PBS pH  $7.4$ , for a bare electrode (background; a) and for electrodes modified with AuNPs (b), PdNPs (c) and Pd-AuNP-3 (d). NPs concentration:  $1.45 \times 10^{12}$  NPs/mL.

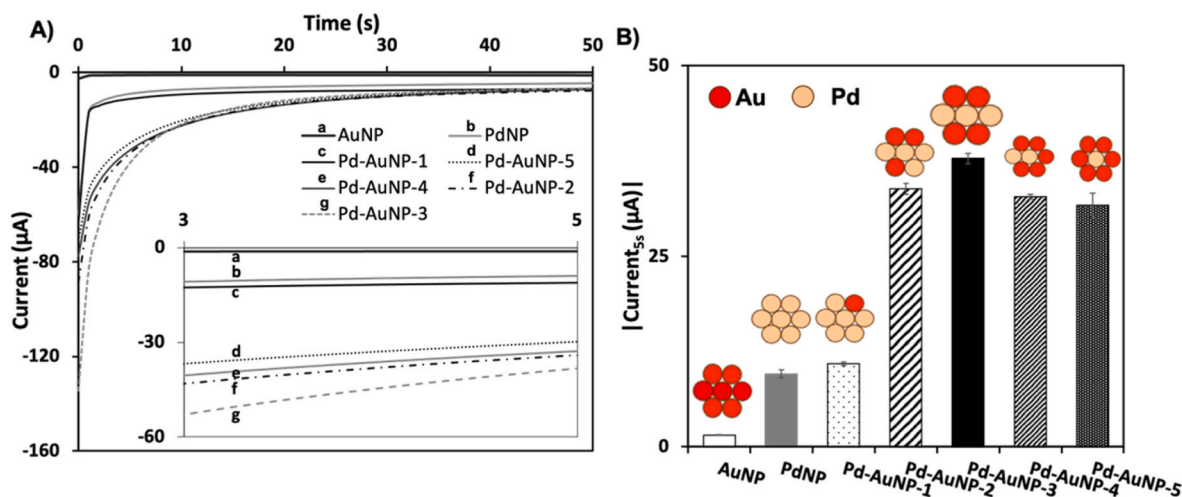


Fig. 4. Electrochemical characterization of Pd-AuNPs with different Au content. A. Chronoamperograms recorded at  $-0.45$  V for  $50$  s in PBS  $10$  mM pH  $7.4$  for AuNPs (a), PdNPs (b), Pd-AuNP-1 (c), Pd-AuNP-2 (f), Pd-AuNP-3 (g), Pd-AuNP-4 (e) and Pd-AuNP-5 (d). Inset corresponds to the region from  $3$  s to  $5$  s and from  $0$   $\mu$ A to  $-60$   $\mu$ A. B. Comparison of the analytical signal (absolute value of current recorded at  $5$  s) for each NPs. Data are given as average  $\pm$  SD ( $n = 3$ ). NPs concentration:  $1.45 \times 10^{12}$  NPs/mL. NPs composition as detailed in Table 1.

The developed immunosensor takes advantage of the use of MB as platforms to facilitate separation and minimizing matrix effects (Ahmadi et al., 2021; de la Escosura-Muñiz et al., 2016) (Fig. 6B). The advantages of the MB-based immunoassays are well-known. First, the fact that the reactions take place in liquid phase, with stirring, allows to improve their kinetics, reducing the incubation times to approximately  $20$  min (typically  $90$  min for assays performed in solid phase). The magnetic separation performed after each incubation step also allows to pre-concentrate the sample, which leads to improved sensitivities. Moreover, such separation after capturing the analyte allows to remove the rest of compounds present in the sample which may interfere in the electrochemical measurement. This leads to a reduction of matrix effects and to an increase in selectivity.

Briefly, biotinylated monoclonal anti-hyaluronidase antibody (biotin anti-HYAL) was immobilized onto streptavidin-modified commercial magnetic beads and the conjugate was incubated with increasing concentrations of hyaluronidase. The resulting complex was put in contact with the MBs-hyaluronidase conjugate, forming the final

immunosandwich. The use of antibodies as recognition elements confers the immunosensor with selectivity against hyaluronidase.

The resulting complex was placed on a SPCE, to which working electrode was attracted by the action of a small external magnet placed on its reverse side. The analytical method consists in applying a potential of  $-0.45$  V in chronoamperometric mode and measuring the current recorded at  $5$  s (analytical signal), as optimized for the Pd-AuNP-3 determination.

The absolute value of this current increases with the Pd-AuNP-3 concentration, due to their catalytic activity toward the ORR. So, when higher is the concentration of hyaluronidase in the immunoassay, higher is the amount of the Pd-AuNPs-3 tags, being the signals correlated with the analyte concentration, as shown in Fig. 7A.

Dose-response experiments were performed in the range of  $125$ – $4600$  ng/mL of hyaluronidase with a good linear relationship ( $r = 0.9982$ ) according to the following equation:

$$|Current_{5s}| (\mu A) = 0.003 [Hyaluronidase] (ng/mL) + 0.4432$$



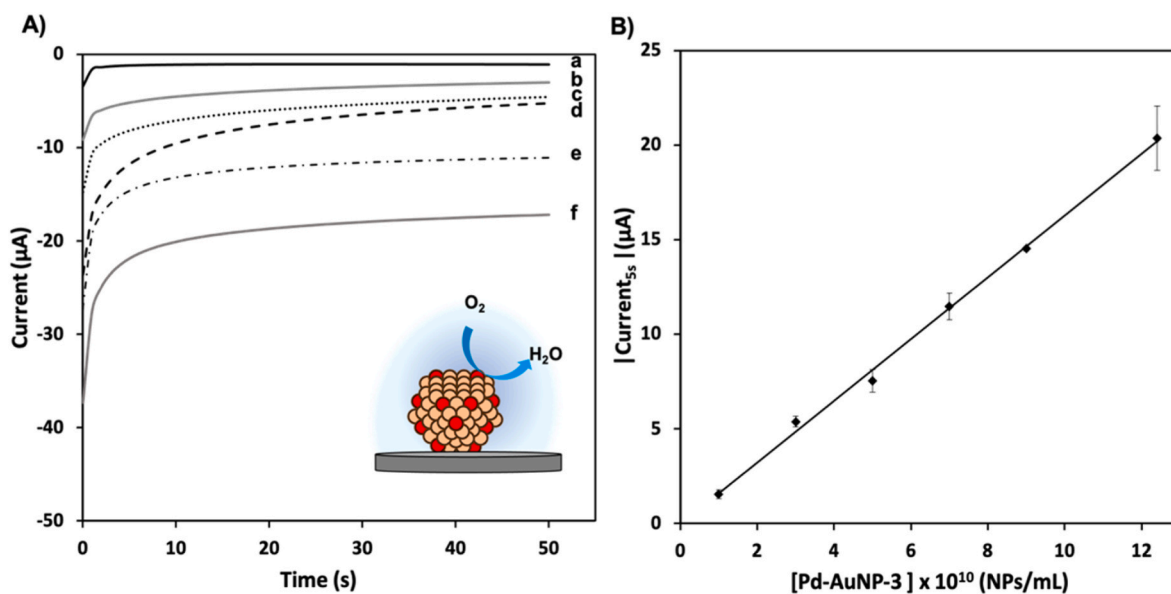


Fig. 5. A. Chronoamperograms recorded at  $-0.45$  V during 50 s in 10 mM PBS pH 7.4 for increasing concentrations of Pd-AuNP-3:  $1.00 \times 10^{10}$  NPs/mL (a),  $3.00 \times 10^{10}$  NPs/mL (b),  $5.00 \times 10^{10}$  NPs/mL (c),  $7.00 \times 10^{10}$  NPs/mL (d),  $9.00 \times 10^{10}$  NPs/mL (e) and  $1.20 \times 10^{11}$  NPs/mL (f). B. Relationship between the analytical signal (current at 5 s) and Pd-AuNP-3 concentration. Data are given as average  $\pm$  SD ( $n = 3$ ).

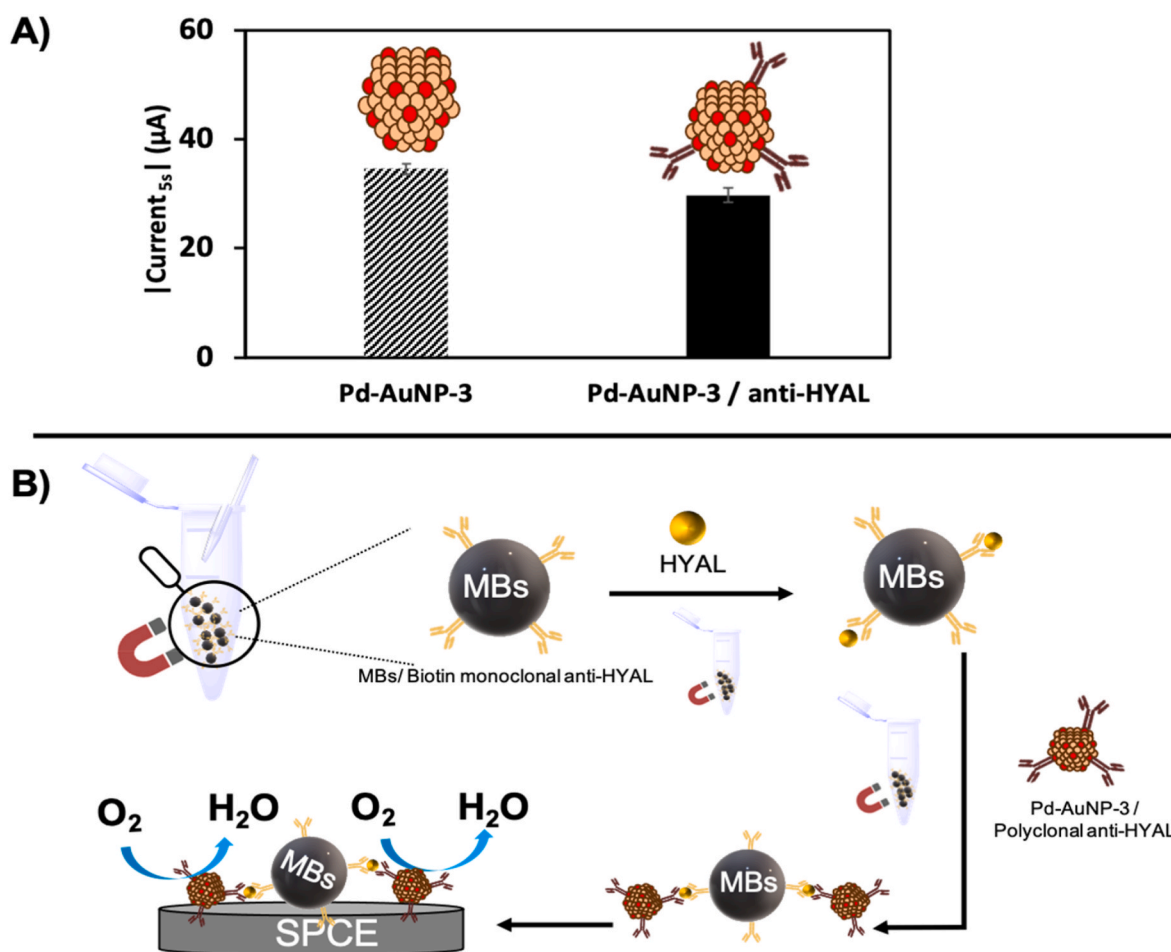
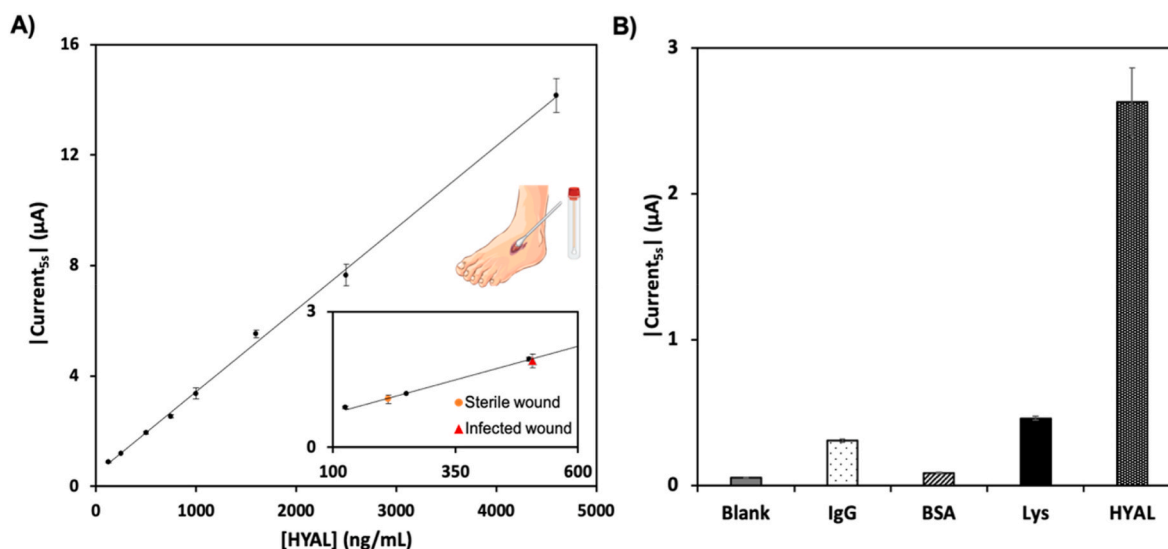


Fig. 6. A. Comparison of the analytical signals (coming from chronoamperograms obtained applying a potential of  $-0.45$  V and measuring the current recorded at 5 s) for Pd-AuNP-3 and Pd-AuNP-3/anti-HYAL conjugate. Data are given as average  $\pm$  SD ( $n = 3$ ). B. Schematic representation of the immunosensor developed for the detection of hyaluronidase (HYAL) using Pd-AuNP-3 tags and magnetic beads (MBs) platforms.





**Fig. 7.** A. Calibration plot signals (coming from chronoamperograms obtained applying a potential of  $-0.45$  V and measuring the current recorded at 5 s) obtained for standard solutions of hyaluronidase (from 125 to 4600 ng/mL) as well as the analytical signals obtained for swab exudates from patients with sterile (circle) and infected (triangle) ulcers (inset). Data are given as average  $\pm$  SD ( $n = 3$ ). B. Sensor response to different potential interferences, all of them at a concentration of 750 ng/mL. Data are given as average  $\pm$  SD ( $n = 3$ ).

The obtained LOD, calculated as three-times the SD of the intercepted divided by the slope was 50 ng/mL, equivalent to 0.02 U/mL (437 U/mg). The reproducibility of the method was also good with an RSD below 8% ( $n = 3$ ).

The obtained LOD is one of the lowest found in the biosensors-related bibliography (Table 2), demonstrating the excellent performance of our method based on the use of Pd-AuNP-3 tags.

### 3.4. Selectivity studies and hyaluronidase determination in chronic wound exudates

Bacterial identification in chronic wound exudates in a short time and with a high selectivity is desirable for achieving a better screening methodology in wound infection handling. For that reason, attaining an analytical method with a high selectivity and good performance in real samples is advantageous. In this context, the use of MBs in the here developed immunosensor supposes a major advantage as they allow to separate biomolecules from complex samples, reducing matrix effects (Ahmadi et al., 2021; de la Escosura-Muñiz et al., 2016).

Selectivity of the Pd-AuNP-3 based immunosensor was evaluated against common analytes present in human samples, as it is BSA, IgG and lysozyme, another well-known infection biomarker (Hasmann et al., 2011; Mota et al., 2021; Silva et al., 2020). Analytical signals recorded

for each condition were insignificant comparing with hyaluronidase (Fig. 7B), even in the presence of common wound exudate biomolecules as lysozyme. Thus, the Pd-AuNP-3/MBs based immunosensor had enhanced selectivity to hyaluronidase sensing without significant interferences.

Moreover, the immunosensor was evaluated in real samples obtained from exudates of patients with open wounds, being one from a patient with a sterile wound and the other one from an infected wound (Fig. 7A, inset). The hyaluronidase concentration was directly extrapolated from the calibration curve, considering the low matrix effects observed in the presence of MBs. It can be clearly observed a difference between the hyaluronidase concentration detected in a clean ( $213 \pm 18$  ng/mL;  $0.09 \pm 0.008$  U/mL) and an infected wound ( $507 \pm 40$  ng/mL;  $0.22 \pm 0.017$  U/mL), attesting the suitability of the immunosensor to discriminate between them.

These levels are much lower than the provided by the gold standard turbidimetric assay, which has a linear range from 2 to 5 U/mL (Chen et al., 2020). This makes it difficult to apply this method for validation. In addition, turbidimetric method requires a complex methodology that implies the use of hyaluronic acid for the enzymatic reaction, in contrast with the simplicity of our immunosensor.

Moreover, there is not a clear consensus in bibliography about the expected levels of hyaluronidase in infected and non-infected samples.

**Table 2**  
Comparison with other reported biosensors for hyaluronidase detection.

Sensing principle	Transduction technique	Limit of detection (U/mL)	Sample	Ref
Bimetallic gold/silver nanoclusters-gold nanoparticles as fluorescence quencher	Fluorescence	0.3	Spike and recovery	Liu et al. (2019)
Conjugated polymer nanoparticles and Au nanorods	Fluorescence	0.003	Spike and recovery	Wang et al. (2022)
Water soluble fluorescence molybdenum disulfide quantum dots quenched by hyaluronic acid gold nanoparticles	Fluorescence	0.7	Spike and recovery	Gu et al. (2016)
Carbon Dot/Naphthalimide and hyaluronic acid Förster resonance energy transfer (FRET) mechanism	Fluorescence	0.09	Not tested	Raj et al. (2021)
Electrostatic interaction between hyaluronic acid and $Ru(bpy)_3^{2+}$	Electrochemiluminescence	0.33	Spike and recovery	Li et al. (2018)
Methylene blue-hyaluronic acid complexes and enzymolysis through hyaluronidase	Differential pulse voltammetry (DPV)	0.28	Urine samples	Li et al. (2021)
Nanopores blocking by hyaluronidase	Differential pulse voltammetry (DPV)	64	Bacteria culture	de la Escosura-Muñiz et al. (2019)
Pd-AuNP-3/MB immunosensor based on electrocatalytic activity toward the ORR	Chronoamperometry	0.02	Exudates from human wounds	This work

Considering this, and the limitations of the turbidimetric assay, our immunosensor provides a useful tool for further carefully evaluation in a high number of patient samples. A threshold value for discriminating infected and non-infected samples should be further defined for a practical application of this method in a real scenario.

#### 4. Conclusions

In this work, we study for the first time the role that slight changes into the Pd/Au proportion have in the electrocatalytic activity of bimetallic Pd-AuNPs toward the oxygen reduction reaction (ORR), together with their application as novel tags for the determination of an infection biomarker in chronic wound exudates.

The selective introduction of gold atoms on the palladium nano-cluster, following a galvanic substitution procedure, is quantitatively evaluated by STEM-EDX analysis. Our findings indicate that, the synergy between both metals is strongly enhanced when the amount of gold is controlled and occupies the more reactive positions of the cluster, affecting the obtained electrocatalytic activity. This is of key relevance, since it is observed that an excess of gold leads to a decrease in such activity. These findings may be of great interest not only for the biosensing application given in this work, but also for applications such as energy converting on fuel cells.

The optimal Pd-AuNPs (70% Pd, 30% Au) are used as tags, taking advantage of the bio-functionalities of gold present in the cluster, in an electrochemical immunosensor for the detection of hyaluronidase wound infection biomarker, using magnetic beads (MBs) platforms. The low matrix effects inherent to the use of MBs platforms allow us to discriminate between wound exudates with both sterile and infected ulcers without sample pre-treatment, meeting the clinical requirements. This novel electrocatalytic immunoassay has the advantage, over common methods for NP tags electrochemical detection, of the signal generation in the same neutral medium where the immunoassay takes place (10 mM PBS pH 7.4), avoiding the use of additional and hazardous reagents, bringing it closer to their use as point-of-care devices. This is of particular relevance in highly integrated systems such as lateral-flow assays, where our Pd-AuNPs have also potential interest, since their optical properties (violet color with maximum of absorbance at 530 nm) allows to postulate them as tags for dual electrochemical/optical detection.

#### Declaration of competing interest

The authors declare that they have no known competing financial interests or personal relationships that could have appeared to influence the work reported in this paper.

#### Acknowledgements

This work has been supported by the CTQ2017-86994-R and MCI-21-PID2020-115204RB-I00 projects from the Spanish Ministry of Economy and Competitiveness (MINECO) and the Spanish Ministry of Science and Innovation (MICINN) respectively, and the FC-GRUPIN-ID/2018/000166 project from the Asturias Regional Government. C. Toyos-Rodríguez thanks the MICINN for the award of a FPI Grant (PRE2018-084953). A. de la Escosura-Muñiz also acknowledges the MICINN for the “Ramón y Cajal” Research Fellow (RyC-2016-20299). The authors acknowledge the Chronic Ulcers Unit of the Hospital Universitario Central de Asturias (HUCA) and specially to Susana Valerdiz for providing the real samples used in this work.

#### References

Ahmadi, M., Ghoorchian, A., Dashtian, K., Kamalabadi, M., Madrakian, T., Afkhami, A., 2021. *Talanta* 225, 121974.  
 Ambrosi, A., Castañeda, M.T., Killard, A.J., Smyth, M.R., Alegret, S., Merkoçi, A., 2007. *Anal. Chem.* 79, 5232–5240.

Baptista-Pires, L., de la Escosura-Muñiz, A., Balsells, M., Zuaznabar-Gardona, J.C., Merkoçi, A., 2019. *Electrochem. Commun.* 98, 6–9.  
 Bayda, S., Adeel, M., Tuccinardi, T., Cordani, M., Rizzolio, F., 2020. *Molecules* 25, 112.  
 Brust, M., Walker, M., Bethell, D., Schiffrin, D.J., Whyman, R., 1994. *J. Chem. Soc., Chem. Commun.* 801–802, 0.  
 Campbell, C.T., 2004. *Science* 306, 234–235.  
 Cao, L., Cai, J., Deng, W., Tan, Y., Xie, Q., 2020. *Anal. Chem.* 92, 16267–16273.  
 Carneiro, P., Morais, S., Pereira, M.C., 2019. *Nanomaterials* 9, 1663.  
 Chen, D., Zhu, X., Tao, W., Kong, Y., Huang, Y., Zhang, Y., Liu, R., Jiang, L., Tang, Y., Yu, H., Hao, Q., Yang, X., Zou, H., Chen, J., Lu, Y., Zhang, H., Li, W., 2020. *J. Contr. Release* 324, 545–559.  
 Clinton, A., Carter, T., 2015. *Lab. Med.* 46, 277–284.  
 de la Escosura-Muñiz, A., Ambrosi, A., Merkoçi, A., 2008. *TrAC Trends Anal. Chem. (Reference Ed.)* 27, 568–584.  
 de la Escosura-Muñiz, A., Sánchez-Espinel, C., Díaz-Freitas, B., González-Fernández, A., Maltez-da Costa, M., Merkoçi, A., 2009. *Anal. Chem.* 81, 10268–10274.  
 de la Escosura-Muñiz, A., Merkoçi, A., 2010. *Expert Opin. Med. Diagn.* 4, 21–37.  
 de la Escosura-Muñiz, A., Parolo, C., Merkoçi, A., 2010a. *Mater. Today* 13, 24–34.  
 de la Escosura-Muñiz, A., Maltez-da Costa, M., Sánchez-Espinel, C., Díaz-Freitas, B., Fernández-Suarez, J., González-Fernández, A., Merkoçi, A., 2010b. *Biosens. Bioelectron.* 26, 1710–1714.  
 de la Escosura-Muñiz, A., Plichta, Z., Horák, D., Merkoçi, A., 2015. *Biosens. Bioelectron.* 67, 162–169.  
 de la Escosura-Muñiz, A., Baptista-Pires, L., Serrano, L., Altet, L., Francino, O., Sánchez, A., Merkoçi, A., 2016. *Small* 12, 205–213.  
 de la Escosura-Muñiz, A., Ivanova, K., Tzanov, T., 2019. *ACS Appl. Mater. Interfaces* 11, 13140–13146.  
 Doria, G., Conde, J., Veigas, B., Giestas, L., Almeida, C., Assunção, M., Rosa, J., Baptista, P.V., 2012. *Sensors* 12, 1657–1687.  
 Gu, W., Yan, Y., Zhang, C., Xian, Y., 2016. *ACS Appl. Mater. Interfaces* 8, 11272–11279.  
 Han, A., Zenilman, J.M., Melendez, J.H., Shirliff, M.E., Agostinho, A., James, G., Stewart, P.S., Mongodin, E.F., Rao, D., Rickard, A.H., Lazarus, G.S., 2011. *Wound Repair Regen.* 19, 532–541.  
 Han, G., Ceilley, R., 2017. *Adv. Ther.* 34, 599–610.  
 Han, J.-J., Li, N., Zhang, T.-Y., 2009. *J. Power Sources* 193, 885–889.  
 Hasmann, A., Wehrschuetz-Sigl, E., Kanzler, G., Gewessler, U., Hulla, E., Schneider, K.P., Binder, B., Schintler, M., Guebitz, G.M., 2011. *Diagn. Microbiol. Infect. Dis.* 71, 12–23.  
 Hassan, A.-R.H.A.-A., de la Escosura-Muñiz, A., Merkoçi, A., 2015. *Biosens. Bioelectron.* 67, 511–515.  
 Holzinger, M., Le Goff, A., Cosnier, S., 2014. *Front. Chem.* 2, 63.  
 Huizhi, K., Wang, L., O'Donoghue, M., Cao, Y.C., Tan, W., 2008. *Nanoparticles for Biosensors* 583–621 (Chapter 15).  
 Hynes, W.L., Walton, S.L., 2000. *FEMS Microbiol. Lett.* 183, 201–207.  
 Iglesias-Mayor, A., Amor-Gutiérrez, O., Costa-García, A., de la Escosura-Muñiz, A., 2019. *Sensors* 19, 5137.  
 Iglesias-Mayor, A., Amor-Gutiérrez, O., Novelli, A., Fernández-Sánchez, M.-T., Costa-García, A., de la Escosura-Muñiz, A., 2020. *Anal. Chem.* 92, 7209–7217.  
 Järbrink, K., Ni, G., Sönnergren, H., Schmidtchen, A., Pang, C., Bajpai, R., Car, J., 2016. *Syst. Rev.* 5, 152.  
 Kusunoki, K., Kudo, D., Hayashi, K., Chida, Y., Todoroki, N., Wadayama, T., 2021. *ACS Catal.* 11, 1554–1562.  
 Lara, S., Pérez-Potti, A., 2018. *Biosensors* 8, 104.  
 Li, Z., Chen, H., Zhuo, Z., Huang, D., Luo, F., Chen, L., Wang, J., Guo, L., Qiu, B., Lin, Z., 2018. *Sensor. Actuator. B Chem.* 275, 409–414.  
 Li, Z.-X., Zhang, J.-L., Wang, J., Luo, F., Qiu, B., Guo, L.-H., Lin, Z.-Y., 2021. *J. Anal. Test.* 5, 69–75.  
 Lim, D.-H., Wilcox, J., 2012. *J. Phys. Chem. C* 116, 3653–3660.  
 Liu, Q., Yan, X., Lai, Q., Su, X., 2019. *Sensor. Actuator. B Chem.* 282, 45–51.  
 Ma, R., Lin, G., Zhou, Y., Liu, Q., Zhang, T., Shan, G., Yang, M., Wang, J., 2019. *Comput. Mater.* 5, 78.  
 Maduraiveeran, G., 2021. *Mater. Lett.* 283, 128763.  
 Mahnic, A., Breznik, V., Bombek Ihan, M., Rupnik, M., 2021. *Front. Med.* 8, 607255.  
 Maltez-da Costa, M., de la Escosura-Muñiz, A., Nogués, C., Barrios, L., Ibáñez, E., Merkoçi, A., 2012. *Small* 8, 3605–3612.  
 Maltez-da Costa, M.M., de la Escosura-Muñiz, A., de Merkoçi, A., 2010. *Electrochem. Commun.* 12, 1501–1504.  
 Melendez, J.H., Frankel, Y.M., An, A.T., Williams, L., Price, L.B., Wang, N.-Y., Lazarus, G. S., Zenilman, J.M., 2010. *Clin. Microbiol. Infect.* 16, 1762–1769.  
 Mota, F.A.R., Pereira, S.A.P., Araújo, A.R.T.S., Passos, M.L.C., Saraiva, M.L.M.F.S., 2021. *TrAC Trends Anal. Chem. (Reference Ed.)* 143, 116405.  
 Nørskov, J.K., Rossmeisl, J., Logadottir, A., Lindqvist, L., Kitchin, J.R., Bligaard, T., Jónsson, H., 2004. *J. Phys. Chem. B* 108, 17886–17892.  
 Rahman, S.T., Rhee, K.Y., Park, S.-J., 2021. *Nanotech. Rev.* 10, 137–157.  
 Raj, P., Lee, S., Lee, T.Y., 2021. *Materials* 14, 1313.  
 Rivas, L., de la Escosura-Muñiz, A., Pons, J., Merkoçi, A., 2014. *Electroanalysis* 26, 1287–1294.  
 Rößner, L., Armbrüster, M., 2019. *ACS Catal.* 9, 2018–2062.  
 Schmidtchen, Helene Wolff, Carita H. A., 2001. *Acta Derm. Venereol.* 81, 406–409.  
 Serra, R., Grande, R., Butrico, L., Rossi, A., Settimo, U.F., Caroleo, B., Amato, B., Gallelli, L., de Francis, S., 2015. *Ther* 13, 605–613.  
 Sha, J., Paul, S., Dumeignil, F., Wojcieszak, R., 2019. *RSC Adv.* 9, 29888–29901.  
 Silva, N.H.C.S., Garrido-Pascual, P., Moreirinha, C., Almeida, A., Palomares, T., Alonso-Varona, A., Vilela, C., Freire, C.S.R., 2020. *Biol. Macromol.* 165, 1198–1210.  
 Singh, P., Buttry, D.A., 2012. *J. Phys. Chem. C* 116 (19), 10656–10663.  
 Spindelov, J.S., Wiecek, A., 2007. *Phys. Chem. Chem. Phys.* 9, 2654.

- Stern, R., Jedrzejewski, M.J., 2006. *Chem. Rev.* 106, 818–839.
- Tammeveski, L., Erikson, H., Sarapuu, A., Kozlova, J., Ritslaid, P., Sammelselg, V., Tammeveski, K., 2012. *Electrochem. Commun.* 20, 15–18.
- Tang, J., Tang, D., 2015. *Microchim. Acta* 182, 2077–2089.
- Tian, X., Lu, X.F., Xia, B.Y., Lou, X.W., David, 2020. *Joule* 4, 45–68.
- Toshima, N., Kanemaru, M., Shiraishi, Y., Koga, Y., 2005. *J. Phys. Chem. B* 109, 16326–16331.
- Toyos-Rodríguez, C., García-Alonso, F.J., de la Escosura-Muñiz, A., 2020. *Sensors* 20, 4748.
- Verbanic, S., Shen, Y., Lee, J., Deacon, J.M., Chen, I.A., 2020. *npj Biofilms Microbiomes* 6, 21.
- Wang, A., Liu, X.Y., Mou, C.-Y., Zhang, T., 2013. *J. Catal.* 308, 258–271.
- Wang, H.-Y., Weng, C.-C., Yuan, Z.-Y., 2021. *J. Energy Chem.* 56, 470–485.
- Wang, Q., Fu, W., Ma, R., Lu, Q., Liu, Z., Yao, J., Liu, Q., Zhang, X., Zhao, H., 2022. *Dyes Pigm* 197, 109844.
- Wang, X., Choi, S.-I., Roling, L.T., Luo, M., Ma, C., Zhang, L., Chi, M., Liu, J., Xie, Z., Herron, J.A., Mavrikakis, M., Xia, Y., 2015a. *Nat. Commun.* 6, 7594.
- Wang, X., Vara, M., Luo, M., Huang, H., Ruditskiy, A., Park, J., Bao, S., Liu, J., Howe, J., Chi, M., Xie, Z., Xia, Y., 2015b. *J. Am. Chem. Soc.* 137, 15036–15042.
- Welch, C.M., Compton, R.G., 2006. *Anal. Bioanal. Chem.* 384, 601–619.
- Wittenberg, N.J., Haynes, C.L., 2009. *WIREs Nanomed. Nanobiotechnol.* 1, 237–254.
- Wu, Z.-P., Caracciolo, D.T., Maswadeh, Y., Wen, J., Kong, Z., Shan, S., Vargas, J.A., Yan, S., Hopkins, E., Park, K., Sharma, A., Ren, Y., Petkov, V., Wang, L., Zhong, C.-J., 2021. *Nat. Commun.* 12, 859.
- Zhang, H., Watanabe, T., Okumura, M., Haruta, M., Toshima, N., 2012. *Nat. Mater.* 11, 49–52.
- Zhao, D., Xu, B.-Q., 2006. *Angew. Chem. Int. Ed.* 45, 4955–4959.
- Zhou, X., Willems, R.J.L., Friedrich, A.W., Rossen, J.W.A., Bathoorn, E., 2020. *Antimicrob. Resist. Infect. Control* 9, 130.



# Novel magnetic beads with improved performance for Alzheimer's disease biomarker detection

C. Toyos-Rodríguez<sup>a,b</sup>, A. Llamedo-González<sup>c,d</sup>, D. Pando<sup>c</sup>, S. García<sup>e</sup>, J.A. García<sup>f</sup>, F. J. García-Alonso<sup>b,d</sup>, A. de la Escosura-Muñiz<sup>a,b,\*</sup>

<sup>a</sup> NanoBioAnalysis Group-Department of Physical and Analytical Chemistry, University of Oviedo, Julián Clavería 8, 33006 Oviedo, Spain

<sup>b</sup> Biotechnology Institute of Asturias, University of Oviedo, Santiago Gascon Building, 33006 Oviedo, Spain

<sup>c</sup> Nanovex Biotechnologies S.L., Parque Tecnológico de Asturias Edificio CEEI, 33428 Llanera, Spain

<sup>d</sup> NanoBioAnalysis Group-Department of Organic and Inorganic Chemistry, University of Oviedo, Julián Clavería 8, 33006 Oviedo, Spain

<sup>e</sup> Department of Psychology, University of Oviedo, Oviedo, Spain

<sup>f</sup> NanoBioAnalysis Group-Department of Physics, University of Oviedo, Calvo Sotelo s/n, 33007 Oviedo, Spain

## ARTICLE INFO

### Keywords:

Magnetic beads  
Magnetic nanoparticles  
Immunosensors  
Alzheimer's disease  
Electrochemical detection

## ABSTRACT

Magnetic beads (MBs) have been notably used as platforms in biosensing thanks to their magnetic behavior as they allow to simplify purification and separation by preconcentrating the sample and also to minimize matrix effects, what facilitates the analysis of real samples. Even though it exists a variety of commercially available ones, there is still great interest to develop alternative MBs with improved performance. In this work, we propose the synthesis of novel, reliable and low-cost MBs by colloidal assembly of zinc doped magnetite for their use as electrochemical immunosensing platforms. First, zinc doped magnetite  $Zn_xFe_{3-x}O_4$  nanoparticles (ZnFeNPs) of a diameter of  $13 \pm 3$  nm and a saturation magnetization of 81 emu/g were synthesized and encapsulated in a polymeric matrix of poly(lactic-co-glycolic) acid (PLGA), generating polymeric MBs that were covered with polyethyleneimine (PEI) (MB@PEI), obtaining particles of  $96 \pm 16$  nm. The PEI external layer provides MBs with a higher degree of encapsulation and stability and with functional groups that convert MB@PEI particles in versatile tools for their use as immunosensing platforms. In order to compare the suitability of the obtained MBs with commercially available ones, the affinity protein neutravidin (NAV) was linked to the MB@PEI surface through glutaraldehyde crosslinking. The obtained MB@NAV exhibited a significantly higher saturation magnetization than commercially available NAV-modified MBs, and also a better reproducibility (RSD of 4% for MB@NAV and 12% for commercial MBs) and enhanced surface functionalization ability when used as immunosensing platforms in a model assay using gold nanoparticle tags. As proof-of-concept of application in real samples, MB@NAV were finally applied for the detection of Tau protein, a well-known Alzheimer's Disease (AD) biomarker, with a detection limit (LOD) of 63 ng/mL and an excellent performance in human serum samples.

## 1. Introduction

Magnetic particles (MPs), those containing metals like iron or nickel as elements, oxides, or mixed oxides, have emerged as relevant materials in many different areas including bioimaging [1], drug delivery [2], wastewater treatment [3], biosensing [4,5] or in the isolation of complex matrices [6] among other applications.

MPs are typically used in the nanoscale range, from which superparamagnetic nanoparticles (SPIONs) are very appreciated by their stability and low toxicity [7]. In the nanoscale, the magnetic properties of these particles are size-dependent [8]. At lower diameters, lower than

20 nm, their saturation magnetization ( $M_s$ ) increases with increasing particle size, regardless of particle shape. Up to 20 nm, the upper superparamagnetic limit [9] their remanent magnetization ( $M_r$ ) starts to increase [10,11]. These SPIONs form stable liquid dispersions at room temperature [9] and exhibit high mobilities in the presence of external magnetic fields [12]. The most widely used route for the synthesis of SPIONs is the thermal decomposition of iron complexes as it generates high crystalline products with low polydispersity [13].

The reduced size of SPIONs entails, however, a low magnetic moment ( $m$ ), what difficulties their functionalization without losing their magnetic behavior. An effective way to circumvent this difficulty is

\* Corresponding author.

E-mail address: [alfredo.escosura@uniovi.es](mailto:alfredo.escosura@uniovi.es) (A. de la Escosura-Muñiz).

<https://doi.org/10.1016/j.microc.2022.107211>

Received 14 October 2021; Received in revised form 20 December 2021; Accepted 12 January 2022

Available online 19 January 2022

0026-265X/© 2022 The Author(s). Published by Elsevier B.V. This is an open access article under the CC BY license (<http://creativecommons.org/licenses/by/4.0/>).

doping magnetite nanoparticles with  $\text{Zn}^{2+}$  ions, what enhances their magnetic properties, particularly its Ms, that increases significantly with the incorporation of a modest percentage of zinc(II) ions [14–16].

Another common way to increase magnetism is the encapsulation of magnetic nanoparticles into the so-called magnetic beads (MBs) that is, polymer spheres containing nanomagnetic particles randomly dispersed [17–19], thus the resulting material remains superparamagnetic but exhibits a fast response to external magnetic fields [20]. Accordingly, the employment of ZnFeNPs improves the magnetic moment of the MBs they are part of [21], taking advantage of both strategies.

There are a huge number of polymers that can be used to synthesize MBs, including poly(lactic-co-glycolic acid) (PLGA) [21–25]. PLGA is a biocompatible, biodegradable polymer widely used for encapsulation of different compounds for diagnosis in biomedicine as it is approved by the Food and Drug Administration (FDA) and the European Medicines Agency (EMA) [26,27].

The use of MBs in immunosensing is extensive as they are interesting tools for the immobilization of biological recognition elements due to their high surface-to-volume ratio. As they can be moved by an external magnetic field, they allow the pre-concentration and separation of analytes of interest from complex samples, thus minimizing matrix effects [28–31]. Although the extensive use of commercially available MBs, there is still a great interest in obtaining alternative MBs for an improved performance [32,33].

Among the wide variety of analytes detected using MBs as immunosensing platforms, it is worthy to mention their application for the detection of Alzheimer's disease (AD) biomarkers [34–38]. AD is an untreatable and debilitating neurodegenerative disorder that affected more than 50 million people in 2019 and that is considered as the current main cause of dementia [39]. The diagnosis of AD is currently based on imaging techniques, mainly magnetic resonance imaging (MRI) for detecting abnormalities in patient brains [40] and the detection through immunohistochemistry and enzyme linked immunosorbent assay (ELISA) of cerebrospinal fluid (CSF) and blood plasma biomarkers [41].

Amyloid beta ( $\text{A}\beta$ ) peptides plaques and hyperphosphorylated microtubule-associated protein Tau stand out from the biomarkers used for AD diagnostics. Tau protein is the main microtubule associated protein of the brain, that regulates axonal growth, transport or neuronal polarity through its phosphorylation. But, an hyperphosphorylation of this protein has been associated to the development of several neurodegenerative diseases, including AD [42–46].

In patients with AD, levels of Tau protein reach values of 195 pg/mL in cerebrospinal fluid (CSF) samples [47], although further research is needed to establish reliable methodologies for sample acquisition and measurement that reduce the variability observed in the clinic between protein levels and the development of the disease [48,49].

In this work, ZnFeNPs with a high magnetization were synthesized following a thermal-decomposition procedure and used for the formation of MBs by encapsulation using PLGA as coating polymer. The obtained MB@PLGA were subsequently coated with polyethyleneimine (PEI) for increasing encapsulation and stability and providing the MBs with external functional groups for facilitating the ulterior bioconjugation of the affinity protein neutravidin (NAV) through glutaraldehyde crosslinking. The obtained MB@NAV were used as immunosensing platforms in a model immunoassay using gold nanoparticles (AuNPs) as labels, proving their suitability in immunosensing. Their performance was compared with that of commercially available MBs, showing comparable results with an increased reproducibility (RSD of 4% vs 12%) and an enhanced surface functionalization ability for the immobilization of specific antibodies. As proof-of-concept of application in real samples, MB@NAV were also implemented for the detection of Tau protein with a LOD of 63 ng/mL and a good performance in human serum samples.

## 2. Experimental

### 2.1. Reagents and materials

Benzyl ether 98%, glutaraldehyde solution grade II 25%, iron (III) acetylacetonate 97%, neutravidin, oleic acid 90%, polyethylenimine, branched Mw ~ 25.000, poly(lactic-co-glycolic acid) (PLGA) Resomer® RG 503H 50:50, polyvinyl alcohol (PVA) 31.000–50.000 wt 87–89% hydrolyzed, albumin, from bovine serum (BSA), anti-Human IgG ( $\gamma$ -chain specific)-Biotin, gold (III) chloride trihydrate 99.9%, Human IgG greater than 95% (HPLC grade), anti-Tau antibody, clone 12, from mouse and Tau-441 protein were purchased from Sigma-Aldrich (Spain). Zinc (II) acetylacetonate 95%, 2-propanol hyper grad LiChrosol®, tri-sodium citrate trihydrate and Tween-20 detergent were obtained from Merk Millipore (Spain). Petroleum ether 40/60, streptavidin-modified magnetic beads (M–280) and biotinylated Tau monoclonal antibody (BT2) were purchased from Thermo Fisher Scientific (Spain). Dichloromethane anhydrous (0.001% water) was obtained from VWR International Eurolabs (Spain) and oleylamine (approximate C-18 content 80–90%) was obtained from Acros Organics (Spain). Polyclonal rabbit anti-mouse immunoglobulin (used as control) was purchased from Dako Products /Agilent (USA).

Solutions were prepared, unless otherwise stated, using ultrapure water (18.2 M $\Omega$ -cm @ 25 °C) taken from a Millipore Direct-Q 3 UV purification system purchased from Millipore Ibérica S.A. (Spain). Phosphate buffer electrolyte solution was prepared using as precursors sodium chloride, potassium chloride, disodium hydrogen phosphate and potassium dihydrogen phosphate all obtained from Merck (Germany). Two different buffers were used in the MB bioconjugation process: a binding and washing (B&W) buffer composed of 0.1 M PBS pH 7.2 solution with 0.05% (v/v) Tween-20 and a blocking buffer (BB) consisted in 0.1 M PBS pH 7.2 solution with 5% (w/v) BSA.

### 2.2. Instrumentation

A transmission electron microscopy (TEM), either a JEOL JEM 2100 HRTEM and a JEOL2000 EXII TEM were used for size characterization of the as-synthesized nanoparticles. Size distribution was obtained by measuring the diameter of each particle with ImageJ software. Dynamic light scattering (DLS) was also performed using a Malvern Instruments Zetasizer Nano SZ with a solid-state He–Ne laser (wavelength  $\lambda = 633$  nm).

X-ray powder diffraction (XRPD) was used to obtain the composition profile of the ZnFeNPs and the crystallinity size of the particles, using  $\text{CuK}\alpha_{1,2}$  radiation ( $\lambda = 1.54056$  Å and 1.54439 Å) in a Bragg-Brentano reflection configuration, on a PHILIPS X' PERT PRO Analytical diffractometer in a  $2\theta$  range of 15–90°, with a step size of 0.03 using bulk magnetite as comparison. Infrared spectroscopy (IR) was performed using a Fourier transform infrared spectroscopic (FTIR) Spectrometer Paragon 1000 from PerkinElmer (USA) using KBr pressed disks.

Inductively coupled plasma mass spectrometry (ICP-MS) analysis was done using a Triple Quad 8800 ICP-QQQ from Agilent equipped with a concentric nebulizer with double-class glassy spray chamber to correlate the composition of zinc present in the nanoparticles. Additionally, magnetic measurements were performed at room temperature using a PPMS-14 T (Physical Property Measurement System).

A rotary evaporator IKA® RV8, from VWR International, was used for the MBs synthesis. A MagRack® 6 provided by Sigma-Aldrich (Spain) was used for magnetic separation processes. A MSC-100 cooling thermo shaker from Labolan (Spain) was used for the immunoassay incubations. Purification of AuNPs before and after bioconjugation with antibodies was done using a thermostatic centrifuge (Rotanta 460 R) from Hettich (Germany).

Electrochemical measurements were done using a  $\mu$ Autolab type II controlled by Autolab GPES software from Metrohm (Switzerland). Screen-printed carbon electrodes (SPCEs, ref DRP-110) and their



connector to the potentiostat (ref. DRP-DSC) were obtained from Metrohm DropSens S.L. (Spain). The SPCEs have a conventional three-electrode configuration including a working and counter electrode both composed of carbon and a silver pseudoreference electrode. A magnetic support for SPEs (DRP-MAGNET-700) purchased from Metrohm DropSens S.L. (Spain) was used for the electrochemical measurements with the MBs.

### 2.3. Synthesis and characterization of ZnFeNPs

ZnFeNPs were synthesized following a previously published procedure [50] with slight modifications. For the synthesis, 4 mmol Fe(acac)<sub>3</sub> and 0.68 mmol Zn(acac)<sub>2</sub> were dispersed in a mixture of 20 mL dibenzyl ether, 2.8 mL oleylamine and 2.7 mL oleic acid previously deoxygenated by purging Ar for 30 min. The mixture was placed in a three-necked round-bottom flask and heated with vigorous mechanical stirring, refrigeration, and inert atmosphere until reflux. When reflux was achieved, the reaction was maintained for 15 min under the same conditions. Afterwards, heating was removed, and the reaction was maintained at vigorous stirring for 15 min more, completing the first heating step. Then, a second heating step was performed by reconnecting the heating source and maintaining the reaction under reflux for 2 h. After this time, heating was removed again, and the reaction was maintained under stirring for 30 min, when it was separated and let it cool down. The obtained particles were purified by washing with a mixture 1:1 in volume of 2-propanol and light petroleum ether using an external magnetic disk and dried under vacuum. Dried particles were reconstituted in 2-propanol at a concentration of ~ 100 mg/mL.

The obtained NPs were characterized through TEM, XRDP, IR, ICP and magnetic measurement of the room temperature hysteresis loops.

### 2.4. Synthesis and characterization of magnetic beads (MBs)

MBs were synthesized following a water in oil emulsion procedure. First, 1.0 mL of ZnFeNPs suspension in 2-propanol was added to 2.0 mL of a 25 mg/mL PLGA solution in dimethylformamide (DMF) in a 15 mL centrifuge tube and vortexed for 15 s. The mixture was then transferred to a 50 mL centrifuge tube containing 15 mL of PVA 2% solution and then vortexed for 30 s and homogenized using a Branson® digital sonifier S450D during 1 min in pulses of 1 s (30 pulses/min) at a 65% amplitude. The PLGA encapsulated MBs were transferred to a one-necked round bottom flask that contained 10 mL of PVA 1% solution and the suspension was stirred at 100 rpm, 20 °C and 950 mbar for 45 min using a rotary evaporator in order to toughen the synthesized MBs. Next, the obtained MBs were washed three times with water using an external magnetic disk, and then resuspended in water for a final concentration of 10 mg/mL.

TEM, DLS (both size and  $\zeta$ -potential), IR and magnetic measurement of the room temperature hysteresis loops were used for the characterization of the MBs obtained here and after further functionalization.

### 2.5. MBs conjugation with neutravidin

MB@PLGA were also functionalized with a layer of PEI for further conjugation with neutravidin (NAV) through glutaraldehyde linking. First, 1.0 mL of MBs with a concentration of 10 mg/mL in water were transferred to a 1.5 mL LoBind Eppendorf® and separated from the supernatant using a MagRack® 6 from Sigma-Aldrich. Then 1.0 mL of 4.0 mg/mL aqueous solution of PEI was added to the MBs and stirred using a Vortex for 1 h. The MB@PEI were washed three times with water by using the magnetic rack MagRack® and, then 1.0 mL of 2.5% glutaraldehyde solution. The mixture was maintained under stirring in the Vortex during 30 min. After that, the reaction was washed three times with water using the MagRack® and, again with the supernatant removed, 1.0 mL of a 0.8 mg/mL solution of NAV in PBS 0.1 M pH 7.2 was added. This suspension was stirred during 6 h using a Vortex and the

excess of NAV was removed by washing three-times with PBS 0.1 M pH 7.2 using the MagRack®. Finally, the MB@NAV were suspended in 1 mL of PBS 0.1 M pH 7.2 and maintained under refrigeration until its use.

### 2.6. Synthesis of AuNPs and conjugation with antibodies

AuNPs were synthesized following the method developed by Turkevich et al. [51]. Briefly, 100 mL of a solution  $2.94 \times 10^{-4}$  M of gold (III) chloride trihydrate were reduced by 2.5 mL of an aqueous solution  $3.88 \times 10^{-2}$  M of tri-sodium citrate dihydrate at boiling point and under vigorous stirring for 15 min. Then, the reaction was moved to a cold magnetic stirrer and maintained under vigorous stirring for 30 min. Past this time, 690  $\mu$ L of the as-synthesized AuNPs ( $9.00 \times 10^{14}$  NPs/mL) were transferred to a 1.5 mL LoBind Eppendorf® tube and centrifuged at 7500 g, 20 °C for 30 min in the presence of 0.025% Tween-20. The supernatant was removed and 700  $\mu$ L of 2 mM trisodium citrate solution pH 7.3 were added. For the initial direct immunoassay (Section 2.7.), on this solution, 57.5  $\mu$ L of 100  $\mu$ g/mL antibody (human IgG for positive samples and mouse-IgG for negative control) were added and the solution was incubated for 60 min at 25 °C at gentle stirring. Finally, the solution was centrifuged at 7500 g, 4 °C for 20 min and the pellet was resuspended in 0.1 M PBS pH 7.2 with the addition of 1% BSA.

For the sandwich immunoassay for Tau protein detection (Section 2.8.), AuNPs were conjugated with Anti-Tau antibody, following the same procedure with the addition of Anti-Tau antibody in a concentration of 40  $\mu$ g/mL.

### 2.7. Direct immunoassay for the evaluation of MB@NAV performance as immunosensing platforms

For the evaluation of the ability of MB@NAV to be used as platforms in an immunoassay, they were conjugated with a biotinylated-anti-human IgG (anti-HIgG). Briefly, 15  $\mu$ L of a solution 10 mg/mL of MB@NAV were transferred to a 0.5 mL LoBind Eppendorf® tube and washed three-times with B&W buffer using a MagRack®. Then, MB@NAV were re-suspended in 108  $\mu$ L of B&W buffer, and 42  $\mu$ L of anti-HIgG (200  $\mu$ g/mL) were added. The solution was incubated during 30 min at 25 °C and 650 rpm in a Thermo Shaker incubator. After this step, MB@NAV/anti-HIgG were washed three times with B&W buffer and resuspended in 150  $\mu$ L of BB solution followed by an incubation period of 1 h at 25 °C and 650 rpm to prevent from unspecific absorption by blocking any remaining active sites. MB@NAV/anti-HIgG were then washed three times with B&W buffer and the supernatant removed. Then, 150  $\mu$ L of AuNPs conjugated with human IgG (HIgG-AuNPs) were added and the solution was incubated for 30 min at 25 °C and 650 rpm. After this step, MB@NAV/anti-HIgG/HIgG were separated and washed two times with B&W buffer and two times with 0.1 M PBS pH 7.2 using a MagRack®. The final product was resuspended in 150  $\mu$ L of 0.1 M PBS pH 7.2. Negative control assays were performed following the same experimental procedure but using mouse IgG (mIgG-AuNPs) instead of HIgG-AuNPs.

The electrochemical measurements were done taking advantage of the potential of AuNPs as catalysts of hydrogen evolution reaction (HER), following a previously optimized procedure [52,53]. For these measurements, 20  $\mu$ L of sample were placed on the working area of a SPCEs above a magnetic support and 20  $\mu$ L of a 0.2 M HCl solution were added. Electrochemical measurements were done by applying an initial potential of + 1.35 V for 60 s and then measuring by chronoamperometry at a fixed potential of -1.00 V for 300 s. The absolute value of the current at 300 s was chosen as the analytical signal.

The same procedure was performed with commercially available streptavidin-modified magnetic beads, for comparison purposes.

### 2.8. Sandwich immunoassay for Tau protein detection

A similar procedure to the previously described for the direct

immunosensor was done here for the detection of Tau protein. Briefly, 10  $\mu\text{L}$  of the obtained MB@NAV were re-suspended to a final volume of 150  $\mu\text{L}$  with B&W buffer and washed three-times with the same buffer. Then, MB@NAV were re-suspended in 108  $\mu\text{L}$  of B&W buffer and 42  $\mu\text{L}$  of biotinylated anti-Tau antibody (15  $\mu\text{g}/\text{mL}$ ) were added. The solution was incubated during 30 min at 25  $^{\circ}\text{C}$  and 650 rpm in a Thermo Shaker incubator. After incubation MB@NAV/anti-Tau were washed three-times with B&W buffer, and 150  $\mu\text{L}$  of BB solution were added and incubated for 60 min in the same conditions. Then, another washing step was performed, and 100  $\mu\text{L}$  of Tau protein was added in concentrations ranging from 50 to 750 ng/mL and incubated for 30 min. After the incubation, MB@NAV/anti-Tau/Tau conjugate was washed three-times with B&W buffer and 150  $\mu\text{L}$  of the conjugate of AuNPs with anti-Tau antibody were added for the incubation during 60 min at the same conditions.

The final product was washed twice with B&W buffer and twice with 0.1 M PBS pH 7.2 and measured in SPCEs above a magnetic support with the addition of 20  $\mu\text{L}$  of the final product and 20  $\mu\text{L}$  of 0.2 M HCl, using the same electrochemical procedure as in the direct immunoassay.

### 2.9. Spike and recovery protocol

Spike and recovery experiment was performed to evaluate if the Tau protein detection was affected by the human serum matrix. A pool of serum samples of healthy patients obtained from the University Program for Seniors of Oviedo University, from the Memory Workshop from the Popular University, from Rocas Senior Center, from Gijón-Sur Integrated Cultural Center, from Ateneo Integrated Cultural Center, and from San Agustín Senior Social Center (Spain) were used for such purpose. They met the following criteria: (1) no history of past or current psychiatric or neurological disorders and (2) a score higher than 26 in the Mini-Mental State Examination (MMSE). Also, subjects with acute comorbidities were excluded.

The serum was spiked with different concentrations of Tau (50 and 750 ng/mL) and then evaluated in the immunoassay ( $n = 3$  for each sample), following the same experimental procedure than the described in section 2.8. The analytical signals were compared with those obtained

for the standard samples in PBS buffer, calculating the % recovery of the analytical signal in the real matrix sample.

## 3. Results and discussion

### 3.1. Synthesis and characterization of ZnFeNPs

ZnFeNPs have been proposed as an alternative to conventional SPIONs since it is known that the introduction of  $\text{Zn}^{2+}$  ions at the tetrahedral sites of SPIONs may increase the magnetic properties of these particles [54]. For that reason, their use in the formation of superparamagnetic MBs by encapsulation in polymeric matrixes has been postulated as an alternative to traditional SPIONs based MBs in order to improve magnetism without the need to increase the particles size. In this work, ZnFeNPs have been synthesized following a previously published thermal-decomposition method developed by our group but using an appropriate mixture of  $\text{Zn}(\text{acac})_2$  and  $\text{Fe}(\text{acac})_3$  instead of using only  $\text{Fe}(\text{acac})_3$  [50]. This method has advantages over electrochemical-based synthetic routes [55,56] in terms of simplicity, reproducibility and size-controllability [11,57].

Figure 1.A. represents an electron micrograph of ZnFeNPs and the corresponding size distribution. The average size distribution of ZnFeNPs is  $13 \pm 3$  nm with a spherical shape and appropriate polydispersity. ZnFeNPs were also characterized by X-ray powder diffraction (XRPD) (Fig. 1.B.). Compared to the standard  $\text{Fe}_3\text{O}_4$ , ZnFeNPs have a similar profile. To estimate the crystallinity domain size of the nanoparticles, a LeBail fitting method was performed using magnetite as standard sample, showing an average apparent size of  $15 \pm 9$  nm, a value that is within the range of that observed by TEM, also indicating that the ZnFeNPs are monocrystalline.

Composition of ZnFeNPs was also studied by ICP-MS, that provided a Zn/Fe ratio of 12:88 ( $\pm 1$ ), what indicates that the obtained NPs are doped with Zn. Additionally, it was proven that little modifications in the Zn/Fe ratio do not affect significantly their magnetic behavior (Table S1.). ZnFeNPs were also characterized by IR (Fig. 1.C.), showing a broad band at  $570\text{ cm}^{-1}$ , due to solid-state vibrations of ferrites. The obtained ZnFeNPs were covered by oleic acid, what is confirmed by the

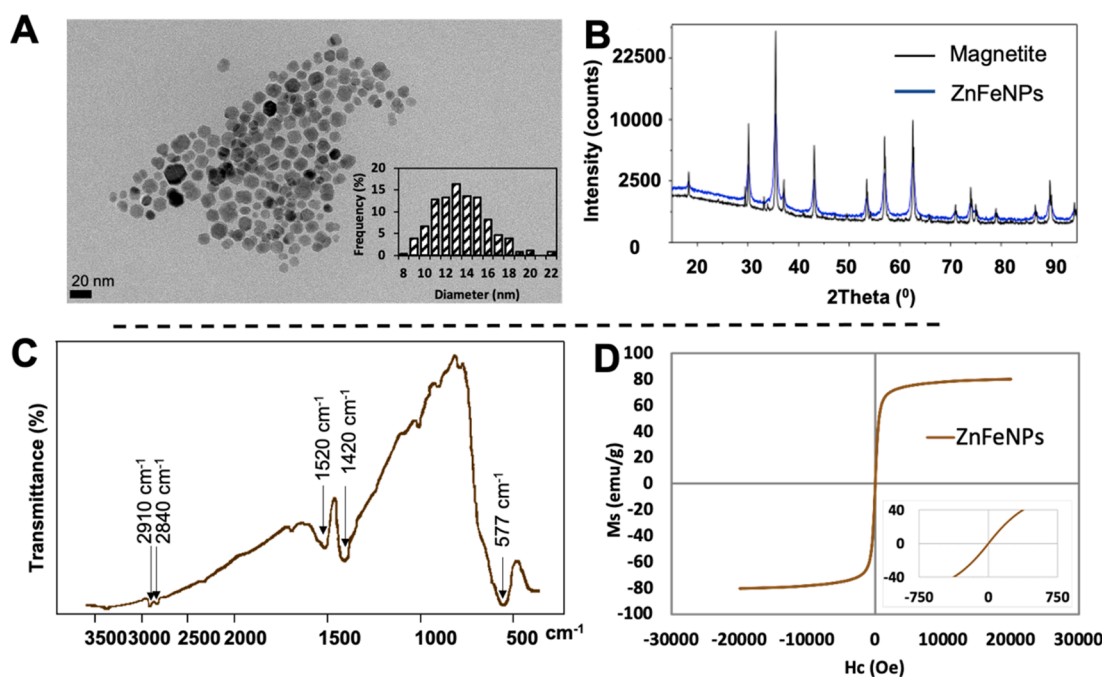


**Fig. 1.** Characterization of ZnFeNPs. **A.** Electron micrographs of ZnFeNPs and size distribution histogram showing an average size diameter of 13 nm; **B.** XRPD analysis of ZnFeNPs compared to magnetite as reference material. ZnFeNPs pattern presents a broadened profile; **C.** IR spectrum of ZnFeNPs; and **D.** Hysteresis curve of ZnFeNPs that shows a superparamagnetic behavior and a  $M_s$  of 81 emu/g (inset shows amplified the low-field region of the hysteresis curve).

presence of absorption bands of the oleate at  $\sim 2910\text{ cm}^{-1}$ , w, and  $\sim 2840\text{ cm}^{-1}$ , w (CH stretching), and  $\sim 1520\text{ cm}^{-1}$ , w, br and  $\sim 1420\text{ cm}^{-1}$ , w, br (symmetric and antisymmetric stretching of  $-\text{COO}$ ). This IR spectra is equal to the previously described for magnetite NPs [50] what suggests that the incorporation of Zn ions is by doping of the magnetite nanoparticles, as expected.

The magnetic hysteresis curve of ZnFeNPs (Fig. 1.D.) showed a superparamagnetic behavior at room temperature, with a coercivity of 3 Oe and a saturation magnetization (Ms) of  $81 \pm 1\text{ emu/g}$ , which is much higher than the previously described for magnetite NPs obtained by the same synthetic method (12 Oe and  $70\text{ emu/g}$ ) [50]. Similar increases in the value of Ms have been described for other zinc doped magnetite [14–16,54].

### 3.2. Synthesis and characterization of magnetic beads (MBs)

The obtained ZnFeNPs were used for the formation of MBs following the procedure described in Fig. 2, based on previously published methods with some modifications [58–60]. A dispersion of ZnFeNPs in 2-propanol was mixed with PLGA in DMF solution and incorporated into an aqueous phase of PVA, following a water in oil emulsion method. The contact of these two phases facilitates the assembling of ZnFeNPs and PLGA, leading to the formation of the MBs. PLGA is a biocompatible polymer widely used in drug delivery due to its effective encapsulation capacity and control release [61], what provides a great versatility to the MBs obtained in this work [62,63]. MB@PLGA were also coated with a layer of PEI (MB@PEI) in order to achieve an improved encapsulation and stability. Also, PEI was selected as it facilitates the conjugation due to i) the primary amine groups of PEI and to ii) the well-known proton sponge effect of this polymer, associated to its high positive charge that facilitates the electrostatic interaction with negatively charged biomolecules [64,65].

In order to obtain MBs suitable for their use as immunosensing platforms, the synthesized MB@PEI need to be functionalized with affinity proteins. To facilitate the comparison of the MBs synthesized in this work with commercially available ones, neutravidin (NAV) affinity protein was selected for the conjugation. NAV is, together with streptavidin, a biotin-recognition protein normally used as molecular recognition element in biosensing [66]. In this work, NAV was incorporated through glutaraldehyde as a crosslinker, thanks to its high reactivity [67]. This methodology may also be applied to different affinity proteins, thus increasing the versatility of the obtained MBs.

The obtained MBs were characterized in terms of size, DLS,  $\zeta$ -potential, IR and magnetic behavior by measuring the hysteresis loops at room temperature.

First, MBs were morphologically characterized, showing a spherical

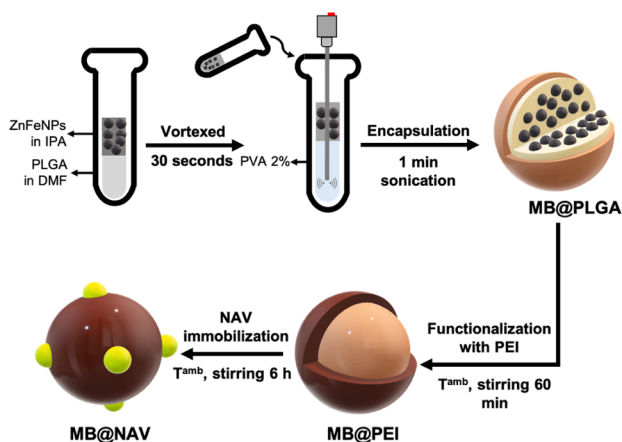


Fig. 2. Schematic representation of the encapsulation-based assembly method for the synthesis of MB@NAV.

shape and an enhanced dispersity with an average diameter of  $89 \pm 18\text{ nm}$  for MB@PLGA,  $96 \pm 16\text{ nm}$  for MB@PEI and  $117 \pm 19\text{ nm}$  for MB@NAV (Fig. 3.A.) obtained from the TEM images. It is worthy mention that the encapsulation observed in the MB@PLGA is slightly worse as noticed in the left side inset in Fig. 3.A., while this state is corrected after the incorporation of PEI. The presence of external NAV is correlated with the increased size of the final NP, as detected by DLS.

As it can be clearly seen, each MB is constituted by a large number of individual ZnFeNPs. Considering the average volume of a MB and the average volume of a single ZnFeNP, it has been estimated that each MB is constituted by approximately 260 individuals ZnFeNPs (assuming that there are no holes inside the particle).

Measurement of the hydrodynamic size of the as-synthesized MBs indicates a change in the diameter of the particles after functionalization, going from  $182\text{ nm}$  of MB@PLGA (Polydispersity index (PDI) of 0.098),  $216\text{ nm}$  for MB@PEI (PDI of 0.147) to  $414\text{ nm}$  (PDI 0.318) after the incorporation of NAV (Fig. 3.B.), what tallies with the presence of this high molecular weight protein ( $\sim 60\text{ kDa}$ ). It is also worthy to mention that an increase in the PDI of the particles is also noticed, what suggests that the conjugation with NAV slightly favor aggregation compared to previous steps.

Functionalization has also been confirmed by measuring the  $\zeta$ -potential of MBs, which represents the external electrical potential in the surface of the suspended particles [68]. The  $\zeta$ -potential (Fig. 3.C.) of MB@PLGA suspended in milli-Q water was of  $-10 \pm 5\text{ mV}$  due to the presence of external carboxylic groups own of acid terminations of the PLGA used. After the coating with PEI, the  $\zeta$ -potential changed to a positive value of  $27 \pm 6\text{ mV}$ , corresponding to the presence of amine groups, confirming the successful incorporation of PEI.  $\zeta$ -potential of MB@NAV measured in PBS 0.1 M pH 7.2 shifts from  $27 \pm 6\text{ mV}$  to  $-10 \pm 5\text{ mV}$ , what correlates with the charge of NAV near its isoelectric point (pH 6.3) [69].

In order to furtherly confirm the functionalization, MBs were characterized by IR (Fig. 3.D.). The presence of the poly(lactic-co-glycolic) matrix in MB@PLGA nanoparticles is denoted mainly by the band at  $1752\text{ cm}^{-1}$ , due to the ester carbonyl group ( $\nu_{\text{C=O}}$ ) of the copolymer. It should be noticed the relative intensities of the peaks at  $1422$  and  $1384\text{ cm}^{-1}$  in the same IR spectrum, assignable to the C–H bending vibrations of the  $\text{CH}_3$  and  $\text{CH}_2$  groups. The stronger intensity of the band at  $1384\text{ cm}^{-1}$  indicates the presence of abundant methyl groups, as it is expected for the lactic repeating unit in PLGA [70]. Other absorptions of interest are those at  $1167$  and  $1090\text{ cm}^{-1}$ , due to the C–O–C groups of the polyester.

On the other hand, the most characteristic band of the PEI assigned to N–H bending should appear at  $1576\text{ cm}^{-1}$  [71]. However, in the infrared spectrum of the MB@PEI this peak is almost completely hidden by a  $\delta_{\text{OH}}$  band at  $1636\text{ cm}^{-1}$ , probably due to the presence of water. It should be mentioned that the intensities of the peaks at  $1422$  and  $1384\text{ cm}^{-1}$  are very similar, as expected, considering the predominant presence of  $\text{CH}_2$  groups in PEI. Additionally, bands corresponding to PLGA still remain, confirming that the incorporation of PEI does not remove the previously present PLGA.

Moreover, the presence of NAV could not be clearly identified through IR due to the multiple functional groups that compose this protein and to the previous structure of the MBs, although it could be seen an increase in the signal corresponding to  $\sim 1545\text{ cm}^{-1}$ . This peak corresponds to amide II band of the secondary amides present in the NAV protein.

Magnetic behavior of all the obtained MBs was measured at room temperature (Fig. 3.E.). The saturation magnetization (Ms) of MB@PLGA was of  $54 \pm 2\text{ emu/g}$ , while after the coating with PEI this value increased to  $63 \pm 5\text{ emu/g}$ . Although it should be expected a decrease in Ms with the increase of non-magnetic components [72], the higher degree of encapsulation observed through TEM measurements for MB@PEI and the purification stages performed after functionalization has allowed us to separate and purify those MBs with an increased



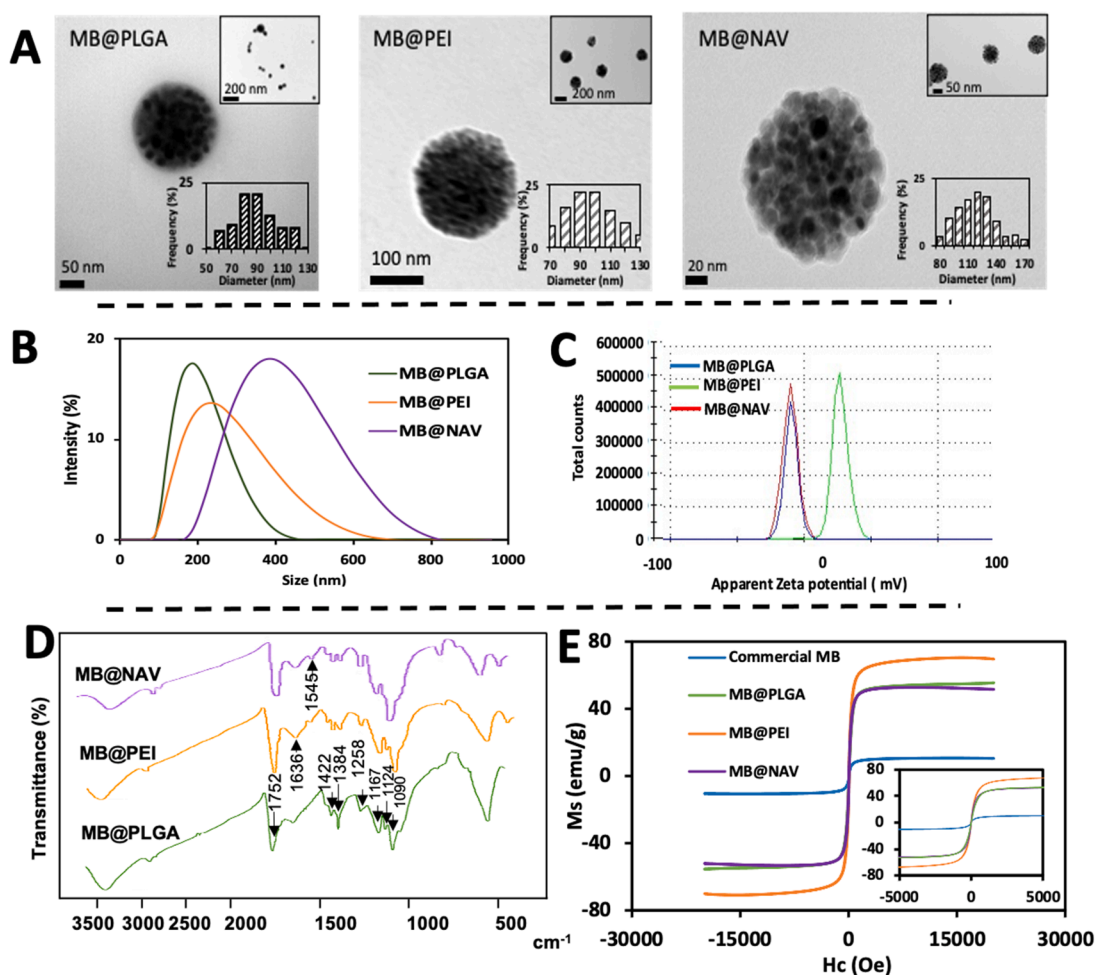


**Fig. 3.** Characterization of MBs. **A.** TEM micrographs of MB@PLGA, MB@PEI and MB@NAV and the corresponding size distribution histogram. An inset of higher magnification is included in the right side of the micrographs; **B.** Hydrodynamic diameter of all MBs in which it is observed a change after functionalization; **C.**  $\zeta$ -potential showing a shift from a negative value for MB@PLGA (external carboxylic groups) to a positive value for MB@PEI (external amine groups) and again, to a negative value after the incorporation of NAV (external imine groups); **D.** IR spectrum of MB@PLGA, MB@PEI and MB@NAV; and **E.** Hysteresis curves of MB@PLGA (54 emu/g), MB@PEI (63 emu/g), MB@NAV (54 emu/g) and the commercially available MBs (11 emu/g). Inset represents an amplification of the low-field region of the hysteresis curves.

magnetic saturation, what could explain the improvement observed.

Regarding superparamagnetic behavior, MB@PLGA present a reduced remanence with a coercivity of 10 Oe, what indicates that the clustering of individual ZnFeNPs into MBs allows to maintain the superparamagnetic behavior of the individual nanoparticles. This value increases to 14 Oe after the incorporation of PEI. Regarding the magnetic behavior of MB@NAV, it is observed a slight decrease in the Ms (from  $63 \pm 5$  emu/g to  $54 \pm 1$  emu/g) and an increase in the coercivity (from 14 to 16 Oe) of the particles. Commercially available MB were also measured for comparison purposes, showing a Ms of 11 emu/g with a coercivity of 2 Oe. The low value of total  $m$  noticed for such MBs is probably due to the high proportion of non-magnetic material, as previously reported [21].

### 3.3. Direct immunoassay for the evaluation of MB@NAV performance

A direct immunoassay was performed for i) the evaluation of the ability of the MB@NAV to be used as immunosensing platforms and ii) as a comparison of the performance of the MB@NAV with that of the commercial MBs. Both MB@NAV and commercial MBs were bioconjugated with biotinylated anti-human IgG (anti-HIgG) and let to react with human IgG (HIgG), previously conjugated with AuNP tags. Mouse IgG (MIgG) conjugated with AuNPs was used as negative control

(Fig. 4.A.). Electrochemical detection was based on the electrocatalytic activity of AuNPs toward the hydrogen evolution reaction (HER) [73], by applying a potential of  $-1.0$  V during 300 s, selecting the value of the current recorded at 300 s as the analytical signal [52,74].

Figure 4.B. shows the chronoamperograms recorded during the stage of hydrogen ion electroreduction for the different assays evaluated. An increase in the catalytic current is clearly observed for the positive assays compared with the control ones. The comparison of the average analytical signals and their standard deviation ( $n = 3$ ) shown in Fig. 4.C. suggest that MB@NAV have a better performance than the commercial ones. First, positive samples provide higher signals, which suggests an enhanced ability of the MB@NAV to capture antibodies. Moreover, the signals recorded for negative control samples were smaller for the MB@NAV, what may indicate a lower unspecific absorption of protein/AuNP conjugates. In addition, the reproducibility obtained with MB@NAV was better than that of the commercial MBs, giving a relative standard deviation (RSD) of 4% (RSD of 12% for commercial MBs).

### 3.4. Sandwich immunoassay for the detection of Tau protein using MB@NAV

Once evaluated the ability of the MB@NAV to efficiently act as immunosensing platform, they were applied for the detection of Tau

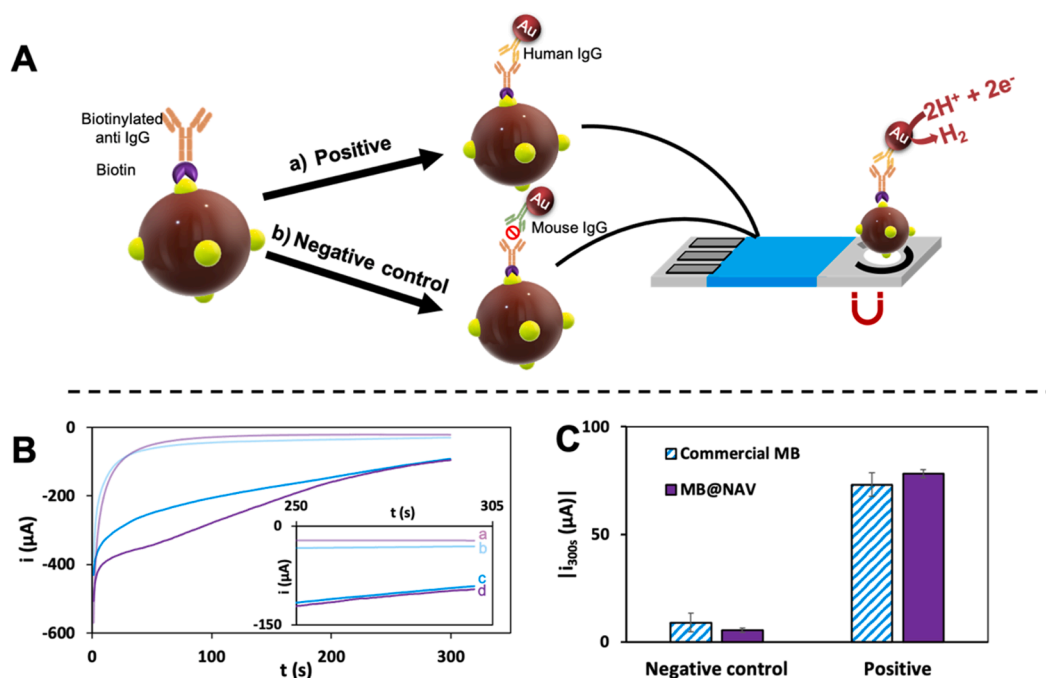


**Fig. 4.** Direct immunoassay for the evaluation of MB@NAV performance. **A.** Schematic representation of the direct immunoassay performed for the evaluation of the MB@NAV performance; **B.** Chronoamperograms recorded by applying a potential of  $-1.00$  V for 300 s in 1 M HCl for: a. Negative control with MB@NAV, b. negative control with commercial MBs, c. positive control with commercial MBs and d. positive control with MB@NAV (inset shows an amplification of the region near 300 s); **C.** Current obtained at 300 s (analytical signal) for the negative control and positive control with both MB@NAV synthesized in this work (purple) and commercial MBs (blue lines). Background current of  $16.5 \mu\text{A}$  corresponding to the hydrogen evolution in the bare carbon electrode was subtracted from all measurements.

protein, an AD biomarker, in a sandwich immunoassay format. The structure of the immunoassay is schematized in Fig. 5.A. Briefly, a biotinylated anti-Tau antibody was immobilized on the MB@NAV and the conjugate was then incubated with samples containing concentrations of Tau protein ranging from 50 to 750 ng/mL, in a dose-response assay. The sandwich was then completed with anti-Tau antibody conjugated with AuNPs, that were detected based on the HER reaction, as described above.

The results obtained are represented in Fig. 5.B. and depict that there is a direct correlation between the catalytic current recorded and the

concentration of Tau protein. Fig. 5.C. shows that there is a good linear relationship between the two parameters in the range 50–750 ng/mL, with a correlation coefficient of 0.9963, according to the equation:

$$\text{Current}_{300\text{s}} = 0.1264[\text{Tau}](\text{ng/mL}) + 63.043$$

The limit of detection (LOD) was calculated as three times the standard deviation of the intercepted divided by the slope, resulting in a value of 63 ng/mL. The method showed an excellent reproducibility, with an average relative standard deviation (RSD) of 4 % ( $n = 3$ ).

Tau protein has been selected as model analyte in our proof-of-

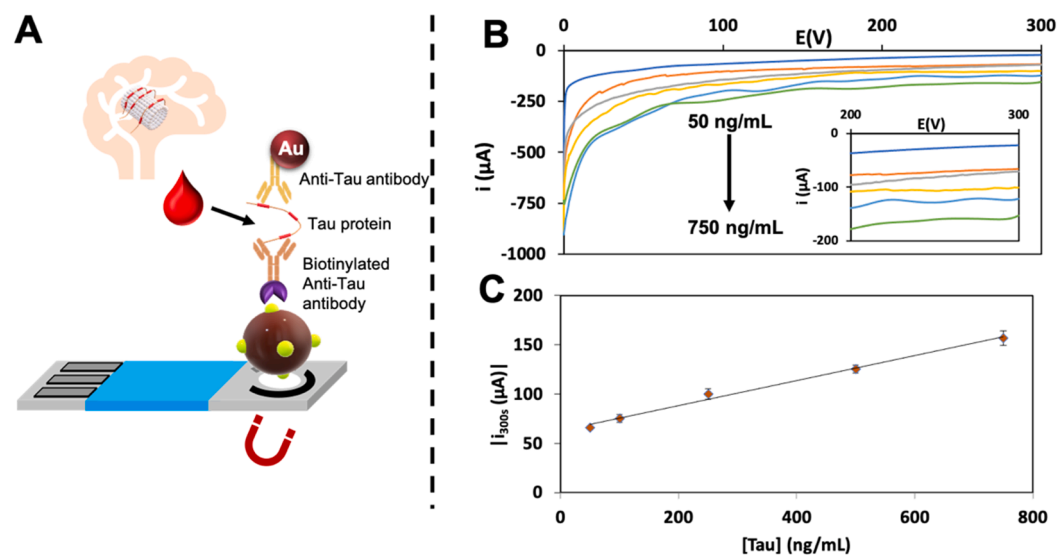


**Fig. 5.** **A.** Schematic representation of the biosensor used for the detection of Tau protein by the immobilization of biotinylated anti-Tau antibodies onto MB@NAV; **B.** Chronoamperograms recorded by applying a potential of  $-1.00$  V for 300 s in 0.1 M HCl for each Tau concentration ranging between 50 and 750 ng/mL. Inside, an inset of the signal recorded at the region near 300 s; **C.** Calibration curve of the current recorded at 300 s for each Tau concentration.

concept, instead of i.e. hyperphosphorylated one due to the following reasons. Although there is still controversy on the clinical implications of total Tau protein as predictor of neurodegeneration [75,76] and its role in AD, there is no consensus on hyperphosphorylated Tau (p-tau) too, as it is not clear which p-tau isoform is more relevant in AD. Even though p-tau181 has been mainly stated as AD biomarker in blood [77], the role of p-tau217 has also stood out [78,79]. The difference between both isoforms relies on the amino acid residue that is phosphorylated. These clinical results point out that the mechanism of action of Tau protein in AD still requires further investigation. For these reasons, the identification of Tau protein as proof-of-concept is an extended practice in immunosensing for AD diagnostics [36].

This is why we have selected Tau protein as analyte in our proof-of-concept work. It is worthy to highlight that our biosensing system may be easily adapted to the determination of p-tau, just using suitable antibodies that are commercially available.

### 3.5. Tau protein analysis in human serum samples: Spike and recovery

The final objective of the development of an analytic biosensor is the detection of biomolecules in real samples. In this context, it has been evaluated the performance of the biosensor in a serum sample of cognitively healthy patients, demonstrating the selectivity of the analytical method in the real scenario. For that purpose, a spike and recovery method was performed obtaining a high recovery rate at levels around 85–89% (Table 1). These results indicate that the presence of other components in real samples do not significantly interfere in the accurate detection of Tau protein, opening the way to the use of the here described methodology to the evaluation of samples from AD patients.

## 4. Conclusions

In this work, we report a novel method for obtaining magnetic beads (MBs) with improved performance as immunosensing platforms, which is applied for the detection of Tau protein, an Alzheimer's disease biomarker in human serum.

First, ZnFeNPs were obtained by a thermal-decomposition method, demonstrating that the doping with Zn atoms of the magnetite nanoparticles, clearly enhances their magnetic behavior. The obtained ZnFeNPs are used for the formation of MBs by encapsulation in a PLGA polymeric matrix. In order to facilitate their use as immunosensing platform, MB@PLGA were first functionalized with PEI and then NAV was furtherly immobilized on their surface. In all cases, MBs maintained their superparamagnetic behavior with high saturation magnetization values, assuring that encapsulation of single nanoparticles works as a way of maintaining magnetism while allowing further functionalization. Moreover, the saturation magnetization obtained for the as-synthesized MB@NAV was significantly higher than that of commercial MBs, constituting an important practical advantage.

The performance of MB@NAV in a direct immunoassay for detecting HlgG using AuNPs as labels showed lower RSD for MB@NAV compared to commercial MBs, thus improving the reproducibility of the assay. Moreover, the lower and higher net currents recorded with MB@NAV for control and positive samples respectively suggested that the here described MBs provide lower non-specific adsorptions as they have a greater surface functionalization ability.

These results prove the effectivity of the obtained MB@NAV as immunosensing platforms, and their versatility opens the way to their use for a wide variety of applications.

The developed immunosensor for Tau protein detection constitutes just a proof-of-concept of the potential ability of such MBs to be used as immunosensing platforms for an interesting application in real samples. The low matrix effects (high recoveries) observed in human serum samples demonstrate the excellent performance of our MBs in a real scenario. Although the detection limit obtained in our proof-of-concept study (63 ng/mL) is higher than the required for AD diagnostics (pg/mL

**Table 1**  
Spike and recovery assay data.

Sample	Spiked Tau (ng/mL)	Current in PBS (μA)	Current in real sample (μA)	Recovery (%)
Serum from cognitively healthy subjects	50	−66,12	−56,15	85%
	750	−156,8	−139,0	89%

levels in human serum), the versatility of both the MBs and the nanoparticle tags allow to make feasible further optimizations for meeting such clinical needs. On the one hand, it is well-known that the magnetic separation performed after each incubation step allows to pre-concentrate the sample. This means that higher sample volumes than the evaluated in our work (100 μL) may be assayed, capturing a higher amount of the AD biomarker. After removing the supernatant, MBs may be re-suspended in a smaller volume, leading to the sample pre-concentration. Regarding the tag, current research in our group (and others) is focused on alternative bimetallic nanoparticles with electrocatalytic properties that can be detected at lower levels than the AuNPs.

Such studies, together with a careful evaluation of patient samples will be object of future research.

## Declaration of Competing Interest

The authors declare that they have no known competing financial interests or personal relationships that could have appeared to influence the work reported in this paper.

## Acknowledgements

This work has been supported by the CTQ2017-86994-R and MCI-21-PID2020-115204RB-I00 projects from the Spanish Ministry of Economy and Competitiveness (MINECO) and the Spanish Ministry of Science and Innovation (MICINN) respectively and the FC-GRUPIN-ID/2018/000166 project from the Asturias Regional Government. C. Toyos-Rodríguez thanks the MICINN for the award of a FPI Grant (PRE2018-084953). A. de la Escosura-Muñiz also acknowledges the MICINN for the “Ramón y Cajal” Research Fellow (RyC-2016-20299).

## Appendix A. Supplementary data

Supplementary data to this article can be found online at <https://doi.org/10.1016/j.microc.2022.107211>.

## References

- [1] S. Mirza, M.S. Ahmad, M.I.A. Shah, M. Ateeq, in: *Metal Nanoparticles for Drug Delivery and Diagnostic Applications*, Elsevier, 2020, pp. 189–213, <https://doi.org/10.1016/B978-0-12-816960-5.00011-2>.
- [2] L.H. Reddy, J.L. Arias, J. Nicolas, P. Couvreur, Magnetic nanoparticles: design and characterization, toxicity and biocompatibility, pharmaceutical and biomedical applications, *Chem. Rev.* 112 (11) (2012) 5818–5878, <https://doi.org/10.1021/cr300068p>.
- [3] S.C.N. Tang, I.M.C. Lo, Magnetic nanoparticles: essential factors for sustainable environmental applications, *Water Res.* 47 (8) (2013) 2613–2632, <https://doi.org/10.1016/j.watres.2013.02.039>.
- [4] Y. Xu, E. Wang, Electrochemical biosensors based on magnetic micro/nano particles, *Electrochim. Acta* 84 (2012) 62–73, <https://doi.org/10.1016/j.electacta.2012.03.147>.
- [5] M. Ahmadi, A. Ghoorchian, K. Dashtian, M. Kamalabadi, T. Madrakian, A. Afkhami, Application of magnetic nanomaterials in electroanalytical methods: A review, *Talanta* 225 (2021) 121974, <https://doi.org/10.1016/j.talanta.2020.121974>.
- [6] A.-H. Lu, E.L. Salabas, F. Schüth, Magnetic Nanoparticles: Synthesis, Protection, Functionalization, and Application, *Angew. Chem. Int. Ed.* 46 (8) (2007) 1222–1244, <https://doi.org/10.1002/anie.200602866>.
- [7] R.B. Nasir Baig, M.N. Nadagouda, R.S. Varma, Magnetically retrievable catalysts for asymmetric synthesis, *Coord. Chem. Rev.* 287 (2015) 137–156, <https://doi.org/10.1016/j.ccr.2014.12.017>.

- [8] Y.-T. Chen, A.G. Kolhatkar, O. Zenasni, S. Xu, T.R. Lee, Biosensing Using Magnetic Particle Detection Techniques, *Sensors* 17 (2017) 2300, <https://doi.org/10.3390/s17102300>.
- [9] L. Li, Y. Yang, J. Ding, J. Xue, Synthesis of Magnetite Nanooctahedra and Their Magnetic Field-Induced Two-/Three-Dimensional Superstructure, *Chem. Mater.* 22 (10) (2010) 3183–3191.
- [10] Q. Li, C.W. Kartikowati, S. Horie, T. Ogi, T. Iwaki, K. Okuyama, Correlation between particle size/domain structure and magnetic properties of highly crystalline Fe<sub>3</sub>O<sub>4</sub> nanoparticles, *Sci Rep.* 7 (2017) 9894, <https://doi.org/10.1038/s41598-017-09897-5>.
- [11] D. Ling, T. Hyeon, Chemical Design of Biocompatible Iron Oxide Nanoparticles for Medical Applications, *Small* 9 (9-10) (2013) 1450–1466, <https://doi.org/10.1002/smll.201202111>.
- [12] C.G.C.M. Netto, H.E. Toma, L.H. Andrade, Superparamagnetic nanoparticles as versatile carriers and supporting materials for enzymes, *J. Mol. Catal. B Enzym.* 85–86 (2013) 71–92, <https://doi.org/10.1016/j.molcatb.2012.08.010>.
- [13] K. Aguilar-Arteaga, J.A. Rodríguez, E. Barrado, Magnetic solids in analytical chemistry: A review, *Anal. Chim. Acta* 674 (2) (2010) 157–165, <https://doi.org/10.1016/j.aca.2010.06.043>.
- [14] J.-T. Jang, H. Nah, J.-H. Lee, S. Moon, M. Kim, J. Cheon, Critical Enhancements of MRI Contrast and Hyperthermic Effects by Dopant-Controlled Magnetic Nanoparticles, *Angew. Chem. Int. Ed.* 48 (7) (2009) 1234–1238, <https://doi.org/10.1002/anie.200805149>.
- [15] J.M. Byrne, V.S. Coker, E. Cespedes, P.L. Wincott, D.J. Vaughan, R.A.D. Patrick, G. van der Laan, E. Arenholz, F. Tuna, M. Bencsik, J.R. Lloyd, N.D. Telling, Biosynthesis of Zinc Substituted Magnetite Nanoparticles with Enhanced Magnetic Properties, *Adv. Funct. Mater.* 24 (17) (2014) 2518–2529, <https://doi.org/10.1002/adfm.201303230>.
- [16] I. Castellanos-Rubio, O. Arriortua, L. Marcano, I. Rodrigo, D. Iglesias-Rojas, A. Barón, A. Olazagoitia-Garmendia, L. Olivi, F. Plazaola, M.L. Fdez-Gubieda, A. Castellanos-Rubio, J.S. Garitaonandia, I. Orue, M. Insausti, Shaping Up Zn-Doped Magnetite Nanoparticles from Mono- and Bimetallic Oleates: The Impact of Zn Content, Fe Vacancies, and Morphology on Magnetic Hyperthermia Performance, *Chem. Mater.* 33 (9) (2021) 3139–3154, <https://doi.org/10.1021/acs.chemmater.0c04794>.
- [17] O. Philippova, A. Barabanova, V. Molchanov, A. Khokhlov, Magnetic polymer beads: Recent trends and developments in synthetic design and applications, *Eur. Polym. J.* 47 (4) (2011) 542–559, <https://doi.org/10.1016/j.eurpolymj.2010.11.006>.
- [18] Z. Lu, Y. Yin, Colloidal nanoparticle clusters: functional materials by design, *Chem. Soc. Rev.* 41 (21) (2012) 6874, <https://doi.org/10.1039/c2cs35197h>.
- [19] J. Guo, W. Yang, C. Wang, Magnetic Colloidal Supraparticles: Design, Fabrication and Biomedical Applications, *Adv. Mater.* 25 (37) (2013) 5196–5214, <https://doi.org/10.1002/adma.201301896>.
- [20] N.C. Bigall, C. Wilhelm, M.-L. Beoutis, M. García-Hernandez, A.A. Khan, C. Giannini, A. Sánchez-Ferrer, R. Mezzenga, M.E. Matera, M.A. García, F. Gazeau, A.M. Bittner, L. Manna, T. Pellegrino, Colloidal Ordered Assemblies in a Polymer Shell—A Novel Type of Magnetic Nanobeads for Theranostic Applications, *Chem. Mater.* 25 (7) (2013) 1055–1062, <https://doi.org/10.1021/cm3036746>.
- [21] J. Park, M.D. Porter, M.C. Granger, Colloidally Assembled Zinc Ferrite Magnetic Beads: Superparamagnetic Labels with High Magnetic Moments for MR Sensors, *ACS Appl. Mater. Interfaces* 9 (23) (2017) 19569–19577, <https://doi.org/10.1021/acsami.7b03182>.
- [22] S.H. Chun, S.W. Shin, L. Amornkitbamrung, S.Y. Ahn, J.S. Yuk, S.J. Sim, D. Luo, S. H. Um, Polymeric Nanocomplex Encapsulating Iron Oxide Nanoparticles in Constant Size for Controllable Magnetic Field Reactivity, *Langmuir* 34 (43) (2018) 12827–12833, <https://doi.org/10.1021/acs.langmuir.7b04143>.
- [23] S.-J. Lee, H.-J. Kim, Y.-M. Huh, I.W. Kim, J.H. Jeong, J.-C. Kim, J.-D. Kim, Functionalized Magnetic PLGA Nanospheres for Targeting and Bioimaging of Breast Cancer, *J Nanosci Nanotechnol.* 18 (3) (2018) 1542–1547, <https://doi.org/10.1166/jnn.2018.14220>.
- [24] N. Schleich, P. Sibret, P. Danhier, B. Ucakar, S. Laurent, R.N. Muller, C. Jérôme, B. Gallez, V. Préat, F. Danhier, Dual anticancer drug/superparamagnetic iron oxide-loaded PLGA-based nanoparticles for cancer therapy and magnetic resonance imaging, *Int. J. Pharm.* 447 (1-2) (2013) 94–101, <https://doi.org/10.1016/j.ijpharm.2013.02.042>.
- [25] S.-J. Lee, J.-R. Jeong, S.-C. Shin, J.-C. Kim, Y.-H. Chang, K.-H. Lee, J.-D. Kim, Magnetic enhancement of iron oxide nanoparticles encapsulated with poly(D, L-lactide-co-glycolide), *Colloids Surf., A* 255 (1-3) (2005) 19–25, <https://doi.org/10.1016/j.colsurfa.2004.12.019>.
- [26] A. Jonderian, R. Maalouf, Formulation and In vitro Interaction of Rhodamine-B Loaded PLGA Nanoparticles with Cardiac Myocytes, *Front. Pharmacol.* 7 (2016), <https://doi.org/10.3389/fphar.2016.00458>.
- [27] L. Gomes dos Reis, W.-H. Lee, M. Svolos, L.M. Moir, R. Jaber, N. Windhab, P. M. Young, D. Traini, Nanotoxicologic Effects of PLGA Nanoparticles Formulated with a Cell-Penetrating Peptide: Searching for a Safe pDNA Delivery System for the Lungs, *Pharmaceutics* 11 (2019) 12, <https://doi.org/10.3390/pharmaceutics11010012>.
- [28] T.A.P. Rocha-Santos, Sensors and biosensors based on magnetic nanoparticles, *TrAC* 62 (2014) 28–36, <https://doi.org/10.1016/j.trac.2014.06.016>.
- [29] J. Pansieri, M. Gerstenmayer, F. Lux, S. Mériaux, O. Tillement, V. Forge, B. Larrat, C. Marquette, Magnetic Nanoparticles Applications for Amyloidosis Study and Detection: A Review, *Nanomaterials* 8 (2018) 740, <https://doi.org/10.3390/nano8090740>.
- [30] M. Pedrero, S. Campuzano, J.M. Pingarrón, Magnetic Beads-Based Electrochemical Sensors Applied to the Detection and Quantification of Bioterrorism/Biohazard Agents, *Electroanalysis* 24 (2012) 470–482, <https://doi.org/10.1002/elan.201100528>.
- [31] L. Fabiani, M. Saroglia, G. Galatà, R. De Santis, S. Fillo, V. Luca, G. Faggioni, N. D'Amore, E. Regalbutto, P. Salvatore, G. Terova, D. Moscone, F. Lista, F. Arduini, Magnetic beads combined with carbon black-based screen-printed electrodes for COVID-19: A reliable and miniaturized electrochemical immunosensor for SARS-CoV-2 detection in saliva, *Biosens. Bioelectron.* 171 (2021) 112686, <https://doi.org/10.1016/j.bios.2020.112686>.
- [32] K.E. Luo, K.-B. Jeong, S.-M. You, D.-H. Lee, Y.-R. Kim, Molecular Rearrangement of Glucans from Natural Starch To Form Size-Controlled Functional Magnetic Polymer Beads, *J. Agric. Food Chem.* 66 (26) (2018) 6806–6813, <https://doi.org/10.1021/acs.jafc.8b01590>.
- [33] K. Luo, D.-H. Lee, H.J. Adra, Y.-R. Kim, Synthesis of monodisperse starch microparticles through molecular rearrangement of short-chain glucans from natural waxy maize starch, *Carbohydr. Polym.* 218 (2019) 261–268, <https://doi.org/10.1016/j.carbpol.2019.05.001>.
- [34] A. Iglesias-Mayor, O. Amor-Gutiérrez, A. Novelli, M.-T. Fernández-Sánchez, A. Costa-García, A. de la Escosura-Muñiz, Bifunctional Au@Pt/Au core@shell Nanoparticles As Novel Electroanalytical Tags in Immunosensing: Application for Alzheimer's Disease Biomarker Detection, *Anal. Chem.* 92 (10) (2020) 7209–7217, <https://doi.org/10.1021/acs.analchem.0c00760>.
- [35] L. Rivas, A. de la Escosura-Muñiz, J. Pons, A. Merkoçi, Alzheimer Disease Biomarker Detection Through Electroanalytical Water Oxidation Induced by Iridium Oxide Nanoparticles, *Electroanalysis* 26 (2014) 1287–1294, <https://doi.org/10.1002/elan.201400027>.
- [36] C.A. Razzino, V. Serafin, M. Gamella, M. Pedrero, A. Montero-Calle, R. Barderas, M. Calero, A.O. Lobo, P. Yáñez-Sedeño, S. Campuzano, J.M. Pingarrón, An electrochemical immunosensor using gold nanoparticles-PAMAM-nanostructured screen-printed carbon electrodes for tau protein determination in plasma and brain tissues from Alzheimer patients, *Biosens. Bioelectron.* 163 (2020) 112238, <https://doi.org/10.1016/j.bios.2020.112238>.
- [37] C. Toyos-Rodríguez, F.J. García-Alonso, A. de la Escosura-Muñiz, Electrochemical Biosensors Based on Nanomaterials for Early Detection of Alzheimer's Disease, *Sensors* 20 (2020) 4748, <https://doi.org/10.3390/s20174748>.
- [38] A. de la Escosura-Muñiz, Z. Plichta, D. Horák, A. Merkoçi, Alzheimer's disease biomarkers detection in human samples by efficient capturing through porous magnetic microspheres and labelling with electrocatalytic gold nanoparticles, *Biosens. Bioelectron.* 67 (2015) 162–169, <https://doi.org/10.1016/j.bios.2014.07.086>.
- [39] P. Scheltens, K. Blennow, M.M.B. Breteler, B. de Strooper, G.B. Frisoni, S. Salloway, W.M. Van der Flier, Alzheimer's disease, *The Lancet* 388 (10043) (2016) 505–517, [https://doi.org/10.1016/S0140-6736\(15\)01124-1](https://doi.org/10.1016/S0140-6736(15)01124-1).
- [40] A. Kaushik, R.D. Jayant, S. Tiwari, A. Vashist, M. Nair, Nano-biosensors to detect beta-amyloid for Alzheimer's disease management, *Biosens. Bioelectron.* 80 (2016) 273–287, <https://doi.org/10.1016/j.bios.2016.01.065>.
- [41] B. Shui, D. Tao, A. Florea, J. Cheng, Q. Zhao, Y. Gu, W. Li, N. Jaffrezic-Renault, Y. Mei, Z. Guo, Biosensors for Alzheimer's disease biomarker detection: A review, *Biochimie* 147 (2018) 13–24, <https://doi.org/10.1016/j.biochi.2017.12.015>.
- [42] K. Iqbal, F. Liu, C.-X. Gong, I. Grundke-Iqbal, Tau in Alzheimer Disease and Related Tauopathies, *CAR* 7 (2010) 656–664, <https://doi.org/10.2174/156720510793611592>.
- [43] K. Iqbal, A. del C. Alonso, C.-X. Gong, S. Khatoon, J.-J. Pei, J.Z. Wang, I. Grundke-Iqbal, Mechanisms of neurofibrillary degeneration and the formation of neurofibrillary tangles, in: K. Jellinger, F. Fazekas, M. Windisch (Eds.), *Ageing and Dementia*, Springer Vienna, Vienna, 1998: pp. 169–180. [https://doi.org/10.1007/978-3-7091-6467-9\\_15](https://doi.org/10.1007/978-3-7091-6467-9_15).
- [44] K. Iqbal, T. Zaidi, G. Wen, I. Grundke-Iqbal, P. Merz, S. Shaikh, H. Wisniewski, I. Alafuzoff, B. Winblad, Defective brain microtubule assembly in Alzheimer's disease, *The Lancet* 328 (8504) (1986) 421–426.
- [45] Y. Zhou, J. Shi, D. Chu, W. Hu, Z. Guan, C.-X. Gong, K. Iqbal, F. Liu, Relevance of Phosphorylation and Truncation of Tau to the Etiopathogenesis of Alzheimer's Disease, *Front. Aging Neurosci.* 10 (2018) 27, <https://doi.org/10.3389/fnagi.2018.00027>.
- [46] H. Braak, E. Braak, I. Grundke-Iqbal, K. Iqbal, Occurrence of neurofibrillary threads in the senile human brain and in Alzheimer's disease: A third location of paired helical filaments outside of neurofibrillary tangles and neuritic plaques, *Neurosci. Lett.* 65 (3) (1986) 351–355, [https://doi.org/10.1016/0304-3940\(86\)90288-0](https://doi.org/10.1016/0304-3940(86)90288-0).
- [47] P. Carneiro, S. Morais, M.C. Pereira, Nanomaterials towards Biosensing of Alzheimer's Disease Biomarkers, *Nanomaterials* 9 (2019) 1663, <https://doi.org/10.3390/nano9121663>.
- [48] V. Serafin, M. Gamella, M. Pedrero, A. Montero-Calle, C.A. Razzino, P. Yáñez-Sedeño, R. Barderas, S. Campuzano, J.M. Pingarrón, Enlightening the advancements in electrochemical bioanalysis for the diagnosis of Alzheimer's disease and other neurodegenerative disorders, *J. Pharmaceut. Biomed.* 189 (2020) 113437, <https://doi.org/10.1016/j.jpba.2020.113437>.
- [49] L.C. Brazaca, I. Sampaio, V. Zucolotto, B.C. Janegitz, Applications of biosensors in Alzheimer's disease diagnosis, *Talanta* 210 (2020) 120644, <https://doi.org/10.1016/j.talanta.2019.120644>.
- [50] C. Toyos-Rodríguez, J. Calleja-García, L. Torres-Sánchez, A. López, A.M. Abu-Dief, A. Costa, L. Elbaile, R.D. Crespo, J.S. Garitaonandia, E. Lastra, J.A. García, F. J. García-Alonso, A Simple and Reliable Synthesis of Superparamagnetic Magnetite Nanoparticles by Thermal Decomposition of Fe(acac)<sub>3</sub>, *Journal of Nanomaterials* 2019 (2019) 1–10, <https://doi.org/10.1155/2019/2464010>.



- [51] J. Turkevich, P.C. Stevenson, J. Hillier, A study of the nucleation and growth processes in the synthesis of colloidal gold, *Discuss. Faraday Soc.* 11 (1951) 55–75, <https://doi.org/10.1039/d9f511100055>.
- [52] M.-d. Costa, A.d. la Escosura-Muñoz, A. Merkoçi, Electrochemical quantification of gold nanoparticles based on their catalytic properties toward hydrogen formation: Application in magnetoimmunoassays, *Electrochem. Commun.* 12 (11) (2010) 1501–1504, <https://doi.org/10.1016/j.elecom.2010.08.018>.
- [53] A. de la Escosura-Muñoz, C. Sánchez-Espinel, B. Díaz-Freitas, Á. González-Fernández, M. Maltez-da Costa, A. Merkoçi, Rapid Identification and Quantification of Tumor Cells Using an Electrocatalytic Method Based on Gold Nanoparticles, *Anal. Chem.* 81 (24) (2009) 10268–10274, <https://doi.org/10.1021/ac902087k>.
- [54] W. Szczerba, J. Zukrowski, M. Przybylski, M. Sikora, O. Safonova, A. Shmeliov, V. Nicolosi, M. Schneider, T. Granath, M. Oppmann, M. Straßer, K. Mandel, Pushing up the magnetisation values for iron oxide nanoparticles via zinc doping: X-ray studies on the particle's sub-nano structure of different synthesis routes, *Phys. Chem. Chem. Phys.* 18 (36) (2016) 25221–25229, <https://doi.org/10.1039/C6CP04221J>.
- [55] M. Rivero, A. del Campo, Á. Mayoral, E. Mazario, J. Sánchez-Marcos, A. Muñoz-Bonilla, Synthesis and structural characterization of Zn<sub>x</sub>Fe<sub>3-x</sub>O<sub>4</sub> ferrite nanoparticles obtained by an electrochemical method, *RSC Adv.* 6 (46) (2016) 40067–40076, <https://doi.org/10.1039/C6RA04145K>.
- [56] M. Jouyandeh, J.A. Ali, M. Aghazadeh, K. Formela, M.R. Saeb, Z. Ranjbar, M. R. Ganjali, Curing epoxy with electrochemically synthesized Zn Fe<sub>3</sub>-O<sub>4</sub> magnetic nanoparticles, *Prog. Org. Coat.* 136 (2019) 105246, <https://doi.org/10.1016/j.porgcoat.2019.105246>.
- [57] A. Ali, H. Zafar, M. Zia, I. ul Haq, A.R. Phull, J.S. Ali, A. Hussain, Synthesis, characterization, applications, and challenges of iron oxide nanoparticles, *NSA*. Volume 9 (2016) 49–67. <https://doi.org/10.2147/NSA.S99986>.
- [58] J. Mosafar, K. Abnous, M. Tafaghodi, H. Jafarzadeh, M. Ramezani, Preparation and characterization of uniform-sized PLGA nanospheres encapsulated with oleic acid-coated magnetic-Fe<sub>3</sub>O<sub>4</sub> nanoparticles for simultaneous diagnostic and therapeutic applications, *Colloids Surf., A* 514 (2017) 146–154, <https://doi.org/10.1016/j.colsurfa.2016.11.056>.
- [59] X. Liu, M.D. Kaminski, H. Chen, M. Torno, L. Taylor, A.J. Rosengart, Synthesis and characterization of highly-magnetic biodegradable poly(D, L-lactide-co-glycolide) nanospheres, *J. Control. Release* 119 (1) (2007) 52–58, <https://doi.org/10.1016/j.jconrel.2006.11.031>.
- [60] R. Singh, P. Kesharwani, N.K. Mehra, S. Singh, S. Banerjee, N.K. Jain, Development and characterization of folate anchored Saquinavir entrapped PLGA nanoparticles for anti-tumor activity, *Drug Dev Ind Pharm.* 41 (11) (2015) 1888–1901.
- [61] F. Mohamed, C.F. van der Walle, Engineering Biodegradable Polyester Particles With Specific Drug Targeting and Drug Release Properties, *J. Pharm. Sci.* 97 (1) (2008) 71–87, <https://doi.org/10.1002/jps.21082>.
- [62] Y. Zhang, M. García-Gabilondo, A. Rosell, A. Roig, MRI/Photoluminescence Dual-Modal Imaging Magnetic PLGA Nanocapsules for Theranostics, *Pharmaceutics*. 17 (2020) 16.
- [63] J. Ghitman, E.I. Biru, R. Stan, H. Iovu, Review of hybrid PLGA nanoparticles: Future of smart drug delivery and theranostics medicine, *Mater. Des.* 193 (2020) 108805, <https://doi.org/10.1016/j.matdes.2020.108805>.
- [64] S. Nimesh, in: *Gene Therapy*, Elsevier, 2013, pp. 197–223, <https://doi.org/10.1533/9781908818645.197>.
- [65] C. Olbrich, U. Bakowsky, C.-M. Lehr, R.H. Müller, C. Kneuer, Cationic solid-lipid nanoparticles can efficiently bind and transfect plasmid DNA, *J. Control. Release* 77 (3) (2001) 345–355, [https://doi.org/10.1016/S0168-3659\(01\)00506-5](https://doi.org/10.1016/S0168-3659(01)00506-5).
- [66] *Surf. Interface Anal.* (2002) 5.
- [67] I. Migneault, C. Dartiguenave, M.J. Bertrand, K.C. Waldron, Glutaraldehyde: behavior in aqueous solution, reaction with proteins, and application to enzyme crosslinking, *Biotechniques* 37 (2004) 12.
- [68] G.W. Lu, P. Gao, in: *Handbook of Non-Invasive Drug Delivery Systems*, Elsevier, 2010, pp. 59–94, <https://doi.org/10.1016/B978-0-8155-2025-2.10003-4>.
- [69] I. Barinaga-Rementería Ramírez, L. Ekblad, B. Jergil, Affinity partitioning of biotinylated mixed liposomes: effect of charge on biotin-NeutrAvidin interaction, *J. Chromatogr. B Biomed. Sci. Appl.* 743 (1-2) (2000) 389–396, [https://doi.org/10.1016/S0378-4347\(00\)00065-7](https://doi.org/10.1016/S0378-4347(00)00065-7).
- [70] J. Coates, Interpretation of Infrared Spectra, A Practical Approach, in: R.A. Meyers (Ed.), *Encyclopedia of Analytical Chemistry*, John Wiley & Sons, Ltd, Chichester, UK, 2006: p. a5606. <https://doi.org/10.1002/9780470027318.a5606>.
- [71] F. Wang, P. Liu, T. Nie, H. Wei, Z. Cui, Characterization of a Polyamine Microsphere and Its Adsorption for Protein, *IJMS*. 14 (2012) 17–29, <https://doi.org/10.3390/ijms14010017>.
- [72] W. Wu, Q. He, C. Jiang, Magnetic Iron Oxide Nanoparticles: Synthesis and Surface Functionalization Strategies, *Nanoscale Res Lett.* 3 (2008) 397–415, <https://doi.org/10.1007/s11671-008-9174-9>.
- [73] T.D. Tran, M.T.T. Nguyen, H.V. Le, D.N. Nguyen, A. Truong, P.D. Tran, Gold nanoparticle as an outstanding catalyst for the hydrogen evolution reaction, *Chem. Commun.* 54 (2018) 3363–3366, <https://doi.org/10.1039/C8CC00038G>.
- [74] M. Espinoza-Castañeda, A. de la Escosura-Muñoz, G. González-Ortiz, S.M. Martín-Orúe, J.F. Pérez, A. Merkoçi, Casein modified gold nanoparticles for future theranostic applications, *Biosens. Bioelectron.* 40 (1) (2013) 271–276, <https://doi.org/10.1016/j.bios.2012.07.042>.
- [75] M.P. Pase, A.S. Beiser, J.J. Himali, C.L. Satizabal, H.J. Aparicio, C. DeCarli, G. Chêne, C. Dufouil, S. Seshadri, Assessment of Plasma Total Tau Level as a Predictive Biomarker for Dementia and Related Endophenotypes, *JAMA Neurol.* 76 (5) (2019) 598, <https://doi.org/10.1001/jamaneurol.2018.4666>.
- [76] M.A. Sugarman, H. Zetterberg, K. Blennow, Y. Tripodis, A.C. McKee, T.D. Stein, B. Martin, J.N. Palmisano, E.G. Steinberg, I. Simkin, A.E. Budson, R. Killiany, M. K. O'Connor, R. Au, W.W.Q. Qiu, L.E. Goldstein, N.W. Kowall, J. Mez, R.A. Stern, M.L. Alosco, A longitudinal examination of plasma neurofilament light and total tau for the clinical detection and monitoring of Alzheimer's disease, *Neurobiol. Aging* 94 (2020) 60–70, <https://doi.org/10.1016/j.neurobiolaging.2020.05.011>.
- [77] T.K. Karikari, T.A. Pascoal, N.J. Ashton, S. Janelidze, A.L. Benedet, J.L. Rodriguez, M. Chamoun, M. Savard, M.S. Kang, J. Theriault, M. Schöll, G. Massarweh, J.-P. Soucy, K. Höglund, G. Brinkmalm, N. Mattsson, S. Palmqvist, S. Gauthier, E. Stomrud, H. Zetterberg, O. Hansson, P. Rosa-Neto, K. Blennow, Blood phosphorylated tau 181 as a biomarker for Alzheimer's disease: a diagnostic performance and prediction modelling study using data from four prospective cohorts, *The Lancet Neurology*. 19 (5) (2020) 422–433, [https://doi.org/10.1016/S1474-4422\(20\)30071-5](https://doi.org/10.1016/S1474-4422(20)30071-5).
- [78] S. Janelidze, E. Stomrud, R. Smith, S. Palmqvist, N. Mattsson, D.C. Airey, N. K. Proctor, X. Chai, S. Shcherbinin, J.R. Sims, G. Triana-Baltzer, C. Theunis, R. Lemmon, M. Mercken, H. Kolb, J.L. Dage, O. Hansson, Cerebrospinal fluid p-tau<sub>217</sub> performs better than p-tau<sub>181</sub> as a biomarker of Alzheimer's disease, *Nat Commun.* 11 (2020) 1683, <https://doi.org/10.1038/s41467-020-15436-0>.
- [79] E.H. Thijssen, R. La Joie, A. Strom, C. Fonseca, L. Iaccarino, A. Wolf, S. Spina, I. E. Allen, Y. Cobigo, H. Heuer, L. VandeVrede, N.K. Proctor, A.L. Lago, S. Baker, R. Sivasankaran, A. Kieloch, A. Kinshar, L. Yu, M.-A. Valentin, A. Jeromin, H. Zetterberg, O. Hansson, N. Mattsson-Carlsson, D. Graham, K. Blennow, J. H. Kramer, L.T. Grinberg, W.W. Seeley, H. Rosen, B.F. Boeve, B.L. Miller, C. E. Teunissen, G.D. Rabinovici, J.C. Rojas, J.L. Dage, A.L. Boxer, Plasma phosphorylated tau 217 and phosphorylated tau 181 as biomarkers in Alzheimer's disease and frontotemporal lobar degeneration: a retrospective diagnostic performance study, *The Lancet Neurology*. 20 (9) (2021) 739–752, [https://doi.org/10.1016/S1474-4422\(21\)00214-3](https://doi.org/10.1016/S1474-4422(21)00214-3).



# Towards the maximization of nanochannels blockage through antibody-antigen charge control: Application for the detection of an Alzheimer's disease biomarker

Celia Toyos-Rodríguez<sup>a,b</sup>, Francisco Javier García-Alonso<sup>b,c</sup>, Alfredo de la Escosura-Muñiz<sup>a,b,\*</sup>

<sup>a</sup> NanoBioAnalysis Group-Department of Physical and Analytical Chemistry, University of Oviedo, Julián Clavería 8, 33006 Oviedo, Spain

<sup>b</sup> Biotechnology Institute of Asturias, University of Oviedo, Santiago Gascon Building, 33006 Oviedo, Spain

<sup>c</sup> NanoBioAnalysis Group-Department of Organic and Inorganic Chemistry, University of Oviedo, Julián Clavería 8, 33006 Oviedo, Spain

## ARTICLE INFO

### Keywords:

Nanochannels  
Nanopores  
Biosensor  
Tau protein  
Alzheimer's disease

## ABSTRACT

Although size and charge effects in nanochannels have been previously approached for electrochemical immunosensing, as far as we know, thorough studies on the effect of both the antibody and the antibody/antigen immunocomplex charges at different pHs have not been deeply reported. In this context, we present here an unprecedented study of such parameters, applied also for the first time for the detection of an Alzheimer's disease (AD) biomarker. AD detection is currently based in time consuming and expensive techniques, so that the development of alternative analytical strategies for facilitating its diagnosis is still a need. To reach that purpose, we propose here the development of a nanochannel-based system for the electrochemical monitoring of Tau protein, an important AD biomarker. Tau protein is selectively captured by specific antibodies immobilized in the inner walls of the nanochannels of nanoporous alumina membranes. The captured Tau protein blocks the nanochannel and difficulties the passage of red-ox indicator ions, which is voltammetrically monitored using an indium tin oxide/poly(ethylene terephthalate) (ITO/PET) electrode as transducer. The charges of both the antibody and the Tau antigen at different pHs and their effect on the diffusion of the red-ox indicator ions to the electrode are carefully evaluated to maximize the electrostatic blocking of the nanochannels upon the immunocomplex formation. The developed biosensing system allows the determination of Tau protein with a detection limit of 4.3 ng/mL, which is within the range of clinical interest, showing also excellent recovery percentages in human plasma samples.

## 1. Introduction

Neurodegenerative diseases are multifactorial pathologies that act on the central and peripheral nervous system [1]. The incidence of these pathologies increases among age, so that the rise in life expectancy is expected to worsen their burden [2]. From all of them, Alzheimer's disease (AD) is the most common, affecting 30% of people older than 85 years, a value that is increasing in a 6–8% yearly [3,4]. AD neurodegeneration manifests at initial stages with episodes of memory loss and evolves to deterioration in cognition, temporal space disorientation and the incapacity to carry out quotidian activities [5,6].

The incapacitating condition of this pathology has also a relevant impact both socially and economically, with a burden of €232 billion in

2015 [7].

For that reason, a rapid detection is a major concern and, in this process, AD biomarkers, between which Tau protein is included, have been identified as a research priority [8].

Tau protein plays a pivotal role in the development of several neurodegenerative diseases, known as tauopathies [9]. AD, frontotemporal lobar dementia (FTD) [10] or corticobasal degeneration (CBD) are some of them. In the case of AD, Tau is related with the formation of neurofibrillary tangles (NFTs) [11]. All of it, constitutes Tau as a common pathological hallmark in neurodegeneration, so that its detection is desirable for the sensitive diagnosis of AD and other neurodegenerative disorders.

Tau proteins acts as a neuronal microtubule-associated protein that

\* Corresponding author at: NanoBioAnalysis Group-Department of Physical and Analytical Chemistry, University of Oviedo, Julián Clavería 8, 33006 Oviedo, Spain.

E-mail address: [alfredo.escosura@uniovi.es](mailto:alfredo.escosura@uniovi.es) (A. de la Escosura-Muñiz).

<https://doi.org/10.1016/j.snb.2023.133394>

Received 7 November 2022; Received in revised form 22 December 2022; Accepted 18 January 2023

Available online 19 January 2023

0925-4005/© 2023 The Author(s). Published by Elsevier B.V. This is an open access article under the CC BY license (<http://creativecommons.org/licenses/by/4.0/>).

regulates axonal growth and neuronal polarity, as it is mainly found associated to axons [12]. In the normal human brain, Tau regulates the assembly of tubulin into microtubules [13]. This regulation is mediated by the phosphorylation of Tau protein, however, an hyperphosphorylation of this protein increases its tendency to aggregate and to assemble into pair helical filaments (PHFs) and later in the formation of intracellular NFTs, highly related with AD [14–17]. The formation of NFTs has also been related with  $\beta$ -amyloid ( $A\beta$ ), a relevant AD biomarker [18], as according to the amyloid cascade hypothesis [19], Tau hyperphosphorylation occurs following ( $A\beta$ ) deposition [20,21].

Current Tau protein detection is based on enzyme-linked immunosorbent assay (ELISA), mass spectrometry or surface plasmon resonance among other techniques [22–24]. But these procedures are time-consuming and expensive, so that they are not suitable for their use as generalized screening methods. For that reason, the development of optical and electrochemical biosensors for the detection of AD biomarkers has increased among the last years, obtaining promising results [25,26]. However, most of these approaches are based on sandwich-based or competitive assays, depending on the analyte size, requiring the use of labels. The complexity of these procedures is meant to be reduced by the implementation of label-free strategies, for what the use of nanochannels as biosensing platforms stands out [27,28].

In the 50's Wallace Coulter developed the first microchannel-based biosensing device [29]. The mechanism of action of this system is based on the detection of changes in the electrical conductance between two chambers connected by a microchannel when an analyte passes through it. From this first device, several improvements have been done until reaching nanometer channel systems [30], able to detect biomolecules as ssDNA following the so-called stochastic sensing [27,31].

In the development of nanochannel-based systems, the use of naturally pore forming biomolecules such as pore forming toxins has also been exploited [31,32]. However, these biological systems in occasions lack from stability and are suitable just for small size molecules, so that alternative systems such as solid-state nanochannels have been postulated [33]. As an example of them, nanoporous alumina membranes show up. They are characterized by having reduced pore sizes while maintaining an enhanced pore density, what increases the available surface area [34]. These membranes have already been used for the electrochemical detection of proteins [35], DNA [36], enzymes [37] or *in situ* monitoring of cell secreted proteins [38] and anti-virulence agents [39], using screen printed carbon electrodes (SPCEs) or indium tin oxide/poly(ethylene terephthalate) (ITO/PET) electrodes. The excellent filtering properties and low unspecific adsorption of proteins shown by this material has made it ideal for the analysis of samples with complex matrixes. However, the detection of AD biomarkers is seldom studied within nanochannels [40].

In this context, we propose here a novel approach for the detection of Tau protein using nanoporous alumina membranes as sensing platforms and ITO/PET electrodes as transducers. The analytical detection technique used is based on the blockage of the signal, both steric and electrostatic, due to the presence of increasing concentrations of Tau protein, captured by specific antibodies. Moreover, the effect of the pH in the blockage capacity and the performance in real plasma samples has also been investigated. The developed biosensor is the first approach, to our knowledge, in which nanochannels are used for Tau protein detection.

## 2. Materials and methods

### 2.1. Reagents and equipment

(3-aminopropyl) triethoxysilane (APTES), amyloid beta protein ( $\beta$ -amyloid), avidin from egg white, bovine serum albumin (BSA), N-(3-Dimethylaminopropyl)-N'-ethylcarbodiimide hydrochloride (EDC), N-Hydroxysulfosuccinimide sodium salt (sulfo-NHS), Tau-441 (1–441) protein, plasma from human (prepared from donors pooled blood),

potassium ferrocyanide  $K_4[Fe(CN)_6]$ , (2-(N-morpholino) ethanesulfonic acid) (MES) and Tris (tris(hydroxymethyl) aminomethane)-HCl (Tris-HCl) were purchased from Sigma-Aldrich (Spain). Anti-Tau monoclonal antibody (BT2) was purchased from Thermo Fisher Scientific (Spain).

Buffer solutions used were 0.1 M MES pH 5.0, and 0.1 M Tris-HCl at pH 6.5, 7.2 and 9.0 and they were all prepared in ultrapure water (18.2 M $\Omega$ -cm @ 25 °C) obtained from a Millipore Direct-Q® 3 UV purification system from Millipore Ibérica S.A (Spain).

Nanoporous alumina membranes (Whatman® Anodisc™ filters, 13 mm diameter, 60  $\mu$ m thickness, 100 nm pore) were obtained from VWR International Eurolabs (Spain). ITO/PET sheets (surface resistivity 60  $\Omega$ /sq) were obtained from Sigma-Aldrich (Spain). ITO/PET was used in pieces of 43  $\times$  20 mm as electrochemical transducers. As reference electrode a silver/silver chloride from CH Instruments, Inc (United States of America) was used, while a platinum wire from Alfa Aesar (United States of America) was selected as counter electrode.

The electrochemical measurements were performed inside a methacrylate electrochemical cell using an Autolab PGSTAT-10 (Eco Chemie (Netherlands)) connected to a PC and controlled by Autolab GPES software. The nanoporous membranes were characterized using a scanning electron microscope (SEM) MEB JOEL-6100 (Japan).

### 2.2. Methods

#### 2.2.1. Nanoporous alumina membranes functionalization and anti-Tau antibody immobilization

Anti-Tau antibodies were immobilized in the inner walls of the nanochannels of the nanoporous alumina membranes following a previously optimized procedure, consisting in the functionalization of the alumina with amino groups through a silanization protocol, followed by the immobilization of the antibody through the peptide bond, using the EDC/NHS chemistry (see Fig. S1 at the Supplementary Material) [41].

Briefly, nanoporous membranes were immersed in ultrapure water and boiled for 1 h. This boiling step is done both for cleaning them and activate the hydroxyl groups present in the surface, what favours the latter silanization process. [42]. Then, the membranes were dried under a nitrogen flow and then plunged into a 5% APTES solution in acetone for 1 h. The solution was withdrawn, and the membranes were washed three times with pure acetone. After that, they were dried at 120°C for 30 min. After this process, the silanized membranes could be stored for weeks without losing their activity.

For the optimization of the immobilization of anti-Tau antibodies in the inner wall of the nanochannels, 30  $\mu$ L of a solution of 5 mM EDC/sulfo-NHS in MES pH 5, containing different concentrations of the anti-Tau antibody (0.5, 1, 10 and 50  $\mu$ g/mL) were placed on the top side of the membrane and left at room temperature for incubation for 2 h. Control assays were performed in Tris-HCl 10 mM pH 7.00 without antibody being added. After this incubation, membranes were placed on top of a rack and gently washed with Tris-HCl 10 mM pH 7.00 buffer (see Fig. S2 at the Supplementary Material).

#### 2.2.2. Immunoassay for Tau capturing in the nanochannels

For that purpose, 30  $\mu$ L of solutions containing increasing concentrations of Tau protein (5–100 ng/mL) were placed on the membranes and left for incubation at room temperature during 3 h. Then, membranes were put on top of a rack and thoroughly cleaned with Tris-HCl 10 mM. To achieve an enhanced variation between control samples and Tau-containing ones, pH of the final buffer solution used for cleaning and measuring was adjusted, thus trying at pH 7.00, 8.24 and 9.00. Control assays were performed using the same procedure but without the addition of Tau protein.

To evaluate the selectivity of the developed sensor, the above-described methodology was followed for 100 ng/mL solutions of  $\beta$ -amyloid, avidin and BSA solutions instead of that of Tau protein.

Long-term stability of the membranes was also evaluated by storing a set of anti-Tau antibody modified membranes at 4°C for one month and

adding a 100 ng/mL Tau solution at different time points.

### 2.2.3. Cell set-up and electrochemical measurements

The electrochemical measurements were performed fixing the nanoporous membrane on top of an ITO/PET electrode, using a methacrylate cell. First, the membrane was placed with the filtering side up on top of the conductive side of the ITO/PET electrode. The electrode was introduced between two pieces of methacrylate, one of them with a hole that delimitates the ITO/PET working electrode area and the electrochemical cell. Then, the whole system was adjusted with screws to avoid liquid leakage. Ag/AgCl and a Pt wire were used as reference and counter electrodes respectively.

For the electrochemical measurement, the electrochemical cell was filled with 400  $\mu\text{L}$  of a 10 mM solution of  $\text{K}_4[\text{Fe}(\text{CN})_6]$  red-ox indicator. Then, a pre-treatment at  $-0.55\text{ V}$  was applied for 30 s and immediately after, a differential pulse voltammetric (DPV) scan between  $+0.1\text{ V}$  and  $+1.3\text{ V}$  was done applying a step potential of 10 mV, a modulation amplitude of 50 mV and at a scan rate of 33.5 mV/s. As a result, the oxidation of  $[\text{Fe}(\text{CN})_6]^{4-}$  to  $[\text{Fe}(\text{CN})_6]^{3-}$  was observed and the correspondent peak current at approximately  $+0.6\text{ V}$  was selected as analytical signal.

Measurements were performed in triplicate, using different nanoporous alumina membranes and ITO/PET electrodes.

The whole time required for performing the analysis (from the step of adding the sample containing the antigen), including also mounting the cell, is of around 4 h (for 20 membranes: analysis of 20 samples) or 6 h (for 60 membranes: analysis of 60 samples). Using more cells simultaneously, the number of analysis could be further increased, estimating 1 h more per each 20 membranes (i.e. 8 h for analysing 100 samples).

### 2.2.4. Spike and recovery assay

Spike and recovery is fundamental for the evaluation of the performance of a biosensor in complex samples. A plasma sample from healthy patients was used for such purpose. This experiment was performed by spiking the plasma sample with different concentrations (5 and 25 ng/mL) of Tau protein ( $n = 3$  for each sample). Then, the spiked samples were evaluated in the nanochannels-based sensing system, being finally calculated the % of recovery of the analytical sample in plasma, compared with the obtained in non-spiked plasma.

## 3. Results and discussion

### 3.1. Sensing principle for Tau protein detection: optimization of the main parameters involved

In this work, commercial nanoporous alumina membranes with a nominal pore diameter of 100 nm (real average diameter of  $108 \pm 16\text{ nm}$ , Fig. S3 at the Supplementary Material) were selected as sensing platforms due to their easy functionalization, filtering capacities and low unspecific adsorption of proteins. Membranes were first characterized by scanning electron microscopy showing a regular and well dispersed morphology (Fig. 1A).

The principle of the developed biosensor is based on the nanochannels blocking by the Tau protein captured by the specific antibody. In the presence of this protein, the flow of the  $[\text{Fe}(\text{CN})_6]^{4-}$  red-ox indicator through the nanochannels is reduced, due to both steric and electrostatic impediments (Fig. 1B). This is monitored through the decrease in the voltammetric oxidation of  $[\text{Fe}(\text{CN})_6]^{4-}$  to  $[\text{Fe}(\text{CN})_6]^{3-}$  which is evaluated using the electrochemical set-up detailed at methods section, with ITO/PET working electrodes (Fig. 1C). Compared to screen-printed carbon electrodes (SPCEs), previously used together with

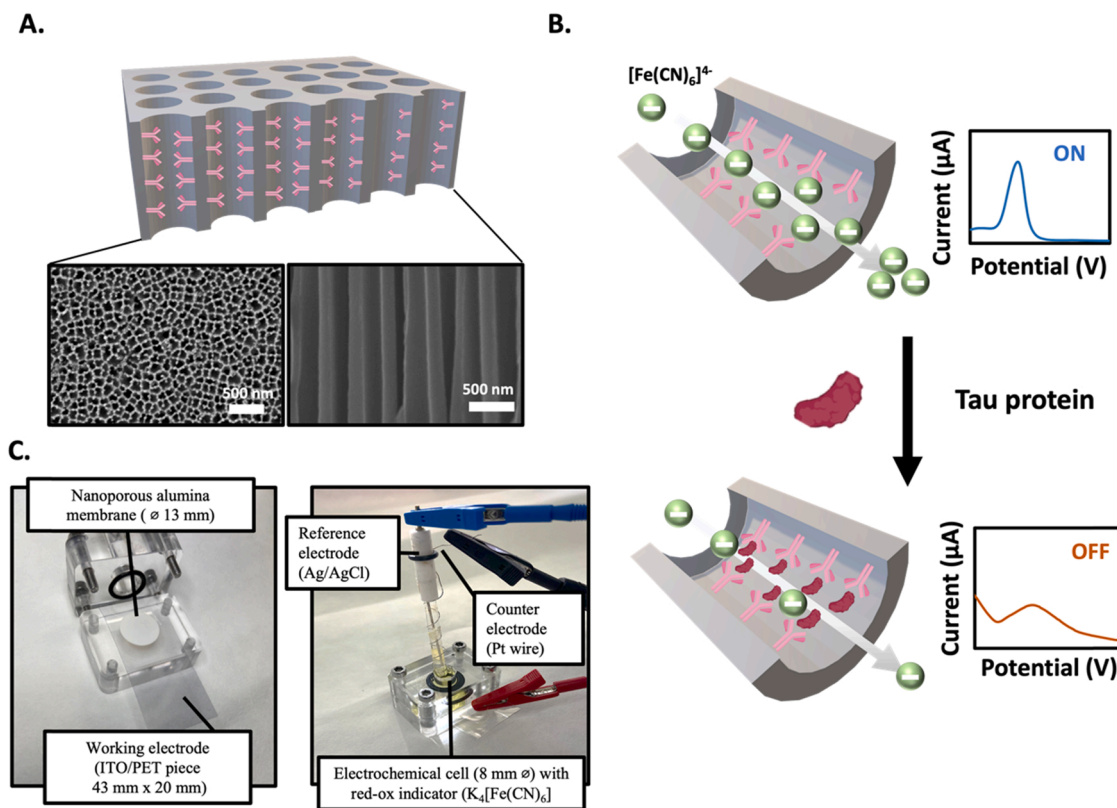


**Fig. 1.** A. Schematic representation of the pore distribution inside a nanoporous alumina membrane accompanied by SEM micrographs of both top view (left) and cross-section view (right) of the membranes. B. Schematic representation of the principle of the biosensor developed, based on the nanochannels blocking by the Tau protein captured by specific antibodies, which hinders the diffusion of  $[\text{Fe}(\text{CN})_6]^{4-}$  to the electrode, leading to a decrease in its voltammetric oxidation to  $[\text{Fe}(\text{CN})_6]^{3-}$ . C. Electrochemical set-up used in this sensing device.



nanoporous alumina membranes in nanochannels-based electrochemical biosensing systems [43], ITO/PET electrodes show important advantages for such particular application. The use of SPCEs as transducers in these systems suffered from important limitations related to: (i) the membrane covers the three electrodes (reference, counter and working), inducing not wanted blocking of the reference electrode, which leads to unstable signals; (ii) the roughness of the working carbon electrode makes difficult the assembling with the membrane, leading to irreproducibility in the signals. In contrast, our experimental set-up allows to improve the system performance, overcoming such limitations. The flatter surface of the ITO/PET electrode allows to improve the membrane/electrode assembling and consequently the system reproducibility. The use of external counter and reference electrodes avoids the electrodes blocking with the membrane, giving much more stable signals. Moreover, the flexibility and biocompatibility of the ITO/PET make it ideal for future applications in wearable electrochemical sensing [44].

### 3.1.1. Optimization of anti-Tau antibody concentration

As detailed in *methods* section, anti-Tau antibodies are immobilized in the inner walls of the nanochannels through the peptide bond, taking advantage of the carbodiimide chemistry. The minimum concentration for a total covering of the nanochannels surface was evaluated by monitoring the certain blocking effect that the antibodies by themselves exert toward the diffusion of the red-ox indicator ion through to the electrode. This blockage could be associated to both steric and electrostatic effects, as the size of an antibody is considered to be around

10–15 nm [45,46], while the size of the ions of  $[\text{Fe}(\text{CN})_6]^{4-}$  is lower than 1 nm.

Therefore, the first step performed was the immobilization of different anti-Tau antibody concentrations to study the blockage produced. The degree of blockage in the signal has been calculated as described in Eq. 1:

$$\text{Index of Antibody Current Blockage } (\Delta I_{\text{ab}}) (\%) = \left( \frac{I_0 \text{ bare membrane} - I \text{ antibody modified membrane}}{I_0 \text{ bare membrane}} \right) \times 100 \quad (1)$$

where  $I$  is the value of the peak current corresponding to the voltametric oxidation of  $[\text{Fe}(\text{CN})_6]^{4-}$  to  $[\text{Fe}(\text{CN})_6]^{3-}$ . The use of this parameter as analytical signal in this experiment has helped to normalize the results and obtain a better conclusion.

Anti-Tau antibody in concentrations ranging from 0.5 to 50  $\mu\text{g}/\text{mL}$  was evaluated. The isoelectric point (pI) of the antibody is a key parameter for the selection of the adequate buffer in which the  $[\text{Fe}(\text{CN})_6]^{4-}$  red-ox indicator solution is prepared. Previous experiments have confirmed that the pI for Tau antibodies is between 5 and 8 [47] but these values could vary depending on the species in which the antibody has been generated. In this regard, the monoclonal anti-Tau antibody used in this work has been produced in mouse, being the antibody an IgG1 kappa light chain that is associated with a pI of 6.4 [48].

In view of this information, and with the aim of taking advantage of the electrostatic hindrance for this optimization, a Tris-HCl buffer at pH

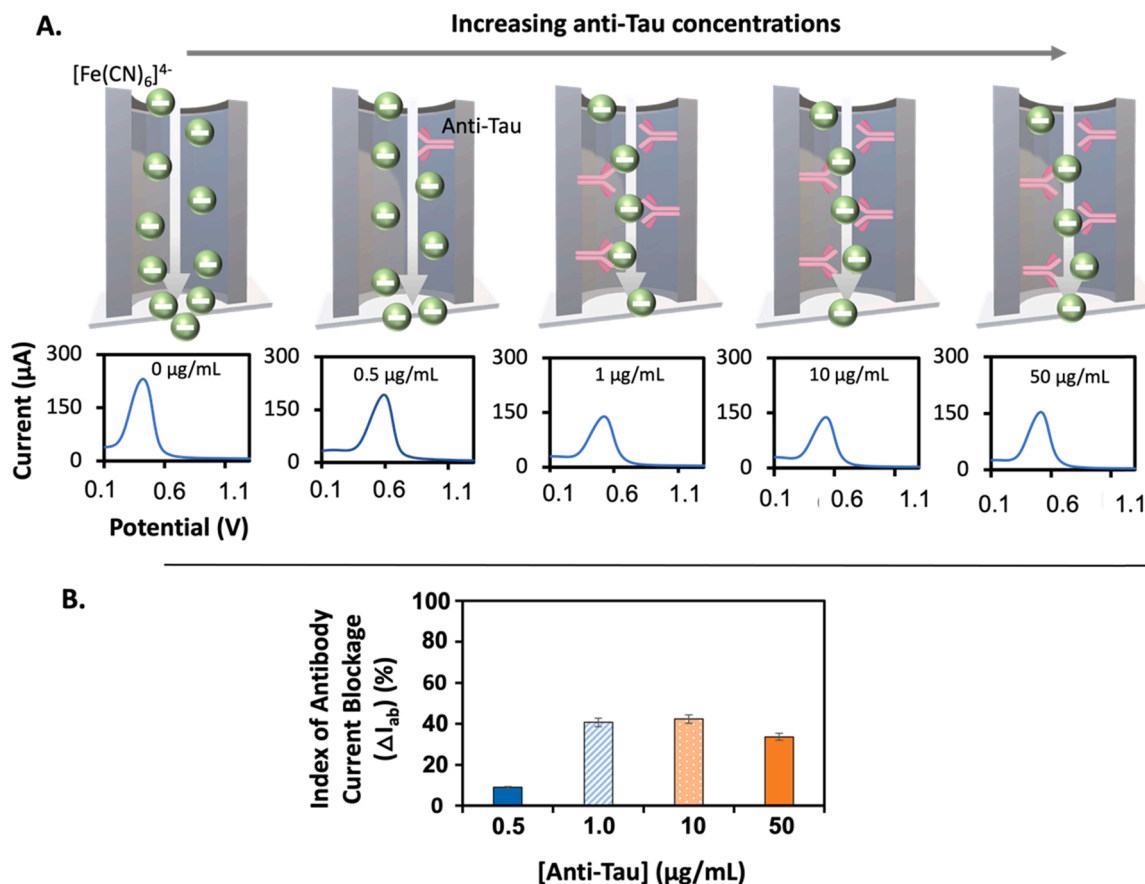


**Fig. 2.** Optimization of the concentration of anti-Tau antibody immobilized inside the nanochannels. A. (Up) Schematic illustration of the different situations with different amounts of antibody immobilized and the blockage on the diffusion of the  $[\text{Fe}(\text{CN})_6]^{4-}$  red-ox indicator ions; (Down) Differential pulse voltammograms (DPV) recorded for each concentration of anti-tau antibody concentration evaluated, using a 10 mM  $\text{K}_4[\text{Fe}(\text{CN})_6]$  solution in 10 mM Tris-HCl buffer at pH 7.00, applying a pre-concentration potential of  $-0.55$  V for 30 s and scanning from  $+0.1$  V to  $+1.3$  V at a step potential of 10 mV, a modulation amplitude of 50 mV and a scan rate of 33.5 mV/s; B. Comparative representation of the index of antibody current blockage (as defined in Eq. 1) for different anti-Tau antibody concentrations. Data are given as average  $\pm$  SD ( $n = 3$ ).

of 7.00 was selected as  $[\text{Fe}(\text{CN})_6]^{4-}$  solution media, so as to have the antibodies negatively charged which should exert a certain repulsion to the diffusion of the  $[\text{Fe}(\text{CN})_6]^{4-}$  ions. This is translated into an increased blockage of the analytical signal. By selecting this pH, a further confirmation of the pI of the antibody could be done in an easy-to-manage form.

As shown and illustrated in Fig. 2A, the increasing amount of anti-Tau antibody produces a gradual decrease in the voltammetric signal, reaching a saturation for 1  $\mu\text{g}/\text{mL}$ . This behaviour is consistent with our hypothesis, suggesting that the presence of the negatively charged antibodies is hindering the diffusion of the negatively charged red-ox indicator ions. In terms of blockage in the signal (Fig. 2B) at a concentration of 0.5  $\mu\text{g}/\text{mL}$  the index of blockage produced is of 9% while this value is notably enlarged to 41% with a slight increase in the concentration to 1  $\mu\text{g}/\text{mL}$ . This value is maintained at higher concentrations, reaching 42% for 10  $\mu\text{g}/\text{mL}$ , what indicates that the saturation of the nanochannels has been achieved and the increase in anti-Tau antibody concentration is not translated into a greater immobilization of them inside the nanochannel. The slight decrease to 34% observed for 50  $\mu\text{g}/\text{mL}$  is probably due to the saturation of the signal. These results suggest that the minimum amount of anti-Tau antibody giving the total covering of the nanochannels corresponds to a concentration of 1  $\mu\text{g}/\text{mL}$ , which was selected as optimum for the development of the immunoassay.

### 3.1.2. Immunoassay for Tau protein capturing inside the channels and optimization of the pH of the measuring buffer

After the optimization of the anti-Tau antibody concentration, immunoassays were performed for Tau protein capturing inside the nanochannels. The Tau protein molecule has a size of 69–75 nm in a non-phosphorylated form while this value slightly increases in a hyperphosphorylated form [49]. Considering the presence of anti-Tau antibodies (of around 10–15 nm) in the inner walls of the nanochannels (real average diameter of 108 nm), the capturing of the Tau protein would highly increase the steric blockage of the signal, still allowing the  $[\text{Fe}(\text{CN})_6]^{4-}$  red-ox indicator ions diffusion.

Moreover, proteins may have a positive or negative external net charge depending on the pH of the measurement solution. This charge will contribute to the signal blockage by electrostatic interactions of the nanochannel due to charge repulsion between the negative ions of the red-ox indicator and the biomolecule. For that reason, to have the maximum blockage by low concentrations of Tau protein, the optimum pH for the buffer used during measurements was evaluated.

In this experiment, a fixed concentration of Tau protein of 100 ng/mL was used. Tau protein behaves as a dipole containing two domains, a N-terminal region which has a pI of 3.8, and a C-terminal region with a pI of 10.8. Tau protein also contains a proline-rich domain with a pI of 11.4. However, posttranslational modifications of this protein could clearly modulate these dipoles [50]. For that reason, the use of a measuring pH that allows to detect a wider range of Tau protein forms is desirable for the real implementation of the biosensor developed in this work for further clinical samples analysis.

In this work, the model Tau-441, recombinant protein, the longest human brain Tau isoform (441 amino acids) was used [51]. The pI value for Tau-441 used was also theoretically calculated using ProtParam tool following previously published procedures (see Fig. S4 at the Supplementary Material) [50,52], providing a pI value of 8.24 which correlates with previously reported values [53].

Taking into consideration this information, pH values of 7.00, 8.24 and 9.00 were used for preparing the 10 mM  $\text{K}_4[\text{Fe}(\text{CN})_6]$  red-ox indicator solutions for studying the effect of the pH in the nanochannels blockage, as defined in Eq. 2:

$$\text{Index of Tau Current Blockage } (\Delta I_{\text{Tau}}) (\%) = \left( \frac{I_0 \text{ antibody modified membrane} - I_{\text{immunoassay}}}{I_0 \text{ antibody modified membrane}} \right) \times 100 \quad (2)$$

It is worthy to mention that according to the pI of the anti-Tau antibodies, they should remain negatively charged for all the pH values evaluated, being their inherent blockage effect considered as a constant background which does not affect the biosensing system.

According to the scheme represented in Fig. 3A at a pH of 8.24, equivalent to the pI of Tau-441, the protein molecules are uncharged, so not electrostatic effects should be induced by the presence of the protein inside the nanochannels. However, a noticeable blockage in the current up to a 32% index (as defined in Eq. 2) is measured, suggesting that steric impediments (size above 69–75 nm in a nanochannel of 100 nm in diameter) have an important contribution in hindering the diffusion of the red-ox indicator ions.

At a pH of 7.00, which is below the pI value of Tau-441, the net charge of the protein is positive, so this should induce an electrostatic attraction effect to the  $[\text{Fe}(\text{CN})_6]^{4-}$  ions and consequently an increase in the voltammetric signal. This is corroborated by the decrease in the blockage index (18%) obtained, as depicted in Fig. 3B, induced by the steric blockage of the protein (size above 69–75 nm in a nanochannel of 100 nm in diameter).

Interestingly, increasing the pH to 9.00, a value which is higher than the pI of the Tau-441, the protein is negatively charged, impeding the diffusion of the  $[\text{Fe}(\text{CN})_6]^{4-}$  ions. This leads to a dramatic increase in the current blockage index to 73% (Fig. 3B). According to these results, pH 9.00 is selected as the optimum value for obtaining the maximum response regarding the analytical signal. Moreover, this pH value allows to cover a wide spectrum of pIs, so that all variants of Tau protein, independently of their phosphorylation state and isoform, could be detected with a high precision. The quite basic pH does not significantly affect the chemical stability of the ferro/ferricyanide pair as it has been previously stated that this redox molecule retains its activity even at pH 14 [54]. Although a small decrease in the analytical signal is recorded at pH 9.00, compared to measurements at pH 7.00, the use of normalized blocking indexes eliminates the impact of these small variations in the result, facilitating comparison between different conditions.

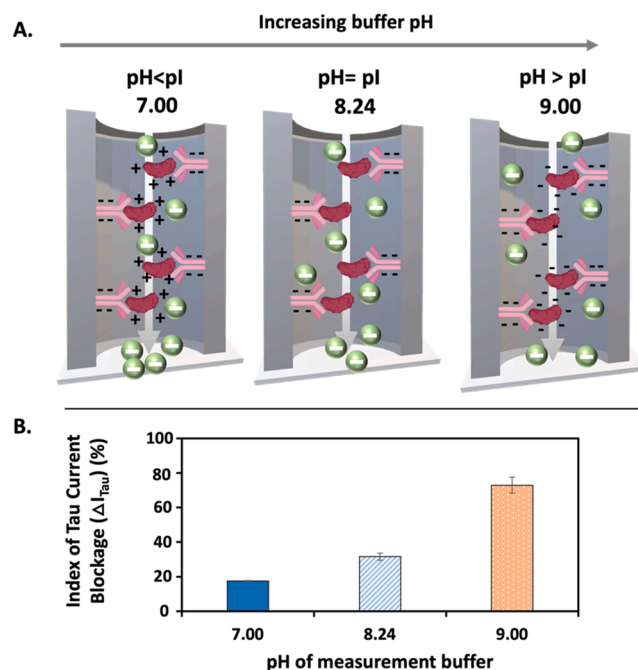


Fig. 3. Effect of the pH of the measurement buffer in the analytical system. A. Representation of the different charges of both anti-Tau antibody and Tau protein depending on the pH of the measurement solution and how it affects the diffusion of the  $[\text{Fe}(\text{CN})_6]^{4-}$  red-ox indicator ions through the channel; B. Effect of the pH on the index of Tau current blockage (as defined in Eq. 2) represented by the average  $\pm$  SD ( $n = 3$ ).

### 3.2. Electrochemical detection of Tau protein

After the optimization of the main parameters involved in the detection of Tau protein, the biosensor developed was used for the determination of different concentrations of this biomarker. The Tau protein incubation is performed at a pH 7.00, as the immunoreaction has been proved to be more efficient and stable at such pH value [55]. After this incubation step, electrochemical measurements are performed using a  $[\text{Fe}(\text{CN})_6]^{4-}$  redox solution in a buffer at pH 9.00. At this pH value, the Tau protein is negatively charged, what optimizes the blockage obtained, as proved in previous sections. Due to the short duration of the measurement, the chemical stability of the antigen-antibody interaction should not be compromised at such basic pH.

As expected, the presence of increasing concentrations of Tau protein leads to a decrease in the voltammetric peak current corresponding to the oxidation of the red-ox indicator  $[\text{Fe}(\text{CN})_6]^{4-}$  to  $[\text{Fe}(\text{CN})_6]^{3-}$  at approximately + 0.6 V (Fig. 4A), which is the analytical signal selected for the quantitative analysis. It was found a linear relationship between such analytical signal and the Tau protein concentration within the range 5–100 ng/mL (Fig. 4B) with a correlation coefficient ( $r$ ) of 0.9981, adjusted to this equation:

$$\text{Peak current } (\mu\text{A}) = -0,112 [\text{Tau}] (\text{ng/mL}) + 20,4 \quad (3)$$

The biosensing system developed has a limit of detection (LOD), calculated as three times the standard deviation of the intercepted divided by the slope) of 4.32 ng/mL and an appropriate reproducibility with a relative standard deviation (RSD) of 9%. Although there is a quite controversy in the bibliography on the expected levels of Tau protein in plasma of both healthy and AD patients, in the particular case of the immunoassays, the literature suggests that the found Tau levels strongly depend on the specific anti-Tau antibody used. Some reported immunoassays [56] have shown that the Tau protein is present in AD patients plasma at levels of around 60 ng/mL, which are above the detection limit of our immunoassay. This suggests that our methodology is potentially suitable for the determination of Tau protein in the real

scenario. Anyway, a careful evaluation of different antibodies may be necessary for the real implementation of this technology.

Our methodology is faster and cheaper than ELISA kits, since neither competitive assays nor the use of labels are required. Moreover, our approach benefits of the low cost and portability of the potentiostats used for the electrochemical detection [57], which is ideal for a point-of-care detection of Alzheimer's disease.

### 3.3. System selectivity and long-term stability

Selectivity of the biosensor was evaluated against common analytes present in human samples, as  $\beta$ -amyloid, another common AD biomarker, avidin and BSA (Fig. 4C). It has been observed that the blockage produced in the presence of the abovementioned analytes is lower than 20%, what supposes an irrelevant value compared to the one obtained by Tau protein (61%), proving the selectivity of the method.

Additionally, long-term stability of the developed sensor has been preliminary addressed by storing a set of anti-Tau antibody modified membranes at 4°C for one month and evaluating the response for a 100 ng/mL Tau solution at different time points. As shown at the [Supplementary Material](#) (Fig. S5), the response of the system was stable and reproducible for at least 21 days, noticing a decrease after 30 days of storage. Although this aspect requires further optimization, the preliminary stability observed suggests that the antibody-modified membranes could be stored ready for the sample analysis, which would only involve the steps of the sample incubation on the membrane, washing and measuring buffer adding.

### 3.4. System performance in real samples

Tau protein is well-known to be a suitable biomarker for the detection of AD and other neurodegenerative disorders, as high levels of this protein are present in cerebrospinal fluid (CSF) and plasma samples of patients with different pathologies [58].

The main obstacle to overcome for measuring Tau protein is the

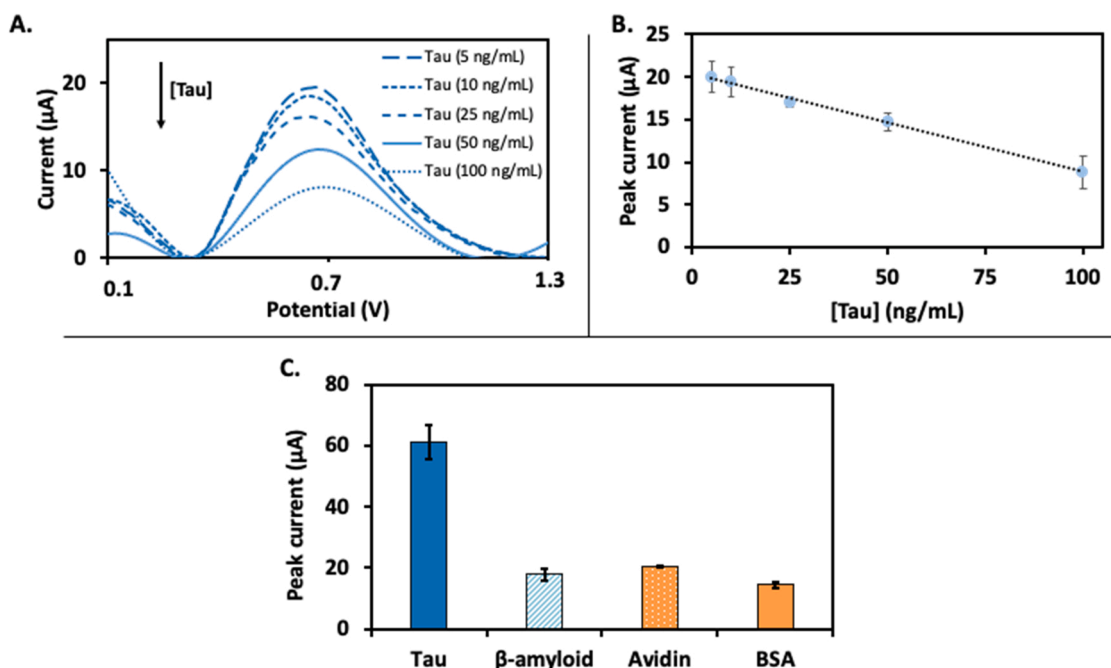


**Fig. 4.** Tau protein detection through antibody recognition inside the nanochannels. A. Differential pulse voltammograms (DPV) recorded for different Tau concentrations, using as red-ox indicator 10 mM  $\text{K}_4[\text{Fe}(\text{CN})_6]$  in buffer at pH 9.00. Anti-Tau antibody concentration: 1  $\mu\text{g/mL}$ . Pre-concentration potential: - 0.55 V for 30 s; scan range: + 0.1 V to + 1.3 V; step potential: 10 mV; modulation amplitude: 50 mV; scan rate: 33.5 mV/s. B. Calibration curve obtained by representing the analytical signal (value of the peak current at +0.6 V)  $\pm$  SD ( $n = 3$ ), obtained for the different concentrations of Tau protein assayed. C. Selectivity assay using a concentration of 100 ng/mL of Tau protein,  $\beta$ -amyloid, avidin or BSA.

complexity of real samples as possible interferences could occur [59,60]. For addressing this drawback, nanoporous alumina membranes are suitable platforms, as it is well known that this material has a low protein adsorption rate, acting as efficient filter in complex matrixes [41, 43].

For evaluating this issue, a spike and recovery procedure was performed in plasma samples adding different Tau concentrations spiked in commercial plasma from healthy patients. The plasma samples are then added, in substitution of Tau protein dissolved in buffer solution, in the incubation step. After that a 10 mM  $K_4[Fe(CN)_6]$  in buffer at pH 9.00 red-ox solution was used for measuring the decrease in current produced by Tau protein, hence assuring that both antibody and antigen are negatively charged and maximizing electrostatic blockage. The spiked assay showed an excellent recovery rate at levels around 95% (Table 1). These results clarify that the performance of the biosensor is not altered by the presence of interfering compounds, thus opening the way to its use for the detection of AD.

#### 4. Conclusions

Tau protein, a well-known AD biomarker, has been detected in this work using a novel nanochannel-based platform. The mechanism of this biosensor is based on the voltammetric determination of the blockage that Tau protein produces to the diffusion of the red-ox indicator  $[Fe(CN)_6]^{4-}$ . It was already known that both steric and electrostatic interactions affect the nanochannel blockage obtained, but the contribution of both components of the antigen-antibody pair used in nanochannels-based immunosensors was less research. Our findings confirm that the control of the charge of both components by changing the buffer measurement pH is required to maximize the blockage upon the immunocomplex formation. Considering antibody pI is particularly crucial not only for the overall blockage obtained but also to properly select the antibody concentration required in the immunoassay, reducing the concentration needed and thus the immunosensor cost.

In the main, our method let detecting Tau protein with a good performance in human real samples and with a LOD of 4.3 ng/mL, which is in correlation with clinical values and with those detected by gold-standard techniques. It is worthy to mention that our methodology does not require neither labels nor competitive assays. As far as we know, this is the first time that Tau protein is detected through a nanochannel-based electrochemical sensor. This label-free sensor allows to detect Tau protein in a cheaper and faster approach, getting closer to clinical practice requirements, opening the way to a point-of-care diagnosis of AD.

Overall, our findings related the effect of both the anti-Tau antibody and the anti-Tau/Tau immunocomplex charges on the nanochannels-based biosensing system may be extended to any other antibody/antigen pair, just paying attention to the isoelectric point of such proteins, targeting applications in medicine, food analysis and environmental control among others.

#### CRedit authorship contribution statement

**Celia Toyos-Rodríguez:** Conceptualization, Experimental work, Formal analysis, Writing – original draft. **Francisco Javier García-Alonso:** Conceptualization, Supervision, Funding acquisition. **Alfredo de la Escosura-Muñiz:** Conceptualization, Data curation, Supervision, Writing – review & editing, Funding acquisition. All authors have given approval to the final version of the manuscript.

#### Declaration of Competing Interest

The authors declare that they have no known competing financial interests or personal relationships that could have appeared to influence the work reported in this paper.

**Table 1**

Spike and recovery assay data in plasma for Tau concentrations of 5 and 25 ng/mL, corresponding to the lower and medium values of the calibration curve.

Sample	Spiked Tau (ng/mL)	Current in PBS ( $\mu$ A)	Current in real sample ( $\mu$ A)	Recovery (%)
Plasma from healthy subjects	5.00	18.9	18.2	96.3
	25.0	17.0	16.3	95.6

#### Data Availability

Data will be made available on request.

#### Acknowledgements

This work has been supported by the MCI-21-PID2020-115204RB-I00 project from the Spanish Ministry of Science and Innovation (MICINN), the CTQ2017-86994-R project from the Spanish Ministry of Economy and Competitiveness (MINECO) and the SV-PA-21-AYUD/2021/51323 project from the Asturias Regional Government. C. Toyos-Rodríguez thanks the MICINN for the award of a FPI Grant (PRE2018-084953). A. de la Escosura-Muñiz also acknowledges the MICINN for the “Ramón y Cajal” Research Fellow (RyC-2016-20299).

#### Appendix A. Supporting information

Supplementary data associated with this article can be found in the online version at [doi:10.1016/j.snb.2023.133394](https://doi.org/10.1016/j.snb.2023.133394).

#### References

- [1] A.D. Gitler, P. Dhillon, J. Shorter, Neurodegenerative disease: models, mechanisms, and a new hope, *Dis. Model. Mech.* 10 (2017) 499–502, <https://doi.org/10.1242/dmm.030205>.
- [2] G. Deuschl, E. Beghi, F. Fazekas, T. Varga, K.A. Christoforidi, E. Sipido, C. L. Bassetti, T. Vos, V.L. Feigin, The burden of neurological diseases in Europe: an analysis for the global burden of disease study 2017, *Lancet Public Health* 5 (2020) e551–e567, [https://doi.org/10.1016/S2468-2667\(20\)30190-0](https://doi.org/10.1016/S2468-2667(20)30190-0).
- [3] H. Checkoway, J.I. Lundin, S.N. Kelada, Neurodegenerative diseases, *IARC Sci. Publ.* 163 (2011) 407–419.
- [4] C.P. Ferri, M. Prince, C. Brayne, H. Brodaty, L. Fratiglioni, M. Ganguli, K. Hall, K. Hasegawa, H. Hendrie, Y. Huang, et al., Global prevalence of dementia: a delphi consensus study 366 (2005) 6.
- [5] Alzheimer Association 2018 Alzheimer's Disease Facts and Figures; 2019; pp. 1–88.
- [6] E. Joe, J.M. Ringman, Cognitive symptoms of Alzheimer's disease: clinical management and prevention, *BMJ* (2019) l6217, <https://doi.org/10.1136/bmj.l6217>.
- [7] A.A. Tahami Monfared, M.J. Byrnes, L.A. White, Q. Zhang, The humanistic and economic burden of Alzheimer's disease, *Neurol. Ther.* 11 (2022) 525–551, <https://doi.org/10.1007/s40120-022-00335-x>.
- [8] H. Shah, E. Albanese, C. Duggan, I. Rudan, K.M. Langa, M.C. Carrillo, K.Y. Chan, Y. Joannette, M. Prince, M. Rossor, et al., Research priorities to reduce the global burden of dementia by 2025, *Lancet Neurol.* 15 (2016) 1285–1294, [https://doi.org/10.1016/S1474-4422\(16\)30235-6](https://doi.org/10.1016/S1474-4422(16)30235-6).
- [9] Y.-L. Gao, N. Wang, F.-R. Sun, X.-P. Cao, W. Zhang, J.-T. Yu, Tau in neurodegenerative disease, 175–175, *Ann. Transl. Med.* 6 (2018), <https://doi.org/10.21037/atm.2018.04.23>.
- [10] Hutton, M.; Lendon, C.L.; Rizzu, P.; Baker, M.; Froelich, S.; Houlden, H.; Pickering-Brown, S.; Chakraverty, S.; Isaacs, A.; Grover, A.; et al. Association of Missense and 5'-Splice-Site Mutations in Tau with the Inherited Dementia FTDP-17. 1998, 393, 4.
- [11] R. Medeiros, D. Baglietto-Vargas, F.M. LaFerla, The role of tau in Alzheimer's disease and related disorders: role of tau in AD and related disorders, *CNS Neurosci. Ther.* 17 (2011) 514–524, <https://doi.org/10.1111/j.1755-5949.2010.00177.x>.
- [12] K. Iqbal, F. Liu, C.-X. Gong, I. Grundke-Iqbal, Tau in Alzheimer disease and related tauopathies, *Curr. Alzheimer Res.* 7 (2010) 656–664, <https://doi.org/10.2174/156720510793611592>.
- [13] M.D. Weingarten, A.H. Lockwood, S.Y. Hwo, M.W. Kirschner, A protein factor essential for microtubule assembly, *Proc. Natl. Acad. Sci.* 72 (1975) 1858–1862, <https://doi.org/10.1073/pnas.72.5.1858>.
- [14] Iqbal, K.; del C. Alonso, A.; Gong, C.-X.; Khatoon, S.; Pei, J.-J.; Wang, J.Z.; Grundke-Iqbal, I. Mechanisms of Neurofibrillary Degeneration and the Formation of Neurofibrillary Tangles. In *Ageing and Dementia*; Jellinger, K., Fazekas, F.,



- Windisch, M., Eds.; Journal of Neural Transmission. Supplementa; Springer Vienna: Vienna, 1998; Vol. 53, pp. 169–180 ISBN 978-3-211-83114-4.
- [15] K. Iqbal, T. Zaidi, G.Y. Wen, I. Grundke-Iqbal, P.A. Merz, S.S. Shaikh, H. M. Wisniewski, I. Alafuzoff, B. Winblad, Defective brain microtubule assembly in Alzheimer's Disease, *Lancet* 2 (1986) 421–426.
- [16] Y. Zhou, J. Shi, D. Chu, W. Hu, Z. Guan, C.-X. Gong, K. Iqbal, F. Liu, Relevance of phosphorylation and truncation of tau to the etiopathogenesis of Alzheimer's Disease, *Front. Aging Neurosci.* 10 (2018) 27, <https://doi.org/10.3389/fnagi.2018.00027>.
- [17] H. Braak, E. Braak, I. Grundke-Iqbal, K. Iqbal, Occurrence of neurofibrillary threads in the senile human brain and in Alzheimer's disease: a third location of paired helical filaments outside of neurofibrillary tangles and neuritic plaques, *Neurosci. Lett.* 65 (1986) 351–355, [https://doi.org/10.1016/0304-3940\(86\)90288-0](https://doi.org/10.1016/0304-3940(86)90288-0).
- [18] R.J. O'Brien, P.C. Wong, Amyloid precursor protein processing and Alzheimer's disease, *Annu. Rev. Neurosci.* 34 (2011) 185–204, <https://doi.org/10.1146/annurev-neuro-061010-113613>.
- [19] J.A. Hardy, G.A. Giggins, Alzheimer's disease: the amyloid cascade hypothesis, *Science* 256 (1992) 184–185, <https://doi.org/10.1126/science.1566067>.
- [20] R. Ismail, P. Parbo, L.S. Madsen, A.K. Hansen, K.V. Hansen, J.L. Schaldemose, P. L. Kjeldsen, M.G. Stokholm, H. Gottrup, S.F. Eskildsen, et al., The relationships between neuroinflammation, beta-amyloid and tau deposition in Alzheimer's disease: a longitudinal PET study, *J. Neuroinflamm.* 17 (2020) 151, <https://doi.org/10.1186/s12974-020-01820-6>.
- [21] M.J. Pontecorvo, M.D. Devous, M. Navitsky, M. Lu, S. Salloway, F.W. Schaefer, D. Jennings, A.K. Arora, A. McGeehan, N.C. Lim, et al., Relationships between flortaucipir PET Tau binding and amyloid burden, clinical diagnosis, age and cognition, *Brain* (2017) aww334, <https://doi.org/10.1093/brain/aww334>.
- [22] D.L. Sparks, R.J. Kryscio, M.N. Sabbagh, C. Ziolkowski, Y. Lin, C. Liebsack, S. Johnson-Traver, Tau is reduced in AD plasma and validation of employed ELISA methods, *Am. J. Neurodegener. Dis.* 1 (2012) 99–106.
- [23] Y. Liu, H. Qing, Y. Deng, Biomarkers in Alzheimer's disease analysis by mass spectrometry-based proteomics, *Int. J. Mol. Sci.* 15 (2014) 7865–7882, <https://doi.org/10.3390/ijms15057865>.
- [24] A. Hye, J. Riddoch-Contreras, A.L. Baird, N.J. Ashton, C. Bazenet, R. Leung, E. Westman, A. Simmons, R. Dobson, M. Sattler, et al., Plasma proteins predict conversion to dementia from prodromal disease, *e2, Alzheimers Dement* 10 (2014) 799–807, <https://doi.org/10.1016/j.jalz.2014.05.1749>.
- [25] M. Ameri, Z. Shabaninejad, A. Movahedpour, A. Sahebkar, S. Mohammadi, S. Hosseindoost, M.S. Ebrahimi, A. Savardashtaki, M. Karimpour, H. Mirzaei, Biosensors for detection of tau protein as an alzheimer's disease marker, *Int. J. Biol. Macromol.* 162 (2020) 1100–1108, <https://doi.org/10.1016/j.ijbiomac.2020.06.239>.
- [26] C. Toyos-Rodríguez, F.J. García-Alonso, A. de la Escosura-Muñiz, Electrochemical biosensors based on nanomaterials for early detection of Alzheimer's disease, *Sensors* 20 (2020) 4748, <https://doi.org/10.3390/s20174748>.
- [27] A. de la Escosura-Muñiz, A. Merkoçi, Nanochannels preparation and application in biosensing, *ACS Nano* 6 (2012) 7556–7583, <https://doi.org/10.1021/nn301368z>.
- [28] A. de la Escosura-Muñiz, A. Merkoçi, Nanochannels for electrical biosensing, *TrAC Trends Anal. Chem.* 79 (2016) 134–150, <https://doi.org/10.1016/j.trac.2015.12.003>.
- [29] W.H. Coulter, High speed automatic blood cell counter and cell size analyzer, *Proc. Natl. Electron Conf.* 12 (1956) 1034–1040.
- [30] S.M. Bezrukov, I. Vodyanov, V.A. Parsegian, Counting polymers moving through a single ion channel, *Nature* 370 (1994) 279–281.
- [31] H. Bayley, P.S. Cremer, Stochastic sensors inspired by biology, *Nature* 413 (2001) 226–230, <https://doi.org/10.1038/35093038>.
- [32] H. Bayley, Membrane-protein structure: piercing insights, *Nature* 459 (2009) 651–652, <https://doi.org/10.1038/459651a>.
- [33] Z.S. Siwy, S. Howorka, Engineered voltage-responsive nanopores, *Chem. Soc. Rev.* 39 (2010) 1115–1132, <https://doi.org/10.1039/B909105J>.
- [34] A. Santos, T. Kumeria, D. Losic, Nanoporous anodic aluminum oxide for chemical sensing and biosensors, *TrAC Trends Anal. Chem.* 44 (2013) 25–38, <https://doi.org/10.1016/j.trac.2012.11.007>.
- [35] A. de la Escosura-Muñiz, A. Merkoçi, Label-free voltammetric immunosensor using a nanoporous membrane based platform, *Electrochem. Commun.* 12 (2010) 859–863, <https://doi.org/10.1016/j.elecom.2010.04.007>.
- [36] A. de la Escosura-Muñiz, A. Merkoçi, Nanoparticle based enhancement of electrochemical DNA hybridization signal using nanoporous electrodes, *Chem. Commun.* 46 (2010) 9007–9009, <https://doi.org/10.1039/c0cc02683b>.
- [37] A. Iglesias-Mayor, O. Amor-Gutiérrez, C. Toyos-Rodríguez, A. Bassegoda, T. Tzanov, A. de la Escosura-Muñiz, Electrical monitoring of infection biomarkers in chronic wounds using nanochannels, *Biosens. Bioelectron.* 209 (2022), 114243, <https://doi.org/10.1016/j.bios.2022.114243>.
- [38] A. de la Escosura-Muñiz, M. Espinoza-Castaneda, A. Chamorro-García, Rodríguez-Hernández, J. Carlos, C. de Torres, A. Merkoçi, In situ monitoring of PTHLH secretion in neuroblastoma cells cultured onto nanoporous membranes, *Biosens. Bioelectron.* 107 (2018) 62–68, <https://doi.org/10.1016/j.bios.2018.01.064>.
- [39] A. de la Escosura-Muñiz, K. Ivanova, T. Tzanov, Electrical evaluation of bacterial virulence factors using nanopores, *ACS Appl. Mater. Interfaces* 11 (2019) 13140–13146, <https://doi.org/10.1021/acsami.9b02382>.
- [40] L. Zhou, H. Ding, F. Yan, W. Guo, B. Su, Electrochemical detection of Alzheimer's disease related substances in biofluids by silica nanochannel membrane modified glassy carbon electrodes, *Analyst* 143 (2018) 4756–4763, <https://doi.org/10.1039/C8AN01457D>.
- [41] A. de la Escosura-Muñiz, A. Merkoçi, A nanochannel/nanoparticle-based filtering and sensing platform for direct detection of a cancer biomarker in blood, *Small* 7 (2011) 675–682, <https://doi.org/10.1002/smll.201002349>.
- [42] W. Ye, Y. Xu, L. Zheng, Y. Zhang, M. Yang, P. Sun, A nanoporous alumina membrane based electrochemical biosensor for histamine determination with biofunctionalized magnetic nanoparticles concentration and signal amplification, *Sensors* 16 (2016) 1767, <https://doi.org/10.3390/s16101767>.
- [43] A. de la Escosura-Muñiz, W. Chunglok, W. Surareungchai, A. Merkoçi, Nanochannels for diagnostic of thrombin-related diseases in human blood, *Biosens. Bioelectron.* 40 (2013) 24–31, <https://doi.org/10.1016/j.bios.2012.05.021>.
- [44] Y. Wang, B. Sun, H. Wei, Y. Li, F. Hu, X. Du, J. Chen, Investigating immunosensor for determination of depression marker-Apo-A4 based on patterning AuNPs and N-Gr nanomaterials onto ITO-PET flexible electrodes with amplifying signal, *Anal. Chim. Acta* 1224 (2022), 340217, <https://doi.org/10.1016/j.aca.2022.340217>.
- [45] Y.H. Tan, M. Liu, B. Nolting, J.G. Go, J. Gervay-Hague, G. Liu, A Nanoengineering Approach for Investigation and Regulation of Protein Immobilization, *ACS Nano* 2 (2008) 2374–2384, <https://doi.org/10.1021/nn800508f>.
- [46] Y. Dong, C. Shanon, Heterogeneous immunosensing using antigen and antibody monolayers on gold surfaces with electrochemical and scanning probe detection, *Anal. Chem.* 72 (2000) 2371–2376, <https://doi.org/10.1021/ac991450g>.
- [47] E.E. Congdon, J.E. Chukwu, D.B. Shamir, J. Deng, D. Ujla, H.B.R. Sait, T. A. Neubert, X.-P. Kong, E.M. Sigurdsson, Tau antibody chimerization alters its charge and binding, thereby reducing its cellular uptake and efficacy, *EBioMedicine* 42 (2019) 157–173, <https://doi.org/10.1016/j.ebiom.2019.03.033>.
- [48] Å. Danielsson, A. Ljunglöf, H. Lindblom, One-step purification of monoclonal IgG antibodies from mouse ascites, *J. Immunol. Methods* 115 (1988) 79–88, [https://doi.org/10.1016/0022-1759\(88\)90312-2](https://doi.org/10.1016/0022-1759(88)90312-2).
- [49] G.C. Ruben, K. Iqbal, I. Grundke-Iqbal, H.M. Wisniewski, T.L. Ciardelli, J. E. Johnson, The microtubule-associated protein tau forms a triple-stranded left-handed helical polymer, *J. Biol. Chem.* 266 (1991) 22019–22027, [https://doi.org/10.1016/S0021-9258\(18\)54739-6](https://doi.org/10.1016/S0021-9258(18)54739-6).
- [50] M. Kolarova, F. García-Sierra, A. Bartos, J. Rícný, D. Ripova, Structure and pathology of tau protein in Alzheimer disease, *Int. J. Alzheimers Dis.* 2012 (2012) 1–13, <https://doi.org/10.1155/2012/731526>.
- [51] P. Weydt, L. Dupuis, Å. Petersen, *Thermoregulatory Disorders in Huntington Disease. Handbook of Clinical Neurology* 157, Elsevier, 2018, pp. 761–775. ISBN 978-0-444-64074-1.
- [52] L. Ferrari, S.G.D. Rüdiger, Recombinant production and purification of the human protein tau, *Protein Eng. Des. Sel.* 31 (2018) 447–455, <https://doi.org/10.1093/protein/gzz010>.
- [53] R. Brandt, N.I. Trushina, L. Bakota, Much more than a cytoskeletal protein: physiological and pathological functions of the non-microtubule binding region of Tau, *Front. Neurol.* 11 (2020), 590059, <https://doi.org/10.3389/fneur.2020.590059>.
- [54] J. Luo, A. Sam, B. Hu, C. DeBruler, X. Wei, W. Wang, T.L. Liu, Unraveling PH dependent cycling stability of ferricyanide/ferrocyanide in redox flow batteries, *Nano Energy* 42 (2017) 215–221, <https://doi.org/10.1016/j.nanoen.2017.10.057>.
- [55] S.C. Devanaboyina, S.M. Lynch, R.J. Ober, S. Ram, D. Kim, A. Puig-Canto, S. Breen, S. Kasturirangan, S. Fowler, L. Peng, et al., The effect of PH dependence of antibody-antigen interactions on subcellular trafficking dynamics, *mAbs* 5 (2013) 851–859, <https://doi.org/10.4161/mabs.26389>.
- [56] T.T. Vu Nu, N.H.T. Tran, E. Nam, T.T. Nguyen, W.J. Yoon, S. Cho, J. Kim, K.-A. Chang, H. Ju, Blood-based immunoassay of tau proteins for early diagnosis of Alzheimer's disease using surface plasmon resonance fiber sensors, *RSC Adv.* 8 (2018) 7855–7862, <https://doi.org/10.1039/C7RA11637C>.
- [57] O. Parlak, Portable and wearable real-time stress monitoring: a critical review, *Sens. Actuators Rep.* 3 (2021), 100036, <https://doi.org/10.1016/j.snr.2021.100036>.
- [58] S. Schraen-Maschke, N. Sergeant, C.-M. Dhaenens, S. Bombois, V. Deramecourt, M.-L. Cailliet-Boudin, F. Pasquier, C.-A. Mauge, B. Sablonnière, E. Vanmechelen, et al., Tau as a biomarker of neurodegenerative diseases, *Biomark. Med.* 2 (2008) 363–384, <https://doi.org/10.2217/17520363.2.4.363>.
- [59] M.L. Chiu, W. Lawi, S.T. Snyder, P.K. Wong, J.C. Liao, V. Gau, Matrix effects—a challenge toward automation of molecular analysis, *J. Assoc. Lab. Autom.* 15 (2010) 233–242, <https://doi.org/10.1016/j.jala.2010.02.001>.
- [60] J.-F. Masson, Consideration of sample matrix effects and “Biological” noise in optimizing the limit of detection of biosensors, *ACS Sens* 5 (2020) 3290–3292, <https://doi.org/10.1021/acssensors.0c02254>.

**Celia Toyos-Rodríguez** received her BSc in Biotechnology in 2017 at the University of Oviedo (Spain). She is now a PhD Student in the NanoBioAnalysis group, Department of Physical and Analytical Chemistry, University of Oviedo under a Pre-doctoral Researcher (FPI) grant. Her research interests focus on the development of electrochemical sensors based on nanomaterials for clinical diagnosis of Alzheimer's Disease and infection.

**Francisco Javier García-Alonso** received his PhD in Chemical Sciences in 1982 from the University of Valladolid (Spain). He is Full Professor in Inorganic Chemistry at the University of Oviedo (Spain) since 2009. His research interests focus on the synthesis of novel inorganic nanomaterials for applications in biosensing.

**Alfredo de la Escosura-Muñiz** holds a PhD in Chemistry (2006) from the University of Oviedo (Spain). As of June 2018 he holds a “Ramon y Cajal” Research Fellowship in the Nanobioanalysis Group, Department of Physical and Analytical Chemistry, University of Oviedo, where he is also a Lecturer in Chemistry. His research interests focus on the

development of biosensing systems based on nanoparticles and nanochannels for point-of-care diagnostic applications.



## Electrical monitoring of infection biomarkers in chronic wounds using nanochannels

Alba Iglesias-Mayor<sup>a</sup>, Olaya Amor-Gutiérrez<sup>a</sup>, Celia Toyos-Rodríguez<sup>a</sup>, Arnau Bassegoda<sup>b</sup>, Tzanko Tzanov<sup>b</sup>, Alfredo de la Escosura-Muñiz<sup>a,c,\*</sup>

<sup>a</sup> NanoBioAnalysis Group - Department of Physical and Analytical Chemistry, University of Oviedo, Julián Clavería 8, 33006, Oviedo, Spain

<sup>b</sup> Grup de Biotecnologia Molecular i Industrial, Department of Chemical Engineering, Universitat Politècnica de Catalunya, Terrassa, Spain

<sup>c</sup> Biotechnology Institute of Asturias, University of Oviedo, Santiago Gascon Building, 33006, Oviedo, Spain

### ARTICLE INFO

#### Keywords:

Nanopores  
Nanochannels  
Wound infection  
Lysozyme  
Peptidoglycan  
Electrochemical detection

### ABSTRACT

Chronic wounds represent an important healthcare challenge in developed countries, being wound infection a serious complication with significant impact on patients' life conditions. However, there is a lack of methods allowing an early diagnosis of infection and a right decision making for a correct treatment. In this context, we propose a novel methodology for the electrical monitoring of infection biomarkers in chronic wound exudates, using nanoporous alumina membranes. Lysozyme, an enzyme produced by the human immune system indicating wound infection, is selected as a model compound to prove the concept. Peptidoglycan, a component of the bacterial layer and the native substrate of lysozyme, is immobilized on the inner walls of the nanochannels, blocking them both sterically and electrostatically. The steric blocking is dependent on the pore size (20–100 nm) and the peptidoglycan concentration, whereas the electrostatic blocking depends on the pH. The proposed analytical method is based on the electrical monitoring of the steric/electrostatic nanochannels unblocking upon the specific degradation of peptidoglycan by lysozyme, allowing to detect the infection biomarker at 280 ng/mL levels, which are below those expected in wounds. The low protein adsorption rate and thus outstanding filtering properties of the nanoporous alumina membranes allowed us to discriminate wound exudates from patients with both sterile and infected ulcers without any sample pre-treatment usually indispensable in most diagnostic devices for analysis of physiological fluids.

Although size and charge effects in nanochannels have been previously approached for biosensing purposes, as far as we know, the use of nanoporous membranes for monitoring enzymatic cleavage processes, leading to analytical systems for the specific detection of the enzymes has not been deeply explored so far. Compared with previously reported methods, our methodology presents the advantages of no need of neither bioreceptors (antibodies or aptamers) nor competitive assays, low matrix effects and quantitative and rapid analysis at the point-of-care, being also of potential application for the determination of other protease biomarkers.

### 1. Introduction

Healing of chronic wounds, affecting 1 to 2 percent of the population in developed countries, represents a major healthcare challenge with important financial burden (Clinton and Carter, 2015) (Järbrink et al., 2016). Chronic wounds are usually heavily colonized with bacteria, while providing bacteria-free environment is a prerequisite for wound healing. An early detection and treatment of infection is one of the most important factors in wound management. Although classical signs of infection - like redness, heat, swelling, exudate production and pain

(Gardner et al., 2001) - are still the main criteria in the clinical examination of the wound status, they are ambiguous and depend on the experience of the healthcare practitioner (Siddiqui and Bernstein, 2010). More precise, but still questioned are the (semi)quantitative microbiological investigations, including the gold-standard biopsy method, a time-consuming technique which is not often carried out in ambulatory clinical practice to avoid patient's morbidity, mostly local bleeding and infection spread (Gardner et al., 2006). The correct microbiological identification of the microorganisms infecting a wound in order to prescribe the suitable antibiotic treatment may take up to 3

\* Corresponding author. NanoBioAnalysis Group - Department of Physical and Analytical Chemistry, University of Oviedo, Julián Clavería 8, 33006, Oviedo, Spain.  
E-mail address: [alfredo.escosura@uniovi.es](mailto:alfredo.escosura@uniovi.es) (A. Escosura-Muñiz).

<https://doi.org/10.1016/j.bios.2022.114243>

Received 8 March 2022; Received in revised form 30 March 2022; Accepted 1 April 2022

Available online 5 April 2022

0956-5663/© 2022 The Authors. Published by Elsevier B.V. This is an open access article under the CC BY license (<http://creativecommons.org/licenses/by/4.0/>).

days to come from the Microbiology lab in many hospitals. Until then, the patient is subjected to a broad-spectrum unspecific antimicrobial therapy with important side effects on human microbiome. For this reason, alternative tools for the rapid detection of infections in chronic wounds are strongly required.

Although physical parameters such as temperature (Matzeu et al., 2011), pH (Trupp et al., 2010) or odour (Persaud, 2005) have been studied as qualitative indicators of wound infection (Cutting and White, 2005) (Caliendo et al., 2013), main efforts have been dedicated in the last decades to the identification of biomolecules which presence in wound exudates evidences a bacterial infection (Yager et al., 2007). Enzymes with increased activity in infected wound fluids are considered as reliable infection biomarkers (Schiffer et al., 2015). Lysozyme (Hasmann et al., 2011) is of special relevance, since it is produced by the human immune system as the main component of the host innate defence mechanism (Osserman et al., 1973). Lysozyme is a glycosidase enzyme (Callewaert and Michiels, 2010) capable of hydrolysing the  $\beta$ -(1,4)-glycosidic bonds between N-acetylmuramic acid and N-acetylglucosamine residues of its native substrate, the peptidoglycan (Salton, 1957), a polymer which constitutes the core component of almost all bacterial cell walls (Rogers et al., 2013). This polymer is composed of linear glycan strands (alternating N-acetylglucosamine and N-acetylmuramic acid residues linked by  $\beta$ -(1,4) bonds) cross-linked by short peptides. Gram positive bacteria have a thick peptidoglycan layer and no outer lipid membrane whilst Gram negative bacteria have a thin peptidoglycan layer and an outer lipid membrane (Vollmer et al., 2008). The presence of high lysozyme activity in serum and urine samples has been associated with chronic granulomatous inflammatory disorders as tuberculosis or sarcoidosis (Jain et al., 2020) and myelomonocytic leukemia (Osserman and Lawlor, 1966), respectively. Moreover, the increase in lysozyme levels in serum is an indicator of active chronic inflammation (Hasmann et al., 2011).

The analysis of lysozyme activity has been traditionally based on its lytic action against the cell wall of *Micrococcus luteus* (*M. lysodeikticus*), by measuring the decrease in turbidity (Shugar, 1952). However, this methodology is affected by the pH, ionic strength and matrix effects, what implies that these parameters must be thoroughly controlled to obtain a proper result (Mörsky, 1983). Colorimetric methods based on i) the release of coloured fragments of Remazol brilliant blue-labelled *Micrococcus luteus* upon hydrolysis (Ito et al., 1992) (Hardt et al., 2003) and ii) peptidoglycan stabilized-gold nanoparticles aggregation after enzymatic cleavage (Fu et al., 2018) have also been proposed for such purpose. However, these methods are laborious and require additional separation steps, having as main drawback the low contrast observed in some procedures between signal and background (Hardt et al., 2003). Chromatographic (Fang et al., 2021) and both antibody (Vidal et al., 2005) and aptamer-based (Ostatná et al., 2017) methods have also been reported for lysozyme detection, suffering from important limitations related to their high cost and the need of bioreceptors.

Biosensing systems based on nanochannels emerge as outstanding tools to overcome these limitations and meet such clinical demand. The use of nanopores/nanochannels has become one of the most promising fields of research in the biosensing area in the last years (de la Escosura-Muñiz and Merkoçi, 2012). Proteins, DNA sequences and viruses have been detected through the so-called stochastic sensing on single natural/artificial nanopores. Special mention deserves the commercial implementation of DNA sequencing systems based on the same principles (Clarke et al., 2009). Nanoporous membranes have also been proposed as platforms for both electrochemical and optical biosensing through the monitoring of the nanochannels steric blockage upon bio-complex formation (de la Escosura-Muñiz and Merkoçi, 2016). The easy functionalization and capacity for mass production of nanoporous alumina have made this material as the most extensively used for such applications (Losic and Santos, 2015). Size and charge effects in nanochannels have been approached for biosensing purposes for more than ten years (Li et al., 2010) (Wang et al., 2012) (Yu et al., 2014) (Wang

et al., 2016) (Zhou et al., 2020). However, the use of nanoporous membranes for monitoring enzymatic cleavage processes, leading to analytical methods for enzyme determination has not been deeply explored so far.

In this context, we propose a novel methodology for the determination of lysozyme using nanoporous alumina membranes as sensing platforms and indium tin oxide/poly(ethylene terephthalate) (ITO/PET) electrodes as transducers. This analytical method is based on the electrical monitoring of steric/electrostatic nanochannels blocking upon peptidoglycan immobilization and further lysozyme digestion of the peptidoglycan leading to unblockage of the nanopores. Steric and electrostatic contributions to the nanopore blocking/unblocking mechanism are thoroughly studied, before analysing samples of wound exudates from both patients with clean and infected ulcers.

Our novel methodology presents important advantages compared with the lysozyme detection methodologies reported so far, related to: i) no need of bioreceptors (antibodies or aptamers); ii) no need of competitive assays; iii) low matrix effects thanks to the filtering-like properties and low protein adsorption rate of the nanoporous alumina membranes; iv) quantitative analysis and v) rapid analysis at the point-of-care, using cheap and portable instruments.

## 2. Experimental section

### 2.1. Chemicals and equipment

(3-aminopropyl) triethoxysilane (APTES), *N*-(3-Dimethylamino-propyl)-*N'*-ethylcarbodiimide hydrochloride (EDC), *N*-Hydroxysulfosuccinimide sodium salt (sulfo-NHS), peptidoglycan from *Bacillus subtilis*, lysozyme from chicken egg white, bovine serum albumin (BSA), avidin from egg white and potassium ferrocyanide  $K_4[Fe(CN)_6]$  were purchased from Sigma-Aldrich (Spain). Hyaluronidase (HYAL) has been purchased from MyBioSource (USA). Lysozyme ELISA Kit used for sample validation was provided by Abcam (UK). Red-ox indicator media used for the electrochemical measurements consisted in 10 mM  $K_4[Fe(CN)_6]$  solutions prepared in different buffers: 0.1 M sodium acetate pH 4.5, 0.1 M MES (2-(*N*-morpholino) ethanesulfonic acid) pH 6.5, and 0.1 M Tris (tris(hydroxymethyl) aminomethane)-HCl pH 7.2. Unless otherwise specified, all buffer reagents and other inorganic chemicals of analytical grade were supplied by Sigma-Aldrich (Spain) and used without further purification. The solutions were prepared in ultrapure water (18.2 M $\Omega$  cm @ 25 °C) obtained with a Millipore Direct-Q® 3 UV purification system from Millipore Ibérica S.A (Spain).

Anodic aluminum oxide (alumina) nanoporous membranes (Whatman® Anodisc™ filters, 13 mm diameter, 60  $\mu$ m thickness, containing 20, 100 or 200 nm pores) and indium tin oxide coated poly(ethylene terephthalate) (ITO/PET) sheets (surface resistivity 60  $\Omega$ /sq) were purchased from Sigma-Aldrich (Spain). The electrochemical transducers were ITO/PET pieces of 43 × 20 mm, defining a working electrode of 8 mm in diameter. Reference and counter electrodes were made of silver/silver chloride (CH Instruments, Inc.; United States of America) and of a platinum wire (Alfa Aesar; United States of America) respectively. A methacrylate electrochemical cell was used for the electrochemical measurements that were performed with an Autolab PGSTAT-10 from Eco Chemie (Netherlands), controlled by Autolab GPES software, connected to a PC. All measurements were carried out at room temperature with a working volume of 400  $\mu$ L. A SANYO MIR-262 incubator purchased from SANYO Electric Co. Ltd. (Japan) was used for the enzymatic incubations with lysozyme at 37 °C. Nanoporous membranes used in this work have been characterized by scanning electron microscopy (SEM). Scanning electron microscopy images were obtained using a JEM-6610 from JEOL (Japan) with an accelerating voltage of 20 kV.

Swabs with exudates from patients with potentially non-infected and infected skin ulcers were provided by the Chronic Ulcers Unit of the Hospital Universitario Central de Asturias (HUCA).



## 2.2. Methods

### 2.2.1. Nanoporous alumina membranes functionalization, peptidoglycan immobilization and enzymatic cleavage by lysozyme

Peptidoglycan immobilization on the inner walls of the nanochannels was performed adapting an experimental procedure previously optimized for antibodies (de la Escosura-Muñiz and Merkoçi, 2011). It consists first in the generation of amino groups in the nanochannels via silanization, followed by carbodiimide-mediated peptidoglycan binding through its carboxyl groups. Briefly, nanoporous alumina membranes were first boiled in ultrapure water for 1 h, so as to clean the membranes and the hydroxyl groups of the alumina, which favour the later silanization process (Ye et al., 2016). After drying in nitrogen, they were immersed in a 5% acetone solution of APTES for 1 h. Then, membranes were washed in acetone and baked at 120 °C for 30 min. After that, 30 µL of peptidoglycan solution in 10 mM MES pH 5 buffer, containing 5 mM EDC/sulfo-NHS, were placed on the filtering side of the membrane and left there for 2 h. A scheme illustrating this procedure is shown at the Supporting Information (Figure S1).

After thoroughly washing with 10 mM Tris-HCl (10 mM ionic strength coming from NaCl) pH 8 buffer, the enzymatic reaction was performed by incubating 30 µL of lysozyme solution (concentration range from 1 to 50 µg/mL) in 10 mM Tris-HCl pH 8 on the membrane filtering side at 37 °C for 30 min. Finally, the membranes were washed again and stored in the measurement buffer before the electrochemical experiments. Control assays were performed following the same protocol but using 10 mM phosphate buffered saline (PBS) pH 7.4 solution instead of peptidoglycan solution (bare silanized nanoporous membranes). Three exudates from clean wound ulcers and three from infected ulcers were analysed following the same experimental procedure but using a 1 to 10 dilution (in 10 mM Tris-HCl pH 8) of the wound exudate instead of lysozyme solution.

Selectivity assays were performed following the same experimental procedure but using a 25 µg/mL concentration of avidin, HYAL and BSA. The long-term stability of the peptidoglycan-modified membranes was evaluated by storing a set of them (peptidoglycan concentration: 5 mg/mL) at 4 °C for one month. The nanochannel blocking was evaluated in different days during this period.

### 2.2.2. Nanoporous cell set-up and electrochemical detection

The design of the experimental set-up for the electrochemical detection using nanoporous alumina membranes is shown in Fig. 1. Nanoporous membranes were physically attached onto the ITO/PET electrode, placing it onto a methacrylate block and putting the membrane with the filtering side up over the electrode surface. Then, a second block containing a hole of 8 mm in diameter was placed onto the

membrane, with an insulating O-ring between them to avoid liquid leakage. Finally, the system was fixed with screws, defining an electrochemical cell that was filled with the 10 mM  $K_4[Fe(CN)_6]$  red-ox indicator solution. All measurements were carried out with a working volume of 400 µL, which was enough to cover the three-electrode system (silver/silver chloride reference electrode, platinum wire counter electrode and ITO/PET working electrode).

A pre-treatment at  $-0.1$  V was applied for 30 s and, immediately after, a differential pulse voltammetric (DPV) scan was performed from  $-0.1$  V to  $+1.1$  V (step potential: 10 mV, modulation amplitude: 50 mV, and scan rate: 20.1 mV/s), resulting in a voltammetric signal due to oxidation of  $[Fe(CN)_6]^{4-}$  to  $[Fe(CN)_6]^{3-}$ , which peak current at approximately  $+0.40$  V was chosen as the analytical signal. The measurements were carried out in triplicate at room temperature under non-stirring conditions. Each measurement was performed with a single nanoporous membrane and an ITO/PET electrode, discarded after the measurement.

## 3. Results and discussion

### 3.1. Nanochannels blockage by peptidoglycan: steric and electrostatic contributions

As illustrated in Fig. 2, it is envisaged that the immobilization of peptidoglycan in the nanochannels produces a blockage in the diffusion of the electroactive species through the nanoporous membranes to the electrochemical transducer surface. Furthermore, it is also expected that the degradation of peptidoglycan by lysozyme will lead to the unblockage of the nanopores.

Such nanochannels blocking after peptidoglycan immobilization can be attributed to a dual effect based on both steric and charge repulsion effects. Considering the size of both peptidoglycan (around 10 nm) (Tulum et al., 2019) and  $[Fe(CN)_6]^{4-}$  red-ox indicator ions ( $<1$  nm), it is expected that in absence of peptidoglycan the red-ox ions can freely flow through the nanochannel to the electrode, whereas the presence of peptidoglycan will hinder their passage due to steric impairments.

On the other hand, it is worthy to note that the peptidoglycan can be negatively charged, positively charged or without a net charge depending on the pH of the measurement buffer solution. Peptidoglycan electronic charge may influence the nanopores blockage due to charge repulsion effects. If the peptidoglycan is negatively charged (working at a pH higher than peptidoglycan's isoelectric point) a repulsion effect between the negative charges of the peptidoglycan and the negative ones from the red-ox indicator ions is expected. This charge repulsion will hinder the ions diffusion to the electrode.

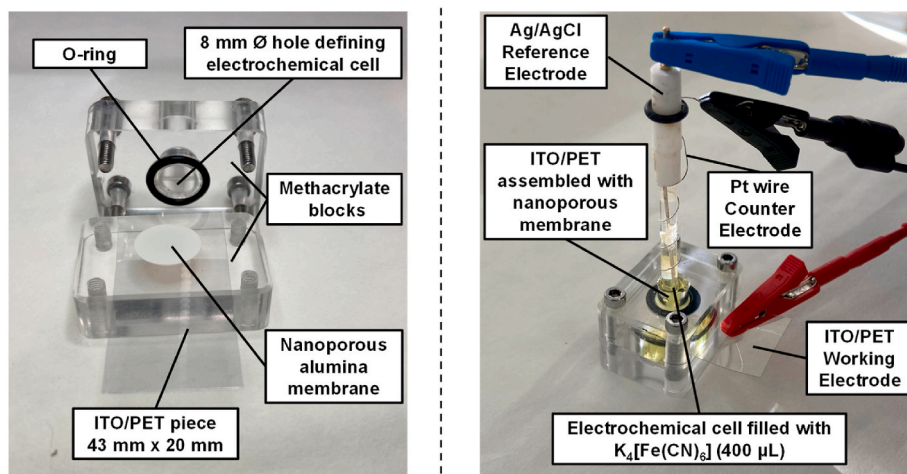


Fig. 1. Experimental set-up for the electrochemical monitoring of the blocking/unblocking of the nanoporous alumina membranes attached to ITO/PET working electrode.

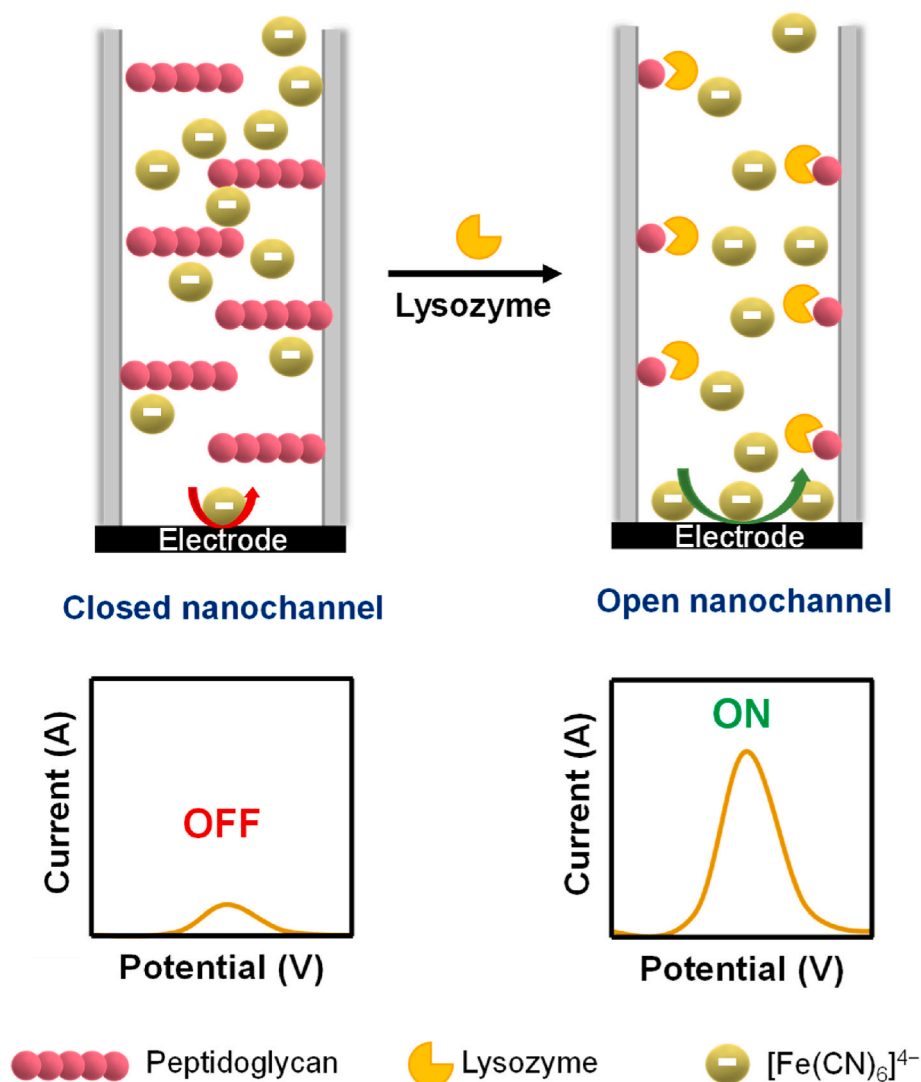


Fig. 2. Scheme (not in scale) of the biosensing system based on nanochannel steric/electrostatic blocking by peptidoglycan and further unblocking after enzymatic cleavage by lysozyme.

Therefore, before carrying out lysozyme determination, a series of optimizations were made with the aim of achieving the maximum steric/electrostatic blocking of the nanochannels by immobilizing peptidoglycan on their inner walls.

With the aim to simplify and normalize the results, in the studies shown along the following sections, the degree of blockage will be expressed in terms of % of decrease in the analytical signal, compared with the one obtained for the bare silanized membrane, calculated as follows:

$$Blockage (\%) = \left| \left( \frac{i_p \text{ peptidoglycan modified membrane} - i_p \text{ bare membrane}}{i_p \text{ bare membrane}} \right) \times 100 \right|$$

### 3.1.1. Effect of the peptidoglycan concentration

The effect of peptidoglycan concentration on the nanochannels blockage and thus on the analytical signal was first studied with

membranes containing nanopores of 20 nm. Peptidoglycan from solutions at different concentrations (1 and 5 mg/mL) was immobilized in the nanochannels through carbodiimide chemistry, as detailed in the methods section. The nanochannels blocking was evaluated by the voltammetric monitoring of the diffusion of the  $[\text{Fe}(\text{CN})_6]^{4-}$  ions in buffer at pH 7.2.

As shown in Fig. 3A, when increasing the amount of peptidoglycan in the nanochannels, the  $[\text{Fe}(\text{CN})_6]^{4-}$  ions diffusion is hindered, probably due to both steric and electrostatic effects, leading to a decrease in the

voltammetric signal from the oxidation of  $[\text{Fe}(\text{CN})_6]^{4-}$  to  $[\text{Fe}(\text{CN})_6]^{3-}$ . As summarized in Fig. 3B, the 18% blocking in the signal recorded at 1 mg/mL peptidoglycan increased up to 47% when using 5 mg/mL peptidoglycan. Higher concentrations were not assayed for cost saving considerations. In view of these results, a peptidoglycan concentration of 5 mg/mL was selected as the optimum for the biosensor development.

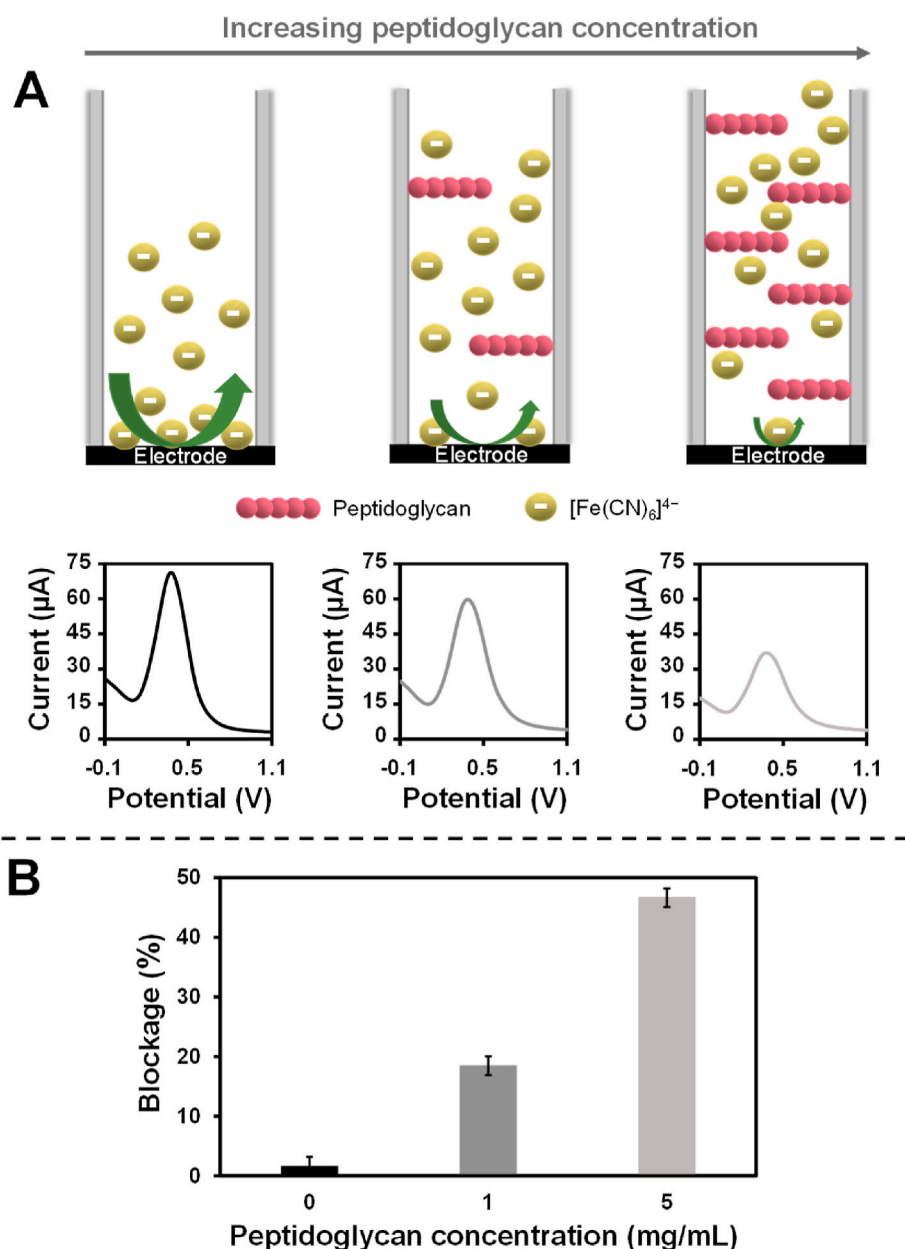


**Fig. 3.** Effect of the peptidoglycan concentration on the nanochannels blockage. (A) Schematic illustration of the different amount of immobilized peptidoglycan, and its effect on the  $[\text{Fe}(\text{CN})_6]^{4-}$  ions diffusion to the electrode. Differential pulse voltammograms registered in 10 mM  $\text{K}_4[\text{Fe}(\text{CN})_6]/0.1$  M (in buffer at pH 7.2) for nanoporous membranes (20 nm pore size), bare silanized (left) and modified with 1 mg/mL (middle) and 5 mg/mL (right) of peptidoglycan. DPV parameters: pre-concentration potential: -0.1 V; pre-concentration time: 30 s; step potential: 10 mV, modulation amplitude: 50 mV, and scan rate: 20.1 mV/s. (B) Comparative bar chart of the signal blockage (expressed in percentage) for different peptidoglycan concentrations. Data are given as average  $\pm$  SD ( $n = 3$ ).

### 3.1.2. Effect of the pH: electrostatic forces involved in nanochannels blocking

pH is a key parameter affecting the ionic transport in nanochannels (Gao et al., 2013) (Li et al., 2013) (Li et al., 2014) (Li et al., 2015) (Zhao et al., 2019). In our particular case, the pH of the measurement buffer solution drives the peptidoglycan electronic charge, affecting the electrostatic forces involved in the nanochannels blocking. Considering the isoelectric point of the peptidoglycan (pI: 6.5) (Yoshida et al., 1996), solutions of the 10 mM  $\text{K}_4[\text{Fe}(\text{CN})_6]$  red-ox indicator were prepared in different buffers at pH below, equal and above this value. Typical buffers for each range of pH were selected: 0.1 M NaAc (for pH 4.5), 0.1 M MES (for pH 6.5) and 0.1 M Tris-HCl (for pH 7.2). The evaluation of any of these buffers at a pH different from their typical value was not considered appropriate. Membranes containing nanopores of 20 nm, where the peptidoglycan is immobilized from a 5 mg/mL solution were used for this study.

As shown in Fig. 4, when the pH of the measurement buffer solution is higher than the pI of the peptidoglycan (pH 7.2), a high blocking (47% decrease in the signal) is observed. These experimental results are in line

with the hypothesis about the effect of the nanochannel charges on the diffusion of  $[\text{Fe}(\text{CN})_6]^{4-}$  anions, which has also been proposed by other authors (Li et al., 2010). At this pH the peptidoglycan is negatively charged, and such charges attract cations and repel anions, forming a negatively charged electric field, also called electrostatic repulsion region. Such restriction region decreases the lane for anions, resulting in a decreased flux of  $[\text{Fe}(\text{CN})_6]^{4-}$  and consequently a lower voltametric signal, what we call a high blockage. However, when working below the pI of the peptidoglycan (pH 4.5), it is positively charged and the situation is the opposite: a positively charged electric field is generated, favoring the pass of  $[\text{Fe}(\text{CN})_6]^{4-}$  anions for keeping neutral charge in the nanochannel, leading to a higher voltametric signal, what we call a low blockage (5% decrease in the signal). At pH of the red-ox indicator medium equal to the pI of the peptidoglycan (pH 6.5), the peptidoglycan molecules are uncharged and the  $[\text{Fe}(\text{CN})_6]^{4-}$  ions diffusion through the nanochannel is neither electrostatically favored nor hindered, obtaining a 15% of signal blockage, probably only due to steric issues.

Considering these findings, in further experiments the electrochemical measurements were performed at the maximum electrostatic

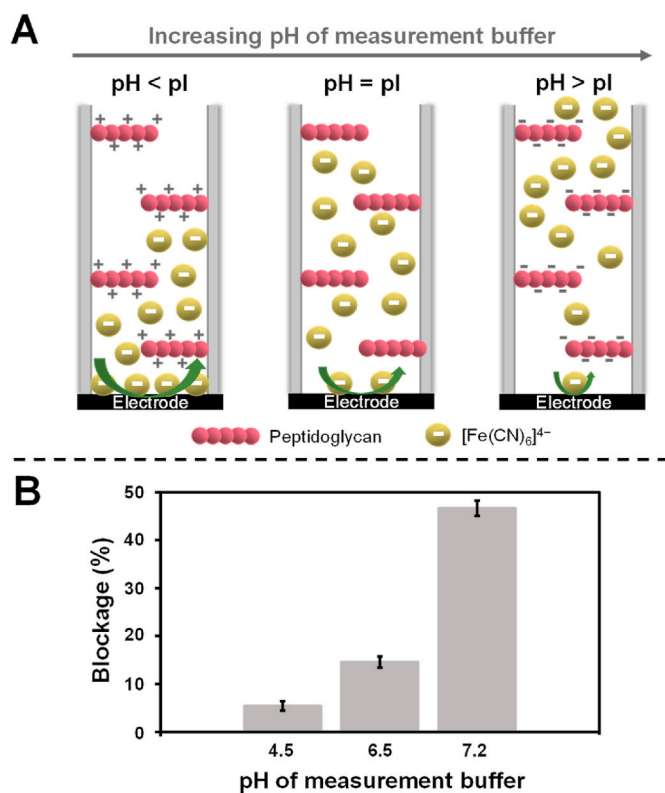


**Fig. 4.** Measurement buffer pH effect on the nanochannels blockage. (A) Schematic illustration of the different net charge of the peptidoglycan (pI: 6.5) depending on the pH of the measurement buffer, and its effect on the [Fe(CN)<sub>6</sub>]<sup>4-</sup> ions diffusion to the electrode. (B) Comparative bar chart of the signal blockage (expressed in percentage) for measurement buffer solutions at different pH. Data are given as average  $\pm$  SD ( $n = 3$ ). Peptidoglycan concentration: 5 mg/mL. K<sub>4</sub>[Fe(CN)<sub>6</sub>] concentration: 10 mM (at different pH measurement buffer solutions).

blockage conditions, that is using a buffer at pH 7.2 as red-ox indicator medium solution.

### 3.1.3. Effect of the nanopore size

The steric blockage of the nanochannels will depend not only on the peptidoglycan concentration but also on the nanopore size, expecting a lower degree of blockage when increasing the nanopore size. Nanoporous membranes containing nanopores of 20 nm, 100 nm and 200 nm were evaluated for such purpose. A peptidoglycan concentration of 5 mg/mL and a red-ox indicator medium solution at pH 7.2 were fixed for this study.

As schematized in Fig. 5A, for the smaller nanopore size (20 nm) the peptidoglycan molecules in the opposite walls of the nanochannels are very close, and this proximity leads to a steric blockage that prevents the flow of [Fe(CN)<sub>6</sub>]<sup>4-</sup> ions. However, when increasing the nanopore size, the distance between the nanochannel walls increases, which facilitates the ions' flow, leading to a decrease in the steric blockage.

From the obtained results (Fig. 5B) it can be concluded that the higher is the nanopore size, the lower the steric blockage. The blocking percentage found for the 20 nm membranes (47%) decreases to 17% when using the intermediate nanopore size (100 nm) membranes, and further to 6% for the higher nanopore size (200 nm) membranes. In line with these results, nanoporous membranes containing pores of 20 nm, for which the maximum signal blocking by the peptidoglycan was achieved, were chosen for lysozyme sensing.

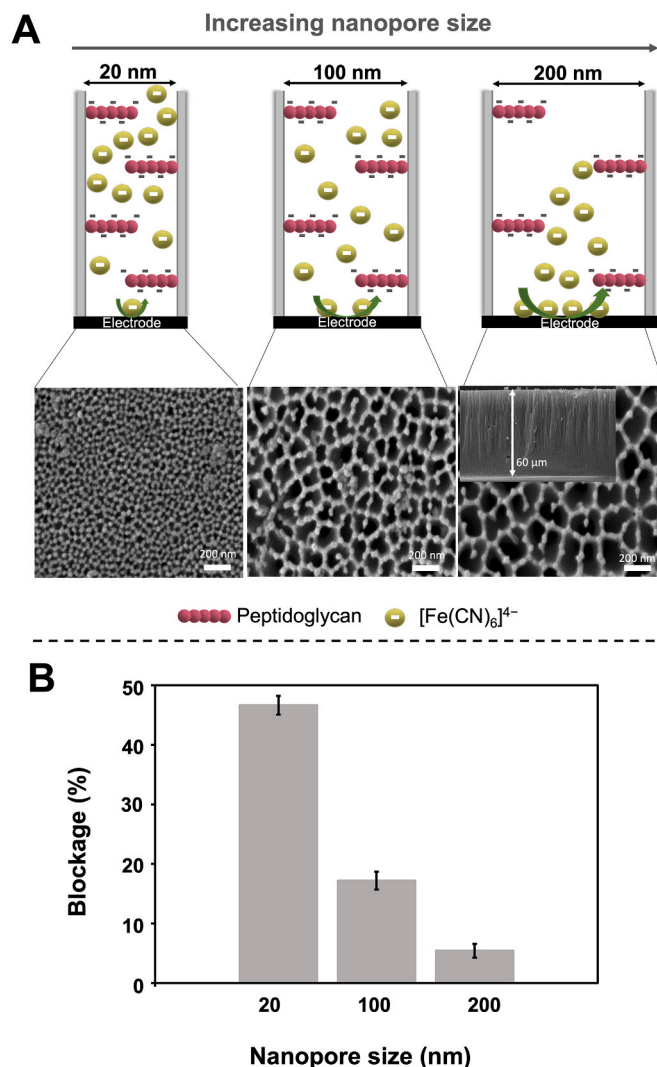


**Fig. 5.** Effect of the nanopore size on the nanochannels blockage. (A) Schematic representation of the effect of different nanopore sizes on the [Fe(CN)<sub>6</sub>]<sup>4-</sup> ions diffusion to the electrode, together with SEM top-view micrographs of the nanoporous membranes. The inset in the image of the 200 nm-pores membrane corresponds to a cross-section view. (B) Comparative bar chart of the signal blockage (expressed in percentage) for nanoporous membranes with different nanopore sizes. Data are given as average  $\pm$  SD ( $n = 3$ ). Peptidoglycan concentration: 5 mg/mL. K<sub>4</sub>[Fe(CN)<sub>6</sub>] concentration: 10 mM (in buffer at pH 7.2).

### 3.2. Electrochemical detection of lysozyme

As previously detailed (Fig. 2), the proposed sensing system is based on the specific cleavage of the  $\beta$ -(1,4)-glycosidic bonds of the peptidoglycan by lysozyme, which leads to the unblockage of the nanochannels. For this purpose, the peptidoglycan-modified membranes were incubated with lysozyme (concentration range from 1 to 50  $\mu$ g/mL) at the optimum conditions for the enzymatic reaction (37  $^{\circ}$ C, 30 min) (Sambrook et al., 1989).

As expected (Fig. 6A), the voltammetric signal obtained for the peptidoglycan-modified membranes (blue continuous line) gradually increases with the amount of lysozyme (dotted lines), evidencing the unblockage of the nanochannels by specific degradation of the peptidoglycan. As a result, the analytical signal ([Fe(CN)<sub>6</sub>]<sup>4-</sup> oxidation peak current at +0.40 V) increases with the lysozyme concentration in the range 0–50  $\mu$ g/mL. Both parameters are adjusted to a linear relationship in the range 0–10  $\mu$ g/mL (Fig. 6B), with a correlation coefficient of 0.9994, according to the following equation:



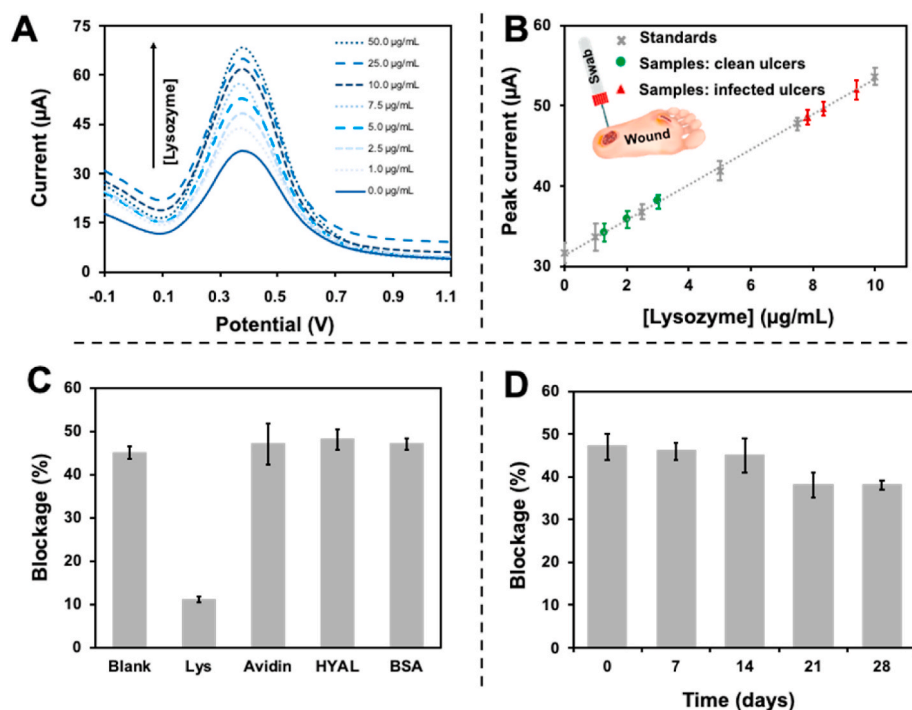


**Fig. 6.** Lysozyme determination through the enzymatic cleavage of peptidoglycan, leading to nanochannels unblockage. (A) Differential pulse voltammograms registered in 10 mM  $K_4[Fe(CN)_6]$ /0.1 M (in buffer at pH 7.2) for 5 mg/mL peptidoglycan-modified membranes (20 nm nanopores) after incubation with increasing concentrations of lysozyme (0–50  $\mu\text{g/mL}$ , from down to up). DPV parameters: pre-concentration potential: -0.1 V; pre-concentration time: 30 s; step potential: 10 mV, modulation amplitude: 50 mV, scan rate: 20.1 mV/s. (B) Calibration plot obtained for standard solutions of lysozyme as well as the analytical signals obtained for swab exudates (diluted 1:10) from three patients with potentially clean ulcers and three patients with clearly infected ones. Data are given as average  $\pm$  SD ( $n = 3$ ). (C) Selectivity study of lysozyme (Lys) detection, evaluated against avidin, hyaluronidase (HYAL) and bovine serum albumin (BSA) (proteins concentration 25  $\mu\text{g/mL}$ ). (D) Long-term stability study of the peptidoglycan-modified membranes (Peptidoglycan concentration: 5 mg/mL).

$$\text{Peak current } (\mu\text{A}) = 2.2 [\text{Lysozyme}] (\mu\text{g/mL}) + 31$$

The method shows a good reproducibility, with a relative standard deviation (RSD) of 5% ( $n = 3$ ). A limit of detection (LOD, calculated as three times the standard deviation of the intercept divided by the slope) of 280 ng/mL of lysozyme was found. This value is in agreement with the obtained by standard ELISA assays (260 ng/mL) (Vidal et al., 2005), being our method considerably simpler, faster and cheaper, without the need of labels or competitive immunoassay formats. This LOD is low enough for detecting lysozyme in wounds, whose concentration is expected to be at  $\mu\text{g/mL}$  levels (Hasmann et al., 2011).

Moreover, the developed methodology presents improved characteristics weight up against other previously reported procedures for lysozyme detection in terms of complexity, assay time, assay cost and point-of-care suitability (Table 1). Although some of the alternative approaches also show low cost and low complexity features, the shorter assay time and the miniaturization/portability of the materials and instruments involved in our nanochannels-based sensing system makes it outstanding for point-of-care analysis.

### 3.3. System selectivity and stability

The selectivity of our system against other proteins that are commonly present in wound exudates, such as avidin, hyaluronidase

(HYAL) and bovine serum albumin (BSA) (at a concentration of 25  $\mu\text{g/mL}$ ), was evaluated. As shown in Fig. 6C, no significant changes in the nanopore blockage were noticed for any of such proteins, as it is observed for lysozyme, demonstrating the excellent selectivity of the system.

The long-term stability of the peptidoglycan-modified membranes was evaluated by storing a set of them at 4  $^{\circ}\text{C}$  for one month. The nanochannel blocking was evaluated in different days during this period. As shown in Fig. 6D, the response of the system was stable and reproducible for at least 14 days, noticing a decrease in the effectivity of the immobilized peptidoglycan after 21 days of storage. The response was then stable at least after 28 days. A longer-term stability study was not considered.

### 3.4. Lysozyme determination in chronic wound exudates

The detection of excessive lysozyme levels in wound exudates is a sign of infection. This would allow to monitor the evolution of the healing status of the wound and to assess the effectiveness of the applied therapies.

Nanoporous alumina membranes are ideal platforms for such real application, thanks to their ability to also act as filter of biomolecules (de la Escosura-Muñiz and Merkoçi, 2011) (de la Escosura-Muñiz et al., 2013) (Espinoza-Castañeda et al., 2015), which also allows *in situ* studies on live cells and bacteria cultures (de la Escosura-Muñiz et al., 2018) (de

**Table 1**

Analytical characteristics of different methodologies for lysozyme detection, in terms of limit of detection (LOD), assay time, assay cost, complexity and point-of-care suitability.

Method	LOD (ng/mL)	Assay time (min)	Assay cost (estimated, €)	Complexity	Point-of-care suitability	Ref.
ELISA	260	120–240	8–15	High <sup>a</sup>	NO	Vidal et al. (2005)
Colorimetric lytic activity against <i>Micrococcus lysodeikticus</i>	7800	120	4–5	Medium	NO	Hasmann et al. (2011)
Peptidoglycan stabilized-gold nanoparticles aggregation	35	90–120	4–5	Low	NO	Fu et al. (2018)
Nanochannels	280	40	4–5	Low	YES	This work

<sup>a</sup> High complexity related to the need of a considerably number of reagents (antibodies, enzymes-substrates, etc.) and incubation/washing steps.

la Escosura-Muniz et al., 2019). It is well-known that alumina has a low protein adsorption rate, what is indeed the reason for its use as a filtering material. This filter-like property minimizes matrix effects in the analytical signal, allowing for the direct detection of lysozyme, without any pre-treatment of the sample. As detailed in the experimental section, swab exudates from three patients with potentially bacteria-free skin ulcers and three patients with infected ones were analysed following the experimental procedure previously detailed for lysozyme standard solutions. Dilution of the swab exudates to a 1:10 ratio was necessary to obtain analytical signals within the range of the calibration curve. As observed in Fig. 6B, substantially different analytical signals were obtained for infected and non-infected samples evidencing the ability of our method to discriminate them. The concentration of lysozyme in each sample was directly extrapolated from the calibration curve, taking advantage of the above detailed low matrix effects noticed when working with alumina membranes. In this way, lysozyme concentrations of  $30 \pm 5$ ,  $13 \pm 2$  and  $20 \pm 3$   $\mu\text{g/mL}$  were estimated in the clean ulcer samples while these values notably increase to  $78 \pm 6$ ,  $83 \pm 6$  and  $94 \pm 9$   $\mu\text{g/mL}$  for the infected ones. The observed behaviour correlates with the few existing literature reporting the lysozyme levels in such kind of samples (Hassmann et al., 2011) which found levels at  $\mu\text{g/mL}$  in both clean and infected ulcers, being notably higher for the infected ones, thus validating the feasibility of our system for the wound infection screening in a real scenario. Two of the wound exudates were also analysed by ELISA technique (see Figure S2 at the Supporting Information), providing a value of 28  $\mu\text{g/mL}$  for the clean ulcer sample and 76  $\mu\text{g/mL}$  for the infected one, what correlates with the values obtained by our method ( $30 \pm 5$   $\mu\text{g/mL}$  and  $78 \pm 6$   $\mu\text{g/mL}$  respectively for such samples).

#### 4. Conclusions

We have demonstrated that the infection biomarker lysozyme can be detected in chronic wound exudates using nanoporous alumina membranes, owing to the enzymatic cleavage of the peptidoglycan substrate used for blocking the alumina nanochannels. Both steric and electrostatic contributions are of key relevance for maximizing the nanochannels blocking by the substrate, which allows detecting low levels of lysozyme. Our findings suggest that while steric blocking is highly dependent on the pore size and the peptidoglycan concentration, the electrostatic blocking mainly depends on the pH of the red-ox indicator solution used for the voltammetric measurements. As far as we know, this is the first time that nanoporous membranes are used for electrochemical monitoring of enzymatic cleavage processes through the unblocking of previously blocked nanochannels, leading to an analytical method for the enzyme determination.

Our electrical method reached a lysozyme detection limit of 280 ng/mL, which is low enough for detecting lysozyme in wounds, with a good selectivity and long-term stability. This result is in line with previous reports based on ELISA assays, being our method faster and cheaper, without the need of labels or competitive immunoassay formats.

The proposed method is of particular interest for the discrimination of exudates from infected and non-infected wounds without sample pretreatment, taking advantage of the low protein absorption rate and thus outstanding filtering properties of the nanoporous alumina membranes. The increased levels of lysozyme in infected ulcer samples (around 85  $\mu\text{g/mL}$ ) compared with non-infected ones (around 21  $\mu\text{g/mL}$ ) correlate with previously reported data for wound fluids, demonstrating the feasibility of our system for the early wound infection diagnosis in the clinical scenario. Early diagnosis would allow to select a correct treatment, avoiding patients' disability and saving resources for hospitalization. Furthermore, the miniaturization and low cost of the proposed analytical methodology would allow its implementation in out-of-hospital settings as well.

#### Declaration of competing interest

The authors declare that they have no known competing financial interests or personal relationships that could have appeared to influence the work reported in this paper.

#### Acknowledgements

This work has been supported by the MCI-21-PID2020-115204RB-I00 project from Spanish Ministry of Science and Innovation (MICINN) and the SV-PA-21-AYUD/2021/51323 project from the Asturias Regional Government. A. Iglesias-Mayor thanks the Spanish Ministry of Education, Culture and Sports (MECD) for the award of a FPU Grant (FPU2014/04686). O. Amor-Gutiérrez and A. de la Escosura-Muñiz thank the University of Oviedo for the "Plan de Apoyo y Promoción de la Investigación" grant (PAPI-18-PF-13) and the "Ayudas Proyectos Emergentes 2019" project (PAPI-19-EMERG-17) respectively. C. Toyos-Rodríguez thanks the MICINN for the award of a FPI Grant (PRE2018-084953). A. de la Escosura-Muñiz also acknowledges the MICINN for the "Ramón y Cajal" Research Fellow (RyC-2016-20299). The authors acknowledge the Chronic Ulcers Unit of the Hospital Universitario Central de Asturias (HUCA) and specially to Prof. Víctor Asensi and Susana Valerdez for providing the real samples used in this work.

#### Appendix A. Supplementary data

Supplementary data related to this article can be found at <https://doi.org/10.1016/j.bios.2022.114243>.

#### References

- Caliendo, A.M., Gilbert, D.N., Ginocchio, C.C., Hanson, K.E., May, L., Quinn, T.C., Tenover, F.C., Alland, D., Blaschke, A.J., Bonomo, R.A., Carroll, K.C., Ferraro, M.J., Hirschhorn, L.R., Joseph, W.P., Karchmer, T., MacIntyre, A.T., Reller, L.B., Jackson, A.F., 2013. Better tests, better care: improved diagnostics for infectious diseases. *Clin. Infect. Dis.* 57, S139–S170. <https://doi.org/10.1093/cid/cit578>.
- Callewaert, L., Michiels, C.W., 2010. Lysozymes in the animal kingdom. *J. Biosci.* 35, 127–160. <https://doi.org/10.1007/s12038-010-0015-5>.
- Clarke, J., Wu, H.C., Jayasinghe, L., Patel, A., Reid, S., Bayley, H., 2009. Continuous base identification for single-molecule nanopore DNA sequencing. *Nat. Nanotechnol.* 4, 265–270. <https://doi.org/10.1038/nnano.2009.12>.
- Clinton, A., Carter, T., 2015. Chronic wound biofilms: pathogenesis and potential therapies. *Lab. Med.* 46, 277–284. <https://doi.org/10.1039/LMBNSWKU4JPN750>.
- Cutting, K.F., White, R.J., 2005. Criteria for identifying wound infection-revisited. *Ostomy/Wound Manag.* 51, 28–34.
- de la Escosura-Muñiz, A., Chunglok, W., Surareungchai, W., Merkoçi, A., 2013. Nanochannels for diagnostic of thrombin-related diseases in human blood. *Biosens. Bioelectron.* 40, 24–31. <https://doi.org/10.1016/j.bios.2012.05.021>.
- de la Escosura-Muñiz, A., Espinoza-Castañeda, M., Chamorro-García, A., Rodríguez-Hernández, C.J., de Torres, C., Merkoçi, A., 2018. In situ monitoring of PTHLH secretion in neuroblastoma cells cultured onto nanoporous membranes. *Biosens. Bioelectron.* 107, 62–68. <https://doi.org/10.1016/j.bios.2018.01.064>.
- de la Escosura-Muniz, A., Ivanova, K., Tzanov, T., 2019. Electrical evaluation of bacterial virulence factors using nanopores. *ACS Appl. Mater. Interfaces* 11, 13140–13146. <https://doi.org/10.1021/acsami.9b02382>.
- de la Escosura-Muñiz, A., Merkoçi, A., 2016. Nanochannels for electrical biosensing. *TrAC Trends Anal. Chem. (Reference Ed.)* 79, 134–150. <https://doi.org/10.1016/j.trac.2015.12.003>.
- de la Escosura-Muñiz, A., Merkoçi, A., 2012. Nanochannels preparation and application in biosensing. *ACS Nano* 6, 7556–7583. <https://doi.org/10.1021/nn301368z>.
- de la Escosura-Muñiz, A., Merkoçi, A., 2011. A nanochannel/nanoparticle-based filtering and sensing platform for direct detection of a cancer biomarker in blood. *Small* 7, 675–682. <https://doi.org/10.1002/sml.201002349>.
- Espinoza-Castañeda, M., Escosura-Muñiz, A., de la, Chamorro, A., Torres, C. de, Merkoçi, A., 2015. Nanochannel array device operating through Prussian blue nanoparticles for sensitive label-free immunodetection of a cancer biomarker. *Biosens. Bioelectron.* 67, 107–114. <https://doi.org/10.1016/j.bios.2014.07.039>.
- Fang, X., Wang, Z., Sun, N., Deng, C., 2021. Magnetic metal oxide affinity chromatography-based molecularly imprinted approach for effective separation of serum and urinary phosphoprotein biomarker. *Talanta* 226, 122143. <https://doi.org/10.1016/j.talanta.2021.122143>.
- Fu, F., Li, L., Luo, Q., Li, Q., Guo, T., Yu, M., Song, Y., Song, E., 2018. Selective and sensitive detection of lysozyme based on plasmon resonance light-scattering of hydrolyzed peptidoglycan stabilized-gold nanoparticles. *Analyst* 143, 1133–1140. <https://doi.org/10.1039/c7an01570d>.

- Gao, H.L., Zhang, H., Li, C.Y., Xia, X.H., 2013. Confinement effect of protonation/deprotonation of carboxylic group modified in nanochannel. *Electrochim. Acta* 110, 159–163. <https://doi.org/10.1016/j.electacta.2012.12.080>.
- Gardner, S.E., Frantz, R.A., Doebbeling, B.N., 2001. The validity of the clinical signs and symptoms used to identify localized chronic wound infection. *Wound Repair Regen.* 9, 178–186. <https://doi.org/10.1046/j.1524-475X.2001.00178.x>.
- Gardner, S.E., Frantz, R.A., Saltzman, C.L., Hillis, S.L., Park, H., Scherubel, M., 2006. Diagnostic validity of three swab techniques for identifying chronic wound infection. *Wound Repair Regen.* 14, 548–557. <https://doi.org/10.1111/j.1743-6109.2006.00162.x>.
- Hardt, M., Guo, Y., Henderson, G., Laine, R.A., 2003. Zymogram with remazol brilliant blue-labeled *Micrococcus lysodeikticus* cells for the detection of lysozymes: example of a new lysozyme activity in Formosan termite defense secretions. *Anal. Biochem.* 312, 73–76. [https://doi.org/10.1016/S0003-2697\(02\)00443-8](https://doi.org/10.1016/S0003-2697(02)00443-8).
- Hasmann, A., Wehrschuetz-Sigl, E., Kanzler, G., Gewessler, U., Hulla, E., Schneider, K.P., Binder, B., Schintler, M., Guebitz, G.M., 2011. Novel peptidoglycan-based diagnostic devices for detection of wound infection. *Diagn. Microbiol. Infect. Dis.* 71, 12–23. <https://doi.org/10.1016/j.diagmicrobio.2010.09.009>.
- Ito, Y., Yamada, H., Imoto, T., 1992. Colorimetric assay for lysozyme using *Micrococcus luteus* labeled with a blue dye, remazol brilliant blue R, as a substrate. *Chem. Pharm. Bull.* 40, 1523–1526.
- Jain, R., Yadav, D., Puranik, N., Guleria, R., Jin, J.-O., 2020. Sarcoidosis: causes, diagnosis, clinical features, and treatments. *J. Clin. Med.* 9, 1081. <https://doi.org/10.3390/jcm9041081>.
- Järbrink, K., Ni, G., Sönnergren, H., Schmidtchen, A., Pang, C., Bajpai, R., Car, J., 2016. Prevalence and incidence of chronic wounds and related complications: a protocol for a systematic review. *Syst. Rev.* 5, 152. <https://doi.org/10.1186/s13643-016-0329-y>.
- Li, C.Y., Ma, F.X., Wu, Z.Q., Gao, H.L., Shao, W.T., Wang, K., Xia, X.H., 2013. Solution-pH-modulated rectification of ionic current in highly ordered nanochannel arrays patterned with chemical functional groups at designed positions. *Adv. Funct. Mater.* 23, 3836–3844. <https://doi.org/10.1002/adfm.201300315>.
- Li, C.Y., Tian, Y.W., Shao, W.T., Yuan, C.G., Wang, K., Xia, X.H., 2014. Solution pH regulating mass transport in highly ordered nanopore array electrode. *Electrochem. Commun.* 42, 1–5. <https://doi.org/10.1016/j.elecom.2014.01.020>.
- Li, C.Y., Wu, Z.Q., Yuan, C.G., Wang, K., Xia, X.H., 2015. Propagation of concentration polarization affecting ions transport in branching nanochannel array. *Anal. Chem.* 87, 8194–8202. <https://doi.org/10.1021/acs.analchem.5b01016>.
- Li, S., Li, J., Wang, K., Wang, C., Xu, J., Chen, H., Xia, X., Huo, Q., States, U., 2010. A nanochannel array-based electrochemical device for quantitative label-free DNA analysis. *ACS Nano* 4, 6417–6424.
- Losic, D., Santos, A., 2015. Nanoporous Alumina: Fabrication, Structure, Properties and Applications. Springer Series in Materials Science. [https://doi.org/10.1007/978-3-319-20334-8\\_5](https://doi.org/10.1007/978-3-319-20334-8_5).
- Matzeu, G., Losacco, M., Parducci, E., Pucci, A., Dini, V., Romanelli, M., Di Francesco, F., 2011. Skin temperature monitoring by a wireless sensor. *IECON Proc. (Industrial Electron. Conf.)* 3533–3535. <https://doi.org/10.1109/IECON.2011.6119881>.
- Mörsky, P., 1983. Turbidimetric determination of lysozyme with *Micrococcus lysodeikticus* cells: reexamination of reaction conditions. *Anal. Biochem.* 128, 77–85. [https://doi.org/10.1016/0003-2697\(83\)90347-0](https://doi.org/10.1016/0003-2697(83)90347-0).
- Osserman, E.F., Klockars, M., Halper, J., Fischel, R.E., 1973. Effects of lysozyme on normal and transformed mammalian cells. *Nature* 243, 331–335. <https://doi.org/10.1038/246421a0>.
- Osserman, E.F., Lawlor, D.P., 1966. Serum and urinary lysozyme (muramidase) in monocytic and monomyelocytic leukemia. *J. Exp. Med.* 125, 921–952.
- Ostatná, V., Kasalová-Vargová, V., Kékedy-Nagy, L., Černocká, H., Ferapontova, E.E., 2017. Chronopotentiometric sensing of specific interactions between lysozyme and the DNA aptamer. *Bioelectrochemistry* 114, 42–47. <https://doi.org/10.1016/j.bioelechem.2016.12.003>.
- Persaud, K.C., 2005. Medical applications of odor-sensing devices. *Int. J. Low. Extrem. Wounds* 4, 50–56. <https://doi.org/10.1177/1534734605275139>.
- Rogers, H.J., Perkins, H.R., Ward, J.B., 2013. *Microbial Cell Walls and Membranes*. Springer.
- Salton, M.R.J., 1957. The properties of lysozyme and its action on microorganisms. *Bacteriol. Rev.* 21, 82–100. <https://doi.org/10.1128/membr.21.2.82-100.1957>.
- Sambrook, J., Fritsch, E.F., Maniatis, T., 1989. *Molecular Cloning: A Laboratory Manual*. Cold Spring Harbor, 1989. Cold Spring Harbor Laboratory, New York.
- Schiffer, D., Tegl, G., Heinzle, A., Sigl, E., Metcalf, D., Bowler, P., Burnet, M., Guebitz, G.M., 2015. Enzyme-responsive polymers for microbial infection detection. *Expert Rev. Mol. Diagn.* 15, 1125–1131. <https://doi.org/10.1586/14737159.2015.1061935>.
- Shugar, D., 1952. The measurement of lysozyme activity and the ultra-violet inactivation of lysozyme. *Biochim. Biophys. Acta* 8, 302–309. [https://doi.org/10.1016/0006-3002\(52\)90045-0](https://doi.org/10.1016/0006-3002(52)90045-0).
- Siddiqui, A.R., Bernstein, J.M., 2010. Chronic wound infection: facts and controversies. *Clin. Dermatol.* 28, 519–526. <https://doi.org/10.1016/j.clindermatol.2010.03.009>.
- Trupp, S., Alberti, M., Carofoglio, T., Lubian, E., Lehmann, H., Heuermann, R., Yacoub-George, E., Bock, K., Mohr, G.J., 2010. Development of pH-sensitive indicator dyes for the preparation of micro-patterned optical sensor layers. *Sensor. Actuator. B Chem.* 150, 206–210. <https://doi.org/10.1016/j.snb.2010.07.015>.
- Tulum, I., Tahara, Y.O., Miyata, M., 2019. Peptidoglycan layer and disruption processes in *Bacillus subtilis* cells visualized using quick-freeze, deep-etch electron microscopy. *Microscopy* 68, 441–449. <https://doi.org/10.1093/jmicro/dfz033>.
- Vidal, M.-L., Gautron, J., Nys, Y., 2005. Development of an ELISA for quantifying lysozyme in hen egg white. *J. Agric. Food Chem.* 53, 2379–2385. <https://doi.org/10.1021/jf048692o>.
- Vollmer, W., Blanot, D., de Pedro, M.A., 2008. Peptidoglycan structure and architecture. *FEMS Microbiol. Rev.* 32, 149–167. <https://doi.org/10.1111/j.1574-6976.2007.00094.x>.
- Wang, C., Liu, H.L., Li, Y.Q., Cao, J., Zheng, B., Xia, X.H., Feng, F., 2016. A novel device of array nanochannels integrated electrochemical detector for detection of amyloid  $\beta$  aggregation and inhibitor screening. *Electrochem. Commun.* 66, 25–28. <https://doi.org/10.1016/j.elecom.2016.02.016>.
- Wang, C., Xu, J., Chen, H., Xia, X., 2012. Mass transport in nanofluidic devices. *Sci. China Chem.* 55, 453–468. <https://doi.org/10.1007/s11426-012-4542-9>.
- Yager, D.R., Kulina, R.A., Gilman, L.A., 2007. Wound fluids: a window into the wound environment? *Int. J. Low. Extrem. Wounds* 6, 262–272. <https://doi.org/10.1177/1534734607307035>.
- Ye, W., Xu, Y., Zheng, L., Zhang, Y., Yang, M., Sun, P., 2016. A nanoporous alumina membrane based electrochemical biosensor for histamine determination with biofunctionalized magnetic nanoparticles concentration and signal amplification. *Sensors* 16, 1767. <https://doi.org/10.3390/s16101767>.
- Yoshida, H., Kinoshita, K., Ashida, M., 1996. Purification of a peptidoglycan recognition protein from hemolymph of the silkworm, *Bombyx mori*. *J. Biol. Chem.* 271, 13854–13860. <https://doi.org/10.1074/jbc.271.23.13854>.
- Yu, J., Zhang, L., Xu, X., Liu, S., 2014. Quantitative detection of potassium ions and adenosine triphosphate via a nanochannel-based electrochemical platform coupled with G-quadruplex aptamers. *Anal. Chem.* 86, 10741–10748. <https://doi.org/10.1021/ac502752g>.
- Zhao, X.P., Zhou, Y., Zhang, Q.W., Yang, D.R., Wang, C., Xia, X.H., 2019. Nanochannel-ion channel hybrid device for ultrasensitive monitoring of biomolecular recognition events. *Anal. Chem.* 91, 1185–1193. <https://doi.org/10.1021/acs.analchem.8b05162>.
- Zhou, Y., Liao, X., Han, J., Chen, T., Wang, C., 2020. Ionic current rectification in asymmetric nanofluidic devices. *Chin. Chem. Lett.* 31, 2414–2422. <https://doi.org/10.1016/j.ccl.2020.05.033>.